ABSTRACT BOOK

Collaborating Today,
Innovating Tomorrow in
Abdominal Radiology

ACAR 2026

THE 13th ASIAN CONGRESS OF ABDOMINAL RADIOLOGY

MARCH 19(Thu) - 21(Sat), 2026
Grand Walkerhill Seoul, Seoul, Korea

www.ACAR2026.org

ABSTRACT BOOK

Hosted by

ACAR ASAR

KSAR 대한복부영상의학회 Korean Society of Abdominal Radiology

대한비뇨생식영상의학회 The Korean Society of Urogenital Radiology

Supported by

KOREA TOURISM ORGANIZATION

SEOUL METROPOLITAN GOVERNMENT

ACAR 2026

THE 13th ASIAN CONGRESS OF ABDOMINAL RADIOLOGY

Daily Program

Mar. 19 (Thu.)

Mar. 20 (Fri.)

Mar. 21 (Sat.)

DAILY PROGRAM

MARCH 19 (Thu)

09:00-10:20 **[PBL01] Problem-based learning 1: Thinking Like an Expert** (Eng.) [Room A] Vista 1

Chairs Young Hwan Lee (Wonkwang University School of Medicine, Wonkwang University Hospital, Korea)
Min Ju Kim (Korea University College of Medicine, Korea University Anam Hospital, Korea)

09:00-09:30 PBL01-1 **Knowledges & Challenges: Retroperitoneum**
Dow-Mu Koh (Royal Marsden Hospital, UK)

09:30-09:55 PBL01-2 **Knowledges & Challenges: Spleen**
Kyowon Gu (Sungkyunkwan University School of Medicine, Samsung Medical Center, Korea)

09:55-10:20 PBL01-3 **Knowledges & Challenges: Infection**
Subin Heo (University of Ulsan College of Medicine, Asan Medical Center, Korea)

09:00-10:20 **[SS01] Scientific Session 1 (ABD): Advances in Pancreatic Imaging: Emerging Techniques and Clinical Applications** (Eng.) [Room B] Vista 2

Chairs Kyung Sook Shin (Chungnam National University College of Medicine, Chungnam National University Hospital, Korea)
Hong Il Ha (Hallym University Sacred Heart Hospital, Korea)

09:00-09:15 SS01-1 **Imaging of Pancreatic NET: From Differentials to Prognostication**
Raju Sharma (All India Institute of Medical Sciences, New Delhi, India)

09:15-09:25 SS01-2 **MRI-Derived Bone Marrow Fat Fraction and Body Composition Predict Chemotherapy-Induced Myelosuppression and Survival in Pancreatic Cancer**
Weinuo Qu (Tongji Hospital Tongji Medical College Huazhong University of Science and Technology, China)

09:25-09:35 SS01-3 **Deep Learning CT Signature for Predicting Occult Liver Metastases and Neoadjuvant Therapy Benefit in Pancreatic Ductal Adenocarcinoma: A Multicenter Retrospective Study**
Ben Zhao (Zhongda Hospital Medical School of Southeast University, China)

09:35-09:45 SS01-4 **U-Shaped Adiposity Thresholds Defining an Obesity Paradox in Gastroenteropancreatic Neuroendocrine Tumors: A Multicenter Prognostic Study with Biological Correlates**
Weinuo Qu (Tongji Hospital Tongji Medical College Huazhong University of Science and Technology, China)

09:45-09:55 SS01-5 **Magnetic Resonance T2-weighted Imaging Radiomics Deep Learning Model to Predict Pancreatic Mucinous Neoplasms**
Xu Fang (Changhai Hospital of Naval Medical University, China)

09:55-10:05 SS01-6 **From Echoes to Contrast: Improving Reporting Standards and Timing of Imagings Delivery in Acute Pancreatitis**
Kevin Xuan Hong Tang (Hampshire Hospitals NHS Foundation Trust, UK)

10:05-10:20 SS01-7 **Imaging of IgG4-Related Disease: Focus on Pancreas and Biliary Tract Manifestation**
Ankur Goyal (All India Institute of Medical Sciences, New Delhi, India)

DAILY PROGRAM

MARCH 19 (Thu)

09:00-10:20 **[SF01] Special Focus 1: Fibroid and Adenomyosis** (Eng.)

[Room C] Grand 1

Chairs Byung Chul Kang (Yonsei University College of Medicine, Severance Hospital, Korea)
Sung Bin Park (University of Ulsan College of Medicine, Asan Medical Center, Korea)

09:00-09:25 SF01-1 **MR Screening and Monitoring for Leiomyoma and Adenomyosis: Updates**
Jungjae Park (Chungnam National University College of Medicine, Chungnam National University Hospital, Korea)

09:25-09:50 SF01-2 **Role of MRI: A Perspective on the Differentiation of the Fibroids from Sarcomas**
Jeong Woo Kim (Korea University College of Medicine, Korea University Guro Hospital, Korea)

09:50-10:15 SF01-3 **Focal Management of Uterine Fibroids and Adenomyosis: Advances in MR-guided Therapy**
Young-sun Kim (Women's Medical Science Center, MINT Hospital, Korea)

10:15-10:20 **Q&A**

09:00-10:20 **[SS02] Scientific Session 2 (ABD): HCC Imaging for Clinical Decision-Making** (Eng.)

[Room D] Grand 4+5

Chairs Min Woo Lee (Sungkyunkwan University School of Medicine, Samsung Medical Center, Korea)
Jeong Eun Lee (Chungnam National University College of Medicine, Chungnam National University Hospital, Korea)

09:00-09:10 SS02-1 **LI-RADS CT/MRI Nonradiation Treatment Response Assessment Version 2024 for Detecting Local Recurrence of Surgically Resected Hepatocellular Carcinoma**
Justin Tse (Stanford University, USA)

09:10-09:20 SS02-2 **LI-RADS Nonradiation Treatment Response Algorithm v2024: Enhanced Performance with Ancillary Features on Hepatobiliary MRI versus CT**
Jaeseung Shin (Sungkyunkwan University School of Medicine, Samsung Medical Center, Korea)

09:20-09:30 SS02-3 **Performance of LI-RADS Nonradiation Treatment Response Algorithm version 2024 on MRI for Transarterial Chemoembolization Plus Systemic Therapy in HCC**
Liuji Sheng (West China Hospital Sichuan University, China)

09:30-09:40 SS02-4 **Clinical Efficacy of CT Iodine Map in Evaluating Treatment Effect of TACE plus RFA for HCC**
Eun Ji Lim (Chosun University College of Medicine and Chosun University Hospital, Korea)

09:40-09:50 SS02-5 **Identification of Benefit Subgroups from Heterogeneous Effects of Adjuvant Transarterial Chemoembolization in Hepatocellular Carcinoma Using Causal Model**
Tianyi Xia (Zhongda Hospital Medical School of Southeast University, China)

09:50-10:00 SS02-6 **Predictive Value of Gd-EOB-DTPA-Enhanced MRI Features for VETC Subtypes and Proportions and Their Combined Prognostic Significance in Hepatocellular Carcinoma**
Hanjun Zhang (The Fourth Affiliated Hospital of Soochow University, China)

10:00-10:10 SS02-7 **Gd-EOB-DTPA-enhanced MRI-based Fractal Analysis for Preoperative Evaluation of Vessels Encapsulating Tumor Clusters and Microvascular Invasion in Hepatocellular Carcinoma**
Dan Liu (West China Hospital, China)

DAILY PROGRAM

MARCH 19 (Thu)

10:10-10:20 SS02-8 **Value of Preoperative Contrast-Enhanced CT-based Radiomics for Predicting CK19-Positive Hepatocellular Carcinoma**
Yawen Wang (Zhongda Hospital Southeast University, China)

11:10-12:00 [PL01] Plenary Lecture (Eng.)
[Room A+B] Vista 1+2

Chair: Jeong Min Lee (Seoul National University College of Medicine, Seoul National University Hospital, Korea)

11:10-12:00 PL01-1 **AI in Radiology**
Seong Ho Park (University of Ulsan College of Medicine, Asan Medical Center, Korea)

12:10-13:10 [LS01] Luncheon Symposium 1: Advancing Patient-Centered Care with Bayer: mpMRI and personalized CT Protocols (Eng.)
Bayer
[Room A+B] Vista 1+2

Chairs: Jeong Yeon Cho (Seoul National University College of Medicine, Seoul National University Hospital, Korea)
Jin-Young Choi (Yonsei University College of Medicine, Severance Hospital, Korea)

12:10-12:40 LS01-1 **Navigating Prostate Cancer Diagnosis: Insights from the PROKOMB Trial on MRI-Based Biopsy Decision-Making**
Charlie Hamm (Charité University Hospital, Germany)

12:40-13:10 LS01-2 **From Theory to Practice: Implementing Personalized Contrast Injection Protocols in Daily CT Workflow**
Hsin-Yu Chen (National Taiwan University Hospital, Chinese Taipei)

12:10-13:10 [LS02] Luncheon Symposium 2: Advancing MRI Diagnostics: Enhancing Safety, Precision, and Clinical Outcomes (Eng.)
Guerbet
[Room C] Grand 1

Chair: Jeong Min Lee (Seoul National University College of Medicine, Seoul National University Hospital, Korea)

12:10-12:15 **Welcome & Opening Remarks**
Jeong Min Lee (Seoul National University College of Medicine, Seoul National University Hospital, Korea)

12:15-12:35 LS02-1 **Latest Trend & Clinical Research on Gadolinium-Based Contrast Agents**
Yu-Ting Kuo (Chi Mei Medical Center, Chinese Taipei)

12:35-12:55 LS02-2 **High-Relaxivity Contrast in Liver MRI: Detection, Characterization, and Treatment Assessment of Liver Lesions**
PiYi Chang (Taichung Veterans General Hospital, Chinese Taipei)

12:55-13:10 **Panel Discussion & Q&A**

DAILY PROGRAM

MARCH 19 (Thu)

13:30-14:50 **[SF02] Special Focus 2: Deep Dive into HCC** (Eng.) — [Room A] Vista 1

Chairs: Myeong-Jin Kim (Yonsei University College of Medicine, Severance Hospital, Korea)
Bang-Bin Chen (National Taiwan University Hospital, Chinese Taipei)

13:30-13:50 SF02-1 **Histopathologic & Molecular Classification of HCC**
Haeryoung Kim (Seoul National University College of Medicine, Seoul National University Hospital, Korea)

13:50-14:10 SF02-2 **Imaging Signatures of HCC Subtypes**
Jin-Young Choi (Yonsei University College of Medicine, Severance Hospital, Korea)

14:10-14:30 SF02-3 **Current Status & Future of Non-invasive Diagnosis of HCC**
Sang Hyun Choi (University of Ulsan College of Medicine, Asan Medical Center, Korea)

14:30-14:50 SF02-4 **Prognostic Stratification of HCC with Imaging Biomarkers**
Hanyu Jiang (West China Hospital, Sichuan University, China)

13:30-14:50 **[RC01] Refresher Course 1: Transplantation Imaging** (Eng.) — [Room B] Vista 2

Chairs: Woo Kyoung Jeong (Sungkyunkwan University School of Medicine, Samsung Medical Center, Korea)
Romamtiezer Sahat Matondang (University of Indonesia, Indonesia)

13:30-13:50 RC01-1 **Imaging of Liver Transplantation**
Kyoung Won Kim (University of Ulsan College of Medicine, Asan Medical Center, Korea)

13:50-14:10 RC01-2 **Imaging of Pancreas Transplantation**
Se Jin Choi (University of Ulsan College of Medicine, Asan Medical Center, Korea)

14:10-14:30 RC01-3 **Imaging of Kidney Transplantation**
Seo Yeon Youn (The Catholic University of Korea, College of Medicine, Seoul St. Mary's Hospital, Korea)

14:30-14:50 RC01-4 **Imaging of Post-BM Transplantation**
Sun Kyung Jeon (Seoul National University College of Medicine, Seoul National University Hospital, Korea)

13:30-15:00 **[RC02] Refresher Course 2: Updates of GY Malignant Tumors** (Eng.) — [Room C] Grand 1

Chairs: Sung Eun Rha (The Catholic University of Korea, College of Medicine, Seoul St. Mary's Hospital, Korea)
Kang-Lung Lee (Taipei Veterans General Hospital, Chinese Taipei)

13:30-13:55 RC02-1 **The Implications of the 2023 New FIGO Stage in Endometrial Cancer from a Radiologist's Perspective**
Stephanie Nougaret (Montpellier Cancer Institute, France)

13:55-14:20 RC02-2 **Optimizing Cervical Cancer Staging with Advanced MR Imaging: A Practical Guide for Radiologist**
Tsukasa Saida (Institute of Medicine, University of Tsukuba, Japan)

DAILY PROGRAM

MARCH 19 (Thu)

14:20-14:45 **O-RADS for Assessment of Adnexal Lesions: Why, When and How**
RC02-3 Lori M. Strachowski (University of California, San Francisco, USA)

14:45-15:00 **O-RADS Case Examples with Pearls and Pitfalls**
RC02-4 Lori M. Strachowski (University of California, San Francisco, USA)

13:30-14:50 [SS03] Scientific Session 3 (ABD): IBD Imaging: Standardization and Innovation (Eng.)

[Room D] Grand 4+5

Chairs Young Hoon Kim (Seoul National University College of Medicine, Seoul National University Bundang Hospital, Korea)
Sung Kyoung Moon (Kyung Hee University College of Medicine, Kyung Hee University Hospital, Korea)

13:30-13:40 **Redefining Radiological Criteria for Small Bowel Stricture in Crohn's Disease: Effects of a 2.5 cm Pre-stenotic Dilatation Threshold on Stricture Prevalence and Prognosis**
SS03-1 Hae Young Kim (University of Ulsan College of Medicine, Asan Medical Center, Korea)

13:40-13:50 **Pre-procedural Imaging Assessment Predicts Endoscopic Passability in Crohn's Disease: Performance of SAR-Based Stricture Criteria and Imaging Predictors of Failed Endoscopic Passage**
SS03-2 Ziman Xiong (Tongji Hospital Tongji Medical College Huazhong University of Science and Technology, China)

13:50-14:00 **Current Status of Inflammatory Bowel Disease in China and the Establishment and Interpretation of the IBD-RADS System: A Multicenter Study and Clinical Translation**
SS03-3 Yaqi Shen (Tongji Hospital Tongji Medical College Huazhong University of Science and Technology, China)

14:00-14:10 **Rethinking Anorectal Cancer Surveillance Using MRI in Crohn's Disease**
SS03-4 Hae Young Kim (University of Ulsan College of Medicine, Asan Medical Center, Korea)

14:10-14:20 **Beyond Surgery: Time-varying Impact of Medical Therapy and Baseline CT Enterography Features on Long-term Surgical Avoidance in Crohn's Disease**
SS03-5 Xiaonan Yang (Tongji Hospital Tongji Medical College Huazhong University of Science and Technology, China)

14:20-14:30 **Toward Precision Surgery: YOLO-assisted Radiomics and Body Composition Fusion for Predicting Surgical Complexity in Crohn's Disease**
SS03-6 Xiaonan Yang (Tongji Hospital Tongji Medical College Huazhong University of Science and Technology, China)

14:30-14:40 **Reducing Misdiagnosis of Appendiceal Mucinous Neoplasms: The Impact of Structured Training on Radiologists' Preoperative Diagnostic Performance**
SS03-7 Ziman Xiong (Tongji Hospital Tongji Medical College Huazhong University of Science and Technology, China)

14:40-14:50 **Discussion (Q&A)**

15:10-16:00 [HL01] ESGAR Honorary Lecture (Eng.)

[Room A+B] Vista 1+2

Chair Chang Hee Lee (Korea University College of Medicine, Korea University Guro Hospital, Korea)

15:10-16:00 **Imaging the Small Bowel in IBD-Where are we now**
HL01-1 Stuart Taylor (University College London, UK)

DAILY PROGRAM

MARCH 19 (Thu)

16:40-18:00 **[SF03] Special Focus 3: Imaging Assessment in Metabolic Liver Disease: From MASLD to HCC** (Eng.)

[Room A] Vista 1

Chairs Cher Heng Tan (Tan Tock Seng Hospital, Singapore)
Seung Soo Lee (University of Ulsan College of Medicine, Asan Medical Center, Korea)

16:40-17:00 SF03-1 **Epidemiology, Pathophysiology & Clinical Outcome of MASLD & MASH**
Han Ah Lee (Chung-Ang University College of Medicine, Chung-Ang University Seoul Hospital, Korea)

17:00-17:20 SF03-2 **Non-invasive Imaging Assessment of MASLD and MASH**
Jeong Min Lee (Seoul National University College of Medicine, Seoul National University Hospital, Korea)

17:20-17:40 SF03-3 **More Than Weight: Advanced Imaging of Body Composition in Obesity**
Kyung Won Kim (University of Ulsan College of Medicine, Asan Medical Center, Korea)

17:40-18:00 SF03-4 **HCC in MASLD- Risk, Surveillance & Diagnostic Challenges**
Ijin Joo (Seoul National University College of Medicine, Seoul National University Hospital, Korea)

16:40-18:00 **[RC03] Refresher Course 3: State-of-the-Art Biliary Imaging** (Eng.)

[Room B] Vista 2

Chairs Yong Eun Chung (Yonsei University College of Medicine, Severance Hospital, Korea)
Hsien Min Low (Tan Tock Seng Hospital, Singapore)

16:40-17:00 RC03-1 **Cholangiopathies: Imaging-based Approaches for Diagnosis**
Maria Antonietta Bali (Università Cattolica del Sacro Cuore, Italy)

17:00-17:20 RC03-2 **Beyond Diagnosis: Preoperative Staging & Resectability Assessment for Extrahepatic Cholangiocarcinoma**
Bohyun Kim (The Catholic University of Korea, College of Medicine, Seoul St. Mary's Hospital, Korea)

17:20-17:40 RC03-3 **IPNB: Detection, Differential & Risk Assessment**
Hyo Jung Park (University of Ulsan College of Medicine, Asan Medical Center, Korea)

17:40-18:00 RC03-4 **The 2026 KSAR Consensus Statement for IPNB**
Dong Ho Lee (Seoul National University College of Medicine, Seoul National University Hospital, Korea)

16:40-18:00 **[SS04] Scientific Session 4 (GU): GU Issues 1** (Eng.)

[Room C] Grand 1

Chairs Deuk Jae Sung (Korea University College of Medicine, Korea University Anam Hospital, Korea)
Rudolf Kuhn (National Kidney and Transplant Institute, Philippines)

16:40-16:50 SS04-1 **Computed Tomography-Based Unsupervised Clustering Identifies Clusters Associated with Progression Free Survival in Clear Cell Renal Cell Carcinoma**
Jae Hyon Park (Armed Forces Daejeon Hospital, Korea)

16:50-17:00 SS04-2 **Preoperative MRI Model for Predicting Inferior Vena Cava Wall Invasion in Renal Cell Carcinoma with Tumor Thrombus**
Xuewei Wen (The First Medical Center, Chinese PLA General Hospital, China)

DAILY PROGRAM

MARCH 19 (Thu)

17:00-17:10 SS04-3 **Multicenter Validation of Bosniak Classification, Version 2019 for Class III-IV Aggressive and Any Cancer Prediction**
Justin Tse (Stanford University, USA)

17:10-17:20 SS04-4 **Construction and Clinical Validation of a Cascaded Deep Learning System for Classification of Benign and Malignant Solid Small Renal Masses Based on MRI**
Mengqiu Cui (The First Medical Center, Chinese PLA General Hospital, China)

17:20-17:30 SS04-5 **Comparative Outcomes of Ultrasound-Guided radiofrequency ablation and Robotic Partial Nephrectomy in Localized Renal Tumors: A Propensity-Matched Prospective Cohort Analysis**
Jong Woo Park (Seoul National University College of Medicine, Seoul National University Hospital, Korea)

17:30-17:40 SS04-6 **Utility of Multi-Model Diffusion MRI for Stratifying High-Risk Complications in Renal Transplant Recipients**
Kangwen He (Tongji Hospital Tongji Medical College Huazhong University of Science and Technology, China)

17:40-17:50 SS04-7 **Diffusion Lacunae in Placenta Accreta Spectrum (PAS): Game Changer in PAS Imaging**
Shinya Fujii (Tottori University, Japan)

17:50-18:00 **Discussion (Q&A)**

16:40-18:00 [SS05] Scientific Session 5 (ABD): Hot Topics in Body Imaging (Eng.)

[Room D] Grand 4+5

Chairs: Won Chang (Seoul National University College of Medicine, Seoul National University Bundang Hospital, Korea)
Jaeseung Shin (Sungkyunkwan University School of Medicine, Samsung Medical Center, Korea)

16:40-16:50 SS05-1 **Effects of Shortening Preparative Fasting Time before Contrast-enhanced CT on the Incidence of Acute Adverse Drug Reactions: An Observational Study**
Yunseo Choi (University of Ulsan College of Medicine, Asan Medical Center, Korea)

16:50-17:00 SS05-2 **Clinical Impact of a High-Relaxivity Gadolinium Contrast Agent in Liver MRI**
PiYi Chang (Taichung Veterans General Hospital, Chinese Taipei)

17:00-17:10 SS05-3 **Deep Learning-based Prediction of Hospitalization for Patients with Abdominal Symptoms during Emergency Department Triage: Combining Initial Abdominal Radiography and Early Clinical Information**
Yeo Eun Han (Korea University College of Medicine, Korea University Anam Hospital, Korea)

17:10-17:20 SS05-4 **An End-to-End Deep Learning Model Based on Non-Contrast CT Images of Patients with Liver Cirrhosis for Predicting Hepatocellular Carcinoma**
Shifan Liu (Zhongda Hospital Medical School of Southeast University, China)

17:20-17:30 SS05-5 **Dynamic CT-Derived Body Composition Changes During Neoadjuvant Therapy as Prognostic Biomarkers in Pancreatic Cancer: Development and Validation of a Survival Nomogram**
Hsin-Yu Chen (National Taiwan University Hospital, Chinese Taipei)

17:30-17:40 SS05-6 **Real-World Radiologist–LLM Reasoning Patterns in Abdominal Imaging: Insights for Designing Personalized AI Copilots**
Choongwui Cho (Hanil general Hospital, Korea)

DAILY PROGRAM

MARCH 19 (Thu)

17:40-17:50 **Evaluation of DeepSeek's Diagnostic Efficacy in Liver Diseases Based on Imaging Findings**
SS05-7 Jinqi Zhang (National Cancer Center National Clinical Research Center for Cancer Cancer Hospital Chinese Academy of Medical Sciences and Peking Union Medical College, China)

17:50-18:00 **Discussion (Q&A)**

DAILY PROGRAM

MARCH 20 (Fri)

09:00-10:20 **[RC04] Refresher Course 4: Recent Updates in Body Imaging** (Eng.) — [Room A] Vista 1

Chairs: Jeong Min Lee (Seoul National University College of Medicine, Seoul National University Hospital, Korea)
Gigin Lin (Chang Gung University Memorial Hospital, Chinese Taipei)

09:00-09:20 **Recent Technical Innovations in DWI**
RC04-1 Ryan L. Brunsing (Stanford University, USA)

09:20-09:40 **Pioneering Clinical Applications of 5T Abdominal MRI**
RC04-2 Liang Zhu (Peking Union Medical College Hospital, China)

09:40-10:00 **Low-field MRI in 2026: Challenges & Opportunities**
RC04-3 Michael Ohliger (University of California, San Francisco, USA)

10:00-10:20 **Beyond the Protons: Multi-nuclei Body MRI**
RC04-4 Satoshi Goshima (Hamamatsu University School of Medicine, Japan)

08:00-10:20 **[JS01] Joint Symposium 1 (ACAR meets China)** (Eng.) — [Room B] Vista 2

Chairs: Chang Hee Lee (Korea University College of Medicine, Korea University Guro Hospital, Korea)
Haiyi Wang (Chinese PLA General Hospital, China)

08:00-08:05 **Welcome address 1**
Jeong Min Lee (Seoul National University College of Medicine, Seoul National University Hospital, Korea)

08:05-08:10 **Welcome address 2**
Haiyi Wang (Chinese PLA General Hospital, China)

08:10-08:30 **AI in Abdominal Imaging**
JS01-1 Yanqi Huang (Guangdong Provincial People's Hospital (Guangdong Academy of Medical Sciences), Southern Medical University, China)

08:30-08:50 **Building LLM-Powered Workflows in Abdominal Radiology: Agents, Tools, and Governance**
JS01-2 Jeong Hyun Lee (Sungkyunkwan University School of Medicine, Samsung Medical Center, Korea)

08:50-09:10 **Imaging in Informing Indivisualized Treatment in HCC**
JS01-3 Hanyu Jiang (West China Hospital, Sichuan University, China)

09:10-09:20 Break

09:20-09:40 **Imaging of Hilar Tumors: What the Surgeon wants to know**
JS01-4 Hsien Min Low (Tan Tock Seng Hospital, Singapore)

09:40-10:00 **Diagnostic Approach to Multiple Solid Renal Lesions on CT and MR Imaging: The SWISS Principle**
JS01-5 Haiyi Wang (Chinese PLA General Hospital, China)

10:00-10:20 **Primary Staging of Rectal Cancer: ESGAR MRI Consensus Update and Dual-Energy CT Potentials**
JS01-6 Masashi Asano (Gifu University, Japan)

DAILY PROGRAM

MARCH 20 (Fri)

09:00-10:20 **[RC05] Refresher Course 5: GU Specific Diagnostic Classification Systems** (Eng.) [Room C] Grand 1

Chairs: Chan Kyo Kim (Sungkyunkwan University School of Medicine, Samsung Medical Center, Korea)
Masahiro Jinzaki (Keio University School of Medicine, Japan)

09:00-09:25 RC05-1 **PI-RADS Essential and Updates**
Anwar Padhani (Mount Vernon Cancer Centre, UK)

09:25-09:50 RC05-2 **VI-RADS: Multiparametric MRI for Staging and Management of Bladder Cancer**
Li-Jen Wang (Linkou Chang Gung Memorial Hospital, Chinese Taipei)

09:50-10:15 RC05-3 **Clear Cell RCC Likelihood Score: Principles and Clinical Applications**
Taek Min Kim (Seoul National University College of Medicine, Seoul National University Hospital, Korea)

10:15-10:20 **Discussion (Q&A)**

09:00-10:20 **[SS06] Scientific Session 6 (ABD): HCC Imaging: From LI-RADS to Prognostic Insights** (Eng.) [Room D] Grand 4+5

Chairs: Tae Wook Kang (Sungkyunkwan University School of Medicine, Samsung Medical Center, Korea)
Ji Soo Song (Jeonbuk National University Medical School, Jeonbuk National University Hospital, Korea)

09:00-09:10 SS06-1 **LI-RADS Treatment Response Assessment Version 2024: Clinical and Radiologic Predictors of LR-TR Viable after Radioembolization**
Sung-Hua Chiu (Stanford University School of Medicine & Tri-Service General Hospital, Chinese Taipei)

09:10-09:20 SS06-2 **Inter-reader Reliability and Diagnostic Performance of the LI-RADS CEUS Nonradiation TRA v2024**
Jeremy Jia Qi Soon (Changi General Hospital, Singapore)

09:20-09:30 SS06-3 **Radiological Characteristics of Hepatocellular Carcinoma in Cirrhotic vs Non-Cirrhotic Liver on Multiphasic CT: A Comparative Study**
Adinda Amalia (Dr Cipto Mangunkusumo National General Hospital, Indonesia)

09:30-09:40 SS06-4 **Prognostic Implications of Washout Timing in Hepatocellular Carcinoma: A Multicenter Cohort Study**
Yingyi Wu (West China Hospital Sichuan University, China)

09:40-09:50 SS06-5 **Preoperative Predicting Tumor-Specific Vascular Patterns on Contrast-Enhanced CT and Their Prognostic Implications for Solitary BCLC 0-A Hepatocellular Carcinoma**
Wanli Zhang (Guangzhou First Peoples Hospital, China)

09:50-10:00 SS06-6 **Intraindividual Comparison of Promising Prognostic Features between CT and MRI in Patients with Hepatocellular Carcinoma**
Xinyuan Jia (West China Hospital Sichuan University, China)

10:00-10:10 SS06-7 **Intraindividual Concordance and Discordance in CT and MRI LI-RADS Categorization in Hepatocellular Carcinoma: Impact on Postsurgical Prognosis**
Yong Jun Jung (University of Ulsan College of Medicine, Asan Medical Center, Korea)

10:10-10:20 **Discussion (Q&A)**

DAILY PROGRAM

MARCH 20 (Fri)

10:40-12:00 **[SF04] Special Focus 4: All About Pancreatic Cysts** (Eng.) — [Room A] Vista 1

Chairs: Takamichi Murakami (Kobe University Graduate School of Medicine, Japan)
Jung Hoon Kim (Seoul National University College of Medicine, Seoul National University Hospital, Korea)

10:40-11:00 SF04-1	**Pathologic Classification of Pancreatic Cystic Neoplasm** Hee Young Na (Seoul National University College of Medicine, Seoul National University Bundang Hospital, Korea)
11:00-11:20 SF04-2	**Pancreatic Cysts: Latest Guidelines & Supporting Evidences** Ji Hye Min (Sungkyunkwan University School of Medicine, Samsung Medical Center, Korea)
11:20-11:40 SF04-3	**Pancreatic Cysts: Key Recommendations from the SAR DFP** Elizabeth Hecht (Weill Cornell Medicine, USA)
11:40-12:00 SF04-4	**Pancreatic Cysts: Key Suggestions from KSAR PCN Study Group** Jeong Hee Yoon (Seoul National University College of Medicine, Seoul National University Hospital, Korea)

10:40-12:00 **[RC06] Refresher Course 6: Imaging of Tumors in GI Tract** (Eng.) — [Room B] Vista 2

Chairs: Se Hyung Kim (Seoul National University College of Medicine, Seoul National University Hospital, Korea)
Wey Chyi Teoh (Changi General Hospital, Singapore)

10:40-11:00 RC06-1	**Gastric Cancer: Preoperative T- & N-staging** Jin Woong Kim (Chosun University College of Medicine and Chosun University Hospital, Korea)
11:00-11:20 RC06-2	**Small Bowel NET: Imaging Features and Latest Treatment** Aarti Sekhar (Emory University School of Medicine, USA)
11:20-11:40 RC06-3	**Perirectal Mass: Pearls & Pitfalls in Differentials** Myung-Won You (Yonsei University College of Medicine, Severance Hospital, Korea)
11:40-12:00 RC06-4	**Anal Cancer & Perianal Disease** Seung Ho Kim (Inje University College of Medicine, Haeundae Paik Hospital, Korea)

10:40-12:00 **[SF05] Special Focus 5: Role of AI in GU Imaging** (Eng.) — [Room C] Grand 1

Chairs: Young Taik Oh (Yonsei University College of Medicine, Severance Hospital, Korea)
Shu-Huei Shen (Taipei Veterans General Hospital, Chinese Taipei)

10:40-11:05 SF05-1	**AI in Prostate Cancer: Clinical Performance and Practical Limitations** Jurgen Fütterer (Radboud University Medical Center, The Netherlands)
11:05-11:30 SF05-2	**Advanced Imaging Biomarkers for RCC: A Radiomics and Machine Learning Perspective** Zhen Li (Tongji Hospital, Tongji Medical College, Huazhong University of Science and Technology, China)
11:30-11:55 SF05-3	**AI-Powered MRI Analysis for Bladder Cancer Diagnosis** Mizuho Nishio (Kobe University, Japan)

DAILY PROGRAM

MARCH 20 (Fri)

11:55-12:00 **Discussion (Q&A)**

10:40-12:00 [SS07] Scientific Session 7 (ABD): Imaging Biomarkers in Liver Disease: Emerging Tools & New Frontiers (Eng.)

[Room D] Grand 4+5

Chairs Na Yeon Han (Korea University College of Medicine, Korea University Anam Hospital, Korea)
Seung-seob Kim (Yonsei University College of Medicine, Severance Hospital, Korea)

10:40-10:50 SS07-1 **Diagnostic Accuracy of Artificial Intelligence Based Imaging in Identifying Hepatic Steatosis: A Systematic Review and Meta-analysis**
Robin Antonio (FEU-NRMF, Philippines)

10:50-11:00 SS07-2 **Beyond Biopsy: Imaging-Driven Deep Learning to Flag At-Risk MASH**
Mei Chin Lim (National University Hospital, Singapore)

11:00-11:10 SS07-3 **Assessment of Cardiovascular Risk Using Coronary Artery Calcium Score, Hepato-steatosis, and Myo-steatosis as Imaging Biomarker for Geriatric Population**
Chandan Jyoti Das (AIIMS, India)

11:10-11:20 SS07-4 **CT-Derived Dynamic Body Composition Changes Predict Durable Clinical Benefit to Immunotherapy in Advanced Hepatocellular Carcinoma: Development and External Validation of a Cross-Center Model**
Bang-Bin Chen (National Taiwan University Hospital, Chinese Taipei)

11:20-11:30 SS07-5 **Liver Fibrosis: Explainable Deep learning Network for Automated Staging by Using Equilibrium Enhanced Phase MR Images**
Junhao Zha (Zhongda Hospital Medical School of Southeast University, China)

11:30-11:40 SS07-6 **Deep Learning–Based Quantitative MRI Biomarkers of Liver Function on Gadoxetic Acid–Enhanced MRI: Correlations with Clinical Liver Function Scores**
Seung Ha Cha (Korea University College of Medicine, Korea University Anam Hospital, Korea)

11:40-11:50 SS07-7 **Paradigm Shift in Post-Liver Transplantation Surveillance: A One-Stop Non-Contrast 4D Flow MRI for Integrated Morpho-Hemodynamic and Functional Profiling**
Weinuo Qu (Tongji Hospital Tongji Medical College Huazhong University of Science and Technology, China)

11:50-12:00 **Discussion (Q&A)**

12:20-13:20 [LS03] Luncheon Symposium 3 (Eng.)

SIEMENS Healthineers

[Room A] Vista 1

Chair Jeong Min Lee (Seoul National University College of Medicine, Seoul National University Hospital, Korea)

12:20-13:20 LS03-1 **Implementation and Clinical Impact of Photon Counting CT in Abdominal Imaging**
Michael Brun Andersen (Copenhagen University Hospital Herlev/Gentofte, Denmark)

DAILY PROGRAM

MARCH 20 (Fri)

12:20-13:20 **[LS04] Luncheon Symposium 4: Abdominal CT with High-Iodine Concentration Contrast Media: Clinical Experience Across Asia** (Eng.)
BRACCO LIFE FROM INSIDE
[Room B] Vista 2

Chair Chang Hee Lee (Korea University College of Medicine, Korea University Guro Hospital, Korea)

12:20-12:40 LS04-1 **Optimizing Clinical Outcomes with Iomeron® 400 : The Role of High-Concentration Contrast Media in Modern Diagnostic Imaging**
Hanyu Jiang (West China Hospital, Sichuan University, China)

12:40-13:00 LS04-2 **Dual-Energy CT in the Diagnosis of Gastrointestinal Bleeding**
Joon-Il Choi (The Catholic University of Korea, College of Medicine, Seoul St. Mary's Hospital, Korea)

13:00-13:20 LS04-3 **Protocol Tailoring & Personalization**
Satoshi Goshima (Hamamatsu University School of Medicine, Japan)

12:20-13:20 **[LS05] Luncheon Symposium 5** (Eng.)
GE HealthCare
[Room C] Grand 1

Chair Min Ju Kim (Korea University College of Medicine, Korea University Anam Hospital, Korea)

12:20-12:50 LS05-1 **Patient-Safe Emergency CT: Iso-osmolar Contrast Media and Double Dose Reduction**
Bohyun Kim (The Catholic University of Korea, College of Medicine, Seoul St. Mary's Hospital, Korea)

12:50-13:20 LS05-2 **UGFF: Ultrasound-Guided Fat Fraction – Multiparametric Quantitative Ultrasound for Liver Steatosis Assessment**
Takuma Oguri (Advanced Visualization Solutions, GE HealthCare, Japan)

13:40-14:30 **[HL02] ESUR Honorary Lecture** (Eng.)
[Room A+B] Vista 1+2

Chair Sung Il Jung (Konkuk University School of Medicine, Konkuk University Medical Center, Korea)

13:40-14:30 HL02-1 **Opportunities for Next Generation Imaging for Advanced Prostate Cancer**
Anwar Padhani (Mount Vernon Cancer Centre, UK)

16:40-18:00 **[TCP01] Case Presentation by Trainees** (Eng.)
[Room B] Vista 2

Chairs Eun Sun Lee (Chung-Ang University College of Medicine, Chung-Ang University Seoul Hospital, Korea)
Myoung Seok Lee (Seoul National University College of Medicine, SMG-SNU Boramae Medical Center, Korea)

16:40-16:48 TCP01-1 **Imaging Features of Renomedullary Interstitial Cell Tumor**
Sigyoung Chun (University of Ulsan College of Medicine, Asan Medical Center, Korea)

16:48-16:56 TCP01-2 **Varied Imaging Presentations of Urethral and Penile Malignancies: A Case Series**
Hanxing Xu (Changi General Hospital, Singapore)

16:56-17:04 TCP01-3 **Diagnostic Enigma: Primary Seminal Vesicle Angiosarcoma — A Multimodality Case Report**
Lourdjeanne Luces-Clemente (St Luke's Medical Center Global City, Philippines)

DAILY PROGRAM

MARCH 20 (Fri)

17:04-17:12 **Biliary Necrosis in Liver Lymphoma**
TCP01-4 Daniel Ong (Tan Tock Seng Hospital, Singapore)

17:12-17:20 **Langerhans Cell Histiocytosis Masquerading as an Infective Mass: A Radiologic and Pathologic Challenge**
TCP01-5 Sue En Ong (School of Medical Sciences Universiti Sains Malaysia, Hospital Sultanah Bahiyah, Malaysia)

17:20-17:28 **A Primary Retroperitoneal Hemangioma Initially Misdiagnosed as a Neuroendocrine Tumor with Increased Uptake in Ga-68 DOTATOC PET/CT**
TCP01-6 Jee Yeon Kim (Yonsei University College of Medicine, Severance Hospital, Korea)

17:28-17:36 **Paradox of Budd Chiari Syndrome Caused by Liver Transplantation**
TCP01-7 Katerina Lee (University of Pennsylvania, USA)

17:36-17:44 **When the Pancreas is Caught off Guard: A Rare Case of Contrast-Induced Radiologic Acute Pancreatitis**
TCP01-8 Kenneth Velasco (Rizal Medical Center, Philippines)

17:44-17:52 **Hepatoid Carcinoma of the Pancreas**
TCP01-9 Won-Seok Yoo (Yonsei University College of Medicine, Severance Hospital, Korea)

17:52-18:00 **Discussion (Q&A)**

16:30-18:00 [ACS01] Asian Chapter Session: Safe Use of Contrast Media: Guidelines and Evidence in Asia (Eng.)

[Room C] Grand 1

Chairs Min Hoan Moon (Seoul National University College of Medicine, SMG-SNU Boramae Medical Center, Korea)
Trifonia Pingkan Siregar (Universitas Indonesia, Indonesia)

16:30-16:45 **China Perspectives**
ACS01-1 Yuan-Cheng Wang (Zhongda Hospital, Southeast University, China)

16:45-17:00 **Japan Perspectives**
ACS01-2 Yoshiko Ueno (Kobe University Graduate School of Medicine, Japan)

17:00-17:15 **Chinese Taipei Perspectives**
ACS01-3 Yu-Ting Kuo (Chi Mei Medical Center, Chinese Taipei)

17:15-17:30 **Singapore Perspectives**
ACS01-4 Martin Weng Chin H'ng (Tan Tock Seng Hospital, Singapore)

17:30-17:45 **Korea Perspectives**
ACS01-5 Moon Young Kim (Seoul National University College of Medicine, SMG-SNU Boramae Medical Center, Korea)

17:45-18:00 **Panel Discussion**

DAILY PROGRAM

MARCH 20 (Fri)

16:40-18:00 **[HO01] Hands-on (GU): PI-RADS Version 2.1 Challenge** (Eng.)

[Room D] Grand 4+5

* Pre-registration Required for Hands-on
* Entry subject to seat availability. Inquire with Room D Hands-on staff at 16:40.

Moderator: Sung Il Hwang (Seoul National University College of Medicine, Seoul National University Bundang Hospital, Korea)

Instructors:
Li-Jen Wang (Linkou Chang Gung Memorial Hospital, Chinese Taipei)
Tsutomu Tamada (Kawasaki Medical School, Japan)
Chan Kyo Kim (Sungkyunkwan University School of Medicine, Samsung Medical Center, Korea)
Young Taik Oh (Yonsei University College of Medicine, Severance Hospital, Korea)

16:40-16:55 **Detection and Classification Using PI-RADS 2.1: Critical Points for Interpretation**
HO01-1 Jurgen Fütterer (Radboud University Medical Center, The Netherlands)

16:55-17:10 **Before Starting Interpretation: Pitfalls and Considerations for New PI-RADS Users**
HO01-2 Weon Jang (Jeonbuk National University Medical School, Jeonbuk National University Hospital, Korea)

17:10-18:00 **PI-RADS Challenge / Q&A**

DAILY PROGRAM

MARCH 21 (Sat)

09:00-10:20 **[RC07] Refresher Course 7: Emergency Radiology in Abdomen** (Eng.) — [Room A] Vista 1

Chairs: Joon-Il Choi (The Catholic University of Korea, College of Medicine, Seoul St. Mary's Hospital, Korea)
Kengo Yoshimitsu (Fukuoka University, Japan)

09:00-09:20 **Bowel Obstruction**
RC07-1 Kyoung Doo Song (Sungkyunkwan University School of Medicine, Samsung Medical Center, Korea)

09:20-09:40 **Bowel Ischemia**
RC07-2 Song-Ee Baek (Yonsei University College of Medicine, Severance Hospital, Korea)

09:40-10:00 **Traumatic Injuries in Abdomen**
RC07-3 Cheong-Il Shin (Seoul National University College of Medicine, Seoul National University Hospital, Korea)

10:00-10:20 **Musculoskeletal Emergencies & Urgencies in Abdomen CT**
RC07-4 Jee Won Chai (Seoul National University College of Medicine, SMG-SNU Boramae Medical Center, Korea)

08:20-10:20 **[JS02] Joint Symposium 2 (ACAR meets Vietnam): High-Value Liver MRI with Hepatocyte-Specific Contrast Agent** (Eng.) — [Room B] Vista 2

Chairs: Chang Hee Lee (Korea University College of Medicine, Korea University Guro Hospital, Korea)
Dung Thanh Le (Viet Duc University Hospital, Hanoi, Vietnam)

08:20-08:25 **Welcome address by ACAR**
Jeong Min Lee (Seoul National University College of Medicine, Seoul National University Hospital, Korea)

08:25-08:30 **Welcome address by VSAR**
Dung Thanh Le (Viet Duc University Hospital, Hanoi, Vietnam)

08:30-08:50 **Liver Imaging in Vietnam: Experience from a High-Volume Tertiary Center**
JS02-1 Huyen Duy Mai Le (University Medical Center, Ho Chi Minh City, Vietnam)

08:50-09:10 **Focal Hypointense Lesions on Hepatobiliary Phase of EOB-MRI**
JS02-2 Huu Khuyen Pham (Viet Duc University Hospital, Vietnam)

09:10-09:30 **Fast and Confident: Optimizing High-Yield Abbreviated EOB-MRI**
JS02-3 Jeong Woo Kim (Korea University College of Medicine, Korea University Guro Hospital, Korea)

09:30-09:50 **Hepatocellular Adenoma: Imaging Features and Subtype-Specific MRI Clues**
JS02-4 So Yeon Kim (University of Ulsan College of Medicine, Asan Medical Center, Korea)

09:50-10:10 **From LI-RADS to Asian Guidelines for HCC Diagnosis: Alignments, Differences, and Real-World Pitfalls**
JS02-5 Sunyoung Lee (Yonsei University College of Medicine, Severance Hospital, Korea)

10:10-10:20 **Discussion (Q&A)**

DAILY PROGRAM

MARCH 21 (Sat)

09:00-10:20 **[SS08] Scientific Session 8: GU Issues 2** (Eng.) — [Room C] Grand 1

Chairs: Dae Chul Jung (Yonsei University College of Medicine, Severance Hospital, Korea)
Sang Youn Kim (Seoul National University College of Medicine, Seoul National University Hospital, Korea)

09:00-09:10 SS08-1 **Clinically Available 3T Multi-Pool Chemical Exchange Saturation Transfer MRI for Accurate Diagnosis and Noninvasive Grading of Prostate Cancer**
Kangwen He (Tongji Hospital Tongji Medical College Huazhong University of Science and Technology, China)

09:10-09:20 SS08-2 **Interreader Agreement of PI-QUAL Version 2 for Prostate Magnetic Resonance Imaging Quality Assessment among Nonexpert Readers and Its Clinical Impact in a Targeted Biopsy Cohort**
Nattawut Jiraaram (Chulabhorn Royal Academy, Thailand)

09:20-09:30 SS08-3 **Mapping Tumor Heterogeneity via Habitat Analysis: An Interpretable Machine Learning Model Fusing 18F-PSMA-1007 PET/CT and mpMRI for ISUP Grade Prediction in a Multicenter Study**
Haoli Xu (The First Affiliated Hospital of Wenzhou Medical University, China)

09:30-09:40 SS08-4 **Evaluating the Clinical and Technical Impacts of PI-QUAL Scoring for Prostate MRI Quality Assessment: A Systematic Review**
Kaiwen Cabbabe (Alfred Health, Australia)

09:40-09:50 SS08-5 **Clinical Evaluation of a Low-Concentration, Low-Voltage Protocol for Urothelial Phase Bladder CT**
Yewon Lim (Ewha Womans University Mokdong Hospital, Korea)

09:50-10:00 SS08-6 **Correlation of MRI and Contrast Enhanced Ultrasound for O-RADS and Challenging Pelvic Mass Diagnosis**
Xiaoyang Liu (University of Toronto, Canada)

10:00-10:10 SS08-7 **CT Indicators for Differentiation of Stage 1 Borderline Ovarian Tumors from Stage I Malignant Epithelial Ovarian Tumors**
Soo Yeon Chae (Konkuk University School of Medicine, Konkuk University Medical Center, Korea)

10:10-10:20 **Discussion (Q&A)**

10:55-16:50 **대한복부영상의학회 –대한비뇨생식영상의학회 공동 연수교육** (Korean / AI-TRSL) — [Room A+B] Vista 1+2

10:55-11:00 **Opening remarks**
대한복부영상의학회 수련이사 정용은

11:00-11:30 **CT: Principles of Dynamic Imaging and Use of Intravenous Contrast Agents in Abdominal CT**
Eun-Suk Cho (Yonsei University College of Medicine, Gangnam Severance Hospital, Korea)

11:30-12:00 **CT: Dose Reduction Strategies and Denoising Techniques in Abdominal CT**
Won Chang (Seoul National University College of Medicine, Seoul National University Bundang Hospital, Korea)

12:00-12:30 **Imaging Techniques for the Small Bowel**
Myung-Won You (Yonsei University College of Medicine, Severance Hospital, Korea)

12:30-13:30 **Lunch break**

DAILY PROGRAM

MARCH 21 (Sat)

13:30-14:00 **MRI: Practical Approach to Performing and Interpreting Liver MRI**
So Hyun Park (Seoul National University College of Medicine, Seoul National University Bundang Hospital, Korea)

14:00-14:30 **MRI: Practical Approach to Performing and Interpreting Biliary and Pancreatic MRI**
Hyo Jung Park (University of Ulsan College of Medicine, Asan Medical Center, Korea)

14:30-15:00 **MRI: Practical Approach to Performing and Interpreting Rectal MRI**
Jeongin Yoo (Seoul National University College of Medicine, Seoul National University Hospital, Korea)

15:00-15:15 **Coffee break**

15:15-15:45 **Review and Updates of Kidney & Adrenal MR Protocol**
Eun Ji Lee (Soonchunhyang University College of Medicine, Soonchunhyang University Seoul Hospital, Korea)

15:45-16:15 **Review and Updates of Bladder MR Protocol**
Ki Choon Sim (Korea University College of Medicine, Korea University Anam Hospital, Korea)

16:15-16:45 **Review and Updates of Female Pelvis MR Protocol**
Mi Yeon Park (University of Ulsan College of Medicine, Asan Medical Center, Korea)

16:45-16:50 **Closing remarks**
대한비뇨영상의학회 총무이사 김상윤

ACAR 2026

THE 13th ASIAN CONGRESS OF ABDOMINAL RADIOLOGY

Invited Session

Mar. 19 (Thu.)

! Abstracts can be found by searching with the Presentation Code !

[Problem-based learning 1: Thinking Like an Expert]

PBL01-1

Knowledges & Challenges: Retroperitoneum

Dow-Mu Koh

Royal Marsden Hospital, UK

The retroperitoneum is a continuous, potential space extending from the diaphragm to the pelvic brim. Within this compartment lie the kidneys, adrenal glands, pancreas (body and tail), aorta and inferior vena cava, lymphatic chains, major vessels, ureters, and various neuro-vascular plexuses. Its anatomical subdivisions – pararenal (anterior and posterior), perirenal, and aortocaval – are clinically significant for understanding the origin and spread of disease.

Retroperitoneal masses are broadly classified into benign and malignant lesions depending on the cell / tissue or origin. Benign entities include lipomas, schwannomas, neurofibromas, leiomyomas, adrenal adenomas, pheochromocytomas, cystic lesions (pancreatic pseudocysts, cystic teratomas), and fibromatosis. Malignant causes encompass primary sarcomas (liposarcoma, leiomyosarcoma, malignant peripheral nerve sheath tumour, rhabdomyosarcoma), metastatic disease (renal cell carcinoma, pancreatic carcinoma, colorectal carcinoma, lymphoma), lymphomas, germ cell tumours, and lymphoma-derived masses such as Hodgkin's disease. In addition, inflammatory pseudo-tumours, retroperitoneal fibrosis, and infectious conditions can mimic malignancy on imaging.

The diagnostic work-up of a retroperitoneal mass is a stepwise, multimodality approach. Initial assessment relies on CT or MRI, whose systematic analysis narrows the differential diagnosis by evaluating size, attenuation/signal characteristics (presence of fat/ myxoid/ cystic/ necrotic component), calcifications, vascularity, and relationship to adjacent structures. MRI provides superior soft-tissue contrast and characterisation of cystic versus solid components, while CT is better for detecting calcification and bone invasion. When imaging findings are indeterminate, image-guided core needle biopsy is essential to establish a definitive diagnosis, as many retroperitoneal lesions have non-specific appearances. PET-CT, although more limited, plays a selective role in assessing metabolic activity, staging, differentiating benign from malignant lesions, as well as high-grade from low-grade tumours. PET-CT using selective tracers can help to diagnose specific malignancies (e.g. DOTATATE PET-CT for diagnosis paragangliomas; MIBG PET-CT for diagnosing neuroblastomas).

The learning objectives of this lecture emphasise familiarity with both focal/diffuse and solid/ cystic retroperitoneal lesions and the indications for additional imaging modalities, guiding clinicians toward a targeted, evidence-based diagnostic pathways. This lecture will help radiologists and clinicians with a comprehensive understanding of retroperitoneal anatomy, the spectrum of benign and malignant causes of retroperitoneal mass lesions, and a practical, imaging-driven diagnostic algorithm that integrates CT, MRI, PET-CT, and histopathology to optimise patient care.

[Problem-based learning 1: Thinking Like an Expert]

PBL01-2

Knowledges & Challenges: Spleen

Kyowon Gu

Sungkyunkwan University School of Medicine, Samsung Medical Center, Korea

The spleen is a mesodermal lymphoid organ divided into red pulp for blood filtration and white pulp for immune responses. Its dual closed and open circulation pathways create distinct contrast enhancement patterns. The arterial phase shows a heterogeneous "zebra" pattern, while the portal venous phase exhibits homogeneous enhancement. Since splenic lesions are rare and often asymptomatic, diagnosing them requires a pattern-based approach, categorizing masses by consistency (cystic or solid) and number (solitary or multiple).

For cystic lesions, solitary masses include thin-walled, non-enhancing epithelial cysts and pseudocysts with thick, often calcified walls. Multiple cysts usually indicate multiloculated lymphangiomas or infectious abscesses. Among solitary solid masses, hemangioma is the most common benign lesion, displaying progressive homogeneous enhancement. Hamartomas show early arterial enhancement that equilibrates with the background spleen. Sclerosing angiomatoid nodular transformation (SANT) is uniquely characterized by a spoke-wheel enhancement pattern. For multiple solid masses, littoral cell angiomas exhibit progressive enhancement. Lymphomas, the most common splenic malignancy, typically appear as hypoenhancing masses with restricted diffusion.

Diagnostic pitfalls include inflammatory pseudotumors, which can mimic malignancies but often feature a central fibrous scar with delayed enhancement. Angiosarcomas are aggressive malignancies showing heterogeneous enhancement due to hemorrhage and necrosis. If imaging remains indeterminate, percutaneous core needle biopsy is recommended; it has a very low complication rate and high accuracy, safely preventing unnecessary splenectomy.

[Problem-based learning 1: Thinking Like an Expert]

PBL01-3

Knowledges & Challenges: Infection

Subin Heo

University of Ulsan College of Medicine, Asan Medical Center, Korea

This interactive, problem-based learning session is designed to share and discuss challenging cases of abdominal infections encountered in daily radiologic practice.

During this session, we will review a spectrum of infections involving the solid abdominal organs, gastrointestinal tract, and peritoneum, which may present with a wide range of imaging appearances, including atypical and less familiar patterns.

Through selected cases, we will focus on recognizing these diverse manifestations and identifying subtle but meaningful imaging clues that can help narrow the differential diagnosis.

By participating, you will gain a broader perspective on the variable imaging presentations of abdominal infections and develop a more intuitive, clue-based approach to their interpretation in routine clinical practice.

[Special Focus 1: Fibroid and Adenomyosis]

SF01-1

MR Screening and Monitoring for Leiomyoma and Adenomyosis: Updates

Jungjae Park

Chungnam National University College of Medicine, Chungnam National University Hospital, Korea

MRI is an important imaging tool for diagnosis and monitoring of uterine leiomyomas and adenomyosis, providing high-resolution images. MRI offers anatomical and functional images for assessing size, location, inner characterization for them. For uterine leiomyomas, MRI based characterization is crucial for treatment plan and also for evaluating therapeutic response after specific treatment. MRI is also useful for identifying coexisting conditions of adenomyosis in patients with myomas, because it may influence on the patient's prognosis. The FIGO classification system was developed as a means of uniformly and consistently describing and classifying uterine fibroids in order to facilitate communication, clinical care and research. Accurately classifying uterine leiomyomas allows clinicians to select the best treatment plan for the patient. Differentiating between various types and identifying the subtype is helpful for determining treatment plan and monitoring the treatment response of uterine adenomyosis. The MRI features of adenomyosis include a thickened and ambiguous junctional zone and the presence of T2-bright foci within myometrium, which represent endometrial glands. Recently, MRI-based systems have been provided for more objectivity and consistency in classifying adenomyosis. MRI-based classification system usually utilize involvement pattern, location of adenomyosis.

[Special Focus 1: Fibroid and Adenomyosis]

SF01-2

Role of MRI: A Perspective on the Differentiation of the Fibroids from Sarcomas

Jeong Woo Kim

Korea University College of Medicine, Korea University Guro Hospital, Korea

Uterine smooth muscle tumors range from benign leiomyomas to malignant leiomyosarcomas, with smooth muscle tumors of uncertain malignant potential (STUMP) representing an intermediate entity. Accurate preoperative differentiation is critical because management and prognosis differ markedly. Misdiagnosis may result in unnecessary extensive surgery or undertreatment of aggressive disease.

MRI is the most effective non-invasive modality for evaluating uterine masses. Conventional MRI provides key morphological and signal intensity information, while advanced techniques such as diffusion-weighted imaging (DWI) and dynamic contrast-enhanced (DCE) imaging increase diagnostic accuracy. Leiomyomas typically show well-defined margins and homogeneous low signal intensity on T2-weighted images, sometimes with cystic or hemorrhagic degeneration. In contrast, leiomyosarcomas often present with ill-defined margins, irregular contours, heterogeneous T2 hyperintensity, T1 hyperintense hemorrhage, and central non-enhancing necrosis. Restricted diffusion with low ADC values and central non-enhancement are among the most reliable MRI indicators of malignancy.

Recent studies have developed MRI-based scoring systems and radiomics approaches that integrate multiparametric features to improve diagnostic confidence. Texture analysis of T2-weighted images and ADC maps combined with machine learning models has demonstrated performance comparable to experienced radiologists, supporting the emerging role of artificial intelligence in complex differential diagnosis.

Nevertheless, imaging overlap remains, as atypical or infarcted leiomyomas may mimic sarcomas. Therefore, MRI findings must be interpreted in conjunction with clinical presentation and tumor growth patterns.

This lecture will review characteristic MRI features of fibroids and sarcomas, summarize evidence on advanced imaging techniques, and discuss the evolving role of radiomics and artificial intelligence in improving diagnostic accuracy.

[Special Focus 1: Fibroid and Adenomyosis]

SF01-3

Focal Management of Uterine Fibroids and Adenomyosis: Advances in MR-guided Therapy

Young-sun Kim

Women's Medical Science Center, MINT Hospital, Seoul, Korea

FUS (focused ultrasound) or HIFU (high-intensity focused ultrasound) ablation is increasingly adopted for the treatment of various gynecologic diseases such as uterine fibroid, adenomyosis owing to its merits as non-invasive therapies as well as capability of uterine preservation.

HIFU ablation can be performed under the guidance of either US or MRI. Each method has pros and cons, however, MR-guided HIFU ablation is generally accepted to be safer because of its wider FOV and thermometric monitoring capability.

In screening step before treating uterine fibroids, the operator should consider several factors to improve necrosis rate, which include T2 signal intensity and perfusion of fibroids as well as thickness of subcutaneous fat of the abdominal wall. During treatment, complete necrosis should always be pursed to achieve better long-term clinical outcomes. There are several well-known complications of HIFU ablation which include skin burn, sciatic nerve injury, hematuria, and bowel injury. Complications usually happen when treating too resistant fibroids or in cases the target lesion is located at unfavorable location, which can be predicted, in other words, can be prevented.

HIFU ablation of uterine adenomyosis shares many features with that of fibroids. However, it shows quite different clinical features as well as MRI findings when followed-up in a long term. Follow-up MRI usually shows more recurrences based on imaging than fibroids due to its infiltrative nature of the disease. However, clinical symptoms usually well controlled even in the presence of viable tissues.

In this lecture, MR-guided HIFU therapy for treating uterine fibroid and adenomyosis will be reviewed from its treatment mechanism to strategy to improve long-term clinical outcomes as well as safety.

[Plenary Lecture]

PL01-1

AI in Radiology

Seong Ho Park

University of Ulsan College of Medicine, Asan Medical Center, Korea

This lecture will: (1) summarize the current real-world landscape of artificial intelligence (AI) in abdominal radiology; (2) trace the broader technological evolution of AI in radiology and medicine; and (3) discuss emerging challenges and imperatives for effective, responsible, and sustainable clinical adoption.

To date, the most extensively explored and clinically implemented AI applications in medical imaging have been concentrated in non-abdominal domains, including chest radiography, mammography, bone age assessment, and neuroimaging for intracranial hemorrhage detection. In contrast, abdominal imaging remains one of the least developed subspecialties in terms of clinically impactful AI deployment. Existing commercial AI tools in abdominal radiology are largely peripheral or complementary. Organ and anatomical segmentation for volumetric assessment—such as hepatic segment volumetry—represents one of the few areas approaching meaningful clinical utility, primarily in presurgical planning. Although numerous diagnostic and predictive AI models for abdominal diseases have been reported in the research literature, most offer limited actionable value for patient management and therefore rarely translate into sustainable, real-world clinical tools. Given the high anatomical complexity, disease heterogeneity, and contextual variability inherent to abdominal imaging, developing AI models that achieve academic success, clinical relevance, and commercial viability simultaneously remains particularly challenging.

The lecture will then situate these realities within the broader evolution of AI in medicine—from convolutional neural network (CNN)-based, narrow task-specific systems to transformer-based foundational models, including large language models (LLMs) and large vision-language models (LVLMs). Foundational models exhibit remarkable versatility and emergent capabilities, creating the perception that they can perform "infinite" tasks without task-specific training. However, versatility does not eliminate the fundamental dependence on high-quality, task-relevant data. Transformer architectures excel at extracting and generalizing patterns embedded within their training corpora, but there is no AI without data. Moreover, the development of transformer-based foundational models requires enormous amount of data and computational resources. Therefore, except for a limited number of relatively simplified examinations—such as chest radiography—the creation of a truly multi-task, general-purpose radiology AI based on foundational models (often loosely described as "AGI in radiology") remains largely theoretical and represents a long-term and uncertain prospect. Current state-of-the-art LVLMs are not yet capable of reliably analyzing radiologic images and remain heavily dependent on textual inputs. These limitations are even more pronounced in abdominal imaging, for reasons similar to those that constrained progress during the earlier CNN-based era.

Finally, the lecture will address a critical paradigm shift: the movement from algorithm-centric AI viewpoint toward an AI-assisted human paradigm. This shift toward human-centered adoption is mirrored in evolving regulatory landscapes: for example, South Korea's AI Framework Act, which came into force on January 22, 2026. The prevailing model-centric approach has frequently overlooked the essential dimension of human–AI interaction, thereby hindering effective integration into clinical workflows. Effective, responsible, and sustainable adoption requires more than high algorithmic performance; it demands careful consideration of how clinicians interact with AI outputs, how uncertainty is quantified and communicated, and how responsibility is allocated. Technical adjuncts—such as uncertainty quantification and explainability tools—are necessary but insufficient. Equally important are deliberate efforts to preserve and strengthen core human professional competencies. Radiologists must remain vigilant against automation bias, deskilling, and "never-skilling" among future generations trained in AI-saturated environments. The often-quoted statement, "AI will not replace doctors, but doctors using AI will replace those who do not," merits refinement. A more accurate up-to-date formulation may be: AI will not replace doctors. But doctors who use AI while preserving and strengthening core human skills will replace those who either ignore AI or become dependent on it.

[Luncheon Symposium 1: Advancing Patient-Centered Care with Bayer: mpMRI and personalized CT Protocols]

LS01-1

Navigating Prostate Cancer Diagnosis: Insights from the PROKOMB Trial on MRI-Based Biopsy Decision-Making

Charlie Hamm

Charité University Hospital, Germany

- Background

Prostate cancer (PCa) diagnosis has historically relied on 12-core systematic biopsy (SB), which carries a well-documented risk of overtreatment for low-grade disease and under-detection of high-grade cancer. By 2019, landmark trials (PRECISION, PROMIS, 4M) established that MRI-targeted biopsies outperform SB for clinically significant PCa (csPCa, Grade Group ≥2). A key unanswered question remained: is it safe to omit biopsy entirely when MRI is negative?

The PROKOMB Trial

A prospective, multisite, longitudinal cohort study conducted across 54 community urology practices and 2 tertiary radiology centres (2016–2017). 607 biopsy-naive men with clinically suspected PCa underwent 3T mpMRI (PI-RADS v2). PI-RADS 3–5 men received targeted + systematic biopsy; PI-RADS 1–2 men entered 3-year active monitoring with biannual visits.

Cohort profile: median age 64, PSA 5.8 ng/mL, PSAD 0.14 ng/mL^2, csPCa prevalence 29% — comparable to PRECISION and 4M.

- Key Results

MRI-negative men (PI-RADS 1–2, 48% of cohort): At 3-year follow-up, NPV for csPCa was 96% (95% CI 94–98%). Only 4% harboured GG≥2 disease. Biopsy was avoided in 86% of MRI-negative men and 41% of the total cohort. Rates of incidental low-grade cancer were comparable to a healthy screening population. Conclusion: omitting biopsy after negative MRI is oncologically safe. MRI-positive men: GG≥2 detection rate was 51%, confirming high diagnostic yield of targeted biopsy. 84% of participants completed full follow-up, and only 15% required a follow-up MRI, demonstrating the pathway is feasible in ambulatory care.

- Outlook

With PCa incidence expected to double by 2040, structured, risk-adapted monitoring protocols for MRI-negative and biopsy-negative men are urgently needed. Current EAU guidelines support MRI-first pathways, but further refinement using PSA density, age, and PI-RADS score is required to enhance efficiency and equity of access.

- Conclusions

- MRI-informed biopsy decision-making is oncologically safe

- mpMRI enables targeted biopsies with high csPCa detection
- The MRI-pathway with structured monitoring is feasible in real-world ambulatory care — provided image quality and reader expertise are assured

[Luncheon Symposium 1: Advancing Patient-Centered Care with Bayer: mpMRI and personalized CT Protocols]

LS01-2

From Theory to Practice: Implementing Personalized Contrast Injection Protocols in Daily CT Workflow

Hsin-Yu Chen

National Taiwan University Hospital, Chinese Taipei

This presentation will first outline the challenges and pain points encountered in daily clinical practice, particularly when patient weight, clinical indications, and other key factors change simultaneously and complicate protocol selection. Drawing on the implementation experience of Centargo and the Smart Protocol at NTUH, the talk will highlight how workflow design plays a decisive role in determining the success or failure of protocol adoption. The speaker will also explain the rationale for utilizing the Smart Protocol and its impact on contrast-enhanced CT diagnostic evaluation, using representative patient cases to demonstrate improvements in image quality consistency and optimization of contrast media use. Finally, the future direction of the department will be introduced, including the planned transition to Ultravist 500 mL.

[Luncheon Symposium 2: Advancing MRI Diagnostics: Enhancing Safety, Precision, and Clinical Outcomes]

LS02-1

Latest Trend & Clinical Research on Gadolinium-Based Contrast Agents

Yu-Ting Kuo

Chi Mei Medical Center, Chinese Taipei

The transition from linear to macrocyclic GBCAs represents a critical shift in radiological safety, primarily driven by the need to prevent Nephrogenic Systemic Fibrosis (NSF) and minimize long-term gadolinium retention. While Group I linear agents like Omniscan and Magnevist are now largely obsolete due to their susceptibility to transmetallation—where endogenous ions displace the toxic Gd ion—Group II macrocyclic agents provide a "cage-like" structure that ensures significantly higher kinetic stability.

The latest innovation, gadopiclenol (Elucirem), enhances this stability with a unique molecular design featuring a hydration number of q=2. By doubling the number of water molecules in the inner coordination sphere compared to standard agents (q=1), gadopiclenol achieves a significantly higher relaxivity.

This allows clinicians to utilize a half-dose protocol (0.05 mmol/kg), which has been proven non-inferior to full doses of standard agents like gadobutrol in detecting CNS lesions and enhancing liver or breast pathology. Furthermore, this dose reduction directly addresses growing concerns over anthropogenic gadolinium environmental contamination, as lower injected volumes lead to reduced excretion into wastewater systems and, eventually, the food chain.

[Luncheon Symposium 2: Advancing MRI Diagnostics: Enhancing Safety, Precision, and Clinical Outcomes]

LS02-2

High-Relaxivity Contrast in Liver MRI: Detection, Characterization, and Treatment Assessment of Liver Lesions

PiYi Chang

Taichung Veterans General Hospital, Chinese Taipei

High-relaxivity gadolinium-based contrast agents enhance liver MRI by increasing the efficiency of T1 shortening per millimole of gadolinium, generating stronger signal intensity at lower doses. Gadopiclenol, a macrocyclic high-relaxivity agent, allows a 50% dose reduction (0.05 mmol/kg vs. 0.1 mmol/kg) while maintaining or improving signal-to-noise ratio (SNR) and contrast-to-noise ratio (CNR). In liver imaging, where lesion detection depends on subtle dynamic enhancement patterns, this efficiency directly improves arterial-phase conspicuity and lesion-to-liver contrast.

During the arterial phase, subcentimeter hepatocellular carcinomas (HCCs) often demonstrate brief and subtle hyperenhancement. Higher relaxivity amplifies this transient signal, creating a steeper contrast gradient between lesion and surrounding parenchyma. As a result, small nodules are more clearly delineated, improving detection confidence. The enhanced contrast is not simply increased brightness, but improved lesion-to-background differentiation, which is critical in a noise-limited imaging environment.

Across portal venous and equilibrium phases, strong parenchymal and vascular enhancement preserves multiphasic contrast behavior. This facilitates accurate characterization of hemangiomas, focal nodular hyperplasia (FNH), HCC, and metastases by improving visualization of washout or progressive fill-in patterns. Robust portal vein enhancement also supports assessment of vascular invasion and segmental anatomy.

In post-treatment surveillance after TACE, ablation, or Y-90, detection of viable tumor relies on identifying subtle nodular arterial enhancement within treated zones. High-relaxivity contrast accentuates minimal residual enhancement, improving differentiation between necrosis and viable tissue. Enhanced CNR strengthens confidence in treatment response evaluation and retreatment decisions.

Importantly, reducing gadolinium dose decreases cumulative exposure in patients requiring lifelong surveillance, including those with chronic liver disease. Thus, high relaxivity transforms liver MRI by combining superior dynamic-phase visualization, improved lesion detection, and optimized patient safety at half the conventional dose.

[Special Focus 2: Deep Dive into HCC]

SF02-1

Histopathologic & Molecular Classification of HCC

Haeryoung Kim

Seoul National University College of Medicine, Seoul National University Hospital, Korea

Hepatocellular carcinoma (HCC) demonstrates substantial histopathological and molecular heterogeneity. Increasing recognition of correlations between morphology and molecular alterations has led to the identification of distinct histological variants with important translational implications.

Macrotrabecular-massive HCC, defined by a macrotrabecular pattern in at least 50% of the tumor, is associated with frequent TP53 alterations, FGF19 amplifications, and aggressive behavior. The vessels-encapsulating-tumor-clusters (VETC) pattern is commonly observed in this subtype and represents an adverse prognostic factor. The steatohepatitic subtype shows features resembling steatohepatitis in more than half of the tumor and is more prevalent in patients with metabolic dysfunction–associated steatotic liver disease or alcohol-related liver disease (5–20% of cases). Molecularly, it is characterized by activation of the IL-6/JAK/STAT pathway, while CTNNB1, TERT promoter, and TP53 mutations are less frequent. Although steatohepatitic HCC is associated with less frequent vascular invasion and fewer satellite nodules, its overall prognosis appears comparable to that of conventional HCC. Scirrhous HCC is another variant, associated with TSC1/TSC2 mutations and activation of the TGF-β pathway. Although clinical outcomes remain somewhat controversial, this subtype has been linked to aggressive clinicopathological features, and survival may be poorer than that of conventional HCC, particularly in larger tumors.

CTNNB1 mutations occur in approximately 20–40% of HCCs. These tumors are usually well differentiated, with microtrabecular and/or pseudoglandular patterns, intratumoral cholestasis, and reduced immune infiltration. However, up to 40% lack classic morphological features. Immunohistochemical staining for nuclear β-catenin and diffuse glutamine synthetase expression may serve as surrogate markers, although molecular testing remains the gold standard.

This talk will review the morpho-molecular heterogeneity of HCC and summarize key variants and patterns with clinical relevance.

[Special Focus 2: Deep Dive into HCC]

SF02-2

Imaging Signatures of HCC Subtypes

Jin-Young Choi

Yonsei University College of Medicine, Severance Hospital, Korea

Hepatocellular carcinoma (HCC) comprises a heterogeneous group of tumors with variable biological aggressiveness, reflected by tumor grade, vascular invasion, and pathologic and molecular classifications. Because of both intra-tumoral and inter-tumoral heterogeneity, accurate prognostic stratification is essential yet challenging. While most HCCs demonstrate typical imaging features, approximately 35% can be categorized into specific histologic subtypes according to the WHO 2019 classification. From a molecular perspective, HCC is also broadly divided into proliferative and non-proliferative classes. Although important knowledge gaps remain in the subclassification of HCC, recognition of these subtypes is clinically relevant because it can influence diagnostic strategies and therapeutic decision-making.

Emerging evidence indicates that radiologic features of HCC correlate with underlying histologic and molecular characteristics, thereby reflecting tumor biology. For example, macrotrabecular massive (MTM) HCC is frequently associated with a hypoxic microenvironment and intratumoral necrosis; on imaging, necrotic components that appear hyperintense on T2-weighted images without corresponding dynamic enhancement may suggest this aggressive subtype.

Although imaging findings alone are not yet definitive for subtype diagnosis, they can substantially increase clinical suspicion and guide further evaluation, including targeted biopsy. Early identification of aggressive HCC subtypes through imaging is important because it directly affects treatment planning and prognostic assessment. Continued research into the radiologic signatures of HCC subtypes may ultimately enable more reliable noninvasive classification and provide imaging biomarkers for prognosis, molecular profiling, and prediction of therapeutic response.

[Special Focus 2: Deep Dive into HCC]

SF02-3

Current Status & Future of Non-invasive Diagnosis of HCC

Sang Hyun Choi

University of Ulsan College of Medicine, Asan Medical Center, Korea

Accurate imaging diagnosis plays a central role in the management of hepatocellular carcinoma (HCC), as HCC can often be diagnosed non-invasivssely without histopathologic confirmation in high-risk patients. Given the global burden of HCC and the prognostic impact of early detection, imaging-based diagnosis directly influences treatment allocation and patient outcomes.

International imaging criteria have evolved to standardize diagnostic approaches. In Western countries, LI-RADS-based systems endorsed by AASLD and EASL emphasize specificity and structured categorization. In contrast, Eastern guidelines such as APASL and KLCA-NCC reflect different clinical priorities, including broader treatment eligibility and variations in healthcare systems. These differences result in distinct thresholds for imaging features, contrast agent preference, and interpretation of hepatobiliary phase findings.

Despite its strengths in standardization, LI-RADS has several limitations, including suboptimal sensitivity for definite HCC, moderate inter-reader agreement for certain imaging features, diagnostic complexity, and uncertainty in managing indeterminate observations. These challenges highlight the need for refinement of diagnostic criteria and improved risk stratification strategies.

Beyond binary diagnosis, imaging is increasingly expected to provide prognostic and predictive information. Conventional qualitative features and emerging quantitative approaches, including radiomics and deep learning, show promise in predicting tumor aggressiveness, recurrence risk, microvascular invasion, and treatment response. As imaging evolves from detection to precision stratification, integration of imaging biomarkers with clinical and molecular data may redefine the role of radiology in HCC management.

This lecture will provide an overview of current diagnostic frameworks, discuss their limitations, and explore future directions toward more personalized imaging-based care in HCC.

[Special Focus 2: Deep Dive into HCC]

SF02-4

Prognostic Stratification of HCC with Imaging Biomarkers

Hanyu Jiang

West China Hospital, Sichuan University, China

This lecture does not have an abstract.

[Refresher Course 1: Transplantation Imaging]

RC01-1

Imaging of Liver Transplantation

Kyoung Won Kim

University of Ulsan College of Medicine, Asan Medical Center, Korea

Liver transplantation has been accepted as the effective curative treatment for patients with end-stage hepatic diseases and hepatic tumors. Orthotopic liver transplantation, which involves replacement of the diseased native liver with a whole liver graft from a cadaveric donor, is the most frequently performed technique of liver transplantation worldwide. However, because of the shortage of cadaveric livers, partial liver transplantation including split liver transplantation and living donor liver transplantation has been increasingly used not only for pediatric recipients but for adult recipients.

As liver transplantation becomes commonplace in many centers, the role of radiology is also becoming more and more important in preoperative imaging of liver transplantation recipient (e.g., portal vein patency and potential postoperative steal, staging of hepatocellular carcinoma), preoperative imaging of live liver donor (e.g., hepatic volumetry and assessment of hepatic steatosis), and screening for postoperative complications. For timely detection of vascular complications after liver transplantation, routine meticulous surveillance Doppler US program is important within a first few postoperative days. If Doppler US is inconclusive (particularly for hepatic artery obstruction), a prompt use of second line-up (contrast-enhanced US/CT) would avoid the delay of diagnosis. Sometimes, it is mandatory to compare with preoperative features as reference (for example, portal hypertension-steal in recipient, biliary anatomy in donor). Dedicated radiologist, fully understanding liver transplantation-related issues, will assure timely diagnosis and proper management of postoperative complications in these patients and enhance the role of radiologic studies.

[Refresher Course 1: Transplantation Imaging]

RC01-2

Imaging of Pancreas Transplantation

Se Jin Choi

University of Ulsan College of Medicine, Asan Medical Center, Korea

Pancreas transplantation (PT) remains the standard treatment for patients with insulin-dependent diabetes mellitus (DM), particularly type 1 DM. By restoring endogssenous insulin production, PT helps sustained glycemic control, improves metabolic stability, and reduces complications associated with poorly controlled diabetes and renal failures. Over the past decades, advances in surgical techniques, immunosuppressive regimens, perioperative management, have improved graft survival rates and patient outcomes. Despite these improvements, PT still had higher complication rate than other solid organ transplants, and complication continue to be significant causes of morbidity and graft loss, in addition to rejection. Importantly, graft survival is closely linked to the early recognition and prompt management of these complications. Clinical diagnosis can be challenging because laboratory findings are often nonspecific, and serum markers may not reliably reflect graft viability or early vascular compromise. In this context, imaging plays a central role in both routine postoperative assessment and the evaluation of suspected complications. Radiologists must therefore be familiar not only with the expected imaging appearance of a transplanted pancreas, but also with the complications. Given the complex surgical anatomy, including arterial and venous anastomoses and enteric drainage configurations, a comprehensive multimodality imaging approach is essential. This lecture reviews the fundamental surgical techniques of pancreas transplantation, the normal postoperative imaging findings, and the vascular, parenchymal, and enteric complications encountered in clinical practice.

[Refresher Course 1: Transplantation Imaging]

RC01-3

Imaging of Kidney Transplantation

Seo Yeon Youn

The Catholic University of Korea, College of Medicine, Seoul St. Mary's Hospital, Korea

Pre-transplantation imaging work-up

Multidetector computed tomography is the modality of choice. In donors, it maps renal parenchyma and vascular variants, which is essential for surgical planning. In recipients, it evaluates aortoiliac calcifications; surgeons need a calcification-free arterial segment of at least 3 cm for safe anastomosis.

Perioperative imaging work-up

Duplex ultrasound evaluates major complications. Allograft compartment syndrome uniquely presents with absent cortical flow. Renal vein thrombosis classically shows absent venous flow and reversed diastolic arterial flow. A key diagnostic pitfall: elevated resistive indices (RIs) and reversed diastolic flow are nonspecific, also occurring in acute tubular necrosis (ATN) and acute rejection.

Long-term postoperative imaging and late complications

Long-term surveillance targets chronic rejection and late complications. Chronic rejection causes functional decline with nonspecific ultrasound findings like elevated RIs, making protocol biopsy the diagnostic standard. Transplant renal artery stenosis manifests after 3 months with refractory hypertension. Practical diagnostic clues include an anastomotic peak systolic velocity over 340 to 400 cm/sec and a downstream tardus-parvus waveform.

Neoplastic and unusual conditions in the transplanted patient

Immunosuppression elevates malignancy risk significantly. Renal cell carcinoma risk is 6 times higher in allografts. Urothelial carcinoma carries increased risk, notably in patients with BK virus. Post-transplant lymphoproliferative disorder manifests as a low-attenuation mass encasing the hilum and causing obstruction.

Take-home message: Successful imaging requires understanding surgical anatomy and complication timelines. Precise interpretation empowers prompt, targeted therapies for graft salvage.

References:

1. Catalá V, Martí T, Diaz JM, et al. Use of multidetector CT in presurgical evaluation of potential kidney transplant recipients. RadioGraphics 2010;30:517-531.

2. Sebastià C, Peri L, Salvador R, et al. Multidetector CT of living renal donors: lessons learned from surgeons. RadioGraphics 2010;30:1875-1890.

3. Ghonge NP, Goyal N, Vohra S, et al. Renal transplant evaluation: multimodality imaging of post-

transplant complications. Br J Radiol 2021;94:20201253.

4. Sugi MD, Joshi G, Maddu KK, et al. Imaging of renal transplant complications throughout the life of the allograft: comprehensive multimodality review. RadioGraphics 2019;39:1327-1355.

5. Low G, Crockett AM, Leung K, et al. Imaging of vascular complications and their consequences following transplantation in the abdomen. RadioGraphics 2013;33:633-652.

[Refresher Course 1: Transplantation Imaging]

RC01-4

Imaging of Post-BM Transplantation

Sun Kyung Jeon

Seoul National University College of Medicine, Seoul National University Hospital, Korea

Bone marrow transplantation is widely used for hematologic diseases, and abdominal imaging is essential for detecting post-transplant complications. This lecture focuses on practical CT findings of graft-versus-host disease (GVHD) and infection, emphasizing post-transplant timing and organ-specific patterns.

Acute GVHD typically occurs within 100 days and most often involves the bowel and liver. Intestinal GVHD commonly shows bowel wall thickening, mucosal hyperenhancement, submucosal edema, and mesenteric hyperemia, with possible ileus, ascites, or pneumatosis in severe cases. Chronic GVHD is more variable and may mimic inflammatory or ischemic bowel disease. Hepatic GVHD may show hepatomegaly, periportal edema, heterogeneous enhancement, and cholestatic features, although imaging can be subtle. Infections vary by immune status and timing: early bacterial/fungal infections and later viral infections such as CMV. CT may demonstrate enterocolitis, hepatosplenic candidiasis with multiple small hypoattenuating lesions, or splenic infarcts. CMV colitis can overlap with GVHD but often shows predominant colonic involvement and deep ulceration. Other key entities include sinusoidal obstruction syndrome (hepatomegaly, ascites, periportal edema, patchy enhancement) and post-transplant lymphoproliferative disorder (nodal or extranodal masses).

A structured approach combining timing, clinical context, and imaging patterns improves diagnosis and supports urgent management.

[Refresher Course 2: Updates of GY Malignant Tumors]

RC02-1

The Implications of the 2023 New FIGO Stage in Endometrial Cancer from a Radiologist's Perspective

Stephanie Nougaret

Montpellier Cancer Institute, France

Endometrial cancer is the most common gynecologic malignancy in high-income countries, with an increasing incidence driven by aging populations and metabolic risk factors. Accurate preoperative staging is crucial to guide surgical strategy, lymph node assessment, and adjuvant treatment. In this context, magnetic resonance imaging (MRI) remains the cornerstone of local staging and risk stratification.

The 2023 revision of the FIGO classification introduces major conceptual changes, shifting from a purely anatomic staging system to a risk-oriented framework that integrates histologic subtype, tumor grade, lymphovascular space invasion, and molecular classification. These updates reinforce the central role of MRI as a non-invasive tool capable of providing comprehensive tumor phenotyping before treatment.

Multiparametric MRI allows precise evaluation of myometrial invasion, cervical stromal involvement, and adnexal extension. Beyond conventional staging, MRI contributes to the identification of aggressive disease patterns, such as deep myometrial invasion, diffuse tumor growth, and extrauterine spread, all of which are associated with poorer prognosis. Diffusion-weighted imaging and dynamic contrast-enhanced sequences further improve lesion conspicuity and assessment of tumor aggressiveness.

In the era of FIGO 2023, MRI findings must be interpreted in close correlation with histopathologic and molecular data to support individualized management. MRI plays an increasing role in selecting patients for fertility-sparing treatment, tailoring the extent of surgery, and optimizing multidisciplinary decision-making. Emerging approaches, including radiomics and artificial intelligence, hold promise to extract additional prognostic and predictive information from MRI, potentially enabling true precision imaging in endometrial cancer.

[Refresher Course 2: Updates of GY Malignant Tumors]

RC02-2

Optimizing Cervical Cancer Staging with Advanced MR Imaging: A Practical Guide for Radiologist

Tsukasa Saida

Institute of Medicine, University of Tsukuba, Japan

FIGO 2018 Staging and MRI Protocol Optimization Under the FIGO 2018 staging system, imaging is now essential for accurate stage assignment. T2WI is the fundamental sequence for staging, and it is mandatory to include the oblique axial plane obtained perpendicular to the long axis of the cervix to accurately assess parametrial invasion (PMI). Furthermore, DWI with at least two b-values (Low: 0–50 s/mm^2, High: 800–1000 s/mm^2) is critical. Furthermore, advanced technologies significantly enhance diagnostic performance: 3D-T2WI/DWI with isotropic voxels allows for multi-planar reconstruction in any plane, which is invaluable for tilted or retroflexed uteri. Deep Learning Reconstruction improves signal-to-noise ratio and sharpness by effectively isolating noise, thereby maintaining high spatial resolution.

Assessment of PMI Accurate assessment of PMI is crucial, as it marks the critical transition in clinical management from surgery to concurrent chemoradiotherapy. MRI is superior for identifying PMI. While an intact low-signal stromal ring on T2WI is a reliable negative predictive factor, the loss of this signal—especially when accompanied by spiculated margins, nodular extensions, or vascular encasement—indicates PMI.

WHO Classification and Gastric-type Adenocarcinoma (GAS) The 2020 WHO classification categorizes cervical tumors by their association with HPV. HPV-independent carcinomas, such as GAS, are generally more aggressive and often present a diagnostic challenge. Their typical location near the internal os limits the efficacy of conventional scraping cytology. Radiologically, GAS and its precursor, Lobular Endocervical Glandular Hyperplasia (LEGH), typically present as a multicystic mass with a Cosmos or microcystic pattern containing serous fluid. A key diagnostic feature is the localized proliferation near the internal os; this growth pattern frequently causes displacement of the cervical canal, a finding that effectively distinguishes these lesions from benign, which typically remain midline.

[Refresher Course 2: Updates of GY Malignant Tumors]

RC02-3

O-RADS for Assessment of Adnexal Lesions: Why, When and How

Lori M. Strachowski

University of California, San Francisco, USA

The American College of Radiology's Ovarian-Adnexal Reporting and Data System (O-RADS) is a dual-modality risk stratification tool for adnexal lesions comprised of an ultrasound (US) and magnetic resonance imaging (MRI) arm. US is considered the primary imaging tool for lesion detection and O-RADS US provides characterization and management recommendations. O-RADS MRI is a complementary arm of the system used as a secondary, problem-solving tool providing higher specificity for lesions with solid tissue. This presentation will focus primarily on O-RADS US including the reasons the system was created and basis for support, when the system should be applied and how to assess and score a lesion into one of six assessment categories using an algorithmic approach. A brief overview of O-RADS MRI will also be discussed. At the end of this presentation, the learner will have a better understanding of the role of O-RADS in assessing cancer risk of adnexal lesions based on morphologic features, approved lexicon terminology and rules for system use.

[Refresher Course 2: Updates of GY Malignant Tumors]

RC02-4

O-RADS Case Examples with Pearls and Pitfalls

Lori M. Strachowski

University of California, San Francisco, USA

This presentation will use a case-based format to demonstrate how to apply the Ovarian-Adnexal Reporting and Data System (O-RADS) in everyday clinical practice. Handy tools to assist in scoring an adnexal lesion with O-RADS US and MRI will be demonstrated, including the O-RADS US smartphone calculator and O-RADS MRI web-based calculator. Pitfalls for each modality arm of the system will be included. Pearls will be highlighted to increase the likelihood of accurate characterization and O-RADS success in risk stratification of adnexal lesions.

[ESGAR Honorary Lecture]

HL01-1

Imaging the Small Bowel in IBD-Where are we now

Stuart Taylor

University College London, UK

The use of cross-sectional imaging to evaluate the small bowel in inflammatory bowel disease (IBD) has increased exponentially over the last 10 years. MRI, ultrasound and to a lesser extent CT are now first line tests in the diagnosis and staging of small bowel IBD and play a vital role in disease phenotyping and assessment of treatment efficacy. The lecture will review lessons learnt from the METRIC trial about the relative strengths and weakness of MR enterography and ultrasound in diagnosis and staging of Crohns disease. The validated signs of disease activity on cross sectional imaging will then be presented, along with disease activity scores. The concept of treat to target and in particular transmural healing will be presented, along with new consensus guidelines on the greater use of imaging in the management of IBD patients. Stricture characterization will be discussed and the potential for new functional MRI techniques in assessment of fibrosis. Finally, an approach to the use of MRE and US in day-to-day clinical practice will be presented

[Special Focus 3: Imaging Assessment in Metabolic Liver Disease: From MASLD to HCC]

SF03-1

Epidemiology, Pathophysiology & Clinical Outcome of MASLD & MASH

Han Ah Lee

Chung-Ang University College of Medicine, Chung-Ang University Seoul Hospital, Korea

Epidemiology: A Global Paradigm Shift

Metabolic dysfunction-associated steatotic liver disease (MASLD) has emerged as the most prevalent chronic liver disease worldwide, affecting approximately 25-30% of the global population. The transition from NAFLD to MASLD nomenclature reflects a more precise focus on cardiometabolic risk factors, emphasizing the presence of at least one of five metabolic triggers: overweight/obesity, hyperglycemia, hypertension, high triglycerides, or low HDL cholesterol. The prevalence of MASLD is closely mirrored by the global obesity and type 2 diabetes (T2DM) epidemics. Within this spectrum, Metabolic dysfunction-associated steatohepatitis (MASH) represents the progressive form, characterized by hepatic inflammation and varying degrees of fibrosis. Alarmingly, MASH is rapidly becoming a leading indication for liver transplantation and a primary driver of hepatocellular carcinoma (HCC) globally.

Pathophysiology: The Multi-Parallel Hit Model

The pathogenesis of MASH is complex and multifactorial, moving beyond the traditional "two-hit" hypothesis toward a "multi-parallel hit" model. It begins with insulin resistance, which leads to increased lipolysis in adipose tissue and enhanced de novo lipogenesis in the liver. This results in the accumulation of toxic lipid species, causing lipotoxicity and endoplasmic reticulum (ER) stress. Concurrently, gut dysbiosis and increased intestinal permeability allow the translocation of pathogen-associated molecular patterns (PAMPs) into the portal circulation, triggering innate immune responses via Toll-like receptors. Chronic activation of Kupffer cells and recruitment of proinflammatory macrophages drive hepatic inflammation. This inflammatory milieu activates hepatic stellate cells (HSCs), the principal effectors of fibrosis, leading to the excessive deposition of extracellular matrix. Genetic factors, such as the *PNPLA3* and *TM6SF2* polymorphisms, also play a significant role in determining individual susceptibility and disease progression.

Clinical Outcome: Beyond Liver-Related Events

The clinical progression of MASLD is highly variable. While many patients remain stable, those with MASH are at significant risk of progressing to advanced fibrosis, cirrhosis, and its associated complications, including portal hypertension, hepatic decompensation, and HCC. In addition, cardiovascular disease (CVD) is the leading cause of mortality in patients with MASLD, followed by extrahepatic malignancies. The presence of advanced fibrosis (Stage F3 or F4) is the most robust histological predictor of liver-related mortality. Therefore, early identification of high-risk patients through non-invasive tests (NITs) and liver stiffness measurement is crucial to optimize management and improve long-term survival.

[Special Focus 3: Imaging Assessment in Metabolic Liver Disease: From MASLD to HCC]

SF03-2

Non-invasive Imaging Assessment of MASLD and MASH

Jeong Min Lee

Seoul National University College of Medicine, Seoul National University Hospital, Korea

Metabolic dysfunction-associated steatotic liver disease (MASLD) is the most prevalent chronic liver disease globally, encompassing a spectrum from simple steatosis to metabolic dysfunction-associated steatohepatitis (MASH), fibrosis, and hepatocellular carcinoma. With the advent of effective pharmacotherapies such as resmetirom and incretin-based agents, the non-invasive identification of patients with "at-risk MASH" has become a clinical priority. This lecture reviews the current imaging tools for MASLD assessment, including ultrasound-based techniques (B-mode US, CAP, and elastography), MRI-PDFF for steatosis quantification, and MR elastography for fibrosis staging, in accordance with the latest AASLD and EASL guidelines. Composite imaging scores—FAST, MAST, and MEFIB—are discussed as promising strategies for identifying at-risk MASH without liver biopsy. Emerging multiparametric MRI approaches incorporating corrected T1 mapping and artificial intelligence–driven ultrasound analytics are also highlighted as future directions. As the management paradigm shifts from biopsy-dependent diagnosis to imaging-centric evaluation, radiologists play an increasingly essential role in patient stratification, treatment eligibility assessment, and longitudinal monitoring. Prospective multicenter validation and standardization of imaging protocols remain critical to fully integrate these non-invasive tools into routine clinical practice

[Special Focus 3: Imaging Assessment in Metabolic Liver Disease: From MASLD to HCC]

SF03-3

More Than Weight: Advanced Imaging of Body Composition in Obesity

Kyung Won Kim

University of Ulsan College of Medicine, Asan Medical Center, Korea

For decades, obesity has been defined by body mass index (BMI), a convenient but biologically crude metric. Individuals with identical BMI values often display strikingly different metabolic risks, muscle integrity, and organ-specific fat deposition. Obesity is not merely excess weight; it is a disorder of metabolic architecture. Advanced imaging now allows us to move beyond anthropometry toward biologically meaningful phenotyping.

CT and MRI have transformed body composition analysis from volumetric measurement to tissue characterization. Visceral adipose tissue (VAT) volume correlates with cardiometabolic risk, yet emerging evidence suggests that fat quality may matter more than quantity. Radiomic features, such as attenuation heterogeneity and texture entropy, reflect inflammatory and fibrotic remodeling within adipose tissue. Perivascular fat attenuation, for example, has been linked to coronary inflammation, illustrating how imaging can infer fat biology rather than simply measure fat mass.

Skeletal muscle assessment has undergone a similar evolution. While cross-sectional muscle area at the L3 level remains a surrogate for whole-body muscle mass, muscle attenuation on CT, reflecting myosteatosis, has emerged as a stronger predictor of frailty, chemotherapy toxicity, and mortality. Muscle is increasingly recognized as an endocrine organ; thus, low attenuation may signal metabolic dysfunction rather than structural loss alone. In this context, muscle quality surpasses muscle quantity as a determinant of resilience.

Ectopic fat deposition further reframes obesity as organ-specific disease. Hepatic steatosis, pancreatic fat infiltration, pericardial fat, and even bone marrow adiposity contribute to metabolic vulnerability. MRI-based proton density fat fraction enables precise quantification of these compartments, supporting longitudinal monitoring.

The rise of GLP-1 receptor agonists introduces a new imaging imperative. Rapid pharmacologic weight loss may entail disproportionate lean mass reduction. Imaging-based surveillance is essential to distinguish healthy metabolic remodeling from unintended sarcopenia.

Artificial intelligence now enables automated segmentation of muscle and adipose tissue from routine CT scans. Every abdominal CT has become a latent metabolic dataset. Opportunistic screening transforms diagnostic imaging into a platform for incidental metabolic diagnosis, integrating body composition metrics into clinical workflows.

Obesity is not a single entity but a spectrum of imaging-defined phenotypes: visceral-dominant, sarcopenic, ectopic fat–dominant, or inflammatory adipose subtypes. As quantitative imaging converges with AI and longitudinal analytics, we approach the concept of a metabolic digital twin, a dynamic representation of an individual's evolving body composition.

[Special Focus 3: Imaging Assessment in Metabolic Liver Disease: From MASLD to HCC]

SF03-4

HCC in MASLD- Risk, Surveillance & Diagnostic Challenges

Ijin Joo

Seoul National University College of Medicine, Korea

Metabolic dysfunction–associated steatotic liver disease (MASLD) has emerged as a rapidly increasing underlying liver disease in patients with hepatocellular carcinoma (HCC). While viral hepatitis–related HCC is declining in many regions due to vaccination and antiviral therapies, MASLD-associated HCC continues to rise worldwide, reflecting the global epidemic of metabolic dysfunction and obesity. This epidemiologic shift introduces new challenges in risk assessment, surveillance strategies, and imaging-based diagnosis.

Current surveillance recommendations and noninvasive diagnostic algorithms, including LI-RADS, are primarily designed for patients with cirrhosis or chronic hepatitis B. However, a substantial proportion of MASLD-related HCC develops in noncirrhotic livers. Despite this, noncirrhotic MASLD is not currently considered a target population for routine HCC surveillance or noninvasive imaging diagnosis because the overall annual incidence remains below accepted surveillance thresholds and the pre-test probability of HCC is lower. As a result, considerable research efforts are focused on identifying higher-risk subgroups within MASLD. Advanced fibrosis, the presence of metabolic dysfunction–associated steatohepatitis (MASH), metabolic comorbidities such as diabetes, genetic susceptibility variants—are being investigated as potential modifiers of HCC risk, although no standardized risk model has yet been established. In patients with MASLD-related cirrhosis, surveillance is recommended but presents additional practical challenges. Obesity and hepatic steatosis can substantially reduce ultrasound sensitivity due to acoustic attenuation and heterogeneous parenchymal echotexture, resulting in higher rates of inadequate examinations and potential delays in tumor detection. These limitations have led to growing interest in alternative strategies, including abbreviated MRI protocols.

This lecture will review the evolving epidemiology of MASLD-associated HCC, discuss current evidence and gaps in risk stratification, and address surveillance challenges specific to this population. In addition, imaging characteristics and potential diagnostic pitfalls in MASLD will be examined, with a focus on the application and limitations of LI-RADS in both cirrhotic and noncirrhotic settings.

[Refresher Course 3: State-of-the-Art Biliary Imaging]

RC03-1

Cholangiopathies: Imaging-based Approaches for Diagnosis

Maria Antonietta Bali

Università Cattolica del Sacro Cuore, Roma, Italy

Cholangiopathies encompass a broad and heterogeneous spectrum of disorders affecting the intrahepatic and/or extrahepatic bile ducts arising from different etiologies and consisting of both benign non-neoplastic and malignant neoplastic diseases. A recently proposed etiology-based classification system categorizes cholangiopathies into genetic, immune-mediated, infectious, idiopathic, malignant, and others which includes drug-induced and ischemic injury cholangiopathy.

Despite their diverse etiologies, these conditions often present with overlapping clinical manifestations and laboratory abnormalities, making differential diagnosis challenging. Nevertheless, establishing an accurate diagnosis at an early stage—when possible—is crucial to prevent disease progression leading to secondary biliary cirrhosis with portal hypertension, end-stage liver disease, and an increased risk of malignancy, particularly cholangiocarcinoma. In this context, imaging plays a pivotal role.

Non-invasive imaging modalities, including ultrasound (US), computed tomography (CT), and magnetic resonance imaging (MRI), are all part of the diagnostic work-up. Owing to its wide availability and accessibility, US is typically used as the first-line modality for the detection of bile duct dilatation. Cross-sectional techniques, such as contrast-enhanced computed tomography and magnetic resonance imaging, provide comprehensive assessment of intrahepatic and extrahepatic bile ducts, surrounding liver parenchyma, and extra-biliary extra-hepatic manifestations. MR, in combination with magnetic resonance cholangiopancreatography (MRCP) and diffusion-weighted imaging (DWI), represent the cornerstone for non -invasive biliary imaging. This comprehensive approach allows for highly accurate detection of ductal strictures, irregularities, and segmental involvement, critical for the differential diagnosis together with associated findings involving the liver but also other organs, such as the pancreas and kidneys, significantly contributing to the correct diagnosis.

Importantly, this imaging-based diagnostic framework should be integrated in a multimodality approach including clinical evaluation, laboratory findings, and, when indicated, data from more invasive endoscopy-based imaging techniques to provide personalized management of patients with suspected cholangiopathies.

[Refresher Course 3: State-of-the-Art Biliary Imaging]

RC03-2

Beyond Diagnosis: Preoperative Staging & Resectability Assessment for Extrahepatic Cholangiocarcinoma

Bohyun Kim

The Catholic University of Korea, College of Medicine, Seoul St. Mary's Hospital, Korea

Curative-intent surgery remains the only definitive treatment for extrahepatic cholangiocarcinoma (eCCA), yet only a minority of patients are resectable at presentation. Thus, preoperative imaging must extend beyond diagnosis and function as a surgical roadmap. Accurate delineation of longitudinal biliary spread, assessment of vascular invasion, detection of nodal and distant metastases, and estimation of future liver remnant are critical to avoid futile surgery and to achieve R0 resection.

This lecture provides a structured, MRI-based approach to staging and resectability assessment in perihilar and distal eCCA. Emphasis will be placed on high-quality 2D and 3D MRCP for precise mapping of ductal involvement, multiphasic contrast-enhanced imaging for evaluating portal vein and hepatic artery relationships, and diffusion-weighted imaging for tumor characterization and metastatic detection. Practical considerations, including imaging before biliary drainage and thoughtful contrast agent selection, will be addressed to optimize diagnostic performance.

Key determinants of resectability, including Bismuth–Corlette classification, patterns of tumor–vessel contact (abutment vs. encasement), bilateral second-order duct involvement, contralateral vascular compromise, nodal status, and residual liver volume thresholds, will be integrated into a checklist-based reporting framework. By shifting focus from detection to operative planning, imaging becomes decisively strategic in multidisciplinary management of eCCA.

[Refresher Course 3: State-of-the-Art Biliary Imaging]

RC03-3

IPNB: Detection, Differential & Risk Assessment

Hyo Jung Park

University of Ulsan College of Medicine, Asan Medical Center, Korea

1. Introduction and Definition

Intraductal Papillary Neoplasm of the Bile Duct (IPNB) is defined by the WHO (2019) as a grossly visible premalignant neoplasm characterized by the intraductal growth of biliary-type epithelium. While biliary intraepithelial neoplasia (BilIN) is a microscopic, radiologically undetectable precursor to cholangiocarcinoma (CCC), IPNB is a sizable, radiologically detectable lesion.

2. Pathological Spectrum

IPNB follows a stepwise progression from low-grade to high-grade intraepithelial neoplasia, eventually leading to invasive carcinoma.

IPNB is often considered the biliary counterpart of Pancreatic IPMN. They share similarities in growth patterns (intraductal papillary growth with superficial spread), mucin production, and histopathologic subtypes (gastric, intestinal, pancreatobiliary, oncocytic). However, there are critical differences including the proportion of mucin production and aggressiveness.

A Japan-Korea collaborative consensus categorizes IPNB into two types. Type 1 is characterized by an intrahepatic location, IPMN-like features, frequent mucin production (80%), and a better clinical outcome. In contrast, Type 2 primarily involves the extrahepatic ducts, presenting with complex histological architecture and consistently high-grade features that result in a poorer prognosis

3. Radiological Manifestations:

The imaging features of IPNB are highly heterogeneous, varying by mass visibility, mucin secretion, and location. The radiologic spectrum can be categorized into several primary patterns:

- Intraductal mass with only proximal ductal dilatation.
- Intraductal mass with both proximal and distal ductal dilatation—the most common and unique feature of IPNB.
- Disproportional ductal dilatation without a visible mass, often caused by tiny tumors or mucin hypersecretion.
- Focal aneurysm-like or cystic dilatation of the duct containing the tumor.

4. Differential Diagnosis and Challenges

IPNB must be differentiated from several mimickers including HCC with bile duct invasion, recurrent pyogenic cholangitis, other cystic lesions including choledochal cyst, Caroli’s disaese, and mucinous cystic neoplasms.

5. Risk Assessment and Surgical Management

Tumor invasiveness is strongly correlated with an intraductal visible mass, tumor size, multiplicity, and bile duct wall thickening. Furthermore, significantly lower ADC values on DWI are associated with invasive carcinoma.

Treatment Principles

- Surgical Candidacy: All cases without distant metastasis are candidates for surgery due to the risk of biliary obstruction and progression.
- General Principle: Curative resection with negative margins is the goal, requiring major hepatectomy or bile duct resection.

Post-surgical outcomes for IPNB are generally better than conventional CCC, with a 5-year overall survival rate of approximately 80.9%. Despite curative resection, the recurrence rate is high (approx. 29.3%) due to tumor multiplicity and preoperatively undetected lesions. Consequently, potentially lifelong follow-up is required.

[Refresher Course 3: State-of-the-Art Biliary Imaging]

RC03-4

The 2026 KSAR Consensus Statement for IPNB

Dong Ho Lee

Seoul National University College of Medicine, Seoul National University Hospital, Korea

Intraductal papillary neoplasm of the bile duct (IPNB) is a rare biliary tumor characterized by grossly visible intraductal papillary or villous proliferation of biliary-type epithelium. It represents a histologic continuum ranging from low- and intermediate-grade intraepithelial neoplasia to high-grade dysplasia and invasive carcinoma. Recognized as a precursor of Cholangiocarcinoma, IPNB is distinct from biliary intraepithelial neoplasia and mucinous cystic neoplasm. Lesions may arise in the intrahepatic or extrahepatic bile ducts and can be solitary or multifocal.

Radiologic manifestations are heterogeneous, varying from subtle or radiologically occult lesions to marked bile duct dilatation with or without visible intraductal masses. Given the high frequency of recurrent biliary obstruction and the potential for malignant transformation, treatment is generally recommended regardless of dysplasia grade. Surgical resection is the mainstay of management, and cases with associated invasive carcinoma should be approached similarly to cholangiocarcinoma. Therefore, precise imaging-based assessment of tumor extent is critical for therapeutic planning. However, accurate radiologic evaluation is challenging due to small papillary lesions, multifocality, and superficial spreading patterns. Currently, no standardized imaging guidelines exist regarding optimal imaging modalities or key features that should be systematically evaluated.

To address this gap, the Korean Society of Abdominal Radiology (KSAR) IPNB study group developed consensus recommendations focusing on imaging evaluation. A comprehensive literature review was conducted using PubMed, Embase, and the Cochrane Library. Through hierarchical screening and collaborative discussion, eight key clinical questions and 15 tentative statements were formulated across three domains: imaging techniques, tumor extent evaluation, and post-treatment follow-up. This lecture will present the development process and summarize the key questions and consensus statements. Establishing a standardized imaging-based framework is expected to facilitate systematic evaluation, improve diagnostic consistency, and optimize management strategies for patients with IPNB.

ACAR
2026
THE 13th ASIAN CONGRESS OF ABDOMINAL RADIOLOGY

Invited Session

Mar. 20 (Fri.)

! Abstracts can be found by searching with the Presentation Code !

[Refresher Course 4: Recent Updates in Body Imaging]

RC04-1

Recent Technical Innovations in DWI

Ryan L. Brunsing

Stanford University, USA

In this talk abdominal and pelvic diffusion-weighted imaging (DWI) will be reviewed including basic principles and emerging technologies, discussed through the lens of common clinical applications.

DWI detects the microscopic motion of water in tissue with established clinical applications. However, single-shot SE-EPI DWI (ss-DWI) remains widely in use clinically. While fast, ss-DWI suffers from limited spatial resolution and geometric distortion with quantitative limitations. Motion artifacts and failed fat suppression remain challenging for all DWI methods.

Multi-shot DWI (ms-DWI), reduced-FOV (rFOV) imaging, and non-traditional k-space trajectories can offer improved spatial resolution and reduced distortion. Gradient moment nulling (GMN) can reduce sensitivity to bulk tissue motion. Numerous methods for better phase correction will be discussed. Data binning can reduce motion and improve image sharpness at the cost of scan time. Conversely, simultaneous multi-slice DWI can reduce scan time by factors of 50% or more. Deep-learning reconstruction shows promise for improved SNR and sharpness while preserving quantitative integrity. Practical considerations include gating-based respiratory mitigation and fat suppression reliability will be discussed.

Hardware is central to improved body DWI. Fast, high-performance gradients shorten TE, enabling higher b-values and better diffusion contrast. While this may limit the applications of some DWI methods on older scanners, intelligent diffusion gradient waveform design can help mitigate some hardware limitations.

DWI data can be used to calculate quantitative imaging biomarkers, the most well-known being ADC. Advanced models—ex: IVIM, DKI, SEM, RSI—result in other interesting quantitative metrics that may provide unique clinical information. Some use cases will be briefly discussed.

In sum, abdominal and pelvic DWI is primed for broader clinical use as modern hardware and software enable higher-resolution, robust imaging.

[Refresher Course 4: Recent Updates in Body Imaging]

RC04-2

Pioneering Clinical Applications of 5T Abdominal MRI

Liang Zhu

Peking Union Medical College Hospital, Beijing, China

Recently, an ultra-high gradient 5.0T clinical MR system has been developed and commercialized for whole-body imaging. Its advantages for high-resolution brain imaging and cranial MR angiography over 3.0T systems has already been shown, while evidence concerning its superiority over 3.0T in abdominal applications remains scarce. Here we introduce research updates in this field, especially our preliminary experience of 5.0T pancreatic imaging.

We firstly applied 5.0T MRI/MRCP in patients with pancreatic cystic lesions (PCLs, 2021.10-2023.03). 35 patients with PCLs underwent 5.0T MRI, as well as 3.0T MRI (n=21) and/or multi-detector CT (MDCT, n=33). We found that the subjective image quality, as well as signal-to-noise ratio (SNR) of T1WI was superior with 5.0T, while T2WI, DWI and MRCP was comparable between the two field strengths. The measurement of cyst size and MPD width received excellent consistency across different modalities. 5.0T MRI detected more tiny cysts, intra-cystic septa and communication between cyst and MPD, compared to 3.0T and MDCT. The diagnostic accuracy for the nature of the PCLs was also higher with 5.0T.

We also explored the value of 5.0T MRI for insulinoma surgical planning. In a surgical cohort of insulinomas over 2.5 years (2021.10-2024.2), 41 patients underwent 5.0T MRI, as well as 3.0T MRI (n=20) and/or MDCT (n=39). We compared image quality, lesion-to-pancreas contrast (LPC), MPD clarity and tumor-MPD distance for surgical planning. It turned out that the subjective image quality and SNR of T1WI and DWI was superior with 5.0T, while T2WI was comparable. MDCT demonstrated the best LPC of insulinoma, while 5.0T MRI was better than 3.0T. 5.0T MRI detected 2 insulinomas which were negative with 3.0T. While tumor-MPD distance was clearly visible in 96.0% patients on 5.0T, the distance relationship could be visualized in only 64.0% and 53.8% patients on 3.0T and MDCT, respectively. Therefore, 5.0T MRI could serve as a comprehensive assessment tool for one-stop surgery planning for patients with insulinomas.

Finally, we performed intra-individual comparison of 5.0T and 3.0T multi-phasic contrast-enhanced study in patients with suspected pancreatic lesions (n=46, 2024.10-2025.06). 5.0T MRI demonstrated significantly higher SNR in pre-contrast T1WI, late-arterial phase (LAP) and delayed-phase (DP) images. Enhancement ratio (ER) was higher with 5.0T MRI for LAP and DP as well. 5.0T also achieved significantly higher LPC during the delayed phase. The interobserver agreement and diagnostic confidence for tumor invasion of common hepatic artery and gastroduodenal artery was higher with 5.0T. The diagnostic performance for determining malignancy, detecting liver metastasis and peritoneal metastases were generally comparable.

In summary, 5.0T MRI pancreatic MRI was clinically feasible and demonstrated certain advantages for revealing lesion details and reduce diagnostic uncertainty.

[Refresher Course 4: Recent Updates in Body Imaging]

RC04-3

Low-field MRI in 2026: Challenges & Opportunities

Michael Ohliger

University of California, San Francisco, USA

Applications of MRI in the abdomen and pelvis have expanded dramatically in recent years. Once primarily a problem-solving tool, MRI is now a first-line modality for hepatocellular carcinoma surveillance, prostate cancer evaluation, staging pelvic malignancies, and monitoring chronic liver disease. As clinical demand grows, improving access to MRI has become increasingly urgent. This need has renewed interest in lower-field systems, including 0.55T MRI. Lower field strength reduces costs related to magnet construction and siting, and enables larger bore designs beyond the current 70-cm “wide-bore” systems, improving patient comfort and accommodating larger body sizes.

Although signal-to-noise ratio (SNR) decreases at lower field, several physical properties help compensate. Shorter tissue T1 allows faster repetition times. Longer T2* permits extended readouts with less distortion. Lower specific absorption rate (SAR) enables higher flip angles. Gadolinium relaxivity is higher at lower field, potentially improving contrast enhancement. Susceptibility artifacts, particularly from metallic implants, are also substantially reduced. Modern advances in image acceleration techniques, improved motion management, and machine learning-based denoising and image sharpening further improve 0.55T performance and help offset intrinsic SNR limitations. Together, these developments have made clinically robust abdominal and pelvic imaging feasible at low field.

Despite this progress, challenges remain. Quantitative tissue biomarkers require further validation and achieving the high spatial resolution needed for detailed cancer staging can be difficult. Continued clinical evaluation is necessary to define diagnostic performance relative to established higher-field systems. Looking forward, fully exploiting low-field MRI will often require rethinking acquisition strategies to align with its distinct physical characteristics. While 0.55T systems lower costs, reliance on superconducting magnets and associated infrastructure may still limit accessibility. Further innovation toward even lower-field systems may be necessary to meaningfully expand global access to MRI.

[Refresher Course 4: Recent Updates in Body Imaging]

RC04-4

Beyond the Protons: Multi-nuclei Body MRI

Satoshi Goshima

Hamamatsu University School of Medicine, Hamamatsu, Japan

Proton MRI has become widely established as the cornerstone of clinical imaging, offering exceptional soft tissue contrast and versatility across various anatomical regions. Its widespread availability and continuous technical improvements have made it an indispensable diagnostic tool in modern medicine. However, the growing interest in multinuclear MRI techniques has opened new horizons for metabolic and functional imaging beyond the capabilities of conventional proton imaging.

Among multinuclear approaches, phosphorus-31 MR spectroscopy (^{31}P MRS) and sodium-23 imaging (^{23}Na MRI) have garnered significant attention for body imaging applications. ^{31}P MRS provides valuable insights into cellular bioenergetics by detecting metabolites such as ATP, phosphocreatine, and inorganic phosphate, enabling non-invasive assessment of tissue metabolism in organs like the liver, kidneys, and skeletal muscle. ^{23}Na MRI, on the other hand, offers unique information about tissue viability and cellular integrity by mapping sodium concentration, which is particularly relevant for detecting early pathological changes in various body organs and tumors.

Looking toward the future, hyperpolarized carbon-13 pyruvate metabolic imaging holds tremendous promise. This technique enhances the MR signal by several orders of magnitude, allowing real-time visualization of pyruvate-to-lactate conversion, a key indicator of glycolytic metabolism. This approach could revolutionize cancer imaging by detecting altered metabolic signatures, monitoring treatment response, and differentiating aggressive from indolent tumors. Furthermore, applications in cardiac and hepatic metabolic assessment may provide unprecedented insights into organ dysfunction and disease progression, ultimately advancing personalized medicine approaches.

[Joint Symposium 1 (ACAR meets China)]

JS01-1

AI in Abdominal Imaging

Yanqi Huang

Guangdong Provincial People's Hospital (Guangdong Academy of Medical Sciences), Southern Medical University, China

This lecture provides a comprehensive overview of the current landscape and future directions of artificial intelligence (AI) in abdominal imaging. Focusing on oncologic applications, the presentation explores how AI technologies are transforming conventional radiological practice by extracting quantitative data from medical images, enhancing diagnostic workflows, and enabling predictive modeling for personalized patient management. The lecture is structured into three key thematic sections, each addressing a critical aspect of AI integration from technical foundations to clinical implementation.

The first part of the lecture introduces the paradigm shift from viewing medical images as visual representations to The lecture begins by introducing the paradigm shift from viewing medical images as visual representations to recognizing them as rich sources of quantitative data. Through radiomics and deep learning, routine CT and MRI examinations can be systematically analyzed to extract sub-visual features related to tissue characteristics, tumor heterogeneity, and perfusion dynamics. This quantitative approach transforms standard imaging into a repository of digital biomarkers for precision oncology.

The second part reviews the spectrum of AI applications in abdominal imaging. Automated detection and segmentation algorithms now enable consistent quantification of tumor burden across multiple organs, significantly reducing inter-reader variability and manual workload. Characterization models could assist in differentiating benign from malignant lesions, and tumor subtyping. Most importantly, emerging predictive models integrate imaging phenotypes with clinical and genomic data to forecast treatment response, recurrence risk, and patient survival. These capabilities represent a fundamental shift from descriptive radiology toward predictive and prognostic imaging, positioning AI as a key enabler of personalized cancer care.

The final part addresses challenges in translating AI tools into clinical workflows. Successful implementation requires seamless integration with PACS, model interpretability to build clinician trust, and rigorous external validation across diverse populations and imaging protocols. Regulatory approval, data privacy, and algorithmic fairness must also be carefully addressed.

In conclusion, this lecture aims to equip the audience with an understanding of how AI is reshaping abdominal imaging by automating routine tasks, uncovering hidden biomarkers, and enabling data-driven predictions to augment radiologists' capabilities in multidisciplinary cancer care.

[Joint Symposium 1 (ACAR meets China)]

JS01-2

Building LLM-Powered Workflows in Abdominal Radiology: Agents, Tools, and Governance

Jeong Hyun Lee

Sungkyunkwan University School of Medicine, Samsung Medical Center, Korea

An AI agent is defined as a system where a Large Language Model (LLM) dynamically directs its own processes and tool usage to accomplish tasks, contrasting sharply with rigidly coded workflows. The standardization of these capabilities is rapidly accelerating through open protocols like the Model Context Protocol (MCP), which seamlessly connects AI systems to external data and tools.

LLM-powered workflows are proving highly effective, particularly in human-supervised settings where generative AI significantly improves documentation efficiency without degrading diagnostic accuracy. For complex tasks like structured categorization, the most effective architecture is a hybrid approach that separates LLM feature extraction from deterministic algorithmic computation. This has demonstrated remarkable success, achieving 97% accuracy for O-RADS MRI scoring.

Despite significant industry hype, the true clinical deployment of autonomous agents remains nascent. A recent systematic review revealed that only 3.9% of "agentic AI" papers in neuroradiology actually met the definition of agentic behavior. Furthermore, even frontier models currently achieve only a 67.1% task completion rate on radiology-specific agent benchmarks. Consequently, the default for abdominal radiology should not be a fully autonomous agent, but rather a retrieval-grounded generation architecture.

The integration of agentic systems introduces various risks, notably the potential for compounding errors across multi-step processes. The deployment of these polished AI outputs also introduces the risk of automation complacency and the subsequent degradation of physician skills. From a regulatory perspective, no LLM-based device has been authorized to date. In Europe, most commercial radiology AI systems will be subject to strict "high-risk" regulations under the EU AI Act starting in August 2027. In response to these emerging challenges, professional bodies like the ACR have launched national AI quality assurance programs, emphasizing that institutions must establish continuous performance oversight, as static AI systems are expected to degrade in real-world performance over time.

[Joint Symposium 1 (ACAR meets China)]

JS01-3

Imaging in Informing Indivisualized Treatment in HCC

Hanyu Jiang

West China Hospital, Sichuan University, China

This lecture does not have an abstract.

[Joint Symposium 1 (ACAR meets China)]

JS01-4

Imaging of Hilar Tumors: What the Surgeon wants to know

Hsien Min Low

Tan Tock Seng Hospital, Singapore

Tumours of the liver hilum is often a straightforward diagnosis. However, several imaging features are frequently overlooked by radiologists, but are important considerations for hepatobiliary surgeons. This lecture aims to provide a framework for radiologists in evaluating liver hilar tumours and in the process communicate to the surgeon pertinent details which would affect resection.

[Joint Symposium 1 (ACAR meets China)]

JS01-5

Diagnostic Approach to Multiple Solid Renal Lesions on CT and MR Imaging: The SWISS Principle

Haiyi Wang

Chinese PLA General Hospital, Beijing, China

Multiple solid renal lesions are encountered in daily practice and may represent benign tumors, multifocal RCC, infection/ischemia, urothelial malignancy, or systemic disease. This lecture introduces a practical CT/MR workflow for radiologists using the SWISS principle, helping translate imaging pattern recognition into an efficient differential diagnosis and management-oriented report.

Step 1 (W/I): Well-defined vs ill-defined. First confirm that lesions are truly solid (exclude cysts/hemorrhagic cysts) and assess margins, distribution (bilateral vs unilateral; cortical vs medullary; collecting system involvement), and enhancement. On MRI, integrate T2 signal, DWI/ADC, chemical-shift imaging, and the presence of macroscopic fat or intralesional hemorrhage.

Step 2 (S): Syndromic, Sporadic, Systemic—based on imaging pattern plus clinical context.

For well-defined lesions:

Syndromic patterns suggest hereditary entities such as VHL, HPRCC, BHD, and TSC. Clues include bilaterality, multifocality, associated renal cysts, or extrarenal findings.

Sporadic tumors include RCC, AML (identify macroscopic fat or fat-poor AML clues), and oncocytoma (e.g., spoke-wheel enhancement/central scar—recognizing overlap with RCC). Characterize enhancement (hypervascular vs hypovascular), venous invasion, and metastatic signs to guide urologic decision-making.

For ill-defined lesions, prioritize non-neoplastic and infiltrative processes: pyelonephritis (striated nephrogram, perinephric inflammation, diffusion restriction), renal infarction (wedge-shaped cortical hypoenhancement, possible cortical rim sign), and transitional cell carcinoma when centered on the collecting system with urothelial thickening or hydronephrosis.

Systemic causes can mimic multifocal tumors: IgG4-related disease, lymphoma/leukemia, and metastases, often showing hypovascular infiltrative lesions and relevant history. The key take-home message is to apply SWISS systematically to narrow differentials, recommend targeted clinical correlation/genetic consideration when appropriate, and propose next steps (follow-up MRI, biopsy, or staging) aligned with patient care.

[Joint Symposium 1 (ACAR meets China)]

JS01-6

Primary Staging of Rectal Cancer: ESGAR MRI Consensus Update and Dual-Energy CT Potentials

Masashi Asano

Gifu University, Japan

The European Society of Gastrointestinal and Abdominal Radiology (ESGAR) released an updated consensus in January 2026 for MRI evaluation of rectal cancer, introducing several clinically important refinements. This lecture will provide a structured, consensus-based overview of the key MRI findings required for local staging.

High-resolution T2-weighted imaging remains the standard sequence, with emphasis on tumor location using the sigmoid take-off, the depth of extramural invasion, and the relationship to the mesorectal fascia. Mesorectal fascia involvement is now uniformly defined as a distance of ≤1 mm, including direct tumor extension, tumor deposits, irregular lymph nodes, and extramural vascular invasion (EMVI). Nodal staging has shifted toward a patient-level risk assessment based on morphological characteristics rather than size alone. In addition, updated acquisition protocols aim to improve reproducibility and promote more standardized reporting across institutions.

The potential role of dual-energy CT (DECT) will then be discussed in this lecture. Low-keV virtual monoenergetic images enhance iodine contrast and improve tumor–vessel conspicuity, enabling detection of EMVI with statistically equivalent accuracy to MRI. Our results demonstrate that 40-keV images significantly improve diagnostic performance for detecting EMVI compared with 70-keV images, suggesting a practical alternative when high-quality rectal MRI is unavailable or inconclusive.

In the future, photon-counting CT, with its higher spatial resolution and improved spectral separation, may allow more precise tissue characterization and support the development of quantitative imaging biomarkers, further refining staging and treatment stratification in rectal cancer.

[Refresher Course 5: GU Specific Diagnostic Classification Systems]

RC05-1

PI-RADS Essential and Updates

Anwar Padhani

Mount Vernon Cancer Centre, UK

Prostate MRI is central to the diagnostic pathway for prostate cancer (PCa), reducing unnecessary biopsies, improving the detection of clinically significant disease (csPCa), and limiting overdiagnosis of indolent tumours. The Prostate Imaging Reporting and Data System (PIRADS) version 2.1 is the current international standard for MRI data acquisition and interpretation. This review synthesises the evidence for its use, its strengths and limitations, and future developments. PI-RADS v2.1 improved the assessments of multiparametric MRI (mpMRI) by clarifying technical requirements, zone-specific interpretation rules, and structured reporting recommendations. Its diagnostic performance is well established, particularly for ruling out csPCa and guiding risk-adapted biopsy strategies. However, significant gaps remain. MRI image quality varies substantially across centres, and PI-RADS lacks a mechanism to exclude non-diagnostic scans, resulting in inconsistent classification. Several scoring challenges persist, most notably the ambiguous definition and heterogeneous management of PI RADS 3 lesions, imprecise lesion measurement standards, and limited guidance for central zone and atypical lesions. Gaps include the lack of strategies to assess background tissue changes, atypical malignancies, and infiltrative patterns. Cancer detection specificity and inter-reader agreement remain moderate, with significant discrepancies in transition zone assessments. Artificial intelligence (AI) holds promise for reducing variability, improving lesion detection, and optimising workflow, though rigorous validation and clear human-AI integration frameworks are needed. Advances in deep learning reconstructions improve image quality and enable shorter protocols, thereby supporting the adoption of biparametric MRI. A shift toward risk-based pathways, integrating MRI findings with PSA density and clinical parameters, is reflected in the forthcoming PI RADS Pathway 2026, which aims to standardize global biopsy practice and reduce unnecessary interventions.

[Refresher Course 5: GU Specific Diagnostic Classification Systems]

RC05-2

VI-RADS: Multiparametric MRI for Staging and Management of Bladder Cancer

Li-Jen Wang

Linkou Chang Gung Memorial Hospital, Chinese Taipei

The standard method of diagnosis and staging of Bladder cancer (BCA) is transurethral resection of bl adder tumor (TURBT) for obtaining histological proof of BCA and during TURBT, at least one bladder bi opsy containing muscle layer has been a routine procedure for assessing whether there is muscle inva sion. The confirmation of muscle invasion of BCA is an important step of clinical decision of patients' prognosis and treatment selection based on that muscle invasive bladder cancer (MIBC) has worse pr ognosis than non-
muscle invasive bladder cancer (NMIBC) and thus has different treatment strategies including cystect omy.

Bladder mpMRI could be served as a complimentary role for MIBC and NMIBC differentiation since TURBT assessment could be imprecise. Initial TURBT may sometimes insufficient based on several known facts: (1) high discordant rate to final proof, (2) sometimes absence of muscle layer of biopsy specimens, (3) high under-staging rate up to 50 %. In this context, the Vesical Imaging Reporting and DATA System (VI-RADS) has been thus recently proposed as a standardized guideline for multiparametric MRI (mpMRI) acquisition and interpretation.

VI-RADS used 5 scores to stratify the risk of muscle invasion of BCA: scores 1-2, no muscle invasion; 3, equivocal; 4, muscle invasion; 5, muscle and extravesical fat invasion. Bladder mpMRI used for VI-RADS includes T2 weighted image (T2WI), Diffusion weighted image (DWI)/Apparent diffusion coefficient (ADC), and dynamic contrast enhancement (DCE) pulse sequences for this purpose. T2WI serves as structural category, which is the initial step to be evaluated for confirming intact low signal intensity (SI) line representing no muscle invasion. On the other hand, DWI and DCE are the main pulse sequences to determine the presence of muscle wall invasion if DWI has sufficient quality. The presence of stalk or inner layer of a bladder tumor on mpMRI indicates it is probably a NMIBC and the stalk is more easily delineated on DWI.

The standard treatment of MIBC is cisplatin-based neoadjuvant chemotherapy (CBNAC), followed by radical cystectomy plus bilateral pelvic lymph nodes dissection. There is a high complete response (CR) rate up to 42 % of CBNAC, meaning no residual BCA after CBNAC, which makes bladder sparing strategy appealing to MIBC patients. Bladder mpMRI could assess treatment response of MIBC after neoadjuvant chemotherapy and determine whether bladder sparing treatment is feasible. Thus, neoadjuvant chemotherapy VI-RADS (nacVI-RADS) has been further proposed in 2022. It uses scores 1-5 to assess the likelihood of CR of BCA after treatment. Patients with nac-VIRADS scores 1-2 (i.e.: no residual bladder tumor) could be monitored under active surveillance. nacVI-RADS 3 means partial response (PR) of MIBC patients with tumor downstaging to NMIBC and bladder sparing strategy could be thus a reasonable treatment selection. For MIBC patients shows size reductions of tumors with persistent muscle invasion on post-treatment mpMRI, they are scored as nacVI-RADS 4. nacVI-RADS 5 is scored for patients with no response or even upstaging after treatment and standard of care such as radical cystectomy has been recommended for this kind of patients.

In my talk, I will use case illustrations for demonstrating the principles of VI-RADS and nacVI-RADS scoring. The diagnostic values of VI-RADS and nacVI-RADS with interobserver variabilities among radiologists in the literature, and their clinical implications will be reviewed and discussed as well.

[Refresher Course 5: GU Specific Diagnostic Classification Systems]

RC05-3

Clear Cell RCC Likelihood Score: Principles and Clinical Applications

Taek Min Kim

Seoul National University College of Medicine, Seoul National University Hospital, Korea

The widespread use of cross-sectional imaging has led to an increase in the incidental detection of indeterminate renal masses. Given the high prevalence of benign tumors and the typically indolent behavior of small renal masses, active surveillance has become a common management strategy for these patients. However, clear cell renal cell carcinoma (ccRCC), the most common subtype of RCC, exhibits more aggressive characteristics compared to other RCC subtypes. To assess the likelihood of clear cell RCC using multiparametric MRI, the clear cell likelihood score (ccLS) was developed.

The ccLS can be applied to renal tumors of any size, but it is most valuable for small renal masses (≤4cm). The ccLS is a 5-point Likert scale used to assess the probability of ccRCC based on three major criteria: T2-weighted imaging (T2WI), corticomedullary enhancement, and microscopic fat. It also includes four ancillary features: diffusion-weighted imaging, segmental enhancement inversion, arterial-to-delayed enhancement ratio, and homogeneity. Clinical management strategies based on ccLS scores are as follows: scores of 1-2 indicate active surveillance, scores of 4-5 suggest definitive therapy, and a score of 3 recommends biopsy. Validation studies show a pooled sensitivity of 80% (95% CI 74-85%) and specificity of 76% (95% CI 67%-83%) for identifying ccRCC.

However, ccLS still has limitations for clinical use due to the overlapping imaging features of renal tumors, the presence of aggressive tumors within non-ccRCC subtypes, and inherent drawbacks of MRI, including low availability, limited accessibility, and long acquisition times. To address these limitations, efforts have been made to integrate additional imaging features into the ccLS, expand its use beyond subclassifying RCC subtypes, and develop a CT-based ccLS algorithm. By the end of this lecture, attendees will gain a comprehensive understanding of the ccLS algorithm and its role in improving the diagnostic accuracy of clear cell RCC.

[Special Focus 4: All About Pancreatic Cysts]

SF04-1

Pathologic Classification of Pancreatic Cystic Neoplasm

Hee Young Na

Seoul National University College of Medicine, Seoul National University Bundang Hospital, Korea

Pancreatic cystic neoplasms (PCN) are composed of a heterogeneous group of entities with diverse biological behavior. With the widespread use of high-resolution imaging, detection of pancreatic cysts has increased substantially, creating a need for accurate risk stratification and multidisciplinary management. In this context, pathologic classification of PCN provides the fundamental framework for understanding the clinical behavior and appropriate clinical management of PCN.

Among PCN, intraductal papillary mucinous neoplasm (IPMN) represents the most prevalent entity, followed by mucinous cystic neoplasm (MCN) and serous cystic neoplasm (SCN). It is characterized by a grossly visible (> 10 mm) non-invasive neoplasm composed of mucin-producing epithelial cells forming papillae, arising in the pancreatic ducts. IPMN is further subclassified into main duct, branch duct, and mixed types based on duct involvement, as well as into gastric, intestinal and pancreatobiliary according to histologic phenotype. These classifications are clinically relevant due to their association with differing risks of malignant transformation and prognosis. Intraductal oncocytic papillary neoplasm (IOPN) and intraductal tubulopapillary neoplasm (ITPN) are morphologically and genetically distinct from IPMN and are therefore classified as separate entities.

MCN is defined by a non-invasive locule-forming and typically mucin-producing epithelial neoplasm associated with distinctive ovarian-type stroma, typically occurring in middle-aged women. IPMN, MCN does not communicate with the pancreatic ductal system and harbors ovarian-type stroma. SCN is composed of glycogen-rich cuboidal epithelium forming cystic structures, and also does not communicate with the pancreatic ducts. Additional cystic tumors include SPN and cystic pancreatic neuroendocrine tumors.

Recent advances in molecular pathology have further refined the classification of PCN. Recurrent driver alterations, including KRAS and GNAS mutations in IPMN and MCN, *PRKACA* or *PRKACB fusions in IOPN, BRAF*, *FGFR2*, *MAML2*, *MAML3*, *NRG1*, and *RET fusions in ITPN,* VHL alterations in SCN, and CTNNB1 mutations in SPN, may serve as diagnostic biomarkers, particularly in cyst fluid analyses.

Understanding the pathologic classification of PCN is essential for radiologists and clinicians, as it forms the basis for imaging interpretation, guideline development, and patient management strategies. This lecture will review the current pathologic classification of PCN, highlight key histologic and molecular features, and discuss their clinical implications in multidisciplinary decision-making.

[Special Focus 4: All About Pancreatic Cysts]

SF04-2

Pancreatic Cysts: Latest Guidelines & Supporting Evidences

Ji Hye Min

Sungkyunkwan University School of Medicine, Samsung Medical Center, Korea

The detection of pancreatic cystic lesions (PCLs) has significantly increased due to the widespread use of high-resolution imaging techniques such as CT and MRI. Among these, branch duct intraductal papillary mucinous neoplasms (BD-IPMNs) are the most common, accounting for approximately 80% of cases. Managing these lesions requires a delicate balance between the risk of malignant progression and the potential morbidity of surgical intervention. This lecture focuses on the 2024 Kyoto Guidelines, which provide updated, evidence-based strategies for the diagnosis and management of IPMNs.

A key update in the 2024 Kyoto Guidelines is the refinement of "High-Risk Stigmata" (HRS) and "Worrisome Features" (WF). Notable changes include the classification of an enhancing mural nodule ≥ 5 mm or a solid component as HRS. Additionally, new-onset or acute exacerbation of diabetes mellitus within the past year and a cyst growth rate ≥ 2.5 mm/year have been included as WFs. Furthermore, the guidelines now emphasize the cumulative risk of multiple WFs; the presence of two or more WFs indicates a higher malignancy risk, warranting surgical consideration rather than solely endoscopic ultrasound (EUS) surveillance.

The surveillance protocol has also been refined. For stable, non-surgical BD-IPMNs, discontinuation of surveillance may be considered after five years of stability in patients with small cysts (< 20 mm) without WFs or HRS. Post-operative surveillance indicators have been clarified to include solid mass development, main pancreatic duct (MPD) dilatation, and cyst growth. Radiologists play a pivotal role in this process by accurately identifying these imaging features and guiding clinical decision-making through standardized reporting and the potential use of risk-prediction nomograms.

[Special Focus 4: All About Pancreatic Cysts]

SF04-3

Pancreatic Cysts: Key Recommendations from the SAR DFP

Elizabeth Hecht

Weill Cornell Medical College, USA

This presentation will provide an up-to-date overview of incidental pancreatic cystic lesions, focusing on their rising detection, variable malignant potential, and the persistent uncertainties that challenge both clinicians and patients. We will explore how these lesions generate clinical ambiguity, emotional stress, and substantial financial impact when long-term surveillance is required.

The session will highlight the key imaging features that help refine the differential diagnosis of pancreatic cysts, with an emphasis on practical approaches radiologists can apply in daily practice to enhance diagnostic confidence. Current management guidelines will be reviewed, noting areas of alignment as well as important points of divergence relevant to patient care.

Attention will be given to imaging characteristics associated with higher-risk or worrisome cysts, while underscoring the critical importance of evaluating the entire pancreas—not just the cyst itself—to avoid overlooking synchronous malignancies or other occult pathology elsewhere in the gland or surrounding organs.

Finally, we will discuss the growing movement toward abbreviated protocols, standardized reporting and the use of a clear, consistent lexicon to improve communication, reduce variability, and support more reliable clinical decision-making. This talk aims to equip radiologists with practical insights and a more nuanced framework for navigating these increasingly common and clinically significant findings.

[Special Focus 4: All About Pancreatic Cysts]

SF04-4

Pancreatic Cysts: Key Suggestions from KSAR PCN Study Group

Jeong Hee Yoon

Seoul National University College of Medicine, Seoul National University Hospital, Korea

Pancreatic cystic lesions (PCLs) are increasingly detected on cross-sectional imaging and encompass a broad spectrum ranging from benign entities to lesions with malignant potential. In daily practice, however, radiology reports for pancreatic cysts often show substantial variability across institutions and readers. Inconsistencies arise in the terminology used to describe cyst morphology and key risk-related features, as well as in how these features are measured and documented. Common examples include non-uniform descriptions of cyst size (measurement plane), main pancreatic duct (MPD) diameter and definition of "dilatation," and ambiguous or interchangeable use of terms such as mural nodule, solid component, wall thickening, or septation. Such heterogeneity can complicate longitudinal comparison, impede clear communication with referring clinicians, and potentially lead to inappropriate surveillance intensity or unnecessary additional testing.

Standardized terminology and structured reporting are therefore essential to improve interpretability and clinical utility of imaging reports for PCLs. Beyond providing a descriptive diagnosis, reports should consistently capture a set of core imaging elements that directly inform risk stratification and management decisions. Moreover, for many PCLs, imaging findings do not allow a single definitive diagnosis; rather, radiologists frequently make a potential differentials under uncertainty. Communicating this uncertainty in a transparent and actionable way is critical.

The KSAR Pancreatic Cystic Neoplasm (PCN) Study Group proposes practical recommendations to address these gaps: (1) a set of standardized terms for key imaging descriptors, (2) a minimum required checklist of reportable items to enhance completeness and comparability, and (3) probability-based reporting to convey the likelihood of clinically relevant categories (e.g., IPMN vs. non-mucinous cyst and the presence of worrisome/high-risk features) instead of overly definitive statements. Probability-based reporting aims to align radiologic communication with real-world diagnostic uncertainty, facilitate multidisciplinary decision-making, and support consistent follow-up strategies.

In this talk, I will review representative examples of reporting inconsistency in PCL reporting, highlight why standardization matters, and present the key suggestions from the KSAR PCN Study Group. The overarching goal is to reduce unwarranted variation, improve longitudinal assessment, and deliver clearer, management-oriented information for patients with pancreatic cysts.

[Refresher Course 6: Imaging of Tumors in GI Tract]

RC06-1

Gastric Cancer: Preoperative T- & N-staging

Jin Woong Kim

Chosun University College of Medicine and Chosun University Hospital, Korea

Gastric cancer remains a major global burden, with most cases and deaths concentrated in Asia, especially East Asia. Preoperative staging matters because it guides (1) endoscopic resection vs surgery in early disease and (2) resectability and surgical extent in advanced disease. Terminology should be explicit: Early gastric cancer (EGC) is T1 (T1a mucosal or T1b submucosal) regardless of nodal status, whereas “early-stage” usually refers to stage grouping (often stage I; definitions vary) and should be labeled as clinical (cTNM) or pathologic (pTNM).

CT gastrography (CTG) complements routine contrast-enhanced CT because subtle mucosal lesions, particularly T1a, can be inconspicuous on standard 2D images. CTG uses gastric distension and post-processing (including virtual gastroscopy/virtual endoscopy) to improve lesion detection, localization, and surgical mapping. A practical workflow is to localize the lesion on CTG, then assess depth and perigastric extension on thin-section multiplanar reformats (MPR). CTG does not replace endoscopy and may have blind areas when distension or reconstruction is suboptimal. In daily practice, CTG adoption is limited by time and workflow burden, but feasibility improves with standardized protocols and technician- or automation-assisted reconstructions.

For T staging, a pragmatic approach is to focus on two management-changing discriminators. First, T1a vs ≥T1b is critical because T1a has low nodal risk and may be eligible for endoscopic therapy, while submucosal invasion increases nodal risk and often supports surgery; CTG can improve detection/localization, but very superficial depth discrimination remains limited. Second, ≤T4a vs T4b determines resectability; thin-section CT with high-quality MPR is essential for evaluating perigastric planes and adjacent organs. When invasion is equivocal, positional imaging (e.g., decubitus “sliding sign”) can help, and staging laparoscopy may be considered when uncertainty persists, especially with suspected peritoneal disease.

For N staging, AJCC 8th N category is pathology-based and count-dependent, so CT should emphasize probability-based regional lymph node metastasis (LNM) positive vs negative and clear documentation of suspicious distant nodes. Portal venous phase CT with thin-section MPR is the standard basis. A Node-RADS–oriented composite assessment (size + configuration) is clinically useful: use short-axis diameter (SAD) with station-aware interpretation, and upgrade suspicion using ancillary features such as round shape, irregular/lobulated margin, heterogeneous texture, central necrosis, abnormal enhancement, and clustered nodes. Reporting should provide an actionable regional LNM likelihood statement and explicitly describe any suspicious distant nodal stations. After neoadjuvant therapy, non-enhancing perigastric infiltration and non-enhancing nodes may reflect treated change; cautious interpretation is needed to avoid overstaging.

Small Bowel NET: Imaging Features and Latest Treatment

Aarti Sekhar

Emory University School of Medicine, USA

1. Presentation:
    a. Median presentation: 66 year, increasing incidence with age
    b. Abdominal pain, GIB, flushing / diarrhea, incidental
    c. Lab tests: Chromogranin A, pancreastatin, serotonin, plasma/urine 5-HIAA
        i. Serotonin production leads to local desmoplastic reaction (SBO, kinking)
        ii. Carcinoid syndrome if liver mets – 10% of patients: sweating, flushing, diarrhea
2. Distribution:
    a. NET is 35% of small bowel tumors, 2/3 arise from distal ileum; 54% will be multifocal
        i. Duodenal less common but can obstruct CBD; gastrinoma triangle
    b. 25% associated with genetic syndromes
    c. 50% will have regional or distant mets at diagnosis
        i. Regional LN: desmoplastic reaction from serotonin; calcification
        ii. Distant mets: 67% peritoneum, 62% LN, 48% liver, 43% lung, 24% bone
3. Outcomes
    a. Median overall survival is 103 months, with 5 year survival of 69%
    b. NET are biologically heterogeneous- survival depends on stage and tumor biology
        i. 5 year survival for stage 1+ 2 is 100%, stage 3 is 80%, stage 4 is 34-55%
    c. Ki-67 index >6% and age are most important factors
    d. 2023 WHO categories as below:

WHO Category	Tumor Grade	Degree of Differentiation	Ki-67 Index
Neuroendocrine Tumors	Low (Grade 1)	Well	< 3%
	Intermediate (Grade 2)	Well	3-20%
	High (Grade 3)	Well	> 20
MiNeNs	Variable	Well or Poorly	Variable
Neuroendocrine Carcinomas (small-cell/large-cell)	High Grade	Poorly	> 20

4. Imaging
    a. Capsule endoscopy
    b. CT or MRI – multiphasic with or without enterography
        i. Arterial phase key as 90% of mets are hypervascular
        ii. MRI more sensitive for detecting liver metastases
    c. Ga68 DOTATATE PET – best for G1 and low Ki-67 G2 NETs
        i. Somatostatin receptor 2 and 5 – find mets and determine response to PRRT
    d. FDG-PET for high G2 (Ki-67 >15%) and G3
5. Treatment
    a. Surgery for primary SB tumor
        i. + resectable local disease (nodes not encasing SMA or proximal branches)
        ii. Unresectable if peritoneal dz, NEC or liver dz occupying > 50% of liver
    b. Pharma
        i. Somatostatin analogs (Lanreotide) for symptoms
        ii. PRRT – peptide receptor therapy (Lu-177, Y-90, In-111)
            1. Future: new alpha emitter PRRT
        iii. Cytotoxics: Everolimus (mTOR inhibitor), 5-FU, doxorubicin, Sutent etc
    c. Liver disease
        i. liver directed– resection if can debulk > 90%, TARE, TACE, ablation
        ii. rarely transplant
    d. Sequencing of therapy is not set in stone – tailor to patient and tumor biology

[Refresher Course 6: Imaging of Tumors in GI Tract]

RC06-3

Perirectal Mass: Pearls & Pitfalls in Differentials

Myung-Won You

Yonsei University College of Medicine, Severance Hospital, Korea

1. anatomy and compartmental approach

We will review the overall anatomical spaces include the rectal wall, mesorectum, retrorectal/presacral space, and pelvic floor musculature. High-resolution T2-weighted MRI allows precise delineation of these compartments and helps determine whether a lesion originates from the rectum or represents an extrinsic process.

2. Imaging techniques: MR

MRI is the primary modality for characterization. T2-weighted imaging provides structural detail, diffusion-weighted imaging helps assess cellularity and potential malignancy, and contrast-enhanced T1-weighted sequences evaluate vascularity and enhancement patterns. CT may complement MRI by demonstrating calcification, fat components, or osseous involvement. PET-CT can be useful when malignant transformation or metastatic disease is suspected.

3. Differential diagnosis

** Localize the epicenter→ texture, enhancement check: cystic/solid or fibrotic, plaque-like perirectal lesion → check for pitfalls

Rectal wall origin:

1) epithelial tumor: adenocarcinoma, mucinous adenocarcinoma,

2) subepithelial tumor: lymphoma; neuroendocrine tumor; GIST/leiomyoma (muscularis propria); metastasis or seeding

Mesorectal origin: metastatic lymph nodes; mesorectal inflammatory mass; desmoid-type fibromatosis (post-op/FAP context); solitary fibrous tumor; sarcoma.

Presacral/retrorectal origin:

1) Congenital cystic: tailgut cyst (retrorectal cystic hamartoma), epidermoid/dermoid, duplication cyst

2) Neurogenic: schwannoma, neurofibroma

3) Osseous/neuroaxial: chordoma, anterior sacral meningocele

4) Inflammatory: abscess, granuloma, endometriosis, malackplakia etc.

4. Pitfalls for differentials

• perirectal vs. rectal mass: confirm wall layer origin and epicenter on high-resolution T2 MRI.

• Cystic lesion ≠ benign: tailgut cyst malignant transformation exists; scrutinize mural nodules/solid enhancement.

• Endometriosis as a cancer mimic (rectosigmoid/Douglas pouch/uterosacral ligaments): fibrosis-dominant infiltrative masses can look aggressive.

• Mucin/therapy effect mimics: post-treatment rectal MRI can show fibrosis vs residual tumor challenges—avoid over-reliance on a single sequence; use multiparametric assessment and standardized rectal MRI reporting principles.

• Presacral masses require "aggressive feature" screening (bone erosion, sidewall invasion, neuroforaminal extension) because it changes surgical approach.

Accurate evaluation of perirectal masses requires a structured approach integrating anatomy, multiparametric MRI findings, and clinical context. Understanding key pearls and recognizing potential pitfalls can significantly improve diagnostic confidence and patient management. Through representative cases and pattern-based analysis, radiologists can develop a more practical and reliable strategy for differentiating perirectal lesions.

[Refresher Course 6: Imaging of Tumors in GI Tract]

RC06-4

Anal cancer & Perianal Disease

Seung Ho Kim

Inje University College of Medicine, Haeundae Paik Hospital, Korea

Anal cancer is a rare malignant tumor with a worldwide incidence of approximately 1.5 per 100.000. Most anal cancers are squamous cell carcinomas. Chemoradiation therapy (CRT) is the standard treatment for most anal cancers, and 80-90% of patients achieve a complete remission. While, some patients with small tumors at the perianal skin may be treated with local excision. The 5-year relative survival rate for anal cancer is approximately 70%, according to data from the U.S. National Cancer Institute and American Cancer Society. Survival rates vary significantly by stage: localized (stage I/II, 80%–90%), regional (stage III, 60%), and distant (stage IV, 20%).

MRI is the preferred, state-of-the-art imaging modality for staging, radiotherapy planning, treatment response assessment after CRT and recurrence surveillance of anal cancer. It provides high-contrast, high-resolution images to determine the primary tumor's size, depth of invasion into surrounding tissues (sphincters, pelvic floor), and involvement of regional lymph nodes, which is crucial for managing anal cancer. MRI is considered superior to other modalities for detailed local staging, while FDG-PET/CT is often used to assess for distant metastasis.

High-resolution T2-weighted imaging is the standard, allowing detailed visualization of the anorectal anatomy. External phased-array surface coils are typically used to get detailed, high-resolution images. Advanced techniques such as diffusion-weighted imaging (high b value ≥800) may be used to improve the detection of tumors and the evaluation of treatment response. They are also useful for evaluating potential complications, such as fistulas or abscesses.

T-stage in anal cancer is primarily based on tumor size with the exception of T4 stage which is any size tumor with invasion of adjacent organs. Specifically, T1: tumor < 2 cm; T2: tumor 2-5 cm; T3: tumor > 5 cm.

Nodal involvement is common in anal cancer and ultrasound with fine needle aspiration is usually included in the diagnostic workup for characterization of the inguinal lymph nodes. The metastatic regional lymph nodes are treated with a radiation boost.

[Special Focus 5: Role of AI in GU Imaging]

SF05-1

AI in Prostate Cancer: Clinical Performance and Practical Limitations

Jurgen Fütterer

Radboud University Medical Center, Nijmegen, The Netherlands

Artificial intelligence (AI) is rapidly transforming radiology workflows, particularly in prostate MRI. The growing demand for imaging, combined with workforce shortages and increasing healthcare costs, requires more efficient diagnostic pathways. AI offers opportunities across the entire radiology workflow, from acquisition and image quality improvement to interpretation, reporting, and clinical decision support.

In image acquisition, deep learning reconstruction can accelerate MRI while maintaining diagnostic quality, enabling shorter scan times and improved patient comfort. During interpretation, AI algorithms can perform segmentation, lesion detection, characterization of clinically significant prostate cancer, and staging. Stand-alone performance of AI systems is approaching that of experienced radiologists, while concurrent reading strategies often improve diagnostic accuracy and consistency.

AI also plays a role in management decisions. Integration with pathology and clinical data allows prediction of recurrence risk and supports patient selection for biopsy, treatment, or active surveillance. In controlled reader studies, AI assistance reduces reporting time and increases diagnostic confidence. However, real-world implementation has shown mixed workflow benefits, highlighting that technical performance does not automatically translate into clinical efficiency.

Despite promising results, important challenges remain. False positives persist, many studies are retrospective, and narrow task-based algorithms struggle with incidental findings or complex cases. There is also a gap between research performance and certified clinical software. Questions about responsibility, supervision, and regulation further complicate adoption.

Future progress requires large multicenter prospective studies, benchmarking of commercial systems, and evaluation of outcomes such as quality of life and cost-effectiveness. Ultimately, AI should not replace radiologists but augment them, enabling more standardized, efficient, and patient-centered prostate cancer care.

[Special Focus 5: Role of AI in GU Imaging]

SF05-2

Advanced Imaging Biomarkers for RCC: A Radiomics and Machine Learning Perspective

Yaqi Shen

Tongji Hospital, Tongji Medical College, Huazhong University of Science and Technology, China

Renal cell carcinoma (RCC) is characterized by substantial biological heterogeneity, which poses challenges for accurate risk stratification and individualized management. In recent years, advanced imaging biomarkers derived from radiomics and machine learning have emerged as powerful noninvasive tools for decoding tumor biology beyond conventional morphologic assessment.

This lecture presents a comprehensive overview of how CT-based radiomics and multimodal integration strategies can support multi-level risk stratification in RCC. Radiomics models have demonstrated robust performance in differentiating benign from malignant renal masses, predicting WHO/ISUP nuclear grade and T stage, and identifying patients at risk of metastasis and postoperative recurrence. Importantly, explainable deep learning approaches, such as Grad-CAM visualization, reveal that models frequently focus on biologically relevant regions, including the tumor–fat interface and renal vein, reflecting patterns of perirenal invasion and vascular tumor thrombus.

Beyond tumor-centric analysis, increasing evidence suggests that the tumor microenvironment—particularly peritumoral adipose tissue and visceral fat distribution—provides incremental prognostic value. Imaging biomarkers such as extracellular volume fraction (ECV), perirenal adipose tissue features, and relative visceral fat area demonstrate meaningful associations with tumor aggressiveness and recurrence risk, highlighting RCC as a tumor–ecosystem disease.

Furthermore, multimodal predictive frameworks integrating radiomics, clinical variables, and pathomics consistently outperform single-modality approaches. Such data fusion strategies represent a critical step toward precision oncologic imaging, enabling noninvasive preoperative grading, risk-adapted surgical planning, and personalized surveillance strategies.

Future directions include prospective multi-center validation, standardized radiomics pipelines, and deeper integration of imaging with molecular and genomic data. Advanced imaging biomarkers are poised to become essential components of precision management in RCC.

[Special Focus 5: Role of AI in GU Imaging]

SF05-3

AI-Powered MRI Analysis for Bladder Cancer Diagnosis

Mizuho Nishio

Kobe University Graduate School of Medicine, Japan

Bladder cancer is the sixth most common malignancy in men worldwide. One of the most critical decisions in clinical care is to determine whether bladder cancer is non–muscle-invasive (NMIBC, ≤T1) or muscle-invasive (MIBC, ≥T2), as this staging drives treatment escalation—from transurethral resection of bladder tumor (TURBT) to radical cystectomy and systemic chemotherapy—and strongly influences prognosis and quality of life. TURBT remains the diagnostic gold standard; however, it is invasive, carries risks such as bleeding and perforation, and may lead to understaging of muscle invasion in approximately 20–30% of cases because of specimen quality and sampling limitations. Therefore, an accurate, noninvasive preoperative approach is needed. In response, the Vesical Imaging Reporting and Data System (VI-RADS), a standardized assessment based on multiparametric MRI (mpMRI), has shown excellent performance (AUC ≈ 0.9 or higher). Nevertheless, uncertainty persists in intermediate categories (VI-RADS 2–3), and inter-reader agreement is not always optimal. To address these limitations of VI-RADS, development of bladder cancer AI has been increasingly motivated. This lecture reviews recent MRI-based diagnostic AI and also introduces the speaker's in-house AI models, covering tumor segmentation and NMIBC–MIBC classification on MRI. We further discuss CT-based AI and emerging uses of large language models for bladder cancer imaging workflows. Finally, we outline key barriers to clinical translation focusing on robustness to inter-institutional (scanner/protocol) variation and the lack of rigorous external and prospective validation.

[Luncheon Symposium 3]

LS03-1

Implementation and Clinical Impact of Photon Counting CT in Abdominal Imaging

Michael Brun Andersen

Copenhagen University Hospital and Department of clinical medicine, Copenhagen University, Denmark

The introduction of photon-counting CT (PCCT) in 2021 has the potential to revolutionize CT imaging. However, it is still in its infancy, and many questions remain. Applications, including improvements in the detection and characterization of lesions, have been demonstrated in pancreatic, renal, and colorectal imaging. These applications rely on the higher spatial resolution of PCCT compared to energy-integrating detector CT (EID-CT) or the spectral capabilities of PCCT already known from dual-energy CT (DE-CT); however, these are enhanced in PCCT with the minimization of beam hardening artifacts that negatively influence the DE-CT images in EID-CT.

From a workflow perspective, we need to consider PCCT as a new system, and to utilize the full potential of the scanner, we need to adjust the current protocols used on EID-CT and optimize them depending on the use case. To obtain ultra-high resolution (UHR) images of sufficiently high quality, the dose needs to be increased; however, by optimizing the protocol for scanning only a selected area with UHR, the dose levels can be controlled and kept lower than those of a standard EID-CT protocol. This is combined with the fact that spectral images are always provided, although at a slightly lower resolution, to control the noise levels.

Currently, there are three possible methods for assessing the spectral images provided by PCCT. The first is the assessment of all images at dedicated workstations provided by the manufacturer. However, this method has several limitations. The second is to automatically create a selection of series at the scanner console and send them directly to the PACS. The final possibility is for some manufacturers to directly integrate into PACS, providing a viewer capable of displaying the spectral files provided by the manufacturer.

We need to consider PCCT as a new modality and actively work with the system to optimize protocols, images, and workflows to unlock its full potential and promise.

[Luncheon Symposium 4: Abdominal CT with High-Iodine Concentration Contrast Media: Clinical Experience Across Asia]

LS04-1

Optimizing Clinical Outcomes with Iomeron® 400 : The Role of High-Concentration Contrast Media in Modern Diagnostic Imaging

Hanyu Jiang

West China Hospital, Sichuan University, China

This lecture does not have an abstract.

[Luncheon Symposium 4: Abdominal CT with High-Iodine Concentration Contrast Media: Clinical Experience Across Asia]

LS04-2

Dual-Energy CT in the Diagnosis of Gastrointestinal Bleeding

Joon-Il Choi

The Catholic University of Korea, College of Medicine, Seoul St. Mary's Hospital, Korea

This lecture does not have an abstract.

[Luncheon Symposium 4: Abdominal CT with High-Iodine Concentration Contrast Media: Clinical Experience Across Asia]

LS04-3

Protocol Tailoring & Personalization

Satoshi Goshima

Radiology, Hamamatsu University School of Medicine, Hamamatsu, Japan

This lecture does not have an abstract.

[Luncheon Symposium 5]

LS05-1

Patient-Safe Emergency CT: Iso-osmolar Contrast Media and Double Dose Reduction

Bohyun Kim

The Catholic University of Korea, College of Medicine, Seoul St. Mary's Hospital, Korea

Emergency department (ED) abdominopelvic CT must deliver rapid, reliable diagnoses while minimizing patient risk. A patient-safety–focused strategy is to use iso-osmolar iodinated contrast media (IOCM) while simultaneously reducing both iodinated contrast media (CM) dose and radiation dose ("double dose reduction"). This approach is enabled by low-kVp imaging, which increases iodine attenuation by shifting mean photon energy closer to iodine's K-edge, and by standardizing iodine delivery using a kVp- and weight-adjusted dosing framework such as the "10-to-10" concept (approximately a 10% iodine dose reduction per 10 kVp decrease). To maintain interpretability under reduced dose conditions, noise can be mitigated using iterative or deep-learning reconstruction, and operational consistency in the ED can be supported by a simple lookup-table dosing scheme that minimizes the need for real-time protocol modifications. In an early exploratory experience applying double low-dose CT (DLCT) in young adults undergoing ED CT for suspected appendicitis, DLCT achieved substantial iodine reduction compared with a single low-dose approach that employed low kVp but fixed iodine dosing. Image noise and appendiceal visibility remained comparable, and although organ SNR/CNR decreased as expected, there was no clear signal of reduced diagnostic confidence for appendicitis or alternative diagnoses in this preliminary dataset. Overall, pairing IOCM selection with standardized, patient-tailored iodine dosing and modern reconstruction provides a practical route to safer ED CT by reducing contrast and radiation together without sacrificing the clinical answer, warranting further validation in broader ED populations and practice settings.

[Luncheon Symposium 5]

LS05-2

UGFF: Ultrasound-Guided Fat Fraction – Multiparametric Quantitative Ultrasound for Liver Steatosis Assessment

Takuma Oguri

Advanced Visualization Solutions, GE HealthCare, Japan

Metabolic dysfunction-associated steatotic liver disease (MASLD) represents a growing global health burden. Quantitative ultrasound (QUS) has a potential to quantify liver steatosis. We developed new QUS clinical application Ultrasound-Guided Fat Fraction (UGFF) which predicts MRI-proton density fat fraction (MRI-PDFF) using QUS parameters. In this presentation, we introduce the principle and utility of UGFF.

UGFF predicts MRI-PDFF using following three QUS parameters; attenuation coefficient (AC), integrated backscatter coefficient (IBSC) and signal-to-noise ratio (SNR), which have emerged as quantifiable imaging biomarkers for hepatic steatosis. Each QUS parameter is evaluated using ultrasound B-mode image data, MRI-PDFF is predicted using the parameters and prediction function. The prediction function was developed with 582 chronic liver disease patients which both ultrasound B-mode image data and MRI-PDFF were acquired. AUROCs to diagnose each steatosis grade (≥S1, ≥S2, S3) in the patients were 0.96 for ≥S1, 0.95 for ≥S2 and 0.94 for S3, respectively [Kuroda et. al., Radiology, 309(1), 2023].

In the presentation, we will also introduce clinical advantages/implementation and additional clinical studies, such as a comparison with liver biopsy and validation study for population dependencies.

[ESUR Honorary Lecture]

HL02-1

Opportunities for Next Generation Imaging for Advanced Prostate Cancer

Anwar Padhani

Mount Vernon Cancer Centre, UK

Prostate-specific membrane antigen (PSMA) positron emission tomography (PET) computed tomography (CT), and

whole-body magnetic resonance imaging (WB-MRI) are superior to conventional CT and bone scan imaging for detecting metastatic disease in patients with prostate cancer. While these higher-accuracy imaging methods have

already shown the potential to enhance patient outcomes, a thorough understanding of the relationship between the

treatment landscape and disease volume on conventional imaging, as well as the prognostic significance of the prostate-specific antigen response, is crucial for determining how they can be more effectively incorporated into clinical care. Prospective clinical trials are required to evaluate whether PSMA-PET/CT and WB-MRI can genuinely improve clinically relevant endpoints for patients through precise treatment adaptations. In this lecture, we will explore the specific opportunities of PSMA-PET/CT and WB-MRI as biomarkers across multiple clinical domains, including metastasis detection and staging, disease characterisation and aggressiveness assessment, biopsy target selection, impact on treatment planning, evaluation of therapeutic response, and theranostics. We will highlight the central research questions that require attention.

[Asian Chapter Session: Safe Use of Contrast Media: Guidelines and Evidence in Asia]

ACS01-1

China Perspectives

Yuan-Cheng Wang

Zhongda Hospital, Southeast University, China

In China, the large population base and high imaging volume make contrast media safety an important clinical and public health priority. According to the Chinese Expert Consensus on the Safe Administration of Iodinated Contrast Media (2018), the overall incidence of acute adverse reactions to iodinated contrast agents ranges from 0.32% to 0.64%, with severe reactions occurring in approximately 0.01% to 0.04% of administrations. Although uncommon, severe reactions can be life-threatening and therefore require early recognition and standardized management

Chinese national guidelines emphasize systematic pre-administration risk assessment and stratified management. A prior history of contrast reaction is the most significant predictor of recurrent events, increasing the risk approximately fivefold. Additional risk factors include asthma, multiple drug allergies, and impaired renal function. Routine skin testing is not recommended, and current evidence does not support a causal association between seafood allergy and iodinated contrast hypersensitivity.

Adverse reactions are classified as mild, moderate, or severe. Management is severity-based: observation for mild reactions; oxygen therapy, antihistamines, and intravenous fluids for moderate reactions; and immediate intramuscular epinephrine with activation of emergency protocols for severe reactions.

Post-contrast acute kidney injury (PC-AKI) remains an important safety consideration. Chinese guidelines recommend adequate peri-procedural hydration as the primary preventive strategy and do not support routine prophylactic use of N-acetylcysteine.

For gadolinium-based contrast agents, nephrogenic systemic fibrosis (NSF) is rare but primarily associated with severe renal impairment. Macrocyclic agents are preferred in high-risk patients. Although gadolinium brain deposition has been demonstrated radiologically, no definitive clinical neurological impairment has been established.

This lecture will review current evidence and highlight practical strategies for the safe use of contrast media from a Chinese perspective.

[Asian Chapter Session: Safe Use of Contrast Media: Guidelines and Evidence in Asia]

ACS01-2

Japan Perspectives

Yoshiko Ueno

Kobe University Graduate School of Medicine, Japan

The safe use of contrast media is an essential component of modern diagnostic imaging. In Japan, contrast media administration is guided by evidence-based recommendations developed by academic societies, including the Japanese Radiological Society and the Japanese Society of Nephrology. These guidelines emphasize risk stratification, prevention of adverse reactions, and appropriate clinical decision-making.

This lecture introduces two complementary aspects of contrast media safety in Japan: national clinical guidelines and practical workflow-based safety management in daily radiology practice.

First, current Japanese guidelines for iodinated and gadolinium-based contrast agents will be reviewed. Topics include the prevention and management of acute hypersensitivity reactions, assessment of renal function prior to contrast administration, and recent evidence regarding contrast-associated acute kidney injury. Contemporary understanding suggests that the risk of kidney injury is lower than previously assumed when appropriate patient selection and hydration strategies are applied.

Second, this lecture presents institutional safety workflows commonly implemented in Japanese hospitals. These include standardized pre-contrast screening questionnaires, renal function assessment protocols, informed consent procedures, and multidisciplinary collaboration among radiologists, technologists, and nursing staff. Emergency preparedness and staff education are also important components of contrast safety management.

By integrating guideline-based recommendations with clinical workflow practices, this lecture aims to provide a practical overview of contrast media safety management in Japan.

[Asian Chapter Session: Safe Use of Contrast Media: Guidelines and Evidence in Asia]

ACS01-3

Chinese Taipei Perspectives

Yu-Ting Kuo

Chi Mei Medical Center, Chinese Taipei

This presentation delineates the comprehensive structural and clinical framework established by the Taiwan Radiological Society (TRS) to govern the safe administration of contrast media. Released in September 2023, the updated Manual on Contrast Media serves as a clinical blueprint that harmonizes international standards, such as those from the ACR and ESUR, with specific local regulations mandated by the Taiwan FDA.

Key Governance and Clinical Pillars:

- Organizational Oversight: Managed by the Patient Safety and Medical Imaging Quality Committee, the guidelines provide standardized protocols for over 1,300 radiologists in Taiwan.
- Risk Stratification and Mitigation: The presentation clarifies valid risk factors for Iodine-Based Contrast Media (ICM) reactions, emphasizing that seafood or dairy allergies are not contraindications. It details specific premedication protocols (e.g., the "12+2 Method") and regulations for Metformin management based on eGFR levels.
- Gadolinium-Based Contrast Agents (GBCA): Safety classifications distinguish between macrocyclic (preferred) and linear agents, specifically addressing concerns regarding brain deposition in the dentate nucleus and globus pallidus.
- Special Populations: Evidence-based guidance is provided for pediatric, pregnant, and lactating patients, advocating for shared decision-making regarding breastfeeding suspension.
- Operational Excellence: Standardized safety measures are highlighted, including viscosity management through warming ICM to 37°C and the implementation of uniform Informed Consent Forms to ensure legal protection and patient education.

The 2023 TRS Guidelines underscore a commitment to continuous improvement, operationalizing safety through structured oversight, global data adaptation, and standardized clinical practice to honor the professional contract with the patient.

[Asian Chapter Session: Safe Use of Contrast Media: Guidelines and Evidence in Asia]

ACS01-4

Singapore Perspectives

Martin Weng Chin H'ng

Tan Tock Seng Hospital, Singapore

The presenter will be speaking on the topic of Safe use of Contrast Media in Singapore. This will come from insights gained from "**Reducing Postponements and Revamping the CT Scan Service from Year 2014 to 2023**" in his institution, a project spanning 10 years, which won the highest accolade in the Singapore Ministry of Health National Quality Improvement Conference 2023.

Safe use of contrast media in essence forms part of the delivery of a "service package" requiring collaborative effort between radiologist/radiographer/nurse & other departments. Change has been difficult given the need to undo long-standing beliefs and negotiating dynamic shifts in criteria particularly over the last 10 years. We are pleased that the Singapore Guidelines will soon be formalized based on:

- Recommendations of other professional bodies
- Consensus between local institutions
- Agreement between upstream/downstream stakeholders

3-key aspects will be covered:

- Contrast media: Presentation will focus mainly on administration of Iodinated and Gadolinium-based contrast media in current local practice and recommendations in the upcoming guidelines
- Location: Familiarity in one's own radiology department cannot be overly emphasized, and the importance of an Orientation Programme will be highlighted
- Training & Spread: Methods for maintaining standards, managing complications and sharing this knowledge with the local and international community will be described

[Asian Chapter Session: Safe Use of Contrast Media: Guidelines and Evidence in Asia]

ACS01-5

Korea Perspectives

Moon Young Kim

Seoul National University College of Medicine, SMG-SNU Boramae Medical Center, Korea

This perspective provides a focused overview of the current status and distinctive clinical practices of contrast media safety in South Korea, juxtaposed with recent international standards (e.g., ACR and ESUR guidance). While core principles such as standardized AKI definitions and risk stratification frameworks and the selective withholding of metformin in patients with severely reduced kidney function (e.g., eGFR < 30 mL/min/1.73 m^2) are broadly consistent across guidelines, Korean practice often reflects a more proactive, risk-averse implementation in several key areas.

Notably, some Korean referral hospitals continue to employ more conservative, institution-level eGFR thresholds for prophylactic hydration (e.g., IV < 45 and IA < 60 mL/min/1.73 m^2), even when national guidance aligns with lower thresholds used internationally. Furthermore, institutional protocols have adopted structured strategies for agent substitution and selective diagnostic testing to manage hypersensitivity reactions for both iodinated media and GBCAs. By integrating electronic surveillance and workflow-based safety programs, Korea illustrates a data-informed approach that balances international evidence with localized practice needs.

Key Comparison Table: Korea vs. International Standards

Parameter	Korea (KSR / local practice)	International guidance (ACR / ESUR)
Hydration threshold	Often more conservative at institution level (e.g., IV <45 / IA <60)	Typically lower threshold (often eGFR <30 for high-risk)
Prevention strategy	Agent substitution + selective testing / protocols	Agent substitution; premedication benefit debated/limited
GBCA protocols	Structured class-switching protocols reported in local practice	Primarily emphasize iodinated CM; GBCA safety stratified by agent class
Re-administration interval	Avoid <24 h when feasible	More restrictive in some guidance for severe CKD
Pharmacovigilance	EMR-linked surveillance / workflow programs	Often institution-dependent; variable reporting systems

[Hands-on (GU): PI-RADS Version 2.1 Challenge]

HO01-1

Detection and Classification Using PI-RADS 2.1: Critical Points for Interpretation

Jurgen Fütterer

Radboud University Medical Center, Nijmegen, The Netherlands

Prostate Imaging Reporting and Data System (PI-RADS) version 2.1 is a standardized MRI-based framework designed to detect, localize and risk-stratify clinically significant prostate cancer. The goal of the system is not only lesion detection but also communication and decision support for biopsy and management. Correct interpretation requires understanding that PI-RADS is a rules-based imaging classification reflecting the probability of Grade Group ≥2 cancer rather than a direct diagnosis.

Interpretation should always begin with anatomical zone identification because scoring depends on lesion location. In the peripheral zone, diffusion-weighted imaging (DWI) is the dominant sequence, whereas in the transition zone T2-weighted imaging i dominant. Dynamic contrast enhancement (DCE) plays only a secondary role and mainly upgrades peripheral zone PI-RADS 3 lesions to PI-RADS 4 when positive. Overreliance on DCE is a common error and does not improve performance in lesions that are clearly benign or clearly malignant.

One of the most critical points is recognizing that PI-RADS categories represent likelihood ranges rather than absolute thresholds. PI-RADS 1–2 generally exclude clinically significant cancer, PI-RADS 4–5 strongly suggest it, whereas PI-RADS 3 requires integration with clinical parameters such as PSA density and prior biopsy history. Therefore, MRI should be interpreted within the clinical pathway rather than in isolation.

Frequent pitfalls include misinterpreting prostatitis, post-biopsy hemorrhage, stromal hyperplasia and anterior fibromuscular stroma as tumor. Symmetric transition zone nodules with encapsulation favor benignity, while lenticular, ill-defined, homogeneous low T2 signal lesions with diffusion restriction suggest malignancy. Image quality assessment is essential before scoring; inadequate acquisition invalidates PI-RADS assessment.

Finally, PI-RADS should guide biopsy strategy, not replace clinical judgement. Combining MRI findings with risk stratification reduces unnecessary biopsies while maintaining detection of significant disease. Optimal use of PI-RADS therefore requires technical quality, structured reading, and clinical integration rather than merely assigning categories

[Hands-on (GU): PI-RADS Version 2.1 Challenge]

HO01-2

Before Starting Interpretation: Pitfalls and Considerations for New PI-RADS Users

Weon Jang

Jeonbuk National University Medical School, Jeonbuk National University Hospital, Korea

PI-RADS v2.1 provides a structured framework for lesion detection and risk stratification; however, many interpretive errors occur before the actual scoring process begins. For new users in particular, systematic preparation and careful assessment of image quality are often as important as imaging interpretation. Interpretation should not be performed independently of clinical information. The clinical indication, whether in the setting of biopsy-naïve evaluation, prior negative biopsy, or active surveillance, as well as PSA level, PSA density, and prior treatment history, all influence lesion conspicuity and the level of confidence in reporting.

Nevertheless, PI-RADS is a risk stratification system designed for the detection of clinically significant prostate cancer. It does not represent a histopathologic diagnosis, nor is it a tool for tumor staging. Upgrading a lesion score on the basis of subjective suspicion or excessive reliance on a particular imaging sequence may introduce unnecessary interobserver variability.

New users should first assign a score objectively based on the dominant sequence and subsequently integrate ancillary sequences. Such a structured approach is more effective in reducing interobserver variability than experience alone.

Recent biopsy constitutes a particularly important pitfall. Post-biopsy hemorrhage may produce T1 hyperintensity and diffusion restriction, potentially mimicking clinically significant malignancy. An interval of at least six weeks before performing MRI is generally recommended. Similarly, acute prostatitis or recent mechanical manipulation may result in focal diffusion abnormalities that are not malignant in origin.

PI-RADS presumes adequate technical image quality. However, suboptimal image acquisition is frequently encountered in routine clinical practice. Motion artifacts, susceptibility artifacts caused by rectal gas, and inappropriate field of view positioning can significantly degrade imaging quality.

When image quality is severely compromised, diagnostic reliability declines substantially. In such circumstances, it is appropriate to explicitly acknowledge technical limitations and to interpret findings with caution. The impact of degraded image quality on diagnostic performance should not be underestimated.

ACAR 2026

THE 13th ASIAN CONGRESS OF ABDOMINAL RADIOLOGY

Invited Session

Mar. 21 (Sat.)

! Abstracts can be found by searching with the Presentation Code !

[Refresher Course 7: Emergency Radiology in Abdomen]

RC07-1

Bowel Obstruction

Kyoung Doo Song

Sungkyunkwan University School of Medicine, Samsung Medical Center, Korea

1. Introduction & Modalities

- **Plain Radiography:** While widely available and useful for follow-up, it lacks sensitivity and specificity (misleading in 20-40% of cases).
- **CT:** This is the gold standard. It is essential not just for diagnosis, but for determining the cause and complications.
- **The Goal:** We must move beyond "SBO vs. No SBO" and answer **five specific questions** to guide clinical management (Conservative vs. Surgical).

2. The 5 Key Questions for CT Interpretation

- **Q1: Is there SBO?**
  - Look for small bowel dilatation (>2.5–3 cm) disproportionate to the colon.
  - Identify the transition from dilated to non-dilated bowel.
- **Q2: Where is the Transition Point?**
  - Tracing bowel loops can be time-consuming; use Multi-Planar Reformation (MPR).
  - **Key Sign:** Look for the **"Small Bowel Feces Sign"**—stasis of particulate material mixed with gas immediately proximal to the transition point.
- **Q3: How Severe is the Obstruction?**
  - Differentiate between partial (low/high grade) and complete obstruction.
  - Check for the flow of oral contrast beyond the transition point.
- **Q4: What is the Cause?**
  - **Adhesions (60-75%):** The most common cause. Often a diagnosis of exclusion, but look for the **"Fat Notch Sign"** (extraluminal compression by a band).
  - **Hernias:** Inspect for external hernias and **Internal Hernias** (e.g., Transmesenteric or Petersen's hernia), especially in patients with a history of Roux-en-Y procedures.
  - **Others:** Neoplasms (primary/metastatic), Bezoars, or Gallstones.
- **Q5: Are there Complications? (Crucial Step)**
  - We must rule out **Strangulation** and **Closed-Loop Obstruction**.

- **Closed-Loop:** Look for a C-shaped or U-shaped loop distribution and the **"Whirl Sign"**.
- **Ischemia:** The most specific sign is **decreased bowel wall enhancement**. Also observe mesenteric haziness and engorged veins.
- *Clinical Implication:* The presence of ischemia or closed-loop obstruction is a strong indication for emergency surgery.

3. Conclusion

- A systematic approach answering these five questions minimizes diagnostic error and optimizes surgical timing.

Bowel Ischemia

Song-Ee Baek

Yonsei University College of Medicine, Severance Hospital, Korea

Mesenteric ischemia is resulting from decreased blood flow to the small or large bowel in an acute or chronic setting. CTA is the most appropriate choice for the initial evaluation of both acute and chronic mesenteric ischemia.

1. Acute Mesenteric Ischemia
   - A. High rates of morbidity and mortality, DDx from common causes of acute abdominal pain
   - B. Acute embolism to the SMA (40~50%), acute mesenteric artery thrombosis ischemia (20%-30%), nonocclusive mesenteric ischemia (25%), mesenteric and portal venous thrombosis (5%-15%).
   - C. CTA: first-step imaging approach, CT with VI contrast: May Be Appropriate
   - D. Vascular CT: arterial stenosis, embolism, thrombosis, arterial dissection, and mesenteric vein thrombosis.
   - E. Nonvascular CT: bowel-wall thickening, hypoperfusion and hypoattenuation, bowel dilatation, bowel-wall hemorrhage, mesenteric fat stranding, pneumatosis intestinalis, and portal venous gas.
   - F. A systematic “inside-out” approach: beginning from bowel lumen and outward to the wall, mesentery, vasculature, and extraintestinal viscera
   - G. Pitfalls: mistaking pneumatosis as a sign that is specific for AMI, misinterpretation of adynamic ileus as a benign finding, and pseudopneumatosis.
   - H. Specific features: involved segments of bowel correspond to a vascular distribution.
   - I. Mimic: inflammatory bowel disease, infections, angioedema, and radiation-induced enterocolitis
2. Chronic Mesenteric Ischemia
   - A. Clinical triad of postprandial abdominal pain 30 to 60 minutes, weight loss, and food avoidance.

     May be: Nausea and vomiting, postprandial diarrhea, early satiety, and malabsorption
   - B. Severe atherosclerotic disease, with including fibromuscular dysplasia, median arcuate ligament syndrome, dissection, and vasculitis
   - C. CTA abdomen and pelvis with IV contrast & MRA abdomen and pelvis without and with IV contrast: Usually Appropriate
   - D. May be a multifactorial event dependent on the pace of lesion progression, the ability of the develop collateral vessels, and the site of the lesion.

[Refresher Course 7: Emergency Radiology in Abdomen]

RC07-3

Traumatic Injuries in Abdomen

Cheong-Il Shin

Seoul National University College of Medicine, Seoul National University Hospital, Korea

Abdominal trauma requires rapid and precise diagnostic evaluation to ensure optimal patient outcomes. This presentation highlights the indispensable role of Computed Tomography (CT) as the gold standard in trauma imaging. We will focus on the radiologic assessment of active bleeding and vascular injuries, which play a pivotal role in trauma triage and therapeutic decision-making. Furthermore, this session provides a comprehensive review of the recent updates in the American Association for the Surgery of Trauma (AAST) Organ Injury Scale, including the latest revisions for pancreatic (2024) and renal (2025) injuries. These updates increasingly incorporate imaging-based findings, especially vascular injury and active hemorrhage, reflecting the evolving role of CT in guiding non-operative management, interventional radiology, and surgical decision-making. By integrating optimzed CT protocols and the updated grading systems, this lecture aims to provide practical insights for radiologists to enhance diagnostic accuracy and clinical decision-making in emergency settings.

[Refresher Course 7: Emergency Radiology in Abdomen]

RC07-4

Musculoskeletal Emergencies & Urgencies in Abdomen CT

Jee Won Chai

Seoul National University College of Medicine, SMG-SNU Boramae Medical Center, Korea

The interpretation of abdominal CT traditionally prioritizes visceral pathologies; however, the musculoskeletal framework often harbors critical evidence of emergencies and urgencies that necessitate equal diagnostic attention. While primary focus is directed toward conditions such as appendicitis or bowel ischemia, the vertebral column and abdominal wall frequently contain "silent" pathologies with significant clinical and socioeconomic implications.

Spinal infection, particularly pyogenic spondylodiscitis, represents a critical diagnosis where early detection significantly improves patient outcomes. On CT, the diagnostic hallmarks include ill-defined destruction of adjacent vertebral endplates and narrowing of the intervertebral disc space. Crucially, the identification of these subtle endplate erosions and the assessment of disc space height are often markedly superior on sagittal reformatted images compared to axial or coronal views. The sagittal plane allows for a continuous longitudinal evaluation of the spinal column, facilitating the detection of early inflammatory changes and associated paravertebral or epidural extensions. It is clinically imperative to distinguish these infectious processes from common mimickers such as Schmorl's nodes or active inflammatory changes in Diffuse Idiopathic Skeletal Hyperostosis (DISH).

In the evaluation of fractures suspicious for malignancy, the assessment of structural integrity and neurological risk is paramount. Pathologic fractures often manifest with involvement of the posterior elements or the posterior vertebral wall. The most critical reporting element in these cases is the presence and degree of central canal compromise. Unlike benign osteoporotic collapses, malignant infiltration frequently results in the retropulsion of tumor or bone fragments into the spinal canal. A detailed description of canal narrowing is a mandatory component of the radiologic report, as it serves as a primary determinant for urgent neurosurgical intervention or radiation therapy to preserve neurological function.

Osteoporotic compression fractures, though frequently incidental and asymptomatic at the time of imaging, represent a significant clinical crisis. These fractures are potent predictors of future catastrophic hip fractures and contribute to a substantial socioeconomic burden. Beyond skeletal instability, vertebral collapse induces a "crowding effect" within the torso. The resulting kyphotic deformity physically reduces the volume of the abdominal cavity, compressing the gastrointestinal tract. This mechanical compression leads to early satiety, exacerbation of gastroesophageal reflux disease (GERD), and chronic constipation, ultimately contributing to a systemic decline in nutritional and cardiopulmonary status.

In conclusion, a comprehensive evaluation that extends beyond the viscera to include the spine and abdominal wall is vital for identifying critical musculoskeletal emergencies.

[Joint Symposium 2 (ACAR meets Vietnam): High-Value Liver MRI with Hepatocyte-Specific Contrast Agent]

JS02-1

Liver Imaging in Vietnam: Experience from a High-Volume Tertiary Center

Huyen Duy Mai Le

University Medical Center, Ho Chi Minh City, Vietnam

Across the ASAR region, liver imaging is shaped by heterogeneous disease patterns and resource availability. In Vietnam, a high prevalence of chronic hepatitis B and a substantial burden of parasitic and other infections influence the spectrum of focal liver lesions (FLLs) we see at scale, including HCC, ICC, metastases, and inflammatory masses. Using our high-volume tertiary center as a case study, I will summarize the practical imaging context and how we convert routine care at scale into publishable, regionally relevant evidence.

Given local resource availability and national health-insurance reimbursement requirements in Vietnam, ultrasound is the first-line modality; multiphasic CT is the workhorse for detection, characterization, and staging; and MRI is used selectively, usually with extracellular contrast agents rather than hepatocyte-specific agents. Under high throughput, we rely on protocol standardization, structured probability-based reporting (including LI-RADS when appropriate), and rapid feedback via multidisciplinary tumor boards.

I will highlight three representative works from our center. First, our ACAR poster describes the disease spectrum of FLLs and demonstrates diagnostic performance using a CT-based enhancement-pattern approach with group-specific models. Second, we show that readily available imaging information from dynamic contrast-enhanced CT/MRI with extracellular agents can stratify early recurrence risk after curative HCC resection—an important message in settings where hepatocyte-specific agents are not widely used. Third, we developed an AI/radiomics model for multiphase CT to support scalable lesion classification.

I will close by proposing practical, low-barrier steps for registry building and data sharing that can enable ACAR–VSAR and broader ASAR multicenter collaboration, turning single-center experience into stronger, generalizable regional evidence.

[Joint Symposium 2 (ACAR meets Vietnam): High-Value Liver MRI with Hepatocyte-Specific Contrast Agent]

JS02-2

Focal Hypointense Lesions on Hepatobiliary Phase of EOB-MRI

Huu Khuyen Pham

Viet Duc University Hospital, Vietnam

Hepatobiliary (HB) contrast agents are increasingly becoming valuable diagnostic tools in MRI, offering a wider range of applications as their clinical use expands. Normal liver cells absorb HBs, which are then excreted via bile. This characteristic creates a distinct hepatobiliary phase (HBP), providing valuable insights into liver function and biliary tract anatomical structure. HBs can aid in the diagnosis of a wide range of HB pathologies, from diffuse liver disease to focal liver lesions, and can clarify anatomical details of the biliary system. Reduced signal intensity in the HBP can stem from various diffuse and focal abnormalities, which may or may not be related to bile secretion. Abnormalities may originate from parenchymal, biliary, or vascular causes, or a combination of these within each major group. Recognition of a suboptimal hypointense HB phase is important in the evaluation of focal lesions in patients with cirrhosis of the liver and particularly in those with hepatocellular carcinoma (HCC). Furthermore, signal loss can suggest the invasive nature of malignancies, potentially impacting prognosis.

In this presentation, we focus only on focal lesions in the HBP. We rely on the clinical sign and other sequences to rule out benign lesions hypointense in HBP such as liver cysts and hepatic hemangiomas. We will demonstrate cases suspected of primary or early recurrence of HCC after treatment. We present clinical cases of hypointense in HBP with hyperintense in arterial phase suggesting typical HCC. Cases of focal hypointense in HBP but non-arterial enhancement require close monitoring due to the risk of developing HCC; we discuss the value of DWI sequences in contributing to the diagnosis of focal nodules hypointense in HBP as early HCC, with the potential to predict the development of highly vascular or non-enhancement HCC. This report also shows focal hypointense nodules in HBP in patients who have undergone hepatectomy for HCC. In patients who have undergone hepatectomy, when small nodules with hypeintense in arterial phase and isointense in portal phase when using extracellular contrast agents, it is difficult to differentiate between hepatic perfusion disorders and early-stage recurrent small HCC

[Joint Symposium 2 (ACAR meets Vietnam): High-Value Liver MRI with Hepatocyte-Specific Contrast Agent]

JS02-3

Fast and Confident: Optimizing High-Yield Abbreviated EOB-MRI

Jeong Woo Kim

Korea University College of Medicine, Korea University Guro Hospital, Korea

Hepatocellular carcinoma (HCC) remains a leading cause of cancer-related mortality worldwide. Although ultrasonography is recommended for surveillance in high-risk patients, its limited sensitivity for early-stage HCC has increased interest in abbreviated MRI (AMRI) protocols.

Abbreviated liver MRI aims to shorten examination time while preserving diagnostic performance. Various AMRI strategies have been proposed, including non-contrast AMRI, dynamic contrast-enhanced AMRI, and hepatobiliary phase AMRI (HBP-AMRI). Among them, HBP-AMRI using gadoxetic acid (EOB-MRI) provides high sensitivity and specificity for HCC detection. The HBP, acquired about 15–20 minutes after injection, offers strong liver-to-lesion contrast because most HCCs show reduced OATP expression and appear hypointense compared with the enhancing liver parenchyma.

HBP-AMRI protocols have also shown diagnostic performance comparable to full-protocol MRI for detecting liver metastases while significantly reducing scan time. A streamlined protocol with T2-weighted imaging, diffusion-weighted imaging, and HBP imaging can usually be completed within 15 minutes, improving workflow efficiency and patient convenience.

However, abbreviated protocols have limitations, including false-positive findings, limited characterization without dynamic information, and the need for recall examinations. Adding arterial phase imaging can improve diagnostic confidence and reduce recall. The second-shot arterial phase (SSAP) is a modified injection technique in which a small additional contrast dose is administered to reacquire arterial phase images. This modified injection protocol demonstrated that motion artifacts were reduced while maintaining vascularity in the SSAP images of patients with HCC and hepatic metastasis.

This lecture will present practical strategies to optimize high-yield EOB-MRI protocols while balancing speed and diagnostic confidence in surveillance and oncologic practice.

[Joint Symposium 2 (ACAR meets Vietnam): High-Value Liver MRI with Hepatocyte-Specific Contrast Agent]

JS02-4

Hepatocellular Adenoma: Imaging Features and Subtype-Specific MRI Clues

So Yeon Kim

University of Ulsan College of Medicine, Asan Medical Center, Korea

Hepatocellular adenoma (HCA) is a benign monoclonal hepatocellular tumor with clinically meaningful molecular subtypes. The 2019 WHO classification recognizes HNF1α-inactivated (HHCA), inflammatory (IHCA), β-catenin–activated (βHCA, including βIHCA), sonic hedgehog (shHCA), and unclassified HCA; notably, bleeding and malignant transformation risks differ significantly by subtype.

From an Asia/Korea perspective, HCAs are increasingly detected due to widespread cross-sectional imaging and rising obesity. Asian cohorts exhibit a higher male proportion (up to 70%), low oral-contraceptive exposure (0–29%), and a predominance of IHCA compared with Western data. Consequently, applying Western "one-size" rules—such as routine resection for all male patients—may lead to the overtreatment of low-risk tumors in Asia.

The primary imaging goal with hepatocyte-specific contrast MRI is to identify the high-risk β-catenin–activated group, particularly exon-3 βHCA/βIHCA, as this group drives the majority of HCA-related hepatocellular carcinoma (HCC) risk. On gadoxetic acid MRI, hepatobiliary phase (HBP) iso-to-hyperintensity serves as a key clue for β-catenin activation, which is linked to increased OATP1B3 expression.

A practical Korean approach utilizes an MRI-based scoring system incorporating two features: (1) marked tumor heterogeneity and (2) iso/high HBP signal. An increasing score raises the likelihood of βHCA/βIHCA, guiding the decision for biopsy and focused immunostains or genomic sequencing.

Differential diagnosis remains a pitfall because focal nodular hyperplasia and certain HCCs can also show HBP iso/high signal. Therefore, MRI findings must be interpreted within the clinical context, considering hepatitis risk, hemorrhage, and tumor multiplicity.

In conclusion, clinicians should use hepatocyte-specific MRI to subtype and risk-stratify HCA in an Asia-aware manner. Prioritizing the detection of β-catenin activation helps avoid unnecessary surgery for low-risk phenotypes while allowing for escalation to pathology or genomics when management hinges on HCC risk.

From LI-RADS to Asian Guidelines for HCC Diagnosis: Alignments, Differences, and Real-World Pitfalls

Sunyoung Lee

Yonsei University College of Medicine, Severance Hospital, Korea

Hepatocellular carcinoma (HCC) is the most common primary liver cancer. It is the only malignancy of which the clinical practice for diagnosis is to use imaging without pathological confirmation in high-risk patients; thus, reliable noninvasive imaging criteria are crucial. To achieve consistent diagnosis of HCC, several scientific organizations have proposed imaging-based diagnostic criteria. The imaging criteria differ between geographic areas, reflecting differences in clinical environment and treatment strategies.

The Liver Imaging Reporting and Data System (LI-RADS), endorsed by the American College of Radiology, is a comprehensive system to standardize the terminology, technique, interpretation, reporting, and data collection of liver imaging in patients at risk for HCC [1]. LI-RADS is currently the most widely used noninvasive diagnostic criteria for HCC in radiological studies because it provides detailed definitions for major and ancillary imaging features of HCCs. LI-RADS categorizes an observation according to its probability of HCC (ranging from LR-1 to LR-5) or malignancy but not specific for HCC (LR-M), on the basis of major, ancillary, and LR-M imaging features [1]. LI-RADS 2018 represents the fourth update and has been fully integrated into the American Association for the Study of Liver Disease 2023 HCC Practice Guidance [2]. LI-RADS was developed and modified predominantly based on data from Western countries and was designed to emphasize the specificity and positive predictive value over sensitivity for liver transplant eligibility.

The Korean Liver Cancer Study Group (KLCSG)-National Cancer Center (NCC) HCC practice guidelines were first announced in 2003 and have been revised in 2009 and 2014 [3]. Since then, the Korean Liver Cancer Association (KLCA, formerly KLCSG)-NCC published KLCA-NCC 2018 practice guidelines for the management of HCC and revised in 2022 [3,4]. They provide diagnosis and treatment guideline specific to the Asian who manifest different clinical behaviors of HCC compared to Western population, especially in Korean [4]. The KLCA-NCC 2022 practice guidelines for the imaging diagnosis of HCC has been revised into a non-binary decision algorithm that covers the whole spectrum of observations, similar to LI-RADS [4]. The KLCA-NCC 2022 guidelines categorize an observation into indeterminate, probable HCC, and definite HCC after excluding benign lesions such as cyst or hemangiomas based on bright T2 signal intensity and other malignancies based on targetoid appearance [4]. KLCA-NCC 2022 was designed to favor high sensitivity for the detection of early HCC and early treatment with locoregional therapies.

[1] American College of Radiology. CT/MRI Liver Imaging Reporting and Data System (LI-RADS) version 2018.

[2] Singal AG, Llovet JM, Yarchoan M, et al. AASLD Practice Guidance on prevention, diagnosis, and

treatment of hepatocellular carcinoma. *Hepatology.* 2023;78(6):1922-1965.

[3] Lee S, Kim SS, Chang DR, et al. Comparison of LI-RADS 2018 and KLCA-NCC 2018 for noninvasive diagnosis of hepatocellular carcinoma using magnetic resonance imaging. *Clinical and molecular hepatology.* 2020;26(3):340-351.

[4] 2022 KLCA-NCC Korea practice guidelines for the management of hepatocellular carcinoma. *Clinical and molecular hepatology.* 2022;28(4):583-705

ACAR 2026

THE 13th ASIAN CONGRESS OF ABDOMINAL RADIOLOGY

Oral Presentation

Mar. 19 (Thu.)

! Abstracts can be found by searching with the Presentation Code !

[Scientific Session 1: Advances in Pancreatic Imaging: Emerging Techniques and Clinical Applications]

SS01-1

Imaging of Pancreatic NET: From Differentials to Prognostication

Raju Sharma

All India Institute of Medical Sciences, New Delhi, India

Pancreatic NETs are rare and diverse group of tumors with varied clinical manifestations. They may or may not be associated with clinical symptoms due to hormone production and can be classified into functioning or non-functioning tumors. The clinical picture depends on the hormone or peptide being secreted by the tumor. The talk will cover the entire spectrum of NETs ranging from insulinoma, gastrinoma and non-functioning NETs. The imaging features of pancreatic NETs will be highlighted. The functioning tumors are small in size while the non-functioning tumors are large at presentation. It is these large tumors that have a propensity to undergo necrosis or cystic change. They may occur sporadically or be associated with syndromes like von-Hippel landau, MEN I, tuberous sclerosis and neurofibromatosis.

On ultrasound they are seen as small well defined hypoechoic masses. The larger tumors may show necrosis or cystic change. The presence of peripancreatic nodes and liver metastases point towards malignancy. Contrast enhanced ultrasound may show their hypervascular nature. Endoscopic Ultrasound is a good modality for small NETs and can also be used for EUS guided FNAC.

On multiphase CT the lesions are well circumscribed and hypervascular and show bright enhancement on the late arterial phase. They may not always be hypervascular specially the non-functioning ones. The larger tumors may show necrosis or cystic change. Calcification may be seen especially in non-functioning NETs. On MR these lesions are hypointense on T1 and hyperintense on T2W images and show enhancement on the late arterial phase. MR is good for detection of small liver metastases which are also hypervascular. These tumors express Somatostatin receptors and therefore octreotide scintigraphy and DOTANOC PET-CT are good modalities for their diagnosis and whole-body staging. It is also useful to determine if the patient is suited for peptide receptor radionuclide therapy (PRRT). Insulinomas tend to be small, present with neuroglycopenic symptoms and are more often benign. They may not express SSTR receptors and if PET-CT is negative Exendin PET should be used. Gastrinomas tend to occur in the gastrinoma triangle and present with ulcers in unusual location like second part of duodenum. They are more often malignant and more likely to express somatostatin receptors. The differential diagnosis includes pancreatic ductal adenocarcinoma, hypervascular metastases, serous cystadenoma and intrapancreatic accessory spleen and this will be highlighted with examples. Well differentiated tumors are DOTANOC positive and FDG negative while poorly differentiated tumors are DOTANOC negative and FDG positive.

[Scientific Session 1: Advances in Pancreatic Imaging: Emerging Techniques and Clinical Applications]

SS01-2

MRI-Derived Bone Marrow Fat Fraction and Body Composition Predict Chemotherapy-Induced Myelosuppression and Survival in Pancreatic Cancer

Weinuo Qu[1], Chenxi Lyu[1], Ziling Zhou[1], Jiali Li[1], Zhen Li[1*]

[1] Radiology, Tongji Hospital Tongji Medical College Huazhong University of Science and Technology, China

Chemotherapy-induced myelosuppression (CIM) is a common and serious adverse event in pancreatic cancer, often leading to treatment delay or dose reduction. Reliable imaging biomarkers for individualized CIM risk prediction remain limited. This study aimed to evaluate the predictive value of pre-chemotherapy MRI-derived bone marrow fat fraction (BMFF), abdominal body composition, and baseline laboratory parameters for post-chemotherapy myelosuppression and survival.

This study included 488 pancreatic cancer patients who received myelotoxic chemotherapy, comprising 338 retrospectively enrolled (March 2014–October 2024) and 150 prospectively recruited (November 2024–May 2025) cases. Myelosuppression severity was graded according to CTCAE v5.0, using the most severe hematologic value among day 8, day 14, and pre-cycle-2 measurements after the first chemotherapy cycle. Patients were divided into severe and non-severe CIM groups and further stratified by neoadjuvant versus non-neoadjuvant chemotherapy.

Pre-chemotherapy MRI included dual-echo Dixon T1-weighted FAT and WATER sequences. A 3D U-Net deep learning model was applied for automatic segmentation of vertebral bone marrow and abdominal body composition, including skeletal muscle, subcutaneous, visceral, and intermuscular adipose tissue at Th11–L3 levels for both cross-sectional areas and volumetric indices, normalized by height. BMFF was calculated as FAT / (FAT + WATER). Baseline hematologic, hepatic, renal, metabolic, and protein indices were also analyzed.

Ten machine learning classifiers were used to predict severe CIM: k-nearest neighbors (KNN), Naïve Bayes, logistic regression, QDA, LDA, SVM, decision tree, random forest, extra trees, gradient boosting, XGBoost, and LightGBM. Model performance was assessed using ROC analysis, calibration curves, and decision curve analysis (DCA). Feature interpretability was explored via SHAP analysis. Survival outcomes were evaluated using Kaplan–Meier analysis and multivariate Cox regression.

In the neoadjuvant chemotherapy subgroup, the KNN model achieved the highest performance (AUC = 0.77 in the retrospective cohort; 0.80 in the prospective cohort). Calibration and DCA confirmed good model agreement and clinical applicability. SHAP analysis identified pre-chemotherapy platelet count, BMFF, and absolute neutrophil count as the top contributors to severe CIM prediction. Patients with higher BMFF values exhibited an increased risk of early severe myelosuppression and worse survival trends. Cox regression further supported the prognostic relevance of BMFF in combination with hematologic and metabolic indicators.

MRI-based quantification of bone marrow fat fraction and body composition, combined with systemic laboratory data, enables interpretable prediction of chemotherapy-induced myelosuppression and survival in pancreatic cancer. This integrative imaging–clinical framework provides a potential tool for personalized chemotherapy risk assessment and treatment optimization.

Keywords : Bone Marrow Fat Fraction, Chemotherapy-Induced Myelosuppression, Pancreatic Cancer

[Scientific Session 1: Advances in Pancreatic Imaging: Emerging Techniques and Clinical Applications]

SS01-3

Deep Learning CT Signature for Predicting Occult Liver Metastases and Neoadjuvant Therapy Benefit in Pancreatic Ductal Adenocarcinoma: A Multicenter Retrospective Study

Ben Zhao[1], Zixin Xiao[1], Yiming Li[1], Shenghong Ju[1*]

[1]Radiology, Zhongda Hospital Medical School of Southeast University, China

To develop a deep learning (DL) framework integrating pancreatic tumor and liver imaging features to predict occult liver metastases (OLM) in pancreatic ductal adenocarcinoma (PDAC), thereby guiding personalized neoadjuvant therapy (NAT).

In this multicenter retrospective study (2015-2022), 1,063 patients with PDAC were included: a training cohort (n = 450), internal validation cohort (n = 113), external validation cohort (n = 342), and an NAT cohort (n = 158). We developed a Mamba-based model that integrates multi-phase computed tomography features from both primary tumors and liver regions. Its performance was evaluated using the area under the receiver operating characteristic curves (AUCs). To assess clinical utility, survival outcomes were compared between NAT followed by surgery and upfront surgery groups based on model-defined risk stratification. Finally, radiotranscriptomics analysis was employed to elucidate the underlying biological insights.

The Mamba-based model demonstrated robust performance for predicting the OLM in PDAC, with the AUCs of 0.890 (training), 0.820 (internal validation), and 0.806 (external validation), respectively. Model-defined high-risk patients had significantly shorter progression-free survival (PFS: HR = 1.95, $P < 0.001$) and overall survival (OS: HR = 1.96, $P < 0.001$), independent of clinicopathological factors. Notably, NAT conferred significant OS benefits exclusively in model-defined high-risk patients (17.43 vs. 34.10 months; $P < 0.001$), even after propensity score matching (18.03 vs. 34.10 months; $P = 0.003$), while low-risk patients showed no survival benefit. Furthermore, radiotranscriptomics also revealed the relative biological aggressiveness of high-risk patients.

The proposed Mamba framework enabled accurate prediction of OLM and may serve as a clinically actionable tool for identifying PDAC patients most likely to benefit from NAT.

Overview of model's development, evaluation and clinical utilization. a, The development. of Mamba-based model for the prediction of OLM; **b**, Model evaluation. The performance of Mamba-based model in different cohorts. **c**, clinical utilization. We explore its pitential value in predicting benefit from NAT. **d**, Biological insights. Deciphering the underlying biological interpretation of the Mamba-based model. **e**, Patient inclusion and exclusion across different cohorts. OLM, occult liver metastases; PDAC, pancreatic ductal adenocarcinoma.

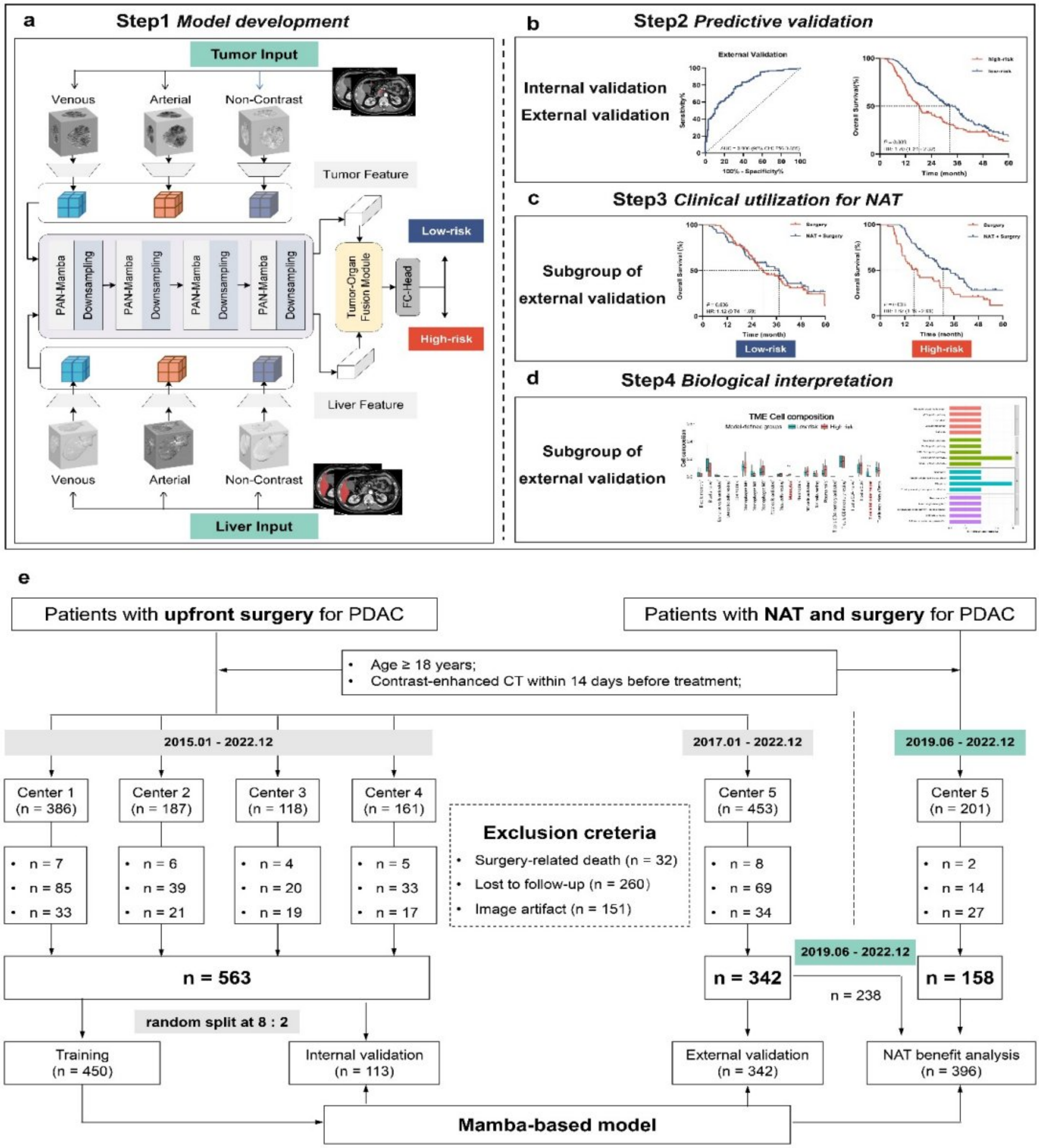

Keywords : Pancreatic ductal adenocarcinoma, Deep learning, Occult liver metastases

[Scientific Session 1: Advances in Pancreatic Imaging: Emerging Techniques and Clinical Applications]

SS01-4

U-Shaped Adiposity Thresholds Defining an Obesity Paradox in Gastroenteropancreatic Neuroendocrine Tumors: A Multicenter Prognostic Study with Biological Correlates

Weinuo Qu[1], Chenxi Lyu[1], Zhibo Wang[1], Jiali Li[1], Zhen Li[1*]

[1]Radiology, Tongji Hospital Tongji Medical College Huazhong University of Science and Technology, China

Accurate preoperative prognostication remains a critical need for gastroenteropancreatic neuroendocrine tumors (GEP-NETs). While 3D body composition metrics from routine CT present a potential noninvasive prognostic solution, their clinical utility remains underexplored and supporting evidence is inconsistent. This multicenter study aimed to investigate their prognostic value and biological relevance.

This multicenter study included 509 GEP-NET patients from 3 hospitals (April 2015 – April 2024). 464 patients from one hospital were randomly assigned to training and validation sets with a ratio of 7:3. Patients from two additional centers comprised the preliminary test set. Skeletal muscle tissue and abdominal fat were automatically segmented with an nnUNetv2-based algorithm, yielding seven 3-D body-composition parameters (BCPs) included subcutaneous fat index (SFI), visceral fat index (VFI), etc. The random survival forest (RSF) algorithm was applied to build the prognostic prediction model. C-index, integrated Brier score (IBS), and time-dependent ROC curves (t-ROC) were used to evaluate the performance. SHapley Additive exPlanations analysis (SHAP) analysis enhanced algorithmic explainability. Partial-dependence plots were used to explore the impact of BCPs, and BCPs were further correlated with Ki-67 and other immunohistochemical markers to establish biological explainability.

For overall survival prediction, the RSF model integrating BCPs, age, BMI, and tumor location achieved C-indexes of 0.981, 0.899, and 0.773 in the training, validation, and test sets, respectively. t-ROC curves showed 1-, 3-, and 5-year AUCs of 0.783, 0.920, and 0.956 in the validation set, and 0.764, 0.789, and 0.750 in the test set. SHAP analysis ranked VFI and SFI as the foremost prognostic predictors. Both extremes of adiposity—subcutaneous fat index (SFI < 400 cm^3/m^3 or > 600 cm^3/m^3) and visceral fat index (VFI < 450 cm^3/m^3 or > 650 cm^3/m^3)—are associated with poor prognosis. Both VFI and SFI were correlated significantly with the Ki-67 proliferation index in GEP-NETs ($p<0.05$).

3D body composition analysis enables individualized survival prediction in GEP-NETs. The validated U-shaped adiposity thresholds (SFI: 400–600 cm^3/m^3; VFI: 450–650 cm^3/m^3) offer clinically actionable targets for nutritional intervention and personalized management.

Araphical Abstract

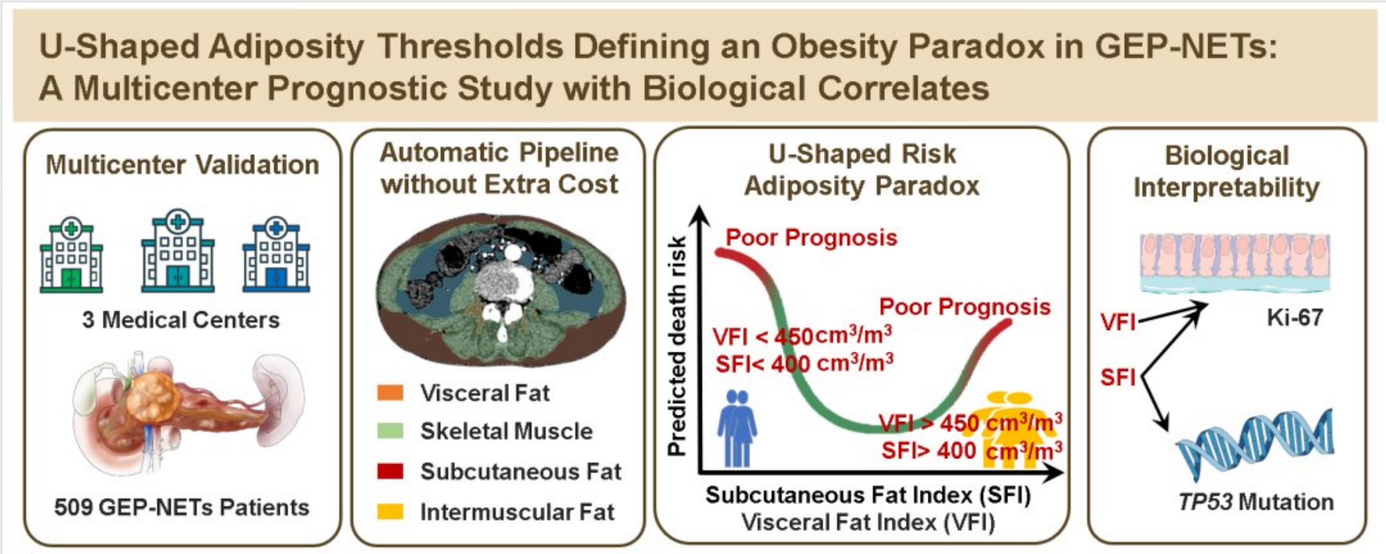

The time-dependent ROC curves for OS prediction. Training set (A); validation set (B); test set (C). ROC curves, Receiver Operating Characteristic curves; OS, overall survival.

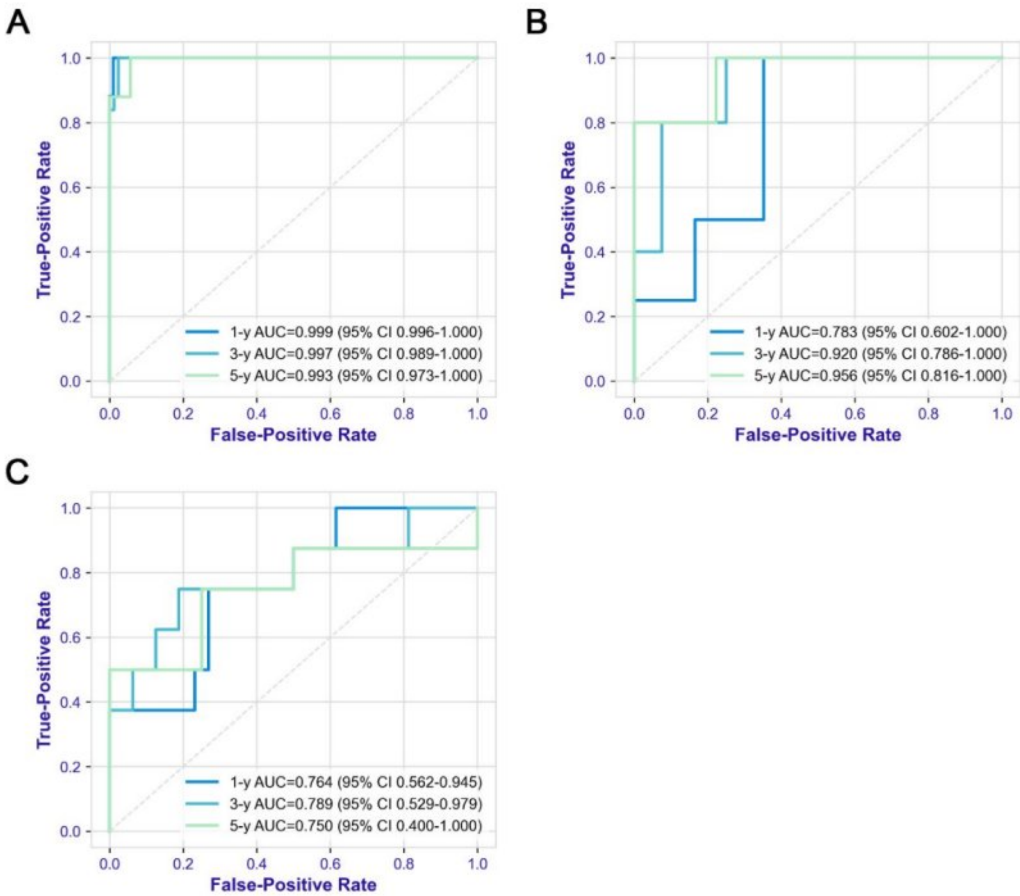

Keywords : Gastroenteropancreatic Neuroendocrine Tumor, Prognosis, Machine Learning

[Scientific Session 1: Advances in Pancreatic Imaging: Emerging Techniques and Clinical Applications]

SS01-5

Magnetic Resonance T2-weighted Imaging Radiomics Deep Learning Model to Predict Pancreatic Mucinous Neoplasms

Xu Fang[1], Chengwei Chen[1], Yun Bian[1*], Li Wang[1], Chengwei Shao[1], Jianping Lu[1]

[1]Radiology, Changhai Hospital of Naval Medical University, China

Intraductal papillary mucinous neoplasms (IPMN) and mucinous cystic neoplasms (MCN) of the pancreas are precancerous, while serous cystadenomas (SCA) have minimal malignant potential. Accurate preoperative differentiation of IPMN/MCN from SCA is critical for guiding treatment and early precancerous screening in pancreatic cystic neoplasm (PCN) patients. This study aimed to develop and validate a T2-weighted imaging (T2WI) radiomics deep learning model for predicting IPMN/MCN.

Retrospective data included 732 pathologically confirmed PCN patients: 252 SCA, 387 IPMN, and 93 MCN from Changhai Hospital (Nov 2011–Apr 2024; split 7:3 into training [n=540] and validation [n=192] sets) and 170 patients (50 SCA, 120 IPMN/MCN) from Shanghai 411 Hospital (Aug 2020–Oct 2023; test set). Lesions were segmented on T2WI and enhanced venous-phase MRI to extract radiomics (3D, peritumoral, habitat) and deep learning (ResNet18, DINOv2) features. Dimensionality reduction yielded feature scores, and logistic regression built three models: conventional (clinical and radiological features), T2WI radiomics-deep learning combined, and enhanced-phase combined. Models were visualized as nomograms; diagnostic efficacy was assessed via ROC (AUC, 95%CI, sensitivity, specificity, accuracy) and clinical utility via decision curve analysis (DCA).

The T2WI and enhanced-phase models used 69 and 73 features, respectively. The conventional model included 4 factors (female, age, pancreatic body and tail, main pancreatic duct dilation); combined models added their respective feature scores. Key AUC values (training/validation/test sets): conventional model (0.805/0.772/0.849), T2WI combined model (0.979/0.932/0.955), enhanced-phase combined model (0.993/0.909/0.920). DCA showed the T2WI combined model was more beneficial than "treat-all as IPMN/MCN" or "treat-all as SCA" at threshold probabilities of 0.02–0.99 (training), 0.1–0.97 (validation), and 0.08–0.98 (test).

The T2WI radiomics deep learning combined model accurately predicts IPMN/MCN. It enables non-invasive, cost-effective classification via non-contrast MRI, guides treatment decisions, and facilitates early precancerous screening in PCN patients.

Keywords : Pancreatic cystic neoplasm, Magnetic resonance imaging, Deep learning

[Scientific Session 1: Advances in Pancreatic Imaging: Emerging Techniques and Clinical Applications]

SS01-6

From Echoes to Contrast: Improving Reporting Standards and Timing of Imagings Delivery in Acute Pancreatitis

Kevin Xuan Hong Tang[1], Muhammad Irfan[1], Elizabeth Daly[1], Adrian Ho[1*]

[1]Radiology, Hampshire Hospitals NHS Foundation Trust, UK

Acute pancreatitis occurs when the pancreas is inflamed rapidly, and is typically caused by gallstones (50%), alcohol (25%) and other causes (25%). Computed Tomography abdomen-pelvis (CTAP) is indicated 72-96 hours after initial onset of symptoms to minimise underestimation of pancreatic necrosis. Ultrasonography of abdomen is recommended within 24 hours after diagnosis. This two-cycle audit aims to evaluate and optimise reporting standards and timelines of imaging delivery of both CTAP and ultrasonography of abdomen according to Royal College of Radiologists (RCR) guidelines.

A retrospective analysis of patients diagnosed with acute pancreatitis between September 2024 and February 2025 in two mid and north Hampshire Hospitals was conducted. Relevant data included referral indications for CTAP, timing of delivery of CTAP and ultrasound abdomen, and reporting details such as pancreatic necrosis, free intraperitoneal fluid and peripancreatic fat stranding. Sustained educational efforts were conducted to panels of radiologists and surgeons before carrying out a prospective analysis between June and August 2025.

Post-intervention, mean compliance of referral indications for CTAP increased from 67% to 88%. Mean reporting CTAP standard increased from 80% to 88% and mean time for initial CTAP assessment increased from 60 to 84 hours. Ultrasound abdomen performed within 24 hours of diagnosis increased from 61% to 72%; average time of ultrasound performance reduced from 53.33 hours to 23.92 hours.

Sustained educational efforts and optimal dissemination of this protocol were effective in improving imaging reporting standards and diagnostic accuracy. These interventions brought local practice standards closer to RCR recommendations for the management of acute pancreatitis.

Keywords : Acute pancreatitis, Ultrasound abdomen, CT abdomen pelvis

Imaging of IgG4-Related Disease: Focus on Pancreas and Biliary Tract Manifestation

Ankur Goyal

All India Institute of Medical Sciences, New Delhi, India

IgG4-related disease (IgG4-RD) is a systemic, immune-mediated fibroinflammatory condition capable of affecting nearly any organ system, though the pancreas and biliary tree are among the most frequently involved sites. The disease is characterized histopathologically by dense lymphoplasmacytic infiltrates rich in IgG4-positive plasma cells, storiform fibrosis, and obliterative phlebitis. From an imaging perspective, IgG4-RD typically presents as tumefactive (tumor-like) lesions or diffuse organ enlargement that can mimic malignancy, often leading to diagnostic challenges. A key feature distinguishing IgG4-RD from malignancies and other inflammatory conditions is its dramatic and rapid response to corticosteroid therapy.

Pancreatic Manifestations: Autoimmune Pancreatitis (AIP) Type 1

Type 1 Autoimmune Pancreatitis (AIP) is the pancreatic manifestation of IgG4-RD and typically affects older males. Radiologically, it presents in three primary morphological patterns: diffuse, focal, and multifocal.

- Diffuse Form: This is the classic presentation, characterized by a diffusely enlarged, "sausage-shaped" pancreas with a loss of normal lobular architecture and featureless borders. On contrast-enhanced CT (CECT), the parenchyma appears hypoattenuating in the arterial phase and shows delayed, homogeneous enhancement due to fibrosis. A hallmark finding, highly specific to AIP, is the "halo sign"—a capsule-like rim surrounding the pancreas that is hypodense on CT and hypointense on T1 and T2-weighted MRI sequences.
- Focal Form: This presentation appears as a focal mass, often in the pancreatic head, which can closely mimic pancreatic ductal adenocarcinoma (PDAC). Key differentiating features include the "duct-penetrating sign," where the main pancreatic duct (MPD) remains visible passing through the mass without complete obstruction, and the "ice pick sign," which is a smooth, tapered narrowing of the upstream duct. Unlike PDAC, focal AIP rarely causes significant upstream ductal dilation (>5mm) or abrupt vascular encasement.
- MRI Features: On MRI, affected pancreatic parenchyma is typically T1-hypointense and T2-hyperintense, while the surrounding capsule is T2-hypointense. Diffusion-weighted imaging (DWI) shows restricted diffusion with significantly lower ADC values compared to pancreatic cancer, aiding in differentiation.

Biliary Manifestations: IgG4-Related Sclerosing Cholangitis (IgG4-SC)

The biliary strictures in IgG4-SC are typically long, continuous, and associated with symmetric wall thickening (>2.5 mm). IgG4-SC is classified into four types based on the location of strictures: Type 1 involves the intrapancreatic bile duct only; Type 2 involves diffuse intra- and extrahepatic strictures; Type 3 involves hilar and distal strictures; and Type 4 involves hilar strictures only.

- Imaging Characteristics: On CT and MRI, the bile duct walls show circular, symmetric thickening with a smooth inner margin and single-layer delayed enhancement. This contrasts with cholangiocarcinoma (CCA), which often shows asymmetric thickening, abrupt cutoff, and double-layer enhancement.
- Differentiation from PSC: Unlike Primary Sclerosing Cholangitis (PSC), which presents with multifocal, short, band-like strictures giving a "beaded" or "pruned-tree" appearance and diverticulum-like outpouchings, IgG4-SC strictures are longer and smoother. Furthermore, IgG4-SC typically spares the biliary epithelium, whereas PSC causes severe epithelial damage.
- Involvement of the gallbladder (IgG4-CC) presents as diffuse wall thickening with preservation of the mucosal layer, reflecting transmural fibrosis. This preservation of the mucosal line helps distinguish IgG4-CC from gallbladder carcinoma.

[Scientific Session 2: HCC Imaging for Clinical Decision-Making]

SS02-1

LI-RADS CT/MRI Nonradiation Treatment Response Assessment Version 2024 for Detecting Local Recurrence of Surgically Resected Hepatocellular Carcinoma

Sung-Hua Chiu[1], Luke Yoon[1], Stephan Altmayer[1], Daniel Delitto[1], Aya Kamaya[1], **Justin Tse[1*]**

[1]Radiology, Stanford University, USA

LI-RADS CT/MRI Nonradiation Treatment Response Assessment (TRA) version 2024 (v2024) specifies that the updated algorithm may be applied for evaluating the surgical margin after hepatocellular carcinoma (HCC) resection. The aim of our study was to compare detection of local recurrences after surgical resection of HCC between LI-RADS CT/MRI Nonradiation TRA v2024 and the LI-RADS CT/MRI Core version 2018 (v2018) diagnostic algorithm.

This retrospective study included patients with surgically resected HCC who underwent at least one postoperative liver CT or MRI performed ≥6 months after surgery. Two radiologists independently reviewed all postoperative CT and MRI examinations in separate sessions, assessing the surgical margin using LI-RADS CT/MRI Nonradiation TRA v2024 and LI-RADS CT/MRI Core v2018, respectively; a third radiologist resolved discrepancies. Local recurrence was defined by v2024 as LR-TR Viable (i.e., masslike enhancement at the margin, in any phase and of any size) and by v2018 as LR-5, LR-M, or LR-TIV.

The study included 200 patients (142 men, 58 women; median age 67 years) with median follow-up of 30.5 months. Interreader agreement for v2024 categorization was substantial (κ=0.71). By v2024, LR-TR Viable at the surgical margin was assigned in 56 (28.0%) patients: on the initial postoperative examination in 21 patients, directly after an LR-Nonviable assignment without intervening LR-TR Equivocal assignment in 31 patients, and after an LR-TR Equivocal assignment in remaining patients (Figure 1). LR-TR Viable was assigned after a median of 5.1 months and at a median size of 1.5 cm. By v2018, LR-5, LR-M, or LR-TIV was assigned at the surgical margin in 53 (26.5%) patients after a median of 12.0 months ($p<.001$) and at a median size of 2.1 cm ($p<.001$). At the time of the 56 initial LR-TR Viable assignments, categories assigned for v2018 were LR-3, LR-4, LR-5, LR-M, and LR-TIV in 21, 10, 18, 3, and 4 patients, respectively (Figure 2). Upgrade of LR-3 and LR-4 observations to LR-5, LR-M, or LR-TIV occurred after a median of 5.1 and 3.0 months, respectively.

v2024 enables detection of postoperative HCC local recurrence in 28% of patients, at an earlier time, and at a smaller size compared to v2018, potentially improving eligibility for timely salvage therapies.

Sankey diagram of all 200 patients, depicting LI-RADS CT/MRI Nonradiation TRA v2024 assignment on first and final postoperative examinations and any intervening assignments. TRA = treatment response algorithm. v2024 = version 2024.

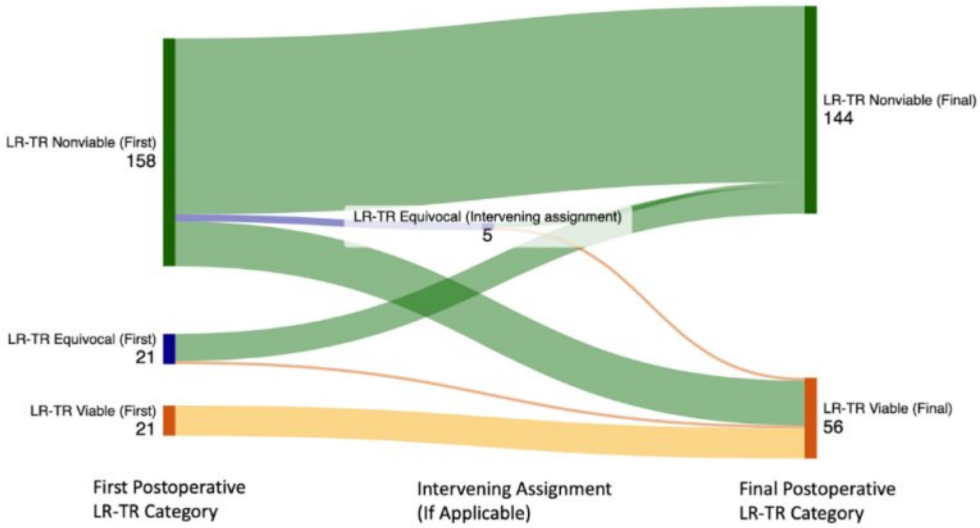

Sankey diagram of 56 patients with at least one assignment of LR-TR Viable, depicting LI-RADS CT/MRI Core v2018 categorization at time of first assignment of LR-TR Viable, final LI-RADS CT/MRI Core v2018 categorization prior to management decision, and management decision. v2018 = version 2018

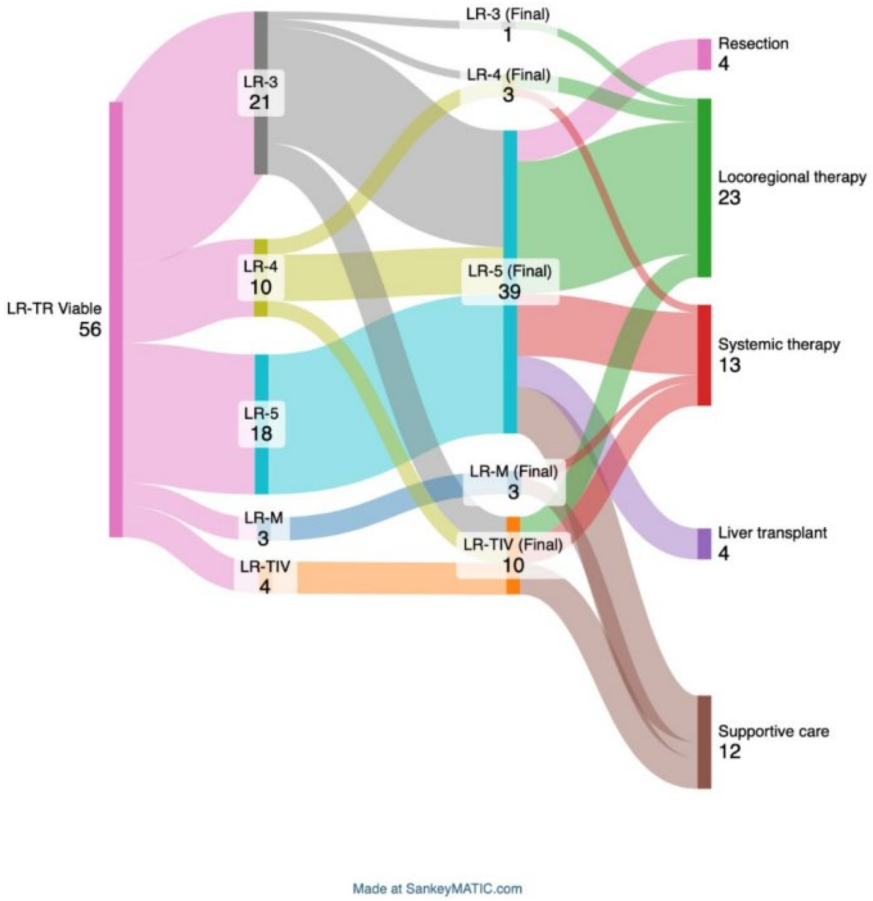

Keywords : Hepatocellular carcinoma, LI-RADS, Treatment response

[Scientific Session 2: HCC Imaging for Clinical Decision-Making]

SS02-2

LI-RADS Nonradiation Treatment Response Algorithm v2024: Enhanced Performance with Ancillary Features on Hepatobiliary MRI versus CT

Jaeseung Shin[1,4], Jeongin Yoo[2], Kyowon Gu[1], Sun-Young Baek[1], Jae Seok Bae[2], Min Woo Lee[1,4], Sang Yun Ha[3], Ji Hye Min[1,4*], Jeong Min Lee[2]

[1]Radiology, Samsung Medical Center, Korea
[2]Radiology, Seoul National University Hospital, Korea
[3]Pathology, Samsung Medical Center, Korea
[4]Radiology, Sungkyunkwan University School of Medicine, Korea

To compare the diagnostic performance of Liver Imaging–Reporting and Data System (LI-RADS) Nonradiation Treatment Response Algorithm (TRA) version 2024 (v2024) with that of LI-RADS TRA version 2017 (v2017) for assessing hepatocellular carcinoma (HCC) viability after locoregional therapy (LRT), and to evaluate the incremental value of ancillary features (AFs) and the relative performance of CT versus hepatobiliary agent (HBA)–enhanced MRI.

This multicenter retrospective study included 245 patients (199 men (81.2%); median age, 61 years) who underwent nonradiation LRT for HCC followed by surgery between January 2018 and December 2021. Among them, 194 (79.2%) underwent both CT and HBA-MRI before surgery. Three radiologists independently applied LI-RADS Nonradiation TRA v2024 (with and without AFs) and v2017 to the largest treated lesion and reached a consensus. Surgical pathology (viable n = 193 [78.8%], complete necrosis n = 52 [21.2%]) was the reference standard. Diagnostic performances were compared with Bonferroni-adjusted McNemar tests; interobserver agreement was assessed with Fleiss κ.

On HBA-MRI, LI RADS Nonradiation TRA v2024 with AFs the highest diagnostic performance (sensitivity 79%, specificity 90%, and accuracy 82%), significantly exceeding v2024 without AFs (sensitivity 66%, accuracy 72%) and v2017 (sensitivity 67%, accuracy 73%) (all $P < .001$), while preserving comparable specificity (v2024 without AFs, 94%; v2017, 94%; $P > .05$). Among 194 paired CT–MRI cases, HBA-MRI with AFs achieved higher sensitivity (79%) and accuracy (81%) than CT with v2024 (64%, 71%; $P < .001$), with similar specificity (93%, 91%, $P = 0.66$). On subgroup analysis, HBA-MRI showed higher accuracy than CT after TACE (81% vs 71%, $P < .001$) but not after ablation (79% vs 79%, $P > .99$). Interobserver agreement for v2024 was substantial on CT ($\kappa = 0.65$) and moderate on HBA MRI ($\kappa = 0.54$).

LI RADS Nonradiation TRA v2024, particularly when AFs are incorporated, improves sensitivity and accuracy for detecting viable HCC after nonradiation LRT compared to v2017. While HBA-MRI with AFs provides the higher sensitivity and accuracy, it yields lower interobserver agreement for LR-TR categorization compared to CT.

Flowchart of patient selection.

LRT = locoregional therapy, HBA-MRI = hepatobiliary agent–enhanced MRI, HCC = hepatocellular carcinoma.

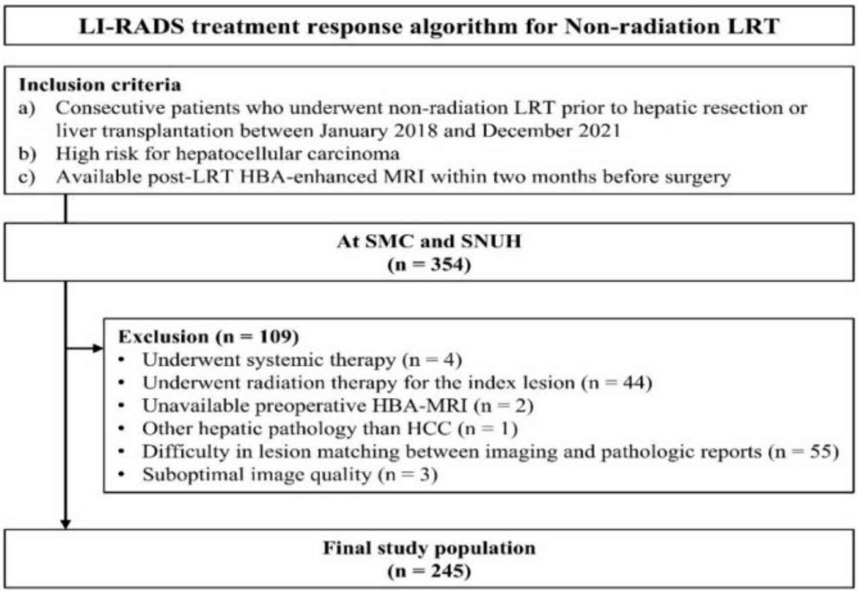

A 70-year-old man with non-B, non-C cirrhosis, 224 days after transarterial chemoembolization and radiofrequency ablation. Dynamic contrast-enhanced T1-weighted images (A, precontrast; B, arterial phase; C, portal venous phase; D, portal venous subtraction) demonstrate equivocal nodular enhancement (arrows) without definite APHE, leading to an LR-TR Equivocal categorization by LI-RADS TRA v2017. However, the lesion shows marked diffusion restriction (arrows) on the (E) diffusion-weighted image (b=800 s/mm^2) and (F) apparent diffusion coefficient map, with corresponding (G) subtle T2 hyperintensity (arrow). The presence of diffusion restriction, an ancillary feature favoring viability, allowed for the lesion to be upgraded to LR-TR Viable according to v2024 criteria. (H) A prior CT shows the treated lesion (arrow). (I) A low-power microscopic image (Hematoxylin and Eosin stain) of the surgical specimen confirms the presence of viable tumor (asterisk), corresponding to a final pathologic diagnosis of incomplete necrosis (80% necrosis).

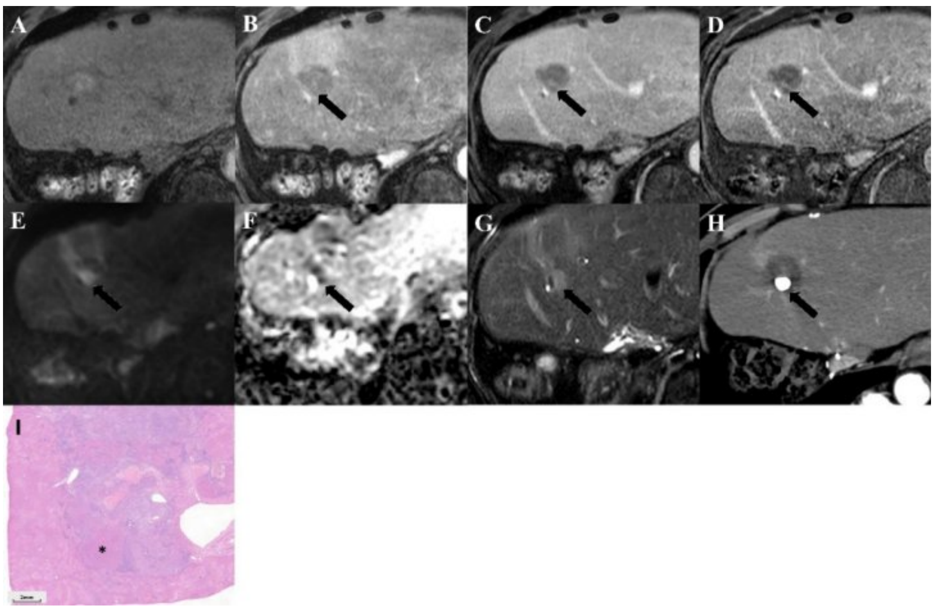

Keywords : LI-RADS, Treatment Response, Diagnostic performance

[Scientific Session 2: HCC Imaging for Clinical Decision-Making]

SS02-3

Performance of LI-RADS Nonradiation Treatment Response Algorithm version 2024 on MRI for Transarterial Chemoembolization Plus Systemic Therapy in HCC

Liuji Sheng[1], Hanyu Jiang[1], Yali Qu[1], Bin Song[1,2], Zheng Ye[1*]

[1]Radiology and Functional and Molecular Imaging Key Laboratory of Sichuan Province, West China Hospital Sichuan University, China
[2]Radiology, Sanya Peoples Hospital, China

The Liver Imaging Reporting and Data System treatment response algorithm version 2024 (LR-TRA v2024) provides a standardized framework for assessing treatment response of hepatocellular carcinoma (HCC) to locoregional therapy. However, its effectiveness in HCC patients undergoing locoregional plus systemic combination therapy remains uncertain. We aimed to investigate the performance of LR-TRA v2024 on MRI in detecting residual HCC following transarterial chemoembolization (TACE) plus systemic therapy.

This single-center retrospective study included consecutive adult patients who received TACE plus systemic therapy for HCC and subsequent surgical resection (July 2019 to November 2023). Patient inclusion and exclusion are illustrated in **Figure 1**. All contrast-enhanced preoperative MRIs were independently evaluated by three blinded radiologists for LR-TR categories and two ancillary features. Postoperative pathology was used as the reference standard for residual tumors, which was further categorized as any (>0%) or major (>10%) residual tumors. When investigating the performances of LR-TR categories, the LR-TR Equivocal category was grouped into the LR-TR Viable category. The diagnostic performances were evaluated using positive (PPV) and negative predictive values (NPV).

51 patients (median age, 56 years; 45 males) with 63 HCCs were included. For the detection of any residual tumor, the per-lesion PPV and NPV of the LR-TR Viable category were 100.0% and 46.9%, respectively; the per-patient PPV and NPV were 100.0% and 45.5%, respectively. For the detection of major residual tumor, the per-lesion PPV and NPV of the LR-TR Viable category were 80.6% and 84.4%, respectively; the per-patient PPV and NPV were 82.8% and 86.4%, respectively. The diagnostic performances of LR-TRA v2024 features and categories based on consensus interpretations are summarized in **Table 1.**

LR-TRA v2024 was effective in evaluating treatment response and detecting residuals of HCC to TACE plus systemic therapy.

Figure 1.

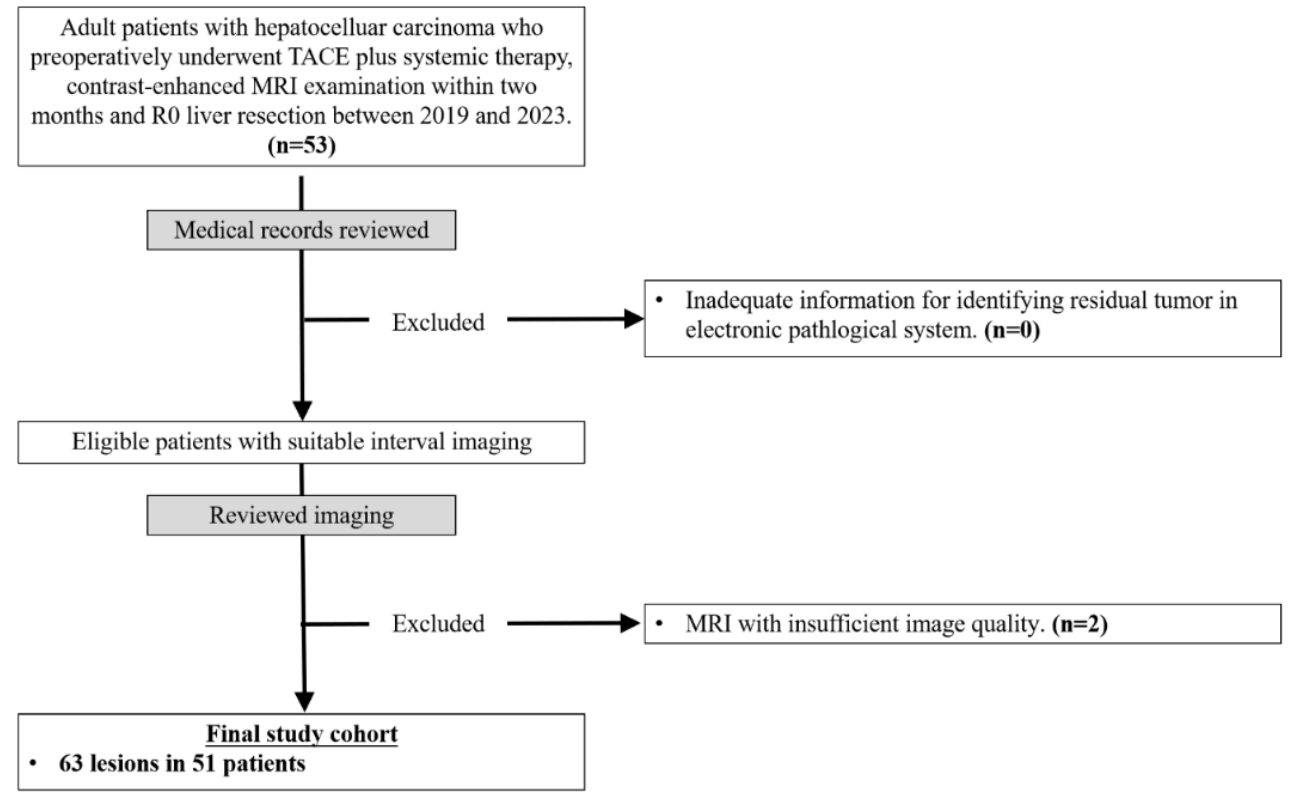

Table 1.

Consensus	Any/ Absence of Any residual viable tumor (non-pCR/ pCR)				
Per-lesion (*n* = 63)	**Masslike arterial phase hyperenhancement†**	**Masslike washout†**	**Masslike enhancement†**	**LR-TR Nonviable category‡**	**LR-TR Viable category†**
Sensitivity	31/48 (64.6) [49.5, 77.8]	21/48 (43.8) [29.5, 58.8]	31/48 (64.6) [49.5, 77.8]	15/15 (100) [78.2, 100]	31/48 (64.6) [49.5, 77.8]
Specificity	15/15 (100) [78.2, 100]	15/15 (100) [78.2, 100]	15/15 (100) [78.2, 100]	31/48 (64.6) [49.5, 77.8]	15/15 (100) [78.2, 100]
PPV	31/31 (100) [NA, NA]	21/21 (100) [NA, NA]	31/31 (100) [NA, NA]	15/32 (46.9) [37.6, 56.4]	31/31 (100) [NA, NA]
NPV	15/32 (46.9) [37.6, 56.4]	15/42 (35.7) [30.2, 41.6]	15/32 (46.9) [37.6, 56.4]	31/31 (100) [NA, NA]	15/32 (46.9) [37.6, 56.4]
Accuracy	46/63 (73.0) [60.3, 83.4]	36/63 (57.1) [44.0, 69.5]	46/63 (73.0) [60.3, 83.4]	46/63 (73.0) [60.3, 83.4]	46/63 (73.0) [60.3, 83.4]
Per-patient (*n* = 51)					
Sensitivity	29/41 (70.7) [54.5, 83.9]	19/41 (46.3) [30.7, 62.6]	29/41 (70.7) [54.5, 83.9]	10/10 (100) [69.2, 100]	29/41 (70.7) [54.5, 83.9]
Specificity	10/10 (100) [69.2, 100]	10/10 (100) [69.2, 100]	10/10 (100) [69.2, 100]	29/41 (70.7) [54.5, 83.9]	10/10 (100) [69.2, 100]
PPV	29/29 (100) [NA, NA]	19/19 (100) [NA, NA]	29/29 (100) [NA, NA]	10/22 (45.5) [34.1, 57.3]	29/29 (100) [NA, NA]
NPV	10/22 (45.5) [34.1, 57.3]	10/32 (31.3) [25.5, 37.7]	10/22 (45.5) [34.1, 57.3]	29/29 (100) [NA, NA]	10/22 (45.5) [34.1, 57.3]
Accuracy	39/51 (76.5) [62.5, 87.2]	29/51 (56.9) [42.2, 70.7]	39/51 (76.5) [62.5, 87.2]	39/51 (76.5) [62.5, 87.2]	39/51 (76.5) [62.5, 87.2]
Per-lesion (*n* = 63)	**>10%/ ≤10% residual viable tumor (non-MPR/ MPR)**				
Sensitivity	25/30 (83.3) [65.3, 94.4]	19/30 (63.3) [43.9, 80.1]	25/30 (83.3) [65.3, 94.4]	27/33 (81.8) [64.5, 93.0]	25/30 (83.3) [65.3, 94.4]
Specificity	27/33 (81.8) [64.5, 93.0]	31/33 (93.9) [79.8, 99.3]	27/33 (81.8) [64.5, 93.0]	25/30 (83.3) [65.3, 94.4]	27/33 (81.8) [64.5, 93.0]
PPV	25/31 (80.6) [66.5, 89.7]	19/21 (90.5) [70.7, 97.4]	25/31 (80.6) [66.5, 89.7]	27/32 (84.4) [70.5, 92.4]	25/31 (80.6) [66.5, 89.7]
NPV	27/32 (84.4) [70.5, 92.4]	31/42 (73.8) [63.6, 82.0]	27/32 (84.4) [70.5, 92.4]	25/31 (80.6) [66.5, 89.7]	27/32 (84.4) [70.5, 92.4]
Accuracy	52/63 (82.5) [70.9, 90.9]	50/63 (79.4) [67.3, 88.5]	52/63 (82.5) [70.9, 90.9]	52/63 (82.5) [70.9, 90.9]	52/63 (82.5) [70.9, 90.9]
Per-patient (*n* = 51)					
Sensitivity	24/27 (88.9) [70.8, 97.6]	17/27 (63.0) [42.4, 80.6]	24/27 (88.9) [70.8, 97.6]	19/24 (79.2) [57.8, 92.9]	24/27 (88.9) [70.8, 97.6]
Specificity	19/24 (79.2) [57.8, 92.9]	22/24 (91.7) [73.0, 99.0]	19/24 (79.2) [57.8, 92.9]	24/27 (88.9) [70.8, 97.6]	19/24 (79.2) [57.8, 92.9]
PPV	24/29 (82.8) [68.5, 91.4]	17/19 (89.5) [68.6, 97.1]	24/29 (82.8) [68.5, 91.4]	19/22 (86.4) [68.1, 94.9]	24/29 (82.8) [68.5, 91.4]
NPV	19/22 (86.4) [68.1, 94.9]	22/32 (68.8) [57.0, 78.5]	19/22 (86.4) [68.1, 94.9]	24/29 (82.8) [68.5, 91.4]	19/22 (86.4) [68.1, 94.9]
Accuracy	43/51 (84.3) [71.4, 93.0]	39/51 (76.5) [62.5, 87.2]	43/51 (84.3) [71.4, 93.0]	43/51 (84.3) [71.4, 93.0]	43/51 (84.3) [71.4, 93.0]

Keywords : Hepatocellular carcinoma, Liver Imaging Reporting and Data System Treatment Response Algorithm, Transarterial chemoembolization plus systemic therapy

[Scientific Session 2: HCC Imaging for Clinical Decision-Making]

SS02-4

Clinical Efficacy of CT Iodine Map in Evaluating Treatment Effect of TACE plus RFA for HCC

Eun Ji Lim[1], Eun Ju Yoon[1*], Jin Woong Kim[1], Jun Hyung Hong[1], Sang Gook Song[1], Hyun Chul Kim[1]

[1]Radiology, Chosun university hospital, Korea

To evaluate added value of CT iodine map in assessing ablative margin (AM) within ablative zone immediately after transarterial chemoembolization (TACE) plus radiofrequency ablation (RFA) for hepatocellular carcinoma (HCC).

This study obtained approval from the institutional review board. It included a total of 41 consecutive patients with 52 HCCs who underwent contrast-enhanced CT with iodine map following the combination therapy with TACE and RFA. To assess the technical success of TACE plus RFA, the AM status within the ablative zones was evaluated on two sets of images: immediate CT image (image set 1) and immediate CT image with iodine map (image set 2). Two radiologists reviewed these images in consensus. The status of the AM was classified into four grades: A (absolutely curative), B (relatively curative), C (relatively non-curative), and D (absolutely non-curative). Additionally, the ability to distinguish the AM was assessed on each image sets using a scoring system to measure diagnostic confidence. The AM was compared on each image set based on the diagnostic criteria of the AM in the one-month follow-up CT imaging. The technical effectiveness of the procedure was evaluated based on one-month follow-up CT imaging. Two sets of images (image set 1 and 2) were reviewed by two radiologists in consensus.

On immediate CT image after RFA, image set 1 was categorized as follows: grade A (n=18), grade B (n=14), grade C (n=18), and grade D (n=2). Image set 2 was categorized as follows: grade A (n=31), grade B 7(n=12), grde C (n=7), and grade D (n=2). According to status of AM, technical success on each image set was determined to be achieved in 32 (61.5%) and 43 (82.7%), respectively (P<.001). Confidence agreement for status of AM on each image set was 2.84 and 3.87, respectively (P<.001). The technical effectiveness was achieved in all of ablation zones on one-month follow-up CT. Based on the one-month follow-up CT, the diagnostic accuracy of technical success was 70.9% and 96.4% for each image set of immediate CT, respectively (P<.001).

CT iodine map can enhance the diagnostic performance of assessing the AM and technical success immediately after TACE plus RFA for HCC.

Keywords : CT iodine map, HCC, Ablative margin

[Scientific Session 2: HCC Imaging for Clinical Decision-Making]

SS02-5

Identification of Benefit Subgroups from Heterogeneous Effects of Adjuvant Transarterial Chemoembolization in Hepatocellular Carcinoma Using Causal Model

Tianyi Xia[1], Yaoyao Yu[1], Lingling Gao[2], Shenghong Ju[1*]

[1]Radiology, Zhongda Hospital Medical School of Southeast University, China
[2]Science and Opto-electronics Engineering, Beihang University, China

Adjuvant transarterial chemoembolization (TACE) after curative resection for hepatocellular carcinoma (HCC) shows conflicting results, likely due to the heterogeneity of treatment effects (HTEs). We aimed to assess HTE and develop a tool to identify patients most likely to benefit from adjuvant TACE.

We retrospectively included HCC patients from 10 tertiary centers (real-world cohort, n = 2,630) between 2012 and 2023 and an independent clinical trial (validation cohort, n = 328). After propensity score matching between patients with and without adjuvant TACE, the real-world cohort was defined as the development cohort (n = 1,632). HTE on overall survival (OS) was assessed using (1) subgroup analyses, (2) Cox regression (risk-based), and (3) causal survival forest (effect-based) in the development cohort. Individual treatment effects were used to inform a policy tree (iATACE), which was validated across various cohorts. Survival analyses were performed using Cox regression and log-rank tests.

A total of 2,958 patients were included (median age, 58 years; 83.6% male). After matching, adjuvant TACE showed no significant average treatment effect on OS [hazard ratio (HR) 0.85, 95% confidence interval (CI) 0.70-1.03, P = 0.1061]. Consistent HTEs were observed across subgroup-, risk-, and effect-based analyses. Patients with microvascular invasion, younger age, or corona enhancement on imaging derived greater survival benefits (P <0.05). The iATACE stratified patients into recommendation subgroups; those in the rec-adjuvant TACE subgroup achieved better survival (HR 0.54, 95% CI 0.43-0.69), while the rec-active surveillance subgroup had poorer outcomes (HR 1.88, 95% CI 1.32-2.67) in the development cohort (P <0.05). The stratified treatment effect was confirmed in the validation and real-world cohorts (P <0.05).

Adjuvant TACE demonstrates significant HTE following curative resection for HCC. An interpretable tool enables the individualized identification of patients likely to benefit from adjuvant TACE, providing a framework for postoperative management.

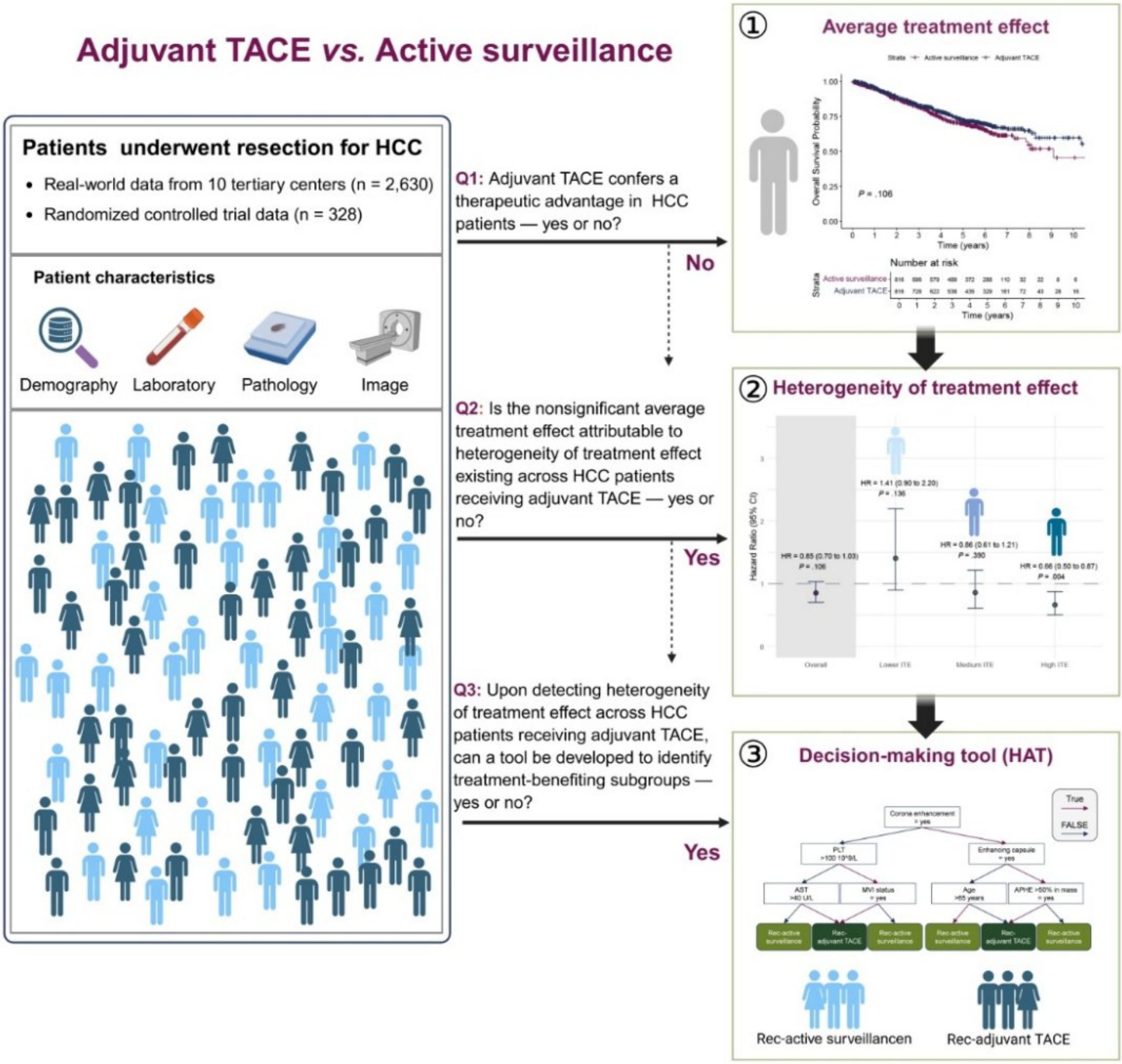

Keywords : Adjuvant transarterial chemoembolization, Hepatocellular carcinoma, Heterogeneity of treatment effects

[Scientific Session 2: HCC Imaging for Clinical Decision-Making]

SS02-6

Predictive Value of Gd-EOB-DTPA-Enhanced MRI Features for VETC Subtypes and Proportions and Their Combined Prognostic Significance in Hepatocellular Carcinoma

Hanjun Zhang[1], Weiguo Zhang[1*]

[1]Radiology, The Fourth Affiliated Hospital of Soochow University, China

Background: The imaging features and prognostic significance of vessels encapsulating tumor clusters (VETC) subtypes and proportions in hepatocellular carcinoma (HCC) are unknown.

Purpose: To identify Gd-EOB-DTPA-enhanced MRI features predicting the subtypes and proportions of VETC in HCC, and to evaluate the prognostic significance of integrating clinicoradiological features with certain VETC phenotypes.

Materials and Methods: This retrospective study included 211 patients with pathologically confirmed HCC who underwent Gd-EOB-DTPA-enhanced MRI between January 2015 and December 2024. Patients were categorized into different VETC subtypes and proportions groups based on pathological analysis. Imaging features predictive of these classifications were identified by using logistic regression analyses, and the prognostic implications of VETC-based stratification were assessed by integrating relevant imaging and clinicopathological indices by using Cox regression analyses.

Results: Macrotrabecular-VETC (MaT-VETC) (≥6 layers cell thickness) was independently associated with satellite nodule (aOR 4.54, 95% CI: 1.46–14.08; P = .009) and low arterial-phase enhancement ratio (aOR 3.33, 95% CI: 1.22-9.17; P = .019) . In multivariable analysis, a complete enhancing capsule (<50%, aOR 2.634, 95% CI:1.463-4.792; P=.001), lower hepatobiliary phase (HBP) lesion-to-liver signal ratio (aOR 0.17, 95% CI: 0.06–0.52; P = .002) and smaller lesion size (aOR 0.51, 95% CI: 0.28–0.94; P = .031) were independent predictors of higher VETC proportion. Elevated AFP (≥300 μg/L) predicted both MaT-VETC (aOR 3.53, 95% CI: 1.12–11.15; P = .031) and higher VETC proportion (aOR 2.32, 95% CI: 1.28–4.23; P = 0.006). MaT-VETC was independently associated with worse overall survival (aHR 2.84, 95% CI: 1.03–7.78; P = .043), whereas a higher VETC proportion showed a nonsignificant trend toward shorter survival (aHR 2.069, 95% CI: 0.781-5.480; P=.143).

Conclusion: Preoperative Gd-EOB-DTPA-enhanced MRI features and elevated AFP levels could be used to predict VETC subtypes and proportions. MaT-VETC was associated with worse overall survival.

Gd-EOB-DTPA-enhanced MR images in an 81-year-old man demonstrate a 7.6-cm hepatocellular carcinoma in the left medial lobe, classified as the MiT-VETC subtype with 20% microtrabecular component. The lesion exhibits arterial phase hyperenhancement (A) and hepatobiliary-phase hyperintensity (B). Corresponding photomicrographs show thin trabeculae (<6 cells) surrounded by vascular spaces (C, hematoxylin–eosin stain; original magnification, ×100) and CD34-positive endothelial rims encompassing over half the tumor area (D, CD34 immunostain; original magnification, ×100). (MiT: Microtrabecular; MaT:Macrotrabecular)

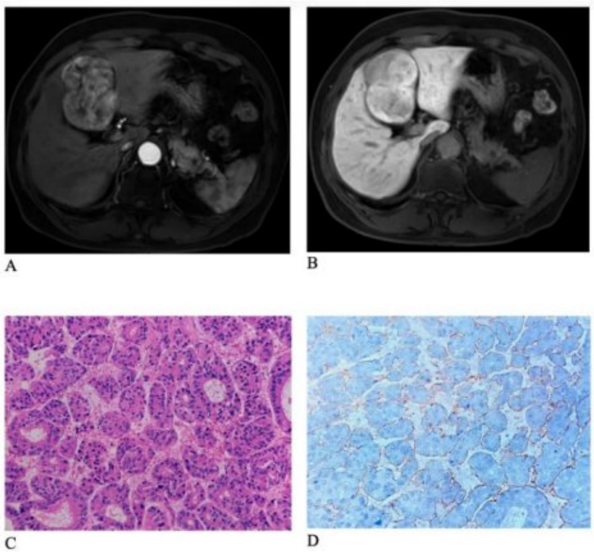

In a 35-year-old man, MR images reveal an 11.5-cm hepatocellular carcinoma in the left hepatic lobe, classified as the MaT-VETC subtype with a 50% macrotrabecular component. The tumor demonstrates predominant arterial hypoenhancement (A) with hepatobiliary-phase hyperintensity (B). Histology reveals thick trabeculae (>6 cells) within vascular spaces (C, hematoxylin–eosin stain; original magnification, ×100) and extensive CD34-positive endothelial encasement (D, CD34 immunostain; original magnification, ×100). (MiT: Microtrabecular; MaT:Macrotrabecular)

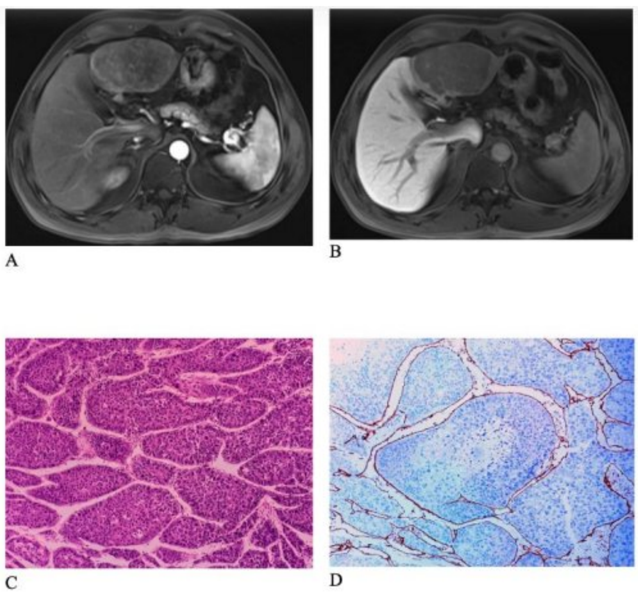

Keywords : VETC, Prognostic and prediction, Gd-EOB-DTPA-enhanced MRI

[Scientific Session 2: HCC Imaging for Clinical Decision-Making]

SS02-7

Gd-EOB-DTPA-enhanced MRI-based Fractal Analysis for Preoperative Evaluation of Vessels Encapsulating Tumor Clusters and Microvascular Invasion in Hepatocellular Carcinoma

Dan Liu[1], Qian Li[1], Feng Che[1], Yi Wei[1], Bin Song[1*]

[1]Radiology, West China Hospital, China

To develop and validate fractal features derived from Gd-EOB-DTPA-enhanced MRI for the preoperative prediction of the vessels encapsulating tumor clusters (VETC) and microvascular invasion (MVI) in patients with hepatocellular carcinoma (HCC).

This retrospective study included 320 patients with histologically confirmed HCC who underwent preoperative Gd-EOB-DTPA- enhanced MRI at a single tertiary medical center. The cohort was chronologically divided into a training set (n = 224) and a test set (n = 96). Based on histopathological assessment of VETC and MVI) patients were stratified into two biological subtypes: VM-HCC+ (defined as VETC+/MVI+, VETC−/MVI+, or VETC+/MVI−) and VM-HCC− (VETC−/MVI−). The fractal dimension (FD) was computed from the hepatobiliary phase (HBP) images using a box-counting algorithm. Conventional qualitative imaging features were also evaluated. Univariate and multivariate logistic regression analyses were performed to identify independent predictors of VM status. A nomogram was constructed for individualized risk estimation. Recurrence-free survival (RFS) was analyzed using the Kaplan–Meier method and compared by the log-rank test.

FD values were significantly higher in the VM-HCC+ group than in the VM-HCC− group ($P < 0.05$). In the test cohort, the FD-based model achieved an area under the receiver operating characteristic curve (AUC) of 0.80 (95% confidence interval [CI]: 0.71–0.89). Multivariate logistic regression analysis identified serum alpha-fetoprotein level, presence of intratumoral artery, and peritumoral hypointensity on HBP as independent predictors of VETC/MVI status. These variables were integrated to construct a clinical-radiological model. Incorporation of FD into this model significantly improved diagnostic performance, with the AUC increasing from 0.67 (95% CI: 0.56–0.78) to 0.82 (95% CI: 0.74–0.90) in the test set ($P < 0.05$). Moreover, patients classified as high-risk by the FD model exhibited significantly shorter RFS compared with thosein the low-risk group ($P < 0.05$).

Fractal analysis based on Gd-EOB-DTPA-enhanced MRI enables quantitative characterization of VETC and MVI status through the fractal dimension. The proposed FD-based model may serve as a noninvasive imaging biamarker for preoperative assessment of tumor biology and prognosis stratification in patients with HCC.

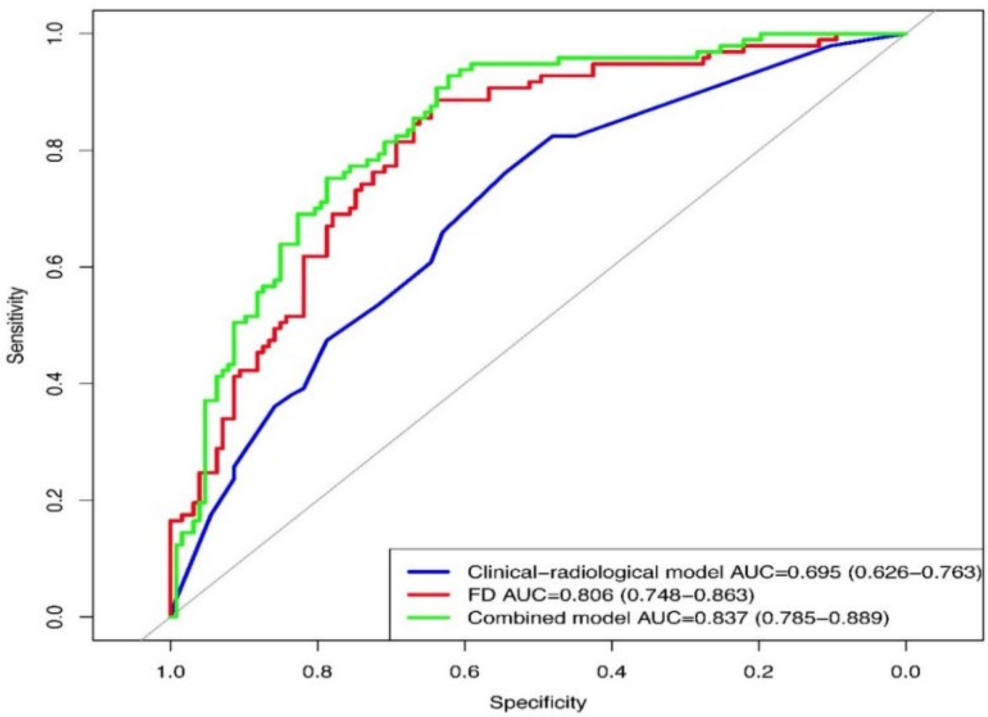

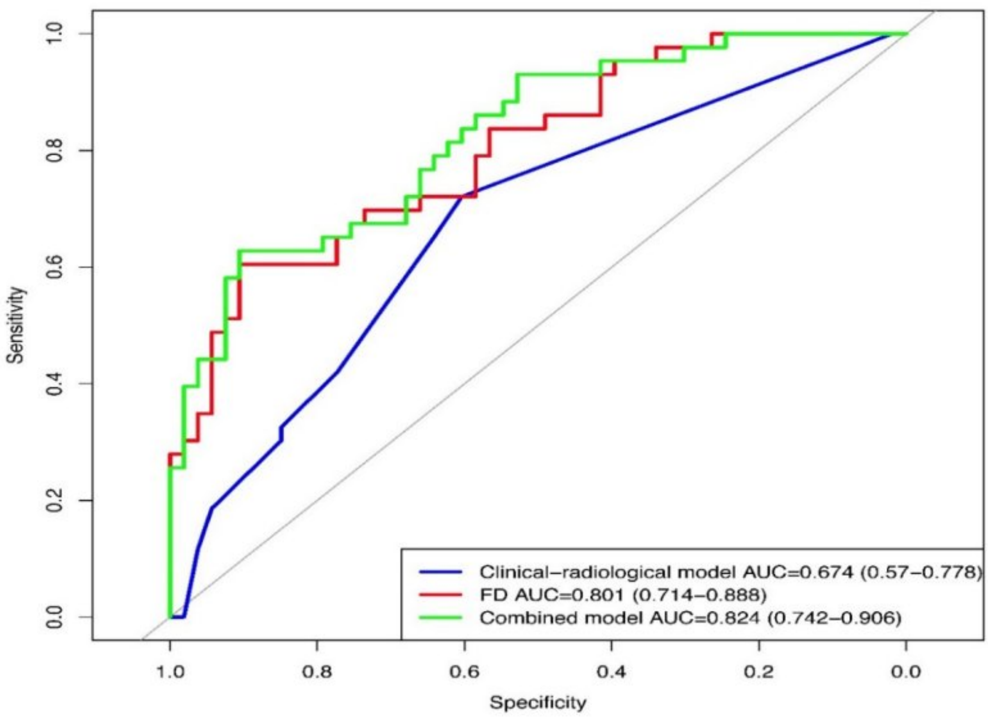

Keywords : Fractal analysis, Hepatocellular carcinoma, Magnetic resonance imaging

[Scientific Session 2: HCC Imaging for Clinical Decision-Making]

SS02-8

Value of Preoperative Contrast-Enhanced CT-based Radiomics for Predicting CK19-Positive Hepatocellular Carcinoma

Yawen Wang[1], Shenghong Ju[1*]

[1]Radiology, Zhongda Hospital Southeast University, China

To develop and validate a radiomics model based on preoperative contrast-enhanced CT for predicting cytokeratin 19 (CK19)-positive hepatocellular carcinoma (HCC), and to investigate its potential clinical application value.

This multi-center retrospective study enrolled patients with pathologically confirmed HCC who underwent preoperative contrast-enhanced CT between February 2012 and November 2023. Based on postoperative immunohistochemical staining results for CK19, patients were categorized into CK19-positive (n=101) and CK19-negative (n=397) groups. Radiomics features were extracted from the tumor region on non-contrast, arterial, and portal venous phase CT images after image registration. In the training cohort, feature dimensionality reduction was performed using Maximum Relevance - Minimum Redundancy (mRMR) and the Least Absolute Shrinkage and Selection Operator (LASSO) regression. A radiomics model was subsequently constructed using logistic regression. The model was validated in internal and external test cohorts using pathology as the gold standard. A hybrid model integrating radiomics features with significant clinical-radiological characteristics was also developed. Model performance for predicting CK19-positive HCC was evaluated using the Area Under the Receiver Operating Characteristic Curve (AUC), and clinical utility was assessed via Decision Curve Analysis (DCA).

A total of 498 patients (median age 57 years; 407 males) were included and allocated into training (n=239), internal test (n=103), and external test (n=156) cohorts. Multivariate logistic regression identified AFP >400 ng/ml (OR=4.05, 95% CI: 2.12–7.74, P<0.01) and peritumoral arterial enhancement (OR=2.15, 95% CI: 1.10–4.23, P=0.026) as independent predictors of CK19-positive HCC. The radiomics model achieved AUCs of 0.68 and 0.77 in the internal and external test cohorts, respectively. The hybrid model demonstrated superior performance, with AUCs of 0.77 and 0.78 in the internal and external test cohorts, respectively.

The hybrid model, integrating preoperative contrast-enhanced CT radiomics features with clinical-radiological indicators, effectively predicts CK19-positive HCC, demonstrating good generalizability and promising clinical utility.

Figure1 : Assessment of models for the ability to predict CK19 status. Areas under the receiver operating characteristic curve (AUCs)

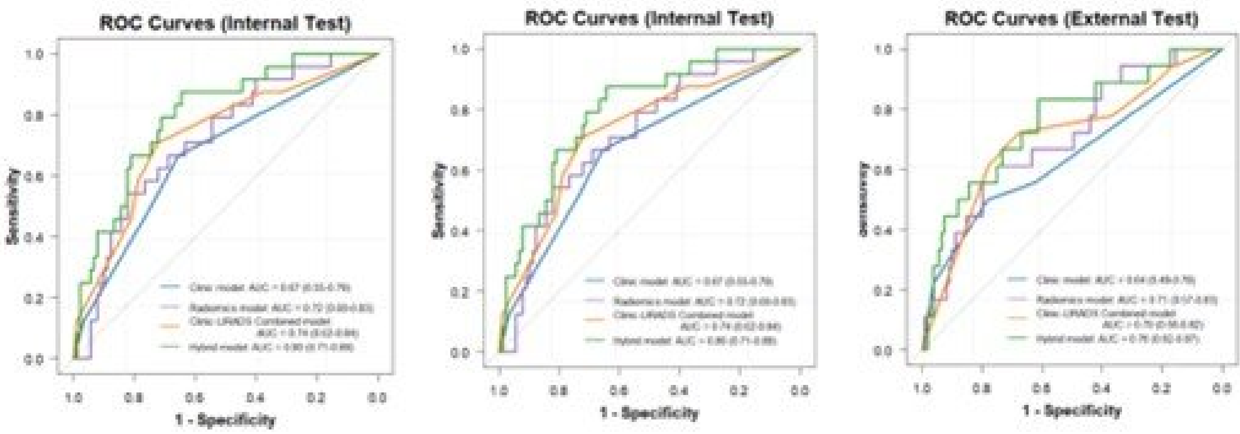

Dataset		Clinic Model	Hybrid Model
Training (n = 268)	Sensitivity (%)	68 (40/59)	80 (47/59)
	Specificity (%)	60 (126/209)	69 (145/209)
	Accuracy (%)	62 (166/268)	72 (192/268)
Internal test (n = 114)	Sensitivity (%)	67 (16/24)	88 (21/24)
	Specificity (%)	66 (59/90)	67 (60/90)
	Accuracy (%)	66 (75/114)	71 (81/114)
External test (n = 127)	Sensitivity (%)	64 (16/25)	76 (19/25)
	Specificity (%)	61 (62/102)	78 (79/102)
	Accuracy (%)	61 (78/127)	77 (98/127)

Keywords : CT Radiomics, Hepatocellular Carcinoma, Cytokeratin 19

[Scientific Session 3: IBD Imaging: Standardization and Innovation]

SS03-1

Redefining Radiological Criteria for Small Bowel Stricture in Crohn's Disease: Effects of a 2.5 cm Pre-stenotic Dilatation Threshold on Stricture Prevalence and Prognosis

Hae Young Kim[1*], Se Jin Choi[1], Eun Sun Choi[1], Jong Keon Jang[1], Seong Ho Park[1]

[1]Radiology, Asan Medical Center, Korea

Traditionally, small bowel stricture in Crohn's disease has been defined as a luminal narrowing with pre-stenotic dilatation >3 cm on imaging. However, there has been a concern that the 3 cm threshold yields low sensitivity for fibrostenosis. Therefore, the Society of Abdominal Radiology, American Gastroenterological Association, and the Society for Pediatric Radiology recently modified their consensus definition, lowering the threshold for pre-stenotic dilatation to ≥2.5 cm. The extent to which the new threshold increases stricture prevalence, and whether patients additionally identified as having a stricture (with pre-stenotic dilatation of 2.5–3 cm) carry an excess risk of adverse clinical outcomes, remain unclear. This study aimed to quantify the increase in stricture prevalence when applying the ≥2.5 cm threshold, and to assess whether risks for adverse outcomes are stratified according to the new diagnostic threshold.

This retrospective study included all consecutive patients who underwent CT enterography in 2017–2018 for routine follow-up of Crohn's disease. Three radiologists retrospectively reviewed CT images and classified patients into three groups: non-stricture, stricture with pre-stenotic dilatation 2.5–3 cm, and stricture with dilatation >3 cm. Stricture prevalence was calculated using both conventional and revised thresholds. Clinical outcomes during median follow-up of 84 months were analyzed using Cox proportional hazards regression and Poisson regression, adjusting for covariates including sex, age at Crohn's disease diagnosis, duration since initial diagnosis, smoking status, history of intestinal resection, small bowel penetration, colonic penetration or stricture, perianal fistula, endoscopically active inflammation, and fecal calprotectin.

Among 1,022 patients, 190 (18.6%) had stricture with pre-stenotic dilatation >3 cm, and 137 (13.4%) had stricture with pre-stenotic dilatation 2.5–3 cm, with stricture prevalence increased from 18.6% to 32.0% using the new threshold. Compared with the non-stricture group, both stricture groups had higher risk for emergency department visit (incidence rate ratio of 2.46 [95% CI, 1.52, 3.98] for 2.5–3 cm group and 2.05 [1.30, 3.23] for >3 cm group; and adjusted hazard ratio [aHR] of 2.13 [1.36, 3.34] and 2.04 [1.34, 3.09] respectively). Presence of stricture was also associated with an increased risk of surgery, particularly in the >3 cm group (aHR, 2.72 [1.70, 4.34]) and to a lesser extent in the 2.5–3 cm group (aHR, 1.79 [1.03, 3.09]). Both stricture groups also had higher risk for symptomatic obstruction (aHR, 8.05 [4.19, 15.48] and 6.57 [3.50, 12.35] for > 3cm group and 2.5–3 cm group respectively) and penetration (aHR, 3.47 [1.74, 6.92] and 4.41 [2.36, 8.24], respectively). Risk for new steroid use was elevated in the 2.5–3 cm group (aHR, 1.68 [1.25, 2.27]) but not in > 3 cm group (aHR, 1.28 [0.95, 1.73]).

Applying the ≥2.5 cm threshold classified an additional 13.4% of patients with CD as having small bowel stricture. Patients with 2.5–3 cm dilatation represent a subgroup characterized by dynamic disease activity and potential for therapeutic modification, but with less irreversible damage than those with >3 cm dilatation. Our findings support the new diagnostic criteria, which enable closer monitoring of this clinically relevant subgroup.

Table . Clinical outcomes according to small bowel stricture noted on baseline CT

	Non-stricture (n = 695)		Stricture [2.5–3 cm] (n = 137)		*P*-value	Stricture [>3 cm] (n = 190)		*P*-value
	Number of patients (%)	aHR (95% CI)	Number of patients (%)	aHR (95% CI)		Number of patients (%)	aHR (95% CI)	
Hospital visit								
ED visit	69 (9.9)	Reference	29 (21.2)	2.13 (1.36, 3.34)	<.001	39 (20.5)	2.04 (1.34, 3.09)	<.001
Ward admission	155 (22.3)	Reference	55 (40.1)	1.93 (1.40, 2.65)	<.001	67 (35.3)	1.73 (1.28, 2.34)	<.001
Surgery	47 (6.8)	Reference	19 (13.9)	1.79 (1.03, 3.09)	0.04	35 (18.4)	2.72 (1.70, 4.34)	<.001
New biologics/small molecule use*	137 (19.7)	Reference	41 (29.9)	1.35 (0.94, 1.94)	0.10	44 (23.2)	1.42 (0.99, 2.02)	0.05
New steroid use	198 (28.5)	Reference	61 (44.5)	1.68 (1.25, 2.27)	0.001	61 (32.1)	1.28 (0.95, 1.73)	0.10
Stricture-specific outcomes†								
Development of symptomatic obstruction	16 (2.3)	Reference	23 (16.8)	8.05 (4.19, 15.48)	<.001	28 (14.7)	6.57 (3.50, 12.35)	<.001
Development/aggravation of penetration	19 (2.7)	Reference	16 (11.7)	3.47 (1.74, 6.92)	<.001	26 (13.7)	4.41 (2.36, 8.24)	<.001

A 37-year-old male with development of symptomatic obstruction during follow-up. (A, B) Coronal-reformatted images of the baseline CT enterography show two small bowel strictures (arrowheads) with pre-stenotic dilatation 2.5–3 cm. The patient had been diagnosed with Crohn's disease 6 years earlier and was on immunomodulator. (C, D) After 35 months of follow-up, the patient presented to emergency department with acute pain, and increased pre-stenotic dilatation of over 3 cm on multipurpose abdomen and pelvis CT acquired without oral contrast.

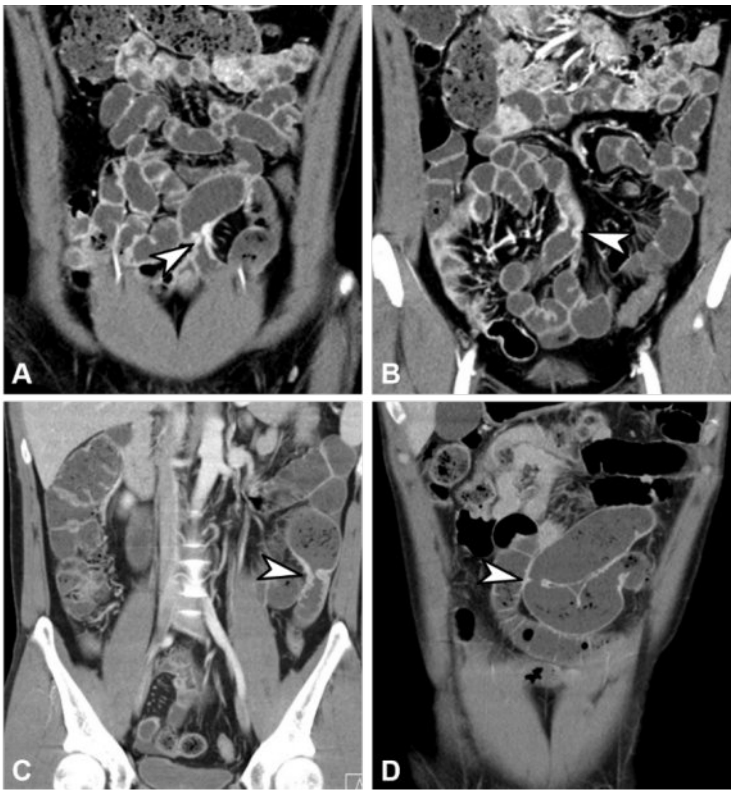

Keywords : Crohn's disease

[Scientific Session 3: IBD Imaging: Standardization and Innovation]

SS03-2

Pre-procedural Imaging Assessment Predicts Endoscopic Passability in Crohn's Disease: Performance of SAR-Based Stricture Criteria and Imaging Predictors of Failed Endoscopic Passage

Ziman Xiong[1*], Zhen Li[1], Yaqi Shen[1]

[1]Radiology, Tongji Hospital of Tongji Medical College of HUST, China

To determine how well radiologic stricture criteria derived from the Society of Abdominal Radiology (SAR) consensus predict whether an endoscope can traverse a diseased bowel segment, and to identify imaging and clinical factors associated with failed endoscopic passage.

In 109 patients who each underwent both CT enterography (CTE) and MR enterography (MRE), we performed segment-level and patient-level analyses. Impassable segments were defined as segments that the endoscope could not traverse during endoscopy because of luminal narrowing or obstruction. First, we tested the SAR imaging definition as a screening tool by comparing all endoscopically impassable segments with all other endoscopically assessed segments to estimate the prediction performance. Second, among segments that readers flagged as suspicious for stricture, we compared impassable versus passable segments and used mixed-effects logistic regression (patient random intercept) and penalized (L2) logistic models to identify independent imaging predictors of impassability. All segment analyses accounted for clustering by patient; patient-level models predicted whether a patient had impassable segments.

After excluding segments unreachable by endoscopy, 512 segments remained (reader-flagged strictures: CTE n=71, MRE n=72). At segment-level, SAR_imaging showed high specificity but moderate sensitivity: CTE sens 38.2%, spec 97.5%, PPV 52.0%, NPV 95.7%, AUC 0.679; MRE sens 61.8%, spec 95.6%, PPV 50.0%, NPV 97.2%, AUC 0.787. Among reader-flagged strictures, wall thickness best predicted impassability (CTE: AUC 0.707, cut-off ≈10.6 mm; MRE: AUC 0.642, cut-off ≈8.0 mm). Penalized multivariable models gave CTE AUC 0.761 (wall thickness OR = 1.36 [1.17 - 1.57]) and MRE AUC 0.663 (OR = 1.22 [1.05 - 1.46]). At patient-level (34/109 patients had ≥1 impassable segment), the count of strictures was associated with endoscopic impassability (CTE: 1 vs 0 OR = 4.28 [1.46–14.08], ≥2 vs 0 OR = 16.19 [2.19–307.31]; MRE: 1 vs 0 OR = 1.12 [0.96–1.36], ≥2 vs 0 OR = 1.27 [1.09–1.48]).

Pre-endoscopic imaging criteria show high specificity and excellent NPV, and wall thickness is the most informative imaging metric for predicting failed endoscopic passage. Patients with multiple strictures are at higher risk of having impassable segments and may require tailored endoscopic planning.

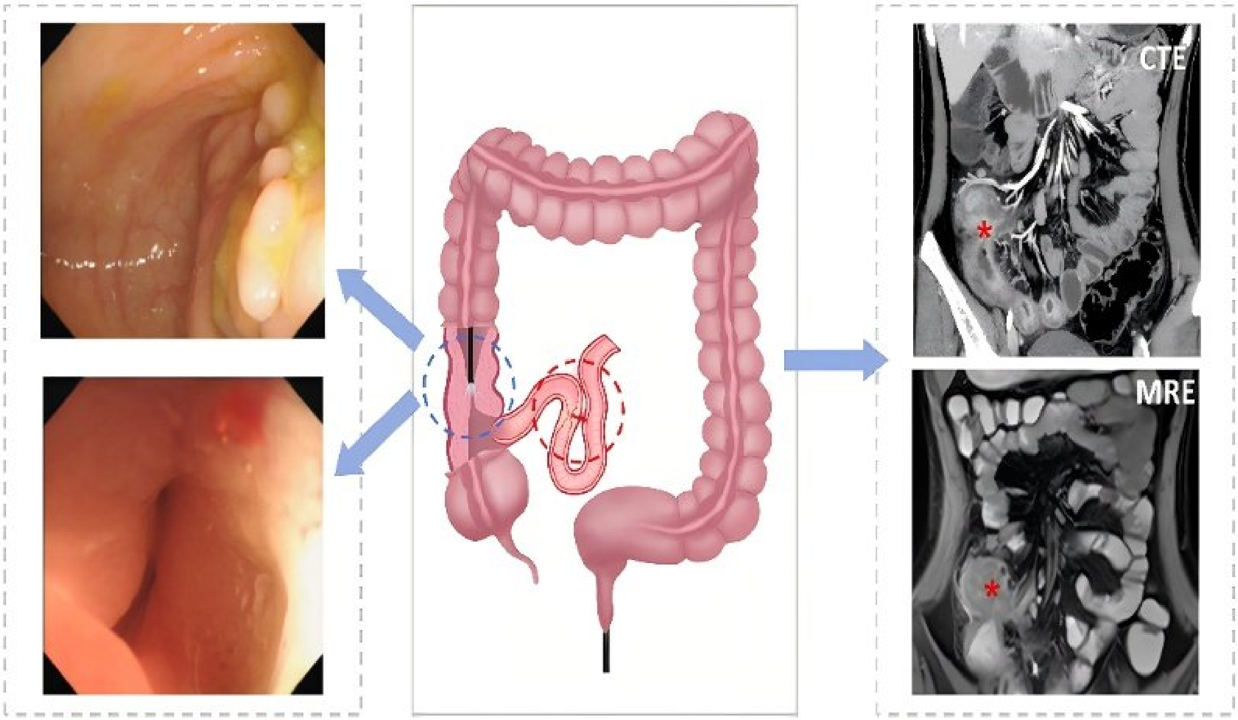

Keywords : Crohn's disease, CT/MR enterography, Endoscopic passability

[Scientific Session 3: IBD Imaging: Standardization and Innovation]

SS03-3

Current Status of Inflammatory Bowel Disease in China and the Establishment and Interpretation of the IBD-RADS System: A Multicenter Study and Clinical Translation

Yaqi Shen[1,2*]

[1]Radiology, Tongji Hospital of Tongji Medical College of HUST, China
[2]Radiology, Shanxi Bethune Hospital Shanxi Academy of Medical Sciences Third Hospital of Shanxi Medical University Tongji Shanxi Hospital, China

Inflammatory bowel disease (IBD) represents a growing global disease burden, with its prevalence rising rapidly in China. Key challenges include diagnostic delays (average 32.0 months), regional disparities (inland vs. coastal areas), and complex differential diagnosis (e.g., intestinal tuberculosis). The absence of a gold standard diagnostic method underscores the critical role of integrating multidisciplinary team (MDT) approaches with imaging technologies to enhance diagnostic efficiency.

Leveraging China's multicenter IBD database, we developed the IBD Reporting and Data System (IBD-RADS) by integrating CT/MRI radiomic features with artificial intelligence technology. This system establishes a graded diagnostic standard (Levels 1-5) by quantifying imaging biomarkers such as visceral fat distribution, intestinal wall enhancement patterns, and fistulas, and underwent multicenter retrospective and prospective validation.

The IBD-RADS system significantly improved the accuracy of differentiating Crohn's disease (CD) from ulcerative colitis (UC) (AUC >0.85). Imaging biomarkers, such as visceral fat predominance, were correlated with disease activity, nutritional status, and treatment failure risk ($p<0.05$). For instance, an imbalance between skeletal muscle and intermuscular fat predicted treatment failure in CD with a hazard ratio (HR) of 1.5 (95% CI: 1.2-1.9). Multicenter validation demonstrated that IBD-RADS has high specificity (>90%) in distinguishing IBD subtypes (e.g., CD vs. intestinal Behçet's disease). Furthermore, the MDT model reduced the time to diagnosis from 79.4 months (pre-2010) to 3.1 months (2015), highlighting the clinical value of imaging synergy.

As a novel imaging tool, the IBD-RADS system addresses standardization challenges in IBD diagnosis and treatment in China through quantitative indicators and AI enhancement. Its integration with genetic background (unique loci in East Asian populations) and clinical parameters provides a basis for personalized treatment.

Keywords : Inflammatory bowel disease, Artificial intelligence, Imaging diagnosis

[Scientific Session 3: IBD Imaging: Standardization and Innovation]

SS03-4

Rethinking Anorectal Cancer Surveillance Using MRI in Crohn's Disease

Hae Young Kim[1], Seong Ho Park[1*], Sung Wook Hwang[2*]

[1]Radiology, Asan Medical Center, Korea
[2]Internal Medicine, Asan Medical Center, Korea

According to recent guidelines, imaging plays a limited role in diagnosing anorectal malignancy associated with perianal fistulizing Crohn’s disease (PFCD). This may be due to insufficient understanding of the histologic spectrum of PFCD-associated cancers, and possibly due to overlap in imaging findings between perianal abscess and mucinous adenocarcinoma arising in PFCD. The purpose of this study was to characterize the epidemiology of malignancies arising in CD—particularly anorectal cancer occurring in the setting of PFCD—and identify factors contributing to their misdiagnosis on imaging.

In this retrospective single-center study, all patients with definite or probable CD enrolled in a prospective inflammatory bowel disease (IBD) registry since 1997 were included. Standardized incidence ratios (SIRs) for cancer development were calculated using national age-, sex-, and calendar year–specific cancer incidence rates. Because SIR does not account for individual-level covariates, multivariable Cox proportional hazards analysis was additionally performed with PFCD modeled as a time-dependent covariate and adjusted for age at CD diagnosis, sex, smoking status, family history of IBD, and Montreal behavior. CT and MRI reports were reviewed to determine whether the diagnosis of anorectal cancer had been missed on imaging. Predictors of missed detection were assessed using multivariable logistic regression.

A total of 5,041 patients with CD were included, of whom 3,669 (72.8%) were male. In total, 2,773 patients (55.0%) had PFCD at diagnosis or developed PFCD during follow-up. During a median follow-up of 125 months (interquartile range, 60–193), 65 cases of small or large bowel cancer, 51 anorectal cancer, and 23 mucinous anorectal cancer were identified. Compared with the general Korean population, the cohort demonstrated substantially elevated cancer incidence, with SIRs of 7.27 (95% CI, 5.61–9.26) for small or large bowel cancer, 10.28 (7.65–13.52) for anorectal cancer, and 57.95 (36.74–86.96) for mucinous anorectal cancer. In multivariable Cox regression, PFCD was not significantly associated with small or large bowel cancer (HR, 1.48 [0.87–2.53]). For anorectal cancer (HR, 1.87 [0.99–3.53]) and mucinous anorectal cancer (HR, 2.67 [0.95–7.51]), estimates were not statistically significant but suggested a tendency toward increased risk in PFCD.

Among 43 patients with anorectal cancer, and CT or MRI performed prior to endoscopy, 19 (44%) had a missed diagnosis. Mucinous histology was the only significant predictor of missed diagnosis (OR, 6.56; 95% CI, 1.38–31.13). Larger tumor size, MRI availability, and more recent calendar year were associated with reduced likelihood of missed diagnosis, although not significantly.

The risk of small or large bowel cancer is elevated in CD, and markedly for mucinous anorectal cancer. The presence of perianal fistula tended to increase the risk of anorectal cancer among patients with CD, although this association did not reach statistical significance. Missed diagnosis of anorectal cancer on imaging was common, especially for mucinous tumors. Greater awareness of the distinctive histologic distribution of anorectal cancers in CD may contribute to enhanced role of imaging in early cancer detection.

A 38-year-old man with Crohn's disease presenting with voiding difficulty that started five days earlier. Axial contrast-enhanced CT images (A, B) demonstrate a large mass involving the anal canal and right ischiorectal/ischioanal fossa. The lesion shows peripheral contrast enhancement without a definite enhancing solid component and was initially misinterpreted as an abscess. The patient had Seton in situ (arrows) for known perianal fistula. Subsequent MR enterography performed within one week (C) revealed that the lesion had a lobulated contour and was composed of numerous locules with hyperintensity on axial fat-saturated T2-weighted image. The mass was pathologically confirmed as mucinous adenocarcinoma.

Keywords : Crohn's disease, Perianal fistula, Mucinous adenocarcinoma

[Scientific Session 3: IBD Imaging: Standardization and Innovation]

SS03-5

Beyond Surgery: Time-varying Impact of Medical Therapy and Baseline CT Enterography Features on Long-term Surgical Avoidance in Crohn's Disease

Xiaonan Yang[1], Ziman Xiong[1], Jiayi Li[1], Zhen Li[1], Yaqi Shen[1*]

[1]Radiology, Tongji Hospital Tongji Medical College Huazhong University of Science and Technology, China

Surgery remains a necessary but undesirable outcome for Crohn's disease (CD), where the real therapeutic goal is not merely to predict surgery but to prevent it through timely and effective medical therapy. Although biologics, immunomodulators, and small-molecule agents have revolutionized CD management, their true long-term protective effect on surgical avoidance remains uncertain. Most existing prognostic models considered only baseline exposures and static predictors, overlooking that medical treatment evolves dynamically with disease activity and clinical response. This study aimed to evaluate whether biologics, immunomodulators, and small-molecule agents truly reduce surgical risk when modeled as time-varying exposures, and to integrate these dynamic therapeutic effects with baseline CT enterography (CTE) features for individualized surgical risk prediction and prevention.

A retrospective cohort of 502 CD patients who underwent baseline CTE and longitudinal follow-up (median 24 months) was analyzed. Baseline variables included clinical characteristics and quantitative CTE metrics. Follow-up data captured initiation, intensification, or discontinuation of biologics, immunomodulators, and small-molecule agents. Medical therapies were encoded as time-varying covariates and analyzed using time-dependent Cox models and marginal structural models (MSM) with inverse probability of treatment weighting (IPTW) to adjust for time-dependent confounders (CRP, albumin, disease activity). The primary endpoint was time-to-surgery, defined as intestinal resection or emergency operation.

During follow-up, 142 patients (28.3%) underwent surgery. Unadjusted analyses showed that biologic use was associated with lower surgical risk ($p < 0.01$). After MSM adjustment, ongoing biologic exposure remained protective but attenuated (HR = 0.71; 95% CI 0.49–1.05; $p = 0.08$). Immunomodulators and small-molecule agents demonstrated complementary benefits, particularly in patients with mild baseline wall thickening (< 5 mm) or limited disease extent. In contrast, severe baseline CTE features—wall thickness ≥ 6 mm, dilation ratio > 3, and abscess formation—remained independent predictors of surgery (HR > 2.0, all $p < 0.01$). The integrated imaging-therapy model achieved superior discrimination (C-index = 0.83) compared with the clinical model alone (C-index = 0.75).

Dynamic modeling revealed that the protective effect of medical therapy on surgical avoidance is context-dependent. Early and sustained use of biologics, immunomodulators, or small-molecule agents confers the greatest benefit among patients with moderate baseline disease activity. These findings emphasize that preventing surgery, rather than merely predicting it, should be the central

therapeutic goal in Crohn's disease. Integrating baseline CTE phenotype with longitudinal therapy dynamics provides a robust framework for precision, imaging-guided management and may inform optimal treatment timing to avert surgical intervention.

Keywords : Crohn's Disease, CT Enterography, Biologic Therapy

[Scientific Session 3: IBD Imaging: Standardization and Innovation]

SS03-6

Toward Precision Surgery: YOLO-assisted Radiomics and Body Composition Fusion for Predicting Surgical Complexity in Crohn's Disease

Xiaonan Yang[1], Ziman Xiong[1], Zhen Li[1], Yaqi Shen[1*]

[1]Radiology, Tongji Hospital Tongji Medical College Huazhong University of Science and Technology, China

Surgical complexity in Crohn's disease (CD) varies substantially among patients and is a key determinant of perioperative outcomes. Conventional indicators fail to capture the anatomic fibrosis, mesenteric inflammation, and systemic nutritional status that underlie technical difficulty. This study aimed to develop a preoperative, CT-based multimodal fusion model integrating YOLO-assisted lesion segmentation, radiomics, deep learning features, and quantitative body composition parameters to predict surgical complexity, using a large multicenter cohort of CD patients.

A total of 714 CD patients from three tertiary centers who underwent intestinal resection with available preoperative CT (≤3 months before surgery) were retrospectively analyzed. A composite Surgical Complexity Score (SCS, 0–12) was defined from operative duration, blood loss, adhesion severity, staged or stoma surgery, and intraoperative complications. Lesions were automatically detected and segmented using YOLOv10-seg, producing pixel-level masks for strictures, fistulas, and abscesses. Radiomics features and deep convolutional embeddings from YOLO's backbone were extracted from segmented regions. L3-level body composition metrics—skeletal muscle area (SMA), skeletal muscle density (SMD), visceral fat area (VFA), and intermuscular fat area (IMFA)—were quantified to assess systemic nutritional and inflammatory status. Features were standardized, harmonized across scanners using ComBat, and filtered for robustness (ICC > 0.85). Gradient boosting and multitask regression models were trained to predict both continuous SCS and high-complexity surgery (SCS ≥ 8). Performance was evaluated by AUC, C-index, mean absolute error (MAE), calibration, and decision curve analysis (DCA), with cross-center validation.

Automatic YOLO segmentation achieved mAP@0.5 = 0.84 and Dice coefficient = 0.80. The fusion model combining radiomics, deep, and body composition features achieved the best performance (AUC = 0.89, MAE = 0.56, C-index = 0.86), outperforming clinical-only (AUC = 0.73) and radiomics-only (AUC = 0.81) models. Low SMD and high IMFA were independently associated with elevated SCS ($\beta > 0$, $p < 0.01$), reflecting the impact of sarcopenic inflammation on operative difficulty. Deep features capturing mural heterogeneity and perienteric inflammation improved discrimination (ΔAUC = +0.05). The model maintained calibration and discrimination across all three centers, confirming robustness and generalizability.

This large-scale, multicenter study demonstrates that YOLO-assisted segmentation combined with radiomics–deep fusion and body composition profiling enables accurate preoperative prediction of

surgical complexity in Crohn's disease. The integrated model quantitatively captures both local inflammatory morphology and systemic nutritional status, providing a reproducible framework for precision surgical planning and risk stratification. These results highlight the translational potential of AI-driven imaging biomarkers to enhance surgical decision-making in inflammatory bowel disease.

Keywords : Crohn's Disease, Deep Learning, Body Composition

[Scientific Session 3: IBD Imaging: Standardization and Innovation]

SS03-7

Reducing Misdiagnosis of Appendiceal Mucinous Neoplasms: The Impact of Structured Training on Radiologists' Preoperative Diagnostic Performance

Ziman Xiong[1], Yaqi Shen[1*], Yufan Wang[1]

[1]Radiology, Tongji Hospital Tongji Medical College Huazhong University of Science and Technology, China

Because appendiceal mucinous neoplasms (AMN) are frequently misdiagnosed as appendicitis or primary ovarian mucinous tumors (POMT), accurate differentiation is clinically challenging. This study aimed to assess whether structured imaging training improves radiologists' ability to distinguish AMN from these mimics and to evaluate its potential impact on gynecologic surgical planning.

This single-center retrospective diagnostic study included pathologically confirmed cases of appendiceal mucinous neoplasms (AMN), appendicitis, and primary ovarian mucinous tumors (POMT) treated between January 2014 and June 2024. To reflect the most clinically relevant diagnostic challenge, only female patients were selected for the evaluation set. Two radiologists with different levels of experience independently reviewed anonymized CT scans to determine lesion origin and type, blinded to clinical information. After a structured AMN-focused training program and a one-month washout, the same cohort was re-evaluated. Diagnostic accuracy, confidence, and interpretation efficiency were compared before and after training.

A total of 100 patients were included, comprising 50 with AMN, 30 with appendicitis, and 20 with POMT. Structured training markedly improved diagnostic performance. Overall localization accuracy increased to 90%. AMN sensitivity rose for both junior and senior readers, while misdiagnosis rates declined substantially. Diagnostic confidence improved, and interpretation time was shortened after training.

Structured imaging training enhances radiologists' ability to recognize AMN, reduces misdiagnosis, and increases efficiency. Accurate preoperative identification of AMN may improve surgical decision-making, minimize intraoperative rupture, and lower the risk of pseudomyxoma peritonei. These findings provide quantitative support for incorporating AMN-focused modules into radiology education and multidisciplinary management.

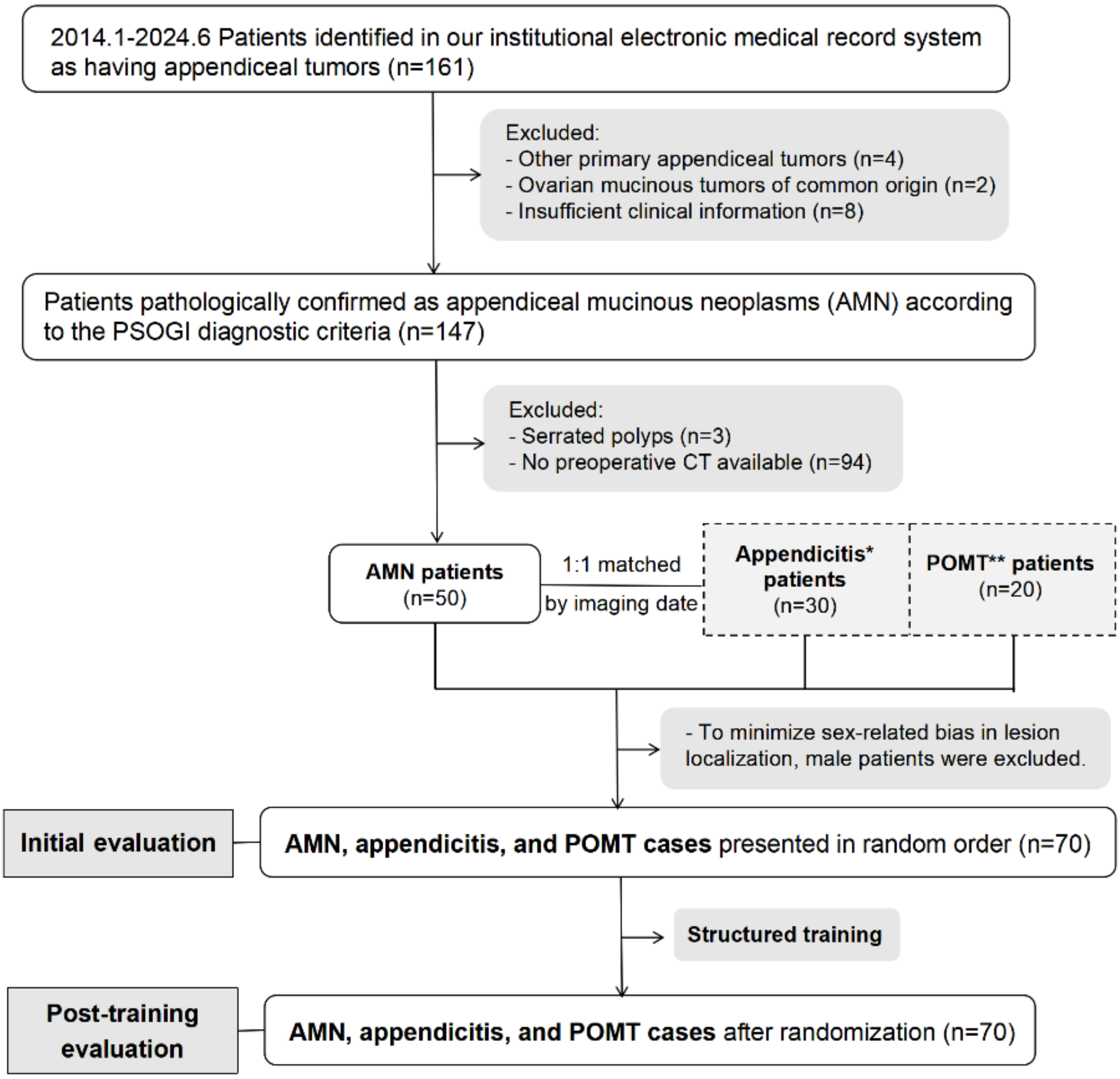

*Appendicitis diagnosed on clinical and imaging grounds.
**Patients with primary ovarian mucinous tumors (POMT) confirmed by postoperative histopathology.

Keywords : Appendiceal Mucinous Neoplasm, CT, Clinical Decision-Making

[Scientific Session 4: GU Issues 1]

SS04-1

Computed Tomography-Based Unsupervised Clustering Identifies Clusters Associated with Progression Free Survival in Clear Cell Renal Cell Carcinoma

Jae Hyon Park[1*], Daeun Choi[2], Minsun Jung[3], Chang Gon Kim[4]

[1]Radiology, Armed Forces Daejeon Hospital, Korea
[2]Radiology, Yonsei University Severance Hospital, Korea
[3]Pathology, Yonsei University Severance Hospital, Korea
[4]Medical Oncology Internal Medicine, Yonsei University Severance Hospital, Korea

This study aimed to develop and validate a radiologic clustering model using CT imaging features to stratify clear cell renal cell carcinoma (ccRCC) patients by prognosis and identify key imaging predictors of 5-year progression free survival (PFS).

This retrospective study included 164 ccRCC patients with multiphase kidney CT and next-generation sequencing (NGS) between September 2003 and October 2024. Qualitative imaging features were extracted, and unsupervised consensus clustering was performed to classify tumors based on radiologic characteristics. A nomogram-based C1 score was derived from features predictive of the high-risk cluster. Model performance was evaluated using C-index and 5-year area under the receiver operating curve (AUC). Genetic alterations and copy number variations (CNVs) were also analyzed for associations with imaging features and survival.

Clustering revealed two distinct radiologic subtypes. Cluster C1 characterized by aggressive behavior such as tumor heterogeneity (p=0.011), exophytic growth pattern (p=0.002), non-smooth margin (p=0.019), and renal sinus extension (p=0.016), and was independently associated with poorer 5-year PFS (p=0.018). The C1 score demonstrated an AUC of 0.992 for predicting cluster C1 in the test-set. Using a cutoff of 0.75, the model achieved 96.3% sensitivity and 96.4% specificity. For predicting 5-year PFS, the C1 score showed moderate performance (AUC 0.65; C-index 0.65), which improved when combined with nodal/distant metastasis and BAP1 mutation status (AUC 0.71; C-index 0.67).

Radiologic clustering using CT features enables non-invasive prognostic stratification of ccRCC. The C1 score derived from this approach may serve as a practical tool to guide surveillance and treatment decisions.

Oncoplot of genetic alterations across ccRCC patients, stratified by radiologic cluster.

The top bar plot shows tumor mutational burden (TMB) for each patient. The bottom bar indicates radiologic cluster assignment (Cluster 1 in red, Cluster 2 in blue).

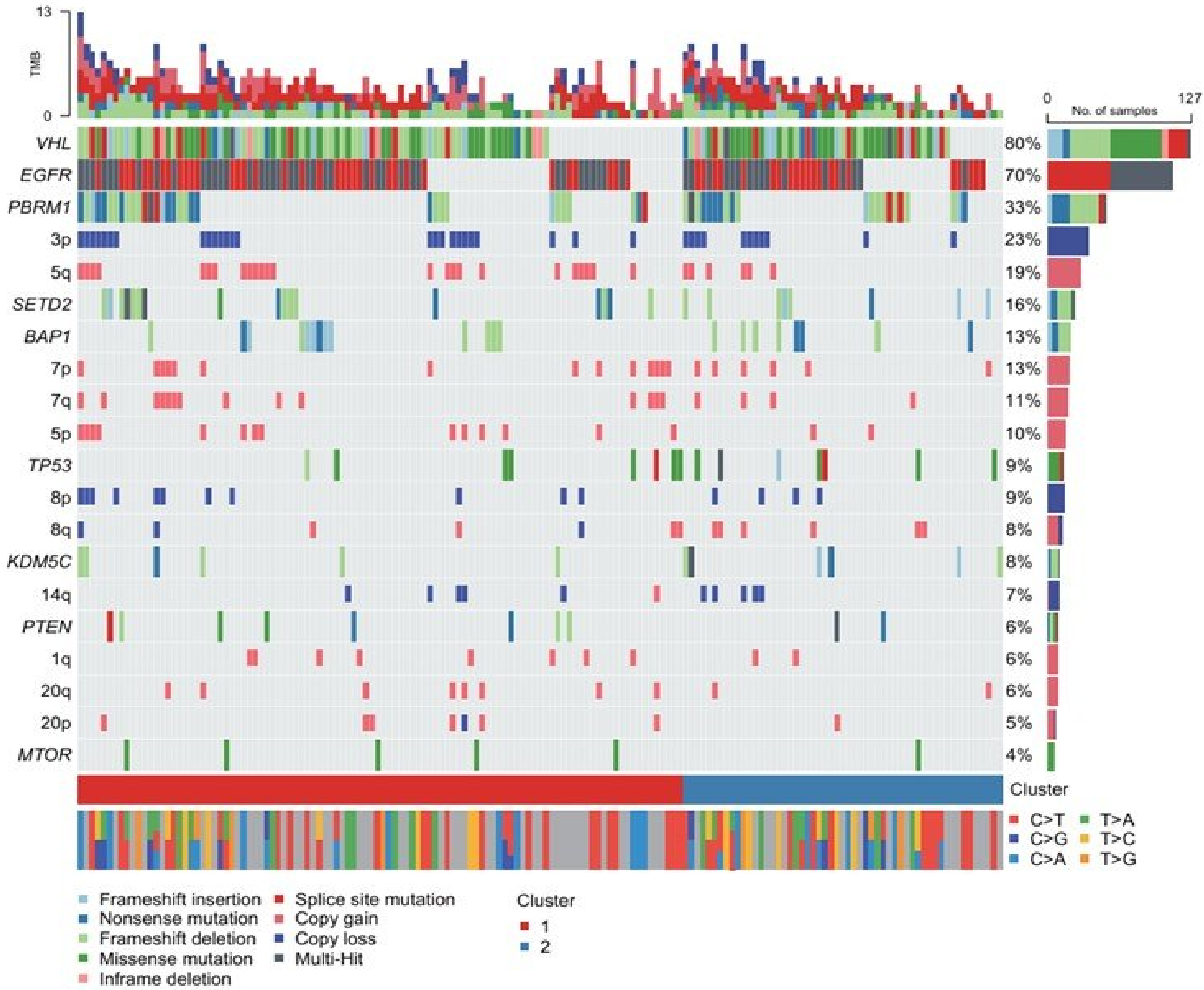

Kaplan-Meier survival analysis stratified by radiologic clusters (C1 vs. C2) in ccRCC patients. Shaded areas represent 95% confidence interval.

(A-B) Cause-specific progression-free survival (PFS) curves for cluster C1 (orange) and C2 (blue) in the training (A), and test (B). In both sets, cluster C1 was associated with significantly poorer 5-year cause-specific PFS.

(C-D) Overall survival (OS) curves for the training (D), and test (E). No statistically significant difference in OS was observed between clusters, although a trend toward worse survival in cluster C1 was noted.

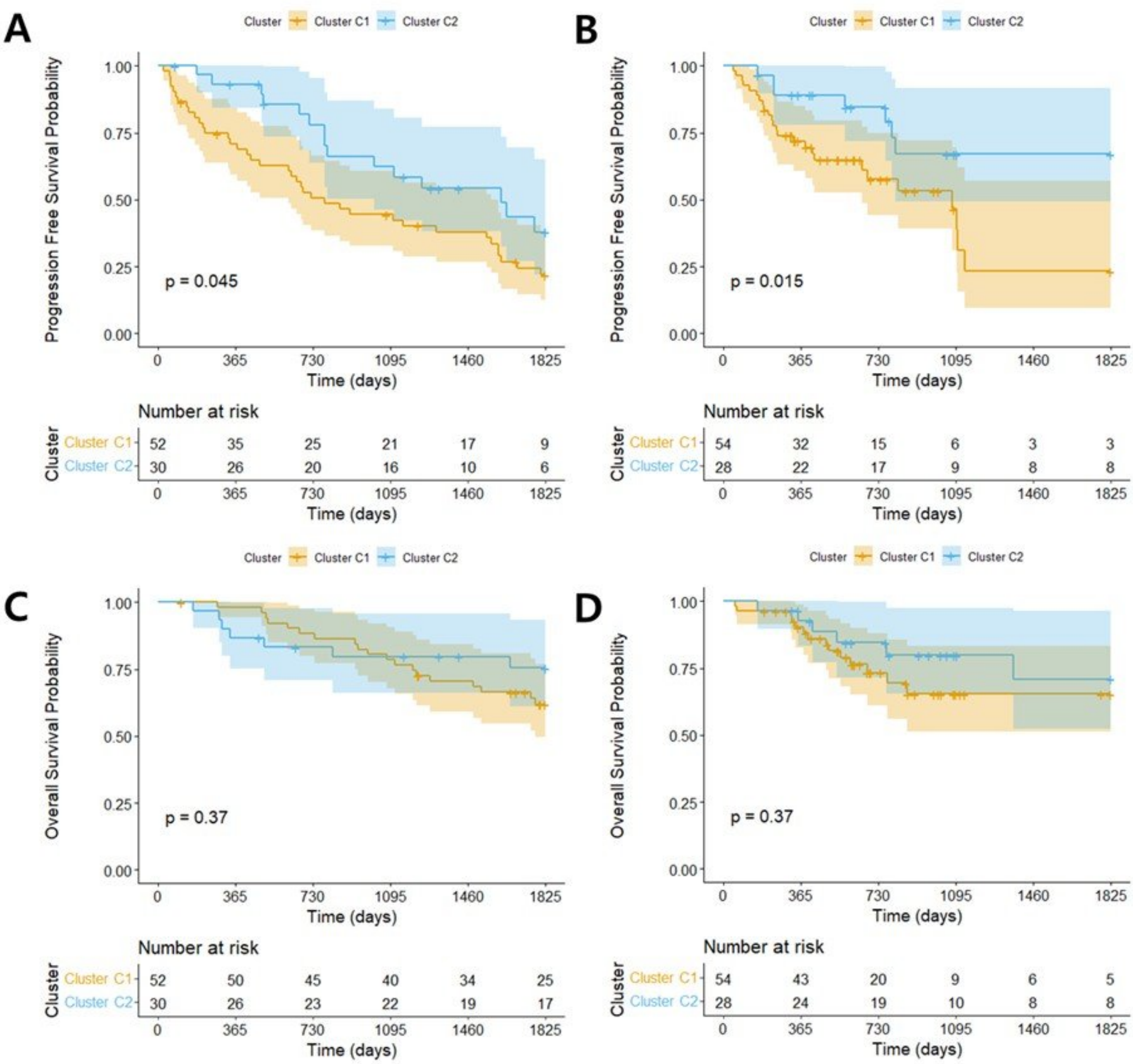

Keywords : Carcinoma, Renal Cell, Cluster Analysis, Progression-Free Survival

[Scientific Session 4: GU Issues 1]

SS04-2

Preoperative MRI Model for Predicting Inferior Vena Cava Wall Invasion in Renal Cell Carcinoma with Tumor Thrombus

Xuewei Wen[1], Shaopeng Zhou[1], Huanhuan Kang[1], Qingbo Huang[2], Xiaohui Ding[3], Haiyi Wang[1*]

[1]Radiology, The First Medical Center of the Chinese PLA General Hospital, China
[2]Urology, The First Medical Center of the Chinese PLA General Hospital, China
[3]Pathology, The First Medical Center of the Chinese PLA General Hospital, China

In patients with renal cell carcinoma (RCC) and inferior vena cava (IVC) tumor thrombus, precise preoperative determination of IVC wall invasion is crucial for surgical planning, as it directly dictates the need for concomitant vascular resection and reconstruction. However, current preoperative imaging assessments primarily rely on subjective overall impressions, which have limited reliability. This study aimed to develop and validate a prediction model based on preoperative multiparametric MRI for the accurate prediction of IVC wall invasion, and to systematically compare its diagnostic performance against individual imaging parameters and subjective radiologic assessments.

This single-center study retrospectively and prospectively enrolled 217 surgically treated RCC patients with IVC tumor thrombus (Training cohort: n=173, January 2005 – December 2023; Temporal validation cohort: n=44, January 2024 – September 2025). Postoperative histopathology served as the reference standard for IVC wall invasion. Quantitative (linear measurements of tumor, vessels, and thrombus) and qualitative (thrombus and vessel wall signal intensity, morphology) imaging features were evaluated. Two specialized abdominal radiologists, blinded to clinical and pathological data, independently provided a subjective overall impression regarding IVC wall invasion; interobserver agreement was also assessed. Variables significant in univariate analysis were incorporated into a multivariable logistic regression model. Diagnostic performance was compared using the Receiver Operating Characteristic (ROC) curve analysis and the DeLong test.

Four independent predictors were identified: Bland Thrombus (OR=3.32, 95% CI: 1.38–8.03), Lumbar Vein Diameter (OR=2.64, 95% CI: 1.23–5.69), Ipsilateral Renal Vein Ostium Diameter (OR=3.64, 95% CI: 1.73–7.63), and Craniocaudal Thrombus Length (OR=3.08, 95% CI: 1.43–6.63). The model demonstrated areas under the curve (AUC) of 0.81 (95% CI: 0.75–0.88) in the training cohort and 0.84 (95% CI: 0.73–0.96) in the validation cohort. Its diagnostic performance was significantly superior to the best single parameter (AUC=0.71) and to the radiologists' subjective assessment (AUC=0.66), with all comparisons being statistically significant ($P < 0.05$).

The developed multiparametric MRI-based prediction model effectively and objectively identifies IVC wall invasion, demonstrating significantly superior diagnostic performance compared to conventional single parameters and subjective assessment. This model holds promise as an improved preoperative risk stratification tool for RCC patients with IVC tumor thrombus, potentially aiding in the formulation of precise surgical plans.

Figure 1. Representative imaging, gross specimen, and histopathologic findings in a patient with renal cell carcinoma with an inferior vena cava (IVC) tumor thrombus (from left to right). (A) Preoperative MRI: panels a1–a4 show the craniocaudal diameter of the tumor thrombus (67.5 mm), associated thrombus, dilated lumbar vein (8.6 mm), and the diameter of the ipsilateral renal vein orifice (28.0 mm), respectively. (B) Gross specimen after radical nephrectomy: b1 shows the resected right kidney and the transected segment of IVC containing tumor thrombus; b2 presents a cross-sectional view of the tumor thrombus within the IVC. (C) Histopathological micrograph (hematoxylin and eosin staining, ×100): the red solid box highlights tumor cells infiltrating the muscular layer of the venous wall, indicating tumor thrombus invasion of the venous wall. PT, primary tumor; TT, tumor thrombus.

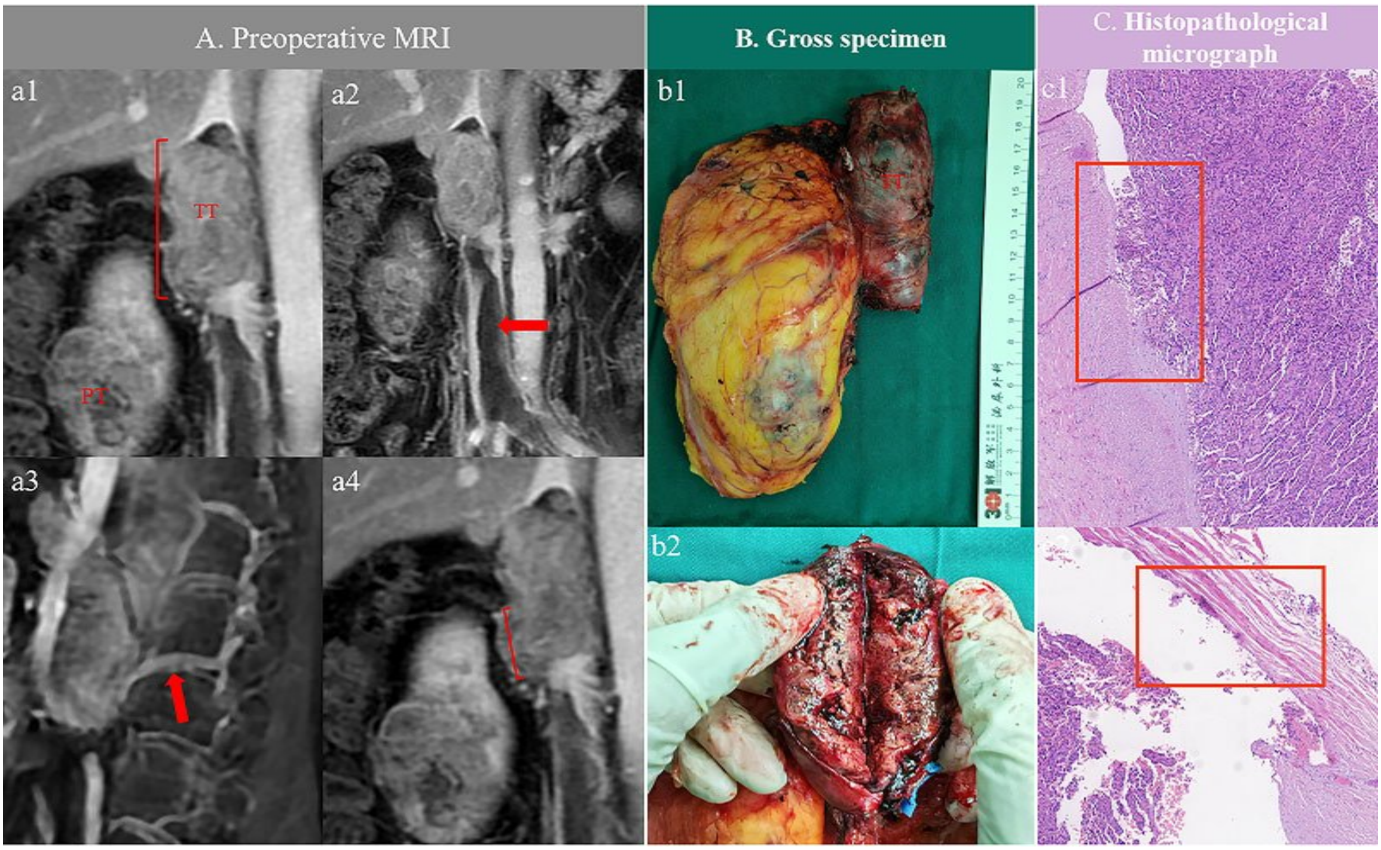

Figure 2. Schematic illustration of quantitative and qualitative MRI parameter measurements. (A) Craniocaudal length of tumor thrombus on coronal image; (B) Ipsilateral renal vein ostium diameter on coronal image; (C) Contralateral renal vein ostium diameter on coronal image; (D) Lumbar vein diameter on sagittal image; (E) Anteroposterior diameter of the inferior vena cava at the renal vein ostium level on axial image; (F) Maximum anteroposterior diameter of the inferior vena cava on axial image; (G) Maximum short-axis diameter of the tumor thrombus on axial image. MRI, magnetic resonance imaging; IVC, inferior vena cava.

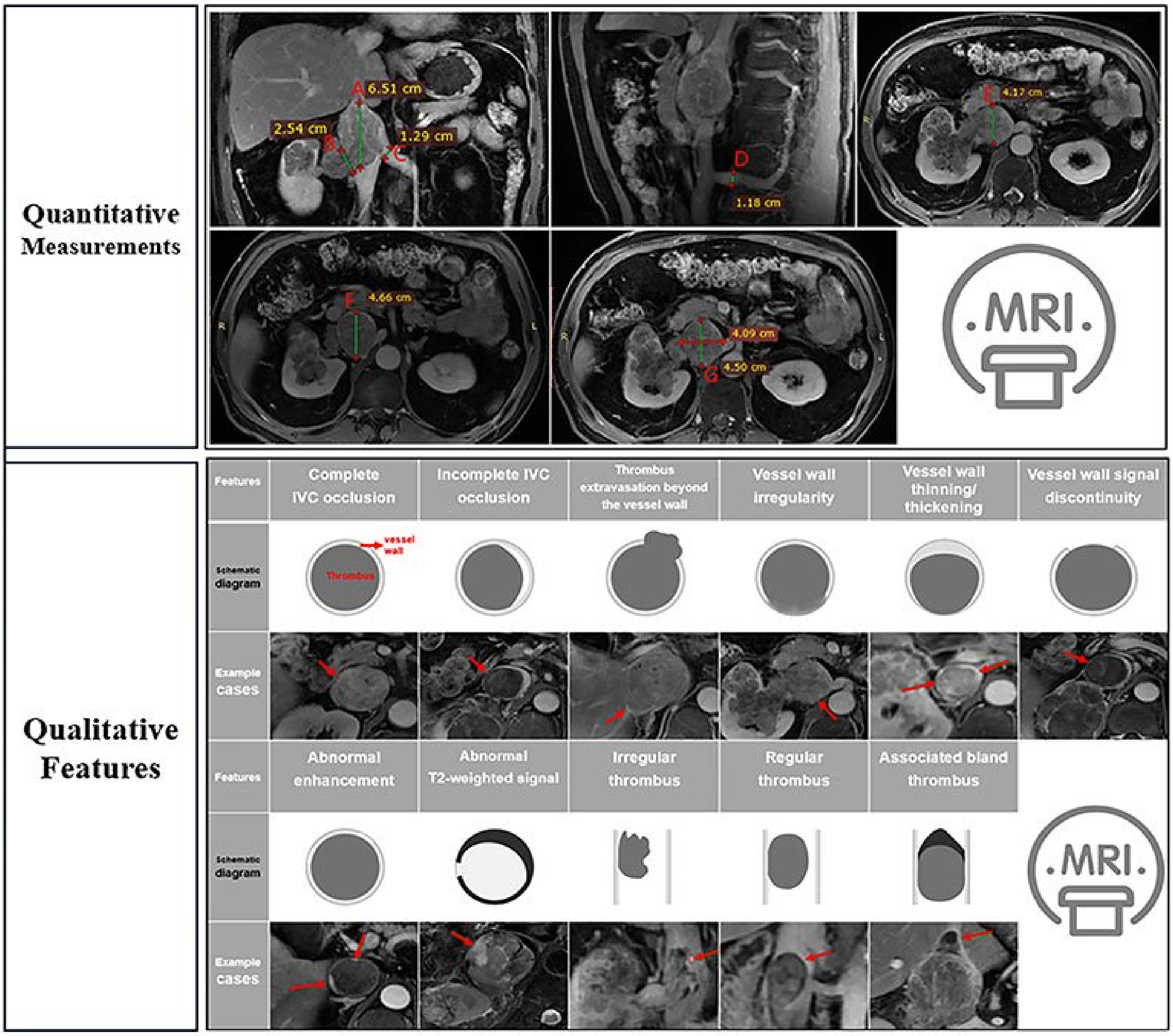

Keywords : Renal Cell Carcinoma, Inferior Vena Cava Tumor Thrombus, Venous Wall Invasion

[Scientific Session 4: GU Issues 1]

SS04-3

Multicenter Validation of Bosniak Classification, Version 2019 for Class III-IV Aggressive and Any Cancer Prediction

Justin Tse[1*], Shokoufeh Khalatbari[2], Matheos Yosef[2], Society of Abdominal Radiology Disease Focused Panel[1], Nicola Schieda[3], Ivan Pedrosa[4], Matthew Davenport[2]

[1]Radiology, Stanford University, USA
[2]Radiology, University of Michigan, USA
[3]Radiology, University of Ottawa, Canada
[4]Radiology, University of Texas MD Anderson Cancer Center, USA

The Bosniak classification system was updated in 2019 (Bosniak v2019) and predicts any cancer rather than aggressive cancer in cystic renal masses. The aims of our study were to determine whether Bosniak v2019 can predict aggressive cancer in addition to any cancer, compare the accuracy of Bosniak III and IV subclassifications, and evaluate the association of nodule size with aggressive cancer and any cancer.

This multicenter, multinational retrospective diagnostic accuracy study included 421 Bosniak III or IV cystic renal masses from 419 patients across 10 institutions in three countries. Pre-treatment renal mass protocol CT or MRI performed within 1 year of resection were reviewed independently by 2 blinded radiologists at each site (20 radiologists). Reference standard was surgical histopathology. Generalized linear mixed models determined risk of aggressive cancer, any cancer, and subclass performance. Agreement was assessed with Gwet's AC1 and intraclass correlation (ICC).

Probability of any cancer was 74.8% for Bosniak III (95% CI: 69.6-79.4%) and 91.0% for Bosniak IV (95% CI: 88.2-93.2%). Probability of aggressive cancer was 10.3% for Bosniak III (95% CI: 7.3-14.3%) and 33.1% for Bosniak IV (95% CI: 29.1-37.3%). Bosniak IV subclasses had significantly higher probability of any cancer and aggressive cancer than Bosniak III subclasses ($p<0.001$ to 0.007; $p<0.001$ to 0.001, respectively). The odds did not significantly differ within Bosniak III ($p=0.56$ to $p=0.99$) or IV ($p=0.10$ to $p=0.74$) subclasses. Nodule size was strongly associated with risk of any cancer (Figure 1; $p=0.01$ [OR 3.8/10 mm]) and aggressive cancer (Figure 2; $p=0.003$ [OR 2.1/10 mm]). Inter-rater agreement was substantial for Bosniak class (Gwet's AC1: 0.70 [95% CI: 0.63-0.77] and good-to-excellent for nodule size (ICC:0.89 [95% CI: 0.85 – 0.91]).

Bosniak v2019 stratifies risk of aggressive cancer and any cancer. Nodule size was strongly associated with aggressive cancer risk. The expert opinion-derived Bosniak v2019 subclass criteria are robustly supported.

Effect of Bosniak IV nodule size on risk of any cancer when overall mass size is fixed at 40 mm (cT1a) or 70 mm (cT1b). Upper bounds are truncated at the calculated diameter at which a spherical nodule would equal 25% of the volume of a mass with given diameter (per Bosniak v2019 rules). Lower bounds are truncated at 4 mm, which is the smallest obtusely marginated nodule size for a Bosniak IV mass.

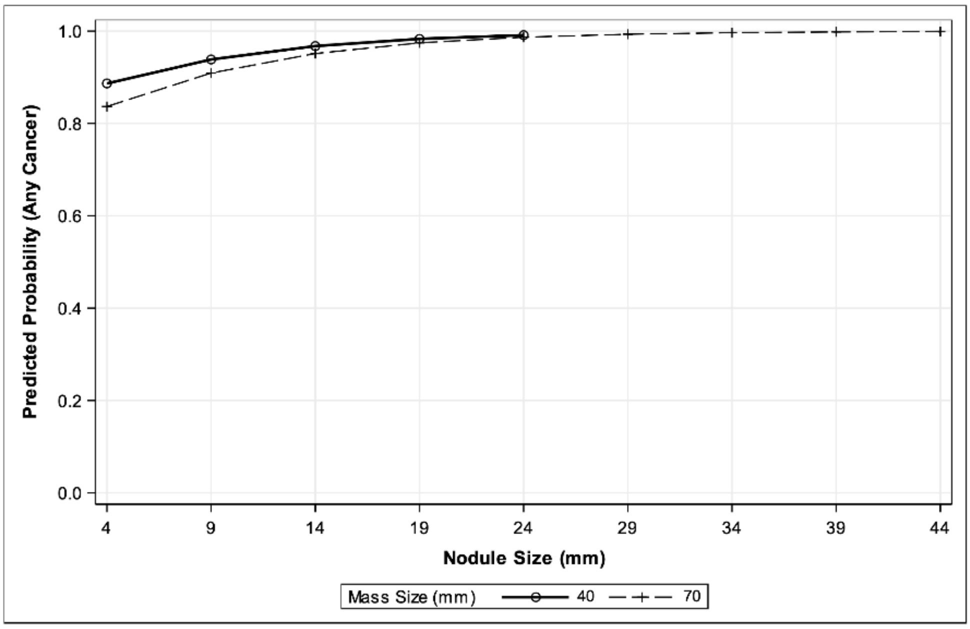

Effect of Bosniak IV nodule size on risk of aggressive cancer when overall mass size is fixed at 40 mm (cT1a) or 70 mm (cT1b). Upper bounds are truncated at the calculated diameter at which a spherical nodule would equal 25% of the volume of a mass with given diameter (per Bosniak v2019 rules). Lower bounds are truncated at 4 mm, which is the smallest obtusely marginated nodule size for a Bosniak IV mass.

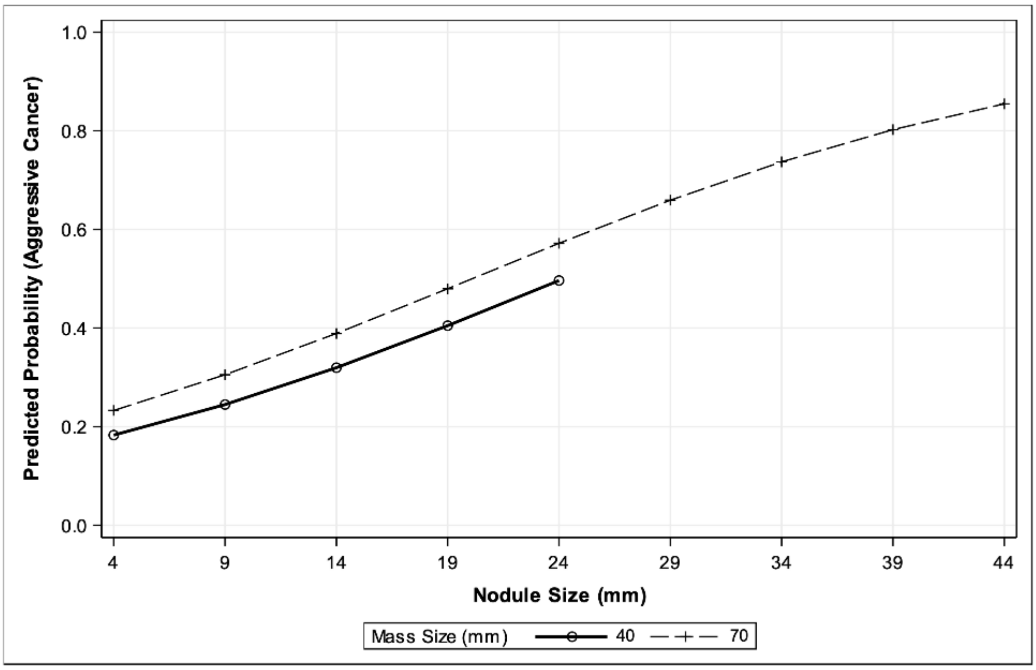

Keywords : Renal cell carcinoma, Cystic renal mass, Bosniak classification

[Scientific Session 4: GU Issues 1]

SS04-4

Construction and Clinical Validation of a Cascaded Deep Learning System for Classification of Benign and Malignant Solid Small Renal Masses Based on MRI

Mengqiu Cui[1], Zilong Zeng[2], Silu Chen[3], Yunfeng Jin[4], He Wang[5], Dawei Yang[6], Haiyi Wang[1*]

[1]Radiology, The First Medical Center Chinese PLA General Hospital, China
[2]School of Medical and Information Engineering, Gannan Medical University, China
[3]Radiology, The Seventh Medical Center Chinese PLA General Hospital, China
[4]CT and MRI, Tonghua Central Hospital, China
[5]Radiology, Peking University First Hospital, China
[6]Radiology, Beijing Friendship Hospital Capital Medical University, China

With the widespread adoption and advancement of imaging technology, the detection rate of small renal masses (SRMs) has significantly increased, accounting for approximately 66% of all renal tumors. However, prior studies indicate that 20% to 30% of surgically resected SRMs are benign, underscoring the persistent challenge in accurately differentiating benign from malignant SRMs. This study aims to develop a cascaded deep learning (DL) system based on multiparametric MRI to achieve automated segmentation and classification of SRM.

A retrospective collection of SRM patients with pathologically confirmed from three institutions was conducted. MRI data from Institution 1 were randomly divided into a training set and an internal test set. Data from other institutions served as external test set. A cascaded DL system was developed, incorporating automated segmentation and benign-malignant classification, using EfficientNet_B4 as the backbone network. We used the Dice Similarity Coefficient (DSC) as the metric for evaluating tumor segmentation performance. Diagnostic performance was evaluated using receiver operating characteristic analysis and compared against three radiologists of varying experience.

A total of 965 SRM patients was concluded. Institution 1 contributed 888 cases, with 712 used for training and 176 as an internal test set; the Institutions 2 and 3 provided 77 cases as an external test set. The median DSC (Q1, Q3) values of the model on the internal test set across the five sequences (T2WI, T1WI, CP, NP, and DP) were 0.822 (0.720, 0.867), 0.714 (0.388, 0.813), 0.828 (0.744, 0.867), 0.836 (0.714, 0.877), and 0.824 (0.738, 0.871), respectively. On the external test set, the median DSC (Q1, Q3) values were 0.789 (0.489, 0.855), 0.659 (0, 0.770), 0.780 (0.629, 0.836), 0.817 (0.667, 0.862), and 0.771 (0.645, 0.852), respectively. The optimal classification model using automated segmentation labels achieved AUCs of 0.936 and 0.786 on internal and external test set, respectively. Performance was comparable to models using manual segmentation (internal: 0.936 vs. 0.944, P=0.629; external: 0.786 vs. 0.815, P=0.671). On the external test set, the model matched the senior radiologist (AUC: 0.786 vs. 0.797, P=0.468) and significantly outperformed the junior radiologist (AUC: 0.786 vs. 0.530, P=0.036). This finding remained consistent in the subgroup of tumors smaller than 3 cm. In terms of the time required for diagnosis, the model's diagnosis time on the test set was significantly shorter than that of

radiologists on both set (all P < 0.05).

The cascaded DL system demonstrated robust performance across multiple centers, enabling non-invasive and efficient discrimination of SRM malignancy, showing promise as a clinical aided tool.

Density plot of the Dice Similarity Coefficient (DSC) for the automated segmentation model on the internal test set (a) and external test set (b).

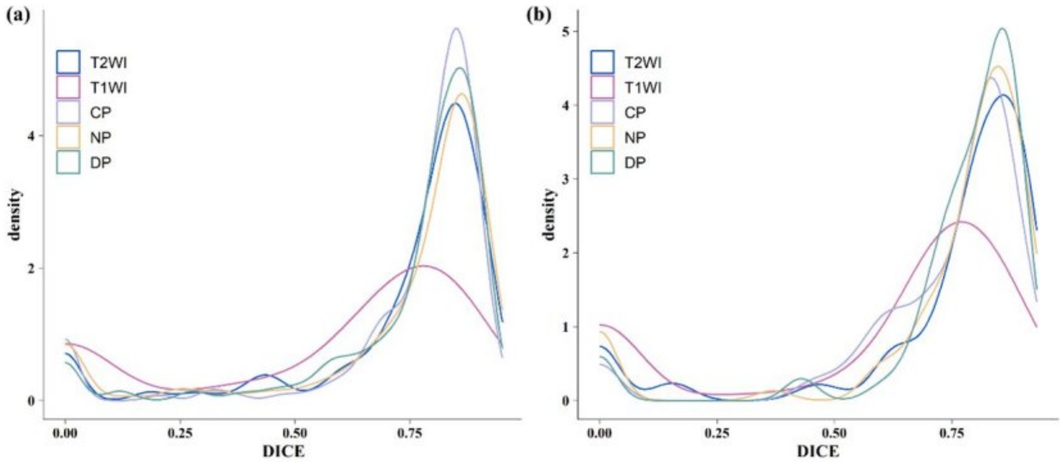

Receiver operator characteristic (ROC) curves of the radiologists with varying experience levels and classification model across test sets. (a) The ROC curves in the internal test set. (b) The ROC curves in the external test set.

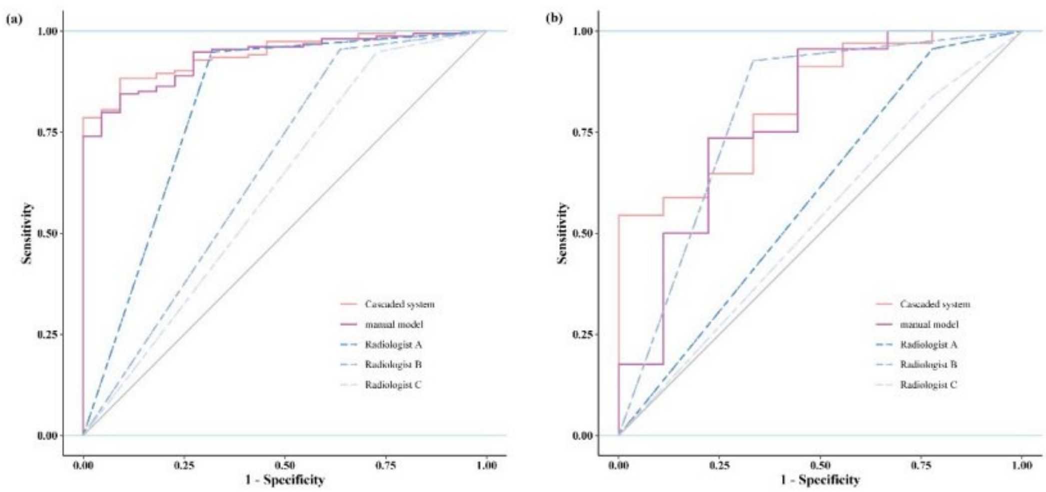

Keywords : Kidney, Small Renal Mass, AI

[Scientific Session 4: GU Issues 1]

SS04-5

Comparative Outcomes of Ultrasound-Guided radiofrequency ablation and Robotic Partial Nephrectomy in Localized Renal Tumors: A Propensity-Matched Prospective Cohort Analysis

Jong Woo Park[1], Ho Hyun Lee[2], Chang Wook Jung[2], Cheol Gwak[2], Sang Youn Kim[1], Taek Min Kim[1], Jang Hee Han[2], June Young Seo[1*]

[1]Radiology, Seoul National University Hospital, Korea
[2]Urology, Seoul National University Hospital, Korea

Ultrasound-guided radiofrequency ablation (USG-guided RFA) has gained attention as a minimally invasive treatment option for renal tumors, particularly in patients with limited surgical eligibility due to comorbidities or advanced age. However, comparative evidence regarding its effectiveness and safety relative to robot-assisted laparoscopic partial nephrectomy (RALPN) remains limited. This study aimed to compare clinical outcomes of USG-guided RFA and RALPN, with a focus on identifying patient subgroups in which RFA may provide distinct advantages.

We analyzed patients who underwent USG-guided RFA or RALPN for localized renal tumors, using data from the SUPER-RCC-Nx prospective cohort at Seoul National University Hospital between June 2021 and June 2025. Propensity score matching (1:2) was performed using age, BMI, tumor size, clinical T stage, Charlson comorbidity index (CCI), nephrometry score, and baseline renal function (creatinine, eGFR). Subgroup analyses were conducted in patients with moderate to high nephrometry scores. Primary outcomes included changes in renal function (baseline vs. 3-month postoperative), and secondary outcomes included operation time, hospital stay, POD#1 visual analog scale (VAS) pain score, complication rates, and oncological outcome.

A total of 861 patients were included in the analysis (RFA: 34; RALPN: 827). The RFA group was significantly older (mean age: 73.8 vs. 57.8 years, $p < 0.001$) and had a higher comorbidity burden ($p < 0.001$). Baseline renal function was poorer in the RFA group, with higher serum creatinine levels (1.38 vs. 0.92 mg/dL, $p = 0.02$) and lower estimated glomerular filtration rate (eGFR; 66.2 vs. 87.4 mL/min/1.73m^2, $p < 0.001$). Tumor size was smaller in the RFA group (1.94 vs. 2.88 cm, $p < 0.001$), while nephrometry scores were comparable between groups ($p = 0.433$). RFA was predominantly performed in older patients or those with limited surgical tolerance. After propensity score matching (PSM), the decline in eGFR at 3 months remained significantly greater in the RFA group (−5.86 vs. −0.60 mL/min/1.73m^2, $p = 0.002$). However, the RFA group demonstrated superior outcomes in various perioperative secondary outcome parameters. Among patients with moderate to high complexity renal tumors, the difference in eGFR decline was not statistically significant (−4.23 vs. −1.78 mL/min/1.73m^2, $p = 0.238$). In this subgroup, RFA was associated with significantly shorter operative time (33.4 vs. 99.0 minutes, $p < 0.001$), reduced hospital stay (1.4 vs. 4.4 days, $p < 0.001$), and lower postoperative day 1 pain scores (VAS 2.1 vs. 4.0, $p < 0.001$). Postoperative complications within 1 and 3 months occurred in 25% of RALPN patients compared to 7.1% of those undergoing RFA. No local recurrence was observed

in either group during the follow-up period.

Ultrasound-guided RFA is a safe and effective alternative to RALPN for small renal tumors, particularly in older patients or those with impaired renal function. In appropriately selected patients with complex tumors, RFA may offer comparable functional outcomes and improved perioperative profiles, supporting its role as a minimally invasive treatment option.

Table 1. Comparison of clinical outcomes of RFA group and RALPN group. RFA group demonstrated superior outcomes in various perioperative parameters. Among the 34 patients who underwent RFA, a second ablation was performed in 4; complete ablation was confirmed in all 34 patients with no recurrence in follow-up CT scans.

	RALPN (N=827)	US-guided RFA (N=34)	*P*-value
Op time (min)	92.1	32.6	**<0.001**
Post-op hospital days	4.4	1.3	**<0.001**
POD#1 VAS score	3.8	1.9	**<0.001**
30d complications (%)	119 (14.4)	3 (8.8)	0.460
≥ C-D grade 2	93 (11.2)	3 (8.8)	1.000
90d complications (%)	124 (15.9)	3 (10.3)	0.058
≥ C-D grade 2	24 (2.9)	2 (5.9)	0.274
Recurrence (%)	9 (1.1)	0 (0.0)	1.000

Figure 1. Demonstration of US-guided RFA. (a), (b) Pre-RFA images of a 1.8 cm sized clear cell RCC on US and contrast enhanced CT. (c) Real-time air bubble formation at the tumor site during RFA procedure. (d) Immediate Post-RFA CT showing no residual enhancement.

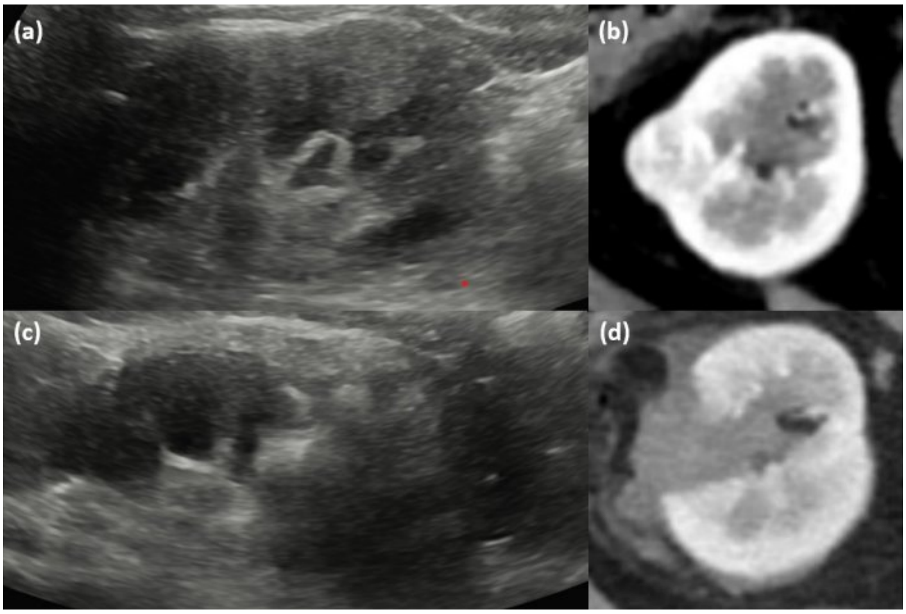

Keywords : USG-guided RFA, RALPN, Comparative study

[Scientific Session 4: GU Issues 1]

SS04-6

Utility of Multi-Model Diffusion MRI for Stratifying High-Risk Complications in Renal Transplant Recipients

Zhouyan Liao[1], **Kangwen He[1]**, Siyuan Ma[1], Gen Chen[1], Jeong Min Lee[2], Zhen Li[1*]

[1]Radiology, Tongji Hospital Tongji Medical College Huazhong University of Science and Technology, China
[2]Radiology, Seoul National University Hospital, Korea

This study aims to develop a noninvasive comprehensive diagnostic protocol based on diffusion weighted imaging (DWI) and clinical indicators to achieve accurate and efficient identification of high-risk complications (rejection, acute kidney injury, viral infection, moderate to severe fibrosis) after renal transplantation.

This prospective study enrolled 120 renal allograft recipients. Quantitative parameters of DWI, intravoxel incoherent motion (IVIM), diffusion kurtosis imaging (DKI), stretched exponential model (SEM), fractional order calculus (FROC) and continuous-time random walk (CTRW) were measured. Clinical and pathological features were also recorded. Univariate and multivariate logistic regression analyses were performed to identify independent clinical and imaging predictors of high-risk complications group. Receiver operating characteristic (ROC) curves were used to evaluate diagnostic performance. Internal validation of the combined model was performed using stratified 5-fold cross-validation and bootstrap resampling to assess model stability and generalizability.

Finally, 101 patients were included. Diffusion coefficients differed significantly between superior and inferior graft function groups across models. DDC_SEM_cortex and HCO_3^- emerged as independent predictors in multivariate analysis. The AUCs for HCO_3-, DDC_SEM_cortex, and their combined model in identifying patients requiring clinical management changes were 0.888, 0.898, 0.941. Internal validation confirmed strong performance (cross-validation AUC 0.938; bootstrap AUC 0.940, 95% CI 0.931–0.943)

Finally, 101 patients were included. Diffusion coefficients differed significantly between superior and inferior graft function groups across models. DDC_SEM_cortex and HCO_3^- emerged as independent predictors in multivariate analysis. The AUCs for HCO_3-, DDC_SEM_cortex, and their combined model in identifying patients requiring clinical management changes were 0.888, 0.898, 0.941. Internal validation confirmed strong performance (cross-validation AUC 0.938; bootstrap AUC 0.940, 95% CI 0.931–0.943)

ROC curves for parameters that showed significant differences between SGF and IGF (such as MD-DKI, ADC, etc.) are shown. In (A) cortical metrics, in (B) medullary metrics. ROC curves for the diagnostic performance of the parameters for differentiating clinical management change group (C).

SGF, superior graft function; IGF, inferior graft function; CTRW, continuous-time random walk model; FROC, fractional order calculus model; SEM, stretched exponential model; DKI, diffusion kurtosis imaging; IVIM, intravoxel incoherent motion; MD, mean diffusivity; MK, mean kurtosis; ADC, apparent diffusion coefficient.

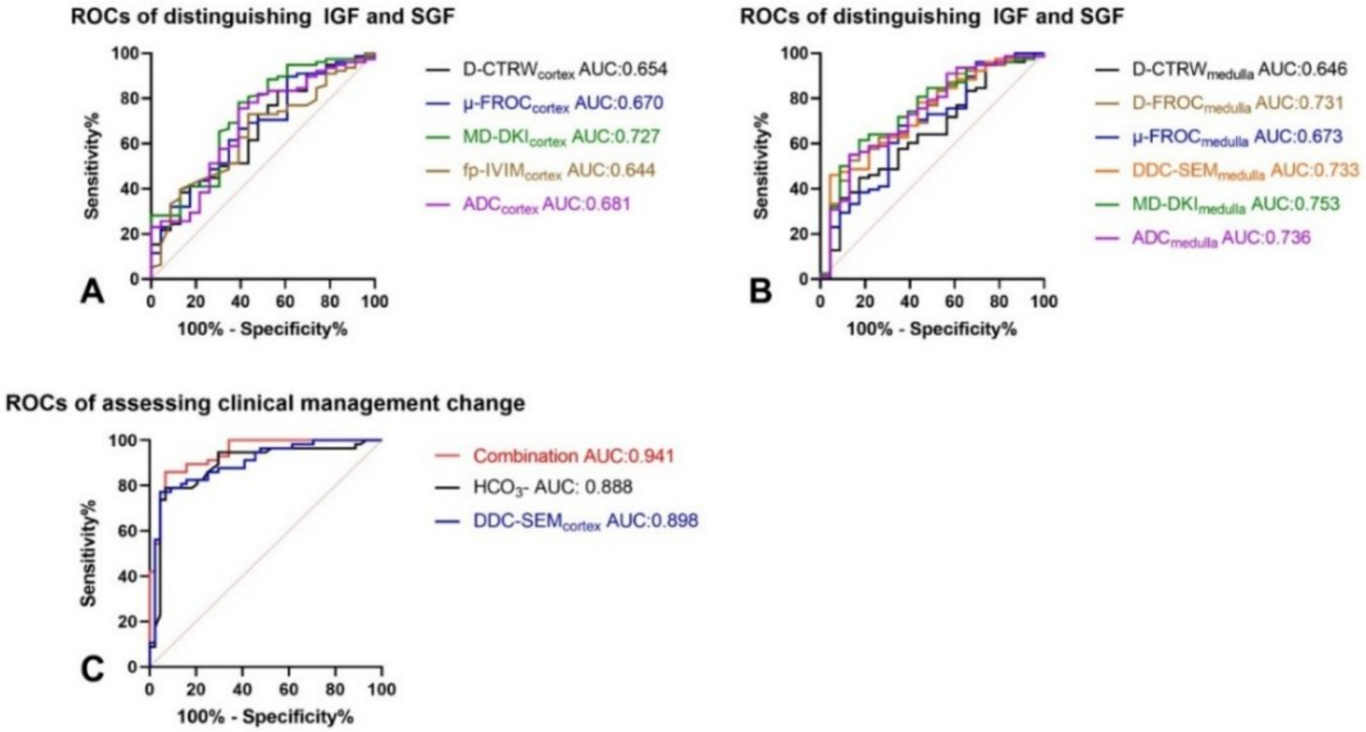

Internal validation and stability assessment of the logistic regression model. A. Fold-wise AUC values from repeated stratified 5-fold cross-validation (10 repeats, 50 folds in total); dashed red line indicates mean AUC. B. Bootstrap distribution of AUCs (n = 200 resamples) based on full-cohort modeling; the vertical dashed line represents the mean AUC. C. Decision curve analysis (DCA) of the model across threshold probabilities, indicating clinical net benefit. D. Calibration curve based on 200 bootstrap resamples; the dashed diagonal line indicates perfect agreement between predicted and observed probabilities.

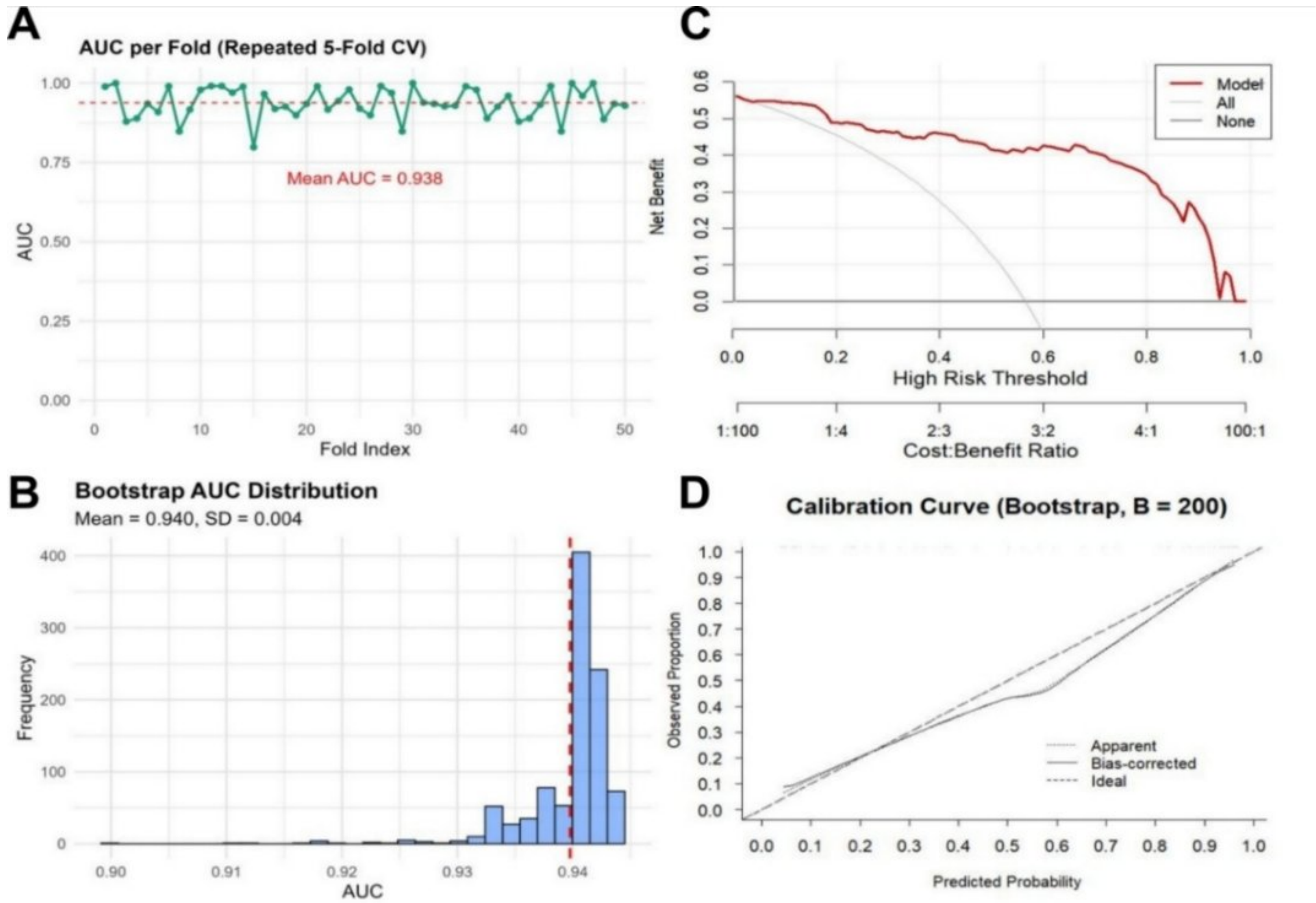

Keywords : Diffusion-weighted imaging, Stretched exponential model, Renal allograft rejection

[Scientific Session 4: GU Issues 1]

SS04-7

Diffusion Lacunae in Placenta Accreta Spectrum (PAS): Game Changer in PAS Imaging

Shinya Fujii[1*], Yuko Iraha[2]

[1]Radiology, Tottori University, Japan
[2]Radiology, Ryukyus University, Japan

Placenta accreta spectrum (PAS) is characterized by abnormal implantation of chorionic villi into the myometrium without an intervening decidua basalis. MRI plays a complementary role to ultrasound in diagnosing PAS and provides additional information useful for surgical planning. Although several MRI features for PAS have been proposed in the consensus statements by SAR and ESUR, accurate diagnosis remains challenging.

Recently, we reported a novel MRI finding on diffusion-weighted imaging (DWI) for diagnosing PAS, termed diffusion lacunae (DL). DL appear as intraplacental ovoid or irregular hypointense areas isointense to amniotic fluid on DWI, with corresponding hyperintensity on ADC maps, and are defined as larger than 1 cm. They are thought to correspond to placental lacunae, the most well-known ultrasound finding suggestive of PAS.

Understanding the formation mechanism of placental lacunae is crucial. In PAS, maternal blood with high velocity from radial arteries flows directly into the intervillous space, distorting the normal placental lobular architecture and resulting in enlargement of intervillous spaces, referred to as placental lacunae. Therefore, DL correspond to areas devoid of villi. We present representative cases of DL with MR–pathologic correlation.

It is also important to recognize exclusion criteria for DL, such as spaces predominantly located peripherally, which may represent the placental marginal sinus. In addition, several mimickers of DL, including placental lakes and decidual septal cysts, can resemble them and potentially lead to misinterpretation. We demonstrate these mimicking intraplacental hypointense lesions on DWI.

In this pictorial review, we highlight the utility and pitfalls of diffusion lacunae in evaluating PAS with MR–pathologic correlation.

Keywords : Placenta, MRI, Diffusion

[Scientific Session 5: Hot Topics in Body Imaging]

SS05-1

Effects of Shortening Preparative Fasting Time before Contrast-enhanced CT on the Incidence of Acute Adverse Drug Reactions: An Observational Study

Yunseo Choi[2], Se Jin Choi[1], Hyo Jung Park[1*], Chong Hyun Suh[1]

[1]Radiology, Asan Medical Center, Korea
[2]University of Ulsan College of Medicine, Korea

Data are limited on whether fasting before contrast-enhanced CT (CECT) prevents adverse drug reactions (ADR) to iodinated contrast media (ICM). This study aimed to assess the impact of shortened preparatory fasting on the incidence of acute ADR to ICM.

This retrospective study included adults undergoing CECT between January–July 2023 (long-NPO; 6-hour fasting for solids and liquids) and January–July 2024 (short-NPO; 3-hour fasting for solids, no liquid restriction). Acute ADRs were analyzed in three sets: (1) all patients, (2) self-controlled (those scanned in both periods), and (3) matched (patients from one period matched using inverse probability of treatment weighting). Acute ADRs were classified as hypersensitivity, physiologic, or emetic reactions. Incidences were compared using log-binomial regression with generalized estimating equations to calculate adjusted risk ratios (RRs). Aspiration pneumonia incidence was also evaluated.

A total of 98,519 adults (mean age ± standard deviation, 60.3 ± 12.7 years; 45679 women [46.4%]) underwent 118,976 CECTs during the long-NPO period, and 98,739 adults (60.6 ± 12.7 years; 45,380 women [46.0%]) underwent 123,459 CECTs during the short-NPO period. The per-patient incidence of acute ADRs was 1.2% (1,216/98,519) and 1.3% (1,284/98,739) in the long- and short-NPO period, respectively. Across all, self-controlled, and matched sets, the incidence of all acute ADRs was not significantly different (adjusted RR, 1.05–1.06; $P \geq .18$). No significant differences between the two periods existed in the rate of acute hypersensitivity, physiologic, or emetic reactions (adjusted RR range, 1.03–1.13; $P \geq .23$). No aspiration pneumonia occurred.

Shortened fasting before CECT was not associated with increased risk of acute ADRs to ICM.

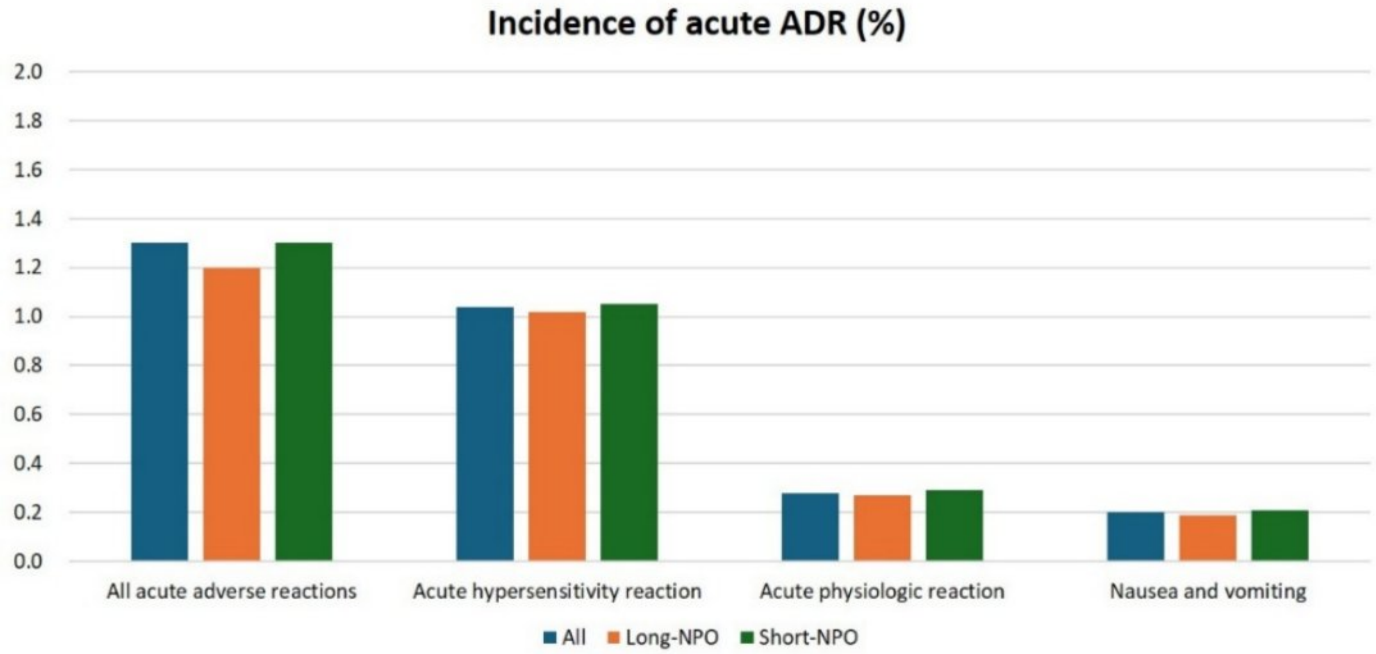

Table. Incidence and relative risk (RR) of acute ADR

	Long-NPO (%)	Short-NPO (%)	RR (95% CI)	P-value
Total cohort	98519 (49.9)	98739 (50.1)		
All acute reactions	1216 (1.2)	1284 (1.3)	1.05 (0.98, 1.14)	0.18
Acute hypersensitivity reaction	1005 (1.0)	1040 (1.1)	1.03 (0.95, 1.13)	0.45
Acute physiologic reaction	271 (0.3)	290 (0.3)	1.07 (0.90, 1.27)	0.46
Nausea and vomiting	186 (0.2)	211 (0.2)	1.13 (0.93, 1.39)	0.23
Self-controlled Set	46062 (50.0)	46062 (50.0)		
All acute reactions	464 (1.0)	491 (1.1)	1.06 (0.95, 1.18)	0.33
Acute hypersensitivity reaction	386 (0.8)	399 (0.9)	1.03 (0.92, 1.16)	0.62
Acute physiologic reaction	98 (0.2)	107 (0.2)	1.09 (0.85, 1.40)	0.51
Nausea and vomiting	68 (0.2)	80 (0.2)	1.18 (0.88, 1.59)	0.27
Matched Set	52457 (49.9)	52677 (50.1)		
All acute reactions	752 (1.4)	793 (1.5)	1.05 (0.94, 1.18)	0.36
Acute hypersensitivity reaction	619 (1.2)	640 (1.2)	1.03 (0.91, 1.17)	0.60
Acute physiologic reaction	173 (0.3)	183 (0.4)	1.06 (0.83, 1.34)	0.65
Nausea and vomiting	118 (0.2)	132 (0.3)	1.11 (0.84, 1.46)	0.47

Keywords : Contrast Media, Adverse Drug Reaction, CT workflow

[Scientific Session 5: Hot Topics in Body Imaging]

SS05-2

Clinical Impact of a High-Relaxivity Gadolinium Contrast Agent in Liver MRI

PiYi Chang[1*]

[1]Medical Imaging, Taichung Veterans General Hospital, Chinese Taipei

High-relaxivity gadolinium-based contrast agents (GBCAs) provide stronger T1 shortening and more robust dynamic enhancement, enabling gadolinium dose reduction while preserving diagnostic quality. These properties may be particularly valuable for HCC diagnosis and post-treatment liver imaging, where subtle residual or recurrent disease and new satellite lesions must be detected early.

Our purpose is to evaluate the clinical impact of a high-relaxivity GBCA on post-treatment follow-up and new lesion detection in Taiwan's first real-world experience.

Twenty consecutive patients undergoing liver MRI for post-treatment surveillance or suspected hepatic lesions received gadopiclenol 0.05 mmol/kg (0.1 mL/kg). Standard multiphase dynamic imaging was performed at 1.5T or 3T. Two abdominal radiologists assessed residual enhancement, new lesion detection, subcentimeter nodules, arterial-phase conspicuity, washout clarity, and visualization of metastatic or satellite lesions. Representative cases were selected to illustrate clinical impact.

Across 20 patients, 28 lesions were detected. Despite the reduced gadolinium dose, gadopiclenol provided strong arterial enhancement and excellent lesion-to-liver contrast. In differential liver lesions—including hemangioma, FNH, and HCC—contrast dynamics were well delineated, supporting confident characterization. In post-treatment cases, subtle residual enhancing foci were clearly visualized, facilitating distinction between recurrence and post-treatment changes. These findings contributed to stage modification and influenced therapeutic decisions in several patients. Tumor recurrence was detected in two cases, including small peripheral lesions that had not been visible on prior examinations performed with conventional macrocyclic GBCAs. Treated lesions also demonstrated sharper borders, improving assessment of viable versus non-viable tissue. No moderate or severe adverse reactions occurred.

Reduced-dose high-relaxivity gadopiclenol enhances the detection of residual disease, new lesions, satellite nodules, and metastatic foci during post-treatment liver MRI follow-up. In addition, the improved dynamic enhancement and lesion-to-liver contrast assist in the accurate differentiation of liver lesions, including hemangioma, FNH, and HCC. These findings support its value for precise surveillance and characterization in patients undergoing locoregional or systemic therapy.

In this arterial-phase MRI, the hepatic hemangioma (black arrow) shows the typical peripheral, nodular, discontinuous enhancement, forming a "puddling" pattern along its margin. This early nodular enhancement helps distinguish hemangioma from hypervascular tumors. With a high-relaxivity contrast agent such as gadopiclenol, the arterial appearance becomes even more conspicuous—stronger T1 shortening and higher lesion-to-liver contrast produce a brighter, sharper peripheral nodule, improving confidence in identifying benign hemangioma features and differentiating it from malignancies that may show washout or heterogeneous enhancement.

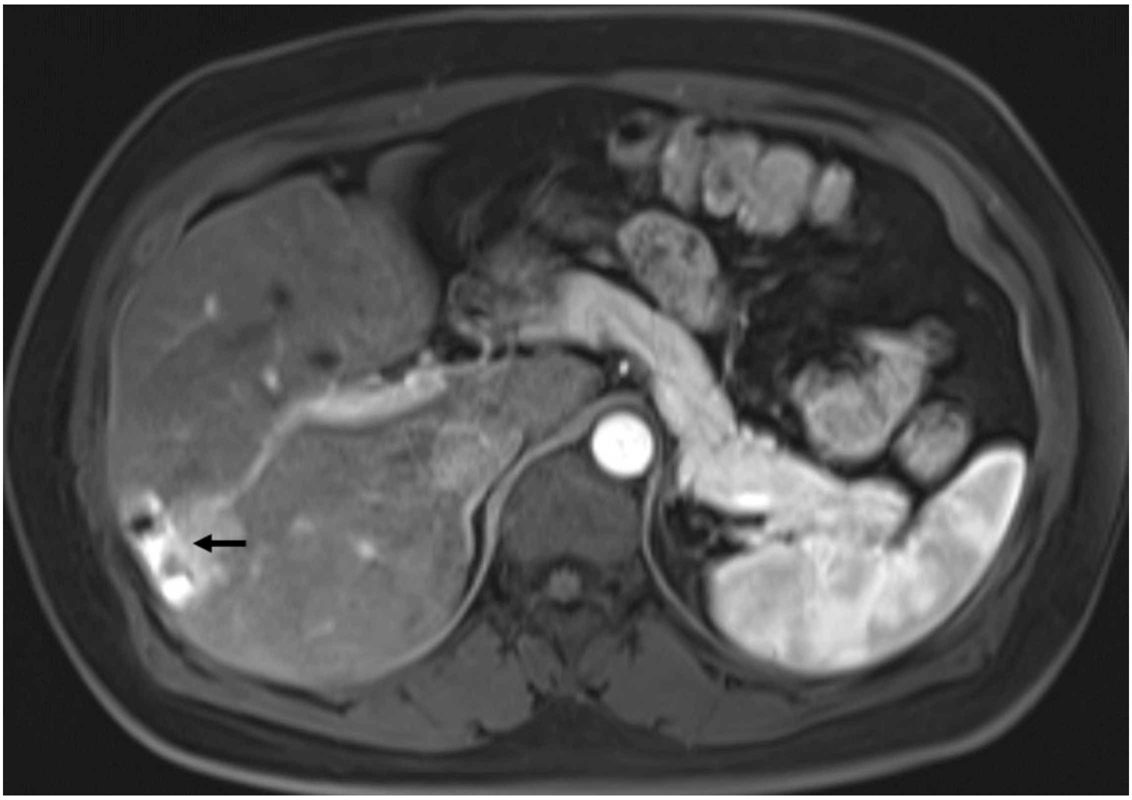

Keywords : Liver MRI, Lesion detection, High-relaxivity gadolinium contrast agent

[Scientific Session 5: Hot Topics in Body Imaging]

SS05-3

Deep Learning-based Prediction of Hospitalization for Patients with Abdominal Symptoms during Emergency Department Triage: Combining Initial Abdominal Radiography and Early Clinical Information

Yeo Eun Han[1,3], Beom Jin Park[1,3*], Yongwon Cho[2], Ki Choon Sim[1,3], Na Yeon Han[1,3], Min Ju Kim[1,3], Deuk Jae Sung[1,3]

[1]Radiology, Korea University Anam Hospital, Korea
[2]Computer Science and Engineering, Soonchunhyang University, Korea
[3]Advanced Medical Imaging Institute, Korea University College of Medicine, Korea

To develop a hospitalization prediction model for patients with abdominal symptoms presenting to the emergency department by applying deep learning involving initial abdominal radiography (AXR) and early clinical information.

This retrospective study included 778 patients (814 visits) with abdominal symptoms who underwent AXR within 3 hours after visiting the emergency department between October and November 2021. The patients were randomly allocated to the training and test sets (n=702 and 112, respectively), and the outcome was discharge (n=560) or hospitalization (n=254; admission, transfer, discharge despite the need for admission). Early clinical information of the patients was collected, including consciousness, vital signs, percutaneous oxygen saturation, symptoms, location and scale of abdominal pain, and medical history, whereas deep features from AXR were extracted using deep learning on DenseNet. With these features, three models – AXR (image model), clinical information (clinical model), and combined (fusion model) - were trained using the random forest algorithm, which was repeated 20 times with 10-fold stratified cross-validation. The models were then validated using the test set, wherein we evaluated the F1 score of the models due to the imbalanced distribution of outcomes. We also evaluated the area under the receiver operating characteristic curve (AUC), accuracy, sensitivity, and specificity. Furthermore, we analyzed the class activation maps, classifying the location of activation based on abdominal findings (gastrointestinal gas, free air, and calcified stones).

For the clinical, image, and fusion models, the F1 score was 0.78, 0.81, and 0.84, the AUC was 0.73, 0.79, and 0.81; the accuracy was 0.68, 0.76, and 0.78; the sensitivity was 0.72, 0.74, and 0.82; and the specificity was 0.67, 0.73, and 0.67, respectively. Overall, the fusion model showed the best performance. In addition, no abdominal findings were found in the activated areas of the AXR in 70% of all negative (discharge) cases and 53% of all positive (hospitalization) cases.

A deep learning model can predict the hospitalization of patients with abdominal symptoms presenting to the emergency department using initial AXR and early clinical information. On AXR, the deep learning model frequently focused on locations that do not contain abdominal findings, implying an unconventional role of AXR in assessing the patient's general condition.

This figure shows the performance of the models.

The area under the ROC curve was **0.73** for the clinical model, **0.79** for the image model, and **0.81** for the fusion model.

Overall, the models incorporating imaging data demonstrated better performance than the clinical model alone.

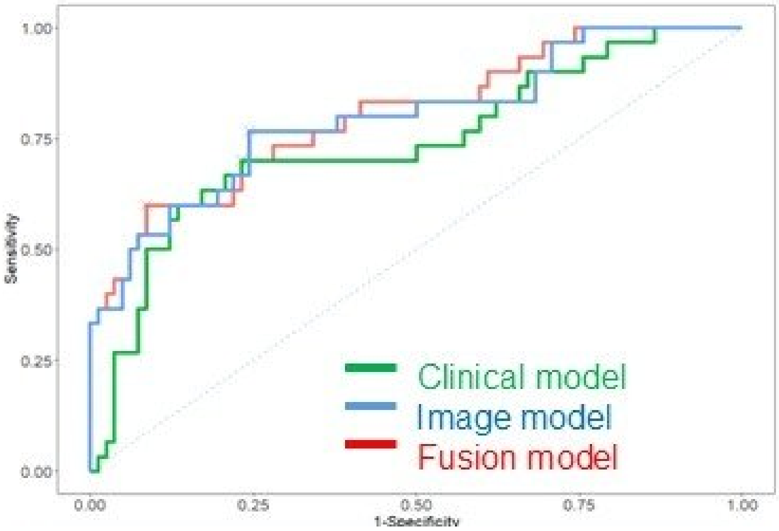

	Clinical model	Image model	Fusion model
F1-score	0.78	0.81	0.84
AUC	0.73 [0.63-0.83]	0.79 [0.70-0.89]	0.81 [0.72-0.90]
Accuracy	0.68	0.76	0.78
Sensitivity	0.72	0.74	0.82
Specificity	0.67	0.73	0.67

Class activation maps (CAMs) of representative cases.

All radiographs demonstrated nonspecific abdominal findings.

The **upper two cases** were predicted as hospitalization by the model. The activated regions commonly overlapped with the degenerative lumbar spine, diaphragm, and sacroiliac joints. The first patient (true positive) was hospitalized for diverticular bleeding, while the second patient (false negative) was later diagnosed with acute appendicitis.

The **lower two cases** were predicted as discharge by the model. The activation patterns were mainly seen in areas of normal bowel gas and soft tissue opacity of the abdomen and pelvis. The first patient (false positive) was discharged after treatment for acute gastroenteritis, and the second patient (true negative) was discharged after Foley catheter change for benign prostatic hyperplasia.

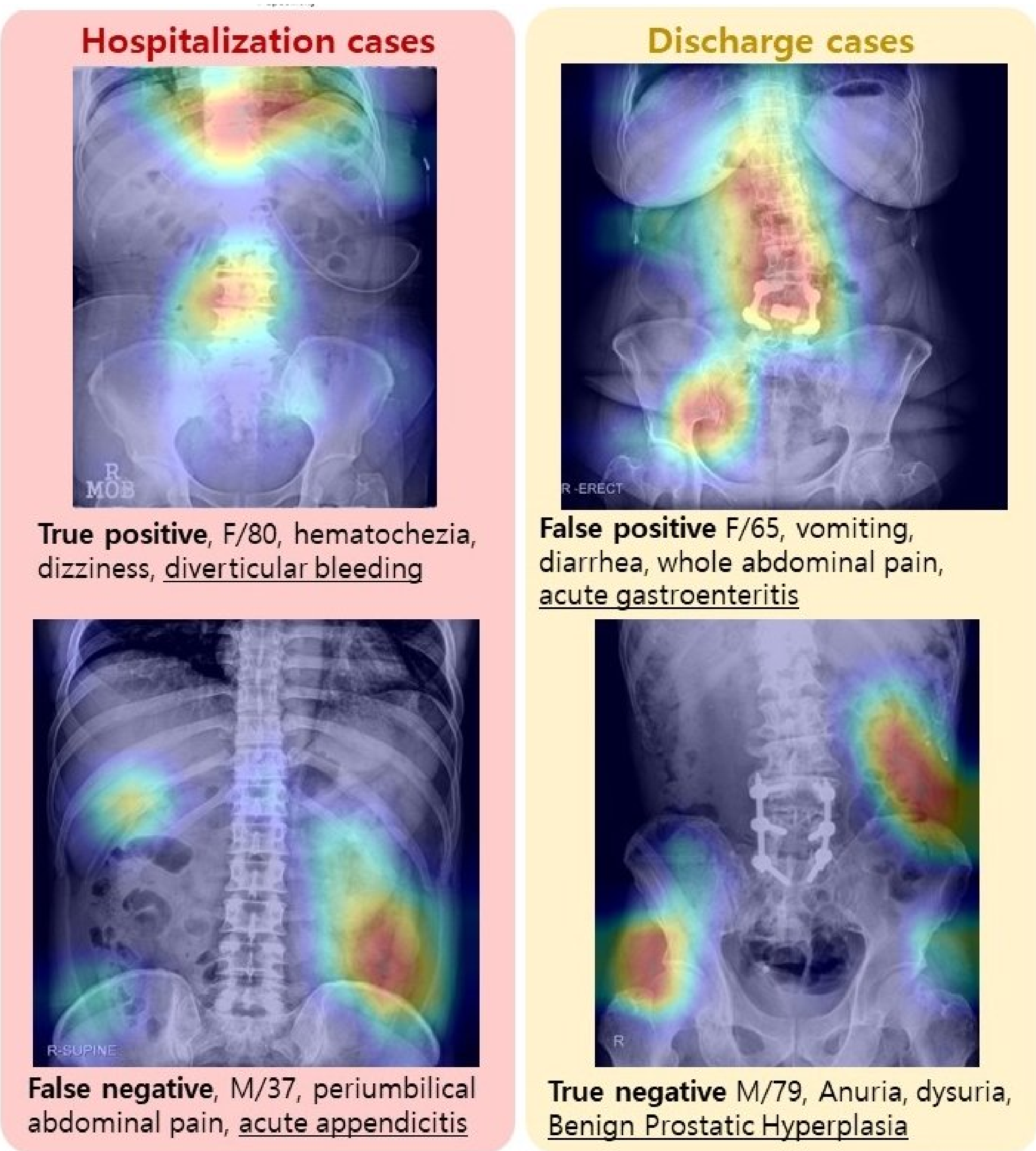

Keywords : Abdominal radiograph, Deep learning, Emergency department

[Scientific Session 5: Hot Topics in Body Imaging]

SS05-4

An End-to-End Deep Learning Model Based on Non-Contrast CT Images of Patients with Liver Cirrhosis for Predicting Hepatocellular Carcinoma

Shifan Liu[1], Shenghong Ju[1*]

[1]Radiology, Zhongda Hospital Medical School of Southeast University, China

Patients with liver cirrhosis face a high risk of developing hepatocellular carcinoma (HCC). However, the effectiveness of current early screening methods remains limited, often resulting in delayed diagnosis and poor outcomes. This study aimed to develop and validate an end-to-end deep learning model based on non-contrast abdominal CT scans to accurately predict the occurrence of HCC 3–12 months in advance among patients with liver cirrhosis.

This prospective study included 703 patients with liver cirrhosis from a single center between June 2018 and January 2020. The median age of the cohort was 48.49 years, with male predominance (86.2%). The median age of patients in the HCC group was significantly higher than that in the NonHCC group (53.58 vs. 47.39 years, $p < 0.001$). The cohort was divided into a training cohort (n = 568) and an external validation cohort (n = 135). Non-contrast abdominal CT images obtained within 3–12 months prior to HCC diagnosis were collected for patients who later developed HCC, while for those who did not develop HCC, images from their final follow-up were used. Based on these data, we constructed a training cohort and developed an early prediction model using deep learning techniques. The optimal model was identified through five-fold cross-validation, and its performance was evaluated in an independent external validation cohort.

We developed a deep learning model named LCPC, which utilizes a fine-tuned ResNet50 architecture to enable end-to-end prediction of HCC within three years in patients with liver cirrhosis, using only non-contrast CT images. In terms of model performance, the area under the curve (AUC) obtained through five-fold cross-validation in the internal training cohort was 0.8180 (95% CI: 0.7950-0.8920); the AUC in the internal validation cohort was 0.8286 (95% CI: 0.7346-0.9137); and the AUC in the independent external validation cohort reached 0.7583 (95% CI: 0.6462-0.8611).

The LCPC model utilizes non-contrast abdominal CT images from patients with liver cirrhosis to enable a prospective and individualized assessment of HCC risk. For patients who have progressed to the decompensated stage, it facilitates the early initiation of the liver donor registration process, thereby gaining valuable preparation time.

Keywords : Liver Cirrhosis, Hepatocellular Carcinoma, Deep Learning

[Scientific Session 5: Hot Topics in Body Imaging]

SS05-5

Dynamic CT-Derived Body Composition Changes During Neoadjuvant Therapy as Prognostic Biomarkers in Pancreatic Cancer: Development and Validation of a Survival Nomogram

Hsin Yu Chen[1], Bang Bin Chen[1*], Yu-Wen Tien[2], Chien-Hui Wu[2]

[1]Radiology, National Taiwan University Hospital, Chinese Taipei
[2]General Surgery, National Taiwan University Hospital, Chinese Taipei

To evaluate whether treatment-related body composition changes quantified from CT imaging serve as prognostic biomarkers in pancreatic cancer patients undergoing neoadjuvant therapy, and to develop a nomogram integrating these dynamic parameters to estimate overall survival (OS).

This retrospective single-center study included 125 patients (M/F = 65/60, mean age 61.5 years) with histologically confirmed pancreatic cancer treated with neoadjuvant therapy between January 2018 and December 2023, withfollow-up completed on October 31, 2025. Contrast-enhanced CT scans at the L3 level were analyzed using TotalSegmentator to quantify skeletal muscle volume and density, subcutaneous and visceral adipose tissue (SATand VAT) volume and density, and vertebral body density. Relative changes were normalized to the interval between baseline and post-treatment imaging. OS was measured from diagnosis to death or last follow-up. Cutoff values for relative changes were determined using the survcut function in R. A multivariable Cox proportional hazards model informed construction of a prognostic nomogram. Model performance was evaluated using a bootstrap-validated C-index, time-dependent ROC analysis, and decision curve analysis.

During a median follow-up of 668 days (IQR, 252–1136), 42 of 125 patients (33.6%) underwent conversion surgery. The median OS was 20.4 months. Changes in skeletal muscle, SAT, and VAT volume and density were eachassociated with OS in univariable analysis ($P < .05$). The final nomogram incorporated seven CT-derived body composition change variables, of which vertebral density ($P = .004$), SAT density ($P < .001$), and skeletal musclevolume ($P = .003$) remained independently associated with OS in the multivariable model. The bootstrap-validated C-index of the nomogram was 0.704 (95% CI, 0.644–0.742). Time-dependent ROC analysis demonstratedconsistent predictive performance at clinically relevant time points, with AUCs of 0.841 (95% CI, 0.750–0.933) at 6 months, 0.822 (95% CI, 0.735–0.908) at 12 months, and 0.720 (95% CI, 0.629–0.812) at 18 months. Risk stratification based on the nomogram score identified three prognostic groups with distinctly different survival outcomes (log-rank $P < .0001$). Decision curve analysis showed greater net clinical benefit of the nomogram compared with individual imaging parameters.

Dynamic changes in skeletal muscle, SAT density, and vertebral density during neoadjuvant therapy reflect prognostic differences in host response and are associated with survival in pancreatic cancer. A CT-based nomogram incorporating these body composition metrics may support individualized risk assessment.

Figure 1. Nomogram for Overall Survival Prediction.

Nomogram integrating seven CT-derived body composition change variables (skeletal muscle volume, skeletal muscle density, subcutaneous adipose tissue volume and density, visceral adipose tissue volume and density, and vertebral body density) to estimate 6-, 12-, and 18-month overall survival probabilities in patients with pancreatic cancer undergoing neoadjuvant therapy. For each variable, a corresponding point value is obtained and summed to generate a total score, which maps to predicted survival probability.

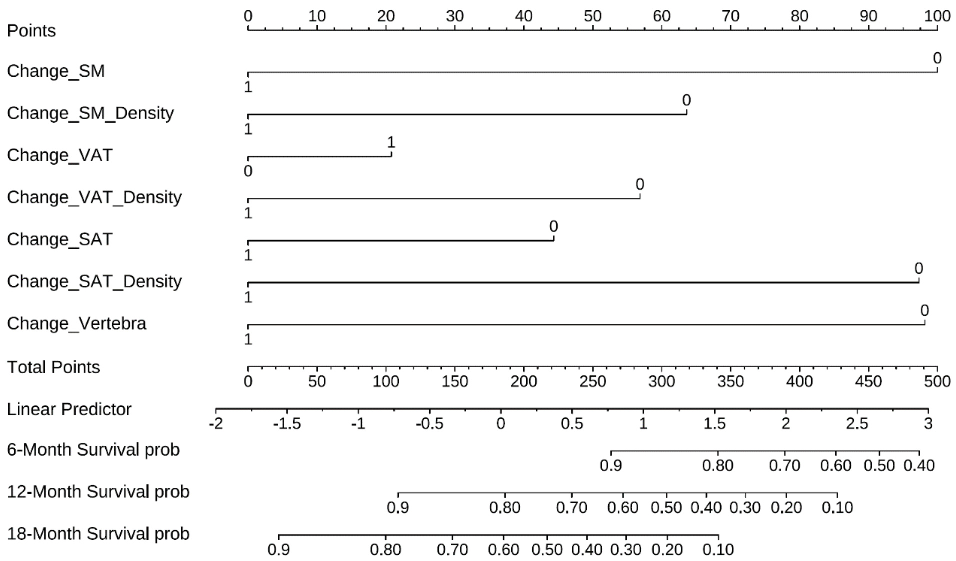

Figure 2. Kaplan–Meier Survival Curves Stratified by Nomogram-Derived Risk Groups.

Overall survival curves for three risk groups determined by total nomogram score. Patients in the high-, intermediate-, and low-risk groups show significantly different survival outcomes (log-rank P < .0001). Shaded areas indicate 95% confidence intervals; numbers at risk are shown below the plot.

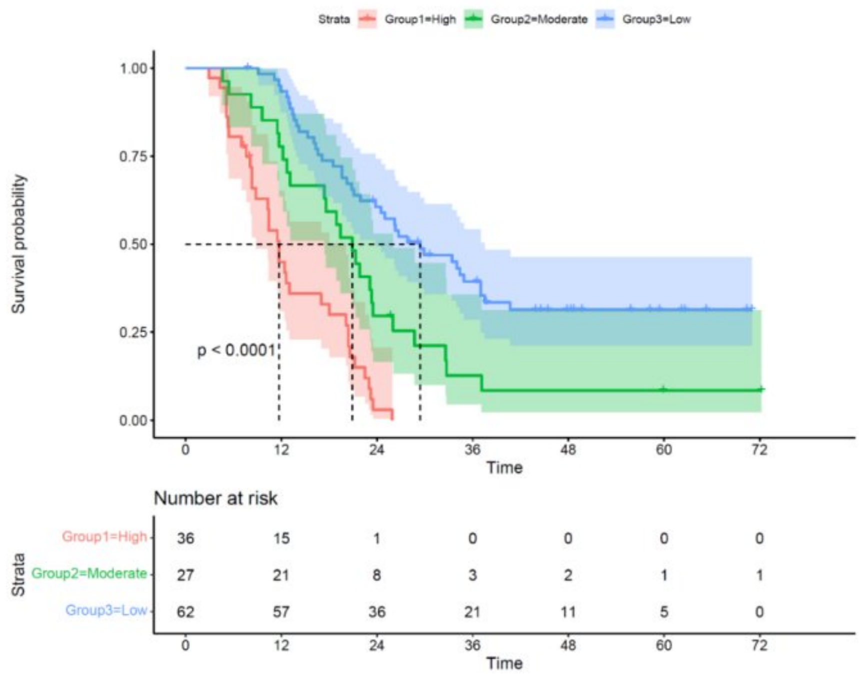

Keywords : Skeletal muscle volume, Visceral adipose tissue, Subcutaneous adipose tissue

[Scientific Session 5: Hot Topics in Body Imaging]

SS05-6

Real-World Radiologist–LLM Reasoning Patterns in Abdominal Imaging: Insights for Designing Personalized AI Copilots

Choongwui Cho[1*]

[1]Radiology, Hanil general hospital, Korea

Large language models (LLMs) are increasingly used in radiology for differential support, clarification, and report refinement. However, how radiologists actually interact with LLMs during real clinical reasoning remains poorly characterized. This study aimed to analyze longitudinal, real-world radiologist–LLM dialogues to delineate their reasoning patterns, role dynamics, and error behaviors and to identify requirements for designing safe, personalized radiology AI copilots.

Ten abdominal imaging cases were selected based on the presence of deep, multi-step reasoning exchanges between an independent radiologist and an LLM. Interactions were coded using the Radiologist–LLM Interaction & Reasoning (RIR) framework, which captures LLM reasoning modes (R-types), radiologist question categories (Q-types), radiologist response behaviors (C-types), and error modes (E-types). Reasoning trajectories, role shifts, prompt–response dynamics, and error-correction processes were analyzed quantitatively and qualitatively. Definitions for all R/Q/C/E subtypes are provided in Appendix A.

Radiologist queries were dominated by differential-development (Q2, 10/10) and pathophysiology (Q3, 7/10), often prompting LLM-driven restructuring of reasoning. Steering responses (C3, 10/10) demonstrated that radiologists consistently maintained diagnostic anchoring. Six clinically meaningful LLM errors appeared across three cases; all were corrected through radiologist-guided revision, underscoring the need for active human oversight. Interactions frequently involved role shifts across inquiry, interpretation, differential expansion, and wording refinement. A reproducible collaboration flow emerged: radiologist sets anchor → LLM structures reasoning → radiologist steers → LLM refines → joint interpretation.

Real-world radiologist–LLM reasoning unfolds through iterative cycles shaped by radiologist anchoring, LLM restructuring, and continuous error correction. Characterizing these behaviors provides practical guidance for developing radiology AI copilots that better support differential reasoning, respond appropriately to radiologist steering, and incorporate safeguards against clinically relevant errors.

Appendix A. RIR Framework and Coding Template

0. Case Metadata
• Case ID:
• Date:
• Modality / Organ system:
• Clinical summary:
• Imaging summary:

1. Dialogue Snapshot
• Radiologist initial input
• LLM first reasoning
• Subsequent dialogue highlights
• Final collaborative output

2. LLM Reasoning Approach Type (R-type)
R1. Descriptor-grounded reasoning *(findings-based analytical reasoning)*
R2. Pattern-recognition reasoning *(morphologic or distribution pattern matching)*
R3. Constraint-based clinical reasoning *(context- or feasibility-driven filtering)*
R4. Differential-expansion & prioritization *(restructuring or reordering DDx)*
R5. Iterative refinement *(stepwise adjustment with new cues or corrections)*

3. Radiologist Question Type (Q-type)
Q1. Descriptor & expression clarification *(clarifying terms, wording, descriptors)*
Q2. Differential diagnosis development *(expanding or prioritizing DDx)*
Q3. Pathophysiology & mechanism inquiry *(asking mechanisms behind findings)*
Q4. Clinical & management consideration *(questions linked to treatment/decision steps)*
Q5. Pitfall & edge-case exploration *(rare mimics & atypical variants)*
Q6. Meta reasoning *(questions about reasoning strategy or rationale)*

4. Radiologist Response Type (C-type)
C1. Disagreement & correction *(explicitly correcting LLM reasoning)*
C2. Agreement & acceptance *(affirming adequacy of LLM reasoning)*
C3. Re-anchoring & steering *(redirecting the reasoning anchor or path)*

5. Error Type (E-type)
E1. Hallucinated detail *(fabricated or ungrounded information)*
E2. Misinterpretation *(incorrect inference from provided findings)*
E3. Overconfidence *(excessive certainty despite ambiguity)*

6. Reasoning Flow Analysis
• Initial anchor
• Key turning point
• Anchor shift
• Final reasoning trajectory

7. Collaboration Pattern
(recognizable interaction structures emerging across radiologist–LLM dialogues)

8. Copilot Design Implication
(principles derived from each case to inform safe and effective AI copilot design)

Appendix B. RIR Result Tables

Appendix B1. RIR coding frequency

Category	Type	Description	Frequency
R-type	R1	Descriptor-grounded reasoning	10
	R2	Pattern-recognition reasoning	10
	R3	Constraint-based clinical reasoning	10
	R4	Differential-expansion & prioritization	9
	R5	Iterative refinement	9
Q-type	Q1	Descriptor & expression clarification	5
	Q2	Differential diagnosis development	10
	Q3	Pathophysiology & mechanism inquiry	7
	Q4	Clinical & management	2
	Q5	Pitfall & edge-case exploration	1
	Q6	Meta reasoning	1
C-type	C1	Disagreement & correction	2
	C2	Agreement & acceptance	9
	C3	Re-anchoring & steering	10
E-type	-	No significant error	6
	E1	Hallucinated detail	1
	E2	Misinterpretation	2
	E3	Overconfidence	2

Appendix B2. Case-level reasoning and copilot implications

Case	Topic	R-type	Q-type	C-type	Errors	Copilot implication
RIR-01	Omental mass	R1 + R2	Q2	C2 + C3	–	Sensitivity to inflammatory vs malignant pattern signatures
RIR-02	Annular pancreas	R3	Q2	C3 + C2	–	Reasoning pathways must incorporate anatomic variants
RIR-03	Linitis plastica	R2	Q2	C2 + C3	–	Strengthened recognition of global infiltrative patterns
RIR-04	DJ stent atrophy	R3 + R5	Q3	C1 + C3 + C2	E2 + E3	Structured consideration of device-related complications
RIR-05	Pancreatic head mass	R1 + R4	Q2	C3 + C2	–	Mechanisms for resolving origin ambiguity
RIR-06	AIP vs PDAC	R1 + R3 + R5	Q2 + Q3 + Q6	C1 + C3	E1 + E2 + E3	Robust evidence guardrails and improved uncertainty signaling
RIR-07	Mild EHD dilation	R1 + R4	Q1 + Q2	C3 + C2	–	Awareness of lab–image mismatches and conservative expression
RIR-08	Tiny PZ lesion	R1	Q1 + Q2	C3 + C2	–	Maintenance of PI-RADS threshold conservatism
RIR-09	TZ PI-RADS 4	R1 + R3	Q2	C2 + C3	–	Incorporation of PSA density into PI-RADS interpretation
RIR-10	Eosinophilic enteritis	R1 + R3 + R5	Q2 + Q3	C2 + C3	E3	Uncertainty calibration for rare or atypical presentations

Keywords : Large language model, Human-AI collaboration, Clinical reasoning

[Scientific Session 5: Hot Topics in Body Imaging]

SS05-7

Evaluation of DeepSeek's Diagnostic Efficacy in Liver Diseases Based on Imaging Findings

Jinqi Zhang[1], Yanfeng Zhao[1], Zheng Zhu[1*], Xiaoyi Wang[1], Bing Feng[1], Xinming Zhao[1]

[1]Diagnostic Radiology, National Cancer CenterNational Clinical Research Center for CancerCancer Hospital Chinese Academy of Medical Sciences and Peking Union Medical College, China

To investigate the accuracy differences between the artificial intelligence (AI) model DeepSeek and radiologists in liver MRI imaging report diagnosis, and to provide evidence for the clinical application of AI-assisted diagnosis.

A retrospective analysis was conducted on imaging findings of 84 patients with pathologically confirmed liver diseases from August 2022 to January 2025. The imaging findings authored by reporting radiologists and reviewing radiologists were processed by the DeepSeek model to generate respective diagnoses. Using pathological results as the gold standard, the diagnostic accuracy of DeepSeek was compared with that of radiologists, and its capability in processing findings from different sources was analyzed.

In distinguishing benign and malignant liver diseases: The accuracy rate of reviewing radiologists was slightly lower than DeepSeek using review findings (90.5% vs. 91.7%), while reporting radiologists demonstrated higher accuracy than DeepSeek with report findings (95.2% vs. 91.7%). Regarding disease diagnosis accuracy: Reviewing radiologists surpassed DeepSeek using review findings (79.8% vs. 73.8%), and reporting radiologists also surpassed DeepSeek with report findings (82.1% vs. 71.4%). DeepSeek exhibited varying diagnostic accuracy when analyzing imaging findings from different categories of reporting radiologists, ranked in descending order as follows: visiting radiologists (76.2%), certified residency-trained radiologists (75.7%), and resident radiologists in training (61.5%).

The diagnostic accuracy of finding-based DeepSeek in liver disease diagnosis may improve with the advancement of radiologists' standardized training and clinical experience accumulation. Although its current performance remains inferior to experienced radiologists, clinicians objectively understand DeepSeek's technical limitations as a diagnostic tool and fully leverage its existing capabilities to maximize the collaborative value of AI in medical decision-making support.

Keywords : Imaging findings, Magnetic resonance imaging, Diagnostic efficacy

ACAR 2026

THE 13th ASIAN CONGRESS OF ABDOMINAL RADIOLOGY

Oral Presentation

Mar. 20 (Fri.)

! Abstracts can be found by searching with the Presentation Code !

[Scientific Session 6: HCC Imaging: From LI-RADS to Prognostic Insights]

SS06-1

LI-RADS Treatment Response Assessment Version 2024: Clinical and Radiologic Predictors of LR-TR Viable after Radioembolization

Sung-Hua Chiu[1,2], Stephan Altmayer[1], Luke Yoon[1], Andrew Kesselman[1], Aya Kamaya[1], Justin Tse[1*]

[1]Radiology, Stanford University School of Medicine, USA
[2]Radiology, Tri-Service General Hospital, Chinese Taipei

To evaluate clinical and radiologic predictors of viability (LR-TR viable) after radioembolization for unresectable hepatocellular carcinoma (HCC).

This retrospective study included HCC patients who underwent radioembolization and had at least 3-month post-treatment imaging follow-up. Treatment response was assessed by two fellowship-trained abdominal radiologists using LI-RADS CT/MRI Radiation TRA v2024 Core; disagreements were settled by a third radiologist. Pre-treatment clinical and radiologic features were evaluated with multivariate analysis, including age, sex, Albumin-Bilirubin (ALBI) grade, alpha-fetoprotein (AFP) level, Eastern Cooperative Oncology Group (ECOG) performance status scale, presence of tumor in vein (TIV), radiologic tumor size, and tumor border (i.e. infiltrative).

A total of 239 HCC patients (182 men, 57 women; median age 65) were included for analyses. Median tumor size was 7.8 cm, with 39% infiltrative and 40% TIV. ALBI grade 1/2/3 was 25%/67%/8%, median AFP was 131 ng/mL, and ECOG 0/1/2 was 44%/49%/7%. After radioembolization, there were 93 (38.9%) lesions categorized as LR-TR Viable, 137 (57.3%) lesions as LR-TR Nonprogressing and 9 (3.8%) lesions as LR-TR Nonviable at the first post-treatment imaging evaluation. At multivariate analysis, only TIV (odd ratio: 1.82, 95% confidence interval (CI): 1.03-3.23, p-value=0.041) and tumor size greater than 5 cm (odd ratio: 2.45, 95% CI:1.09-6.12, p-value=0.040) were significantly associated with LR-TR Viable. Patients with LR-TR Viable had shorter overall survival than those with LR-TR Nonprogressing or Nonviable (44 versus 14 months, p-value

Two radiologic features, TIV and size greater than 5 cm, were significant predictors of LR-TR viable after radioembolization for HCC. This suggests that patients with venous invasion and larger size may be more resistant to radioembolization and may require more intensive or alternative therapies.

Forest plot showing the association between clinical and radiologic features and the prediction of LR-TR Viable. At multivariate analysis, only TIV (odd ratio: 1.82, 95% confidence interval (CI): 1.03-3.23, p-value=0.041) and tumor size greater than 5cm (odd ratio: 2.45, 95% CI:1.09-6.12, p-value=0.040) were significantly associated with LR-TR Viable.

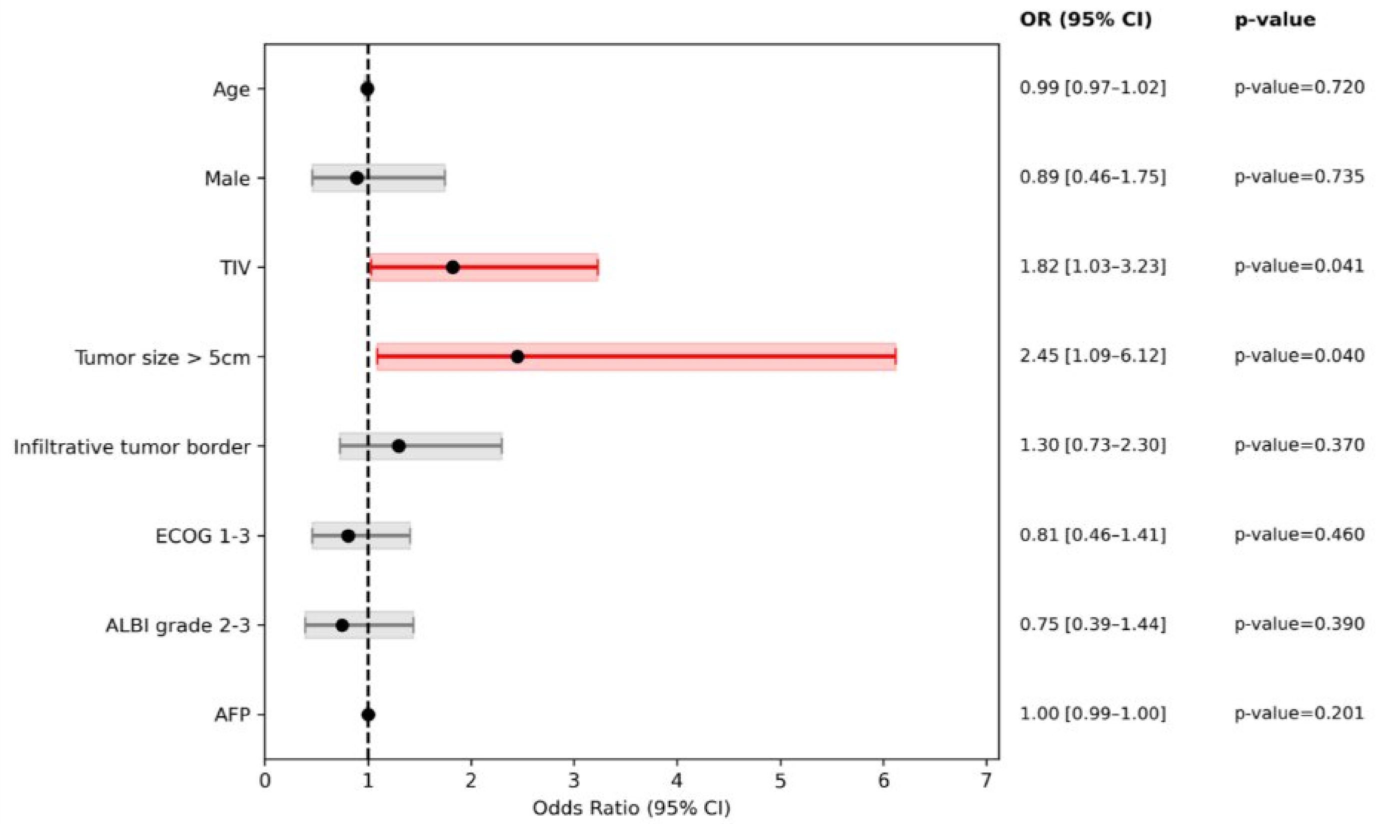

Keywords : LI-RADS, Treatment response algorithm, Radioembolization

[Scientific Session 6: HCC Imaging: From LI-RADS to Prognostic Insights]

SS06-2

Inter-reader Reliability and Diagnostic Performance of the LI-RADS CEUS Nonradiation TRA v2024

Jeremy Jia Qi Soon[1*], Jia Ren Perry Liew[1], Jeremy Jia Hong Lam[1], Wey Chyi Teoh[1]

[1]Radiology, Changi General Hospital, Singapore

Contrast-enhanced ultrasound (CEUS) is increasingly used for post-treatment evaluation of hepatocellular carcinoma (HCC) as an alternative to computed tomography (CT) or magnetic resonance imaging (MRI). In 2024, the American College of Radiology introduced the Liver Imaging Reporting and Data System (LI-RADS) CEUS Nonradiation Treatment Response Assessment (TRA) Version 2024 to standardize assessment of tumor viability after nonradiation locoregional therapy or resection. This study aimed to evaluate the inter-reader reliability and diagnostic performance of this new algorithm.

Three abdominal radiologists and a radiology resident with varying CEUS experience independently assessed 32 CEUS examinations with 39 treated lesions for (i) intralesional tumor viability (Absent/Uncertain/Present), (ii) perilesional tumor viability (Absent/Uncertain/Present), and (iii) final TRA category (TR-Nonviable/Equivocal/Viable) according to LI-RADS CEUS TRA v2024 definitions. Inter-reader agreement was quantified using Cohen's kappa for reader pairs and Fleiss' kappa for all four readers. Pairwise comparisons of Cohen's kappa were performed to explore the effect of reader experience. Diagnostic performance was evaluated using a composite reference standard based on follow-up CT/MRI findings or multidisciplinary consensus regarding tumor viability.

Among 39 lesions, inter-reader agreement across all four readers was substantial for intralesional viability (Fleiss' $\kappa = 0.71$, 95% CI 0.46–0.89), moderate for perilesional viability (Fleiss' $\kappa = 0.43$, 95% CI 0.19–0.62), and moderate for final TRA (Fleiss' $\kappa = 0.53$, 95% CI 0.31–0.69). Pairwise agreement ranged from substantial (Cohen's $\kappa = 0.62$–0.77) for intralesional viability, fair to moderate ($\kappa = 0.30$–0.57) for perilesional viability, and moderate to substantial ($\kappa = 0.45$–0.72) for final TRA category. Pairwise comparisons showed no significant differences in agreement between the most experienced and least experienced pairs.

Majority agreement (≥3 of 4 readers) was high: 94.9% for intralesional viability, 87.2% for perilesional viability, and 87.2% for final TRA category. Full agreement rates across all readers were achieved in 84.6% for intralesional viability, 51.3% for perilesional viability, and 53.9% for final TRA category.

Pooled diagnostic performance was excellent when TR-Equivocal cases were excluded or grouped with TR-Nonviable: sensitivity 100%, specificity 97–98%, PPV 84%, NPV 100%, and accuracy 97–98%. When TR-Equivocal cases were grouped with TR-Viable, specificity decreased to 71% and accuracy to 74%.

The LI-RADS CEUS Nonradiation TRA v2024 demonstrated substantial inter-reader reliability for intralesional tumor viability and strong diagnostic performance across varying reader experience levels.

Majority agreement was high, supporting consistent applicability in clinical and multidisciplinary settings. Lower reproducibility for perilesional findings highlights interpretive challenges in distinguishing benign hyperemia from residual disease. These results affirm the robustness of the new CEUS TRA v2024 framework and support its clinical utility as a standardized, radiation-free tool for post-treatment assessment.

Table 1. Overall inter-reader agreement for LI-RADS CEUS nonradiation TRA v2024 categories (Fleiss' kappa).

	Fleiss Kappa	95% Confidence Interval
Intralesional Viability	0.71	0.46-0.89
Perilesional Viability	0.43	0.19-0.62
Final TRA category	0.53	0.31-0.69

Table 4: Diagnostic performance of LI-RADS CEUS nonradiation TRA v2024 under three analytic approaches.

	TR-equivocal excluded		TR-viable vs (TR-nonviable & equivocal)		TR-nonviable vs (TR-viable & equivocal)	
	Estimate (%)	95% CI (%)	Estimate (%)	95% CI (%)	Estimate (%)	95% CI (%)
Sensitivity	100	79-100	100	79-100	100	79-100
Specificity	97	91-99	98	94-100	71	62-78
PPV	84	60-97	84	60-97	29	17-42
NPV	100	96-100	100	97-100	100	96-100
Diagnostic Accuracy	97	93-99	98	94-100	74	66-80

Keywords : CEUS, LI-RADS, Hepatocellular Carcinoma

[Scientific Session 6: HCC Imaging: From LI-RADS to Prognostic Insights]

SS06-3

Radiological Characteristics of Hepatocellular Carcinoma in Cirrhotic vs Non-Cirrhotic Liver on Multiphasic CT: A Comparative Study

Adinda Amalia[1*], C Rinaldi Lesmana[1], Trifonia Pingkan Siregar[2], Hanna Dwi Wiranti[2], Muhammad Arief Saputra[2]

[1]Internal Medicine, Dr Cipto Mangunkusumo National General Hospital, Indonesia
[2]Radiology, Dr Cipto Mangunkusumo National General Hospital, Indonesia

Hepatocellular carcinoma (HCC) can develop in both cirrhotic and non-cirrhotic livers and Asian real-world data suggest that up to one-third of HCC arises in a non-cirrhotic background. These patients are rarely captured by cirrhosis-based surveillance programs and often present with bulkier tumors and different patterns of portal vein involvement. In many Asian centers, multiphasic computed tomography (CT), rather than gadoxetic magnetic resonance imaging, is still the routine workhorse for HCC imaging. We therefore asked whether CT-based radiological characteristics of HCC differ between cirrhotic and non-cirrhotic livers in our tertiary center, and whether any differences might reflect missed opportunities for earlier detection in the non-cirrhotic group.

We conducted a retrospective case-series of consecutive HCC patients who underwent multiphasic contrast-enhanced CT between 2023 and 2025. Clinical variables (age, sex, Child–Pugh class, ALBI grade, Barcelona Clinic Liver Cancer [BCLC] stage) and imaging features (tumor size, number of lesions, lobar involvement, splenomegaly, main and branch portal vein thrombosis, and portal vein obliteration) were retrieved from electronic records. Patients were classified as cirrhotic or non-cirrhotic using combined clinical, laboratory, and imaging criteria. Radiological features were compared using chi-square tests and t-tests, as appropriate.

Eighty six patients met the inclusion criteria (61 cirrhotic, 25 non-cirrhotic; 87% male; mean age 54.4 ± 11.7 years). Splenomegaly, as a marker of portal hypertension, was substantially more frequent in cirrhotic than non-cirrhotic patients (59% vs 12%). Very large tumors (>7 cm) were frequent in both groups but particularly prominent in non-cirrhotic HCC (67% vs 92%), suggesting later imaging diagnosis despite preserved liver function. Main portal vein thrombosis tended to be more frequent in cirrhotic HCC (33% vs 17%), whereas branch portal vein thrombosis was slightly more common in non-cirrhotic HCC (67% vs 48%). Most cirrhotic patients presented with advanced BCLC stage C or D, while non-cirrhotic patients were more often classified as BCLC C with better liver reserve.

In this Asian multiphasic CT cohort, non-cirrhotic HCC accounted for nearly one-third of cases and typically presented with very large tumors and frequent branch portal vein involvement but far fewer radiological signs of portal hypertension. These contrasting patterns between cirrhotic and non-cirrhotic livers indicate that clinically important HCC can arise outside conventional cirrhosis-based surveillance. Our findings support a reexamination of risk definitions and more tailored imaging approaches for high-risk non-cirrhotic patients in settings where CT remains the main imaging tool.

Keywords : Hepatocellular Carcinoma, Cirrhotic, Non Cirrhotic

[Scientific Session 6: HCC Imaging: From LI-RADS to Prognostic Insights]

SS06-4

Prognostic Implications of Washout Timing in Hepatocellular Carcinoma: A Multicenter Cohort Study

Yingyi Wu[1], Ting Yang[1], Junhan Pan[1], Luna Wang[2], Bin Song[1], Hanyu Jiang[1], Yanshu Wang[1*]

[1]Radiology, West China Hospital Sichuan University, China
[2]Hepatobiliary Surgery and Liver Transplantation, Zhongshan Hospital Fudan University, China

Hepatocellular carcinoma (HCC) is often diagnosed noninvasively through imaging, particularly using MRI with extracellular contrast agents (ECAs), with nonperipheral washout being a key feature. Nonperipheral washout can be observed during the portal venous phase (PVP) or delayed phase (DP), but the prognostic implications of early (PVP) and late (DP) washout remain unclear. This study aims to compare the clinical, histopathologic, and prognostic significance of early and late nonperipheral washout patterns in patients undergoing curative-intent liver resection for BCLC 0/A stage single HCC with Child-Pugh A liver function.

This multicenter, retrospective cohort study included 611 patients between March 2011 and April 2023 **(Figure 1)**. Preoperative MRI with ECAs was performed within two months of surgery. Nonperipheral washout was categorized into three groups: early washout (observed in PVP), late washout (observed only in DP), and no washout. Tumor characteristics, histopathologic features, and imaging findings were evaluated, and recurrence-free survival (RFS) was analyzed. The consistency of imaging feature assessments was evaluated using inter- and intra-rater agreement analyses. Survival outcomes were assessed using Kaplan - Meier and multivariable Cox regression models. Predefined subgroup analyses were performed.

The cohort had a median age of 55 years, with 85% male patients. Chronic hepatitis B was the predominant etiology (88%), and 57% had cirrhosis. The median tumor size was 3.2 cm, with 80% classified as BCLC A stage. The consistency of imaging feature assessments was substantial, with inter-rater agreement for early and late washout at Fleiss' $\kappa = 0.67 - 0.74$. Tumors in the early washout group were larger (3.8 cm vs. 2.8 cm, $p < 0.001$) and more likely to exhibit aggressive features, including the macrotrabecular-massive (MTM) subtype (26.0% vs. 4.6%, $p = 0.001$), Edmondson-Steiner grade III/IV (39.8% vs. 22.1%, $p = 0.002$), and microvascular invasion (MVI) (34.6% vs. 21.1%, $p = 0.014$). Early washout was associated with other aggressive imaging features, such as non-smooth tumor margins (80.9% vs. 60.0%, $p < 0.001$), intratumoral arteries (31.3% vs. 9.5%, $p < 0.001$), and PVP peritumoral hypoenhancement (26.7% vs. 6.3%, $p < 0.001$). In survival analysis, the early washout group had significantly shorter early RFS (adjusted log-rank $p = 0.015$), while overall RFS was comparable between the early and late washout groups (adjusted p = 0.234) **(Figure 2)**. The "no washout" group was used as the reference in Cox regression analysis, where early washout was an independent prognostic factor for both overall RFS (HR 1.41, 95% CI 1.08 - 1.84, $p = 0.012$) and early RFS (HR 1.91, 95% CI 1.32 - 2.76, $p < 0.001$). Subgroup analyses revealed that early washout was associated with shorter overall and early RFS across most subgroups, including those stratified by MRI field strength, cirrhosis status, diffuse fatty change of the background liver, serum AFP levels, tumor sizes, surgery types, and pathological MVI statuses and tumor grades **(Figure 3)**.

In early-stage (BCLC 0/A) hepatocellular carcinoma after curative resection, early non-peripheral washout is an independent predictor of early recurrence and shorter recurrence-free survival, associated with invasive pathological and imaging features.

Figure 1. Flowchart illustrating patient inclusion and exclusion in the study cohort. BCLC = Barcelona Clinic Liver Cancer; HCC = hepatocellular carcinoma; ECA = extracellular contrast agent; LI-RADS = Liver Imaging Reporting and Data System.

Fig.1

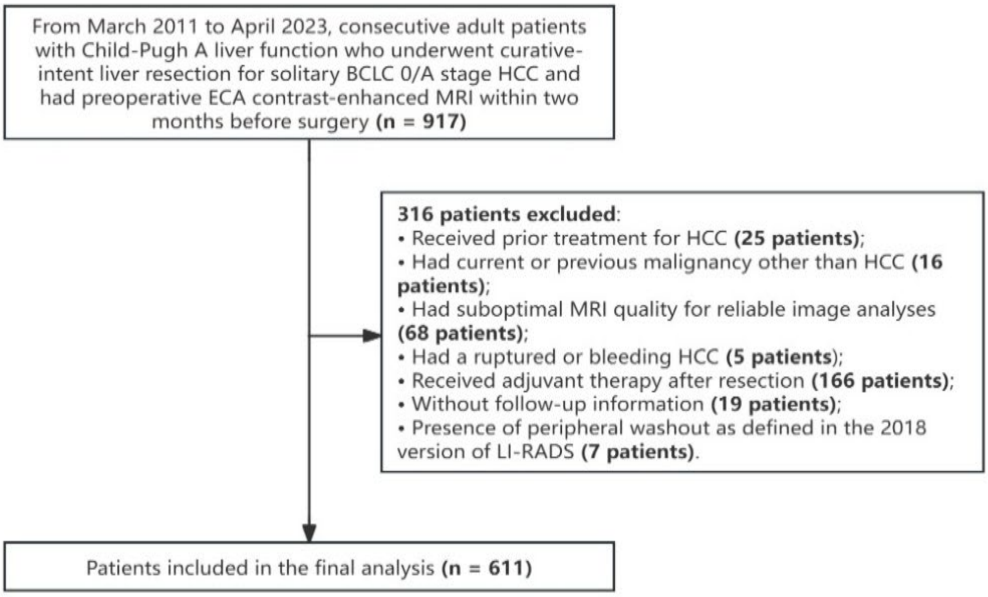

Figure 2. Kaplan-Meier survival curves for overall recurrence-free survival (RFS) and early RFS stratified by washout patterns. Left panel: Overall RFS stratified by nonperipheral washout pattern (No washout, Late washout, Early washout). Early washout was associated with significantly worse overall RFS compared to no washout (adjusted log-rank p < 0.001). No significant difference in overall RFS was observed between late washout and early washout (adjusted log-rank p = 0.234). Right panel: Early RFS stratified by washout patterns. Early washout was associated with significantly shorter early RFS compared to both late washout and no washout (adjusted log-rank p < 0.001 and p = 0.965, respectively), with the difference between late and early washout reaching statistical significance (adjusted log-rank p = 0.015). *Number at risk* for each group is provided below the survival curves.

Fig.2

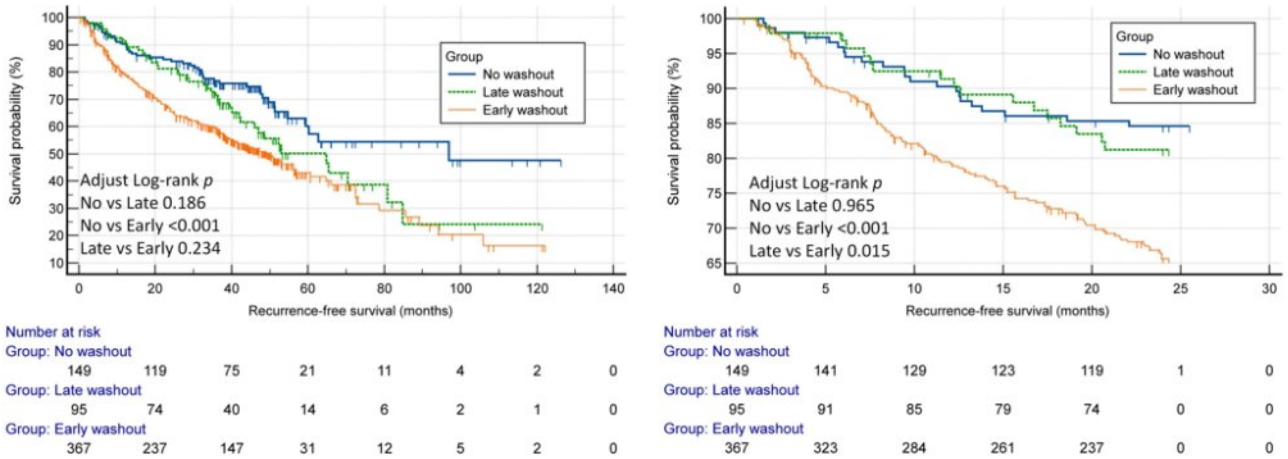

Figure 3. Subgroup analyses of early nonperipheral washout for overall and early recurrence-free survival (RFS). AFP = α-fetoprotein.

Forest plots show subgroup analyses comparing early nonperipheral washout versus no/late washout for (A) overall RFS and (B) early RFS in patients with BCLC 0/A stage hepatocellular carcinoma after curative resection. Hazard ratios (HRs) and 95% confidence intervals (CIs) were derived from Cox proportional hazards models. Early washout was consistently associated with shorter overall and early RFS across most subgroups, including different MRI field strengths, cirrhosis statuses, diffuse fatty change of the background liver, serum AFP levels, tumor sizes, surgery types, as well as pathological microvascular invasion (MVI) statuses and Edmondson-Steiner grades.

Fig.3

A — overall RFS

Variables	n (%)	No/Late washout	Early washout	HR (95%CI)	P
		No. of events/ No. of total			
All patients	611 (100.00)	86/244	182/367	1.71 (1.32 ~ 2.21)	<.001
Cirrhosis					
Absent	239 (39.12)	20/94	55/145	2.10 (1.26 ~ 3.51)	0.005
Present	372 (60.88)	66/150	127/222	1.59 (1.18 ~ 2.14)	0.002
Diffuse fatty change					
Absent	498 (81.51)	75/199	152/299	1.64 (1.24 ~ 2.16)	<.001
Present	113 (18.49)	11/45	30/68	2.08 (1.03 ~ 4.18)	0.04
Field strength					
1.5 T	299 (48.94)	53/118	112/181	1.74 (1.25 ~ 2.41)	<.001
3.0 T	312 (51.06)	33/126	70/186	1.69 (1.11 ~ 2.56)	0.013
Enhancing capsule					
Absent	33 (5.40)	12/28	2/5		
Present	578 (94.60)	74/216	180/362	1.74 (1.33 ~ 2.28)	<.001
Edmondson-Steiner grade					
I/II	406 (66.45)	69/185	106/221	1.43 (1.05 ~ 1.93)	0.021
III/IV	205 (33.55)	17/59	76/146	2.47 (1.45 ~ 4.21)	<.001
Tumor size					
≤ 3cm	277 (45.34)	50/158	55/119	1.64 (1.12 ~ 2.41)	0.011
>3cm	334 (54.66)	36/86	127/248	1.51 (1.04 ~ 2.19)	0.031
Microvascular invasion					
Absent	396 (64.81)	57/184	72/212	1.22 (0.86 ~ 1.73)	0.266
Present	215 (35.19)	29/60	110/155	1.97 (1.31 ~ 2.98)	0.001
AFP					
≤ 400 ng/ml	466 (76.27)	64/198	121/268	1.74 (1.28 ~ 2.36)	<.001
>400 ng/ml	145 (23.73)	22/46	61/99	1.52 (0.94 ~ 2.48)	0.091
Resection extent					
Minor	543 (88.87)	82/230	159/313	1.70 (1.30 ~ 2.22)	<.001
Major	68 (11.13)	4/14	23/54		
Resection type					
Laparoscopic	188 (30.77)	26/83	38/105	1.32 (0.80 ~ 2.18)	0.27
Open surgery	423 (69.23)	60/161	144/262	1.83 (1.35 ~ 2.47)	<.001

B — Early RFS

Variables	n (%)	No/Late washout	Early washout	HR (95%CI)	P
		No. of events/ No. of total			
All patients	611 (100.00)	39/244	120/367	2.29 (1.59 ~ 3.28)	<.001
Cirrhosis					
Absent	239 (39.12)	11/94	40/145	2.60 (1.34 ~ 5.07)	0.005
Present	372 (60.88)	28/150	80/222	2.18 (1.42 ~ 3.35)	<.001
Diffuse fatty change					
Absent	498 (81.51)	32/199	98/299	2.28 (1.53 ~ 3.40)	<.001
Present	113 (18.49)	7/45	22/68	2.30 (0.98 ~ 5.39)	0.055
Field strength					
1.5 T	299 (48.94)	23/118	74/181	2.43 (1.52 ~ 3.88)	<.001
3.0 T	312 (51.06)	16/126	46/186	2.10 (1.19 ~ 3.71)	0.011
Enhancing capsule					
Absent	33 (5.40)	5/28	1/5		
Present	578 (94.60)	34/216	119/362	2.33 (1.59 ~ 3.42)	<.001
Edmondson-Steiner grade					
I/II	406 (66.45)	31/185	64/221	1.88 (1.23 ~ 2.89)	0.004
III/IV	205 (33.55)	8/59	56/146	3.26 (1.55 ~ 6.84)	0.002
Tumor size					
≤ 3cm	277 (45.34)	22/158	31/119	2.02 (1.17 ~ 3.49)	0.012
>3cm	334 (54.66)	17/86	89/248	2.02 (1.20 ~ 3.39)	0.008
Microvascular invasion					
Absent	396 (64.81)	24/184	41/212	1.55 (0.94 ~ 2.57)	0.087
Present	215 (35.19)	15/60	79/155	2.47 (1.42 ~ 4.29)	0.001
AFP					
≤ 400 ng/ml	466 (76.27)	29/198	74/268	2.05 (1.34 ~ 3.16)	0.001
>400 ng/ml	145 (23.73)	10/46	46/99	2.51 (1.26 ~ 4.97)	0.009
Resection extent					
Minor	543 (88.87)	37/230	104/313	2.30 (1.58 ~ 3.35)	<.001
Major	68 (11.13)	2/14	16/54		
Resection type					
Laparoscopic	188 (30.77)	8/83	26/105	2.69 (1.22 ~ 5.95)	0.014
Open surgery	423 (69.23)	31/161	94/262	2.13 (1.42 ~ 3.20)	<.001

Table 1: Differences in clinicopathologic characteristics according to washout pattern.

Characteristic	No Washout (n = 149)	Late Washout (n = 95)	Early Washout (n = 367)	*P* overall	*P* (No vs Late)	*P* (No vs Early)	*P* (Late vs Early)
Age (y)	56.0 (48.0, 64.0)	56.0 (49.0, 64.0)	54.0 (46.0, 63.0)	0.21	-	-	-
Sex				0.31	-	-	-
M	121 (81.2)	82 (86.3)	317 (86.4)				
F	28 (18.8)	13 (13.7)	50 (13.6)				
Chronic liver							
Hepatitis B	134 (89.9)	82 (86.3)	320 (87.2)	0.62	-	-	-
Hepatitis C	2 (1.3)	4 (4.2)	5 (1.4)	0.18	-	-	-
Alcohol use	8 (5.4)	1 (1.1)	18 (4.9)	0.22	-	-	-
MASLD	4 (2.7)	1 (1.1)	8 (2.2)	0.73	-	-	-
Other	0 (0.0)	0 (0.0)	1 (0.3)	>.99	-	-	-
Cryptogenic	9 (6.0)	10 (10.5)	27 (7.4)	0.42	-	-	-
ALBI grade				0.74	-	-	-
1	111 (74.5)	73 (76.8)	285 (77.7)				
2	38 (25.5)	22 (23.2)	82 (22.3)				
Child-Pugh				0.10	-	-	-
5	126 (84.6)	86 (90.5)	299 (81.5)				
6	23 (15.4)	9 (9.5)	68 (18.5)				
BCLC stage				<.001	0.06	<.001	0.003
0	54 (36.2)	20 (21.1)	46 (12.5)				
A	95 (63.8)	75 (78.9)	321 (87.5)				
Size of tumor	2.4 (1.8, 3.0)	2.8 (2.2, 4.0)	3.8 (2.5, 6.0)	<.001	0.013	<.001	<.001
Laboratory							
AFP (ng/mL)	18.8 (3.3, 261.4)	14.6 (3.8, 96.9)	23.9 (4.8, 476.4)	0.11	-	-	-
AST (U/L)	29.0 (24.0, 39.0)	32.0 (24.0, 43.0)	31.0 (25.0, 45.0)	0.23	-	-	-
ALT (U/L)	29.0 (23.0, 50.0)	32.0 (21.0, 46.0)	34.0 (23.0, 51.0)	0.42	-	-	-
TBIL (μmol/L)	14.2 (10.5, 19.3)	14.3 (10.3, 18.7)	14.4 (10.9, 19.0)	0.95	-	-	-
ALB (g/L)	43.9 (39.6, 46.2)	42.8 (40.0, 45.7)	43.4 (40.4, 46.1)	0.76	-	-	-
CREA (μmol/L)	73.0 (64.0, 83.0)	73.0 (64.0, 85.5)	74.0 (65.0, 83.4)	0.43	-	-	-
PLT (×10^9/L)	118.0 (76.0,	132.0 (83.0,	132.0 (91.0,	0.07	-	-	-
Surgical details							
Major	9 (6.0)	6 (6.3)	54 (14.7)	0.005	>.99	0.007	0.03
Open surgery	102 (68.5)	59 (62.1)	262 (71.4)	0.21	-	-	-
Anatomical	13 (27.1)	9 (32.1)	49 (37.4)	0.42	-	-	-
Resection margin	33 (35.9)	17 (36.2)	70 (34.0)	0.93	-	-	-
Intraoperative	5 (3.4)	5 (5.3)	20 (5.4)	0.60	-	-	-
Pathologic							
Cirrsosis	84 (56.4)	56 (59.0)	207 (56.4)	0.90			
Steatosis of liver	19 (25.3)	14 (40.0)	55 (29.3)	0.29			
Edmondson-	38 (25.5)	21 (22.1)	146 (39.8)	<.001	0.876	0.003	0.002
Microvascular	34 (22.8)	26 (27.4)	155 (42.2)	<.001	>.99	0.002	0.014
MTM subtype§	7 (7.5)	2 (4.6)	54 (26.0)	<.001	>.99	<.001	0.001

Note.—Continuous variables are expressed as medians with IQRs in parentheses, while categorical variables are expressed as numbers with percentages in parentheses. Unless stated otherwise, continuous variables were compared using the Kruskal-Wallis test and categorical variables using the χ^2 test. For characteristics with significant differences across all three groups (P All < .05), post hoc pairwise comparisons were performed with Bonferroni correction.

*More than one etiology could be present for each patient.

†Data available for 207 patients (No washout, n=48; Late washout, n=28; Early washout, n=131).

‡Data available for 345 patients (No washout, n=92; Late washout, n=47; Early washout, n=206).

§Data available for 345 patients (No washout, n=93; Late washout, n=44; Early washout, n=208).

Abbreviations: ALBI = albumin-bilirubin, BCLC = Barcelona Clinic Liver Cancer, M = male, MASLD = metabolic dysfunction–associated steatotic liver disease, MTM = macrotrabecular-massive.

Table 2: Differences in LI-RADS features and categories according to washout pattern.

Table 2: Differences in LI-RADS features and categories according to washout pattern

Characteristic	No Washout (n = 149)	Late Washout (n = 95)	Early Washout (n = 367)	*P* overall	*P* (No vs Late)	*P* (No vs Early)	*P* (Late vs Early)
LI-RADS major features							
Nonrim APHE	144 (96.6)	93 (97.9)	335 (91.3)	0.014	>.99	0.036	0.03
Nonperipheral washout	0 (0.0)	95 (100.0)	367 (100.0)	<.001	<.001	<.001	0.74
Enhancing capsule	125 (83.9)	91 (95.8)	362 (98.6)	<.001	<.001	<.001	0.41
Tumor size (cm)†	2.4 (1.8, 3.0)	2.8 (2.2, 4.0)	3.8 (2.5, 6.0)	<.001	0.013	<.001	<.001
LI-RADS ancillary features							
Favoring malignancy, not HCC in particular							
Corona enhancement	43 (28.9)	21 (22.1)	149 (40.6)	<.001	0.42	0.017	0.001
Fat in mass more than liver	48 (32.2)	34 (35.8)	173 (47.1)	0.003	0.87	0.003	0.07
Mild moderate T2 hyperintensity	146 (98.0)	94 (99.0)	359 (97.8)	0.92	-	-	-
Diffusion restriction	148 (99.3)	92 (96.8)	366 (99.7)	0.033	-	-	-
Iron sparing in solid mass	14 (9.4)	10 (10.5)	23 (6.3)	0.26	-	-	-
Favoring malignancy, HCC in particular							
Nonenhancing capsule	5 (3.4)	0 (0.0)	0 (0.0)	0.002	0.007	<.001	>.99
Nodule in nodule architecture	18 (12.1)	24 (25.3)	147 (40.1)	<.001	0.045	<.001	0.008
Mosaic architecture	11 (7.4)	8 (8.4)	117 (31.9)	<.001	>.99	<.001	<.001
Blood products in mass	16 (10.7)	11 (11.6)	113 (30.8)	<.001	>.99	<.001	<.001
LR-M features							
Rim APHE	3 (2.0)	2 (2.1)	28 (7.6)	0.011	>.99	0.016	0.05
Peripheral washout*	0 (0.0)	1 (1.1)	3 (0.8)	0.62	-	-	-
Delayed central enhancement*	5 (3.4)	1 (1.1)	9 (2.5)	0.53	-	-	-
Targetoid restriction*	1 (0.7)	1 (1.1)	9 (2.5)	0.47	-	-	-
Marked diffusion restriction	36 (24.2)	15 (15.8)	99 (27.0)	0.08	-	-	-
Infiltrative appearance*	0 (0.0)	0 (0.0)	9 (2.5)	0.06	-	-	-
Necrosis or severe ischemia	11 (7.4)	21 (22.1)	158 (43.1)	<.001	0.023	<.001	<.001
LI RADS category‡							
4	48 (32.9)	3 (3.2)	3 (0.8)	<.001	<.001	<.001	0.06
5	85 (63.1)	82 (94.7)	306 (89.9)				
M	6 (4.0)	2 (2.1)	32 (9.3)				
Other tumor-related prognostic							
T2 peritumoral hyperintensity	16 (10.7)	12 (12.6)	93 (25.3)	<.001	>.99	<.001	0.008
PVP peritumoral	6 (4.0)	6 (6.3)	98 (26.7)	<.001	0.98	<.001	<.001
Low ADC value	51 (38.9)	28 (33.7)	174 (53.2)	<.001	0.69	0.009	0.002
APHE proportion>50%	142 (95.3)	91 (95.8)	259 (70.6)	<.001	>.99	<.001	<.001
Internal artery	8 (5.4)	9 (9.5)	115 (31.3)	<.001	0.67	<.001	<.001
Complete capsule	74 (49.7)	47 (49.5)	89 (24.3)	<.001	>.99	<.001	<.001
Non-smooth tumor margin	83 (55.7)	57 (60.0)	297 (80.9)	<.001	0.70	<.001	<.001
The VICT2 trait§	24 (16.1)	17 (17.9)	145 (39.5)	<.001	>.99	<.001	<.001
Bilobar involvement*	5 (3.4)	2 (2.1)	16 (4.4)	0.56	-	-	-
Involvement of liver capsule	88 (59.1)	59 (62.1)	249 (67.9)	0.14	-	-	-
Homogenous fat in mass	24 (16.1)	12 (12.6)	71 (19.4)	0.27	-	-	-
Imaging features associated with the severity of underlying liver diseases and portal hypertension							
Ascites	10 (6.7)	3 (3.2)	27 (7.4)	0.34			
Cirrhosis	92 (61.7)	58 (61.1)	222 (60.5)	0.97			
Diffuse fatty change	36 (24.2)	9 (9.5)	68 (18.5)	0.02	0.006	0.20	0.06
Diffuse iron overload	23 (15.4)	13 (13.7)	36 (9.8)	0.16			
Splenomegaly	60 (40.3)	40 (42.1)	153 (41.7)	0.30			

Note.—Data are numbers of patients, with percentages in parentheses, or medians, with IQRs in parentheses. Unless stated otherwise, comparisons were made using the χ^2 test for categorical variables and the Kruskal-Wallis test for continuous variables. For characteristics with significant differences across all three groups (P All < .05), post hoc pairwise comparisons were performed with Bonferroni correction for categorical variables and Dunn's test for continuous and ordinal variables.
Abbreviations: LI-RADS = Liver Imaging Reporting and Data System, APHE = arterial phase hyperenhancement, PVP = portal venous phase, ADC = apparent diffusion coefficient.
*Comparisons were made using the Fisher exact test.
†Continuous or ordinal variables compared using Kruskal-Wallis test with post hoc Dunn's test.
‡Comparisons were made in patients with LI-RADS high-risk status (n=567).
§The VICT2 trait is defined as the presence of portal venous phase peritumoral hypoenhancement; or the presence of both corona enhancement and T2-weighted peritumoral hyperintensity coupled with the absence of a complete capsule.

Table 3: Univariable and multivariable cox regression analyses for recurrence-free survival and early recurrence-free survival.

Table 3: Univariable and Multivariable Cox Regression Analyses for Recurrence-Free Survival and Early-Recurrence-Free Survival

Variable	Recurrence-Free Survival				Early-Recurrence-Free Survival			
	Univariable HR	*P*	Multivariable HR	*P*	Univariable HR	*P*	Multivariable HR	*P*
Age (y)	0.96 (0.72, 1.28)	0.76			0.81 (0.55, 1.19)	0.29		
Sex (M vs F)	0.95 (0.68, 1.34)	0.78			0.97 (0.63, 1.50)	0.90		
α-fetoprotein(>400 ng/mL vs ≤400 ng/mL)	1.53 (1.18, 1.98)	0.001			1.98 (1.43, 2.74)	<0.001	1.50 (1.07, 2.10)	0.02
ALBI grade (grade 2 vs grade 1)	1.10 (0.83, 1.46)	0.49			0.93 (0.64, 1.35)	0.70		
Surgery								
Open surgery (yes vs no)	1.39 (1.05, 1.84)	0.02			1.71 (1.17, 2.50)	0.005		
Major hepatectomy (yes vs no)	1.05 (0.71, 1.55)	0.83			1.11 (0.69, 1.80)	0.66		
Pathology								
Cirrsosis (present vs absent)	1.90 (1.47, 2.46)	<0.001	1.95 (1.51, 2.52)	<0.001	1.65 (1.19, 2.29)	0.003	1.67 (1.20, 2.33)	0.002
Edmondson-Steiner grade (III/IVvs I/II)	1.11 (0.86, 1.43)	0.42			1.42 (1.04, 1.95)	0.03		
Microvascular invasion (present vs absent)	2.61 (2.05, 3.33)	<0.001	2.19 (1.71, 2.79)	<0.001	3.33 (2.43, 4.54)	<0.001	2.59 (1.86, 3.61)	<0.001
Imaging features								
Washout pattern								
Late washout (present vs no washout)	1.64 (1.05, 2.56)	0.03			1.47 (0.72, 2.96)	0.29		
Early washout (present vs no washout)	2.43 (1.72, 3.43)	<0.001	1.41 (1.08, 1.84)	0.012	3.59 (2.14, 6.04)	<0.001	1.91 (1.32, 2.76)	<0.001
Tumor size (cm)	1.12 (1.07, 1.16)	<0.001			1.14 (1.09, 1.20)	<0.001		
BCLC stage (A vs 0)	1.32 (0.96, 1.83)	0.09			1.63 (1.04, 2.56)	0.03		
T2WI peritumoral hyperintensity (present vs absent)	1.44 (1.09, 1.92)	0.01			1.62 (1.14, 2.30)	0.007		
APHE proportion(>50% vs ≤50%)	0.63 (0.16, 2.54)	0.52			0.65 (0.46, 0.94)	0.02		
Internal artery (present vs absent)	1.91 (1.46, 2.50)	<0.001			2.16 (1.55, 3.00)	<0.001		
Nonperipheral washout (present vs absent)	1.60 (1.18, 2.16)	0.003			2.18 (1.40, 3.43)	0.008		
PVP peritumoral hypoenhancement (present vs absent)	1.49 (1.10, 2.02)	0.009			1.81 (1.27, 2.58)	0.001		
Complete capsule (present vs absent)	0.66 (0.50, 0.86)	0.002			0.52 (0.36, 0.75)	0.001		
Non-smooth tumor margin (present vs absent)	1.65 (1.24, 2.20)	0.001			1.93 (1.29, 2.88)	0.001		
Tumor growth subtype (present vs absent)	1.66 (1.31, 2.12)	<0.001			2.02 (1.47, 2.78)	<0.001		
Mosaic architecture (present vs absent)	1.58 (1.20, 2.08)	0.001			1.62 (1.15, 2.28)	0.006		
Blood products in mass (present vs absent)	1.93 (1.48, 2.51)	<0.001	1.62 (1.23, 2.14)	0.006	1.96 (1.41, 2.72)	<0.001		
Necrosis or severe ischemia (present vs absent)	1.78 (1.39, 2.28)	<0.001			1.88 (1.37, 2.57)	<0.001		
The VICT2 trait* (present vs absent)	1.24 (0.95, 1.62)	0.11			1.50 (1.09, 2.07)	0.01		

Note.—Data in parentheses are 95% CIs. To avoid overfitting at the multivariable Cox regression analyses, independent (ie, noncollinear) variables with P < 0.05 at the univariable analyses were analyzed in the multivariable model.
Abbreviations: ALBI = albumin-bilirubin, APHE = arterial phase hyperenhancement, BCLC = Barcelona Clinic Liver Cancer, PVP = portal venous phase, T2WI = T2-weighted imaging.
*The VICT2 trait is defined as the presence of portal venous phase peritumoral hypoenhancement; or the presence of both corona enhancement and T2-weighted peritumoral hyperintensity coupled with the absence of a complete capsule.

Keywords : Hepatocellular Carcinoma, Nonperipheral Washout, Recurrence-Free survival

[Scientific Session 6: HCC Imaging: From LI-RADS to Prognostic Insights]

SS06-5

Preoperative Predicting Tumor-Specific Vascular Patterns on Contrast-Enhanced CT and Their Prognostic Implications for Solitary BCLC 0-A Hepatocellular Carcinoma

Wanli Zhang[1*], Ruimeng Yang[1], Xinqing Jiang[1]

[1]Radiology, Guangzhou First Peoples Hospital, China

Vessels that encapsulate tumor clusters (VETC) and microvascular invasion (MVI) represent two specific vascular patterns in hepatocellular carcinoma (HCC) associated with patients' unfavorable outcomes. This study aimed to investigate the value of qualitative and quantitative contrast-enhanced CT (CECT) features for the noninvasive identification of VETC and/or MVI status in solitary HCC at Barcelona Clinic Liver Cancer (BCLC) 0-A stage, and to assess their prognostic implications.

Patients with surgically confirmed solitary BCLC 0-A HCC and preoperative CECT from two medical centers were retrospectively enrolled. All patients were divided into VM+ (MVI and/or VETC-positive) and VM- (both MVI-negative and VETC-negative) groups based on histopathology. Four predictive models (clinical, CT quantitative, CT qualitative and combined model) integrating clinical and CECT features were developed and external validated for identifying VM+ status in HCC. Models performance was evaluated and compared using receiver operating characteristic curve (ROC) analysis and DeLong tests. Subgroup analysis of the best-performing VM+ prediction model was performed utilizing propensity score matching (PSM) to balance baseline differences between the centers. Postoperative follow-up information was collected to calculate patients' recurrence-free survival (RFS) time. Kaplan-Meier survival curves and multivariate Cox proportional hazards regression analysis were used for survival analysis.

A total of 347 patients (mean age, 56.89 years ± 8.39 [SD]) were enrolled, with 174 VM+ HCC and 173 VM- HCC. The training cohort included 207 patients (173 men, 101 [48.8%] VM+ HCCs), and the external validation cohort had 140 cases (118 men, 73 [52.14%] VM+ HCCs). Both the CT qualitative and quantitative models exhibited good predictive performance for VM+ HCC, with AUCs > 0.71 in the two cohorts. Serum alpha-fetoprotein (AFP) ≥ 200 ng/mL, non-smooth tumor margin, the presence of internal arteries, and the tumor-to-liver density ratio in the portal venous phase (P-TLR) < 0.86 were identified as independent predictors of VM+ HCC. The combined model, incorporating these factors, achieved optimal predictive power, with training and external validating AUCs of 0.778 and 0.794. After PSM, the combined model maintained superior predictive performance, with AUCs of 0.782 and 0.810 in the training and external validation cohorts, respectively. Kaplan-Meier survival analysis demonstrated that patients with VM + HCC had worse 2-year PFS in both two cohorts. A derived VM+ score from the combined model stratified patients effectively, with higher scores associated with significantly shorter 2-year PFS in both the training and external validation cohorts pre- and post PSM. After variables significant in univariate analysis were excluded from the final logistic regression-based

VM+ prediction model, multivariate Cox analysis still identified a VM+ score ≥ 34 and tumor size ≥ 60mm as significant predictors of HCC progression ($P < 0.05$).

The combined model, integrating clinical and CECT-based quantitative and qualitative features, enables non-invasive assessment of VM status in BCLC 0-A stage solitary HCC and effectively stratifies patients according to progression risk.

Table 1. Performances of the four models for predicting VM+ HCC

*DeLong test between combinational model and other three models.

A *P* value less than 0.05 was considered statistically significant, presented in **bold**.

AUC, area under the curve; CI, confidence interval; ACC, accuracy; SEN, sensitivity; SPE, specificity; PPV, positive predictive value; NPV, negative predictive value; VM, vessels that encapsulate tumor clusters (VETC) and/or microvascular invasion (MVI).

Table 1. Performances of the four models for predicting VM+ HCC

Cohort	Model	AUC (95% CI)	ACC	SEN	SPE	PPV	NPV	P^*
Training cohort	Clinical model	0.634 (0.564-0.700)	0.599	0.574	0.623	0.592	0.606	**< 0.001**
	CT qualitative model	0.717 (0.650-0.777)	0.657	0.762	0.557	0.621	0.711	**0.046**
	CT quantitative model	0.741 (0.676-0.800)	0.686	0.703	0.670	0.670	0.703	0.156
	Combined model	0.778 (0.715-0.832)	0.729	0.653	0.802	0.759	0.708	/
External validation cohort	Clinical model	0.707 (0.620-0.793)	0.679	0.685	0.672	0.694	0.662	**0.005**
	CT qualitative model	0.724 (0.640-0.807)	0.650	0.658	0.642	0.667	0.632	**0.037**
	CT quantitative model	0.710 (0.623-0.796)	0.686	0.740	0.627	0.684	0.689	**0.024**
	Combined model	0.794 (0.718-0.870)	0.729	0.753	0.701	0.733	0.723	/

Figure 1. Kaplan-Meier curves of tumor progression-free survival outcomes stratified by VM+ score (a, c, e, g) and VM status (b, d, f, h). a-b, e-f, represented the training cohort; c-d, g-h, represented the external validation cohort. e-f, g-h, were post-PSM. Statistical comparison between survival curves was performed with the log-rank test.

PFS, progression-free survival; PSM, propensity score matching; VM, vessels that encapsulate tumor clusters (VETC) and/or microvascular invasion (MVI).

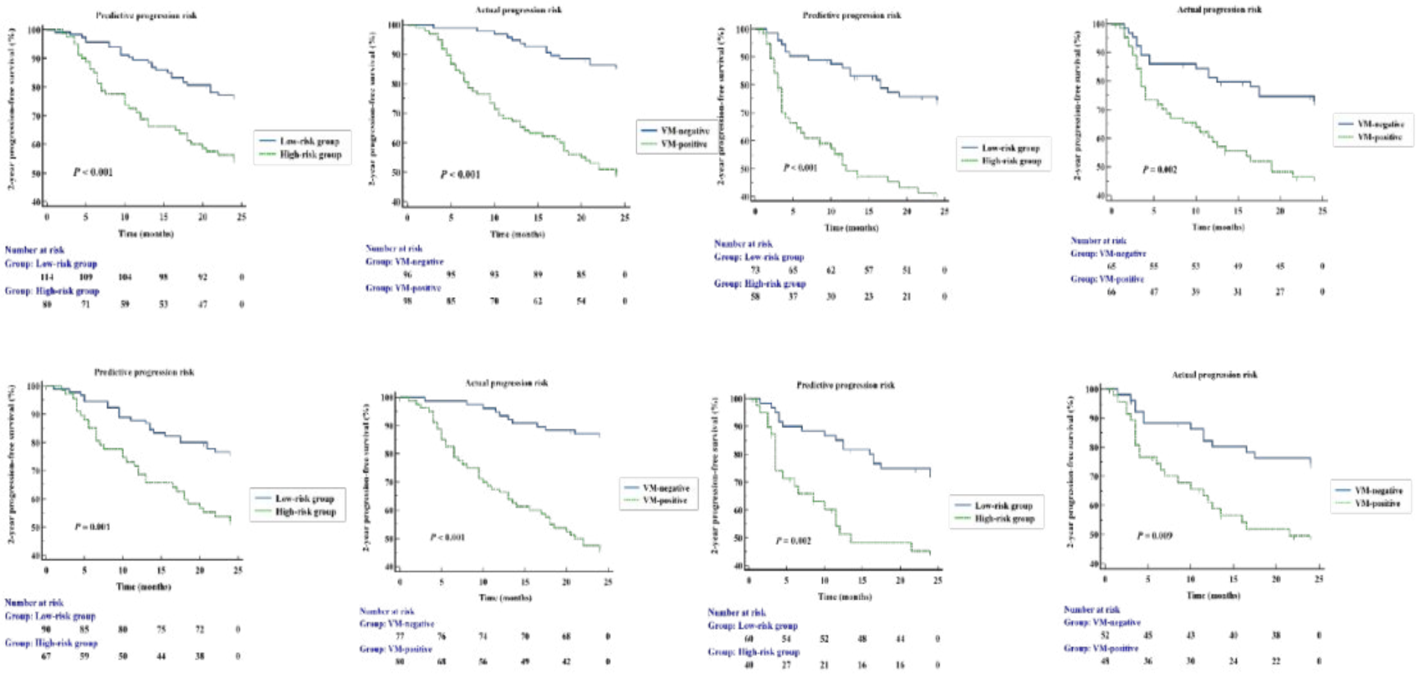

Keywords : Hepatocellular carcinoma, Microvascular invasion, Vessels that encapsulate tumor clusters

[Scientific Session 6: HCC Imaging: From LI-RADS to Prognostic Insights]

SS06-6

Intraindividual Comparison of Promising Prognostic Features between CT and MRI in Patients with Hepatocellular Carcinoma

Xinyuan Jia[1], Yanshu Wang[1], Bin Song[1], Hanyu Jiang[1*]

[1]Radiology, West China Hospital Sichuan University, China

MRI has been extensively validated to provide valuable prognostic information in hepatocellular carcinoma (HCC), yet whether comparable features can be reliably assessed and maintain similar prognostic value on CT remains unclear. This study aimed to comprehensively and intraindividually compare prognostic imaging features of HCC between CT and MRI, and to further assess their predictive performance for histopathologic MVI and early recurrence-free survival (≤2 years, eRFS) in solitary Barcelona Clinic Liver Cancer (BCLC) 0/A stage HCC.

This single-center retrospective study included consecutive patients with solitary BCLC 0/A HCC who underwent both preoperative contrast-enhanced CT and MRI followed by curative resection. Sixteen prognostic imaging features were independently evaluated by two blinded radiologists in randomized order with a 4-week washout. Inter-modality agreement was assessed using the intraclass correlation coefficient (ICC) for continuous variables, and Cohen's κ and Gwet's AC1 for categorical variables. The McNemar test compared feature frequencies. Univariate and multivariate Cox regression analyses identified predictors for eRFS, while logistic regression was performed for microvascular invasion (MVI).

A total of 302 patients (median age, 54 years; 82.5% men) were included. During a median 42-month follow-up, the cumulative eRFS rate was 67.7%. Tumor size showed excellent inter-reader and inter-modality agreement (ICC, 0.99), while most binary features demonstrated moderate-to-good reproducibility after adjusting for prevalence bias (AC1, 0.32–0.96). MRI more frequently depicted complex intratumoral and peritumoral features such as corona enhancement and blood products in mass (all $p<.05$), whereas CT more often showed single-nodular subtype and nonperipheral "washout." The predictive performance for MVI was comparable between CT- and MRI-based models (AUC, 0.755 vs. 0.750; $p=.767$), and both modalities showed similar ability for eRFS prediction (C-index, 0.643 vs. 0.650; $p=.387$).

CT and MRI demonstrated comparable performance to predict both MVI and eRFS, despite modality-specific differences in feature detectability. MRI may offer advantages in depicting peritumoral characteristics, whereas CT remains a clinically feasible tool for prognostic assessment in patients with HCC.

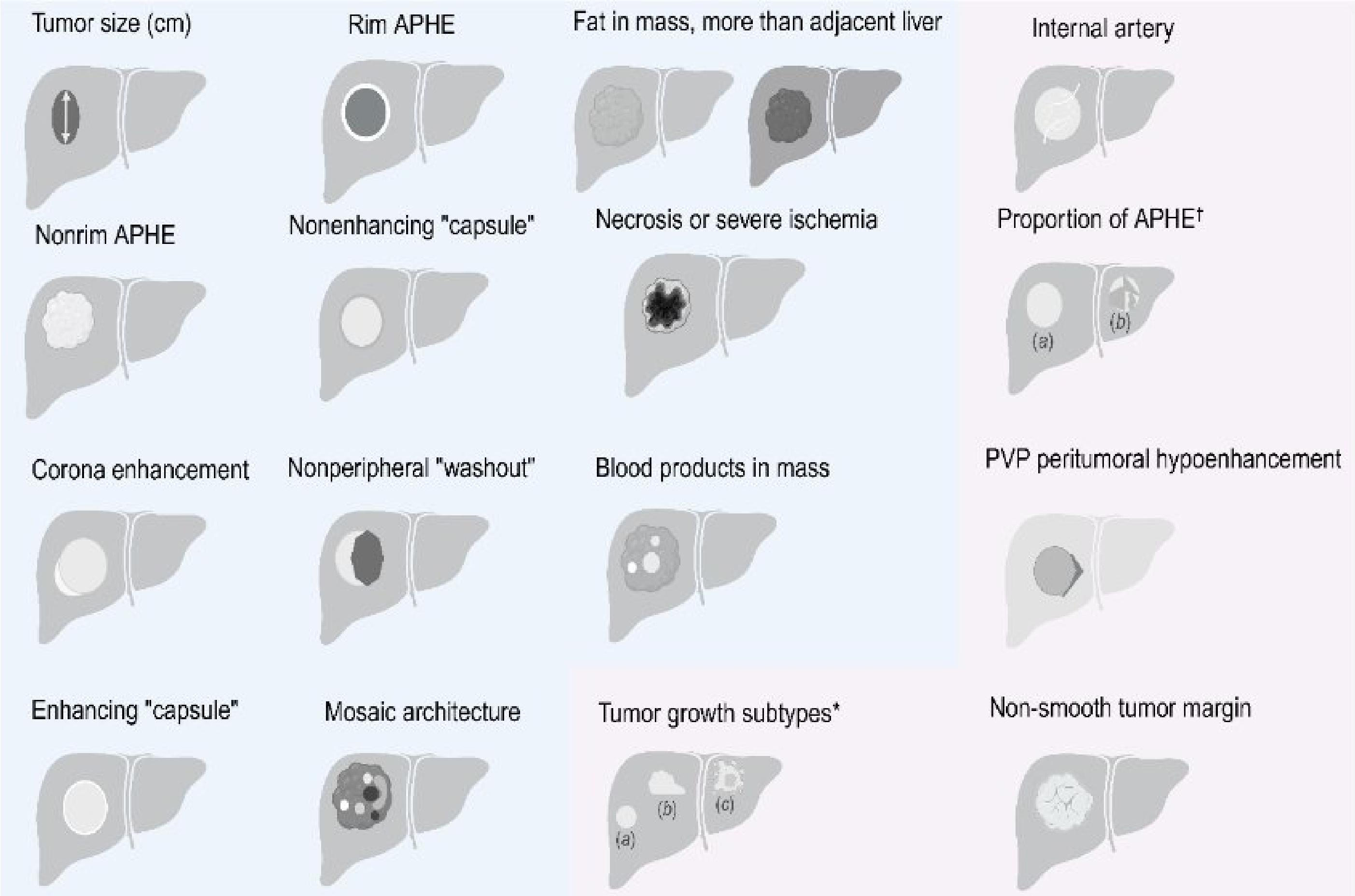

Keywords : Microvascular invasion, CT, MRI

[Scientific Session 6: HCC Imaging: From LI-RADS to Prognostic Insights]

SS06-7

Intraindividual Concordance and Discordance in CT and MRI LI-RADS Categorization in Hepatocellular Carcinoma: Impact on Postsurgical Prognosis

Yong Jun Jung[1], Sang Hyun Choi[1*], Subin Heo[1]

[1]Radiology, Asan Medical Center University of Ulsan College of Medicine, Korea

Substantial discrepancies in Liver Imaging Reporting and Data System (LI-RADS) categorization between CT and MRI have been reported. However, the prognostic implications of such intraindividual concordance patterns in patients with hepatocellular carcinoma (HCC) remain unclear. To assess intraindividual concordance and discordance in LI-RADS categorization between CT and MRI in surgically-resected HCC and to evaluate their impact on early postsurgical recurrence.

This dual-center retrospective study included patients who underwent both CT and MRI prior to hepatic resection between January 2016 and December 2020. For each HCC, the LI-RADS category was independently assigned on CT and MRI. Univariable and multivariable Cox regression analyses were performed to evaluate the association between CT/MRI LI-RADS categorization (LR-M vs. LR-4/5) and 2-year recurrence-free survival (RFS). Patients were classified into three groups according to CT and MRI LI-RADS categorization: both modalities, only one modality, or neither modality. The 2-year RFS was compared among the groups.

A total of 319 patients (mean age, 58.8 years; 248 men) were included with 114 (35.7%) showing discrepant CT/MRI LI-RADS categorizations. The frequency of LR-M categorization was significantly higher on MRI than on CT (21.6% vs. 6.0%, P<0.001). CT (hazard ratio [HR]=2.25, P=0.03) and MRI (HR=2.23, P=0.003) LR-M categorizations were independently associated with two-year RFS. The two-year RFS was lowest, intermediate, and highest in patients with HCCs categorized as LR-M on both modalities (33.3%), only one modality (63.3%), and neither modality (82.8%), respectively (P<0.001).

LI-RADS categorization of HCC frequently differed between CT and MRI. CT/MRI LR-M categorizations were independent predictors of two-year RFS. Recurrence was highest when tumors were classified as LR-M on both modalities.

Kaplan-Meier survival curves of 2-year recurrence-free survivals and overall survival rates stratified by the number of imaging modalities that classified the tumor as LR-M. Patients with HCCs classified as LR-M on both modalities (Group C) demonstrated a lower 2-year recurrence-free survival and overall survival rate, than those with HCCs classified as LR-4/5 on both modalities (Group A) or as LR-M on only one modality (Group B).

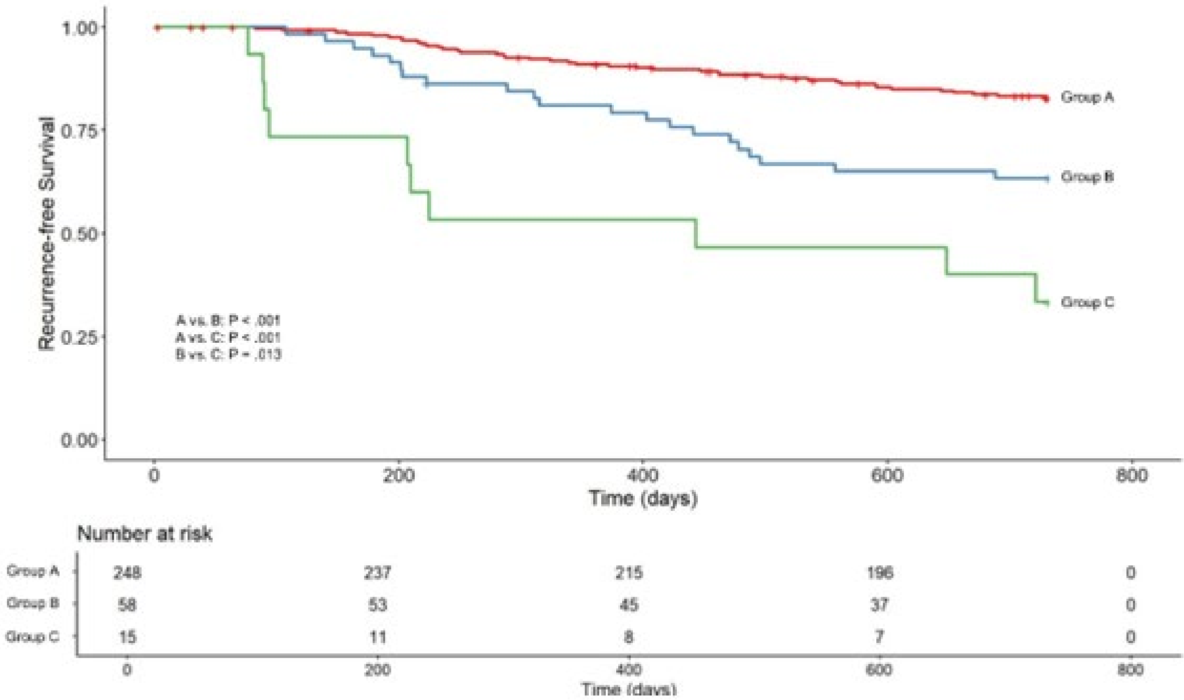
Recurrence-free Survival
1.00
0.75
0.50
0.25
0.00
Group A
Group B
Group C
A vs. B: P < .001
A vs. C: P < .001
B vs. C: P = .013
0
200
400
600
800
Time (days)
Number at risk
Group A 248 237 215 196 0
Group B 58 53 45 37 0
Group C 15 11 8 7 0
Time (days)

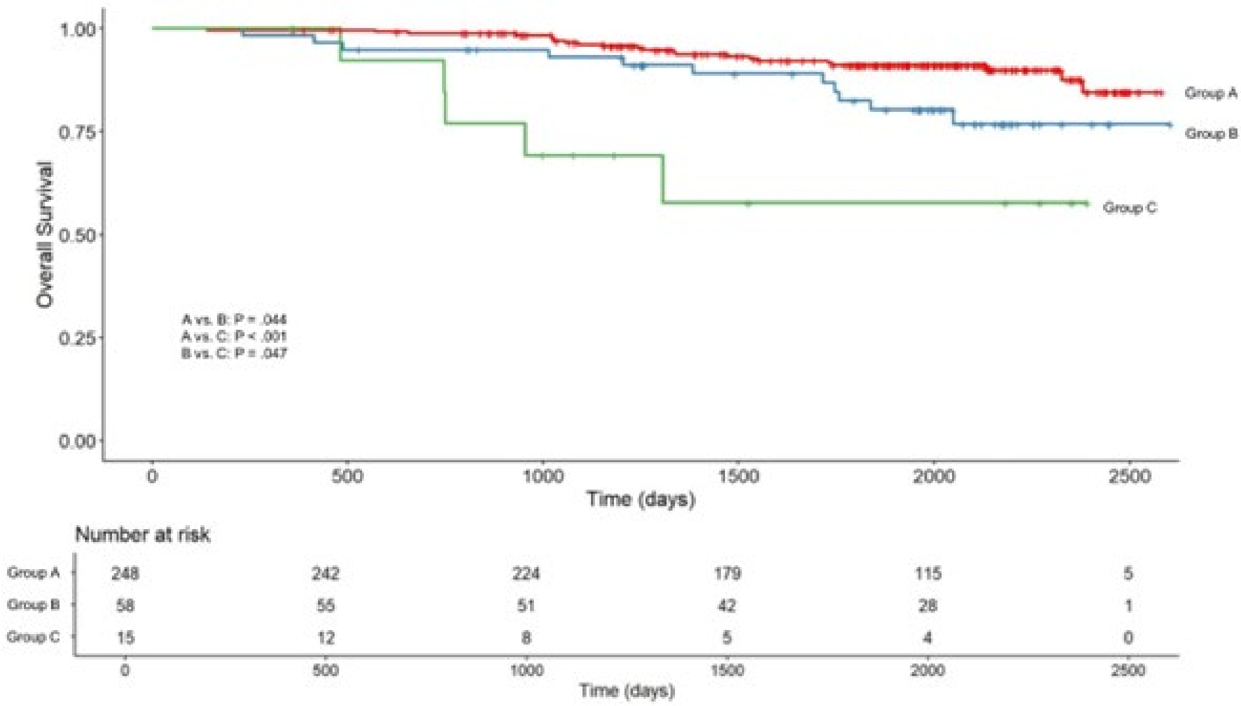
Overall Survival
1.00
0.75
0.50
0.25
0.00
Group A
Group B
Group C
A vs. B: P = .044
A vs. C: P < .001
B vs. C: P = .047
0
500
1000
1500
2000
2500
Time (days)
Number at risk
Group A 248 242 224 179 115 5
Group B 58 55 51 42 28 1
Group C 15 12 8 5 4 0
Time (days)

A 57-year-old man with B-viral liver cirrhosis and surgically proven HCC. (A–C) Axial CT shows a 3.5-cm rim arterial-phase hyperenhancing mass (arrow) in segment 6 (A) with delayed central enhancement in portal venous (B) and delayed-phase (C) images. (D–F) Axial MRI also shows rim arterial-phase hyperenhancement (D) without definite washout or an enhancing capsule on portal venous (E) and transitional-phase (F) images. This HCC was categorized as LR-M on both CT and MRI. Intrahepatic recurrence was observed at 210 days after resection.

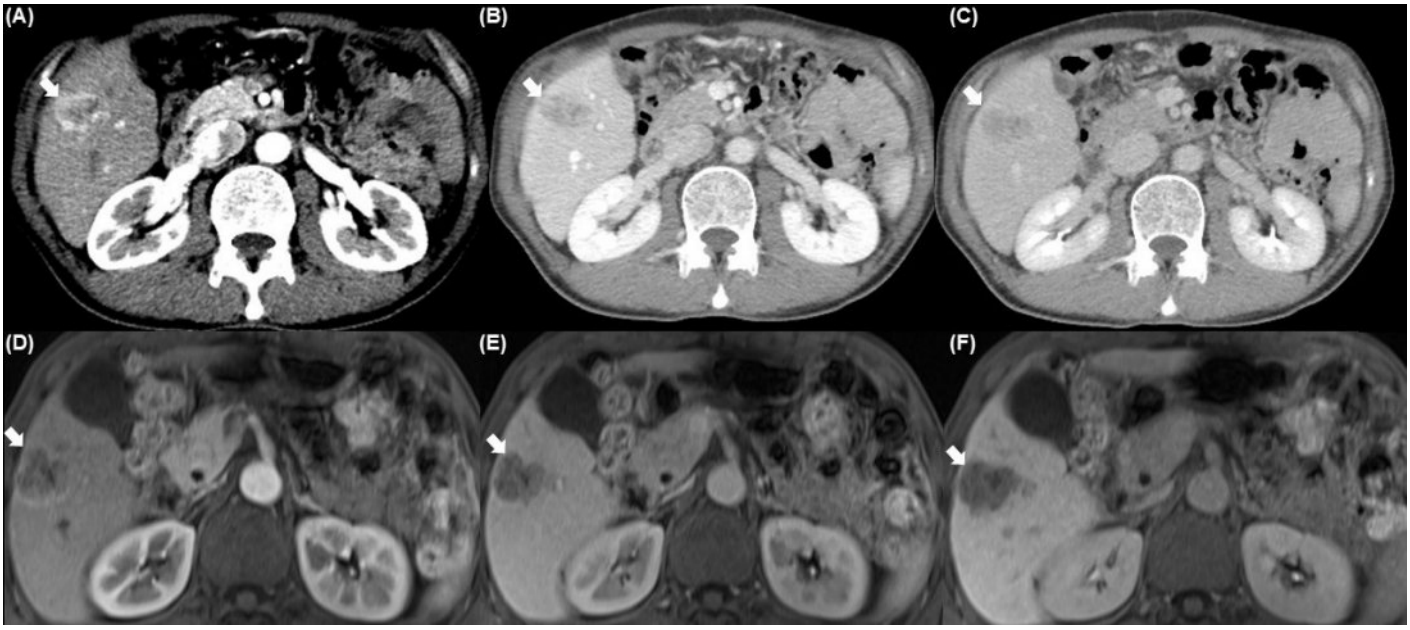

Keywords : Liver Imaging Reporting and Data System, Discrepancy, Prognosis

[Scientific Session 7: Imaging Biomarkers in Liver Disease: Emerging Tools & New Frontiers]

SS07-1

Diagnostic Accuracy of Artificial Intelligence Based Imaging in Identifying Hepatic Steatosis: A Systematic Review and Meta-analysis

ROBIN ANTONIO[1*]

[1]Radiology, FEU-NRMF, Philippines

Introduction. The definitive method for diagnosing fatty liver is pathology. Recent technological advancements have facilitated the integration of artificial intelligence (AI) into the medical field. This systematic study and meta-analysis aims to assess the diagnostic efficacy of image-based artificial intelligence (AI) in detecting hepatic steatosis.

Methods. This was a meta-analysis which included 5 studies with good methodologic quality. Comprehensive searches were conducted in PubMed, Medline, Scopus, Cochrane, and Google Scholar. Only studies published within the last five years were considered to focus on the most recent advancements in AI technologies for the imaging based diagnosis of hepatic steatosis. A combination of keywords related to AI technologies ("Artificial Intelligence", "Machine Learning"), (liver steatosis, hepatic steatosis, fatty liver), and imaging techniques (Ultrasound, "MRI", "CT scans", "deep learning reconstruction") were used. Meta-analysis was performed using inverse variance method to compute for the pooled sensitivity, specificity, and accuracy along with 95% confidence interval.

Results. The pooled sensitivity of of AI based imaging in identifying hepatic steatosis was 91% (95%CI=86% to 95%) while specificity was 90% (95%CI=83% to 95%). The pooled accuracy determined by the SROC curve was 0.92.

Conclusions. AI-based imaging demonstrates high sensitivity and specificity for identifying hepatic steatosis, with a pooled accuracy of 0.92, indicating its potential as a reliable diagnostic tool in clinical practice.

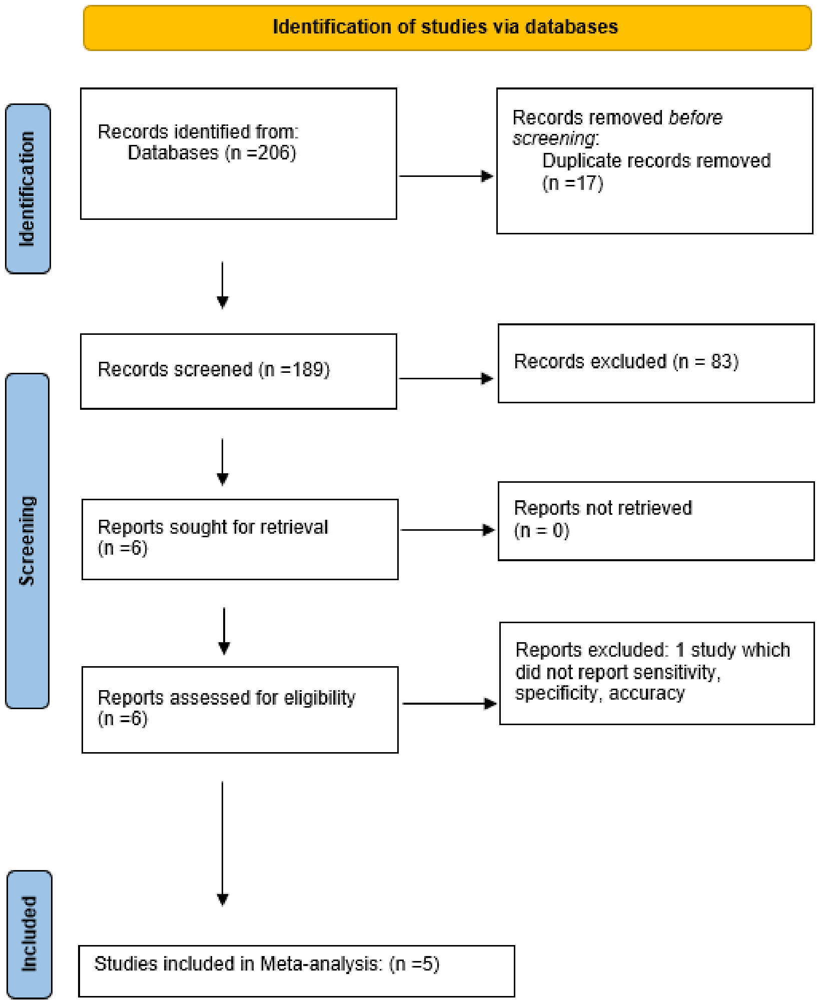

Figure 1. PRISMA Flow Diagram of the Research Study

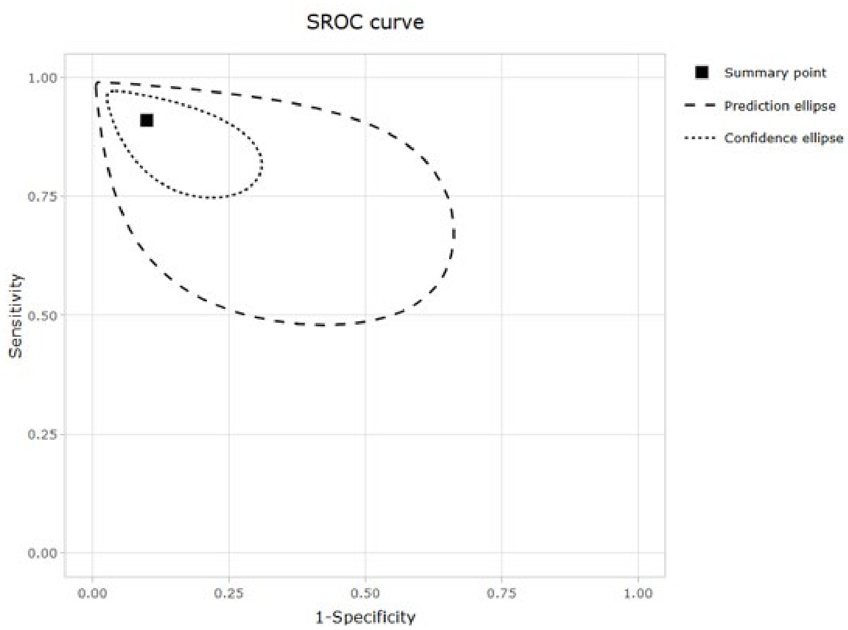

Keywords : Robin, Liver, AI

[Scientific Session 7: Imaging Biomarkers in Liver Disease: Emerging Tools & New Frontiers]

SS07-2

Beyond Biopsy: Imaging-Driven Deep Learning to Flag At-Risk MASH

Mei Chin Lim[1*], Selvakumar Vigneshwaran[4], Jordan Jun Yi Low[5], Nicole Shu Ying Tang[2], Ganakirthana Kalpenya Devi[1], Zongchen Li[1], Samuel Lau[1], Cheng Han Ng[3]

[1]Diagnostic Imaging, National University Hospital, Singapore
[2]Yong Loo Lin School of Medicine, National University of Singapore, Singapore
[3]MedicineDivision of Gastroenterology and Hepatology, National University Hospital, Singapore
[4]Lee Kong Chian School of Medicine, Nanyang Technological University, Singapore
[5]School of Engineering, National University of Singapore, Singapore

Early detection of patients with at-risk MASH (Metabolic dysfunction-Associated Steatohepatitis) is increasingly vital due to the heightened risk of disease progression. Current diagnostics are costly, underscoring the need for timely risk stratification to guide early clinical decision-making. This study investigates the application of a Convolutional Neural Network (CNN) model for the non-invasive prediction of at-risk MASH, through advanced fibrosis and cirrhosis.

Participants were drawn from a multi-ancestral Asian cohort, with a subset undergoing liver biopsy for suspected MASH. Histological activity was graded using the NASH Clinical Research Network (CRN) NAFLD Activity Score (NAS), and liver stiffness was assessed using FibroScan. Clinical profiling included metabolic comorbidities (type 2 diabetes mellitus, hypertension, dyslipidaemia), with covariate adjustments. The CNN was trained to classify patients with potential MASH, defined by fibrosis stage ≥F2 and NAS ≥4, or a FAST score ≥0.35. To improve generalizability and robustness despite noise, data augmentation (±20% rotation and brightness variation) was applied, specifically on the EfficientNetB6 architecture. Liver segmentation was performed using a custom YOLOv11 model, isolating the hepatic region for analysis. Extracted segmentation metrics, namely mask area, shape descriptors, and echogenicity (pixel intensity), were integrated with biopsy and FibroScan data.

Total of 872 patients (M:F =0.72:0.28, Training: Testing=80:20) were analysed with valid data. The custom YOLO model reached mean average precision (mAP@0.5) of 0.549 at 0.5 recall across all classes, and 0.892 specifically for liver masks. Metrics were derived from the segmented masks, including echogenicity based on pixel intensity, mask shape and segmentation area, and integrated with biopsy and FibroScan data. The resulting CNN models demonstrated high predictive performance, achieving an area under the receiver operating characteristic curve (AUC) greater than 0.85 for

This study demonstrates that CNN applied to routine liver imaging, paired with automated liver segmentation and simple image-derived metrics, can non-invasively flag patients at risk for clinically significant MASH. By defining “at-risk” using histologic and composite criteria (fibrosis ≥F2 with NAS ≥4, or FAST ≥0.35), the model speaks directly to decision points that matter for referral and biopsy prioritization. Trained in a multi-ancestral Asian cohort with biopsy, FibroScan, and clinical profiling, the approach achieved AUCs >0.85 across endpoints, while the custom liver segmentation attained strong mask performance, supporting scalable, end-to-end automation. Clinically, these findings suggest a practical triage layer atop ultrasound pathways, potentially reducing reliance on invasive biopsies and

enabling earlier, targeted intervention.

Keywords : Metabolic dysfunction-associated Steatohepatitis, Convolutional Neural Network, Fibrosis

[Scientific Session 7: Imaging Biomarkers in Liver Disease: Emerging Tools & New Frontiers]

SS07-3

Assessment of Cardiovascular Risk Using Coronary Artery Calcium Score, Hepato-steatosis, and Myo-steatosis as Imaging Biomarker for Geriatric Population

CHANDAN JYOTI DAS[1*], IRAM JAMSHED[1], FAIZ SAIFI[1], YASH SHARMA[1], B Nayak[1], SHALIMAR SHALIMAR[1], Avinash CHAKRAWARTY[1], Maroof Ahmad KHAN[1]

[1]Radiodiagnois and Interventional radiology Gastroenterology Geriatrics and Biostatistics, AIIMS, India

Aging is a major health issue, and coronary artery disease (CAD) is the leading cause of death in the elderly and NAFLD patients globally. Percutaneous liver biopsy has been the gold standard for assessing NAFLD and fibrosis, but its invasiveness, complications, and inability to repeat evaluations limit its clinical utility.

Quantifying liver fat using MRI based proton density fat-fraction (PDFF) has shown the most promise. In elderly population, both quantity and quality of skeletal muscle declines which increases the risk of metabolic disorders and CAD. Coronary artery calcium (CAC) measured via non-contrast CT is a robust indicator of atherosclerotic load and future cardiovascular events. In this study, we undertook CT/MRI to asses CAC score, hepato-steatosis and myo-steatosis as risk factor for CAD in geriatric population.

This prospective study was carried out by consecutive geriatric patients with atleast one high-risk criterion (uncontrolled diabetes, hypertension, metabolic syndromeor dyslipidemia) for CAD. Total 110 participants were enrolled in this interim study. CAC scores were derived by CT-imaging and risk was assigned as normal (0), mild (1–99), moderate (100–399) and severe (≥400)for CAD. Sarcopenia and Myo-steatosis was determined from a single axial L3 slice of abdominal CT by calculating Skeletal Muscle Index (SMI) by sex-specific thresholds for men 8.72 cm^2) respectively. The demographic details, BMI, smoking status, alcohol consumptionwere documented and blood samples were collected for biochemical analysis.

In recruited patients (n=110), CAC score was normal(0) in 25.4% (n=28), Mild(1–99) in 38.1% (n=42), Moderate(100–399) in 14.5% (n=16), and Severe(≥400) in 21.8% (n=24). The mean liver fat (MRI-PDFF%) showed increasing trend in CAC score groups: normal 3.59 ± 3.52; mild3.04 ± 1.96;moderate, 3.83 ± 3.61; and severe, 4.39 ± 5.47. The prevalence of abnormal fat fraction (>5%) was consistent across strata (17.9%, 16.7%, 18.8%, 16.7%). The PDFF% is different in geriatric population and >3.5% may be attributed to increased cardiovascular risk.There is decrease in SMI based on CAC severity: 37.37 ± 9.6 in normal, 41.2 ± 12.7 in mild, 36.7 ± 12.3 in moderate and 35.5 ± 15.4 in severe. Sarcopenia burden increases with CAC category with 29–31% in normal and mild, 44% in moderate, and 50% in severe. In both sexes, severe CAC increases risk, nearly half of patients are sarcopenic, with higher share of males (37.5%) than females (12.5%).

Myo-steatosis was frequent overall with 42.9% (normal), 57.1% (mild), 62.5% (moderate), 41.7% (severe) with high prevalence in women (≈69-92% across strata) and lower, more variable in men (20–50%).

Serum sodium and LDL-C were lower with higher CAC (p=0.028 and 0.0315), while total cholesterol was borderline (p=0.0589).

This prospective study shows that CAC with PDFF and myo-steatosis is feasible and reproducible in clinical practice. An early trend of a higher PDFF across mild to severe CAC categories may improve with further patient enrolments. Severe CAC had the lowest SMI which supports the clinical impression that sex-specific CT biomarkers correlates with advanced CAC and sarcopenia.

(A) showing coronary calcium score, (B) showing PDFF, (C) showingSkeletal Muscle Index (SMI) and (D) showing fat muscle area

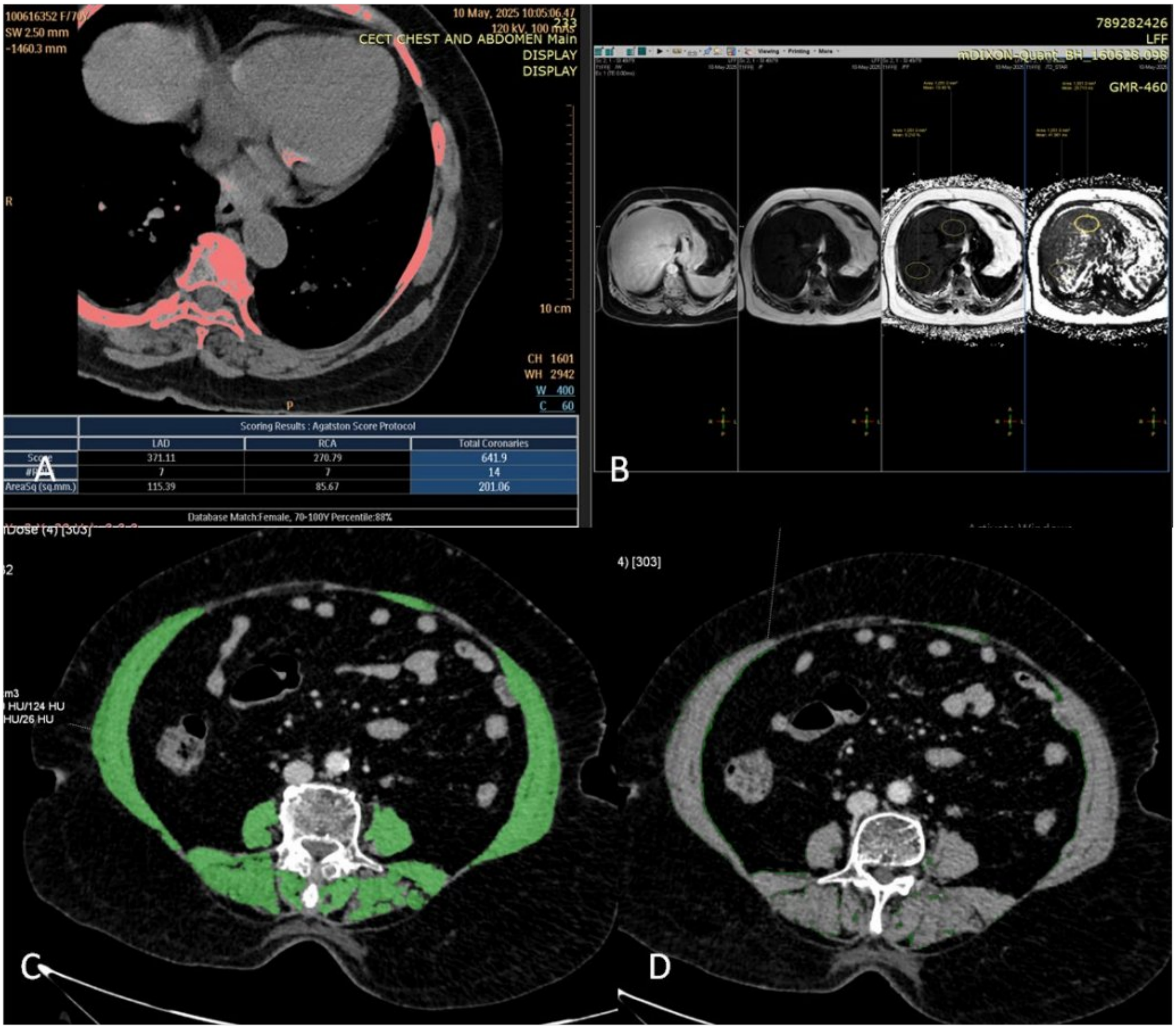

Box plot showing fat fraction mean (%), Skeletal Muscle Index (SMI) and fat muscle area

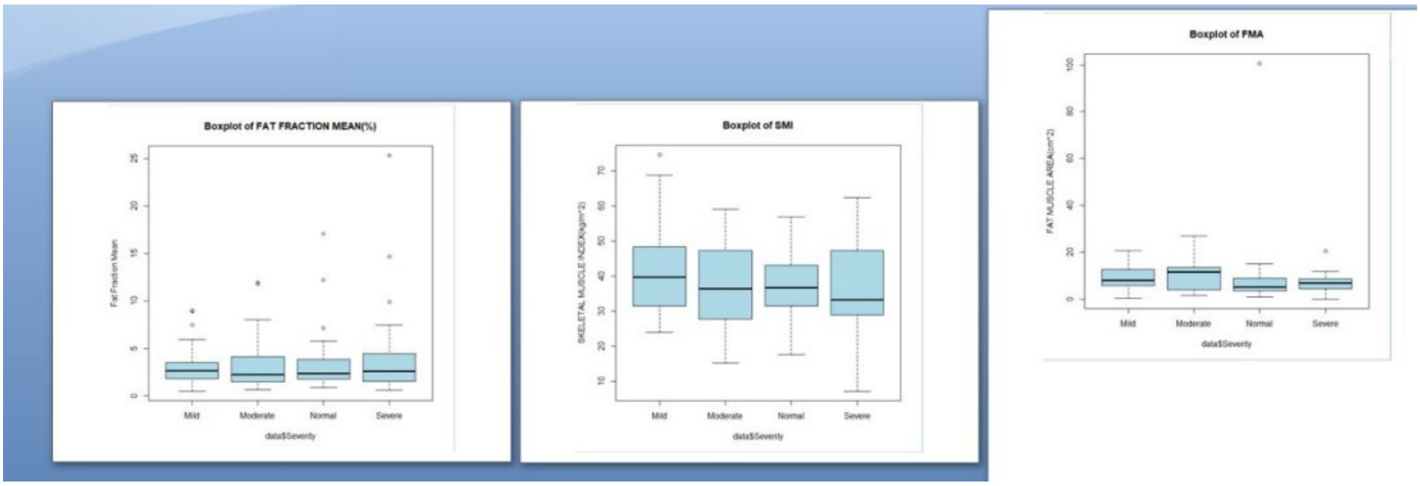

Keywords : Coronary artery calcium (CAC), Myo-steatosis, MRI-PDFF

[Scientific Session 7: Imaging Biomarkers in Liver Disease: Emerging Tools & New Frontiers]

SS07-4

CT-Derived Dynamic Body Composition Changes Predict Durable Clinical Benefit to Immunotherapy in Advance Hepatocellular Carcinoma: Development and External Validation of a Cross-Center Model

Bang-Bin Chen[1*]

[1]Medical Imaging, National Taiwan University Hospital, Chinese Taipei

To determine whether baseline and early on-treatment body composition features extracted from CT imaging are associated with durable clinical benefit (DCB) in patients with advanced hepatocellular carcinoma (HCC) undergoing immunotherapy, and to develop a prediction model with reproducible performance across independent clinical centers.

This retrospective study included a training cohort of 172 patients from National Taiwan University Hospital and an external validation cohort of 33 patients from National Cancer Hospital (2015–2024). All patients had advanced HCC and received immune-based systemic therapy, with follow-up completed on October 31, 2025. DCB was defined as complete response, partial response, or stable disease lasting ≥ 6 months based on RECIST 1.1 evaluation. Contrast-enhanced CT at the L3 level was analyzed using the open-source tool TotalSegmentator to quantify skeletal muscle volume and density, subcutaneous and visceral adipose tissue (SAT and VAT) volume and density, spleen volume, and all vertebral body density. Treatment-related body composition changes were calculated between baseline and the first on-treatment CT and normalized to the imaging interval. Continuous variables were binarized using ROC-Youden optimal cut points derived from the training cohort. Logistic regression with L1 regularization was applied to identify predictors demonstrating stability across centers. Model performance was evaluated using AUC, calibration, and decision curve analysis.

DCB was observed in 74 of 172 patients (43.0%) in the training cohort and 12 of 33 patients (36.4%) in the external validation cohort. Seven variables comprised the final predictive model for DCB, including age, baseline log-transformed alpha-fetoprotein level, Child–Pugh class, change in spleen size, change in skeletal muscle density, change in subcutaneous fat density, and change in visceral adipose tissue volume (all $p < 0.05$). The model yielded an AUC of 0.813 (95% CI, 0.750–0.875) in the training cohort and 0.724 (95% CI, 0.546–0.902) in the validation cohort. Calibration remained acceptable, and decision curve analysis indicated clinical net benefit across relevant decision thresholds.

CT-derived early body composition changes, integrated with baseline clinical features, provide meaningful predictive information regarding immunotherapy durability in HCC. The model demonstrated cross-center stability, suggesting potential clinical applicability. Prospective validation is required.

Figure 1. Multivariable logistic regression model for predicting durable clinical benefit (DCB) in the training cohort (n = 172; 74 with DCB). Odds ratios (ORs) and 95% confidence intervals (CIs) are shown for each variable retained in the final model. Variables included age, baseline log-transformed alpha-fetoprotein level, Child–Pugh class, and interval changes in spleen size, skeletal muscle density, subcutaneous fat density, and visceral adipose tissue volume. All variables demonstrated independent associations with DCB ($p < 0.05$).

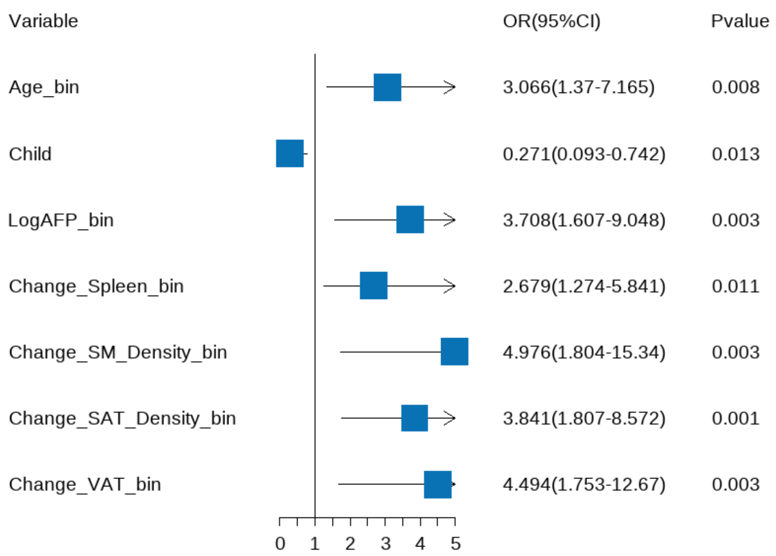

Figure 2. Receiver operating characteristic (ROC) curves for the prediction model in the training cohort (n = 172; AUC = 0.813, 95% CI: 0.750–0.875) and external validation cohort (n = 33; AUC = 0.724, 95% CI: 0.546–0.902). DCB was defined as complete response, partial response, or stable disease lasting ≥ six months according to RECIST 1.1. The difference in performance reflects expected variation between development and external validation settings. The dashed line indicates a reference line for random classification.

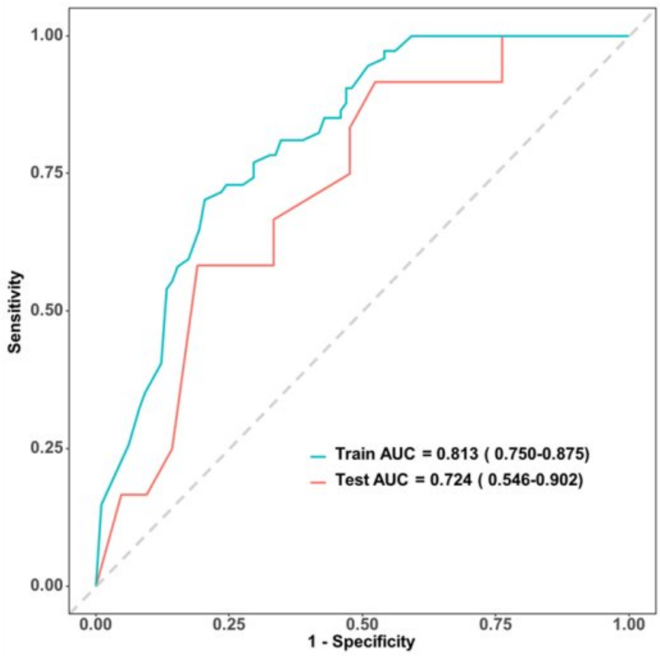

Keywords : Advanced HCC, Body composition, Immunotherapy

[Scientific Session 7: Imaging Biomarkers in Liver Disease: Emerging Tools & New Frontiers]

SS07-5

Liver Fibrosis: Explainable Deep Learning Network for Automated Staging by Using Equilibrium Enhanced Phase MR Images

Junhao Zha[1], Yuancheng Wang[1], Shenghong Ju[1*]

[1]Radiology, Zhongda Hospital Medical School of Southeast University, China

Conventional non-invasive diagnostic modalities, including ultrasound-based liver stiffness measurement (LSM) and serological biomarkers, have been widely adopted in clinical practice. However, their diagnostic accuracy remains limited, often falling short in precisely assessing fibrosis severity. MRI-driven deep learning approaches has opened new avenues for non-invasive, quantitative evaluation of liver fibrosis. This study aimed to develop an nnU-Net model for automated liver segmentation and propose a novel explainable framework integrating multi-task contrastive learning with attention mechanisms to autonomously identify and visualize the discriminative MRI patches for fibrosis staging.

A total of 706 treat-naive chronic hepatitis B patients were eligible for this retrospective study. 655 patients in center 1 between May 2015 and July 2022 were randomized into the training (424), validation (99) and internal test (132) set. 51 patients in center 2 between March 2018 and May 2023 were collected as an external test set. The reference standard was biopsy obtained within 6 months of the MR examinations. This study employed VGG-16 as the backbone architecture, designed to integrate contrastive learning for automated patch selection while simultaneously enhancing the network's discriminative capability for fibrosis classification. Input data were L2-normalized and included equilibrium enhanced phase MR images and LSM. An extraction function returned the top nine probability-ranked patches from the contrastive learning task along with clinically significant fibrosis classification predictions (F≥2). Segmentation performance was quantitatively evaluated using the Dice Similarity Coefficient (DSC) to measure spatial overlap between predicted and ground truth liver masks. All case predictions, labels, and AUCs were systematically recorded. The Integrated Discrimination Improvement (IDI) metric quantified the diagnostic enhancement of the patch-based model over LSM alone.

The nnU-Net model achieved a training set DSC of 0.95 for liver segmentation across 365 cases. For F≥2 fibrosis staging, the AUCs demonstrated sliding changes when averaging predictions from top-ranked patches in the internal test set: 0.818 (single best patch), 0.799 (top two), 0.779 (top three), 0.753 (top four), 0.723 (top five), with performance plateauing beyond five patches. The network achieved AUC values of 0.853 (training), 0.835 (validation), 0.818 (internal test), and 0.805 (external test) for F≥2 fibrosis staging using the "top discriminative patch". A significant difference was observed between the "top discriminative patch" model and the LSM-only approach ($P < 0.0001$), yielding an IDI value of 0.287.

By leveraging self-supervised contrastive learning, the network autonomously identifies diagnostically relevant image patches, reducing dependency on subjective human annotations. The proposed framework provides an accurate, automated, and explainable tool for liver fibrosis staging, and could add vlaue to elastography.

Automated Deep Learning-Based Liver Fibrosis Diagnosis Workflow

Input: L2-normalized equilibrium-phase enhanced MRI images and Liver Stiffness Measurement (LSM). Output: Automated liver segmentation and fibrosis staging with patch-based discriminative feature selection. Key Steps:Liver segmentation using nnU-Net Training with labeled "usable" and "non-usable" image patches, Multi-task network for joint optimization of patch selection and fibrosis classification, Automated patch selection during testing via feature center clustering, End-to-auto automation: patch selection and diagnosis in a unified pipeline.

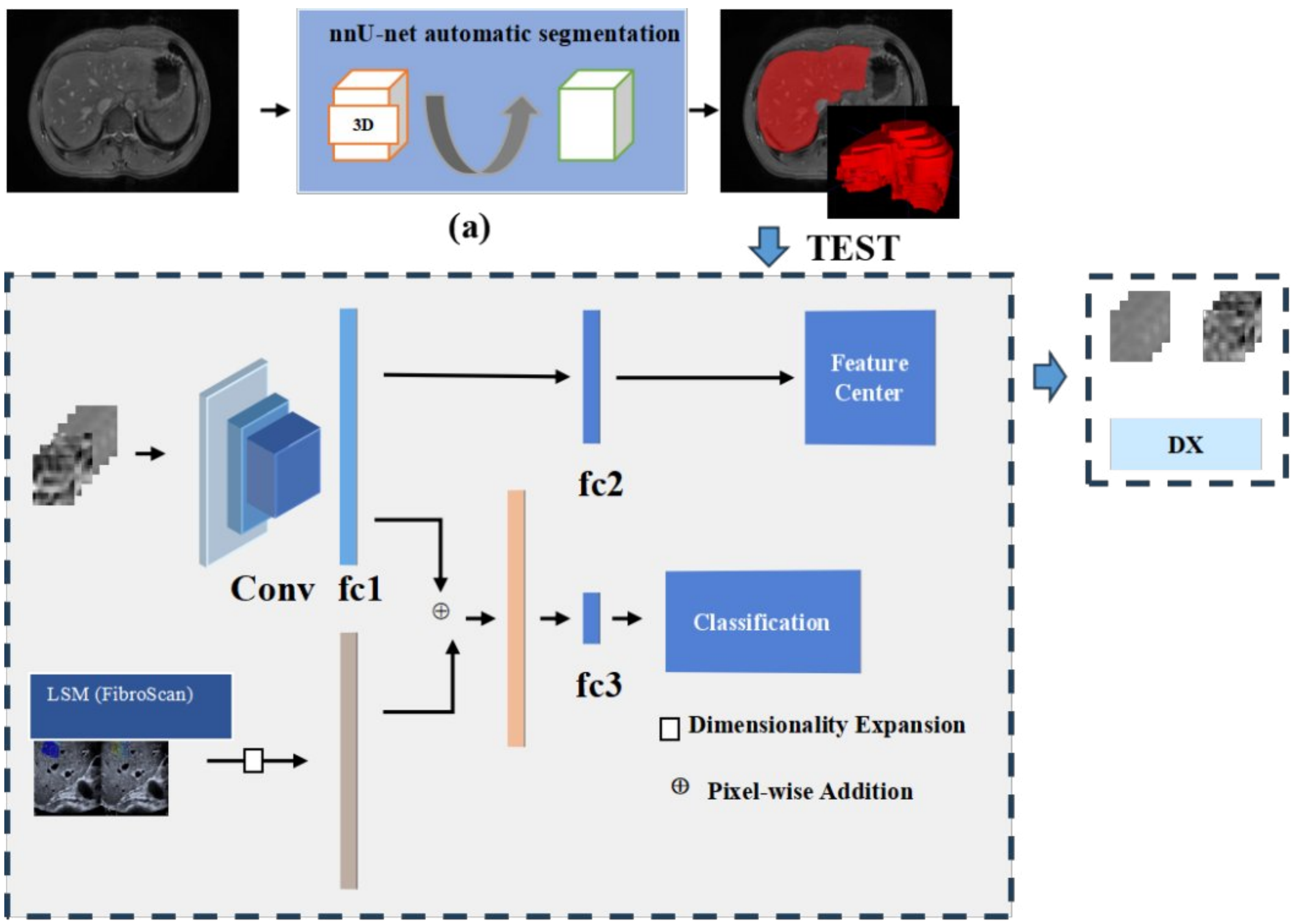

Multi-Task Deep Learning Results

(a) For F≥2 classification, test set performance progressively declined with increasing patch utilization:Top 1 patch: AUC 0.813, Top 2 patches: AUC 0.799, Top 3 patches: AUC 0.779, Top 4 patches: AUC 0.753, Top 5+ patches: AUC stabilized at 0.723.(b) Classification performance using the top discriminative patch across datasets: training set AUC: 0.853,validation set AUC: 0.835, internal test set AUC: 0.818, external test set AUC: 0.805.

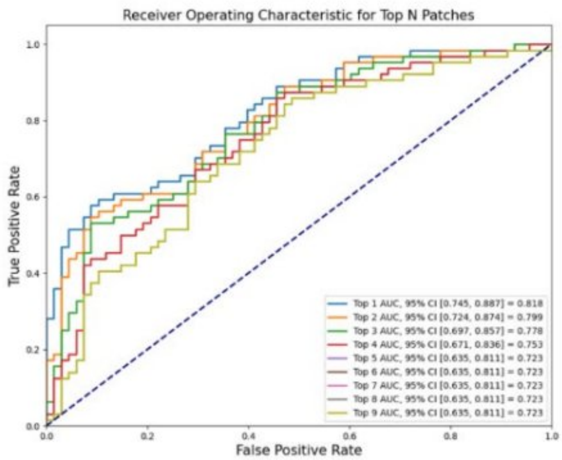

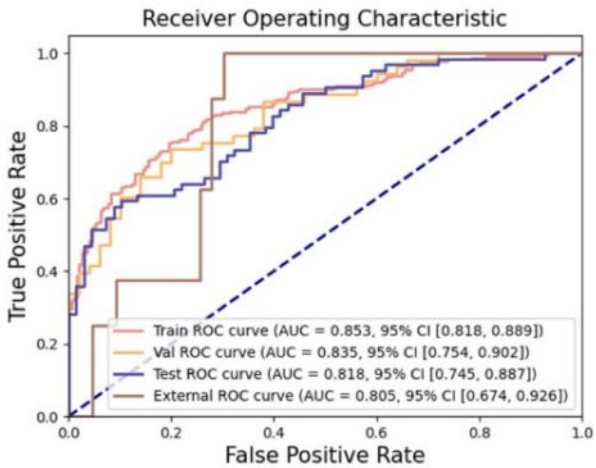

Keywords : Liver fibrosis, MRI, Deep learning

[Scientific Session 7: Imaging Biomarkers in Liver Disease: Emerging Tools & New Frontiers]

SS07-6

Deep Learning–Based Quantitative MRI Biomarkers of Liver Function on Gadoxetic Acid–Enhanced MRI: Correlations with Clinical Liver Function Scores

Seung Ha Cha[1], Na Yeon Han[1*], TaeHun Kim[2,3], Deuk Jae Sung[1], Beom Jin Park[1], Min Ju Kim[1], Ki Choon Sim[1], Yeo Eun Han[1]

[1]Radiology, Korea University Anam Hospital, Korea
[2]Advanced Medical Imaging Institute, Korea University Anam Hospital Korea University College of Medicine, Korea
[3]AI Center, Korea University Anam Hospital Korea University College of Medicine, Korea

Accurate assessment of liver function is essential for clinical management and prognostication in patients with chronic liver disease (CLD). Gadoxetic acid (GA)–enhanced MRI provides both anatomical and functional information based on hepatocellular uptake of contrast agent. This study aimed to develop a deep learning algorithm (DLA) for automated segmentation of GA-enhanced MRI and to investigate whether automatically derived quantitative MRI biomarkers can predict clinical liver function.

A total of 651 GA-enhanced MRIs from patients with histologic or clinical evidence of CLD were retrospectively collected from Anam Hospital (April 2018–February 2025) and Guro Hospital (June 2023–May 2024). Among them, 412 MRIs (291 and 121 from each institution) were manually segmented by radiologists into regions corresponding to the liver, spleen, upper pole of the kidney, portal vein, and bile duct, serving as ground truth. The nnU-Net was trained and validated using 370 cases (90%) and tested on 42 cases (10%). Segmentation performance was evaluated using the Dice similarity coefficient (DSC). For 239 additional MRIs, quantitative parameters including organ volumes and signal intensities (SIs) were automatically extracted using the trained DLA and log-transformed for analysis. Linear regression analyses were conducted to assess associations between MRI-derived parameters and biochemical liver function indices, including the albumin–bilirubin (ALBI) score, Child–Pugh score (CPS), Model for End-Stage Liver Disease (MELD) score, and MELD–Na score. Model performance was evaluated using the coefficient of determination (R^2). Logistic regression and receiver operating characteristic (ROC) curve analyses were performed to assess the predictive performance of MRI parameters for hepatic decompensation.

The deep learning algorithm achieved high segmentation performance, with mean Dice similarity coefficients of 0.990 ± 0.007 for the liver, 0.967 ± 0.029 for the spleen, 0.924 ± 0.089 for the kidney, 0.903 ± 0.071 for the portal vein, and 0.909 ± 0.160 for the bile duct. Multivariable regression models significantly predicted liver function scores, including the ALBI (R^2 = 0.50, $p < 0.001$), Child–Pugh (R^2 = 0.54, $p < 0.001$), MELD (R^2 = 0.41, $p < 0.001$), and MELD–Na (R^2 = 0.42, $p < 0.001$) scores. Log-transformed spleen volume, liver-to-spleen SI ratio, portal vein-to-liver SI ratio, and portal vein-to-kidney SI ratio were consistently identified as common independent predictors across CPS, ALBI, MELD, and MELD-Na scores. In multivariate logistic regression, log-transformed spleen volume (odds ratio =

14.26; 95% CI, 4.11–49.49; $p < 0.001$) and bile duct-to-portal vein SI ratio (odds ratio = 0.29; 95% CI, 0.18–0.48; $p < 0.001$) were independently associated with hepatic decompensation. The combined logistic model demonstrated strong predictive performance for hepatic decompensation (AUC = 0.82), outperforming conventional indices such as the MELD, MELD–Na, and Child–Pugh scores.

Quantitative MRI parameters automatically derived from deep learning–based segmentation can serve as reliable imaging biomarkers for assessing liver function. The proposed algorithm enables reproducible, noninvasive quantification of hepatic function and may complement biochemical tests for evaluating disease severity and predicting clinical outcomes in chronic liver disease.

Keywords : Gadoxetic Acid MRI, Liver Function, Quantitative Imaging

[Scientific Session 7: Imaging Biomarkers in Liver Disease: Emerging Tools & New Frontiers]

SS07-7

Paradigm Shift in Post-Liver Transplantation Surveillance: A One-Stop Non-Contrast 4D Flow MRI for Integrated Morpho-Hemodynamic and Functional Profiling

Weinuo Qu[1], Ziyi Liu[1], Zhen Li[1*]

[1]Radiology, Tongji Hospital of Tongji Medical College of Huazhong University of Science and Technology, China

Current liver transplant surveillance relies on multiple tests, increasing costs and risks. We hypothesized that a single, non-contrast Four-dimensional flow MRI (4D flow MRI) could address this limitation as a unified "one-stop-shop," revolutionizing monitoring by integrating disparate evaluations.

This prospective study enrolled a cohort of liver transplant recipients undergoing long-term follow-up at our institution between August 2024 and September 2025. All patients underwent non-contrast 4D flow MRI, Doppler ultrasonography (DUS) and biochemical testing. The performance of 4D flow MRI was benchmarked against reference standards: balanced turbo field echo (BTFE) for morphology, DUS for hemodynamics, and biomarkers and histology for function.

In transplanted livers, 4D flow MRI provided diagnostically equivalent morphological visualization of key portal venous segments compared to BTFE (all $P>0.05$) with excellent stenosis grading correlation ($r=0.90$, $P < 0.05$). In the hemodynamic study, in the assessment of hemodynamics, the portal venous flow velocity (PVSV) measured by 4D flow MRI demonstrated a significant correlation with DUS measurements ($r=0.82$, $P < 0.0001$). Most importantly, a multiparametric model [portal venous flow (PVF)+PVSV] showed promising utility for identifying inferior graft function (AUC=0.69), while wall shear stress (WSS) exhibited exceptional accuracy for detecting acute rejection (AUC=0.85).

Non-contrast 4D flow MRI establishes a new paradigm for post-transplant care. By integrating morphological, hemodynamic, and functional insights into a single, safe examination, it transcends the limitations of the current fragmented approach, offering a comprehensive solution poised to streamline surveillance and guide precision medicine in liver transplantation.

Paradigm Shift in Post-Liver Transplantation Surveillance: From Fragment Assessments to a One-Stop 4D Flow MRI Solution

In the conventional paradigm, post-liver transplantation surveillance relies on multiple discrete modalities: biochemical tests, Doppler ultrasonography (DUS), and structural MRI (e.g., NCE-MRA). Biochemical profiles (ALT, AST, TBIL and INR) assess liver function indirectly but suffer from time delays and cannot quantify hemodynamics. DUS is limited by operator dependency and angle constraints, while structural MRI also lacks quantitative flow assessment. Although 2D quantitative flow (2D Qflow) technique enables flow velocity measurement, it does not provide three-dimensional vascular anatomy. In summary, the traditional paradigm suffers from fragmentation, information silos, frequent contrast or radiation exposure, as well as inefficiency and high cost. In this study, we propose a novel integrated surveillance paradigm using non-contrast 4D flow MRI, which enables simultaneous evaluation of vascular morphology, hemodynamics, and graft function. This one-stop modality offers comprehensive data integration, avoids contrast or radiation risks, and improves examination efficiency. The shift from the conventional to the novel paradigm marks a transition toward more efficient and holistic post-liver transplantation surveillance. (4D flow MRI=Four-dimensional flow MRI, DUS=Doppler ultrasonography, str-MRI=structural MRI, NCE-MRA=Non-contrast-enhanced Magnetic Resonance Angiography, ALT=Alanine aminotransferase, AST=Aspartate aminotransferase, TBIL=Total bilirubin, INR=International Normalized Ratio, 2D Qflow=two-dimensional flow MRI) (Draw by Figdraw)

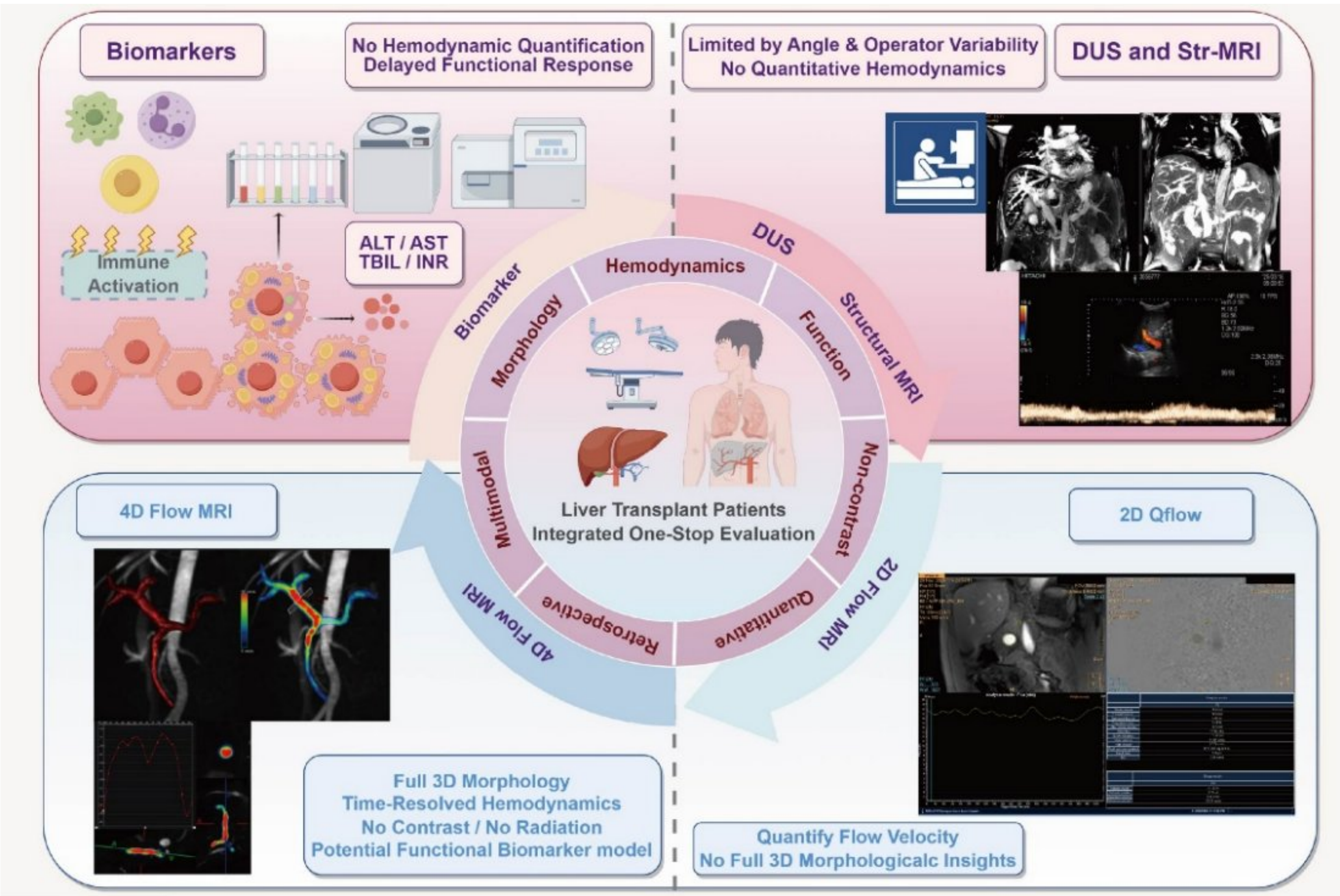

(a)Linear regression and Spearman correlation coefficient between 4D flow and BTFE for the assessment of transplanted liver portal vein stenosis (r = 0.90; P < 0.0001). (b)Scattergram of hemodynamic parameters measured by 4D flow and UDS in portal venous flow velocity (PVSV). Significant correlations in PVSV by 4D flow and DUS were observed(r=0.82;P < 0.0001). (c)Bland–Altman plots of hemodynamic parameters measured by DUS and 4D flow for PVSV. The y-axis reports the %difference (DUS - 4D flow) between the two measurements, while their mean is reported on the x-axis. (d)ROC analysis of various hemodynamic parameters of the transplanted liver portal vein for distinguishing between SGF and IGF. It should be noted that the diagnostic performance is enhanced by combining PVF and PVSV as opposed to using these parameters individually. (e)ROC analysis of the groups with and without acute rejection. It is noted that WSS demonstrated remarkable diagnostic accuracy for acute rejection. (f)The ICC was conducted to evaluate the inter-observer agreement for 4D flow MRI parameters. (SGF = superior graft function, IGF = inferior graft function, PVF = portal venous flow, WSS = wall shear stress, ICC = Intraclass Correlation Coefficient)

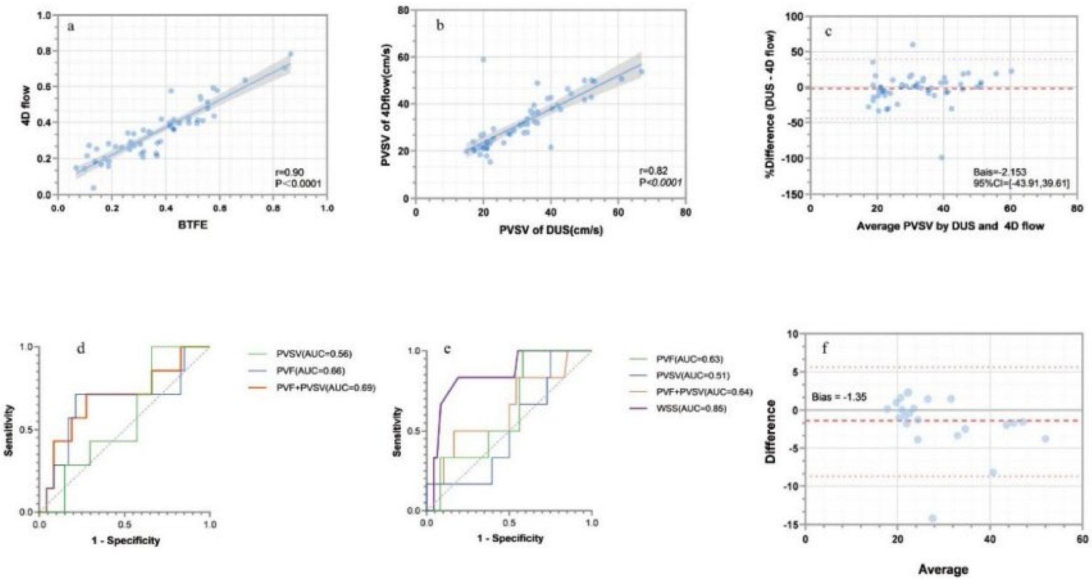

Keywords : Liver transplantation, Four-dimensional flow MRI, Portal venous system

[Case Presentation by Trainees]

TCP01-1

Imaging Features of Renomedullary Interstitial Cell Tumor

Sigyoung Chun[1*], Sung Bin Park[1], Mi Yeon Park[1], Kye Jin Park[1], Mi-Hyun Kim[1], Jeong Kon Kim[1]

[1]Radiology, Asan medical center, Korea

Renomedullary interstitial cell tumor (RMICT), also known as medullary fibroma, is a benign mesenchymal tumor of the kidney that arises from the interstitial cells of the medulla. While these tumors are highly prevalent as small, incidental nodules in autopsy series (reported in up to 50% of cases), clinically symptomatic or radiologically detectable masses are extremely rare. The purpose of this presentation is to describe the imaging features of renomedullary interstitial cell tumor.

In this presentation, we report a case of a renomedullary interstitial cell tumor.

We report a case of a 54-year-old woman who was referred to our hospital due to an incidental renal mass detected on an abdominal CT during a routine health check-up. The tumor was identified as a 1.5 cm well-defined medullary mass, demonstrating low density on CT and low signal intensity on both T1- and T2-weighted MR images. The mass showed mild delayed enhancement. Considering the possibility of a benign tumor, a CT-guided renal mass biopsy was performed. The pathologic results confirmed renomedullary interstitial cell tumor.

Recognizing this disease entity and its benign imaging features is crucial to avoid unnecessary radical nephrectomy for this rare clinical entity.

Keywords :

Renomedullary interstitial cell tumor

[Case Presentation by Trainees]

TCP01-2

Varied Imaging Presentations of Urethral and Penile Malignancies: A Case Series

Hanxing Xu[1*], Jeremy Lam[1]

[1]Diagnostic Radiology, Changi General Hospital, Singapore

Primary urethral and penile malignancies are rare, with histological heterogeneity that includes urothelial carcinoma, squamous cell carcinoma, adenocarcinoma amongst others. Imaging plays a pivotal role in characterising tumour extent and guiding multidisciplinary management. This case series illustrates the clinical and radiological manifestations of urethral and penile malignancies, emphasising diagnostic challenges and teaching points for radiologists.

We retrospectively reviewed four histologically confirmed cases of urethral and penile malignancies diagnosed between 2024–2025 at a tertiary centre. These included:

- One case of male metastatic urethral adenocarcinoma presenting as a perineal abscess;
- One case of male urethral urothelial carcinoma with previous treated bladder and prostate cancers;
- One case of female urethral diverticulum-associated adenocarcinoma;
- One case of male penile squamous cell carcinoma

Clinical presentation, imaging features (CT and/or MRI), and management decisions were collated from the electronic medical record.

The series of four cases demonstrated striking diversity in clinical presentation and imaging features:

1. Metastatic urethral adenocarcinoma presenting as a perineal abscess: A 46-year-old male with dysuria underwent a contrast-enhanced CT perineum which revealed a multiloculated rim-enhancing collection just inferior to the corpus cavernosum. This was surgically drained and later found to harbour biopsy-proven adenocarcinoma on follow-up flexible cystoscopy. MRI demonstrated an irregular T2W heterogeneous, T1W isointense necrotic and heterogeneously-enhancing mass with invasion of the corpus spongiosum and cavernosum. Pancreatic metastasis was also detected on follow-up imaging and biopsy.

2. Urothelial carcinoma recurrence in the urethra: An 86-year-old male with previously treated bladder and prostate cancers developed a urothelial carcinoma of the bulbar/membranous urethra found on follow-up flexible cystoscopy. MRI revealed a T2W isointense and heterogeneously-enhancing mass of the membranous, bulbous and proximal penile urethra, with corpus spongiosum involvement.

3. Adenocarcinoma in female urethral diverticulum: A 66-year-old female with microscopic haematuria was found to have periurethral hypodensities on CT urogram, later characterised on MRI to be a periurethral diverticulum with a T2W mild hyperintense and enhancing mural nodule. This was proven to be a periurethral diverticular adenocarcinoma on biopsy, illustrating the rare malignant transformation of periurethral diverticula.

4. Advanced penile squamous cell carcinoma: A 77-year-old male presented with a fungating penile mass, with MRI revealing an extensive infiltrative penile mass invading the corpora cavernosa, corpus spongiosum, urethra, and scrotal skin. Despite radical penectomy, he developed recurrence within six months.

This series highlights the rarity and heterogeneity of urethral and penile malignancies. Clinical and imaging manifestations may be varied – presenting as abscesses or arising within periurethral diverticula. MRI provides superior soft tissue resolution, accurately delineating tumour extent and local invasion critical for surgical planning. Recognition of atypical imaging presentations can prompt earlier diagnosis and multidisciplinary intervention, improving patient outcomes.

Axial T2W MRI showing a female periurethral diverticulum-associated adenocarcinoma

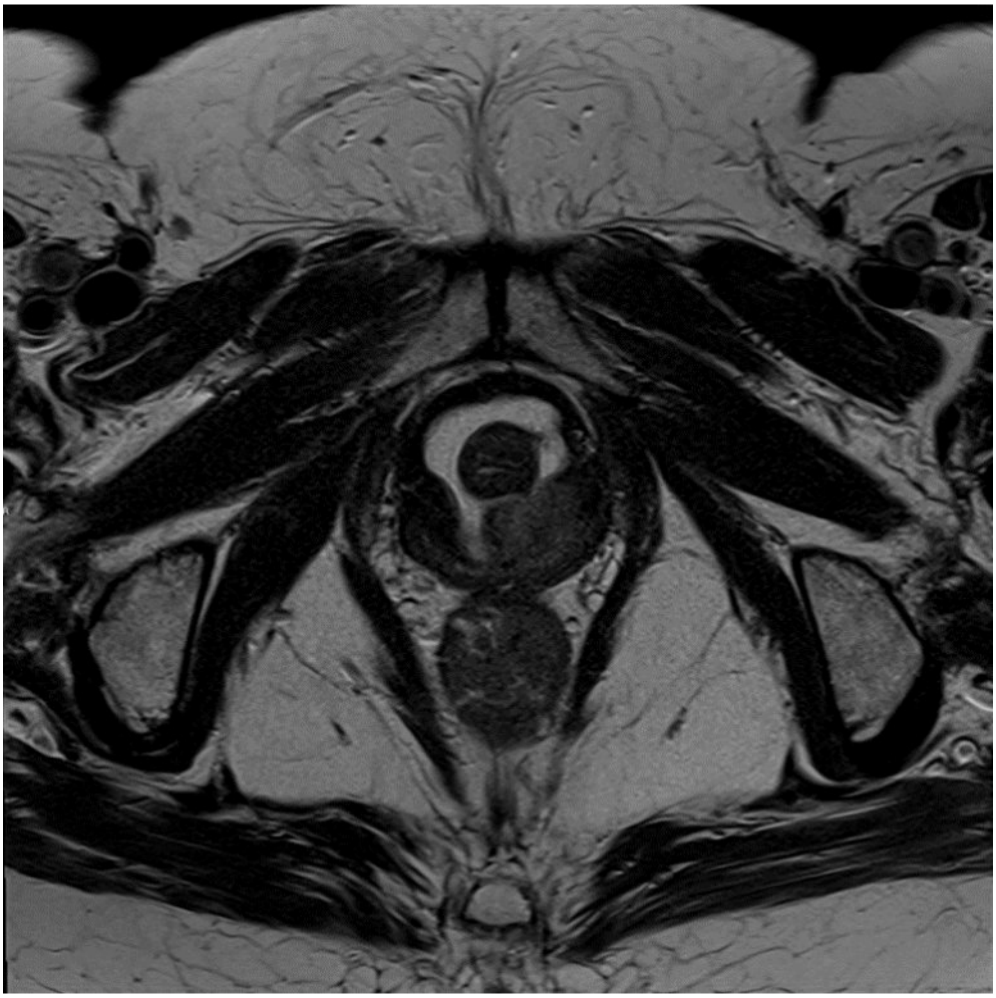

Sagittal T2W MRI showing advanced penile squamous cell carcinoma

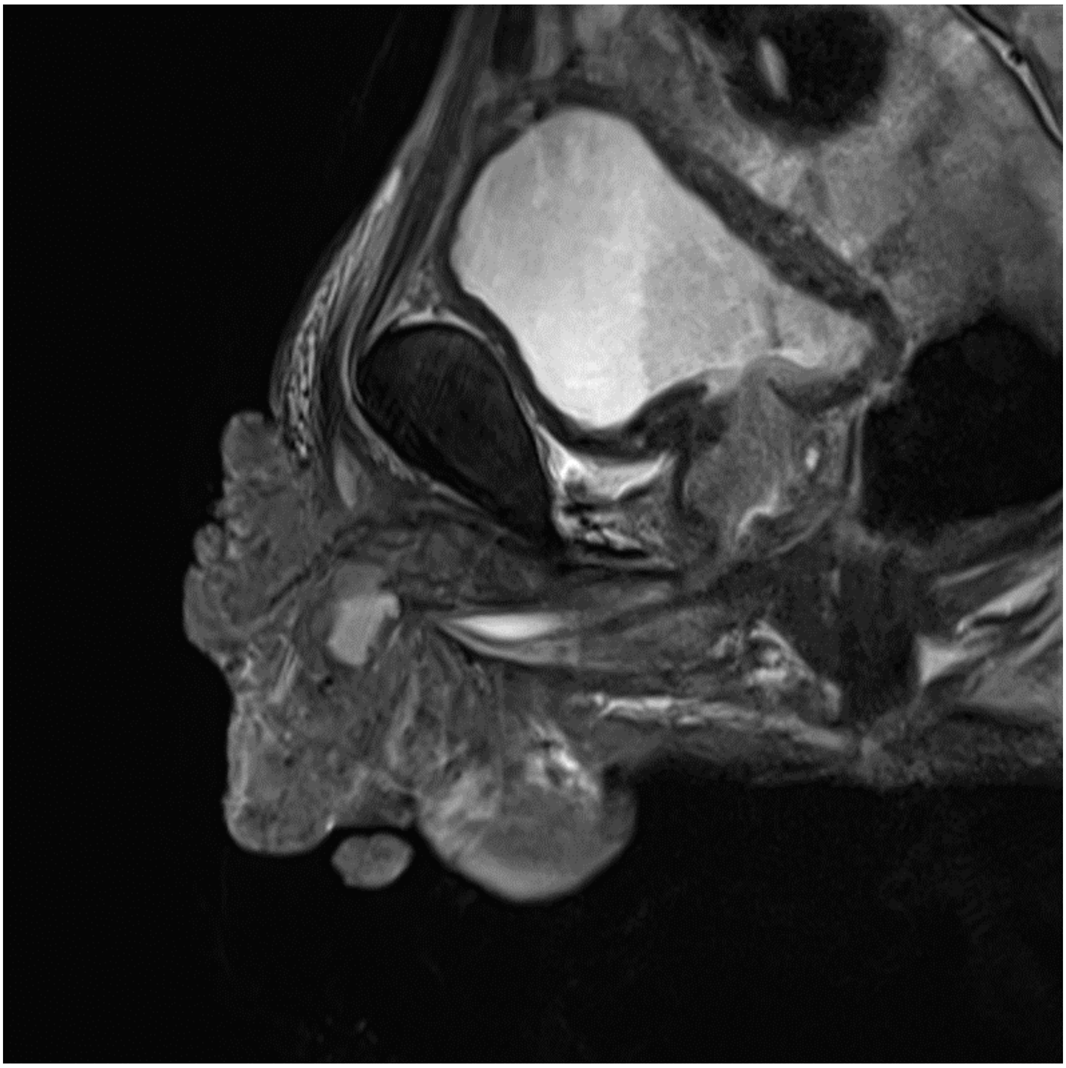

Keywords : Urethral carcinoma, Penile cancer, Imaging features

[Case Presentation by Trainees]

TCP01-3

Diagnostic Enigma: Primary Seminal Vesicle Angiosarcoma — A Multimodality Case Report

Lourdjeanne Luces-Clemente[1*]

[1]Radiology, St Luke's Medical Center Global City, Philippines

Primary angiosarcoma of the seminal vesicle is an exceptionally rare malignant vascular neoplasm, with only a few documented cases worldwide. Seminal vesicle masses, in most instances, represent secondary involvement from adjacent malignancies, most commonly originating from the prostate. Angiosarcomas are highly aggressive vascular tumors with early metastatic spread and poor prognosis. Its nonspecific presentation, often hematuria or pelvic pain, and overlapping imaging features with common urogenital tumors delay recognition, underscoring the role of radiologic evaluation in treatment planning.

This case illustrates a 61-year-old male who presented with recurrent hematuria and a right seminal vesicle mass identified on multimodality imaging. About one year prior to admission, he experienced hypogastric pain and dysuria, initially managed as a urinary tract infection. Six months prior, he developed recurrent hematuria and underwent transurethral resection of the prostate, which revealed benign prostatic hyperplasia. Despite multiple admissions for persistent bleeding, symptoms recurred, and two months before admission, surgical evaluation for suspected malignancy was advised. Upon readmission, he presented with gross hematuria and hematochezia and underwent robotic-assisted excision of seminal vesicle mass and pelvic lymph node dissection.

PET/CT demonstrated a hypermetabolic right seminal vesicle mass with nodal and osseous metastases. Whole abdomen CT also showed a heterogeneously enhancing right seminal vesicle mass with intralesional calcifications, suggestive of malignancy. Robotic excision of the lesion was performed, followed by MRI evaluation to assess for residual tumor, possible local extension, or postoperative complications. Histopathologic examination confirmed primary angiosarcoma of the seminal vesicle, and the patient was subsequently referred for adjuvant chemotherapy and multidisciplinary oncologic follow-up.

This case highlights the aggressive biologic behavior and distinct multimodality imaging features of seminal vesicle angiosarcoma, emphasizing the importance of radiologic-pathologic correlation in early recognition, staging, and management.

Keywords : Seminal Vesicle, Angiosarcoma, Genitourinary

[Case Presentation by Trainees]

TCP01-4

Biliary Necrosis in Liver Lymphoma

Daniel Ong[1], Yi-Wei Wu[1*]

[1]Diagnostic Radiology, Tan Tock Seng Hospital, Singapore

Hepatic lymphoma is a rare condition. Biliary complication such as biliary necrosis is a potential treatment complication. We present a case where a patient with hepatic lymphoma encountered biliary necrosis after combination therapy.

A 77-year-old Chinese male with biopsy proven diffuse large B cell lymphoma was treated with chemotherapy and radiation therapy (RT). He received intensity-modulated radiation therapy (IMRT) of 30.6 Gy/18 fractions to prechemotherapy volume, and 39.6 Gy/18 fractions to the post chemotherapy residual tumor, using concomitant boost technique.

He was later found to have possible biliary necrosis on computed tomography scan. This was later confirmed during an intra-operative cholangiogram done for a percutaneous transhepatic biliary drainage procedure.

This case report demonstrates a rare case of biliary necrosis, possibly related to the natural history of tumor necrosis and treatment (combination therapy), in a patient with hepatic lymphoma.

This case has previously been published in the Journal of Radiology Case Reports: Ong DY, Wu Y-W. Biliary necrosis in liver lymphoma. Journal of Radiology Case Reports 2024;18. doi:10.3941/jrcr.5482.

Figure 1: The right hepatic lobe tumor (hepatic lymphoma) is noted with gas foci within the necrotic component. The right portal vein courses through the necrotic mass and appears attenuated (black arrow). Several dilated intrahepatic ducts are seen connected to the necrotic mass (white arrows). Image insets: Preceding positron emission tomography computed tomography (PET CT) images which demonstrates a fluorodeoxyglucose (FDG)-avid right hepatic lobe mass.

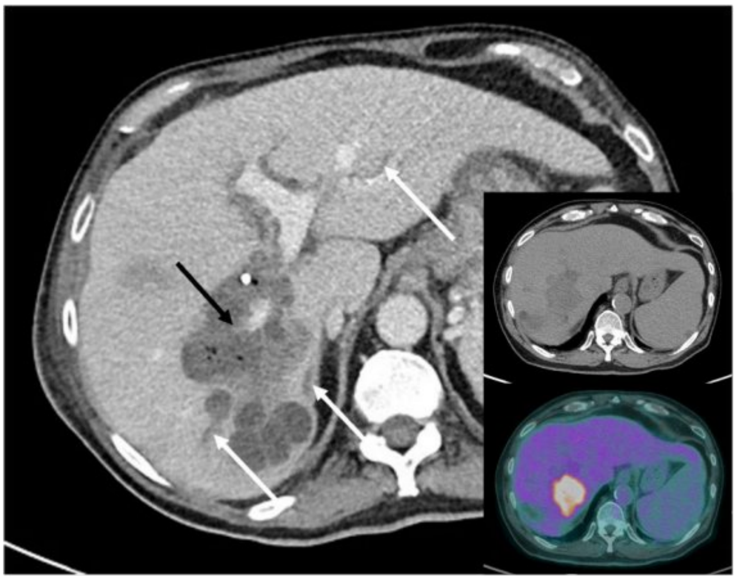

Figure 2 :

Figure 2: Intra-operative cholangiogram during left-sided percutaneous transhepatic biliary drainage procedure demonstrates complete disruption of right-sided ducts (white arrow), compatible with biliary necrosis.

Keywords : Biliary, Necrosis, Lymphoma

[Case Presentation by Trainees]

TCP01-5

Langerhans Cell Histiocytosis Masquerading as an Infective Mass: A Radiologic and Pathologic Challenge

Sue En Ong[1,2], Mohd Syafiek Abdul Haq Saifuddin[2], Noor Diyana Osman[3*]

[1]Radiology, School of Medical Sciences Universiti Sains Malaysia, Malaysia
[2]Radiology, Hospital Sultanah Bahiyah, Malaysia
[3]Biomedical Imaging, Advanced Medical and Dental Institute Universiti Sains Malaysia, Malaysia

Langerhans cell histiocytosis (LCH) is a rare clonal proliferative disorder of dendritic cells that may involve multiple organs but infrequently affects the liver. Hepatic LCH can present with nonspecific symptoms and radiological features that mimic infectious, inflammatory, or malignant lesions, making diagnosis challenging. This case aimed to describe an unusual presentation of hepatic LCH manifesting as a progressively enlarging mass initially presumed to be an abscess, highlighting the role of imaging, biopsy, and multidisciplinary evaluation in achieving the final diagnosis.

We describe a patient who initially presented with short history of bleeding symptoms (spontaneous bruising, gum bleeding) and shortness of breath with 2 months history of intermittent sore throat. Initial laboratory tests revealed anaemia and severe thrombocytopenia. Over the subsequent weeks, the patient developed left lower limb swelling and acute abdominal symptoms.

Serial CT imaging revealed a large iliopsoas mass and a progressively enlarging segment IVa liver lesion. Early biopsy suggested an inflammatory process compatible with an abscess, although the lesion continued to enlarge. The patient subsequently underwent non-anatomical resection of segment IVa, and histopathological examination confirmed **Langerhans cell histiocytosis of the liver**. Postoperative imaging demonstrated residual hepatic disease and interval reduction of lymphadenopathy and iliopsoas mass. Treatment with prednisolone and vinblastine was initiated.

The clinical course was complicated by multiple episodes of sepsis requiring intubation, a confirmed pulmonary embolism on CT pulmonary angiography, and acute cerebral infarction identified on CT brain.

This case illustrates the radiological presentation of hepatic LCH, radiologically mimicking an abscess or malignancy, poses significant diagnostic challenges. Persistent lesion progression despite treatment should prompt reconsideration of the diagnosis and repeat biopsy, especially when imaging suggests an infiltrative or mass-forming process. Radiologists should include LCH in the differential diagnosis of enlarging hepatic masses accompanied by systemic abnormalities and lymphadenopathy. Multimodality imaging, histopathological confirmation, and multidisciplinary management are critical in establishing diagnosis and guiding treatment. This case reinforces that in rare entities like hepatic LCH, radiology often provides the first clue to diagnosis and plays a central role in directing timely and appropriate clinical management.

Keywords : Liver, Langerhans Cell Histiocytosis, Radiology

[Case Presentation by Trainees]

TCP01-6

A Primary Retroperitoneal Hemangioma Initially Misdiagnosed as a Neuroendocrine Tumor with Increased Uptake in Ga-68 DOTATOC PET/CT

Jee Yeon Kim[1], June Park[1*], Hojin Cho[2], Yong Eun Chung[1]

[1]Radiology, Severance Hospital, Korea
[2]Nuclear Medicine, Severance Hospital, Korea

Background

Primary retroperitoneal hemangiomas in adults are extremely rare vascular malformations, accounting for approximately 1–3% of all retroperitoneal tumors. Preoperative diagnosis is often challenging, particularly when lesions do not demonstrate typical imaging features of hemangioma. Ga-68 DOTATOC positron emission tomography/computed tomography (PET/CT) is widely accepted as a reference standard for the evaluation of well-differentiated neuroendocrine tumors owing to its high sensitivity and specificity for somatostatin receptor subtype 2 (SSTR2). However, increased uptake of Ga-68 DOTATOC is not entirely specific to neuroendocrine tumors and may be observed in several benign conditions. We report a rare case of a primary retroperitoneal hemangioma that demonstrated increased Ga-68 DOTATOC uptake and was initially misdiagnosed as a neuroendocrine tumor.

Case presentation

A 40-year-old woman presented with intermittent palpitations, diaphoresis, and a sensation of elevated blood pressure. Physical examination and laboratory findings were unremarkable, and blood pressure measured at presentation was within normal limits. Contrast-enhanced abdominal computed tomography revealed a well-defined, oval-shaped 2.2-cm hypervascular mass in the aortocaval region at the level of the kidneys, showing intense arterial-phase enhancement. Magnetic resonance imaging demonstrated low signal intensity on T1-weighted images and high signal intensity on T2-weighted images, with strong enhancement from the arterial phase persisting into delayed phases. Diffusion-weighted imaging showed high signal intensity. F-18 fluorodeoxyglucose PET/CT demonstrated no significant radiotracer uptake. Based on the hypervascular nature and signal characteristics suggestive of a neuroendocrine tumor, Ga-68 DOTATOC PET/CT was performed and revealed intense radiotracer uptake within the lesion. Considering these imaging findings, a primary retroperitoneal neuroendocrine tumor was suspected, and surgical resection was performed. Histopathological examination confirmed a cavernous hemangioma, establishing the diagnosis of a primary retroperitoneal hemangioma.

Conclusion

This case illustrates that primary retroperitoneal hemangioma may demonstrate increased uptake on Ga-68 DOTATOC PET/CT, leading to potential misdiagnosis as a neuroendocrine tumor. Although Ga-68 DOTATOC PET/CT has high diagnostic accuracy for neuroendocrine tumors, radiotracer uptake is not entirely specific and may occur in benign conditions such as splenic tissue, inflammatory lesions, osteoblastic activity, and vascular tumors. Increased Ga-68 DOTATOC uptake in hemangiomas has been rarely reported, with proposed mechanisms including SSTR2 expression on vascular endothelial cells or adjacent osteoblastic activity, although the exact mechanism remains unclear. In the present case, retrospective review of CT and MRI findings demonstrated imaging features that were also compatible with hemangioma, including well-defined margins, marked hypervascularity, and high T2 signal intensity. Radiologists and nuclear medicine physicians should be aware that retroperitoneal hemangioma can be a diagnostic pitfall on Ga-68 DOTATOC PET/CT and should be considered in the differential diagnosis of hypervascular retroperitoneal lesions demonstrating increased tracer uptake, particularly when other imaging findings are equivocal.

Figure 1. CT and MRI findings of a retroperitoneal hemangioma involving the aortocaval area in 40-year-old female. The lesion is indicated by an arrow.

Pre-contrast phase CT image shows a 2.2–cm sized well-defined nodular lesion in the aortocaval area at the level of bilateral kidneys (a). In arterial phase CT image, the lesion is heterogeneously enhanced, similar degree to the abdominal aorta (b). On MRI, the nodular lesion shows slightly low signal intensity compared to the muscles on pre-contrast T1-weighted image (c) and markedly high signal intensity on T2-weighted image (d). Dynamic MRI images after gadolinium-EOB-DTPA enhancement show early and persistent enhancement during the hepatic arterial (e) and portal venous (f) phases. On diffusion-weighted image with b = 400 sec/mm^2, the lesion shows a markedly high signal intensity, suggesting diffusion restriction (g).

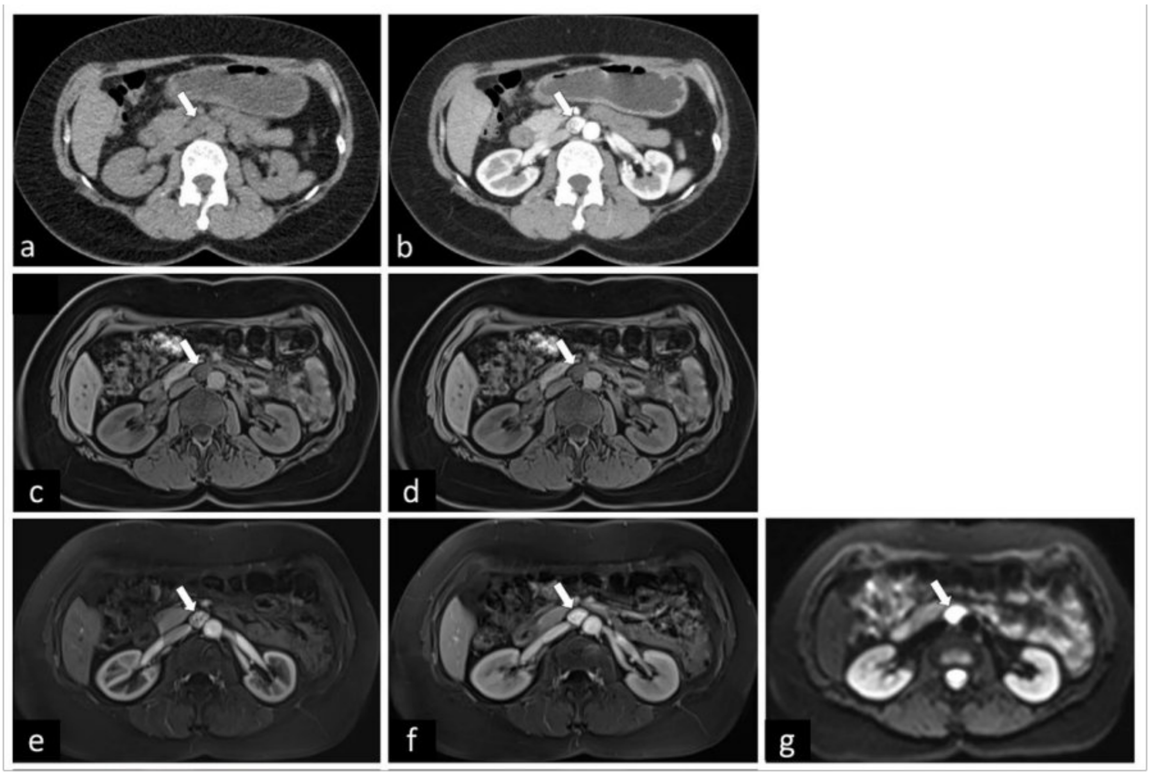

Figure 2. F-18 FDG and Ga-68 DOTATOC PET/CT images of the retroperitoneal hemangioma. (a) The F-18 FDG PET/CT images show no significant uptake in the area of the mass lesion (SUV_{max} = 1.8). (b) The Ga-68 DOTATOC PET/CT images show increased uptake in the same area of the mass lesion (SUV_{max} = 12.7).

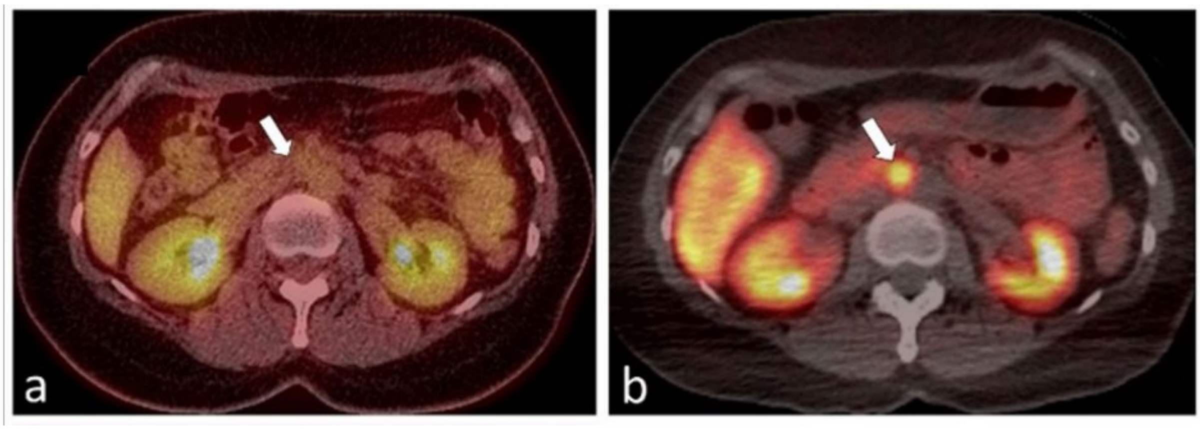

Keywords : Hemangioma, Retroperitoneal space, Neuroendocrine tumor

[Case Presentation by Trainees]

TCP01-7

Paradox of Budd Chiari Syndrome Caused by Liver Transplantation

Katerina Lee[1*]

[1]Diagnostic Radiology, University of Pennsylvania, USA

A 64-year-old female with autoimmune hepatitis induced cirrhosis initially presented for orthotopic liver transplantation. Her hospital recovery was prolonged due to multiple complications, including acute kidney injury, segmental pulmonary embolism, septic and vasogenic shock, aspergillus pneumonia, pancreatitis, and biliary stricture. Since the transplant surgery, the patient had been getting CT abdomen and pelvis almost every 1-2 weeks for medical and procedural management of these complications.

The patient received an enhanced CT examination of the abdomen and pelvis after administration of 85 mL of iopamidol 76% IV solution.

Compared to the most recent CT scan 8 days prior, there was a new right anterior hepatic vein thrombus with a wedge-shaped area of segmental hypoattenuation in segments 7 and 8, reflecting a perfusional abnormality. The portal veins were patent. With the benefit of a prior arterial phase CT exam performed 8 days earlier, the native and anastomosed hepatic arteries were deemed patent, although partially obscured by the biliary stent. No acute source of bacteremia was identified.

Hepatectomy and orthotopic “piggyback” liver transplantation alter hepatic vein/IVC hemodynamics, resulting in increased risk of iatrogenic Budd Chiari syndrome[1]. This is an interesting medical paradox in that the treatment, liver transplantation, is also a cause for the pathology, Budd Chiari syndrome. Published cases of this paradoxical phenomenon report favored involvement of the right hepatic vein[2]. Although not common with rate of less than 3%[3], it can lead to serious complications including graft dysfunction and graft failure, which are associated with mortality rates up to 24%[4,5]. Typically, clinical symptoms develop only when at least two of the three hepatic veins are occluded[6]. Therefore, early diagnosis and intervention are critical in these already immunocompromised transplantation patients.

References

1. Garmpis N, Damaskos C, Prevezanos D, et al. Liver Transplantation and Budd-Chiari Syndrome: When the Cause Becomes the Solution. *Mædica*. 2022;17(2):415-419. doi:10.26574/maedica.2022.17.2.415

2. Aucejo F, Winans C, Henderson JM, et al. Isolated right hepatic vein obstruction after piggyback liver transplantation. *Liver Transplant Off Publ Am Assoc Study Liver Dis Int Liver Transplant Soc*. 2006;12(5):808-812. doi:10.1002/lt.20747

3. Piardi T, Lhuaire M, Bruno O, et al. Vascular complications following liver transplantation: A literature

review of advances in 2015. *World J Hepatol*. 2016;8(1):36-57. doi:10.4254/wjh.v8.i1.36

4. Pandhi MB, Lipnik AJ, Niemeyer MM. Endovascular Treatment of Hepatic Venous Outflow Obstruction after Liver Transplant. *Dig Dis Interv*. 2019;03(4):277-286. doi:10.1055/s-0039-3400494

5. Navarro F, Le Moine MC, Fabre JM, et al. Specific vascular complications of orthotopic liver transplantation with preservation of the retrohepatic vena cava: review of 1361 cases. *Transplantation*. 1999;68(5):646-650. doi:10.1097/00007890-199909150-00009

6. *Regenerative Medicine Applications in Organ Transplantation*. Elsevier Science; 2013.

Figure 1 :

Axial CT image of the abdomen demonstrates right anterior hepatic vein thrombus with a wedge-shaped area of segmental hypoattenuation in segments 7 and 8, reflecting a perfusional abnormality. This was not seen on prior CT abodmen and pelvis a week prior to this exam. Of note, the native and the transplanted hepatic arteries were patent (not visualized on this image).

Keywords : Liver Transplantation Complication, Budd Chiari Syndrome

[Case Presentation by Trainees]

TCP01-8

When the Pancreas is Caught off Guard: A Rare Case of Contrast-Induced Radiologic Acute Pancreatitis

Kenneth Velasco[1], Regina Sy[1*]

[1]Radiology and Imaging Science, Rizal Medical Center, Philippines

Acute pancreatitis is a common inflammatory condition with a wide clinical and imaging spectrum. While gallstones and alcohol account for most cases, drug-induced pancreatitis represents only 0.1–2% of etiologies, and contrast-induced pancreatitis is exceptionally rare, with only isolated reports in the literature. Standard diagnosis requires at least two of the following: characteristic abdominal pain, serum amylase or lipase elevation greater than three times normal, or imaging findings consistent with pancreatitis. Subclinical or radiologic-only pancreatitis—where imaging abnormalities occur without symptoms or enzyme elevation—has been described but remains extremely uncommon.

This case report aims to describe a rare instance of contrast-associated subclinical acute pancreatitis in a young patient with Systemic Lupus Erythematosus (SLE), highlighting the role of imaging in identifying atypical or asymptomatic presentations and emphasizing the importance of recognizing iodinated contrast as a potential trigger.

This is a descriptive case report involving a 22-year-old female with SLE who underwent a whole abdominal triphasic CT scan as part of pre-treatment evaluation for active lupus disease. Clinical symptoms were assessed before and after contrast administration. Serum amylase, lipase, and other laboratory parameters were measured following the scan. CT images from plain, arterial, portal venous, and delayed phases were evaluated for pancreatic enlargement, parenchymal enhancement, and peripancreatic changes. The patient was monitored clinically in the days following the examination, and management decisions were based on clinical status and laboratory results.

The patient had no abdominal pain, nausea, vomiting, fever, or symptoms suggestive of pancreatitis before or after CT imaging. The initial CT phases demonstrated a normal-sized, normally enhancing pancreas without inflammatory changes. However, delayed-phase images showed diffuse pancreatic enlargement (3.6 cm at the head, 3.4 cm at the body, and 4.3 cm at the tail), parenchymal hypoenhancement, loss of normal architecture, and minimal peripancreatic hyperdensities, interpreted as possible contrast extravasation or acute hemorrhage. These findings were compatible with acute pancreatitis, with imaging features suggestive of early necrotizing involvement.

Despite these radiologic findings, the patient remained asymptomatic, and abdominal examination was benign. Serum amylase and lipase were within normal limits, and white blood cell count was unremarkable. With only the imaging criterion met, the case was diagnosed as contrast-associated subclinical (radiologic) acute pancreatitis. The patient was managed conservatively with hydration and observation, remained stable, and subsequently proceeded with the planned immunosuppressive therapy without complication.

Contrast-induced pancreatitis is an exceptionally rare and under-recognized condition with few documented cases. This report presents a unique subclinical, radiologic-only form in a young patient with Systemic Lupus Erythematosus who developed delayed-phase CT findings of pancreatic inflammation immediately after contrast exposure, despite lacking symptoms and having normal amylase and lipase levels. The delayed-phase abnormalities highlight the potential for contrast to cause early microvascular or cellular injury, particularly in patients with immune or microvascular vulnerability. This case underscores the limitations of relying solely on symptoms or enzyme elevation and emphasizes the critical role of imaging in detecting atypical pancreatitis and guiding appropriate clinical management.

Figure 1. Plain (A), arterial (B), and porto-venous (C) phases of the whole abdominal CT scan triphasic study showed a pancreas that is normal in size and parenchymal attenuation. No surrounding fat stranding is noted.

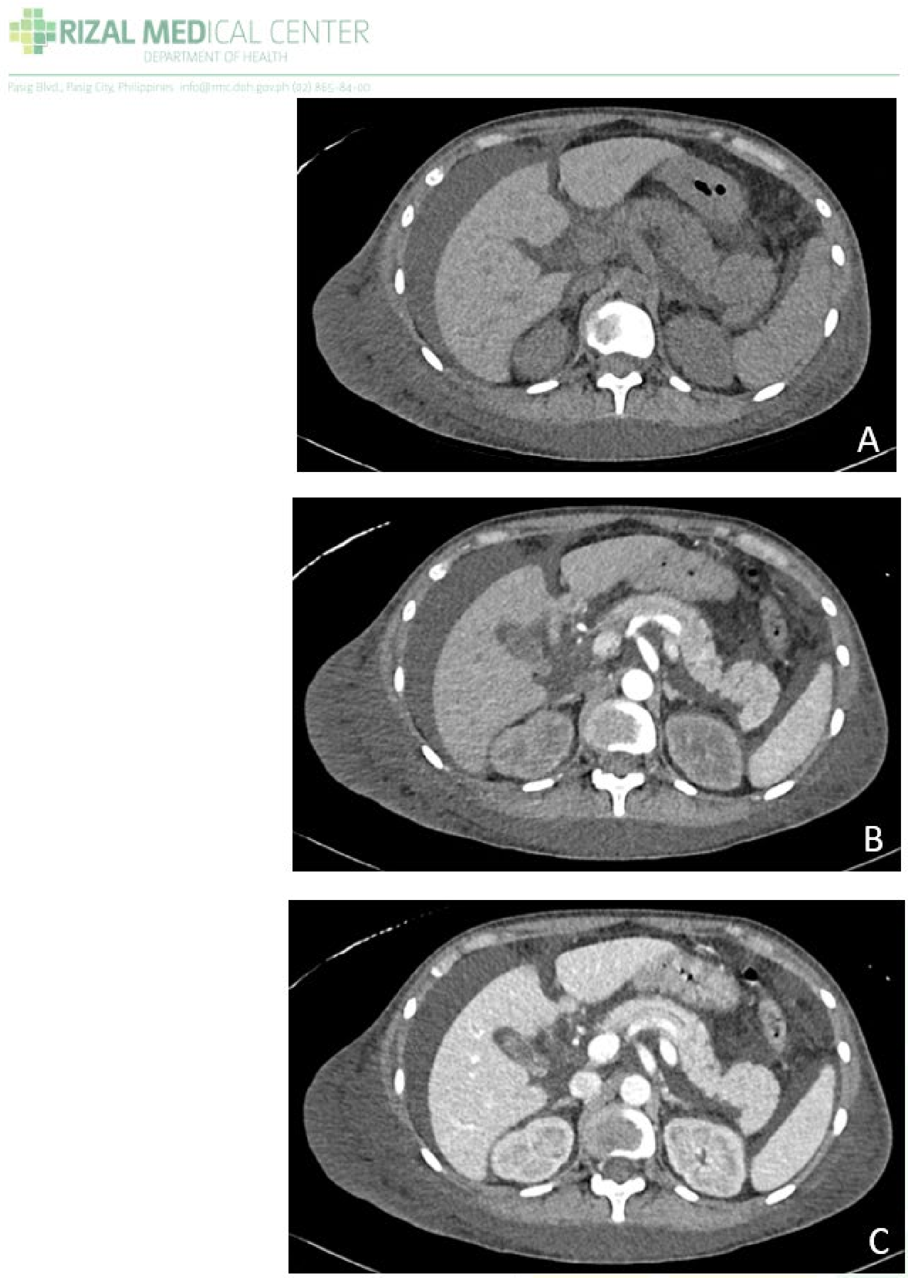

Figure 1. Plain (A), arterial (B), and porto-venous (C) phases of the whole abdominal CT scan triphasic study showed a pancreas that is normal in size and parenchymal attenuation. No surrounding fat stranding is noted.

Figure 2. Delayed whole abdominal CT scan triphasic study revealed diffuse increase in size of the pancreas, measuring approximately 3.6 cm (head), 3.4 cm (body), and 4.3 cm (tail) exhibiting hypoenhancement of its parenchyma and loss of its normal architecture. Minimal peripancreatic hyperdensities (arrow) are also demonstrated, possibly representing contrast extravasation versus acute hemorrhage.

RIZAL MEDICAL CENTER
DEPARTMENT OF HEALTH

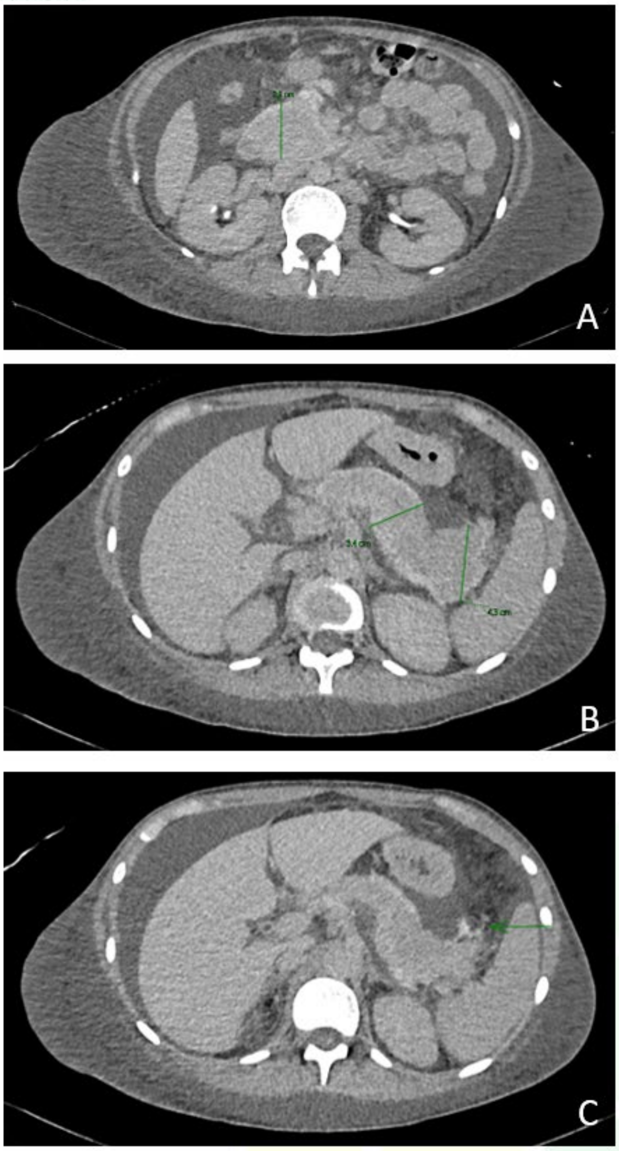

Figure 2. Delayed whole abdominal CT scan triphasic study revealed diffuse increase in size of the pancreas, measuring approximately 3.6 cm (head), 3.4 cm (body), and 4.3 cm (tail) exhibiting hypoenhancement of its parenchyma and loss of its normal architecture. Minimal peripancreatic hyperdensities (arrow) are also demonstrated, possibly representing contrast extravasation versus acute hemorrhage.

Keywords : Contrast-Induced, Radiologic, Pancreatitis

[Case Presentation by Trainees]

TCP01-9

Hepatoid Carcinoma of the Pancreas

Won-Seok Yoo[1], Ja Kyung Yoon[1*], June Park[1], Jin-Young Choi[1]

[1]Radiology, Severance Hospital, Korea

Hepatoid carcinoma is a rare malignant extrahepatic neoplasm with poor prognosis that is histologically similar to hepatocellular carcinoma and often produces alpha-fetoprotein (AFP). It most commonly arises in the stomach, followed by the ovary, whereas pancreatic involvement is exceedingly rare. Hepatoid carcinoma of the pancreas may occur either as a pure form or in combination with other histologic components, including neuroendocrine tumors or pancreatic ductal adenocarcinoma. Here, we describe a case of pure hepatoid carcinoma arising from the pancreas, presenting as a well-defined mass with early hyperenhancement and subsequent washout.

We retrospectively reviewed the abdominal ultrasonography, contrast-enhanced dynamic abdominopelvic CT, contrast-enhanced dynamic MRI, and histopathologic findings of the case.

A 41-year-old man without notable past medical history was found to have a 2.0-cm hypoechoic pancreatic mass in the pancreatic body on abdominal ultrasound during a routine health check-up. The mass was well-defined and showed hypoechogenicity without definite pancreatic duct dilatation. Over a 1-year follow-up period, the lesion increased in size to 2.5 cm. Subsequent contrast-enhanced dynamic abdominopelvic CT revealed a round, hyperenhancing solid pancreatic mass in the body, showing isoattenuation relative to the pancreatic parenchyma on precontrast images and hyperattenuation on arterial, portal venous, and delayed phase images.

Gadolinium-enhanced pancreaticobiliary MRI using gadoterate meglumine (Dotarem; Guerbet SA, Aulnay-sous-Bois, France) demonstrated a 2.5×1.8×1.9 cm well-defined mass confined to the pancreas, showing hypointensity on T1-weighted image. The mass showed homogeneous hypointensity on T2-weighted images compared with the pancreas parenchyma, with signal intensity similar to that of the normal liver parenchyma. No definite dilatation of the pancreatic duct was observed. On dynamic contrast-enhanced T1 images, the mass demonstrated homogeneous enhancement comparable to that of the pancreatic parenchyma in the arterial phase, followed by progressively decreased signal intensity relative to the surrounding pancreas from the portal venous to delayed phases, consistent with a washout pattern. On chemical shift imaging, no significant signal change was observed between in-phase and out-of-phase sequences, suggesting the absence of intratumoral fat or hemorrhage. There was no evidence of distant metastasis in the abdomen and pelvis. Based on these imaging findings, the differential diagnosis included pancreatic neuroendocrine tumor, intrapancreatic accessory spleen, solid pseudopapillary neoplasm, and other mesenchymal tumors of the pancreas. Serum carbohydrate antigen 19-9 (9 IU/mL) and carcinoembryonic antigen (0.48 ng/mL) levels were within normal limits; however, serum AFP levels were not assessed.

Endoscopic ultrasound-guided fine needle aspiration was performed for tissue confirmation.

Histopathologic examination confirmed the diagnosis of hepatoid carcinoma with positive HepPar-1 immunostaining, despite negative AFP immunostaining. The patient underwent curative laparoscopic distal pancreatectomy, and the final histopathologic evaluation consistently confirmed hepatoid carcinoma of the pancreas.

Pancreatic hepatoid carcinoma, although extremely rare, may present with imaging features of arterial phase hyperenhancement and washout resembling typical hepatocellular carcinoma.

Figure 1. Gadoteric acid-enhanced pancreaticobiliary MRI findings of pancreatic hepatoid carcinoma.

A well-defined pancreatic mass located in the body demonstrates hypointensity on T1- and T2-weighted images. On dynamic contrast-enhanced images, the mass shows homogeneous hyperenhancement in the arterial phase, followed by washout on subsequent phases.

AP = arterial phase, PP = portal venous phase, LP = late portal venous phase, TP = transitional phase, HBP = hepatobiliary phase, DWI = diffusion-weighted imaging, ADC = apparent diffusion coefficient, T2FS = fat-suppressed T2-weighted imaging, MRCP = magnetic resonance cholangiopancreatography

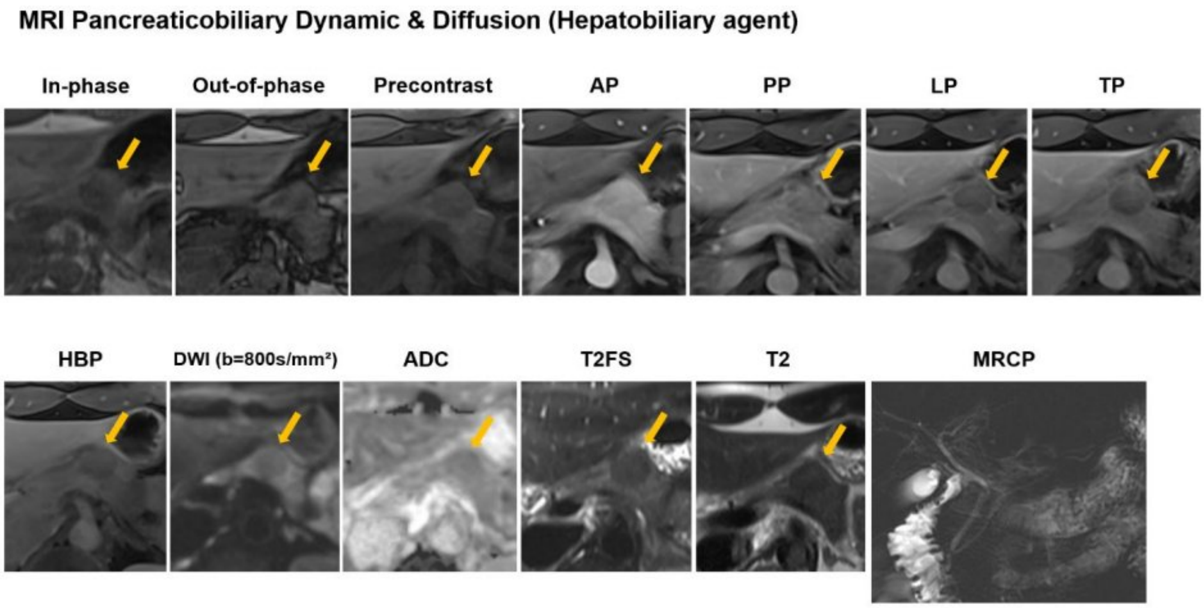

Figure 2. Gross specimen of pancreatic hepatoid carcinoma showing a well-circumscribed, brownish mass confined to the pancreas.

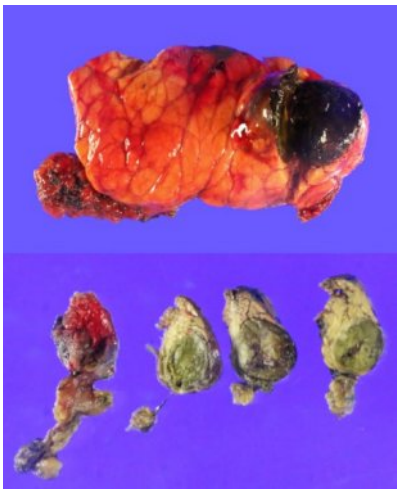

Keywords : Hepatoid carcinoma, Pancreas

ACAR 2026

THE 13th ASIAN CONGRESS OF ABDOMINAL RADIOLOGY

Oral Presentation

Mar. 20 (Sat.)

! Abstracts can be found by searching with the Presentation Code !

[GU Issues 2]

SS08-1

Clinically Available 3T Multi-Pool Chemical Exchange Saturation Transfer MRI for Accurate Diagnosis and Noninvasive Grading of Prostate Cancer

Kangwen He[1*], Zhen Li[1]

[1]Radiology, Tongji Hospital Tongji Medical College Huazhong University of Science and Technology, China

To evaluate the diagnostic value of multi-pool chemical exchange saturation transfer (CEST) MRI on clinically available 3T systems for detecting clinically significant prostate cancer (csPCa) and assessing its correlation with Gleason grade.

In this prospective study, 156 patients with suspected prostate cancer (median age 67 years) underwent multiparametric MRI and multi-pool CEST imaging at 3T. Lorentzian fitting yielded amide proton transfer (APT), water, and magnetization transfer (MT) pool parameters, as well as magnetization transfer ratio asymmetry (MTR_{asym}). The ADC values and T2 mapping values of the lesions were also measured. Parameter stability was assessed in contralateral prostate tissue and obturator internus muscles. Group differences were tested by Wilcoxon signed-rank tests. Univariate and multivariate logistic regression analyses were performed to identify independent risk factors for csPCa. Diagnostic performance was evaluated using ROC curves and compared by DeLong test. Correlations with Gleason grade were analyzed using Spearman coefficients.A subgroup analysis was performed based on prostate zones (PZ or TZ).

CEST parameters demonstrated good stability (coefficients of variation 10–38%, ICCs >0.8). Significant differences in CEST, T2 mapping, and ADC values were observed between csPCa and non-csPCa (all $p < 0.05$). MT derived from multi-pool fitting was an independent predictor of csPCa (OR=0.807, 95% CI=0.682–0.954, p =0.012), with the diagnostic performance (AUC = 0.79) superior to MTRasym (AUC=0.61, p = 0.001). The combination of MT and ADC further improved accuracy (AUC = 0.87, p = 0.001). MT remained robust in both PZ and TZ, while APT showed diagnostic value mainly in PZ. APT in PZ and MT in TZ correlated significantly with Gleason grade (r = 0.31, p = 0.025, and r = –0.49, p = 0.007, respectively).

Multi-pool CEST MRI on 3T provides stable quantitative biomarkers, improves diagnostic performance beyond MTR_{asym}, and yields significant incremental value over ADC, supporting its role as a complementary tool to mpMRI in prostate cancer.

Examples of CEST imaging in prostate.

(A) A 67-year-old male with a serum PSA level of 6.738ng/ml presented with a PI-RADS 3 nodule in the right basal transition zone, characterized by mildly elevated MTR_{asym}, increased amide and MT pool amplitudes, and decreased water pool amplitude on CEST imaging. Targeted biopsy confirmed benign prostatic hyperplasia. (a) T2WI, (b) ADC map, (c) T2 mapping, (d) APTw imaging, (e) APT pool parametric map, (f) MT pool parametric map, (g) water pool parametric map, (h) multi pool lorentzian fitting curves.

(B) A 74-year-old male with a serum PSA level of 28.83ng/ml presented with a PI-RADS 5 nodule in the right mid peripheral zone, showing elevated MTR_{asym}, increased APT and water pool amplitudes, and decreased MT pool amplitude on CEST imaging. Targeted biopsy confirmed prostate cancer with a Gleason score of 4+3. (a) T2WI, (b) ADC map, (c) T2 mapping, (d) APTw imaging, (e) APT pool parametric map, (f) MT pool parametric map, (g) water pool parametric map, (h) multi pool lorentzian fitting curves.

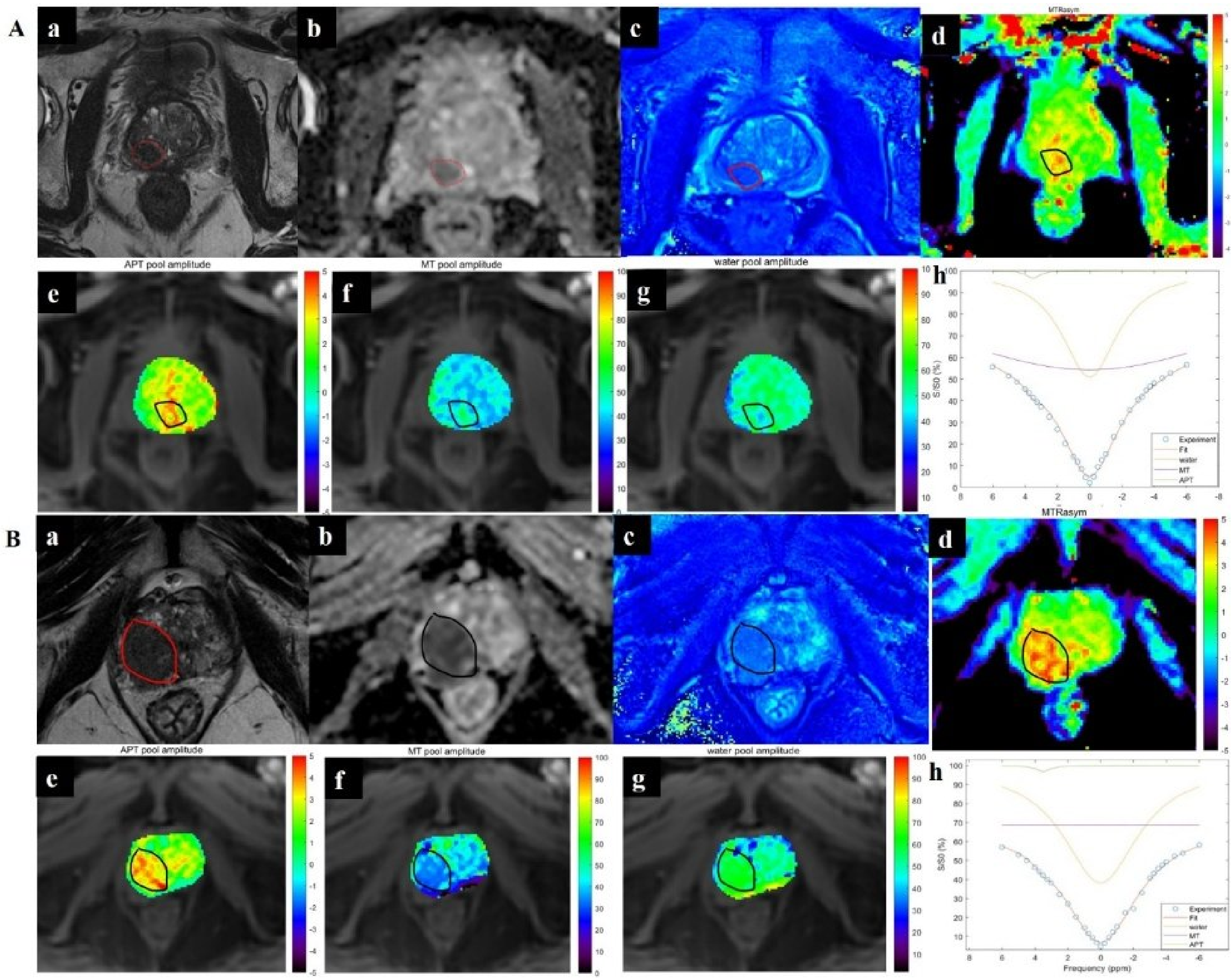

Differences in CEST parameters, ADC, and T2 mapping values were analyzed among benign prostatic lesions and prostate cancers with different Gleason grades **(a)**. The diagnostic performance for distinguishing csPCa from non-csPCa was further evaluated using ROC curves **(b)** and radar charts **(c)**.

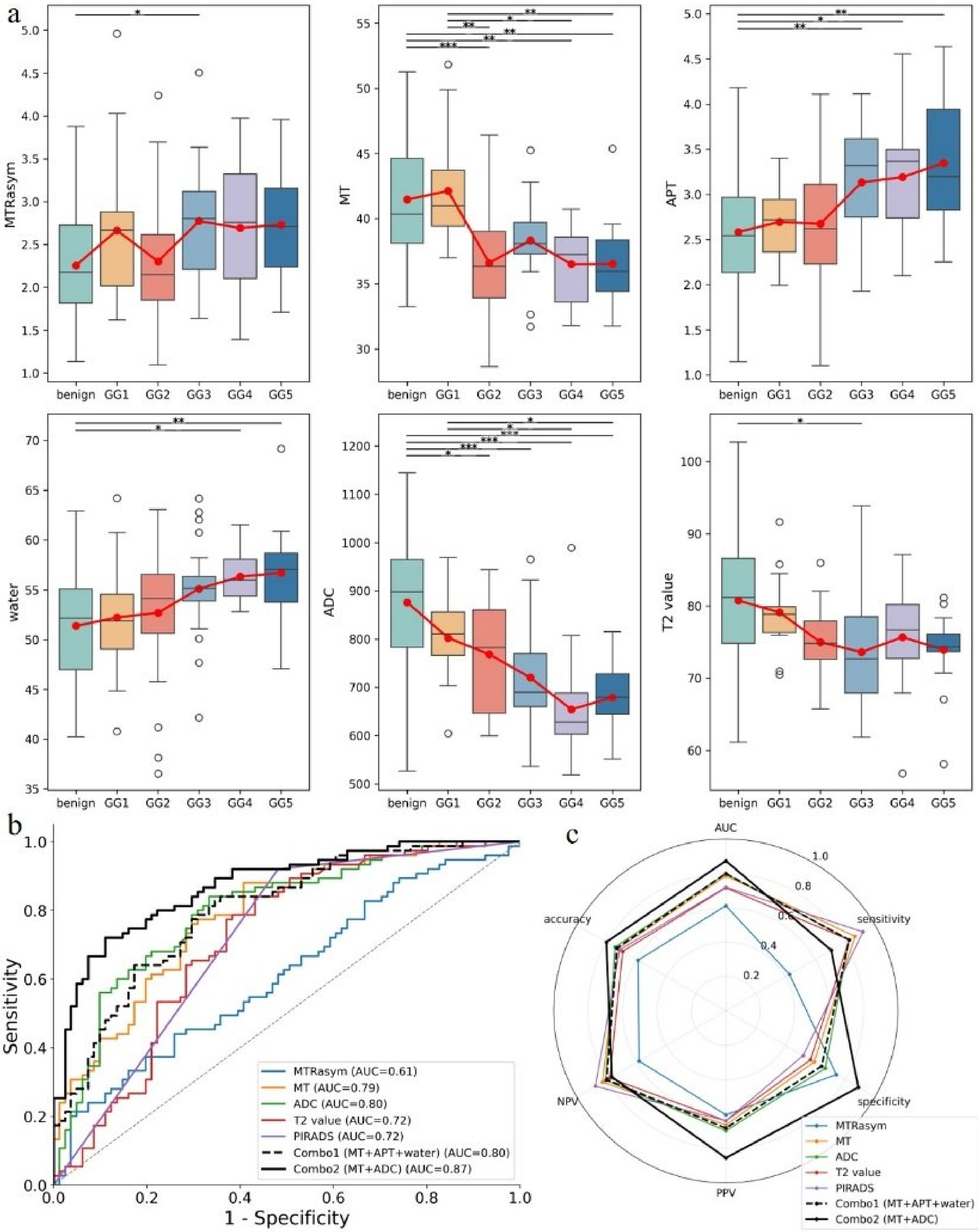

Keywords : Prostate Cancer, Chemical exchange saturation transfer, MRI

[GU Issues 2]

SS08-2

Interreader Agreement of PI-QUAL Version 2 for Prostate Magnetic Resonance Imaging Quality Assessment among Nonexpert Readers and Its Clinical Impact in a Targeted Biopsy Cohort

Nattawut Jiraaram[1], Saksith Warittikoon[1], Panida Wongsansuk[1*]

[1]Diagnostic and Interventional Radiology, Chulabhorn Royal Academy, Thailand

To assess the interreader reliability of PI-QUAL v2—an updated, simplified, and more objective 3-point image-quality scale—and evaluate its impact on prostate magnetic resonance imaging (MRI) diagnostic performance in a targeted biopsy cohort.

In this single-center, retrospective study in Thailand, 100 prostate MRI examinations drawn from both institutional and external sources were scored for image quality by two board-certified body imaging radiologists (one with basic experience and the other a beginner) using PI-QUAL v2. Interreader and intrareader reliability were determined, and associations between PI-QUAL v2 categories, biopsy-confirmed prostate cancer, and diagnostic performance were analyzed.

PI-QUAL v2 showed moderate interreader (Gwet's AC1, 0.59; 78% agreement) and intrareader reliability (0.52 for Reader 1; 0.43 for Reader 2). Sequence-specific agreement was moderate for T2-weighted imaging (T2WI, 0.42) and diffusion-weighted imaging (0.49) and almost perfect for dynamic contrast-enhanced imaging (DCE, 0.95). Cancer detection rates increased with higher PI-QUAL categories across PI-RADS 3–5, reaching significance for PI-RADS 4. Using PI-RADS ≥ 4 as the diagnostic threshold, PI-QUAL 3 achieved the best performance (area under the curve, 0.62 [95% confidence interval, 0.45–0.79]; specificity, 33.3%; positive predictive value, 69.2%; and accuracy, 68.8%).

PI-QUAL v2 showed moderate interreader (Gwet's AC1, 0.59; 78% agreement) and intrareader reliability (0.52 for Reader 1; 0.43 for Reader 2). Sequence-specific agreement was moderate for T2-weighted imaging (T2WI, 0.42) and diffusion-weighted imaging (0.49) and almost perfect for dynamic contrast-enhanced imaging (DCE, 0.95). Cancer detection rates increased with higher PI-QUAL categories across PI-RADS 3–5, reaching significance for PI-RADS 4. Using PI-RADS ≥ 4 as the diagnostic threshold, PI-QUAL 3 achieved the best performance (area under the curve, 0.62 [95% confidence interval, 0.45–0.79]; specificity, 33.3%; positive predictive value, 69.2%; and accuracy, 68.8%).

Keywords : PI-QUAL, Prostate, MRI Quality

[GU Issues 2]

SS08-3

Mapping Tumor Heterogeneity via Habitat Analysis: An Interpretable Machine Learning Model Fusing 18F-PSMA-1007 PET/CT and mpMRI for ISUP Grade Prediction in a Multicenter Study

Haoli Xu[1], Yao[1], Boli Lin[1], Yunjun Yang[1], Shuying Bian[1*]

[1]Radiology, The First Affiliated Hospital of Wenzhou Medical University, China

This study aimed to develop and validate a machine learning prediction model based on multimodal imaging habitat analysis for the preoperative, non-invasive prediction of prostate cancer with an ISUP grade ≥ 3, by integrating information from 18F-PSMA-1007 PET/CT and multiparametric MRI (mpMRI).

This multicenter study retrospectively enrolled 390 patients, who were allocated into a training cohort (n=239), an internal validation cohort (n=102), and an external validation cohort (n=49). All patients underwent preoperative ^{18}F-PSMA-1007 PET/CT and mpMRI, including T2-weighted imaging (T2WI), diffusion-weighted imaging (DWI), and apparent diffusion coefficient (ADC) sequences. Habitat regions were segmented from PET/CT and mpMRI images using the K-means clustering algorithm, from which both habitat-derived radiomic features and traditional radiomic features were extracted, resulting in a total of 15 feature sets. Feature selection was performed using minimum Redundancy Maximum Relevance (mRMR) and the Least Absolute Shrinkage and Selection Operator (LASSO). Predictive models were constructed using support vector machine (SVM), multilayer perceptron (MLP), random forest (RF), linear discriminant analysis (LDA), and logistic regression algorithms. A clinical model was developed by identifying independent predictors through multivariable logistic regression analysis and was compared against a baseline model (bISUP) incorporating biopsy-based ISUP scores. The discriminatory performance of the models was evaluated using the area under the receiver operating characteristic curve (AUC) and the average precision (AP) from precision-recall (PR) curves. The SHapley Additive exPlanations (SHAP) interpretability method was employed to assess feature importance and interpret the optimal machine learning model. Finally, a risk prediction nomogram was developed based on the best-performing combined model, and its predictive accuracy and clinical utility were assessed via calibration curves and decision curve analysis (DCA).

The ITH model, constructed by integrating all habitat-derived features from PET/CT and MRI with the LDA algorithm, demonstrated the optimal performance. It achieved AUC of 0.838, 0.811, and 0.812 in the training, internal validation, and external validation cohorts, respectively, outperforming both the bISUP model (AUCs: 0.775, 0.796, 0.771) and the clinical model (AUCs: 0.768, 0.764, 0.807). SHAP analysis of the ITH model elucidated the contribution and directional impact of key imaging features on its predictions. A combined model was subsequently developed by integrating the ITH model with the bISUP score and clinical predictors, yielding further improved AUCs of 0.877, 0.860, and 0.886 across the three cohorts. The PR curves of the combined model showed excellent performance, with AP values of 0.833, 0.867, and 0.941, and AUC-PR values of 0.830, 0.863, and 0.938 in the training, internal validation, and external validation cohorts, respectively.The risk prediction nomogram based on this combined model exhibited good predictive accuracy. Calibration curves indicated ideal agreement between predictions and observations across all cohorts, and DCA confirmed its significant clinical utility.

The machine learning model integrating multimodal imaging habitat analysis with clinical indicators demonstrated superior and stable performance in predicting high-risk prostate cancer. Its interpretability was further enhanced by SHAP analysis, which provided clear insights into the optimal ITH model. The model exhibited excellent calibration and strong clinical applicability, offering a reliable non-invasive tool for preoperative individualized risk assessment.

Figure 1: Workflow of necessary steps about the study.

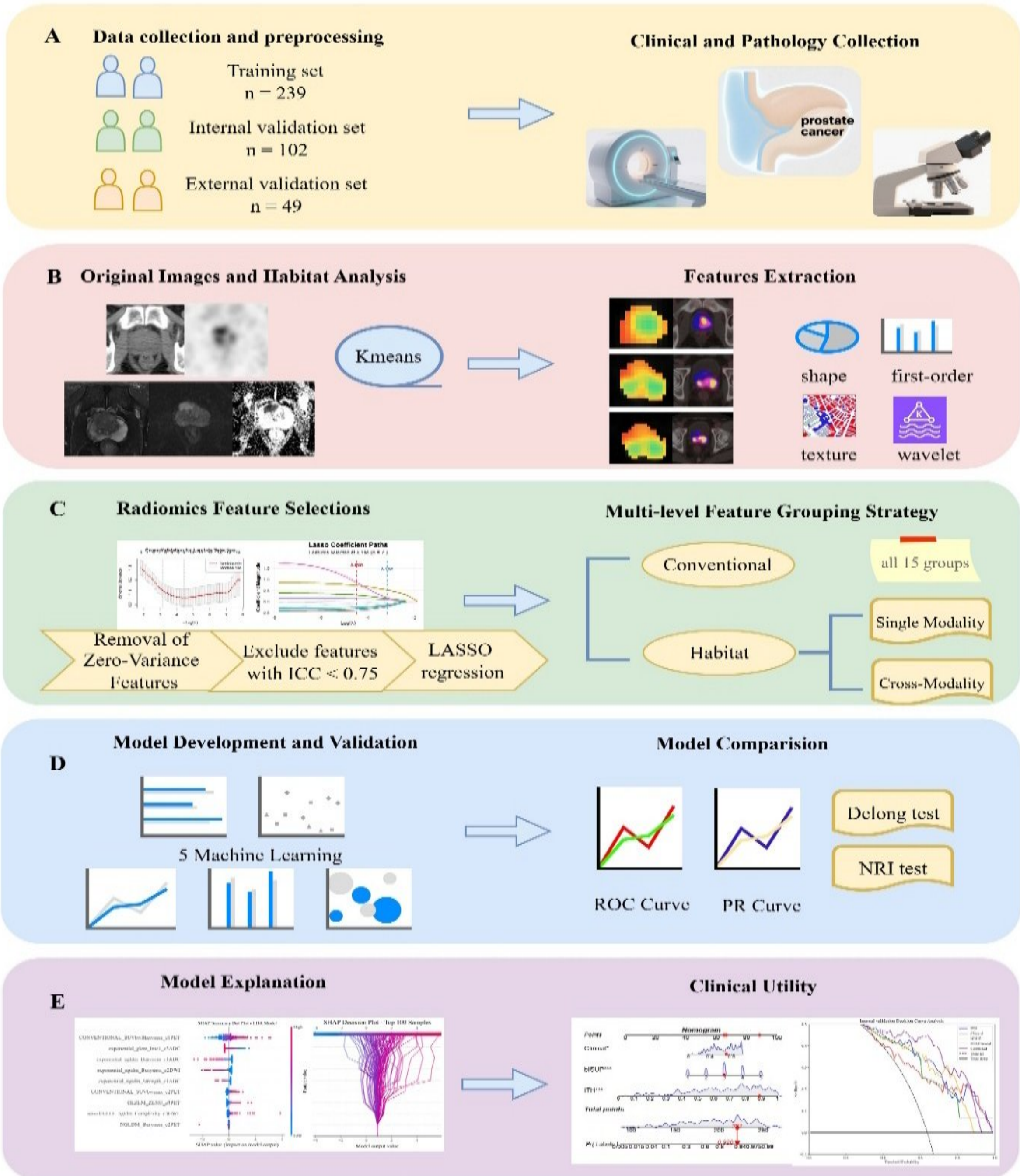

Figure 2: The ROC curves and PR curves of the different models in the train, internal validation and internal validation cohorts.

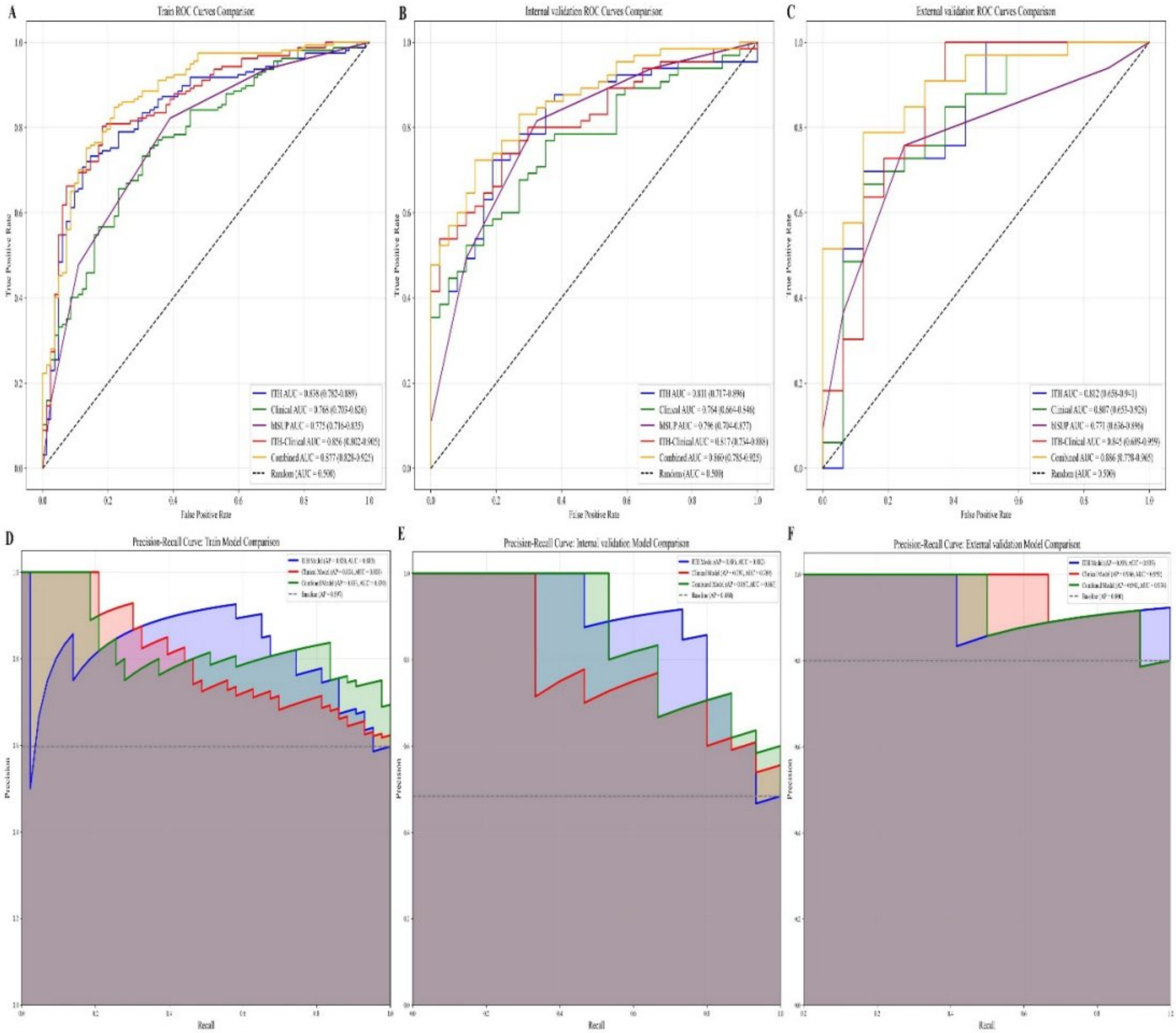

Keywords : Prostate cancer, ISUP grade, Habitat analysis

[GU Issues 2]

SS08-4

Evaluating the Clinical and Technical Impacts of PI-QUAL Scoring for Prostate MRI Quality Assessment: A Systematic Review

Kaiwen Cabbabe[1*], Yihan Li[2], Nathan Ng[3], Charles Li[1], Jyothirmayi Velaga[3]

[1]Radiology, Alfred Health, Australia
[2]Radiology, Peninsula Health, Australia
[3]Radiology, Northern Health, Australia

Prostate multiparametric MRI (mpMRI) is the recommended imaging modality in the diagnostic pathway of prostate cancer, aiding in detection, localisation, staging and risk stratification. High-quality mpMRI is crucial for guiding accurate diagnosis and management decisions. However, substantial variation in mpMRI quality persists across institutions, where acquisition protocols and reader expertise differ widely. To assist with this, the Prostate Imaging Quality (PI-QUAL) score was developed to standardise technical quality assessment of mpMRI. Given its landmark potential, an updated PI-QUAL v2 has also progressed its clinical adoption. Several studies have explored the clinical utility and reproducibility of PI-QUAL, but to date, no systematic review has evaluated the existing literature. This systematic review aims to assess PI-QUAL reproducibility, the factors influencing scoring accuracy, and its impact on diagnostic performance.

This PROSPERO-registered review was performed in accordance with the PRISMA 2020 guidelines. PubMed and Medline were searched for primary studies that assessed PI-QUAL in terms of inter-reader agreement, its relationship with PI-RADS scoring, and its impact on the diagnosis of clinically significant prostate cancer (csPCa) and tumour staging. Methodological quality was assessed using QUADAS-2.

A total of 35 studies were included (30 retrospective, 5 prospective). Inter-reader agreement was reported in 23 studies. Reader agreement was moderate (κ = 0.41-0.60) in 11 studies (47.8%). Stratifying for experience, among expert readers, agreement ranged from moderate to near-perfect (κ = 0.51–0.85), while less-experienced readers showed lower agreement (κ = 0.02–0.59). However, when a training or education programme was introduced before scoring, agreement across all reader groups improved to levels comparable with those of expert readers (κ = 0.58–0.96).

Six studies investigated the relationship between PI-QUAL and PI-RADS scores, of which four found a statistically significant relationship between higher PI-QUAL scores and more definitive PI-RADS calls.

Eleven studies reported a relationship between PI-QUAL and the diagnostic accuracy of csPCa. In nine studies, optimal image quality, as represented by PI-QUAL scores of 4 and 5, demonstrated clinically significant improvements in the ability to rule in or rule out csPCa. All five studies investigating the relationship between PI-QUAL and accurate prostate cancer staging reported that more precise staging is more likely in mpMRI cases that achieved higher PI-QUAL scores.

Three studies evaluated computer-based systems alongside PI-QUAL scoring - one AI tool, one browser-based program, and one deep-learning reconstruction algorithm. Results were heterogeneous, and no system consistently improved PI-QUAL scoring accuracy or reader agreement.

PI-QUAL is a reproducible and clinically meaningful tool that directly strengthens prostate mpMRI interpretation. High PI-QUAL scores improve PI-RADS confidence, increase csPCa detection accuracy, and enable more reliable staging. Structured training substantially improves reproducibility, supporting integration into clinical practice. As mpMRI quality varies widely across institutions, PI-QUAL provides a practical mechanism for standardising image quality. Future research should prioritise validating PI-QUAL v2 in multicenter prospective settings and defining how PI-QUAL can be integrated into clinical workflows. While AI-based tools show theoretical promise for automated quality assessment, current evidence remains limited and inconsistent, underscoring the need for further validation before routine clinical integration.

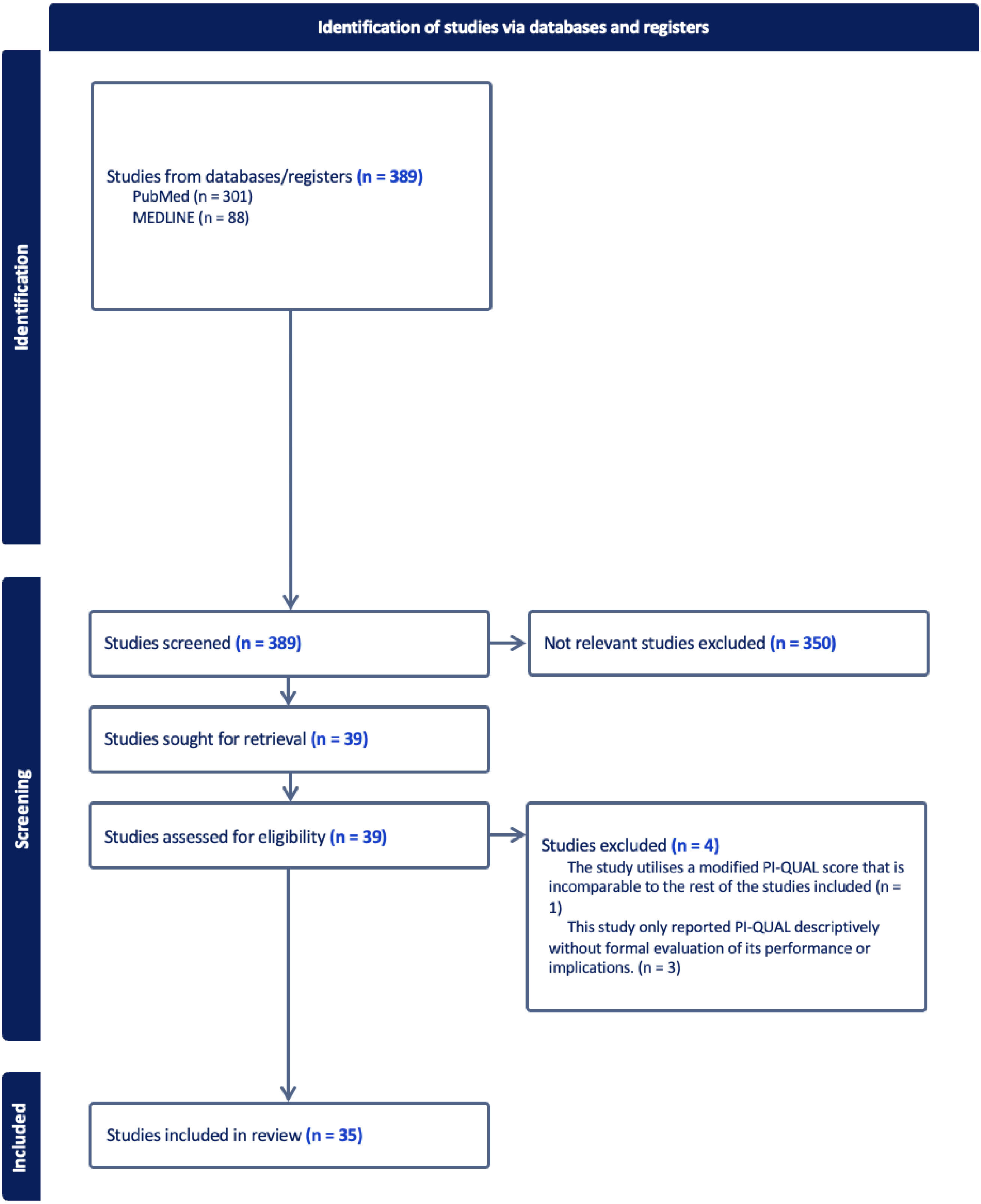

Figure 1: Preferred Reporting Items for Systematic Reviews and Meta-analyses flow diagram showing the outcome of the literature search resulting in the inclusion of full studies in the review.

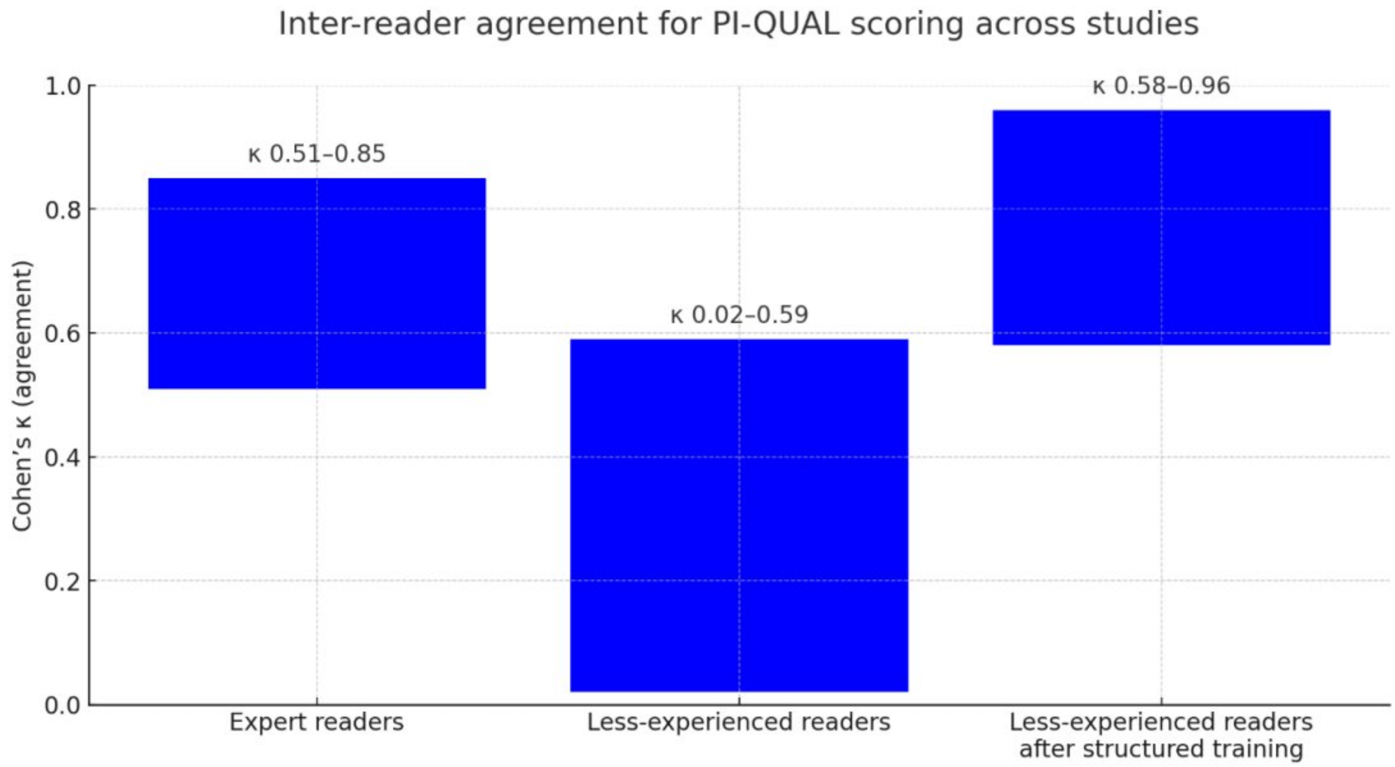

Figure 2: Cohen's κ agreement for PI-QUAL scoring across studies. Each bar spans the κ study range.

Keywords : Prostate MRI, Image Quality, Prostate Cancer

[GU Issues 2]

SS08-5

Clinical Evaluation of a Low-Concentration, Low-Voltage Protocol for Urothelial Phase Bladder CT

Yewon Lim[1], Hyo Jeong Lee[1*]

[1]Radiology, Ewha Womans University Mokdong Hospital, Korea

Iodinated contrast media–related renal toxicity is closely associated with total iodine dose. Reducing iodine concentration and radiation dose in CT may mitigate this risk without compromising diagnostic image quality. This study aimed to compare image quality between a low-concentration, low-voltage protocol and a standard protocol for urothelial phase bladder CT.

Patients who underwent bladder CT using a low-dose (LD) protocol (270 mgI/mL, 90 kVp) between April and July 2024 were retrospectively reviewed. Those with prior bladder CT using the standard-dose (SD) protocol (300 mgI/mL, 100 kVp) were included for paired comparison (n = 47). Qualitative image quality (overall quality, noise, artifact, sharpness, soft-tissue contrast, and lesion conspicuity) was assessed using a 5-point scale. Quantitative measurements of SNR and CNR were obtained from the urine, bladder wall, psoas, aorta, renal cortex, and medulla.

The LD protocol yielded an 11.2% reduction in radiation dose (11.1 ± 3.3 mSv vs. 12.5 ± 3.3 mSv, $p = 0.042$). Subjective image quality was comparable across all parameters, with slightly better soft-tissue contrast in LD ($p = 0.032$). Bladder wall SNR and CNR were non-inferior compared with the standard protocol (SNR: 4.51 ± 1.51 vs. 4.13 ± 0.61, Δ = +0.38, $p = 0.277$; CNR: 3.45 ± 1.45 vs. 3.10 ± 0.79, Δ = +0.35, $p = 0.388$). The LD protocol showed significantly higher SNR and CNR for the aorta and renal cortex.

The low-concentration, low-voltage bladder CT protocol demonstrated non-inferior image quality and diagnostic acceptability compared with the standard protocol, enabling meaningful dose reduction and potential mitigation of contrast-related renal toxicity.

Urothelial phase bladder CT images obtained from the same patient under similar bladder distension conditions. The low-dose (LD) protocol (270 mgI/mL, 90 kVp) shows higher contrast and clearer delineation of the bladder wall compared with the standard-dose (SD) protocol (300 mgI/mL, 100 kVp)

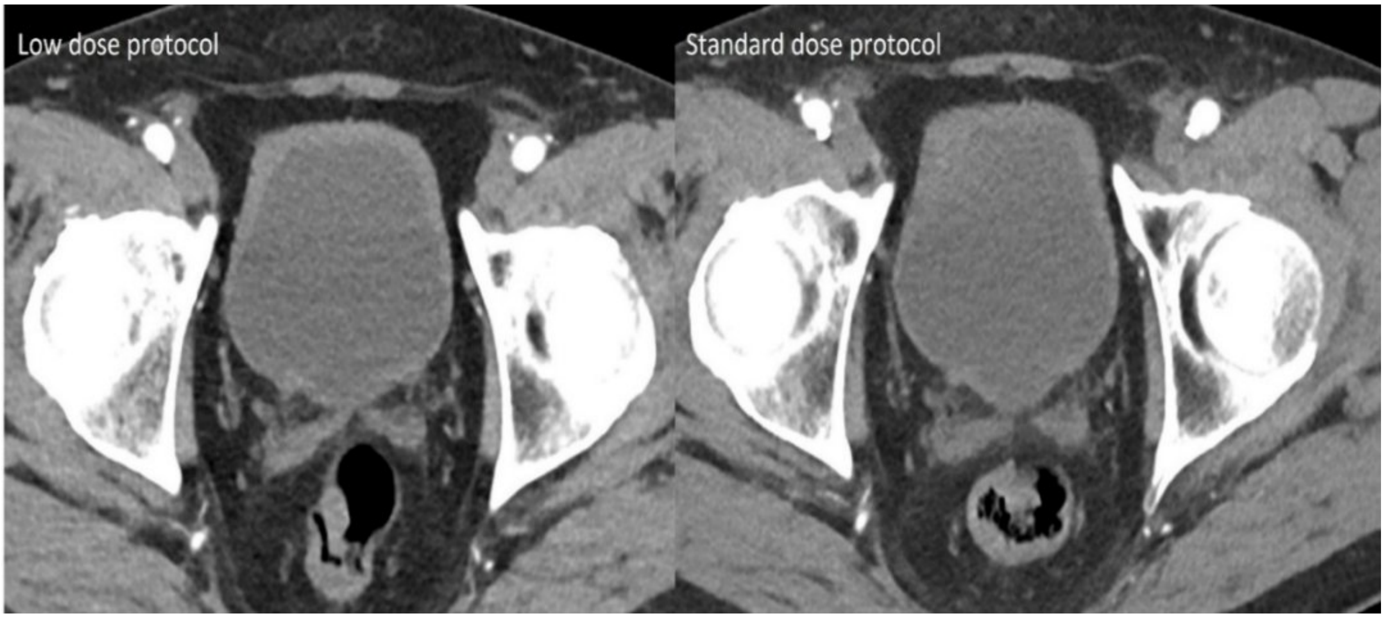

Keywords : CT, Contrast, Bladder

[GU Issues 2]

SS08-6

Correlation of MRI and Contrast Enhanced Ultrasound for O-RADS and Challenging Pelvic Mass Diagnosis

Xiaoyang Liu[1*]

[1]Medical Imaging, University of Toronto, Canada

Accurate characterization of pelvic masses is crucial in the diagnosis and management of pelvic malignancy. MR is the current gold standard for characterization of adnexal lesions; however, utility of MRI may be limited in certain clinical situations such as severe contrast allergy, impaired renal function, misregistration and susceptibility artifacts. Contrast enhanced ultrasound (CEUS) can complement MRI in these situations. This pictorial will explore appearance of benign and malignant lesions in female pelvis in MRI and contrast enhanced ultrasound, and provide case-based approach to O-RADS categorization. Correlation between MRI and CEUS for problem solving and discrepancies will be discussed to better understand the unique advantages and disadvantages of each imaging modalities.

CEUS is an ultrasound tool utilizing intravascular microbubble contrast to characterize lesions. Superior temporal resolution with real time dynamic scanning allows better assessment of subtle enhancement or nodularity. The O-RADS committee is currently working on including CEUS into the new version of O-RADS.

Here we present MRI and CEUS images for benign and malignant pelvic masses. Discussions will be made on condordance and discordance between the two imaging modalities, and how to problem-solve in problematic cases. We wil also discuss how CEUS can be helpful in confirming vascularity, differentiate between benign and malignant lesions in MRI challenging cases and accurate O-RADS categorization. We will also update the audience with recent literatures on this topic for evidence based practice.

Cases to be discussed will include:

1) Right ovarian dermoid with apparent enhancing nodular component on MRI. CEUS confirms no vascularity, suggesting findings on MR was a result of misregistration artifact on the subtraction images.

2) Endometrioma with eccentric nodular enhancing component concerning for malignant degeneration. Pathology proven endometroid adenocarcinoma.

3) Left hemorrhagic lesion with no solid enhancing component on MRI. CEUS confirms enhancing papillary projection. Pathology proven serous cystadenofibroma.

4) Young patient with positive bHCG. Initial ultrasound concerning for molar pregnancy. Patient underwent dilatation and curettage with ongoing bleeding. Post procedure follow up ultrasound shows similar appearance on greyscale. CEUS confirms the area is completely avascular

suggesting evolving avascular retained products.

5) Hemorrhagic cyst with CEUS confirming no internal vascularity.

6-10): One case of each O-RADS 1-5 adnexal lesions will be presented with MRI and CEUS images.

MRI and CEUS are complementary imaging modalities for characterization of adnexal lesions. CEUS can be a helpful adjunct to conventional ultrasound and MRI as a trouble shooting tool in assessment of pelvic masses.

Real time dynamic scanning adds value to static images for confirmation of vascularity.

Helps risk stratify patients to proper management groups depending on malignant potential of the lesion.

Keywords : Mass in female pelvis, MRI contrast enhanced ultrasound correlation, O-RADS

[GU Issues 2]

SS08-7

CT Indicators for Differentiation of Stage 1 Borderline Ovarian Tumors from Stage I Malignant Epithelial Ovarian Tumors

Soo Yeon Chae[2], Min Hoan Moon[1], Hee Sun Park[2], Young Jun Kim[2], Mi Hye Yu[2], Sungeun Park[2], Sung Il Jung[2*]

[1]Radiology, Seoul National University Seoul Metropolitan Government Boramae Medical Center, Korea
[2]Radiology, Konkuk University Medical Center Konkuk University School of Medicine, Korea

Preoperative diagnosis of borderline ovarian tumors (BOTs) is of increasing concern. This study is to assess computed tomography (CT) features in differentiating stage 1 BOTs from stage I malignant epithelial ovarian tumors (MEOTs).

One hundred seventy ovarian masses (97 BOTs and 73 MEOTs) of 141 consecutive patients who underwent preoperative CT imaging before surgery were retrospectively analyzed. Two readers independently and retrospectively reviewed quantitative and qualitative CT features. Multivariate logistic analysis was performed to identify CT features associated with BOTs compared to MEOTs. For the cases with solid component, subanalysis was conducted to further evaluate the relationship between features of solid component and tumor type.

Multivariate logistic analysis demonstrated that larger tumor size ($p < 0.03$ for reader 1, $p = 0.04$ for reader 2) and smaller solid component ($p = 0.0007$ for reader 1, $p = 0.003$ for reader 2) were significantly associated with BOTs compared with MEOTs. In the subanalysis for the cases with solid component, Smaller ($p = 0.01$ for reader 1, $p = 0.001$ for reader 2) and ill-defined ($p = 0.0016$ for reader 1, $p = 0.04$ for reader 2) solid component were significantly associated with BOTs compared with MEOTs.

The tumor size, the margin and size of component of the tumor were useful for differentiating stage 1 BOTs from stage 1 MEOTs on CT.

Keywords : Borderline ovarian tumor, Malignant epithelial ovarian tumor, Computed tomography

ACAR 2026

THE 13th ASIAN CONGRESS OF ABDOMINAL RADIOLOGY

Posters

POSTER PRESENTATION

MARCH 19 (Thu) ** Poster available for viewing throughout the congress.*

16:00-16:40 **Poster Presentation 1 (ISP Format)** (Eng.) Grand Round

Chair Jae Hyun Kim (Seoul National University College of Medicine, Seoul National University Hospital, Korea)

16:00-16:06 **Defecography by Digital Radiography: A Resident's Comprehensive Guide**
ABD-ISP-01 Veronica Elaine Suarez (St Lukes Medical Center - Global City, Philippines)

16:06-16:12 **DECT in Bowel Diseases: A Problem-Solving Tool!**
ABD-ISP-02 Ankur Goyal (All India Institute of Medical Sciences, New Delhi, India)

16:12-16:18 **Exploring Vascular Etiologies of Abdominal Pain with Contrast Enhanced Computed Tomography Scan: A Pictorial Essay**
ABD-ISP-03 Mark Nicholas Reyes (Metropolitan Medical Center, Philippines)

16:18-16:24 **An Oral Dual-Loaded Nanoplatform for CT-Guided, Multi-Modal Therapy of Inflammatory Bowel Disease: Development and Preclinical Evaluation**
ABD-ISP-04 Deepika Singh (SIHAS, India)

16:24-16:40 **Discussion (Q&A)**

16:00-16:40 **Poster Presentation 1** (Eng.) Grand Round

POSTER PRESENTATION

MARCH 19 (Thu) ** Poster available for viewing throughout the congress.*

ABD-Liver-01

Imaging Spectrum of Diffuse Liver Disease

Zhong Yun Lee[1*], Jingli Chong[1], Hsien Min Low[1]
[1]Radiology, Tan Tock Seng Hospital, Singapore

ABD-Liver-02

Safety Profile and Management of Complications After Ablative-Dose Yttrium-90 Resin Microsphere Radioembolisation for Hepatocellular Carcinoma in an Asian Cohort

Hian Liang Huang[1*], Han Chung Low[1], Aaron Kian Ti Tong[1], Kelvin Siu Hoong Loke[1], Si Xuan Koo[1]
[1]Nuclear Medicine and Molecular Imaging, Singapore General Hospital, Singapore

ABD-Liver-03

Imaging Findings Following Yttrium-90 Radioembolisation for Hepatocellular Carcinoma: CT and MRI Appearances with Emphasis on LI-RADS v2024 Treatment Response Categories

Rachel Wei Lian Loh[1*], Jingli Chong[1], Christine Ying Kwok[1], Hsien Min Low[1]
[1]Diagnostic Radiology, Tan Tock Seng Hospital, Singapore

ABD-Liver-04

The Prognostic Impact of MRI Features on Recurrence and Survival after Resection of Hepatocellular Carcinoma is Dependent on Follow-up Time

Fujing Shi[1], Hanyu Jiang[1*]
[1]Radiology, West China Hospital Sichuan University, China

ABD-Liver-05

Imaging Differentiation of Small and Large Duct Intrahepatic Cholangiocarcinoma: CT and MRI Case Review, Imaging Features and Clinical Implications

Anuja Satish Bhave[1*], Christine Kwok[1]
[1]Radiology, National Healthcare Group, Singapore

ABD-Liver-06

Clinicopathologic, MRI and Prognostic Features of Intrahepatic Cholangiocarcinoma According to Cirrhosis Status

Yong Jun Jung[1], Dong Hwan Kim[1*], Sang Hyun Choi[1]
[1]Radiology, Asan Medical Center University of Ulsan College of Medicine, Korea

ABD-Liver-07

Imaging Spectrum of Giant Hepatic Hemangioma with Diffuse Hepatic Hemangiomatosis: Three Case Series

Hyunyu Kang[1], Ki Choon Sim[1*], Min Ju Kim[1], Beom Jin Park[1], Deuk Jae Sung[1], Na Yeon Han[1], Yeo Eun Han[1], Seong Ha Cha[1]
[1]Radiology, Korea University Anam Hospital, Korea

ABD-Liver-08

MRI Features of Sarcomatoid Biliary Carcinomas: An Analysis of Seven Cases Across the Hepatobiliary System

Hao Wu[1], Zheng Zhu[1*], Chunfang Hu[2], Xinming Zhao[1]
[1]Diagnostic Radiology, National Cancer CenterNational Clinical Research Center for CancerCancer Hospital Chinese Academy of Medical Sciences and Peking Union Medical College, China
[2]Pathology, National Cancer CenterNational Clinical Research Center for CancerCancer Hospital Chinese Academy of Medical Sciences and Peking Union Medical College, China

ABD-Liver-09

A Systematic Approach to Focal Liver Lesions from a Radiological Perspective: A Diagnostic Algorithm Utilizing Arterial Phase Enhancement Patterns

Duc Vo Tan[1], Huyen Le Duy Mai[1*], Hy Le Nguyen Gia[1], Phuong Nguyen Nguyen[1], Nhi Nguyen Thi Yen[1], Thuy Do Thi Thanh[1], Duy Nguyen Thanh[1], Viet Tran Doan Khac[1]
[1]Radiology, University Medical Center, Vietnam

POSTER PRESENTATION

MARCH 19 (Thu)

** Poster available for viewing throughout the congress.*

ABD-Pancreas-01

Dual-Phase CT-Based Explainable Radiomics Capturing Spatial-Temporal Heterogeneity for Three-Class Grading and Prognostic Prediction in Pancreatic Neuroendocrine Neoplasms:A Multicenter Retrospective–Prospective Study

Weinuo Qu[1], Chenxi Lyu[1], Chuhuai Wang[1], Jiali Li[1], ShaSha Li[2], Feng Li[3], Zhen Li[1*]
[1]Radiology, Tongji Hospital Tongji Medical College Huazhong University of Science and Technology, China
[2]Radiology, Shanxi Bethune Hospital, China
[3]Radiology, Xiangyang Central Hospital, China

ABD-Biliary-01

SPECT/CT Rules out Bile Leak After Near False-Positive on HIDA Planar Imaging in Complex Postsurgical Abdominal Anatomy

Daniel Kim[1*]
[1]Diagnostic Radiology, The Hospital of the University of Pennsylvania, USA

ABD-Biliary-02

Pictorial Review of Biliary Dilatation in The Context of Malignancy, Focusing on Less Common Pathologies

Yi Ting Lim[1*], Christine Ying Kwok[1]
[1]Diagnostic Radiology, Tan Tock Seng Hospital, Singapore

ABD-Biliary-03

Common Bile Duct Ascariasis

Munkh-Orgil Rentsensambuu[1], Nemekhbayar Purevsuren[1*], Munkhtulga Enkhtur[1]
[1]Radiology, Second State Central Hospital, Mongolia

ABD-CT-01

Correlation between DXA and Hounsfield Unit in Lumbar Spine CT Scan

Munkh-Orgil Rentsensambuu[1], Enkhjargal Davkharbayar[1], Ankhbayar Enkhbaatar[2], Nemekhbayar Purevsuren[3], Munkhtulga Enkhtur[1], Batbayar Ankhjargal[1], Baasanjav Natsag[1], Otgontuya Tsendjav[1], Erdenebulgan Batmunkh[1*]
[1]Diagnostic center SSCH, Radiology, Mongolia
[2]Neurological Surgery - SSCH, Neurological Surgery, Mongolia
[3]Nuclear medicine Center SSCH, Nuclear Medicine, Mongolia

ABD-UGI-01

From Stability to Catastrophe: Evolving Traumatic Diaphragmatic Hernia with Intrathoracic Gastric Volvulus and Perforation in a Teenager

Hui Yun Ong[1,2], Wei Hung Chong[3], Sabariah Mohamed Kassim[2], Rafidah Zainon[4*]
[1]Radiology, School of Medical Sciences Universiti Sains Malaysia, Malaysia
[2]Radiology, Hospital Sultan Abdul Halim, Malaysia
[3]Paediatrics, Hospital Sultanah Bahiyah, Malaysia
[4]Biomedical Imaging, Advanced Medical and Dental Institute Universiti Sains Malaysia, Malaysia

ABD-UGI-02

Baseline DCE-MRI Derived Parameters and MR Signal Intensity Based Logistic Regression Model to Predict Response of Esophageal Squamous Cell Carcinoma to Neoadjuvant Immunochemotherapy

Jingke Li[2], Xurui Liu[1], Tianwu Chen[1*]
[1]Radiology, The Second Affiliated Hospital of Chongqing Medical University, China
[2]Radiology, Affiliated Hospital of North Sichuan Medical College, China

ABD-LGI-02

Spatial Mapping of Tumor Response and Mesorectal Involvement on Pretreatment Contrast-Enhanced CT in Locally Advanced Rectal Cancer

Huiyu Gan[2], Zhen Li[1], Ziman Xiong[1], Ziling Zhou[1*]
[1]Radiology, Tongji Hospital Tongji Medical College Huazhong University of Science and Technology, China
[2]Radiology, Tongji Medical College Huazhong University of Science and Technology, China

POSTER PRESENTATION

MARCH 19 (Thu) ** Poster available for viewing throughout the congress.*

ABD-LGI-03

The Accuracy and Reliability in Detection of Radiologic Signs of Acute Appendicitis Using CT Images Sent Via Mobile Phone Application in Comparison with Medical Grade Workstation Monitor

Vic Emile Bernabe[1*]
[1]*Radiology, Fellow, Philippines*

ABD-Others-01

Apart from Appendicitis: Pictorial Review of Iliac Fossa Pain

Emma Choon Hwee Lee[1*], Rebekah Zhuyi Lee[1], Shuyi Guo[1], Edmond Yang Shan Lim[1], Albert Su Chong Low[1]
[1]*Cardiothoracic and Abdominal Radiology, Singapore General Hospital, Singapore*

ABD-Others-02

Evaluating the Educational Impact of a CT Post-Processing Workshop

Samantha Tan[1*], Shawn Kok[1], Uppaluri Anandswaroop[1], Min-On Tan[1]
[1]*Diagnostic Radiology, Sengkang General Hospital, Singapore*

GU-Uro-01

One-stop Early Noninvasive Evaluation of Renal Allograft Rejection and Fibrosis: Microstructural Mapping via Time-dependent Diffusion MRI

Zhouyan Liao[1], Xiaonan Yang[1], Siyuan Ma[1], Gen Chen[1], Jeong Min Lee[2], Zhen Li[1*]
[1]*Radiology, Tongji Hospital Tongji Medical College Huazhong University of Science and Technology, China*
[2]*Radiology, Seoul National University Hospital, Korea*

GU-Uro-02

Nutcracker Syndrome with Midline Congestion Syndrome and May-Thurner Syndrome: Pathophysiology, Imaging Findings, and Postural Therapeutic Implications

Seung Hyup Kim[1,2,3*], Hyo Jeong Lee[1], Suhnggwon Kim[2], Eungtaek Kang[2], Myung Kim[3], Sang Eun Lee[3], Young Ik Lee[3]
[1]*Radiology, Ewha Womans University Mokdong Hospital, Korea*
[2]*Radiology, Seoul K Nephrology Clinic, Korea*
[3]*Radiology, SNU Healthy Prostate Clinic, Korea*

GU-Uro-03

Integrating Peritumoral Radiomics Improves Preoperative Staging of Clear Cell Renal Cell Carcinoma

Shichao Li[1], Chuhuai Wang[2,3], Mengmeng Gao[1], Kangwen He[1], Zhen Li[1*]
[1]*Radiology, Tongji Hospital of Tongji Medical College of Huazhong University of Science and Technology, China*
[2]*Oncology, Tongji Hospital of Tongji Medical College of Huazhong University of Science and Technology, China*
[3]*MOE Key Laboratory for Biomedical Photonics, Wuhan National Laboratory for Optoelectronics of Huazhong University of Science and Technology, China*

GU-Uro-04

Deep Learning-Based Prediction of Lymph Node Invasion in High-Risk Non-Metastatic Prostate Cancer: Incremental Value of Periprostatic Adipose Tissue

Kangwen He[1], Zhen Li[1*]
[1]*Radiology, Tongji Hospital Tongji Medical College Huazhong University of Science and Technology, China*

GU-Uro-05

Association Between PI-RADS Score and Cancer Detection in Template-Based Transperineal Systematic Prostate Biopsy: Experience from a Rural Single-Center Practice

Leonardo Chung[1], James Sopkin[2], Steve Chung[1*]
[1]*Urology, Illinois Urologic Health Surgeons, USA*
[2]*Statistics, Georgia Institute of Technology, USA*

GU-Uro-06

Prediction of Adverse Pathology in Prostate Cancer Using a Multimodal Habitat Analysis Based on [18F] PSMA-1007 PET/CT and Multiparametric MRI

Yunjun Yang[1], Haoli Xu[1], Shuying Bian[1], Licong Li[1], Cunke Miao[2], Zhifang Pan[2], Heng Lin[2*]
[1]*Radiology, The First Affiliated Hospital of Wenzhou Medical University, China*
[2]*The First School of Medicine School of Information and Engineering, The First Affiliated Hospital of Wenzhou Medical University, China*

POSTER PRESENTATION

MARCH 19 (Thu)

** Poster available for viewing throughout the congress.*

GU-Uro-07

Diagnostic Validity and Inter-reader Reproducibility of the PI-FAB System for Detecting Local Recurrence Following Irreversible Electroporation of Prostate Cancer

Yu Ri Shin[1*], Bohyun Kim[1], Hokun Kim[1], Seo Yeon Youn[1], Sung Eun Rha[1]
[1]Radiology, Seoul St Mary's Hospital, Korea

GU-Uro-08

MRI-Pathology Sizing Discordance in Prostate Cancer: A Lesion-Based Analysis

Honghao Xu[1], Xiaohui Ding[2], Baichuan Liu[1], Xu Bai[1], Jian Zhao[3], Haiyi Wang[1*]
[1]Radiology, First Center of Chinese PLA General Hospital, China
[2]Pathology, First Center of Chinese PLA General Hospital, China
[3]Radiology, Second Center of Chinese PLA General Hospital, China

GU-Uro-10

Rad-VI-RADS: A Fused Radiomics and VI-RADS Model for Improved Detection of Muscle-Invasive Bladder Cancer

Haili Liu[1,2], Yuanhao Ma[1], Huiping Guo[1], Tianran Li[2], Jian Zhao[3], Haiyi Wang[1*]
[1]Radiology, First Medical Center Chinese PLA General Hospital, China
[2]Radiology, Fourth Medical Center Chinese PLA General Hospital, China
[3]Radiology, Second Medical Center Chinese PLA General Hospital, China

POSTER PRESENTATION

MARCH 20 (Fri) ** Poster available for viewing throughout the congress.*

15:50-16:30 Poster Presentation 2 (ISP Format) (Eng.) — Grand Round

Chair: Dong Hwan Kim (University of Ulsan College of Medicine, Asan Medical Center, Korea)

15:50-15:56
ABD-ISP-05
3D Gradient and Spin-Echo MRCP with Deep Learning Reconstruction at 3T: Achieving Non-Inferior Image Quality with Reduced Acquisition Time
Kumi Ozaki (Hamamatsu University School of Medicine, Japan)

15:56-16:02
ABD-ISP-06
Super-Resolution Deep Learning Reconstruction for Three-Dimensional T1-weighted Gradient Echo Imaging in Gadoxetic Acid-Enhanced MRI: Comparison with Conventional and Deep Learning Reconstructions
Kazuma Tsukamoto (Kobe University Hospital, Japan)

16:02-16:08
ABD-ISP-07
Imaging Findings In Early Pancreatic Adenocarcinoma - When the Duct Speaks First
Xinyi Wong (Tan Tock Seng Hospital, Singapore)

16:08-16:14
ABD-ISP-08
Gd-EOB-DTPA-Enhanced MRI for Differentiation of Scirrhous Hepatocellular Carcinoma and Intrahepatic Cholangiocarcinoma in an HBV-Infected Cohort: A bi-center study
Haoran He (The Fourth Affiliated Hospital of Soochow University Suzhou, China)

16:14-16:20
ABD-ISP-09
Diversity of Imaging Features in Intrahepatic Mass-forming Cholangiocarcinoma Across Different Background Liver Conditions
Kazuto Kozaka (Kanazawa University Hospital, Japan)

16:20-16:30
Discussion (Q&A)

15:50-16:30 Poster Presentation 2 (Eng.) — Grand Round

POSTER PRESENTATION

MARCH 20 (Fri) ** Poster available for viewing throughout the congress.*

ABD-Liver-10

Interpreting LI-RADS CEUS Nonradiation TRA v2024: Practical Tips, Pitfalls, and Diagnostic Pearls

Jeremy Jia Qi Soon[1*], Jia Ren Perry Liew[1], Jeremy Jia Hong Lam[1], Wey Chyi Teoh[1]
[1]Radiology, Changi General Hospital, Singapore

ABD-Liver-11

Prognostic Value of Arterial Enhancement Fraction in Unresectable Hepatocellular Carcinoma Following Conversion Therapy

Xinrui Zhou[1], Bin Song[1*]
[1]Radiology, West China Hospital Sichuan University, China

ABD-Liver-12

Deep Learning for Preoperative Microvascular Invasion Prediction in Hepatocellular Carcinoma: A Systematic Review and Meta-Analysis

Bin Song[1*], Zhanfei Tian[1]
[1]Radiology, West China Hospital Sichuan University, China

ABD-Liver-13

Imaging Features of Hepatic Epithelioid Hemangioendothelioma: Two Rare Case Reports and Literature Review

Anh Nguyen Quynh[1*]
[1]Radiology, Hanoi Medical University, Vietnam

ABD-Pancreas-02

Unmasking the Mimics of Pancreatic Cancer

Ankur Goyal[1*], Raju Sharma[1], Krishna Kumar R G[1], Piyush Agarwal[1]
[1]Radiodiagnosis and Interventional Radiology, All India Institute of Medical Sciences New Delhi, India

ABD-Pancreas-03

Integrating Systemic Metabolic Profiles and Dual-Phase CT-Based Habitat Radiomics via Vision Transformer for Predicting the Aggressiveness of Pancreatic Neuroendocrine Neoplasms: A Multicenter Study

Weinuo Qu[1], Chenxi Lyu[1], Zhibo Wang[1], Jiali Li[1], ShaSha Li[3], Feng Li[2], Zhen Li[1*]
[1]Radiology, Tongji Hospital Tongji Medical College Huazhong University of Science and Technology, China
[2]Radiology, Xiangyang Central Hospital, China
[3]Radiology, Shanxi Bethune Hospital, China

ABD-Pancreas-04

Deep Learning-Accelerated Respiratory-Triggered 3D MR Cholangiopancreatography: Sub-Minute Acquisition with Preserved Image Quality

Naoki Yoshida[1,2], Keitaro Sofue[1*], Kazuma Tsukamoto[2], Tomohiro Noda[2], Tatsuya Nishitani[2], Shintaro Horii[2], Yuichiro Somiya[1,2], Akiko Kusaka[2], Tetsuya Wakayama[3], Xucheng Zhu[4], Ty Cashen[5], Takeru Yamaguchi[1], Yoshiko Ueno[1], Takahiro Tsuboyama[1], Izumi Imaoka[1], Takamichi Murakami[1]
[1]Ragiology, Kobe University Graduate School of Medicine, Japan
[2]Center for Radiology and Radiation Oncology, Kobe University Hospital, Japan
[3]MR Clinical Solutions and Research Collaborations, GE HealthCare, Japan
[4]MR Clinical Solutions and Research Collaborations, GE HealthCare, CA, USA
[5]MR Clinical Solutions and Research Collaborations, GE HealthCare, WI, USA

ABD-Biliary-04

Association of Gallbladder Polyps with Intercurrent Degree of Hepatic Steatosis in Patients Who Underwent Abdominal Sonography in a Tertiary Hospital – A Retrospective Study

Charlene Noelle Duante[1], Maynard Redor[1*]
[1]Radiology, FEU-NRMF, Philippines

ABD-UGI-03

Tumor Subregion-based CT Habitat Radiomics to Improve Prediction of Nodal Disease in Esophageal Squamous Cell Carcinoma

Hao Wen[1], Tian-wu Chen[1*], Xu-rui Liu[1]
[1]Radiology, The Second Affiliated Hospital of Chongqing Medical University, China

POSTER PRESENTATION

MARCH 20 (Fri) ** Poster available for viewing throughout the congress.*

ABD-LGI-04

Temporal AI-assisted Compressed Sensing Enables High-resolution, Motion-robust Small-bowel MR Enterography without Antiperistaltic Agents

Ziman Xiong[1*], Xiaopeng Song[2], Wei Mao[2], Zhen Li[1], Yaqi Shen[1]
[1]Radiology, Tongji Hospital of Tongji Medical College of HUST, China
[2]United Imaging Healthcare, China

ABD-LGI-05

Deep Learning–Accelerated Magnetic Resonance Enterography for the Assessment of Crohn's Disease

Sohyun Park[1*]
[1]Radiology, Seoul National University Bundang Hospital, Korea

ABD-LGI-06

CT Utilization in Diagnosing Atypical Causes of Small Bowel Obstruction in the Emergency Room: A Case Series

Jose Ricardo Samson[1], Ma Lourdes Badion[1*]
[1]Radiology, Metropolitan Medical Center, Philippines

ABD-LGI-07

Review of Gastrointestinal Involvement in Vasculitis: Imaging and Biomarker Perspectives

Yaqi Shen[1], Jiayi Li[1*]
[1]Radiology, Tongji Hospital Affiliated with Tongji Medical College of Huazhong University of Science and Technology, China

ABD-LGI-08

Effectiveness of Deep-Learning-Based Denoising Software on Image Quality and Diagnostic Performance of Low-Dose Abdominal CT for evaluation of Acute Appendicitis

Young Hwan Lee[1], Cheonghwan Shin[1], Youe Ree Kim[1]*
[1]Radiology, Wonkwang University Hospital, Korea

ABD-CT-02

Manifestations of Tuberculosis in the Abdomen: A Pictorial Review with Corresponding CT Cases

Phoebe Hay Pui Yeung[1*], Christine Tang[1], Chi Man Chau[1], Lik Fai Cheng[1]
[1]Diagnostic and Interventional Radiology, Princess Margaret Hospital, Hong Kong, China

ABD-Others-03

Vascular or Lymphoid? The Role of Temporal Evolution in Differentiating Splenic Mass Lesions – A Local Case Series

Xu Hao Isaac Tan[1*], Shawn Shi Xian Kok[2], Srinivas Anandswaroop Uppaluri[1], Sandeep Venkatesh Halagatti[1], Aftab Syed[1], Srujana Ganti[1], Sze Ying Yee[1], Yogendra Praveen Mogan[1], Freda Jawan[1], Min On Tan[1]
[1]Radiology, Sengkang General Hospital, Singapore
[2]Radiology, Parkway Radiology, Singapore

ABD-Others-04

Bladder Wall and Rectus Sheath Hematomas as Rare Hemorrhagic Manifestations of Dengue Fever: Importance of CT for Accurate Diagnosis

Abigail Christie[1], Taufik A Wibowo[1,2*]
[1]Radiology, Cipto Mangunkusumo General Hospital Universitas Indonesia, Indonesia
[2]Abdominal Radiology, Cipto Mangunkusumo General Hospital Universitas Indonesia, Indonesia

ABD-Others-05

Wet vs. Dry, Two Faces of Mimicry: Case Series on Tuberculous Peritonitis and Complications

Jose Rafael M. Aldaba[1], Josefina Marie Medina[2*]
[1]Radiology, St. Luke's Medical Center Quezon City, Philippines
[2]Consultant, St. Luke's Medical Center Quezon City, Philippines

ABD-Others-06

When to Suspect Systemic Vasculitis on Abdominal CT?

Raju Sharma[1*], Ankur Goyal[1], Sanchita Gupta[1], Rajendra Behera[1], Shivanand Gamanagatti[1]
[1]Radiology, All India Institute of Medical Sciences, India

POSTER PRESENTATION

MARCH 20 (Fri) ** Poster available for viewing throughout the congress.*

ABD-Others-07

Beyond Active Bleeding: CTA-Guided Culprit Artery Mapping for Targeted Embolization in Acute Gastrointestinal Bleeding.

Viet Tran Doan Khac[1*], Triet Pham Ngoc Minh[1], Viet Dang Quoc[1], Huyen Le Duy Mai[1], Hy Le Nguyen Gia[1], Duc Vo Tan[1], Bac Nguyen Hoang[1]
[1]*Radiology, University Medical Center Ho Chi Minh City, Vietnam*

GU-Uro-11

Fused Pelvic Kidney: A Rare Congenital Fusion Anomaly and Diagnostic Challenge

Mary Grace Yamson[1*]
[1]*Medical Imaging and Therapeutic Radiology, National Kidney and Transplant Institute, Philippines*

GU-Uro-12

Autosomal Recessive Polycystic Kidney Disease in Fraternal Twins: A Case Report with Radiological Review

Raissa Guldam[1], Riza Marquez-Planta[1*]
[1]*Medical Imaging and Therapeutic Radiology, Resident, Philippines*

GU-Uro-13

MRI-based Interpretable Habitat Radiomics for Assessing Synchronous Metastatic Risk in Renal Cell Carcinoma: A Multicenter Study

Xu Bai[1], Haiyi Wang[1*]
[1]*Radiology, Chinese PLA General Hospital, China*

GU-Uro-14

A 11-year Cohort Study Assessing the Management and Outcomes of Renal Injury Focusing on Renal Artery Embolisation at a Level 1 Trauma Centre

Kaiwen Cabbabe[1*], Saman Salaran[1], Samyak Shah[1], Kim Quach[1], Warren Clements[1], Matthew Lukies[1]
[1]*Interventional Radiology, Alfred Health, Australia*

GU-Uro-15

Coexistence of Chromophobe Renal Cell Carcinoma and Perirenal Lipomatous Angiomyolipoma: A Case Report

Jin Yunfeng[1*], Cui Mengqiu[2], Ren Shoujun[1], Li Yuan[1], Yu Pingnian[1], Wang Haiyi[2]
[1]*CT and MRI, Tonghua Central Hospital, China*
[2]*Radiology, The Seventh Medical Center of Chinese PLA General Hospital, China*

GU-Uro-16

Metanephric Adenoma - A Rare Case Report and Literature Review

Linh Tran Thi[1*]
[1]*Radiology, Hanoi Medical University, Vietnam*

GU-Uro-17

Congenital Megacalycosis with Megaureter: A Rare Masquerader of Obstructive Uropathy

Justin Seah[1*], Shawn Kok[2], Min On Tan[1]
[1]*Radiology, Singapore Health Services, Singapore*
[2]*Radiology, Parkway Radiology, Singapore*

GU-Uro-18

A Novel Decision Tree Model Integrating Morphology Variations, ADC ratio and VI-RADS for Detecting Muscle Invasion in Bladder Cancer

Yuanhao Ma[1], Haili Liu[1], Yijian Chen[1], Honghao Xu[1], Xu Bai[1], Jian Zhao[1], Xiaohui Ding[2], Haiyi Wang[1*]
[1]*Radiology, First Medical Center of Chinese PLA General Hospital, China*
[2]*Pathology, First Medical Center of Chinese PLA General Hospital, China*

GU-OBGY-01

Rapidly Enlarging Uterine Mass in a Postmenopausal Breast Cancer Survivor : Differentiating Leiomyosarcoma from Degenerated Leiomyoma

Muhammad Arief Saputra[1*], Trifonia Pingkan Siregar[1], Hanna Dwi Wiranti[1], Adinda Amalia[2], Adila Salsabila[1], Rais Izzan Basyari[1]
[1]*Radiology, Department of Radiology Faculty of Medicine Universitas Indonesia, Indonesia*
[2]*Internal Medicine, Department of Internal Medicine Faculty of Medicine Universitas Indonesia, Indonesia*

POSTER PRESENTATION

MARCH 20 (Fri) ** Poster available for viewing throughout the congress.*

GU-OBGY-02

Massive Ovarian Edema on MRI with Clinicopathologic Correlation

Sung Bin Park[1*], Mi Yeon Park[1], Kye Jin Park[1], Mi-Hyun Kim[1], Jeong Kon Kim[1]
[1]Radiology, Asan Medical Center, Korea

GU-OBGY-03

Bumps and Bellyaches: Unmasking Non-Obstetric Mimics of Acute Abdominal Pain in Pregnancy

Ying Jie Toh[1*], Wenwen Ni[1], Elizabeth Chen[1], Thida Win[1]
[1]Diagnostic and Interventional Imaging, KK Women's and Children's Hospital, Singapore

ACAR 2026

THE 13th ASIAN CONGRESS OF ABDOMINAL RADIOLOGY

Poster Presentation

Mar. 19 (Thu.)

! Abstracts can be found by searching with the Presentation Code !

[Poster Presentation 1 – ISP Format]

ABD-ISP-01

Defecography by Digital Radiography: A Resident's Comprehensive Guide

Veronica Elaine Suarez[1], Rafael Maria Benjamin Echevarria[1*], Franklin Lee[1], Stacey Danica Gosiaco[1], Lourdjeanne Luces-Clemente[1], Seth Gabriel Estanislao[1]

[1]Radiology, St Lukes Medical Center - Global City, Philippines

Defecography, or evacuation proctography, is a useful imaging technique for diagnosing anorectal and pelvic floor disorders, providing a dynamic, real-time evaluation of structure and function. It plays a crucial role in assessing conditions like chronic constipation, fecal incontinence, and rectal prolapse, while also aiding surgical planning. Compared to MRI defecography, fluoroscopic defecography is a more accessible and affordable tool which can still reliably evaluate gravity-dependent and dynamic evacuation in a natural seated position.

This guide synthesizes technical expertise with clinical relevance, offering a comprehensive framework for residents to effectively perform, interpret, and generate detailed reports for defecography that ultimately support the timely and effective management of various anorectal and pelvic floor disorders.

This guide covers the basics of proper image acquisition, including equipment preparation, patient positioning, and scanning technique, while outlining general indications and contraindications for safe study execution. It demonstrates normal anatomy and physiological function during dynamic phases such as straining, resting, and evacuation, providing a baseline for interpretation. Additionally, the text defines essential diagnostic landmarks—specifically the anorectal angle, puborectalis sling, and pelvic floor measurements—and concludes by presenting case examples that emphasize the diagnostic utility of defecography in detecting various anorectal and pelvic floor abnormalities.

Defecography is an indispensable tool for diagnosing complex pelvic floor disorders and aiding in surgical planning. By mastering the acquisition and interpretation techniques presented in this guide, residents can generate detailed, clinically valuable reports that support the timely and effective management of anorectal conditions.

Normal Appearance of the Rectum and Pelvic Floor

- **At rest:** The rectum shows posterior convex rounding parallel to the sacrum. Anal canal is closed. Anorectal angle measures 70-140 degrees. The pelvic floor is located within a few centimeters of the pubococcygeal line
- **During squeezing:** The anorectal junction is pulled anterosuperiorly. The anorectal angle is more acute compared to the resting state. Shortening of the anal canal

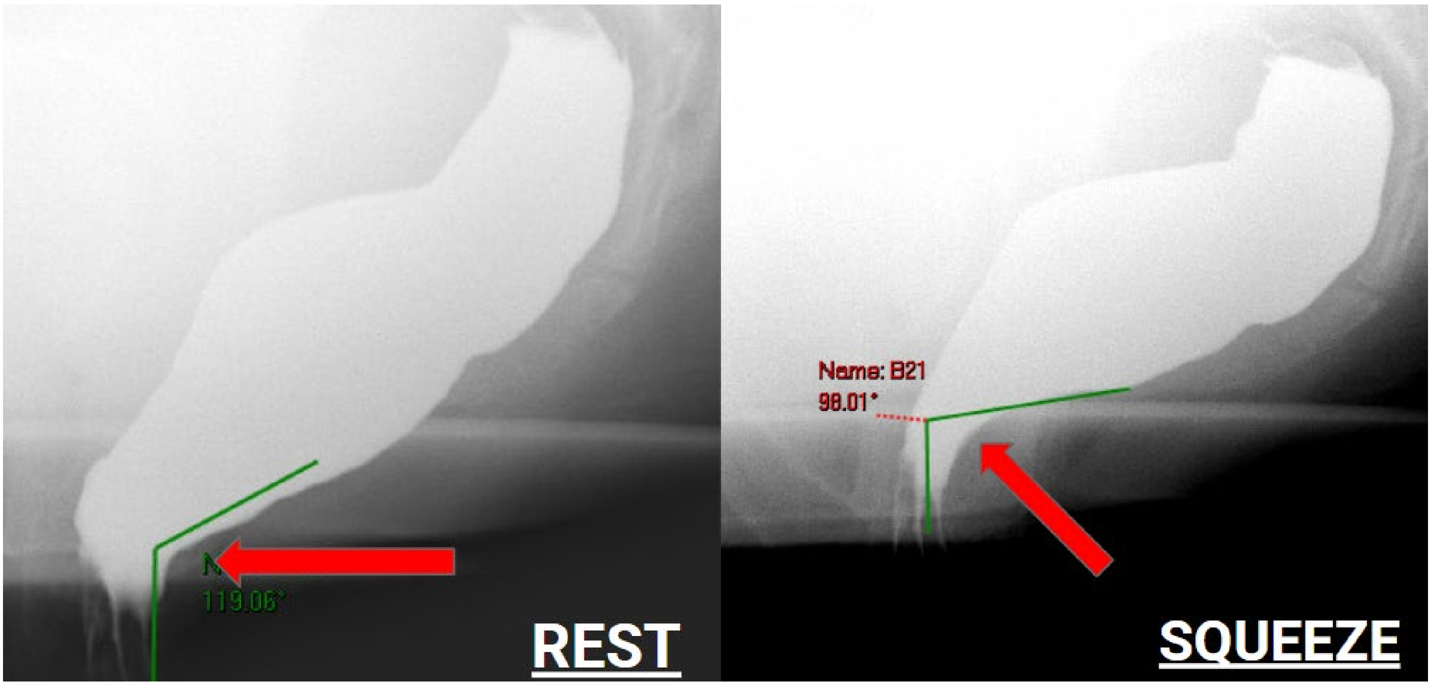

A female patient came in due to constipation.

- **During the resting phase:** There is a normal anorectal angle, albeit higher than average. The anorectal junction lies just above the ischiococcygeal line, denoted by the thin red line and the inferior ischium margin shown by the red arrow. The green and yellow circles reflect the imaged coccyx and anorectal junctions respectively.
- **During the straining phase:** There is further widening of the anorectal angle with descending rectum, causing obscuration of the ischium. At the lowest point of the anorectal junction, it measured 3.7 cm below the starting point at rest.
- **During the evacuation phase**: A focal prominent protrusion is noted along the anterior low rectal wall bulging into the anterior pelvic region
- **During the post-evacuation phase:** Retained contrast material can still be seen in the outpouching, with better delineation of the ischiococcygeal line (red line) far above the anorectal junction.

Overall, these findings are reflective of a **rectocele**. With the presence of a widened anorectal angle at both rest and straining maneuvers, as well as undue caudal migration of the anorectal junction, the diagnosis of a probable **descending perineum syndrome** was made.

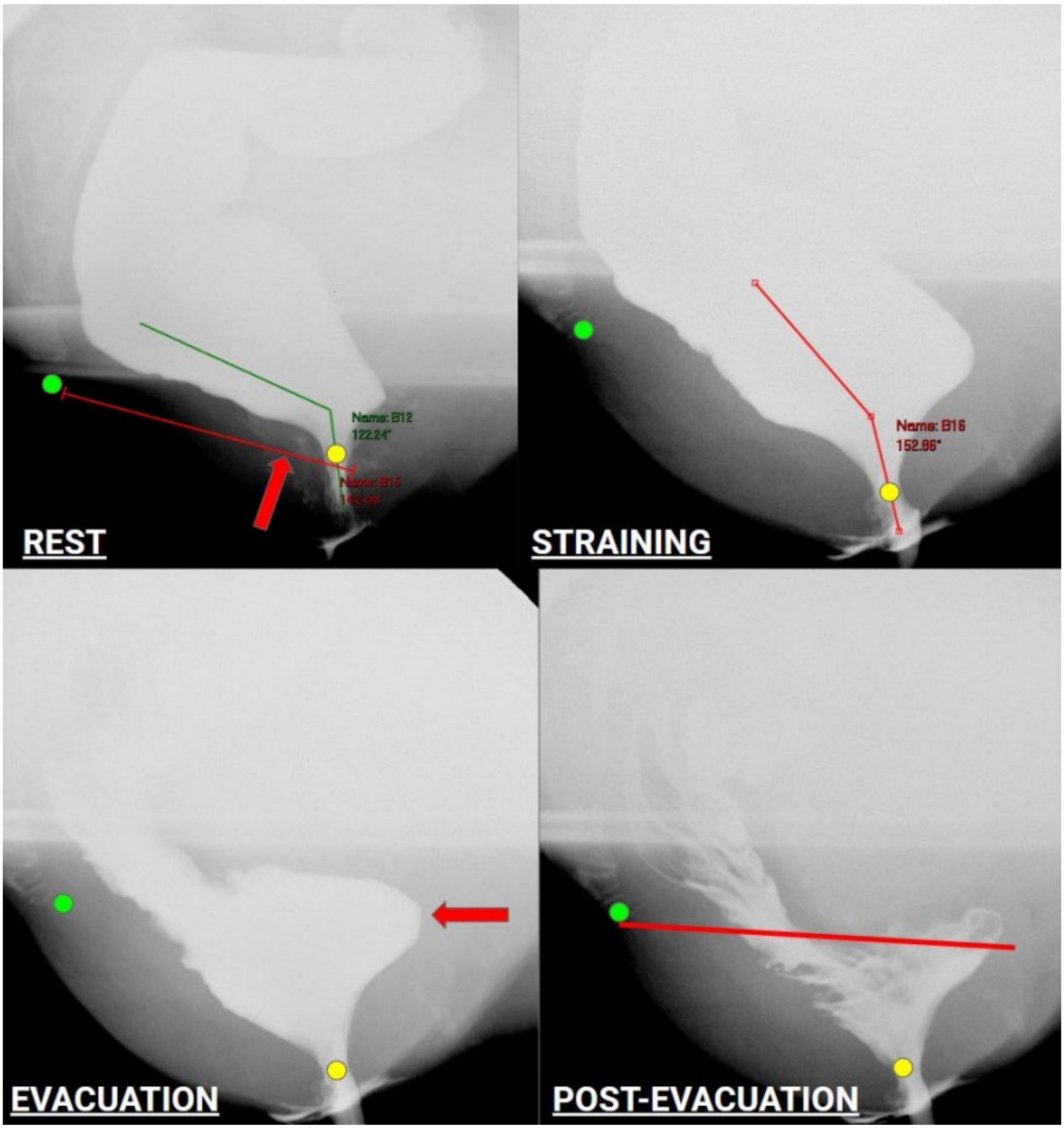

Keywords : Defecography, Digital Radiography, Pelvic Floor Dysfunction

[Poster Presentation 1 – ISP Format]

ABD-ISP-02

DECT in Bowel Diseases: A Problem-Solving Tool!

Ankur Goyal[1*], Raju Sharma[1], Devasenathipathy Kandasamy[1], Rajender Kumar Behera[1], Sanchita Gupta[1]

[1]Radiodiagnosis and Interventional Radiology, All India Institute of Medical Sciences, New Delhi, India

Background: Bowel diseases often pose a diagnostic challenge due to their relative obscurity on CT and may be missed by an inexperienced eye. Dual-energy CT (DECT) may help in such cases by providing a clearer depiction of the findings on monoenergetic low-keV images, iodine-density images and virtual non-contrast (VNC) images.

Aims: To demonstrate the practical applications of DECT in the detection of inflammatory, ischemic and neoplastic bowel diseases.

A retrospective review of DECT cases was done where it helped to make the bowel findings more conspicuous, thus avoiding missed findings.

Cases will be showcased, highlighting the utility of DECT in the following scenarios:

- Detection of subtle abnormal wall thickening and hyperenhancement in Crohn's disease
- Differentiation of abnormal bowel wall thickening from peristalsis-related apparent thickening
- Detection of membrane-type probable strictures
- Detection of serosal metastases
- Detection of small enhancing bowel lesions
- Detection of hyperdense attenuation on VNC in case of intramural hematoma
- Better delineation of ischemic bowel segments
- Better depiction of vascular abnormalities in bowel wall (angiodysplasia / telangiectasias)

DECT may increase the diagnostic confidence of detecting bowel abnormalities and thus may enable optimal management of the patients, saving them from additional investigations even in case of subtle inconspicuous findings.

These subtle areas of bowel wall thickening and hyperenhancement are easily overlooked on routine CT and may be mistaken as due to peristalsis. These are however confidently appreciated iodine density map overlaid on virtual non-contrast images generated from dual-energy dataset

Membrane-type probable strictures in Crohn's disease

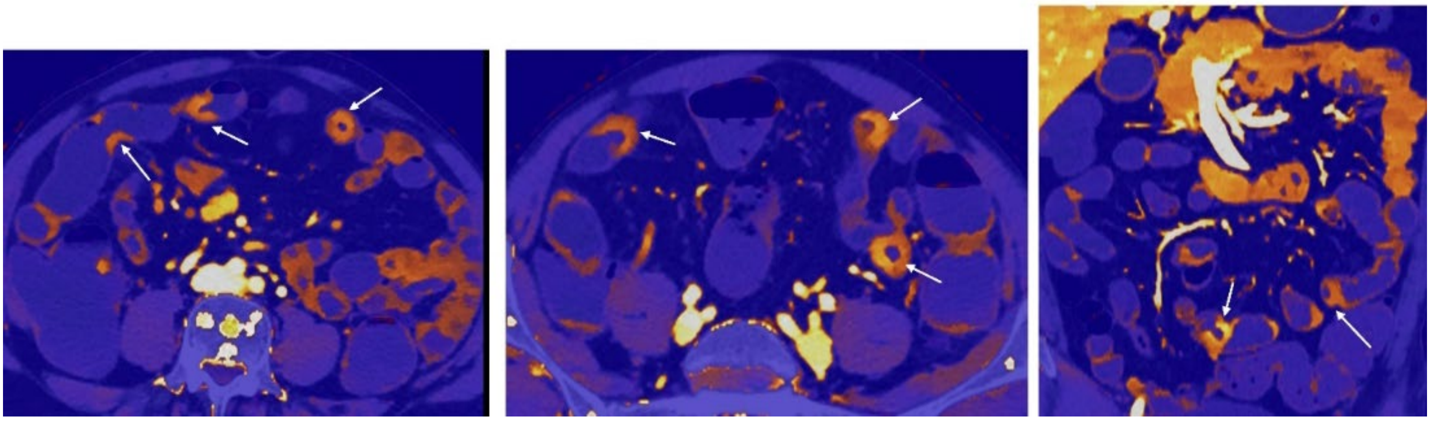

The enhancing deposits along the surface of small bowel loops are much better and confidently appreciated on the monoenergetic low keV image and the iodine density map overlaid on virtual non-contrast image

Serosal metastases in gall bladder carcinoma

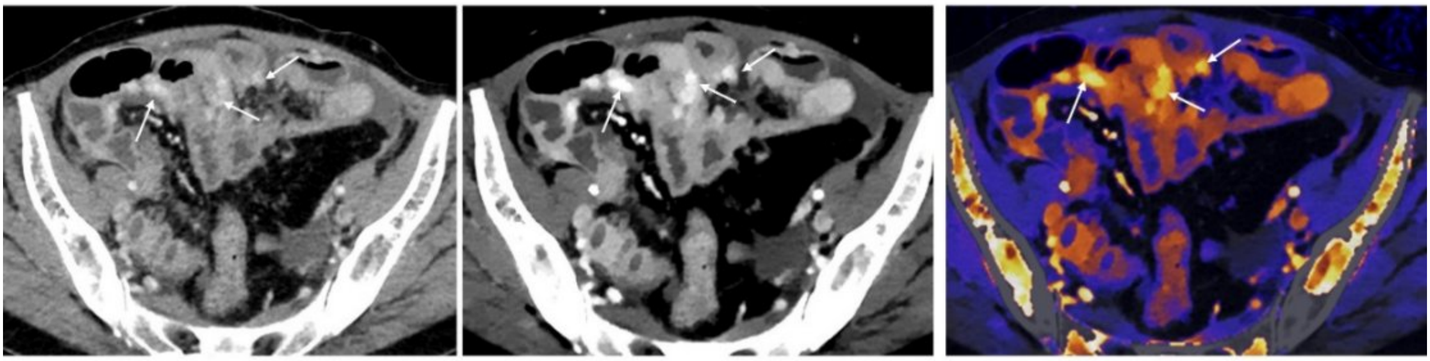

Conventional CECT | Monochromatic Low keV | Iodine density image

Keywords : Dual-energy CT, Bowel diseases, Crohn's disease

[Poster Presentation 1 – ISP Format]

ABD-ISP-03

Exploring Vascular Etiologies of Abdominal Pain with Contrast Enhanced Computed Tomography Scan: A Pictorial Essay

Mark Nicholas Reyes[1*]

[1]Radiology, Metropolitan Medical Center, Philippines

One of the common considerations in patients coming to the emergency department is acute abdominal pain with a variety of causes including appendicitis, diverticulitis, biliary and colic pain, and as well as with a gynecologic etiology. Some may be benign in origin while others may necessitate an emergent surgical management or interventional procedures. Among these, vascular etiology is represented by a small yet significant minority of cases. Moreover, vascular emergencies are often fatal hence timely diagnosis and treatment must be provided.

This study underscores vascular etiologies as underrecognized yet critical causes of acute abdominal pain in emergency settings. It demonstrates the diagnostic superiority of contrast-enhanced CT in detecting arterial and venous pathologies, emphasizing that timely identification is essential for guiding appropriate management and improving patient outcomes.

The standard acquisition protocol include acquisition using 64 MDCT GE Scanner manufactured in WI, USA. For the non-contrast CT, patient is placed on a supine position with both arms elevated above the head. the initial slice was set at 1cm above the dome of the diaphragm up to the inferior margin of the symphysis pubis with a slice thickness of 0.625mm with an interval of 0.5mm Neutral contrast agent is given orally amounting to 400cc and rectally amounting to 200cc prior to the scan. Continuous CT scanning is done during a single breath hold. The subsequent scan is the arterial phase wherein a total of 120cc of non-ionic contrast solution is given at a rate of 3.5 to 5cc/sec using the MEDRAD Salient contrast injection system by Bayer. After which, venous phase is acquired approximately 60 to 70 seconds from the contrast administration. Multiplanar reconstructions are then reviews on a 3D imaging workstation.

This study identified eight key cases representing vascular causes of acute abdomen, including aortic dissections, superior mesenteric artery dissection and thrombosis, mesenteric hypoperfusion, and thrombosis of the portal and superior mesenteric veins. Contrast-enhanced CT consistently revealed critical vascular abnormalities such as intimal flaps, vessel narrowing, abrupt occlusions, absence of flow, and secondary bowel changes like wall thickening and ischemic signs. These results underscore the essential role of contrast-enhanced CT in the timely and accurate detection of both arterial and venous vascular pathologies that can mimic more common abdominal emergencies, thereby enabling early diagnosis and appropriate management.

Often presenting with nonspecific signs, mesenteric ischemia necessitates thorough assessment of the arterial, portal venous, and venous systems for an accurate diagnosis. Reliance solely on patient history and on clinical and laboratory presentations is inadequate, making imaging studies

indispensable. Among the diagnostic options, contrast-enhanced CT stands out as the most dependable and fastest modality, offering detailed visualization of vascular structures within a brief scan time and enabling prompt therapeutic intervention.

Arterial phase of the CECT of the abdomen showing decreased caliber and with diminished flow to the mesenteric arcades of the superior mesenteric artery and inferior mesenteric artery with mucosal wall thickening involving the duodenum, jejunum, and ileum as well as the colonic segments.

Contrast-enhanced computed tomography (CT) scan of the abdomen demonstrating an almost complete occlusion of the portal vein and its main branches. The thrombus is visible as a filling defect within the portal vein lumen (solid black arrow), causing significant reduction in blood flow.

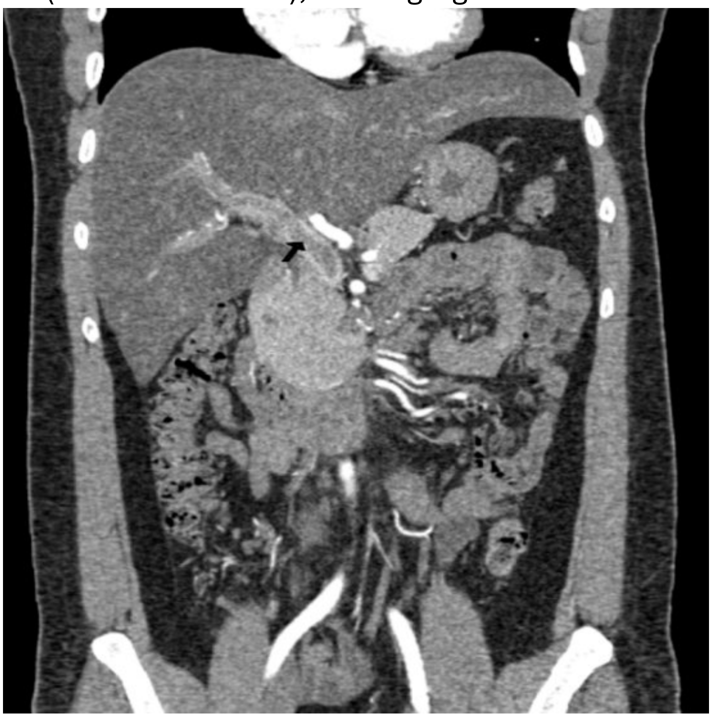

Keywords : Acute Abdominal Pain, Mesenteric Ischemia, Vascular Etiologies of Abdominal Pain

[Poster Presentation 1 – ISP Format]

ABD-ISP-04

An Oral Dual-Loaded Nanoplatform for CT-Guided, Multi-Modal Therapy of Inflammatory Bowel Disease: Development and Preclinical Evaluation

Deepika Singh[1*]

[1]Pharmacy, SIHAS, India

Inflammatory bowel disease (IBD) demands therapeutic systems capable of targeted delivery, mucosal protection, and real-time assessment of disease activity. Multifunctional oral nanoplatforms capable of combining imaging and treatment represent a transformative opportunity. A double-loaded nano-system—incorporating both therapeutic agents and CT-contrast components—may enable simultaneous visualization of inflammation and integrated disease control. To develop and evaluate a multifunctional, double-loaded oral nanoplatform designed for CT imaging–guided and synergistic therapy of IBD in a preclinical model.

A dual-loaded nanoparticle formulation (therapeutic payload + CT contrast agent) was synthesized and characterized for particle size, surface charge, morphology, drug loading efficiency, release kinetics, and X-ray attenuation properties. Stability in simulated gastrointestinal fluids was assessed. Experimental colitis was induced in n rodents. Animals were randomized into healthy control, IBD untreated, free-drug, single-loaded nanoparticle, and dual-loaded nanoplatform groups. In vivo CT imaging evaluated intestinal localization, mucosal retention, and inflammation-related contrast patterns. Therapeutic outcomes were assessed using disease activity index, colon length, histological scoring, inflammatory cytokine quantification (TNF-α, IL-6, IL-1β), oxidative stress markers, and gut barrier integrity assays. Biosafety was evaluated through blood chemistry and organ histology.

The dual-loaded nanoplatform demonstrated excellent GI stability, controlled drug release, and high radiodensity suitable for CT-guided tracking. In vivo imaging confirmed targeted accumulation at inflamed colonic segments with clear contrast delineation. Treatment significantly reduced clinical disease severity, restored epithelial integrity, and decreased inflammatory mediator levels compared with free-drug and single-loaded nanoparticle groups. Oxidative stress and histological injury were substantially mitigated. No systemic toxicity or abnormal organ accumulation was

The multifunctional double-loaded oral nanoplatform provides a powerful theranostic strategy for IBD management, integrating precise CT imaging with potent, localized therapeutic action. This approach shows strong potential for clinical translation as a noninvasive, imaging-guided platform for chronic intestinal inflammation.

Keywords : Inflammatory bowel disease, CT imaging, Theranostics, Dual-loaded nanoparticles

[Poster Presentation 1]

ABD-Liver-01

Imaging Spectrum of Diffuse Liver Disease

Zhong Yun Lee[1*], Jingli Chong[1], Hsien Min Low[1]

[1]Radiology, Tan Tock Seng Hospital, Singapore

Diffuse liver disease encompasses a wide range of pathologies that alter hepatic parenchymal architecture and function. Cross-sectional imaging, particularly CT and MRI, plays a pivotal role in characterizing these disorders, guiding diagnosis, and informing clinical management.

To illustrate and compare the imaging appearances of diffuse liver diseases across multiple etiologies, emphasizing characteristic patterns and key diagnostic clues on CT and MRI.

We showcase our various local cases of diffuse liver disease, obtained from our PACS.

We review the radiologic spectrum of diffuse hepatic pathologies, organised by underlying etiology:

1. Metabolic: Fatty infiltration and iron overload, highlighting signal intensity alterations on in-phase and out-of-phase MRI and susceptibility effects on T2*-weighted imaging.
2. Fibrotic: Morphologic changes and parenchymal texture alterations associated with chronic liver disease and cirrhosis.
3. Neoplastic:* Diffuse infiltrative hepatocellular carcinoma, metastatic disease, and cholangiocarcinoma, focusing on enhancement patterns and diffusion characteristics.
4. Vascular: Imaging features of hepatic infarction, Budd–Chiari syndrome, passive congestion, and hereditary hemorrhagic telangiectasia.
5. Biliary: Patterns seen in primary sclerosing cholangitis, biliary hamartomas, and polycystic liver disease.
6. Post-treatment: Changes following radiotherapy and chemotherapy-induced sinusoidal obstruction.
7. Granulomatous disease: Distinct parenchymal manifestations of infectious and non-infectious granulomatous processe

Diffuse liver diseases exhibit overlapping yet distinguishable imaging features on CT and MRI. Recognizing these characteristic patterns and correlating them with clinical and laboratory data are essential for accurate diagnosis and appropriate management. This pictoral review aims to provide a comprehensive visual guide to aid radiologists in confidently differentiating among the diverse etiologies of diffuse hepatic disease.

MRI liver utilising Primovist contrast media; A: 'in phase', B: 'out phase', C: DWI, D: ADC, E: T2W, F: Arterial, G: Portal venous, H: HPB

Large mass occupying left hepatic lobe extending into right lobe. Signal drop on 'out of phase' sequence in keeping with fat content. Mass is hypovascular, does not show APHE and remaining hypointense compared to background liver with HPB phase defect. Note tumour thrombus in left portal vein extending into right. Appearance suspicious for HCC particularly given the presence of fat.

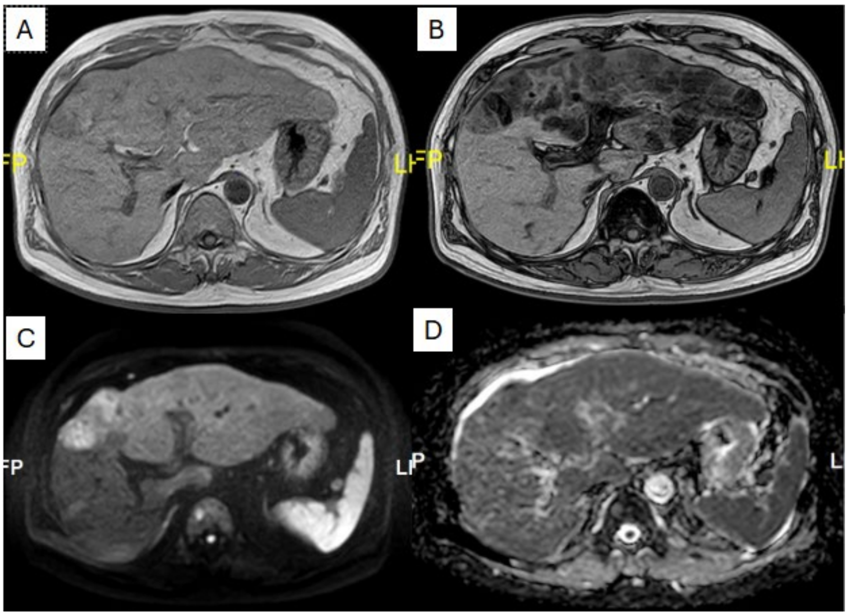

MRI liver utilising Primovist contrast media; A: 'in phase', B: 'out phase', C: DWI, D: ADC, E: T2W, F: Arterial, G: Portal venous, H: HPB

Large mass occupying left hepatic lobe extending into right lobe. Signal drop on 'out of phase' sequence in keeping with fat content. Mass is hypovascular, does not show APHE and remaining hypointense compared to background liver with HPB phase defect. Note tumour thrombus in left portal vein extending into right. Appearance suspicious for HCC particularly given the presence of fat.

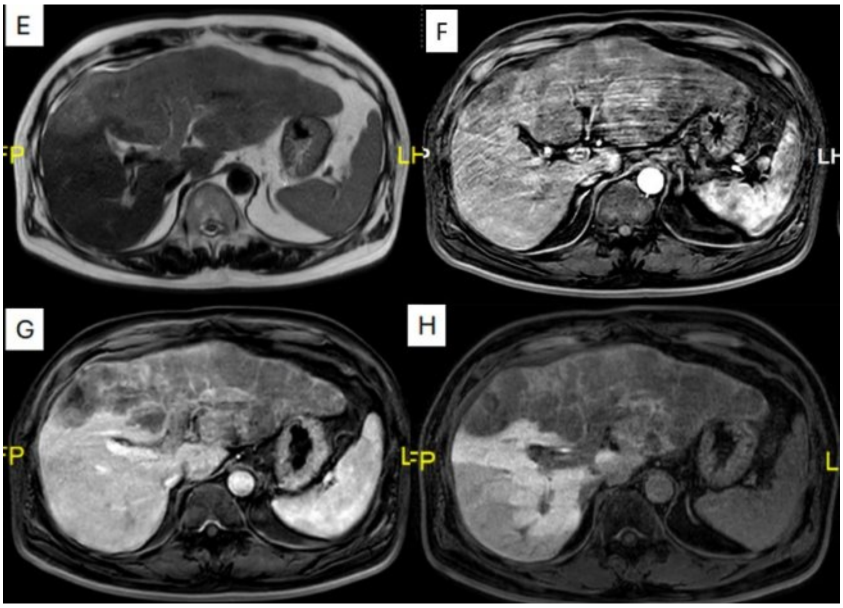

Keywords : Diffuse liver disease

[Poster Presentation 1]

ABD-Liver-02

Safety Profile and Management of Complications after Ablative-Dose Yttrium-90 Resin Microsphere Radioembolisation for Hepatocellular Carcinoma in an Asian Cohort

Hian Liang Huang[1*], Han Chung Low[1], Aaron Kian Ti Tong[1], Kelvin Siu Hoong Loke[1], Si Xuan Koo[1]

[1]Nuclear Medicine and Molecular Imaging, Singapore General Hospital, Singapore

High-dose Yttrium-90 resin microsphere radioembolisation has emerged as an effective treatment for hepatocellular carcinoma, with ablative doses (≥190 Gy) showing promising efficacy outcomes. However, comprehensive safety data for ablative dosing remains limited in Asian populations. We aimed to systematically evaluate the safety profile and adverse event patterns associated with high-dose Y-90 resin microsphere treatments at our institution, with particular focus on identifying treatment-related complications and their clinical management.

We conducted a retrospective clinical audit of all patients with HCC who received high-dose Y-90 resin microsphere radioembolisation (predictive tumour-absorbed dose ≥190 Gy via Tc-99m macroaggregated albumin planning SPECT/CT dosimetry) at Singapore General Hospital Department of Nuclear Medicine and Molecular Imaging between January 2016 and December 2023. All adverse events within 6 months post-treatment were systematically reviewed and graded using CTCAE v5.0 criteria. Events were classified as treatment-related or unrelated based on temporal relationship, clinical presentation, and alternative causative factors including disease progression and concurrent interventions.

Among 68 patients treated with high-dose Y-90 (median age 73 years, median tumour-absorbed dose 262.24 Gy), six patients (8.8%) experienced treatment-related adverse events requiring clinical intervention. Two patients developed possible radiation-induced liver disease, two experienced post-embolisation syndrome, and two developed endoscopically confirmed radiation-induced peptic ulcer disease with identifiable Y-90 microspheres on histology. One ulcer case required endoscopic haemostasis with noradrenaline injection and clip placement, complicated by transient grade 2 anaemia that resolved without transfusion. All patients with hepatic complications recovered liver function either spontaneously or following short-course steroid therapy. Grade 2-3 laboratory abnormalities corresponded to these six patients with treatment-related events. The predictive tumour-absorbed doses for these six patients ranged from 233.52 Gy to 600 Gy, with a median of 349.44 Gy. Four patients had single target artery while the other two had two target arteries. An additional 17 patients experienced adverse events deemed unrelated to Y-90 treatment, attributable to disease progression (n=6), subsequent interventions (n=8), medications (n=2), or unclear aetiology (n=1).

High dose Y-90 resin microsphere radioembolisation has an acceptable safety profile. Radiation-induced liver disease, post-embolisation syndrome, and peptic ulceration represent the primary treatment-related complications, all of which were manageable with appropriate clinical intervention.

The systematic identification and characterisation of these adverse event patterns provides valuable guidance for patient counselling, monitoring protocols, and clinical management strategies in high-dose Y-90 treatments.

Keywords : Radioembolisation, Hepatocellular Carcinoma, Ablative Dose

[Poster Presentation 1]

ABD-Liver-03

Imaging Findings Following Yttrium-90 Radioembolisation for Hepatocellular Carcinoma: CT and MRI Appearances with Emphasis on LI-RADS v2024 Treatment Response Categories

Rachel Wei Lian Loh[1*], Jingli Chong[1], Christine Ying Kwok[1], Hsien Min Low[1]

[1]Diagnostic Radiology, Tan Tock Seng Hospital, Singapore

Yttrium-90 (Y-90) radioembolisation is an established radiation-based locoregional therapy for hepatocellular carcinoma (HCC), inducing necrosis via selective internal radiation. Accurate post-treatment imaging assessment is essential to distinguish expected treatment-related changes from residual viable tumour. The LI-RADS CT/MRI Treatment Response Algorithm (TRA) v2024 introduces a radiation-specific pathway for evaluating treated lesions and provides standardized terminology for categorizing response as Nonevaluable, Nonviable, Nonprogressing, or Viable. Familiarity with these patterns is essential for accurate interpretation and treatment monitoring.

We retrospectively reviewed CT and MRI studies of patients with HCC treated with Y-90 radioembolisation. Representative cases were selected to illustrate the spectrum of LI-RADS v2024 radiation TRA categories. Key imaging features were analyzed across modalities, including mass-like enhancement, washout, T2 signal, diffusion restriction, and hepatobiliary phase findings. Ancillary MRI features such as diffusion restriction and mild-to-moderate T2 hyperintensity were included as supportive indicators of viability when relevant.

Typical Nonviable lesions demonstrated geographic low attenuation on CT and non-enhancing necrotic areas on MRI. Expected post-treatment findings include perilesional hyperemia, capsular retraction and delayed geographic parenchymal enhancement. Nonprogressing lesions demonstrate persistent mass-like enhancement and remain stable or decrease in size over time. Viable lesions showed new or increasing mass-like enhancement, correlating with residual or recurrent tumor. Ancillary MRI features occasionally increased confidence in classifying equivocal lesions as viable.

The LI-RADS v2024 TRA radiation algorithm provides a standardized framework for assessing HCC post-Y-90 radioembolisation. Recognizing the expected imaging spectrum across TRA categories and understanding when ancillary MRI features support the detection of viability enhances diagnostic accuracy and confidence in post-treatment interpretation.

Fig 1. (A) Pre-treatment gadoxetic acid-enhanced MR image in the arterial phase shows a small enhancing lesion in segment 7/8 (white arrow). It demonstrates washout and restricted diffusion (not shown), compatible with hepatocellular carcinoma.

(B, C) On gadoxetic acid-enhanced MRI obtained 3 months post–Y-90 radioembolization, arterial phase subtraction images shows loss of enhancement of the lesion, with peritumoral ring enhancement (white arrow) and adjacent geographic enhancement in the right hepatic lobe (red arrow).

These findings are compatible with post-treatment changes and an LR-TR nonviable lesion.

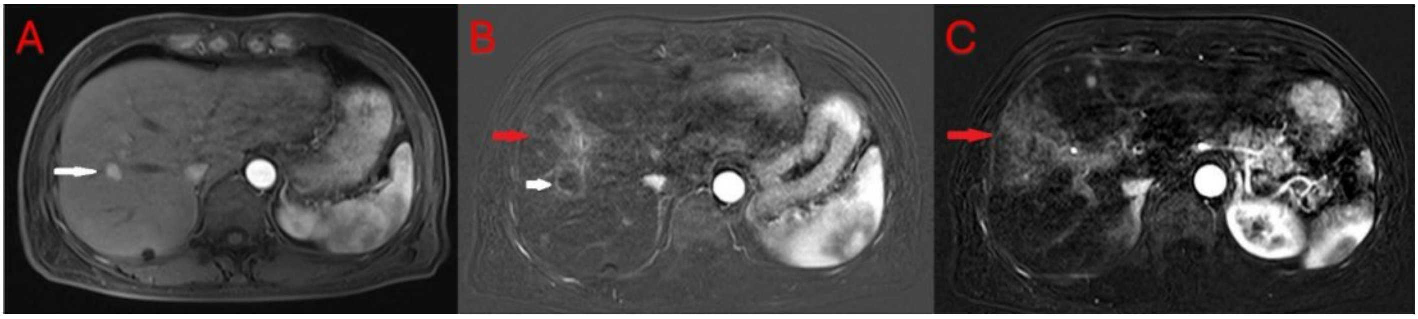

(A, B) Pre-treatment gadoxetic acid-enhanced MR image in the arterial phase (white arrow)shows an enhancing lesion in segment 4A/8 with washout (red arrow), compatible with hepatocellular carcinoma.

(C) On gadoxetic acid-enhanced MRI obtained 3 months post–Y-90 radioembolization, arterial phase subtraction images show decreased tumour enhancement with central necrosis. A small nodular focus of mass-like enhancement is seen at the posterior margin of the treatment zone (white arrow). (D) This finding persists but remains stable on MRI performed 6 months post–Y-90 radioembolization, without interval intervention, compatible with an LR-TR nonprogressing lesion.

(E,F) On follow-up MRI 12 months post–Y-90 radioembolization, a new nodular arterially enhancing lesion is seen at the anterior aspect of the treatment zone (white arrow) without definite washout (not shown) but demonstrates mild T2-weighted hyperintensity (red arrow), suspicious for a LR-TR viable lesion.

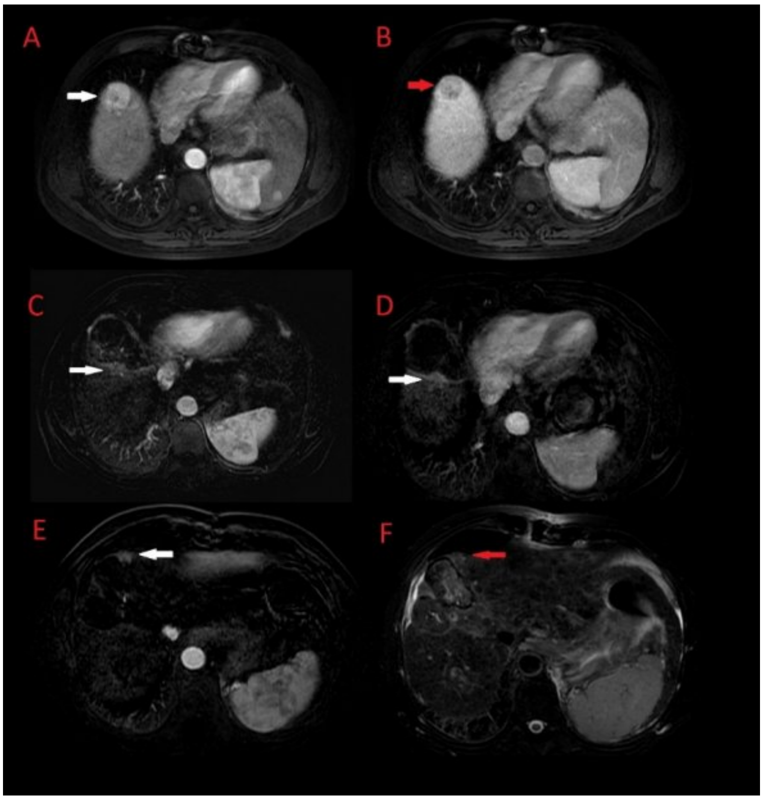

Keywords : Y-90 radioembolisation, LIRADS, Treatment response assessment

[Poster Presentation 1]

ABD-Liver-04

The Prognostic Impact of MRI Features on Recurrence and Survival after Resection of Hepatocellular Carcinoma is Dependent on Follow-up Time

Fujing Shi[1], Hanyu Jiang[1*]

[1]Radiology, West China Hospital Sichuan University, China

The prognostic impact of MRI features, laboratory, and pathological factors following curative resection of hepatocellular carcinoma (HCC) may vary with time,but this phenomenon is not systematically evaluated.The conventional reliance on the Proportional Hazards assumption, which neglects temporal changes in risk factors, may result in hazard ratio estimates that lack temporal specificity. We aimed to evaluate the Proportional Hazards assumption and model time-by-covariate interactions to characterize how the prognostic influence of MRI features, laboratory markers, and pathological characteristics on recurrence-free survival (RFS) evolves after curative HCC resection.

We conducted a retrospective cohort study of 896 patients with pathologically confirmed HCC who underwent curative-intent resection between 2011 and 2023 and had preoperative MRI within 3 months (median follow-up: 22.3 months). Baseline factors included routinely assessed MRI features, preoperative laboratory indicators, and pathological characteristics. The primary endpoint was RFS (time from surgery to first recurrence or death). We used Cox regression models incorporating time-by-covariate interactions (modeled linearly or via restricted cubic splines) to describe time-varying effects. Factors significant in univariable analyses were included in multivariable models to estimate and visualize time-dependent hazard ratios (tdHRs).

Twelve factors were independently associated with RFS in multivariable Cox analysis, including AFP, γ-glutamyl transferase, platelet count, NLR, tumor number,Size of the dominant tumor, portal vein width, peritumoral hypoenhancement, APHE proportion, MRI field strength, microvascular invasion, and resection extent. Time-covariate interaction analysis revealed time-varying effects for six factors: AFP, platelet count, dominant tumor size, APHE proportion, MRI field strength, and microvascular invasion. The remaining six factors showed a relatively constant prognostic impact. Time-dependent Hazard Ratio curves illustrated highly heterogeneous temporal patterns across these predictors.

In this single-center cohort, we demonstrate that a subset of MRI features (e.g., APHE proportion, field strength), laboratory markers (e.g., AFP, platelets), and pathological factors (microvascular invasion) exhibit time-varying associations with RFS following curative HCC resection. Modeling time-covariate interactions and presenting time-dependent Hazard Ratios may potentially reveal dynamic prognostic patterns that could be obscured by the standard proportional hazards assumption. If validated in larger, multi-center cohorts, incorporating these time-varying effects into postoperative risk assessment could offer certain advantages in improving risk stratification and may contribute to more individualized surveillance and management strategies for HCC patients.

Keywords : Hepatocellular carcinoma, Time-varying effects, Prognosis

[Poster Presentation 1]

ABD-Liver-05

Imaging Differentiation of Small and Large Duct Intrahepatic Cholangiocarcinoma: CT and MRI Case Review, Imaging Features and Clinical Implications

Anuja Satish Bhave[1*], Christine Kwok[1]

[1]Radiology, National Healthcare Group, Singapore

Intrahepatic cholangiocarcinoma (ICC) is the second most common primary liver tumor after hepatocellular carcinoma (HCC), accounting for approximately 10–20% of hepatobiliary malignancies. Grossly, ICC is classified into three subtypes: mass-forming, periductal infiltrating, and intraductal growing, with the mass-forming type being the most prevalent. Histologically, numerous terms have historically been used to describe similar tumors. Following the 2019 WHO classification, ICCs are categorized as large duct (LD) or small duct (SD) subtypes, which differ in etiology, molecular characteristics, growth patterns, and clinical behavior.

Both SD and LD subtypes can present as mass-forming intrahepatic cholangiocarcinomas (IMCCs). Differentiating their distinct imaging features is crucial, as it may significantly impact treatment planning.

On CT, SD ICCs commonly show peripheral hyperenhancement and well-defined, lobulated contours, while LD ICCs often lack hyperenhancement and exhibit bile duct encasement, infiltrative margins, and diffuse duct dilation. Lymph node enlargement is more frequent in LD ICCs. MRI features support these differences, with LD tumors displaying infiltrative growth and vascular invasion. Patients with SD ICCs generally have better survival outcomes than those with LD ICCs, mainly due to lower lymphatic spread. Combining key imaging features offers high specificity in distinguishing subtypes, thereby aiding prognosis and treatment planning.

This poster reviews the unique imaging features of SD and LD ICC subtypes and discusses their clinical implications.

Keywords : Intrahepatic Cholangiocarcinoma, Imaging Characteristics, Small Duct Vs Large Duct Subtypes

[Poster Presentation 1]

ABD-Liver-06

Clinicopathologic, MRI and Prognostic Features of Intrahepatic Cholangiocarcinoma According to Cirrhosis Status

Yong Jun Jung[1], Dong Hwan Kim[1*], Sang Hyun Choi[1]

[1]Radiology, Asan Medical Center University of Ulsan College of Medicine, Korea

To compare the clinicopathologic features, MRI characteristics, and long-term survival outcomes of intrahepatic cholangiocarcinoma (ICCA) in patients with and without cirrhosis

We retrospectively analyzed 322 consecutive patients with ICCA who underwent preoperative MRI and curative-intent resection between 2010 and 2018 at a tertiary referral institution. Two abdominal radiologists independently reviewed MRI features. The clinical, pathologic, and MRI findings of cirrhotic and non-cirrhotic patients were compared. Recurrence-free survival (RFS), overall survival (OS), and prognostic factors were evaluated using Kaplan–Meier analysis, the log-rank test, and Cox proportional hazard regression analysis.

Among 322 patients (mean age, 62.5 ±10.0 years; 198 men), 50 (15.5%) had histologic cirrhosis. Compared with non-cirrhotic patients, cirrhotic patients had smaller tumors (4.1 vs. 5.4 cm; p=.002), earlier-stage disease (p=.010), and more frequent purely massforming morphology (98.0% vs. 86.8%; p=.022). On MRI, cirrhotic ICCAs were more often located peripherally (84.0% vs. 58.8%; p=.001) and demonstrated higher rates of non-rim arterial enhancement (22.0% vs. 4.4%; p<.001) and non-peripheral washout (20.0% vs. 4.0%; p<.001). By contrast, bile duct invasion (14.0% vs. 58.5%; p<.001) and vascular invasion (14.0% vs. 57.7%; p<.001) were less common. While cirrhosis itself was not associated independently with RFS or OS, tumor size (hazard ratio [HR]=1.01 for RFS; HR=1.01 for OS), multiplicity (HR=1.80/1.84), arterial-phase enhancement pattern (HR=2.25/2.64), vascular invasion (HR=1.66/1.72), and resection margin status (HR=1.50/1.49) were significant prognostic factors (all p<.05).

ICCA demonstrates distinct clinicopathologic and MRI features depending on cirrhosis status; however, postoperative survival is influenced primarily by tumor-related factors rather than by cirrhosis.

Kaplan–Meier curves showing recurrence-free survival (A) and overall survival (B) according to cirrhosis status.

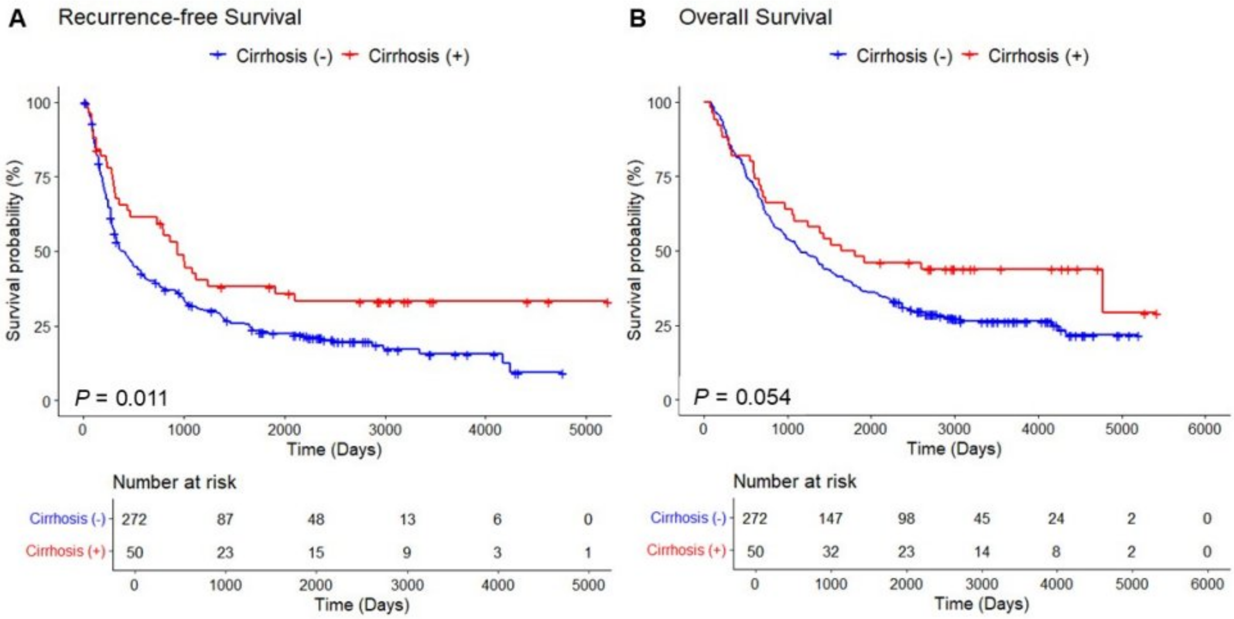

Gadoxetic acid-enhanced MR images of a 56-year-old man with intrahepatic cholangiocarcinoma in alcoholic liver cirrhosis. (A) Axial pre-contrast T1-weighted image showing a lobulated mass measuring 3.4 cm (arrows) located in the peripheral portion ofsegment II. (B) Fat-suppressed T2-weighted image showing no evidence of peritumoral bile duct invasion. (C) Arterial-phase image showing non-rim enhancement of the mass (arrow), (D) followed by non-peripheral washout on the portal-venous phase (arrows). (E) Hepatobiliary phase image showing hypointensity without a targetoid appearance (arrow). (F) Diffusion-weighted image showing non-targetoid diffusion restriction (arrow). The patient underwent left lateral segmentectomy. Histopathological examination confirmed a purely mass-forming type intrahepatic cholangiocarcinoma in a cirrhotic liver. No tumor recurrence occurred during 114 months of follow-up after resection.

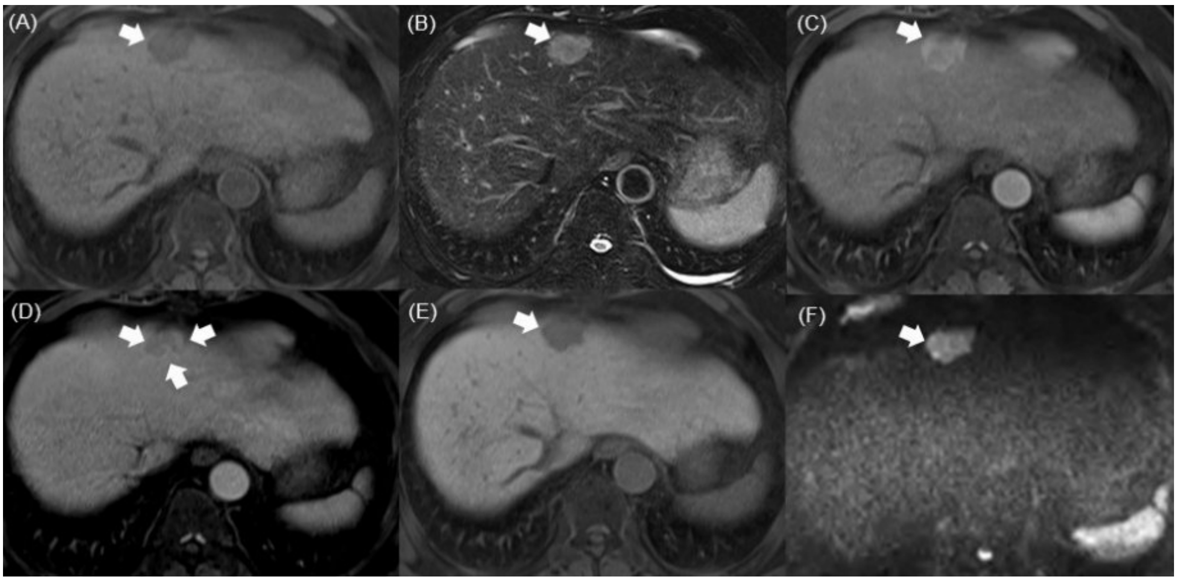

Keywords : Cirrhosis, Prognosis, Magnetic Resonance Imaging

[Poster Presentation 1]

ABD-Liver-07

Imaging Spectrum of Giant Hepatic Hemangioma with Diffuse Hepatic Hemangiomatosis: Three Case Series

Hyunyu Kang[1], Ki Choon Sim[1*], Min Ju Kim[1], Beom Jin Park[1], Deuk Jae Sung[1], Na Yeon Han[1], Yeo Eun Han[1], Seong Ha Cha[1]

[1]Radiology, Korea University Anam Hospital, Korea

Giant hepatic hemangioma accompanied by diffuse hepatic hemangiomatosis is a rare entity in adults and can mimic infiltrative hepatic malignancies. While individual case reports have described its imaging characteristics, larger case series remain limited. This study aims to summarize the radiologic features and clinical characteristics of patients with giant hemangioma and coexisting diffuse hepatic hemangiomatosis.

A retrospective radiologic database search was performed using the keyword **"diffuse hepatic hemangiomatosis."** Thirteen adult patients with imaging findings suspicious for diffuse hepatic hemangiomatosis were identified. Clinical information, laboratory data, contrast-enhanced CT, multiphasic liver MRI, and available pathology reports were reviewed. Imaging features—including enhancement patterns, lesion distribution, and associated hepatic abnormalities—were systematically analyzed.

A total of **13 patients** met the imaging criteria for diffuse hepatic hemangiomatosis. Among them, **9 patients** had both CT and MRI available for comprehensive radiologic evaluation. Typical imaging findings included peripheral nodular enhancement with progressive fill-in in giant hemangiomas and innumerable small T2-hyperintense nodules consistent with diffuse hepatic hepatic hemangiomatosis. **Pathologic confirmation was obtained in 3 patients**, all demonstrating cavernous hemangioma or hemangiomatosis without evidence of malignancy. However, one of them subsequently required an additional hepatectomy due to progression of diffuse hepatic hemangiomatosis. Follow-up imaging demonstrated overall stability in the majority of cases.

This case series highlights characteristic radiologic findings of giant hepatic hemangioma with diffuse hemangiomatosis in adults. Recognition of this pattern is essential to avoid misdiagnosis as infiltrative malignancy. CT and MRI provide complementary diagnostic information, and pathology—though not always required—can confirm the vascular benign nature. Conservative management appears appropriate in patients with preserved liver function and stable imaging features.

Liver MRI in a 46-year-old woman demonstrates a giant hemangioma measuring 23 cm in maximal diameter, replacing the left hepatic lobe. Diffuse signal alteration is observed in both the right anterior and posterior sections, with numerous subtle T2 hyperintense foci. These foci exhibit lower signal intensity on delayed and hepatobiliary phase images compared with the normal right posterior section.

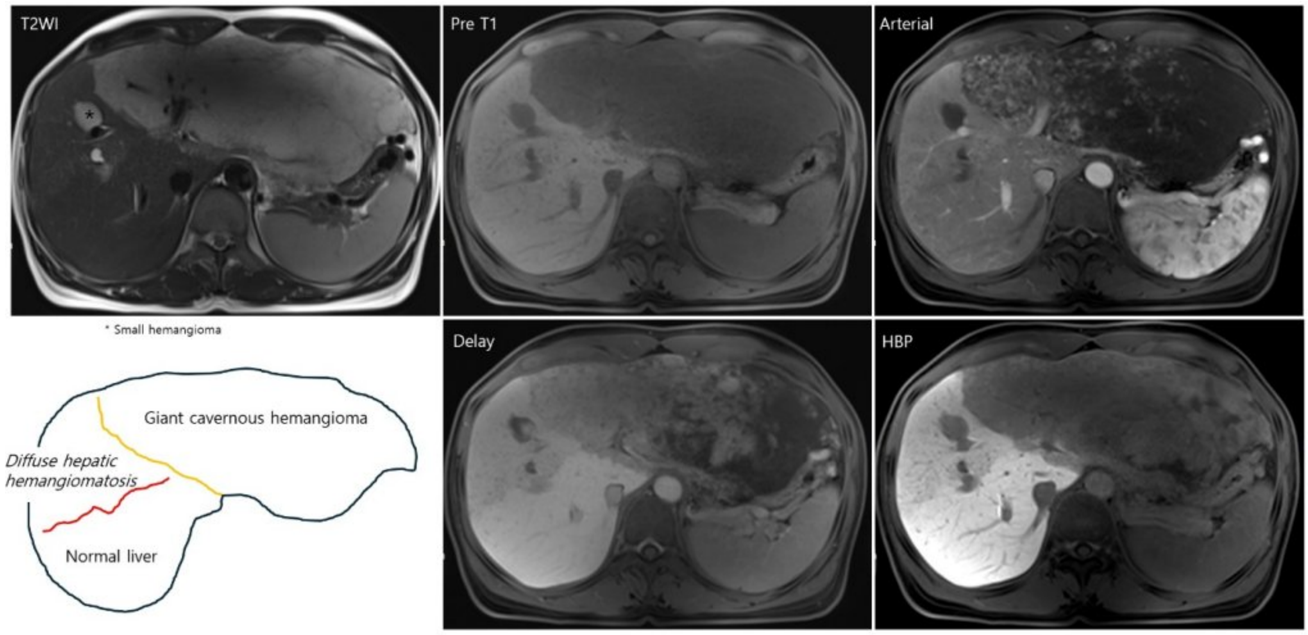

Serial liver dynamic CT scans obtained at one-year intervals demonstrate a gradual increase in the extent of numerous ill-defined enhancing areas in the right anterior section during the arterial phase. The patient subsequently underwent right anterior sectionectomy, and the lesion was confirmed as diffuse hepatic hemangiomatosis.

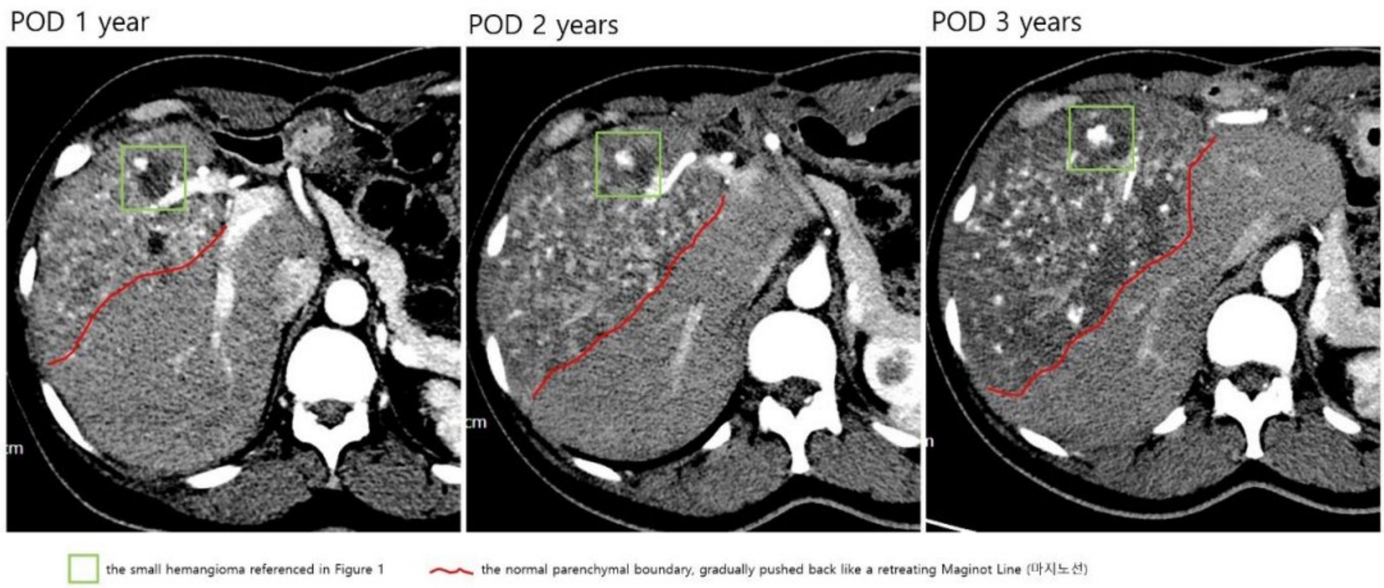

Keywords : Hemangioma, Hemangiomatosis, Giant Hemangioma

[Poster Presentation 1]

ABD-Liver-08

MRI Features of Sarcomatoid Biliary Carcinomas: An Analysis of Seven Cases Across the Hepatobiliary System

Hao Wu[1], Zheng Zhu[1*], Chunfang Hu[2], Xinming Zhao[1]

[1]Diagnostic Radiology, National Cancer CenterNational Clinical Research Center for CancerCancer Hospital Chinese Academy of Medical Sciences and Peking Union Medical College, China
[2]Pathology, National Cancer CenterNational Clinical Research Center for CancerCancer Hospital Chinese Academy of Medical Sciences and Peking Union Medical College, China

Sarcomatoid transformation of biliary carcinoma is an extremely rare variant of hepatobiliary cancer. It is characterized by a biphasic pattern of both epithelial and spindle-cell components, and it follows a clinically aggressive course. MRI features remain incompletely characterized, particularly across different biliary locations. This study aimed to summarize the MRI characteristics of pathologically proven sarcomatoid biliary carcinomas and identify imaging clues that may assist preoperative recognition.

We retrospectively reviewed seven consecutive patients with histologically confirmed sarcomatoid biliary carcinoma who underwent preoperative contrast-enhanced MRI at a single tertiary cancer center between 2018 and 2025. Clinical data, tumor markers, operative records and pathological findings were collected. All patients underwent upper-abdominal MRI including T1-weighted, T2-weighted fat-suppressed, diffusion-weighted imaging (DWI) with apparent diffusion coefficient maps, and multiphase contrast-enhanced sequences. Two abdominal radiologists independently evaluated lesion morphology, growth pattern, signal characteristics, enhancement behavior, necrosis, biliary involvement, vascular relationships and extrahepatic spread, reaching consensus on discrepant findings.

The cohort comprised four men and three women (mean age, 67 years). Lesions were located in the intrahepatic bile ducts (n = 5), extrahepatic bile duct (n = 1) and gallbladder (n = 1). All tumors appeared as irregular masses or segmental wall thickening, predominantly hypointense on T1 and heterogeneously hyperintense on T2 with diffusion restriction. Dynamic imaging most commonly showed peripheral or heterogeneous arterial enhancement with progressive but incomplete centripetal filling and persistent portal/delayed enhancement; classic arterial hyperenhancement with wash-out and a smooth capsule, typical for HCC, was absent in all cases. Central necrosis was frequent, and bile duct dilatation or ductal cut-off was seen in lesions abutting the hepatic hilum or extrahepatic bile duct. CA19-9 was elevated in six of seven patients, whereas alpha-fetoprotein remained within the normal range in all, supporting a biliary rather than hepatocellular origin. Recurrence or metastasis was observed in several patients during follow-up, reflecting the tumors' aggressive biological behavior.

Sarcomatoid biliary carcinomas demonstrate a distinctive MRI pattern. Recognition of this pattern together with associated upstream ductal changes may heighten radiologic suspicion for sarcomatoid differentiation within biliary malignancies and support more targeted diagnostic evaluation in the

preoperative setting.

Figure 1. A 68-year-old man presenting with abdominal discomfort and abdominal distension for 6 months. (a) T1 hypointense; (b) T2 fat-suppressed heterogeneously hyperintense; (c) DWI hyperintense; (d) arterial peripheral/heterogeneous enhancement; (e) portal progressive but incomplete centripetal filling; (f) delayed persistent enhancement with central necrosis.

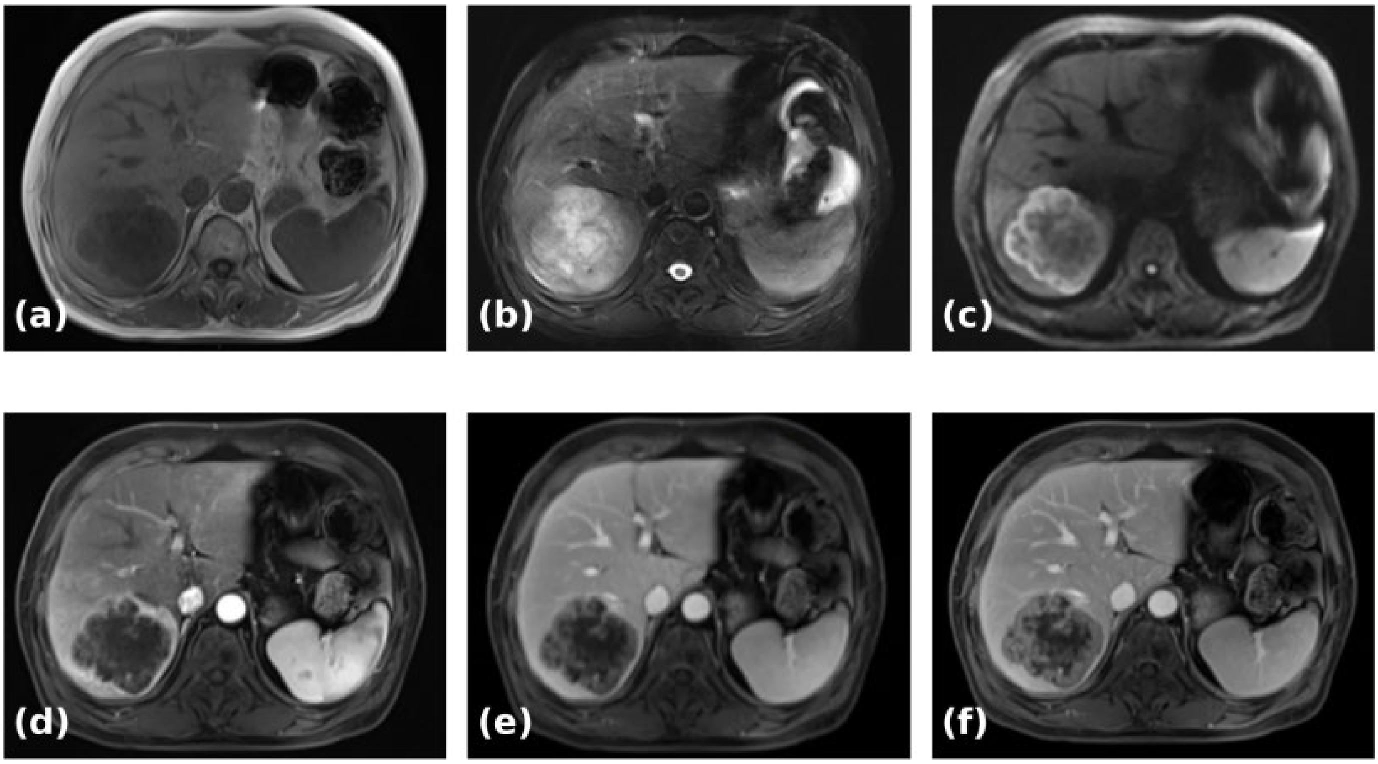

Keywords : Sarcomatoid Biliary Carcinomas, MRI Features

[Poster Presentation 1]

ABD-Liver-09

A Systematic Approach to Focal Liver Lesions from a Radiological Perspective: A Diagnostic Algorithm Utilizing Arterial Phase Enhancement Patterns

Duc Vo Tan[1], Huyen Le Duy Mai[1*], **Hy Le Nguyen Gia[1]**, Phuong Nguyen Nguyen[1], Nhi Nguyen Thi Yen[1], Thuy Do Thi Thanh[1], Duy Nguyen Thanh[1], Viet Tran Doan Khac[1]

[1]Radiology, University Medical Center, Vietnam

This study proposes a systematic diagnostic approach by categorizing focal liver lesions (FLLs) into three groups based on late arterial phase (LAP) enhancement patterns: Non-rim arterial phase hyperenhancement (APHE); rim APHE; and non-APHE. This approach adopts the LI-RADS framework because of its reliability and clinical applicability. The objective was to develop group-specific diagnostic models to enhance differential diagnosis and clinical decision-making.

A retrospective analysis was conducted on 1537 FLLs (non-rim APHE: n = 1240; rim APHE: n = 148; non-APHE: n = 149). All lesions were confirmed by either histopathology or accepted alternative criteria in cases where pathological results were unavailable. For each group, the distribution of pathological entities was recorded. To accommodate the distinct pathological spectrums, clinical priorities of each group, and varying management strategies for different tumor types in current clinical guidelines, tailored statistical strategies were employed: multinomial logistic regression was used for multi-class differentiation within non-rim and non-APHE groups, while a two-step multivariable logistic regression was used to develop a sequential diagnostic model for the rim APHE group.

1. **Non-rim APHE group:** The most frequent entities were hepatocellular carcinoma (HCC, 62%), followed by hepatic hemangioma (HH, 33%) and focal nodular hyperplasia (FNH, 4%). The diagnostic model was structured as a decision tree incorporating age, viral hepatitis, enhancement similar to the blood pool, and central scar (Figure 1A). This model achieved an overall accuracy of 0.989 in differentiating these lesions.

2. **Rim APHE group:** Neoplastic lesions predominated over inflammatory ones (3:1 ratio). Among malignancies, liver metastases (LM) were 2.6 times more common than primary liver cancers (PLC). *A two-step diagnostic approach* was established: *the first model* (WBC, size, location, capsular retraction, perilesional perfusion alteration) differentiating inflammatory from neoplastic lesions demonstrated a diagnostic performance with an AUC of 0.979 (Figure 1B); *the second model* (HBV, size, number, capsular retraction, venous thrombosis) distinguishing PLC from LM showed a diagnostic performance with an AUC of 0.949 (Figure 1C).

3. **Non-APHE group:** The most common entities were inflammatory lesions (53%), followed by LM (25.5%), HCC (10.7%), and intrahepatic cholangiocarcinoma (ICC, 8.1%). A multiclass model was developed using multiplicity, portal venous phase rim enhancement, and tumor in vein to

characterize these lesions (Figure 1D). This model yielded a diagnostic performance with an overall AUC of 0.812.

This systematic approach provides a robust radiological framework for FLL diagnosis by offering a unified diagnostic pathway that streamlines the evaluation of diverse non-invasive criteria typically scattered across various clinical practice guidelines. By integrating clinical and laboratory data with imaging features, these models provide high diagnostic performance across all groups, effectively narrowing differential diagnoses and facilitating individualized patient management.

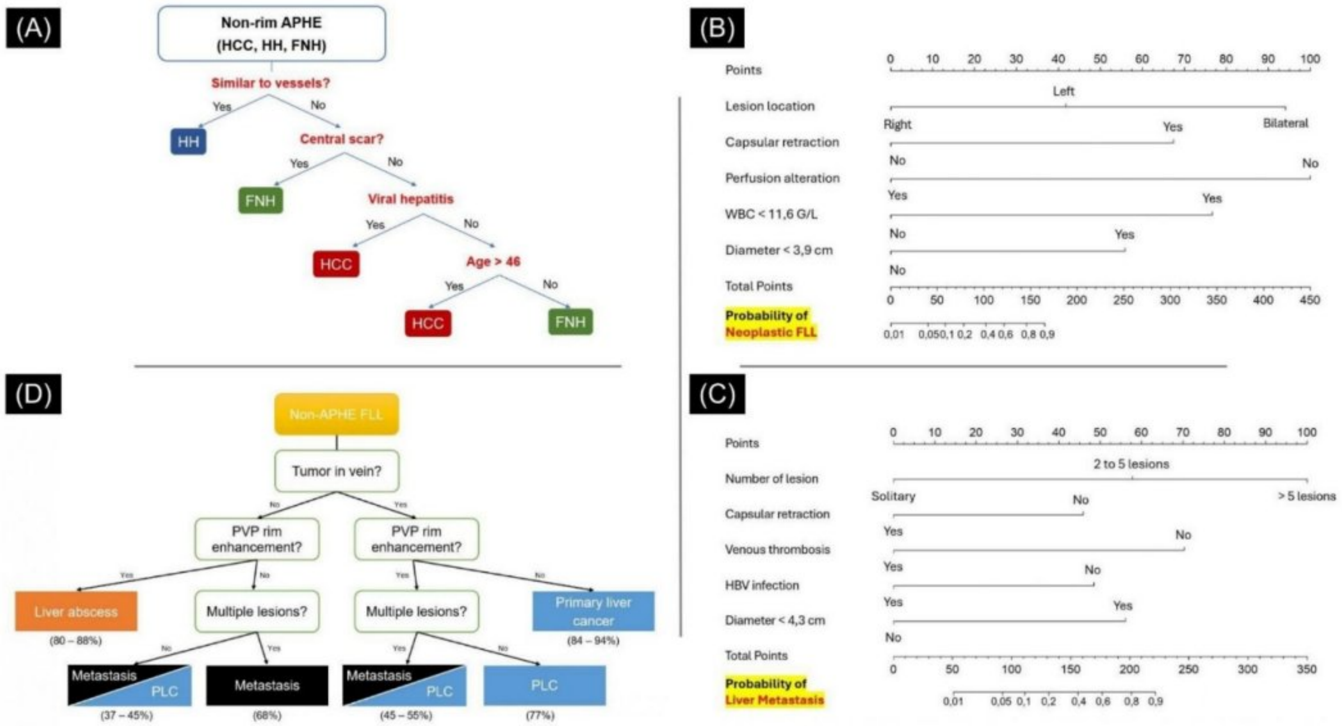

Figure 1. Proposed diagnostic models for characterization of focal liver lesions

(A) *Decision tree for the differential diagnosis of FLLs with non-rim APHE*

(B, C) *Two-step diagnostic nomograms for FLLs with rim APHE*

(D) *Decision tree for the differential diagnosis of FLLs with non-APHE*

ILLUSTRATIVE CASES

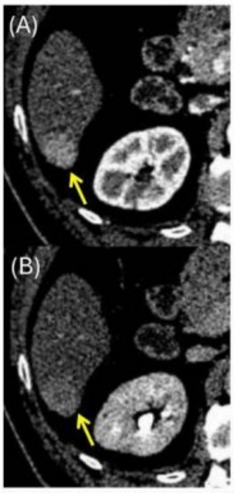

(A) Late arterial phase; (B) Portal venous phase

Case 1: A 62 y.o. female patient with a history of chronic hepatitis B infection. CECT imaging revealed a FLL with non-rim APHE in late arterial phase (→)

Imaging Features: The lesion appeared hyperattenuating compared to the surrounding liver parenchyma; no central scar was identified.

Model-based diagnosis: 99.93% probability of HCC

Outcome: HCC was confirmed by histopathology

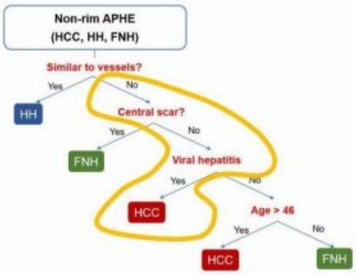

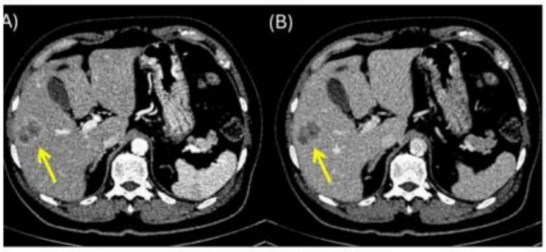

(A) Late arterial phase; (B) Portal venous phase

Case 2: An 81 y.o. male patient with a history of rectal adenocarcinoma, underwent laparoscopic low anterior resection one year prior. Follow-up CECT revealed a FLL with rim APHE in segment V (→). Lab result: HBV (-); WBC 12.2 G/L

Model-based diagnosis:

Step 1 (Inflammation vs. Neoplasm): Score 155 → **87%** probability of **neoplasm**

- ✓ *Key features*: WBC 12.2 G/L, right lobe, 3.5 cm, no capsular retraction, no perfusion hyperplasia

Step 2 (PLC vs. LM): Score 220 → **90%** probability of **LM**

- ✓ *Key features*: Solitary lesion, 3.5 cm, no capsular retraction, no venous thrombosis, HBV negative

Outcome: LM of adenocarcinomatous origin (confirmed by histopathology result after liver resection)

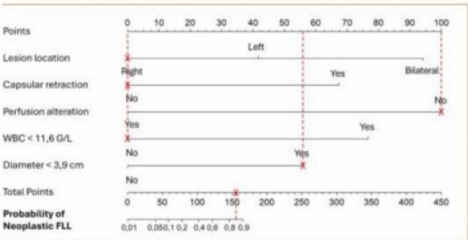

Nomogram 1: Differentiating neoplasm from inflammatory lesion

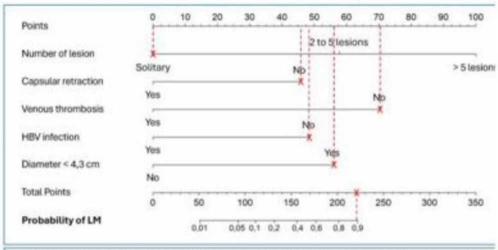

Nomogram 2: Differentiating liver metastasis from primary liver cancer

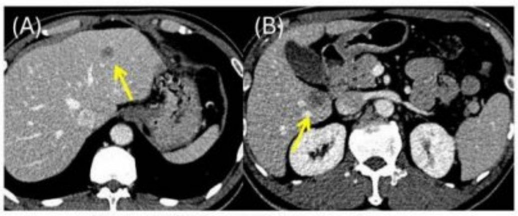

(A) Late arterial phase; (B) Portal venous phase

Case 3: A 55 y.o male patient with a history of colon cancer. Lab result: elevated CEA and CA 19-9 levels

Follow-up CECT: FLLs with non-APHE

- ✓ Key feature: Multiple lesions, no tumor in vein, and no rim enhancement in PVP

Model-based diagnosis: 68% probability of metastasis

Outcome: Liver metastatic

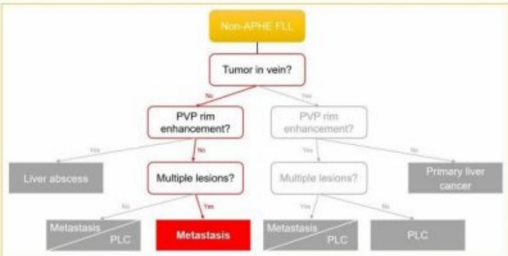

Decision tree for the differential diagnosis of FLLs with non-APHE

Keywords : Focal Liver Lesions, Arterial Phase Enhancement Patterns, Systematic Approach

[Poster Presentation 1]

ABD-Pancreas-01

Dual-Phase CT-Based Explainable Radiomics Capturing Spatial-Temporal Heterogeneity for Three-Class Grading and Prognostic Prediction in Pancreatic Neuroendocrine Neoplasms:A Multicenter Retrospective–Prospective Study

Weinuo Qu[1], Chenxi Lyu[1], Chuhuai Wang[1], Jiali Li[1], ShaSha Li[2], Feng Li[3], Zhen Li[1*]

[1]Radiology, Tongji Hospital Tongji Medical College Huazhong University of Science and Technology, China
[2]Radiology, Shanxi Bethune Hospital, China
[3]Radiology, Xiangyang Central Hospital, China

Accurate preoperative grading and prognostic stratification of pancreatic neuroendocrine neoplasms (P-NENs) remain challenging due to their high intratumoral heterogeneity, sampling limitations and limited interpretability of conventional radiomics models. Dual-phase contrast-enhanced CT provides rich hemodynamic information that may reveal biologically meaningful spatial–temporal heterogeneity.

This multicenter study enrolled 461 patients with pathologically confirmed P-NENs from three institutions, including 398 retrospective and 63 prospective cases. Arterial- and venous-phase contrast-enhanced CT images were processed using a dual-pipeline nnUNet-based automatic segmentation framework: one for precise tumor ROI delineation and another for volumetric body composition segmentation (skeletal muscle, visceral, subcutaneous, and intermuscular fat). A 9-dimensional feature vector integrating arterial enhancement, venous washout, local texture, and gradient characteristics was extracted voxel-wise to model dynamic enhancement behavior. Guided by sparse expert point annotations in 118 representative tumors, a hierarchical prior learning and constrained clustering algorithm segmented each tumor into three biologically interpretable subregions—necrotic, intermediate, and hypervascular—reflecting explicit arterial–venous enhancement patterns. From these, three quantitative heterogeneity indices were constructed: the Dynamic Enhancement Heterogeneity Index (DEHI), Spatial Heterogeneity Index (SHI), and Distribution Diversity Index (DDI). In parallel, conventional habitat radiomics features were extracted from arterial and venous tumor ROIs. Clinical, imaging, and body composition features were integrated for multi-class classification (G1–G2–G3) using recursive feature elimination (RFE) and Ridge regression under 5-fold stratified cross-validation.Model performance was evaluated across internal, external, and prospective cohorts. Prognostic validation was performed using Kaplan–Meier and Cox regression analyses.

Expert-guided habitat clustering produced subregions with significantly different enhancement characteristics, confirming radiological heterogeneity. Among 38 candidate models, seven representative algorithms were compared. The Random Forest (RF_Moderate) model achieved the best generalization, with macro-AUCs of 0.80 (internal), 0.78 (external), and 0.83 (prospective); weighted-AUCs of 0.77, 0.79, and 0.80; RPS values of 0.29, 0.30, and 0.28; and MAE of 0.36,0.44,0.36,

respectively. Calibration curves demonstrated good agreement between predicted and observed grades, and confusion matrices indicated balanced classification across cohorts. SHAP analysis revealed that DEHI, DDI, and relative intermuscular adipose tissue were the most influential predictors of tumor grade. Survival analysis based on model-derived risk stratification showed clear separation among high-, intermediate-, and low-risk groups (log-rank $p < 0.05$).

This study presents an explainable AI workflow integrating dual-phase enhancement-guided tumor habitat clustering, quantitative heterogeneity indices, body composition quantification, and multi-parametric modeling for preoperative grading and prognostic prediction in P-NENs. The proposed framework demonstrated strong generalizability and interpretability across multicenter cohorts, offering a non-invasive and reproducible tool for precision risk assessment.

Keywords : Pancreatic Neuroendocrine Neoplasms, Spatial–Temporal Heterogeneity, Explainable Radiomics

[Poster Presentation 1]

ABD-Biliary-01

SPECT/CT Rules out Bile Leak After Near False-Positive on HIDA Planar Imaging in Complex Postsurgical Abdominal Anatomy

Daniel Kim[1*]

[1]Diagnostic Radiology, The Hospital of the University of Pennsylvania, USA

Bile leak complications include abscess, sepsis, and even death. However, diagnosis is difficult with the presentation nonspecific, including abdominal pain and nausea.1 HIDA scan is useful to diagnose bile leak, but its limited spatial resolution has resulted in vast published sensitivities of 50-100%.2 Incorporating SPECT/CT can significantly improve sensitivity and localize positive cases.1,3 Despite this, there is hesitation with adding SPECT/CT after planar imaging due to patient radiation, costs, and scheduling/staffing limitations.4,5 This case demonstrates the value of SPECT/CT by ruling out bile leak in a postsurgical patient after HIDA planar imaging was almost interpreted as a false positive.

Five days after Whipple, patient became febrile and altered. CT abdomen showed a loculated collection in the porta hepatis, concerning for biloma (Figure 1A-B). A HIDA was ordered to evaluate for bile leak.

On planar imaging, HIDA initially showed focal radiotracer uptake overlying the level of the porta hepatis, potentially supporting bile leak (Figure 1D-E). Approximately 40 minutes later, this area lost radiotracer uptake (Figure 1F). Due to altered postoperative anatomy, a SPECT/CT was performed for further characterization.

SPECT/CT showed no radiotracer uptake at the porta hepatis collection (Figure 2A-B). Rather, the focal radiotracer uptake on planar imaging corresponded to radiotracer at the pancreaticojejunal blind pouch and limb at the level of the collection (Figure 2C-D). SPECT/CT confirmed no bile leak. Patient was instead thought to have a postoperative seroma with fevers from cholangitis and did not require interventions.

SPECT/CT was able to rule out biliary leak after equivocal planar imaging due to overlapping surgically altered bowel and area of interest. HIDA planar imaging alone may have resulted in a false positive and unwarranted interventions. Despite concerns of supplemental radiation, staffing/logistic hurdles, and costs, the diagnostic clarity SPECT/CT offers can change management, and the threshold for obtaining a SPECT/CT especially in a postsurgical patient should be low.

References:

1. Schertz, P. J.; et al. Biliary Leaks: Multidisciplinary Approach to Diagnosis and Treatment. RadioGraphics 2024
2. Matesan, M.; et al. Biliary Leak in the Postsurgical Abdomen….Semin. Nucl. Med. 2017

3. Tian Yue, K.; et al. Imaging Postoperative Bile Leaks...SPECT/CT Scintigraphy. Clin. Nucl. Med. 2010

4. Van Den Wyngaert, T.; et al. SPECT/CT: Standing on...J. Nucl. Med. 2020

5. Wale, D. J. Advances in Radionuclide Imaging...Semin. Roentgenol. 2025

CT abdomen pelvis (A) axial and (B) coronal slices demonstrating a loculated collection at the porta hepatis extending into the lesser curvature of the stomach. C-F show subsequent HIDA planar imaging. (C) There is hepatic and pancreaticojejunal limb radiotracer uptake at minute 14 from radiotracer administration. From minute 27 (D) to minute 38 (E), there is increasing focal radiotracer uptake (red arrow) overlying the epigastric region and at the expected level of the porta hepatis collection. At minute 66 (F), this area starts to lose radiotracer uptake with remaining radiotracer uptake largely confined to the bowel.

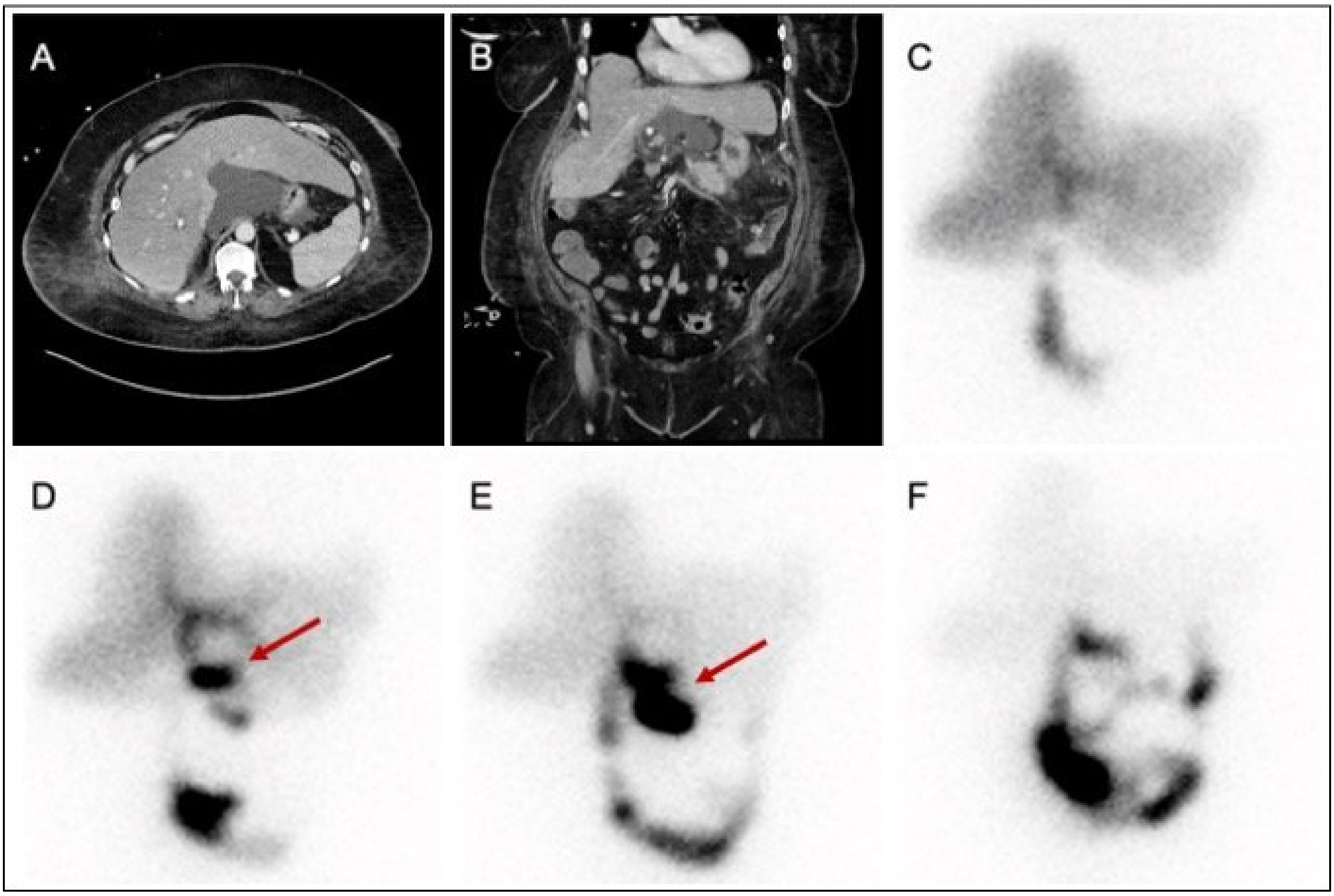

SPECT/CT abdomen after acquisition of HIDA planar imaging and 90 minutes after radiotracer administration. Coronal (A) and axial (B) slices show no radiotracer uptake at the porta hepatis collection (dashed circle). Radiotracer uptake near the level of the porta hepatis at the pancreaticojejunal blind pouch (C, arrow) and the pancreaticojejunal limb (D, arrowhead). This corresponds to the radiotracer uptake seen at the epigastric region in Figure 1.

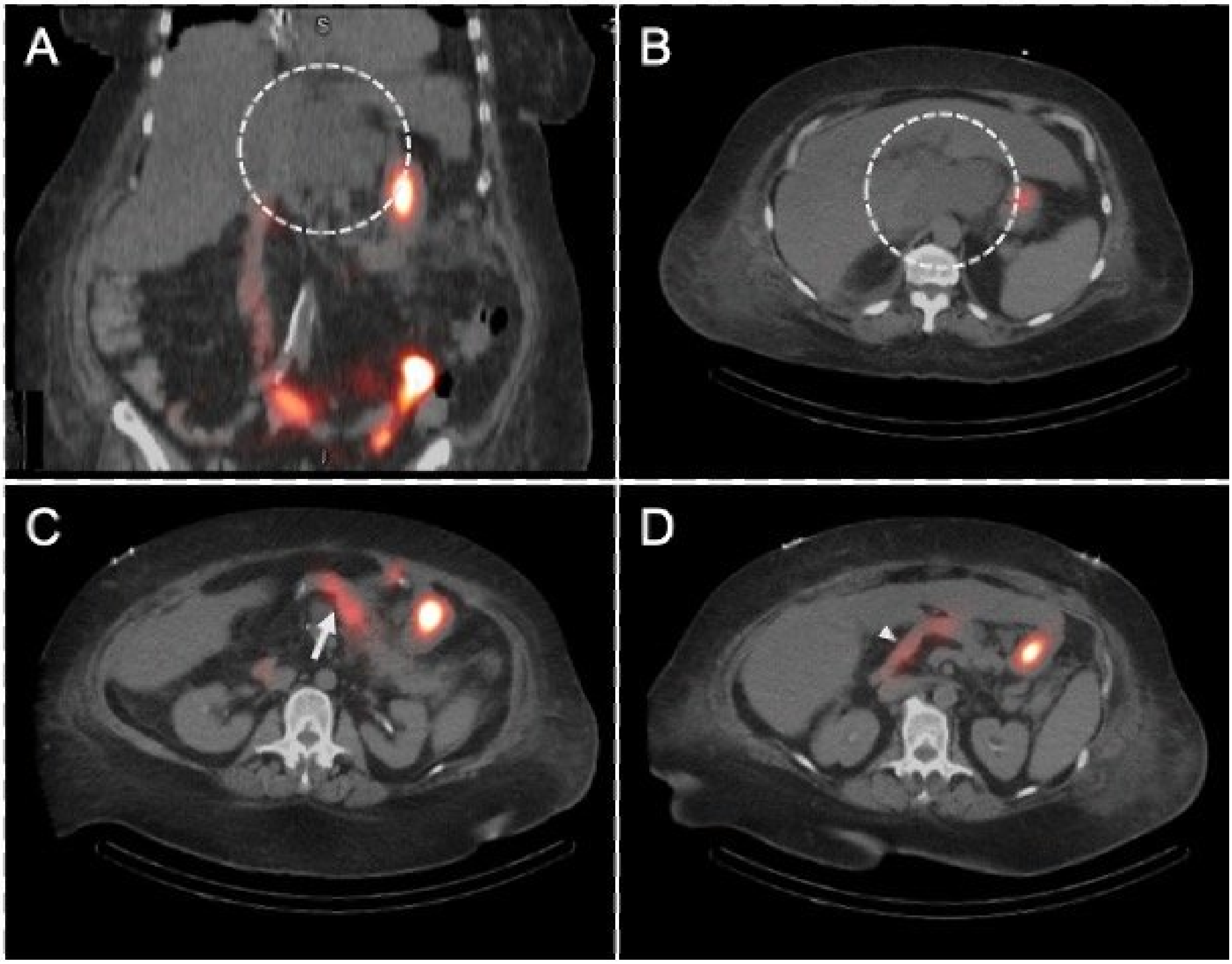

Keywords : Bile Leak, SPECT/CT, Postoperative Seroma

[Poster Presentation 1]

ABD-Biliary-02

Pictorial Review of Biliary Dilatation in the Context of Malignancy, Focusing on Less Common Pathologies

Yi Ting Lim[1*], Christine Ying Kwok[1]

[1]Diagnostic Radiology, Tan Tock Seng Hospital, Singapore

Biliary dilatation in the context of tumours is often associated with primary tumours of the biliary tree such as cholangiocarcinoma or intraductal papillary neoplasms of the bile duct (IPNB). The degree of biliary dilatation varies depending on the subtype of cholangiocarcinoma (intraductal, mass forming or periductal infiltrating) as well as the degree of mucin production and tumour proliferation in IPNB's.

Less commonly, biliary dilatation can also be seen in metastatic disease (which commonly arises from the colon or pancreas) or direct extension from a primary hepatic parenchymal lesion such as hepatocellular carcinoma (HCC).

Whilst clinical history may be helpful in narrowing the differential diagnosis, it is important for the radiologist to be familiar with the spectrum of possible etiologies and distinguish their various imaging differences, in order to guide management and facilitate timely treatment. This can be particularly challenging when patients first present with locally extensive disease, making it hard to ascertain the exact origin.

Bile duct involvement in metastasis and HCC has also shown to have prognostic implications with poorer outcomes noted and is also thus crucial to identify on imaging.

In this pictorial review, we will introduce several cases of bile duct dilatation by various tumours including colorectal metastasis and HCC and compare their imaging features with that of intrahepatic cholangiocarcinoma. We will showcase both the overlapping imaging features as well as the differences in order to help the reader gain familiarity to the various pathologies. Our case series of each of these tumours on CT and MRI have all been correlated with histology results.

Keywords : Biliary, Dilation, Uncommon

[Poster Presentation 1]

ABD-Biliary-03

Common Bile Duct Ascariasis

Munkh-Orgil Rentsensambuu[1], Nemekhbayar Purevsuren[1*], Munkhtulga Enkhtur[1]

[1]Radiology, Second State Central Hospital, Mongolia

Approximately 33% of the global population is estimated to be infected with ascariasis [1]. In the western rural regions of Mongolia, the prevalence of Ascaris infection has been reported to reach up to 12.8% [2]. In studies conducted in countries with high prevalence of ascariasis, it has been reported that cases of acute cholangitis with concurrent ascariasis and stones occur in approximately 1–5% of all patients[3]. Ascaris is primarily inhabits the human small intestine. In certain cases, mature worms aberrantly migrate into the biliary tract, including the common bile duct (CBD), leading to a condition known as biliary ascariasis [4]. Such migration can result in partial or complete obstruction of the biliary tree, potentially causing serious complications such as acute cholangitis, cholecystitis, and pancreatitis [6].

A 22-years-old man was presented at our emergency department with complaints of abdominal pain, vomiting with yellow-green color, and nausea. The symptoms started 4 days ago. This male herder. Laboratory tests were leukocytosis, biochemical tests ALP, BILD, GGT and ALT were elevated. Abdominal examination revealed tenderness in the epigastric region, with no guarding, rigidity, or signs of peritoneal irritation. Chest X-ray was within in normal limits.

ULTRASOUND EXAMINATION:
- *In the gallbladder, there is a stone of 0.8cm in size in the body portion (Fig. 1a Blue arrow).*
- *The CBD is dilated to 1.0 cm (Fig. 1b Green arrow).*
- *The bile ducts inside and outside the liver are dilated up to 0.8cm in size (Fig. 1c Red arrow).*

MRCP EXAMINATION:
- *Common bile duct ascariasis Tree line sign (Fig. 2a,2b Red arrow).*

ERCP EXAMINATION:
- *CBD checked with balloon and basket, multiple parasites around 0.8x0.5 cm in size discharged (Fig. 3 Green arrow).*
- *Also, stones around 0.6x0.5 cm in sizes together with dark colored bile discharged (Fig. 3 Blue arrow).*

The characteristic sonographic features of a worm in the common bile duct include a long, linear, parallel echogenic strip, usually without acoustic shadowing [4]. However, in this case the anechoeic lumen was not seen as the lumen disappears once the worm dies and coiling can occur as the worm shrivels up and becomes smaller. The diameter of the coiled structure in our case was 0.8x0.5 cm, while a live worm is generally 8 to 10 cm long. Abdominal ultrasonography, which is the first modality for evaluation of such patients, can allow biliary ascariasis to be diagnosed in 85% of cases. Magnetic resonance imaging (MRI) shows “eye-glass” appearances of ascaris in the bile duct [4]. This case demonstrates an unusual appearance of a dead ascaris and stones with dark colored bile on ERCP.

Ultrasonography has highly effective in the diagnosis. Radiologist remain vigilant and familiar with the radiologic sign of parasitic infections to ensure timely and accurate diagnosis.

- In the gallbladder, there is a stone of 0.8cm in size in the body portion (Fig. 1a Blue arrow).
- The CBD is dilated to 1.0 cm (Fig. 1b Green arrow).
- The bile ducts inside and outside the liver are dilated up to 0.8cm in size (Fig. 1c Yellow arrow).
- Dilatation of the CBD is indicative of a possible obstruction; therefore, an MRCP was performed for further evaluation.

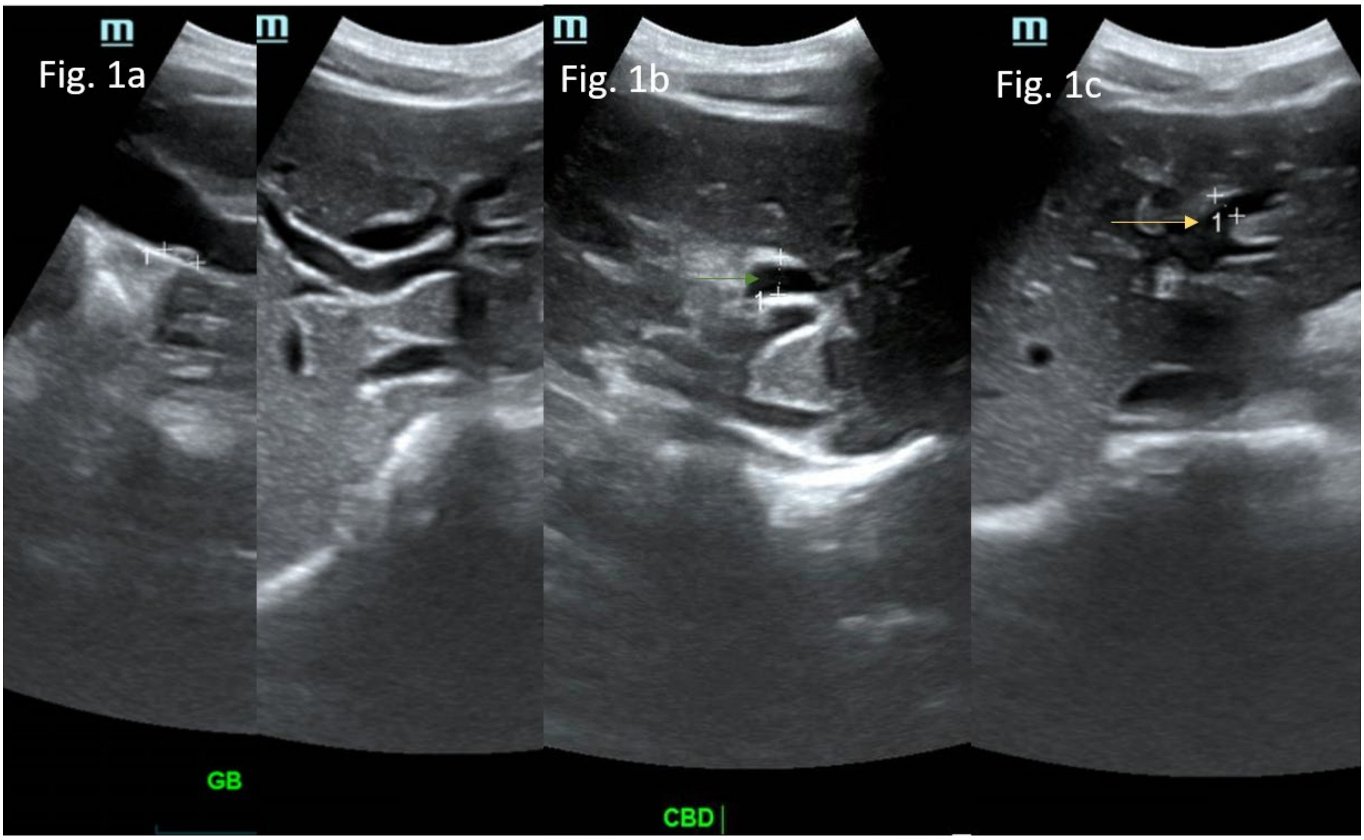

- MRCP shows similar shadow in the lower end of CBD. The central area of low density is also seen (Fig. 2a,2b,2c Yellow arrow).
- The bottom part of the gallbladder contains a stone with a diameter of 0.3cm with low density. (Fig. 2a Blue arrow).
- The bile is thick and contains sediment.

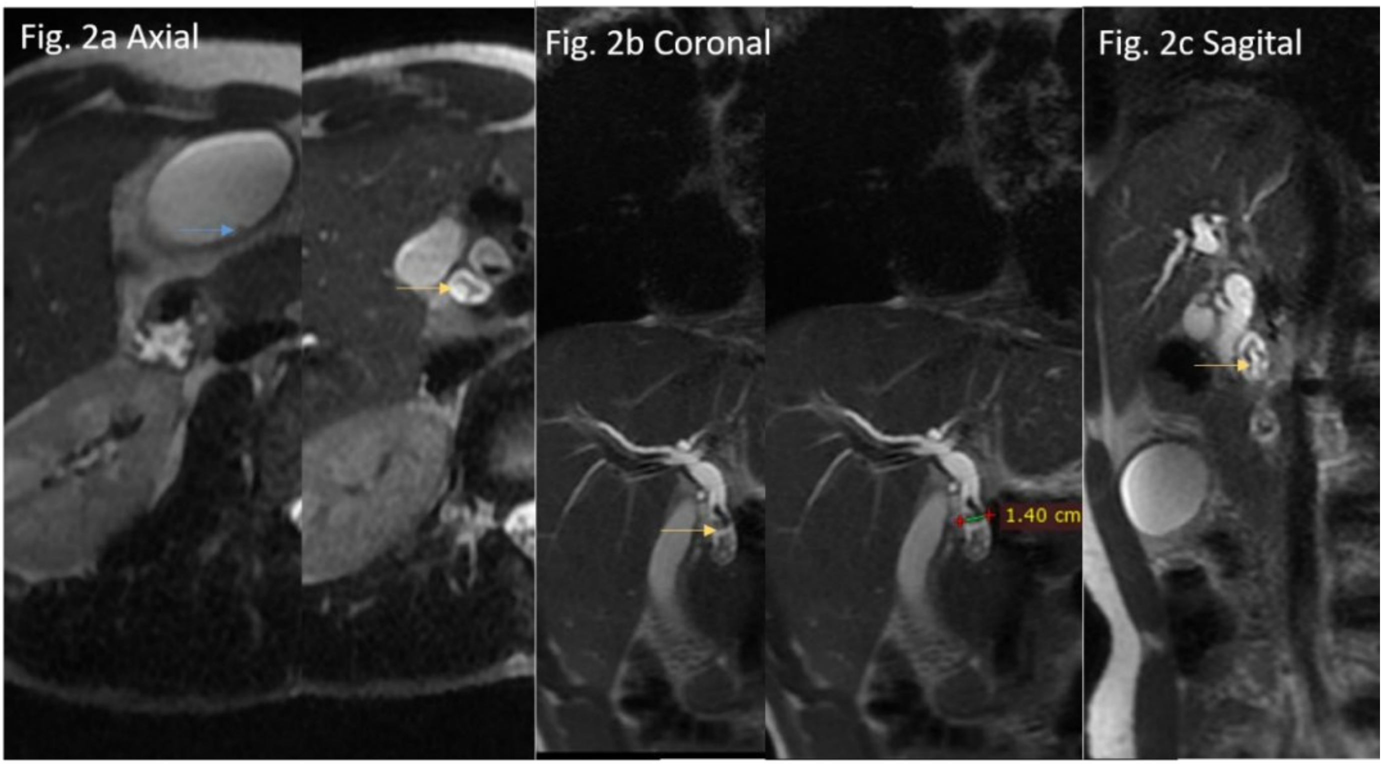

Keywords : Common Bile Duct Ascariasis, Ascariasis, Dilatation of the CBD

[Poster Presentation 1]

ABD-CT-01

Correlation between DXA and Hounsfield Unit in Lumbar Spine CT Scan

Munkh-Orgil Rentsensambuu[1], Enkhjargal Davkharbayar[1], Ankhbayar Enkhbaatar[2], Nemekhbayar Purevsuren[3], Munkhtulga Enkhtur[1], Batbayar Ankhjargal[1], Baasanjav Natsag[1], Otgontuya Tsendjav[1], Erdenebulgan Batmunkh[1*]

[1]Diagnostic center SSCH, Radiology, Mongolia
[2]Neurological surgery- SSCH, Neurological surgery, Mongolia
[3]Nuclear medicine center SSCH, Nuclear medicine, Mongolia

Osteoporosis of the spine can be assessed using CT scans performed for other indications without the use of additional radiation. In order to accurately assess osteoporosis with CT scans and monitor changes in bone mineral density values, reference values for people with osteoporosis are needed. The aim of this study was to use lumbar spine CT scans to assess osteoporosis and to correlate CT scan values (Hounsfield units HU) with DXA T-scores.

The study was conducted using a retrospective study design and the results were analyzed using Stata-19 software. The data of the study participants were extracted from the electronic medical system. The study included 229 patients aged 30-95 years who underwent abdominal CT and DXA examinations between 2020 and 2025. Patients with implants and previous spinal fractures who underwent surgery were excluded because of the difference in HU values. After the exclusion criteria, 137 patients out of 229 patients participated in the study. The results were calculated using the patients' age, gender, CT lumbar spine density, and osteoporosis T-score data from the electronic data, and the descriptive and analytical results were combined. The statistical significance threshold was set at 0.05 when calculating the analytical results. To determine the HU value of CTG, the HU value of L1-L4 vertebrae in 137 patients was measured for each vertebra at 3 levels along the axial axis / the upper part of the vertebra, the middle part, and the lower part / the trabecular part of the vertebral body and calculated the value. To make the measurement accurate, the largest ROI value was taken without including the cortical bone edge. The 3 values were averaged to determine the average HU value for each lumbar vertebra. The measurement was performed twice independently by 2 radiologists and 2 resident physicians.

T-scores were obtained from the data of the bone scan (DXA) for the L1-L4 vertebrae.

HU values decreased steadily with age for each vertebra and were significantly different between age groups ($p<0.001$). There was a significant positive correlation between HU values and bone mineral density and T-score ($p<0.001$). According to the World Health Organization guidelines, the T-score of the spine was classified into three groups: normal (-1.0 or higher), osteopenia (-1.0 and greater than -2.5), and osteoporosis (-2.5 or lower). In this study, (the mean HU of the spine in normal subjects was 112.0±58 ~ T-score ≥-1.0), (the mean HU of osteopenia subjects was 69.1±31.1 ~ -1.0 A mean HU value below 69 is considered to be a high risk of osteoporosis.

This study found that the HU value of the lumbar spine area consistently decreases with age. HU values and a strong positive correlation with the T-score of bone mineral density from DXA analysis also indicate that HU values based on CT scans may be clinically important in identifying bone diseases such as osteoporosis.

To drawing a circular ROI at 3 levels along the axial axis / the upper part of the vertebra, the middle part, and the lower part / including the trabecular part of the vertebral body.

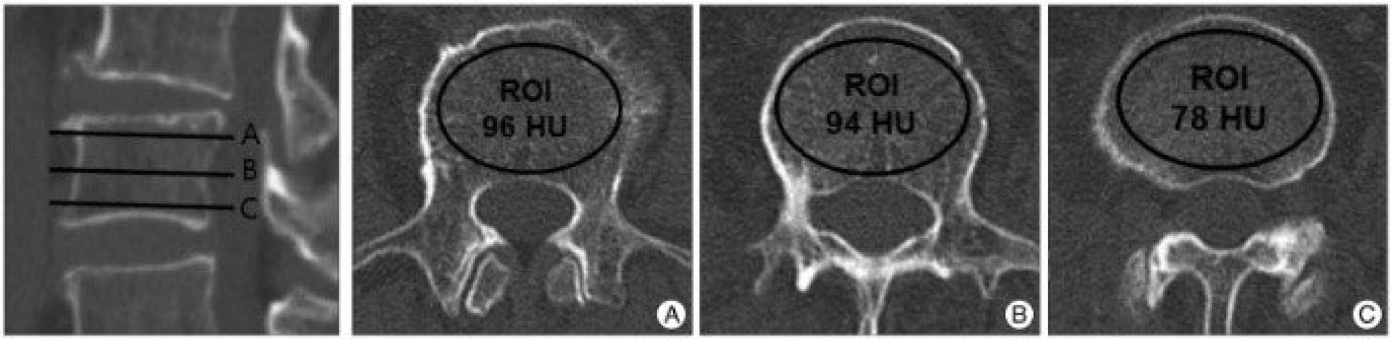

The HU value of each vertebra decreased steadily with age and was significantly different between age groups (p<0.001) [Figure 1]. There was a significant positive correlation between HU value and bone mineral density and T-score (p<0.001). [Figure 2]. According to the World Health Organization guidelines, the T-score of the spine was classified into three groups: normal (-1.0 or higher), osteopenia (-1.0 and greater than -2.5), and osteoporosis (-2.5 or lower). In this study, (the mean HU of the spine in normal subjects was 112.0±58 ~ T-score ≥-1.0), (the mean HU of osteopenia subjects was 69.1±31.1 ~ -1.0 [Figure 3].

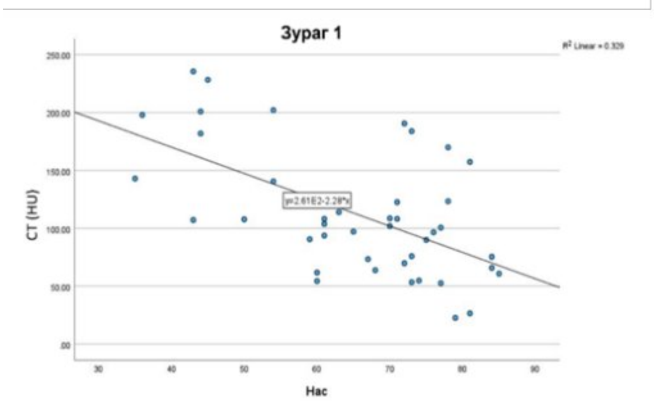

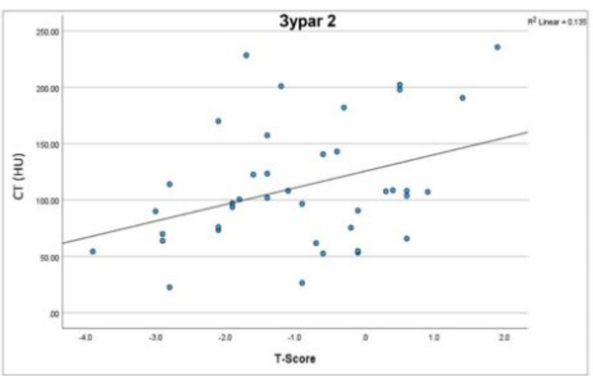

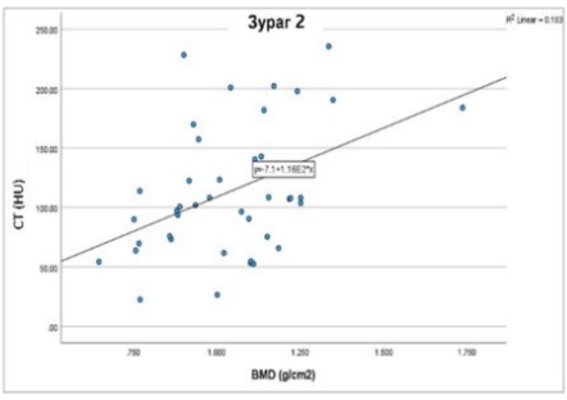

3ypar-3

T-SCORE		HOUNSFIELD UNITS Mean and standard deviation
NORMAL	≥-1.0	112.0±58
OSTEOPENIC	-1.0<T-score < -2.5	69.1±31.1
OSTEOPOROTIC	-2.5≤	55.6±30.6

Keywords : CT (HU) in Lumbar Spine, Bone Mineral Density, Osteoporosis

[Poster Presentation 1]

ABD-UGI-01

From Stability to Catastrophe: Evolving Traumatic Diaphragmatic Hernia with Intrathoracic Gastric Volvulus and Perforation in a Teenager

Hui Yun Ong[1,2], Wei Hung Chong[3], Sabariah Mohamed Kassim[2], Rafidah Zainon[4*]

[1]Radiology, School of Medical Sciences Universiti Sains Malaysia, Malaysia
[2]Radiology, Hospital Sultan Abdul Halim, Malaysia
[3]Paediatrics, Hospital Sultanah Bahiyah, Malaysia
[4]Biomedical Imaging, Advanced Medical and Dental Institute Universiti Sains Malaysia, Malaysia

Traumatic diaphragmatic hernia (TDH) is rare and often presents with nonspecific gastrointestinal symptoms, particularly when a history of trauma is absent or initially unrecognized. Delayed diagnosis increases the risk of life-threatening complications. This study aims to describe a catastrophic case of delayed TDH complicated by intrathoracic gastric volvulus followed by gastric perforation in an initially stable teenager, emphasizing the radiological findings, diagnostic challenges and clinical deterioration.

We conducted a detailed clinical, radiological and operative review of a 14-year-old boy who presented with progressive gastrointestinal symptoms over three days, without an initially disclosed traumatic event. Diagnostic evaluation included serial laboratory tests, chest and abdominal radiography, and contrast-enhanced CT of the thorax. Subsequent endoscopy, emergency imaging, operative findings and histopathological results were analyzed to delineate the sequence of pathological events and identify factors contributing to clinical decline.

Initial imaging revealed a large left diaphragmatic hernia with herniation of abdominal organs and intrathoracic gastric volvulus, without CT evidence of ischemia or perforation. Despite alarming radiological abnormalities, the patient remained clinically stable, and semi-emergent surgical repair was planned. On day 5 of hospital admission, he developed acute back pain, dyspnea and clinical deterioration. Emergency endoscopy revealed congested gastric mucosa and inability to pass the instrument. Condition worsened when he developed cardiac arrest 30 minutes after the endoscopy procedure. A previously undisclosed minor fall three days before presentation was revealed during resuscitation. Repeat imaging demonstrated acute intrathoracic gastric perforation with tension pneumothorax. Emergency thoracoabdominal surgery confirmed a 5 × 8 cm left diaphragmatic defect, herniated viscera, a necrotic gastric segment, and a 1 cm gastric perforation. Despite operative repair and maximal supportive care, the patient progressed to refractory shock and multiorgan failure, resulting in death.

This case underscores the insidious nature of traumatic diaphragmatic hernia, particularly when the precipitating trauma is minor or initially unrecognized. Even in clinically stable patients, delays in diagnosis can precipitate progressive visceral herniation, gastric volvulus, ischemia and ultimately fatal intrathoracic perforation. Prompt and comprehensive radiological evaluation, coupled with a heightened index of suspicion for occult trauma is crucial. Early surgical intervention remains essential

to prevent catastrophic morbidity and mortality.

Figure 1. *Serial chest radiographs.*

(A) Chest radiograph in erect position revealed grossly distended stomach shadow with fluid level in left hemithorax. The subsequent chest radiograph on Day 3 (B) revealed worsening stomach dilatation with mediastinal shift to the right. Air-fluid level was not apparent as it was taken in supine position. The dotted stomach outline shows appearance of 'Upside down stomach' with inferior pointing pylorus. The tip of the distal feeding tube is projected coiled at the mid-thoracic region. (C) Hyperexpanded left hemithorax with absence of bronchovascular markings, significant widening of left intercostal spaces and depression of left hemidiaphragm. Gross gastric distension was seen within the left hemithorax. There was also significant mediastinal shift to the right with almost complete collapse of the right lung. Taken together, the radiographic findings were most likely representing acute intrathoracic gastric perforation with tension pneumothorax. (D) Post-operative chest radiograph shows re-expansion of bilateral lungs.

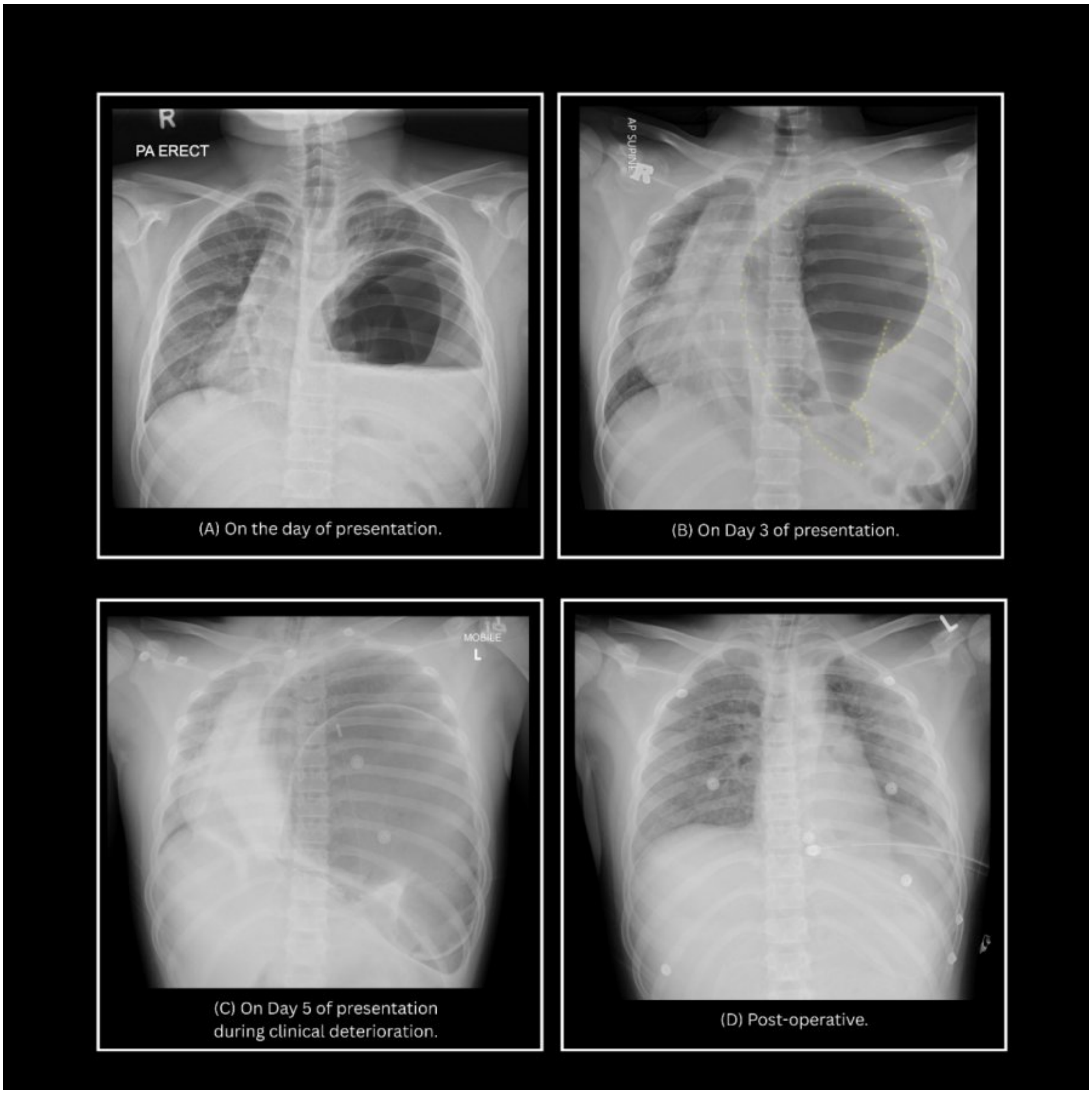

Figure 2. *Contrast-enhanced CT of the thorax in mediastinal window.*

(a) Coronal, **(b)** Sagittal, and **(c)** Axial images. Arrows (→) demonstrate a left posterolateral diaphragmatic defect. Asterisks (*) denote the markedly distended, herniated stomach with abnormal orientation, including a downward-directed pylorus and reversal of the greater and lesser curvatures. Despite significant gastric dilatation, characteristic "beaking" is observed at the gastroesophageal junction (red arrowhead) and at the distal gastric outflow tract (blue arrowhead), reflecting luminal tapering at the sites of twist. A malpositioned and coiled Ryle's tube is identified by the green dashed arrow (-->). Ovals (○) highlight herniated abdominal contents, including the spleen, pancreatic tail, transverse colon, and proximal duodenum. Left lung atelectasis is indicated by pink star (★) with associated mediastinal shift. No CT evidence of strangulation, ischemia, or perforation is present.

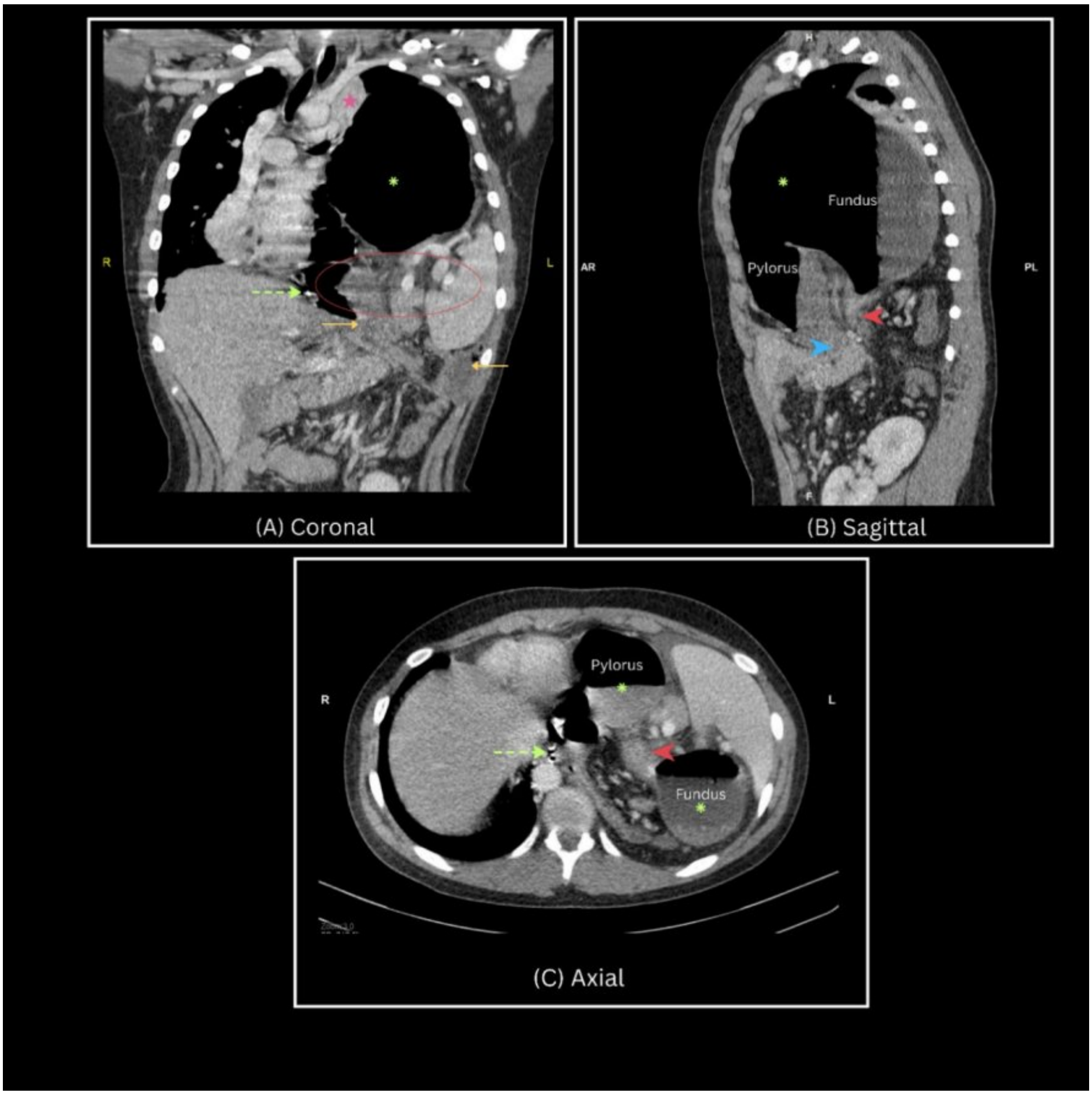

Keywords : Traumatic Diaphragmatic Hernia, Intrathoracic Gastric Volvulus, Intrathoracic Gastric Perforation

[Poster Presentation 1]

ABD-UGI-02

Baseline DCE-MRI Derived Parameters and MR Signal Intensity Based Logistic Regression Model to Predict Response of Esophageal Squamous Cell Carcinoma to Neoadjuvant Immunochemotherapy

Jingke Li[2], **Xurui Liu[1]**, Tianwu Chen[1*]

[1]Radiology, The Second Affiliated Hospital of Chongqing Medical University, China
[2]Radiology, Affiliated Hospital of North Sichuan Medical College, China

It is important to predict response of esophageal squamous cell carcinoma (ESCC) to neoadjuvant immunochemotherapy for treatment decision-making. This study aimed to explore whether dynamic contrast-enhanced MRI (DCE-MRI) derived parameters and MR signal intensity can predict the response.

82 consecutive ESCC patients undergoing pretherapeutic DCE-MRI, T_2WI and T_1WI followed by neoadjuvant immunochemotherapy were prospectively enrolled, among which patients from Institution 1 were randomly stratified into training (n=52) and internal validation (n=15) cohorts, and those from Institution 2 were assigned to external validation cohort (n=15). K^{trans}, K_{ep} and V_e of ESCC and their standard deviation (SD) were generated based on DCE-MRI, mean and SD of MR signal intensity on T_1WI and T_2WI were also obtained, and coefficient of variation (CV) of these parameters were calculated. In training cohort, all parameters were statistically compared between responders and non-responders. Predictive effectiveness of individual parameters with statistical difference, and the parameters based logistic regression models were evaluated using area under the receiver operating characteristic curve (AUC) in three cohorts.

Mean and SD of K_{ep} (K_{ep}_Mean and K_{ep}_SD, respectively) and T_2WI signal intensity (T_2WI_Mean and T_2WI_SD, respectively) in responders were higher than in non-responders (all P-values <0.05), among which, K_{ep}_Mean could best predict the responsiveness with AUCs of 0.858, 0.768 and 0.870; and the model (T_2WI_Mean+T_2WI_SD+K_{ep}_Mean+K_{ep}_SD) demonstrated superior predictive performance (AUCs: 0.928, 0.911 and 0.907) in training, internal and external validation cohorts, respectively.

Combination of mean and SD of K_{ep}, and T_2WI signal intensity could well predict immunochemotherapy responsiveness of ESCC.

Baseline DCE-MRI derived parameters and MR signal intensity based logistic regression model to predict response of esophageal squamous cell carcinoma to neoadjuvant immunochemotherapy

Aim: To explore whether dynamic contrast-enhanced MRI (DCE-MRI) derived parameters and MR signal intensity can predict response of esophageal squamous cell carcinoma (ESCC) to neoadjuvant immunochemotherapy.

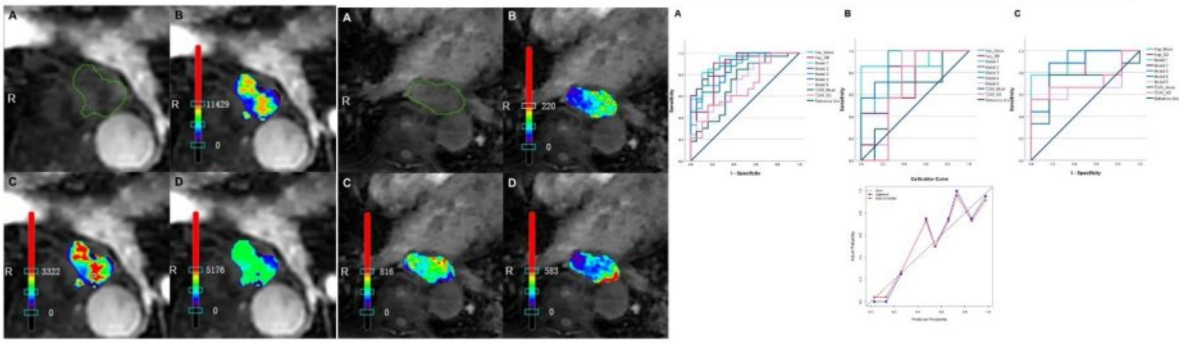

Conclusion: Combination of mean and standard deviation of countercurrent rate and T_2WI signal intensity could well predict immunochemotherapy responsiveness of ESCC.

Keywords : Esophageal squamous cell carcinoma, Neoadjuvant chemotherapy, Dynamic contrast-enhanced MRI

[Poster Presentation 1]

ABD-LGI-02

Spatial Mapping of Tumor Response and Mesorectal Involvement on Pretreatment Contrast-Enhanced CT in Locally Advanced Rectal Cancer

Huiyu Gan[2], Zhen Li[1], **Ziman Xiong[1]**, Ziling Zhou[1*]

[1]Radiology, Tongji Hospital Tongji Medical College Huazhong University of Science and Technology, China

[2]Radiology, Tongji Medical College Huazhong University of Science and Technology, China

Patients with locally advanced rectal cancer (LARC) exhibit significant heterogeneity in response to neoadjuvant chemoradiotherapy (NCRT), and there is an urgent need for accurate preoperative prediction to guide treatment decision-making. This study aims to explore spatiotemporal features from large-scale multi-center contrast-enhanced computed tomography (CECT) data to construct quantitative spatiotemporal models for tumor response in LARC patients to NCRT.

This study retrospectively collected CECT and clinical information of 337 pathologically confirmed LARC patients from three centers. Annotation of tumors and the mesorectum on dual-phase (arterial and venous) CECT images for all cases was performed by two radiologists using the interactive contouring function of the TOMOSAM plugin in 3D Slicer. The cohort was randomly partitioned into training (70%), validation (20%), and test sets (10%). Radiomic extraction yielded 1,223 features per phase (arterial and venous). Pathologic response to CRT was assessed histopathologically and graded using the American Joint Committee on Cancer (AJCC) tumor regression grade (TRG) system (0–3). Treating TRG as a four-class outcome, we evaluated the performance of the radiomics-based multiclass classifier using a one-vs-rest scheme with macro-averaged receiver operating characteristic(ROC) area under the curve(AUC). We trained thirteen models using AdaBoost, Gradient Boosting, LightGBM, and additional baselines to predict tumor involvement, mesorectal involvement, and a combined outcome. Two input schemes were evaluated: (1) single-phase arterial (A) or venous (V) data and (2) a dual-phase V–A difference design, which leverages multiphasic information for improved detectability. Bayesian optimization was used for hyperparameter tuning and 3-fold stratified cross-validation was applied to evaluate model stability.

Among the total population, TRG0 accounts for 9.7%, TRG1 for 13.3%, TRG2 for 41.5%, and TRG3 for 35.5%. In the tumor model, arterial phase achieves the highest AUC, at 0.7844; in the mesorectum model, the V-A difference exhibits the best performance, with an AUC of 0.7527. Meanwhile, across Phases A, V, and V-A difference, the tumor model consistently demonstrates better performance than mesorectum , with respective ΔAUC values of 0.057, 0.0384, and 0.0097.

The tumour-mesorectum model can effectively explain the spatiotemporal changes of tumors in LARC after NCRT by integrating longitudinal features across multiple phases pre- and post-NCRT and characteristics of different spatial regions. It provides a quantitative tool for evaluating tumor response and mesorectal involvement, and addressing poor efficacy prediction accuracy.However, the study is limited by its retrospective design, which may introduce inherent selection bias and affect the

generalizability of the findings.

Fig.1 OVR ROC(per-class faint,macro bold). Thirteen solid lines reflect the AUC values of thirteen tumor models constructed using V-A differences. The dashed lines are the boundary lines of the filled area for the performance fluctuation interval corresponding to the model's ROC curve

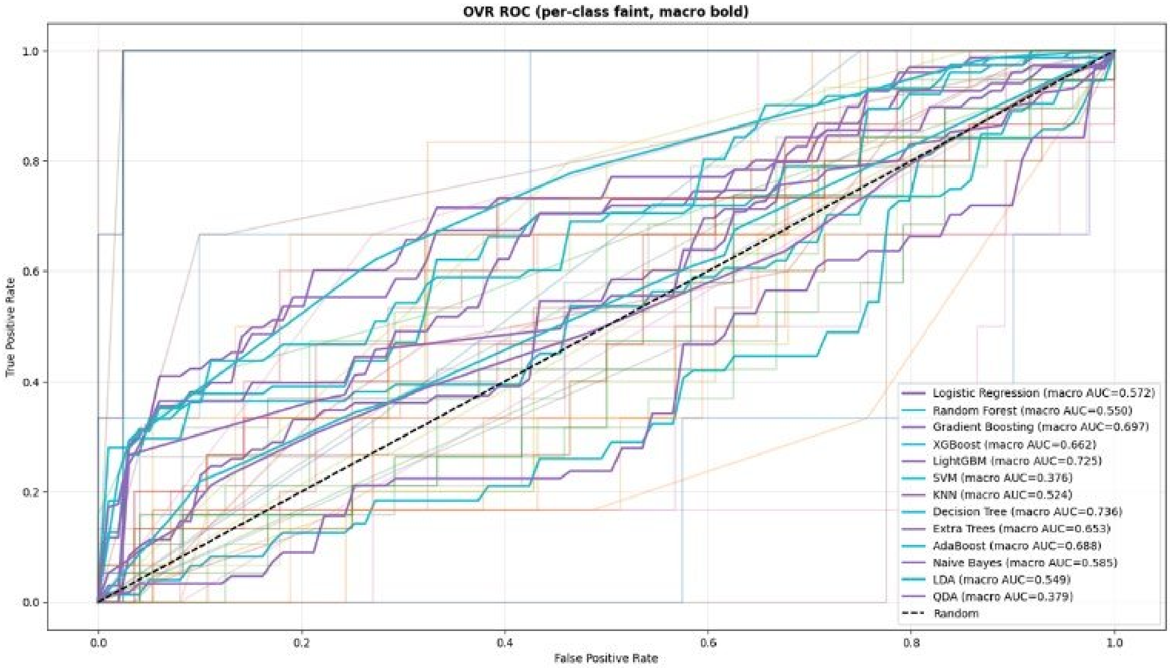

Fig.1 OVR ROC(per-class faint,macro bold). Thirteen solid lines reflect the AUC values of thirteen tumor models constructed using V-A differences. The dashed lines are the boundary lines of the filled area for the performance fluctuation interval corresponding to the model's ROC curve

Fig.2 (a) displays Clinical Impact Curves of the optimal Gradient Boosting model constructed from the arterial phase tumor model for each class , with the x-axis representing the decision threshold and the y-axis denoting relevant metrics. (b) presents calibration curves of the Gradient Boosting model for each class, where the dashed line “Perfect” indicates ideal calibration between mean predicted probability and fraction of positives. (c) shows confusion matrices for tumor models constructed from arterial phase, venous phase, and venous minus arterial phase (min) images, respectively; rows denote actual classes, columns denote predicted classes, and color intensity encodes prediction counts

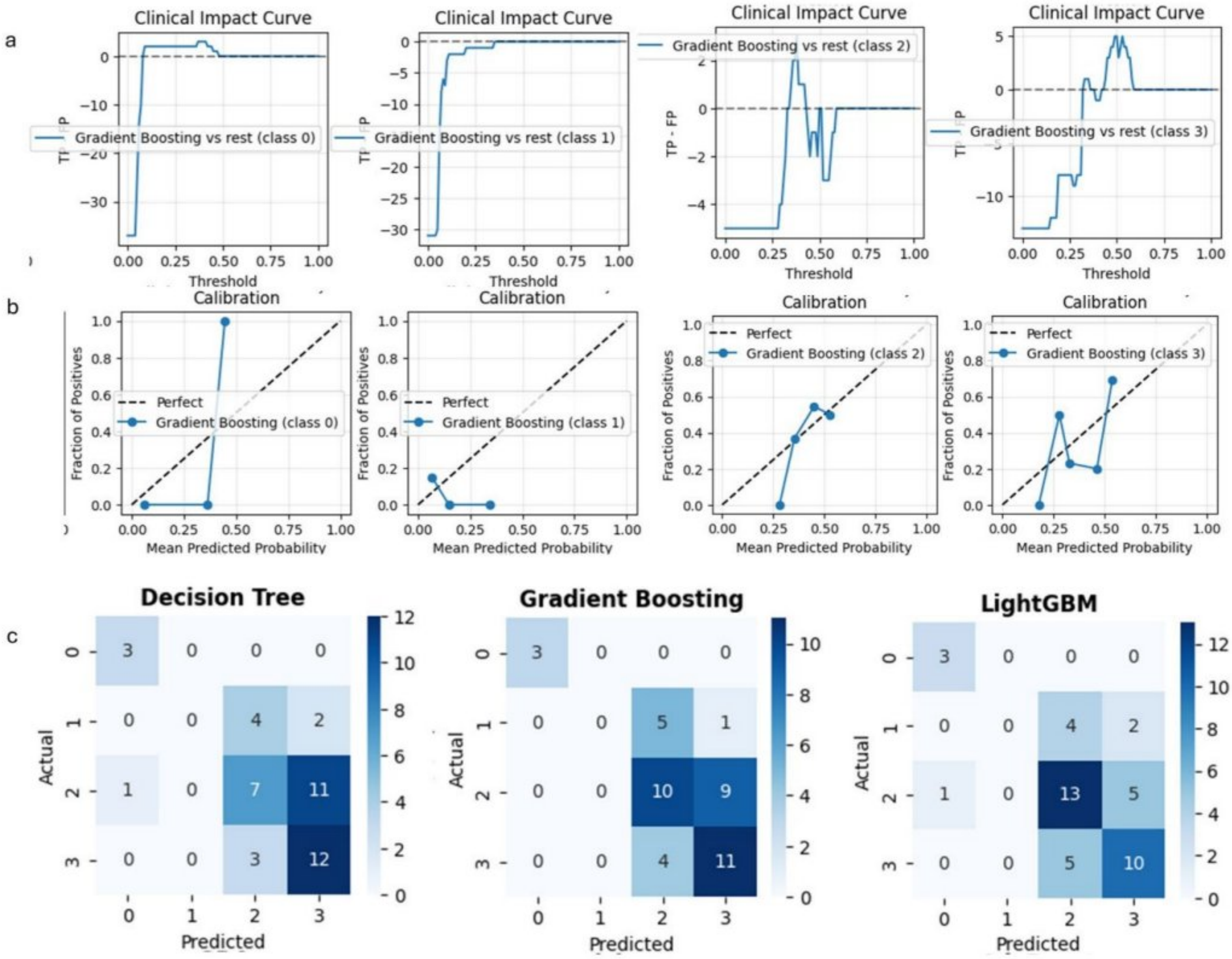

Fig.5 (a) displays Clinical Impact Curves of the optimal Gradient Boosting model constructed from the venous phase mesorectum model for each class .(b) presents calibration curves of the Gradient Boosting model for each class. (c) shows confusion matrices for mesorectum models constructed from arterial phase, venous phase, and venous minus arterial phase (min) images, respectively

Keywords : Locally Advanced Rectal Cancer, CT, Spatiotemporal Mapping

[Poster Presentation 1]

ABD-LGI-03

The Accuracy and Reliability in Detection of Radiologic Signs of Acute Appendicitis Using CT Images Sent Via Mobile Phone Application in Comparison with Medical Grade Workstation Monitor

Vic Emile Bernabe[1*]

[1]Radiology, Fellow, Philippines

The use of mobile or smartphones is very popular in the current times. It has also already been used in the healthcare setting, which may range from patient consultation to monitoring several health conditions, as well as promoting easier communication among the healthcare team. In many settings, physicians now often communicate with one another by sending radiographic pictures through mobile or smartphones, which helps with emergency triaging and transfer decision-making. In line with this, the study aimed to determine the accuracy and reliability of taking CT images using mobile or smartphones, and using these images to diagnose acute appendicitis.

Appendicitis is one of the most common complaints that warranted abdominal emergency surgery worldwide and a prominent cause of acute abdominal discomfort. Finding more convenient ways to diagnose and hasten the diagnosis of the condition will warrant more optimal management that will pave the way to better patient outcomes.

A cross-sectional diagnostic validation study was conducted at the Department of Radiology of Far Eastern University- Dr. Nicanor Reyes Medical Foundation from June 2024 to July 2024. Fifty CT images were retrospectively selected by one radiology consultant using medical records of patients with available confirmation of definitive positive or negative appendicitis (half positive and half negative cases) and previous CT findings based on the standard image generated from the medical grade monitor reports. The radiology residents that participated were given 10 CT images each generated using a mobile phone (Apple Iphone 10) taken in a medical-grade workstation monitor (5 definite positive and definite negative cases of appendicitis). The participating five 4th year radiologists were blinded on the patient diagnosis and previous findings based on the standard image generated from the medical grade monitor reports.

There was high/good sensitivity (96%), specificity (88%), positive predictive value (88.9%), and negative predictive value (95.6%) of using abdominal CT images taken by mobile phone camera for diagnosing acute appendicitis. A concordance level of 94.0% (p=0.004) was observed between CT images taken by mobile phone camera and image generated from medical-grade workstation monitor.

There is high accuracy and concordance of CT images taken on a medical-grade workstation monitor via mobile phone camera in the detection of acute appendicitis. This method can be a cost-effective and efficient way to quickly assess patients in emergency situations where immediate medical attention is required. However, further studies are needed to validate the reliability and consistency of

this approach across different healthcare settings and patient populations.

Table 1. Sensitivity, specificity, positive predictive value, and negative predictive value of using abdominal CT images taken by mobile phone camera for diagnosing acute appendicitis.

	Definitive positive	Definitive negative	Sensitivity (95%CI)	Specificity (95%CI)	PPV (95%CI)	NPV (95%CI)	Accuracy
Positive in Mobile phone camera	24 (96.0)	3 (12.0)	96% (80.5-99.3)	88% (70.0-95.8)	88.9% (71.9-96.2)	95.6% (79.0-99.2)	92% (81.2-96.8)
Negative in Mobile phone camera	1 (4.0)	22 (88.0)					

A concordance level of 94.0% (p=0.004) was observed between CT images taken by mobile phone camera and image generated from medical-grade workstation monitor.

Table 2. Level of concordance between abdominal CT images taken by mobile phone camera and image generated from medical-grade workstation monitor

	Positive in standard image	Negative in standard image	Concordance Correlation Coefficient	p-value
Positive in Mobile phone camera	24 (96.0)	2 (8.0)	0.94 (0.83 to 0.98	0.004
Negative in Mobile phone camera	1 (4.0)	23 (92.0)		

Keywords : Acute Appendicitis, Teleradiology, Radiologist

[Poster Presentation 1]

ABD-Others-01

Apart from Appendicitis: Pictorial Review of Iliac Fossa Pain

Emma Choon Hwee Lee[1*], Rebekah Zhuyi Lee[1], Shuyi Guo[1], Edmond Yang Shan Lim[1], Albert Su Chong Low[1]

[1]Cardiothoracic and Abdominal Radiology, Singapore General Hospital, Singapore

Acute iliac fossa pain is a common and sometimes challenging clinical presentation. It is frequently assessed with CT and diagnoses encountered extends beyond acute appendicitis. This pictorial review aims to illustrate the diverse spectrum of pathologies that may present with iliac fossa pain and highlight the findings on CT. Imaging plays a key role in accurate diagnosis and aids clinical decision-making in this acute presentation.

We present CT images from patients whom we have encountered in our clinical practice who presented with acute iliac fossa pain. The characteristic imaging appearances of a wide range of conditions manifesting with iliac fossa pain and their key clinical correlations are illustrated through representative CT cases.

This pictorial review covers a wide range of conditions that may manifest as iliac fossa pain including appendicitis and its mimics (epiploic appendagitis, Meckel's diverticulitis), colonic pathology (malignancy, diverticulitis, foreign body perforation), gynaecological conditions (ovarian torsion, pelvic inflammatory disease), urinary tract pathology (ureteric calculus), and less common causes such as iliac vein thrombosis and musculoskeletal causes.

Awareness of the diverse radiologic manifestations of iliac fossa pain is essential for timely and accurate diagnosis by the radiologist. A systematic, anatomy-based approach enables detection of subtle imaging features and improves diagnostic confidence in making an accurate diagnosis in the presentation of acute iliac fossa pain.

Keywords : Iliac fossa pain, Appendicitis

[Poster Presentation 1]

ABD-Others-02

Evaluating the Educational Impact of a CT Post-Processing Workshop

Samantha Tan[1*], Shawn Kok[1], Uppaluri Anandswaroop[1], Min-On Tan[1]

[1]Diagnostic Radiology, Sengkang General Hospital, Singapore

Post-processing tools such as dual-energy analysis, lung perfusion mapping, and vascular reconstruction are increasingly essential in modern CT interpretation, yet remain inconsistently taught across radiology residency programs. This study aimed to evaluate the educational impact of a dedicated hands-on Syngo.via post-processing workshop and to assess the need for incorporating structured post-processing training into the radiology curriculum.

A three-hour case-based workshop was conducted using Siemens Syngo.via workstations. Sixteen participants (R3–R4 residents, associate consultants, and junior radiographers) completed pre- and post-workshop surveys assessing prior exposure, understanding of post-processing concepts, confidence in using tools such as dual-energy applications and MPR/MIP/3D reconstructions, and perceived relevance to clinical practice. Quantitative responses were measured using Likert scales, and qualitative free-text responses were thematically analyzed.

Most of the participants had not attended a prior CT post-processing workshop before. Pre-workshop understanding of post-processing software was low (median score 2/5). Confidence in independently performing basic post-processing was similarly limited (median 2/5), and several participants reported little awareness of advanced applications such as lung perfusion or vessel analysis tools.
Post-workshop surveys demonstrated marked improvement. Participants reported significantly greater understanding of Syngo.via functions (median 4/5) and increased confidence in performing MPRs, DECT analysis, and vascular measurements (median 4/5). All participants agreed that the workshop was beneficial and that post-processing training should be formally incorporated into residency teaching. Common suggestions for improvement included increasing workstation licenses, providing more supervised hands-on time, and offering follow-up modules covering additional software platforms.

This expanded 16-participant evaluation confirms a clear training gap in CT post-processing and demonstrates that a focused Syngo.via workshop substantially improves trainee understanding, confidence, and perceived clinical relevance. The consistent endorsement for structured post-processing education supports integrating such workshops into the radiology residency curriculum and expanding access across training sites to ensure radiologists are equipped to utilise modern CT capabilities effectively.

Keywords : Education, Post-processing CT

[Poster Presentation 1]

GU-Uro-01

One-stop Early Noninvasive Evaluation of Renal Allograft Rejection and Fibrosis: Microstructural Mapping via Time-dependent Diffusion MRI

Zhouyan Liao[1], **Xiaonan Yang[1]**, Siyuan Ma[1], Gen Chen[1], Jeong Min Lee[2], Zhen Li[1*]

[1]Radiology, Tongji Hospital Tongji Medical College Huazhong University of Science and Technology, China

[2]Radiology, Seoul National University Hospital, Korea

Functional MRI offers promise for noninvasive detection of renal allograft injury, but conventional models lack biological specificity. This study aimed to evaluate the clinical utility of time-dependent diffusion MRI (td-dMRI) for detecting rejection and fibrosis in kidney transplant recipients.

In this prospective observational study at a tertiary center in China, adult renal allograft recipients undergoing indication biopsies between April 2024 to June 2025 were enrolled. Exclusion criteria included unstable vitals or MRI contraindications. Microstructural maps from td-dMRI based on a Bayesian method, DWI, intravoxel incoherent motion, diffusion kurtosis imaging, stretched exponential model, fractional order calculus, and continuous-time random-walk model. The diagnostic performances of these microstructural parameters in differentiating different degrees of renal allograft fibrosis (mild, moderate and severe fibrosis) and rejection (no-rejection, acute and chronic rejection) were evaluated by areas under the receiver operating characteristic curves (AUC).

A total of 100 patients (67 males, 33 females) were analyzed. Among them, 41 had acute rejection and 13 had chronic rejection; 67 had mild fibrosis, 19 moderate, and 14 severe fibrosis. td-dMRI-derived $diameter_{cortex}$ significantly distinguished fibrosis grades, while $cellularity_{medulla}$ identified early fibrotic changes. For rejection, $diameter_{cortex}$, fin_{cortex}, and $fp_{medulla}$ differentiated acute rejection, and $D\text{-}CTRW_{cortex}$, fin_{cortex}, $fp_{medulla}$, and $diameter_{cortex}$ distinguished chronic rejection. Combining td-dMRI metrics with clinical variables yielded high AUCs (0·968 for acute, 0·913 for chronic rejection).

This study supports td-dMRI as a biologically meaningful, one-stop contrast-free imaging approach for transplant kidney surveillance. It enables noninvasive detection of structural and cellular changes associated with rejection and fibrosis, even when conventional markers are inconclusive. Integrating td-dMRI with serum biomarkers may improve diagnostic accuracy and reduce unnecessary biopsies, promoting personalized immunosuppression and earlier intervention. Future research should validate its utility in multicenter and longitudinal settings.

Study flow chart showed respective histology images (x 400) of a patient with renal allograft (45 years old, male, with renal allograft IgA nephropathy (Oxford classification: M0E1S1T1C0) and mild, borderline acute T cell-mediated rejection factors (Banff2019: i1,10-1, g0v0, ptc0,MVI=0, ah3, mm2, cil,ctl, cg0, cv2,Til, i-IFTA1, t-IFTA1,C4d(-), SV40T (-)).

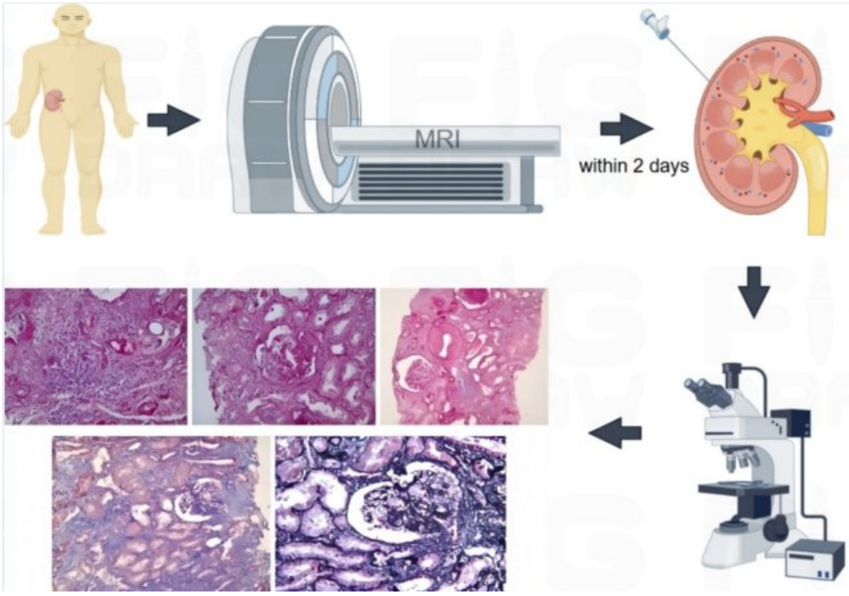

Parameter maps of cellularity, fin, diameter, and Dex calculated by Bayesian estimation from representative no rejection and mild fibrosis (A), acute rejection and moderate fibrosis (B) and chronic rejection and severe fibrosis (C) renal allograft in vivo.

Dex, extracellular diffusivity; fin, intracellular volume fraction.

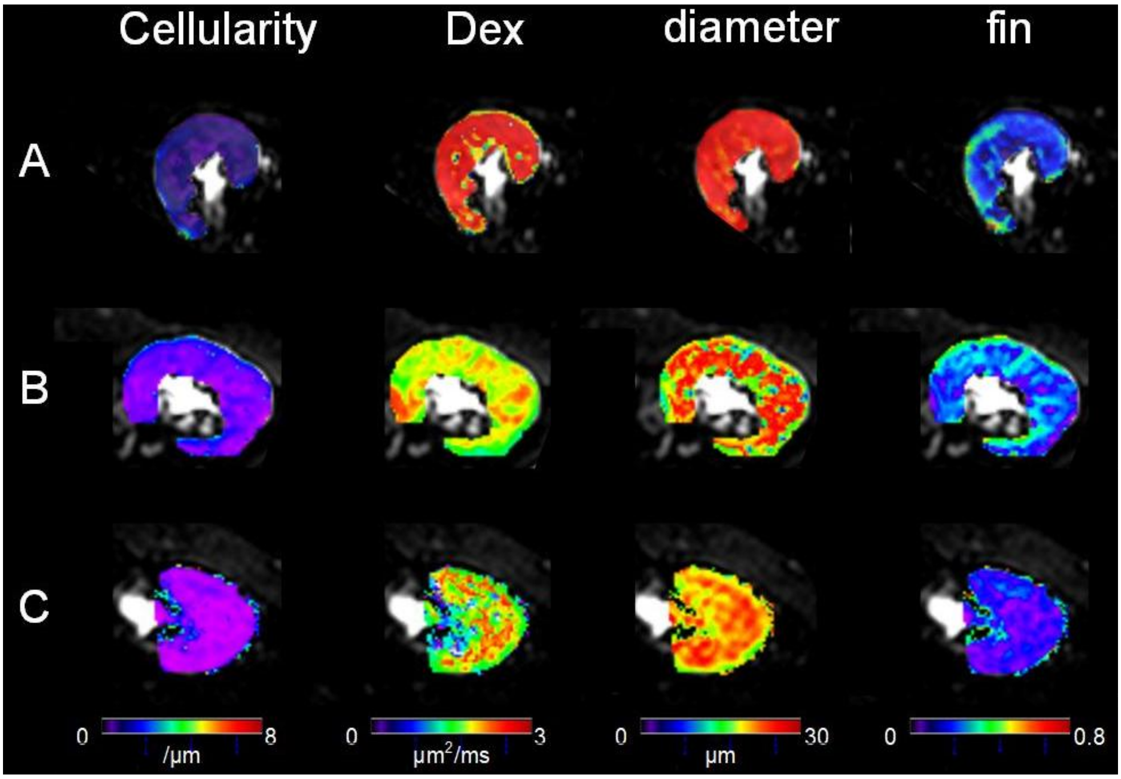

Keywords : Time-dependent diffusion MRI, Renal allograft fibrosis, Renal allograft rejection

[Poster Presentation 1]

GU-Uro-02

Nutcracker Syndrome with Midline Congestion Syndrome and May-Thurner Syndrome: Pathophysiology, Imaging Findings, and Postural Therapeutic Implications

Seung Hyup Kim[1,2,3*], Hyo Jeong Lee[1], Suhnggwon Kim[2], Eungtaek Kang[2], Myung Kim[3], Sang Eun Lee[3], Young Ik Lee[3]

[1]Radiology, Ewha Womans University Mokdong Hospital, Korea
[2]Radiology, Seoul K Nephrology Clinic, Korea
[3]Radiology, SNU Healthy Prostate Clinic, Korea

Nutcracker syndrome (NCS) is increasingly recognized as a more common condition than previously thought, and clinical interest in this entity continues to grow. Hypertension of the left renal vein (LRV) leads to the classical symptoms of NCS, including hematuria, proteinuria, and/or left flank pain. In addition, the development of collateral venous channels may cause a wide spectrum of symptoms, often limited to the left side of the body. Because collateral-related symptoms are highly variable, it is often difficult to suspect NCS based on symptoms alone. Therefore, recognition of characteristic imaging findings and correlation with clinical presentation are essential for diagnosis. Improvement of symptoms with postural modification, particularly by avoiding the supine sleeping posture, strongly suggests that NCS is the underlying cause.

Midline Congestion syndrome (MCS) is a diagnostic term used when patients with NCS develop severe symptoms due to collateral venous congestion predominantly on the left side of the body. Typical examples include left-sided pelvic congestion in women and left-sided varicocele in men; however, venous congestion may occur anywhere from head to toe and cause variety of left-sided symptoms such as pain or discomfort, edema, numbness, tingling sensation, headache, nasal stuffiness, tinnitus, and conjunctivitis. Compression of the left common iliac vein (LCIV) between the right common iliac artery and the vertebral body may cause left lower extremity congestion, known as May-Thurner Syndrome (MTS). MTS frequently coexist in patients with NCS and MCS.

A clinical and imaging database from three institutions (Ewha Womans University Mokdong Hospital, Seoul K Nephrology Clinic, and SNU Healthy Prostate Clinic) included approximately 300 patients diagnosed with NCS based on Doppler ultrasound and/or CT findings and clinical symptoms. Many patients exhibited collateral-related left-sided symptoms that improved with postural modification, leading to a diagnosis of MCS. Among them, 30 patients also demonstrated MTS, presenting with discomfort or edema of the left lower extremity and color Doppler evidence of excessive LCIV compression.

The degree of LRV and LCIV compression is greatest in the supine position and least in the left lateral decubitus position. Patients were advised to avoid supine sleeping and to adopt a left lateral sleeping posture, which led to variable but often significant improvement of symptoms of NCS and MTS.

This scientific exhibition presents the underlying theory, Doppler ultrasound and CT findings, and representative case scenarios illustrating NCS with MCS and MTS.

A 62-year-old woman with nutcracker syndrome and midline congestion syndrome showing tight compression of the left renal vein (LRV) between the abdominal aorta (AA) and superior mesenteric artery (SMA). Note dilated pre-compressed LRV with absent flow signal indicating sluggish flow (asterisks) and bight-colored fast flow in the post-compressed LRV (arrows)

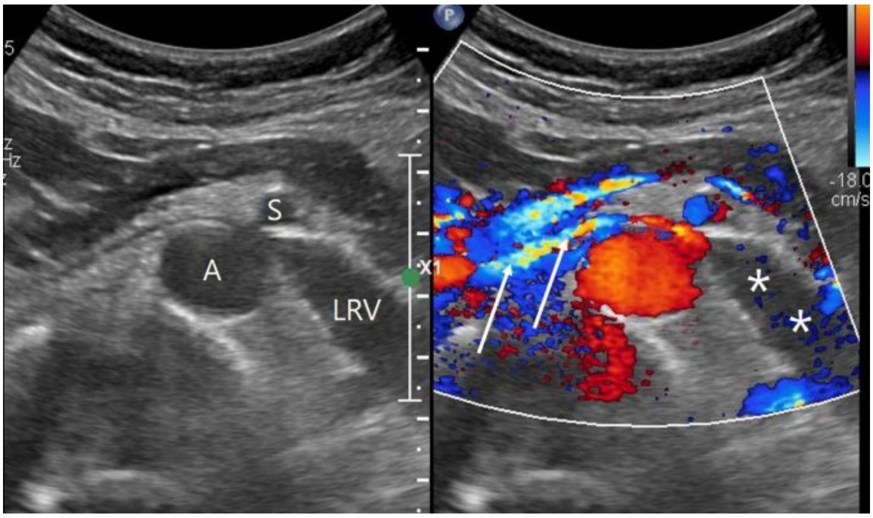

This patient also had May-Thurner syndrome showing compressed left common iliac vein (LCIV) between the right common iliac artery (RCIA) and vertebra (V). Note sluggish flow in the pre-compressed LCIV (asterisks) and bight-colored fast flow in post-compressed LCIV (arrows).

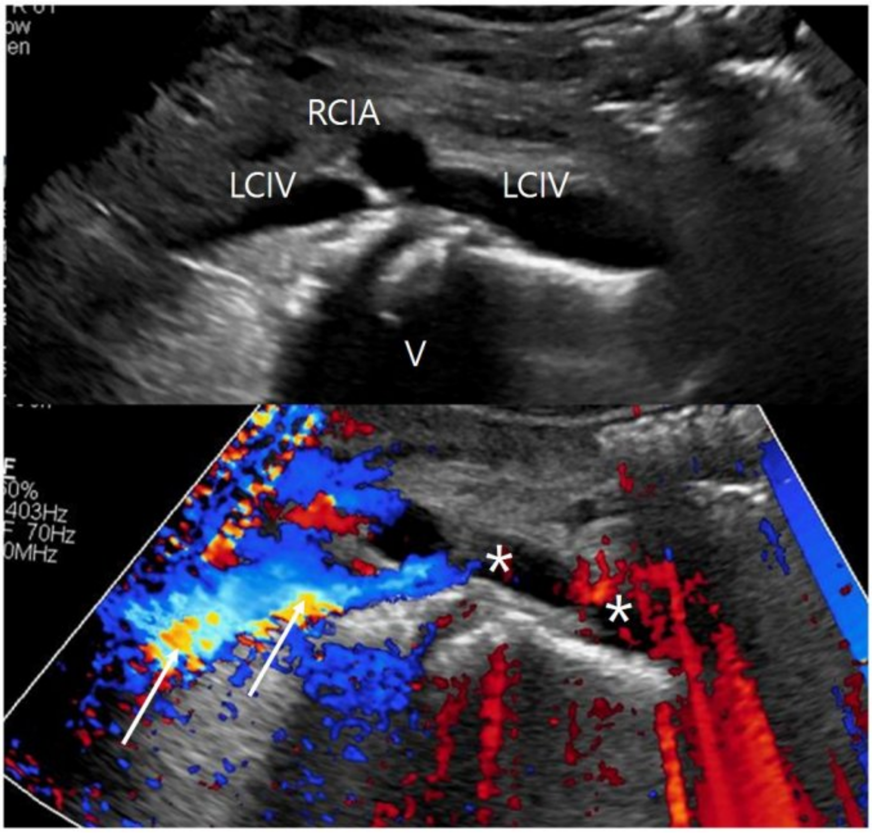

Keywords : Nutcracker syndrome, Midline congestion syndrome, May-Thurner syndrome

[Poster Presentation 1]

GU-Uro-03

Integrating Peritumoral Radiomics Improves Preoperative Staging of Clear Cell Renal Cell Carcinoma

Shichao Li[1], Chuhuai Wang[2,3], Mengmeng Gao[1], **Kangwen He[1]**, Zhen Li[1*]

[1]Radiology, Tongji Hospital of Tongji Medical College of Huazhong University of Science and Technology, China
[2]Oncology, Tongji Hospital of Tongji Medical College of Huazhong University of Science and Technology, China
[3]MOE Key Laboratory for Biomedical Photonics, Wuhan National Laboratory for Optoelectronics of Huazhong University of Science and Technology, China

Accurate preoperative staging of clear cell renal cell carcinoma (ccRCC) is essential for determining surgical strategy and patient prognosis. However, conventional imaging primarily emphasizes intratumoral features, while early extrarenal invasion often manifests as subtle alterations in the peritumoral tissue. This study aimed to evaluate the diagnostic value of peritumoral radiomics and to test whether integrating peritumoral and intratumoral features improves the prediction of pathological staging in ccRCC.

This multicenter retrospective study included 1,240 patients with pathologically confirmed cT1b–T2a ccRCC. Tumor and peritumoral regions were automatically segmented using nnU-Net, and 107 quantitative radiomic features were extracted from each region. Four machine learning classifiers—logistic regression, support vector machine, decision tree, and random forest—were developed based on tumor-only, peritumor-only, and combined features. Model performance was assessed using AUC, sensitivity, specificity, and accuracy across internal and external cohorts. DeLong tests were used for statistical comparison, and SHAP analysis was applied to interpret feature contributions and tumor–peritumor interactions.

In the internal validation cohort, the Combined Radiomics model achieved an AUC of 0.800, outperforming both the Tumor-only (AUC 0.787, $p = 0.798$) and Peritumor-only (AUC 0.709, $p = 0.020$) models, with consistent trends in external validation. SHAP analysis revealed that 30 of the top 40 predictive features originated from the peritumoral region, with peritumor_shape_Maximum3DDiameter ranked highest. Dependence plots demonstrated nonlinear tumor–peritumor interactions, indicating that the integrated model captures cross-regional morphological cues reflective of early local invasion.

Peritumoral tissue harbors distinct morphological and textural cues that complement intratumoral features in identifying early invasion. Integrating peritumoral and intratumoral radiomics enables more accurate, interpretable preoperative staging of ccRCC and may guide individualized surgical decision-making.

Workflow of radiomics-based staging model.

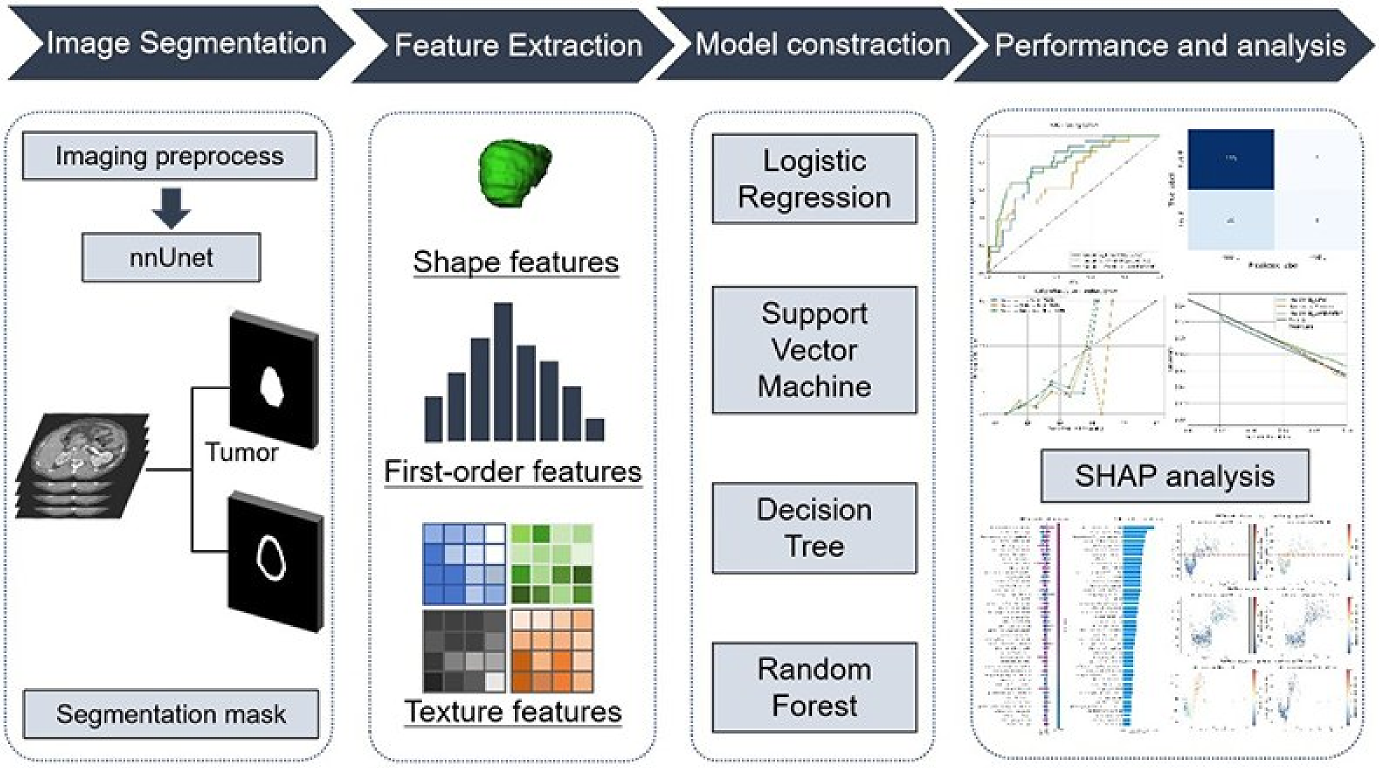

Keywords : Clear cell renal cell carcinoma, Pathological staging, Radiomics

[Poster Presentation 1]

GU-Uro-04

Deep Learning-Based Prediction of Lymph Node Invasion in High-Risk Non-Metastatic Prostate Cancer: Incremental Value of Periprostatic Adipose Tissue

Kangwen He[1], Zhen Li[1*]

[1]Radiology, Tongji Hospital Tongji Medical College Huazhong University of Science and Technology, China

Accurate preoperative prediction of lymph node invasion (LNI) is crucial for individualized treatment planning in patients with high-risk non-metastatic prostate cancer (PCa). While previous studies focused mainly on prostate or tumor features, the potential value of periprostatic adipose tissue (PPAT) remains unexplored. This study aimed to develop an end-to-end deep learning framework for automatic segmentation of the prostate and PPAT, and to evaluate their incremental value in predicting LNI.

We retrospectively collected 356 high-risk non-metastatic PCa patients from two centers who underwent preoperative biparametric MRI (T2-weighted imaging, diffusion weighted imaging, apparent diffusion coefficient), radical prostatectomy, and extended pelvic lymph node dissection. nnUNetv2 was employed to automatically segment the prostate and PPAT, achieving Dice scores of 0.91 and 0.85, respectively.An additional 167 patients with paired prostate MRI and abdominal CT data were included to analyze the correlation between PPAT and whole-body composition. The correlations between MRI-based PPAT and obturator internus muscle and CT-based visceral fat, subcutaneous fat, and skeletal muscle were evaluated. A 3D ResNet-18 classifier was constructed with two strategies: (1) gland-only model and (2) gland+PPAT model. Clinical variables (ag e, PSA, biopsy Gleason grade group, and percentage of positive cores) were integrated with imaging features via late fusion. Model performance was evaluated in an external test cohort (n=49) and compared with the Briganti 2017 nomogram.

The volume of the obturator internus muscle was positively correlated with skeletal muscle volume and BMI (all $p<0.05$). PPAT that automatic segmented based on MRI has no significant correlation with CT based body compositions and BMI, indicating that PPAT is an independent adipose bank. In the external test set, the gland-only model yielded an AUC of 0.59 (95% CI: 0.47–0.70), whereas the gland+PPAT model improved significantly to 0.70 (95% CI: 0.60–0.81, p=0.025), which outperformed the Briganti 2017 nomogram (AUC=0.54, 95% CI: 0.43–0.66, p=0.038). The combined model demonstrated higher sensitivity (75.0%), specificity (64.9%), and accuracy (67.3%) compared with the gland-only model (66.7%, 45.9%, and 51.0%, respectively).

Incorporating PPAT features provides significant incremental value for LNI prediction in high-risk non-metastatic prostate cancer. Combining multi-structural imaging features with clinical variables enhances preoperative risk stratification and decision-making, suggesting potential for guiding individualized surgical planning and avoiding unnecessary lymph node dissection.

The overall framework of this study

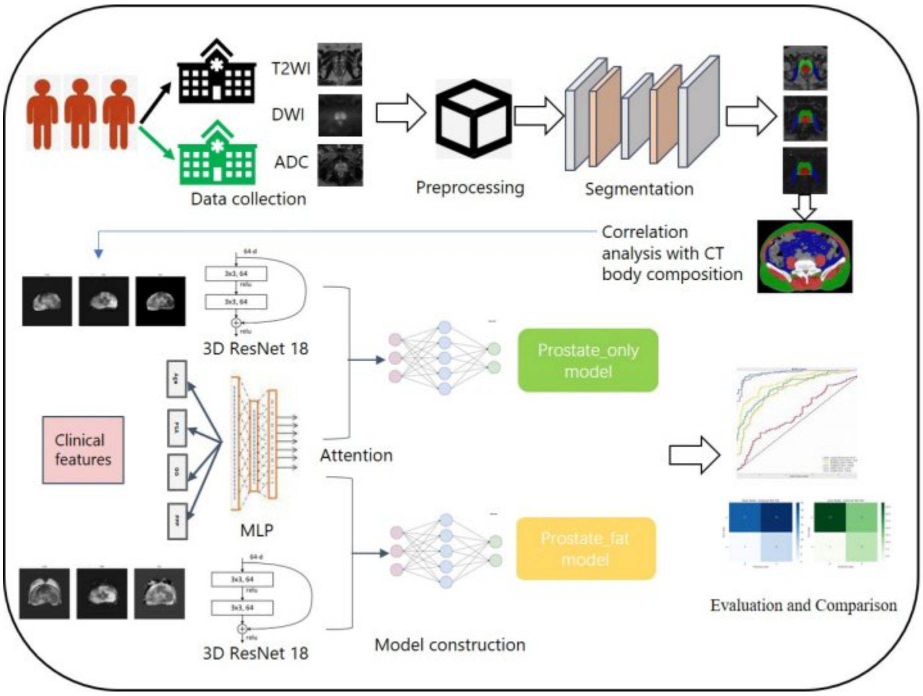

Evaluation of the diagnostic performance of different models on the external dataset. The results show that the **prostate_PPAT model** significantly outperformed both the **prostate_only model** and the **Briganti2017 nomogram** in the external test set.

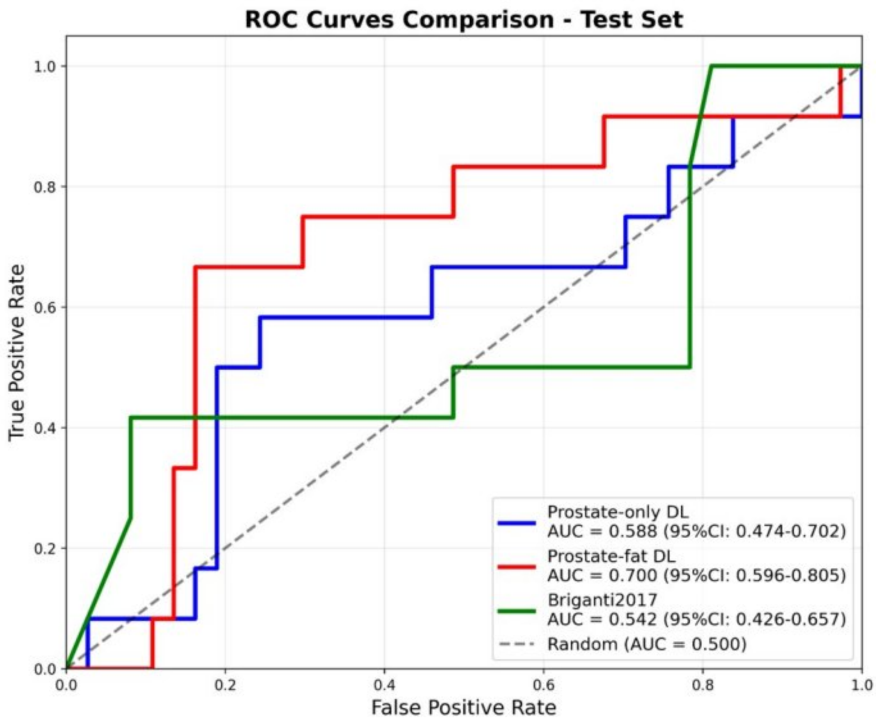

Keywords : Prostate Cancer, Periprostatic Adipose Tissue, Lymph Node Invasion

[Poster Presentation 1]

GU-Uro-05

Association Between PI-RADS Score and Cancer Detection in Template-Based Transperineal Systematic Prostate Biopsy: Experience from a Rural Single-Center Practice

Leonardo Chung[1], James Sopkin[2], Steve Chung[1*]

[1]Urology, Illinois Urologic Health Surgeons, USA
[2]Statistics, Georgia Institute of Technology, USA

Multiparametric MRI (mpMRI) has improved risk stratification for men with prostate cancer. However, its correlation with transperineal (TP) biopsy outcomes in community urology practices is underreported. We evaluated cancer detection across all PI-RADS scores in an office-based setting using a TP 12-core template biopsy approach without real-time image needle guidance.

A retrospective analysis was performed on 109 consecutive men who underwent TP biopsy from May to September, 2025. Each patient had a supine, hospital-based mpMRI followed by a lithotomy, in-office non-contrast perineal low-field MRI (Promaxo Inc, Oakland, CA). Both images were fused for template biopsy planning. All biopsies were performed using a 12-core systematic TP template with attempted lesion targeting but without real-time image needle guidance. All patients were started on prophylactic antibiotics but none had rectal swab testing for fluoroquinolone resistance. PI-RADS scores (1–5, X) were correlated with biopsy positivity. Data analysis was performed using Chi-square test for linear trend and Fisher's exact test.

We found that the prostate cancer detection increased with PI-RADS score: 1 = 4/15 (26.7%), 2 = 2/19 (10.5%), 3 = 5/16 (31.3%), 4 = 11/20 (55.0%), 5 = 19/26 (73.1%) ($p < 0.01$ for trend). PI-RADS 4–5 demonstrated significantly higher detection than 1–3 ($p = 0.004$*). The overall detection was 41.3% when PI-RADS X was included (4/13). No complications occurred in any patient.

In our rural, office-based setting, PI-RADS score strongly correlated with cancer detection using a standard TP template-guided approach without real-time image needle guidance. Even MRI-negative (PI-RADS 1–2) patients showed prostate cancer, reinforcing that our TP approach can detect MRI-occult disease. The TP approach provides a safe, practical, and diagnostically reliable model for community urologists wishing to pursue TP biopsy.

Keywords : Transperineal, MRI, Biopsy

[Poster Presentation 1]

GU-Uro-06

Prediction of Adverse Pathology in Prostate Cancer Using a Multimodal Habitat Analysis Based on [18F]PSMA-1007 PET/CT and Multiparametric MRI

Yunjun Yang[1], Haoli Xu[1], Shuying Bian[1], Licong Li[1], Cunke Miao[2], Zhifang Pan[2], Heng Lin[2*]

[1]Radiology, The First Affiliated Hospital of Wenzhou Medical University, China
[2]The First School of Medicine School of Information and Engineering, The First Affiliated Hospital of Wenzhou Medical University, China

Accurately predicting adverse pathology (AP) in prostate cancer (PCa) patients is crucial for formulating effective treatment strategies. This study aims to develop and validate a multimodal prediction model based on habitat analysis by integrating tumor spatial heterogeneity information from [^{18}F]PSMA-1007 PET/CT and multiparametric MRI (mpMRI) to precisely predict the presence of postoperative AP in PCa patients, and to validate the superiority of multimodal fusion compared to unimodal methods.

A total of 341 PCa patients who underwent radical prostatectomy were retrospectively enrolled. All patients completed standardized preoperative mpMRI (including T2WI, DWI, and ADC sequences) and [^{18}F]PSMA-1007 PET/CT scans. Based on intratumoral heterogeneity, K-means clustering was applied to partition the prostate regions of interest (ROIs) on PET/CT and mpMRI images. Radiomic features were extracted from each habitat, along with traditional radiomic features. Feature selection was then performed using the minimum Redundancy Maximum Relevance (mRMR) and Least Absolute Shrinkage and Selection Operator (LASSO) methods. A random forest machine learning model was used to construct traditional radiomic models and habitat-based models. Multivariate logistic regression analysis identified significant clinical independent predictors, which were integrated with habitat features to build a comprehensive model. Model performance was evaluated using 10-fold cross-validation. The multimodal fusion model combining mpMRI and PET/CT features was compared with individual mpMRI or PET/CT models.

The habitat model demonstrated excellent performance in predicting AP (mpMRI model: AUC = 0.725; PET/CT model: AUC = 0.690; multimodal fusion model: AUC = 0.763), outperforming traditional radiomic models across all modalities (mpMRI model: AUC = 0.699; PET/CT model: AUC = 0.681; multimodal fusion model: AUC = 0.745). The multimodal fusion approach achieved better performance than individual mpMRI or PET/CT models in both habitat and traditional radiomic models. After incorporating clinical factors into the multimodal habitat model, predictive performance further improved, with an AUC of 0.847.

The multimodal fusion model based on habitat analysis, integrating PET/CT and mpMRI, significantly enhances the prediction of adverse pathology in PCa and outperforms traditional radiomic models. This non-invasive approach provides a novel tool for precise preoperative risk assessment, aiding clinical treatment decision-making and improving patient prognosis.

Figure 1. Workflow of the study.

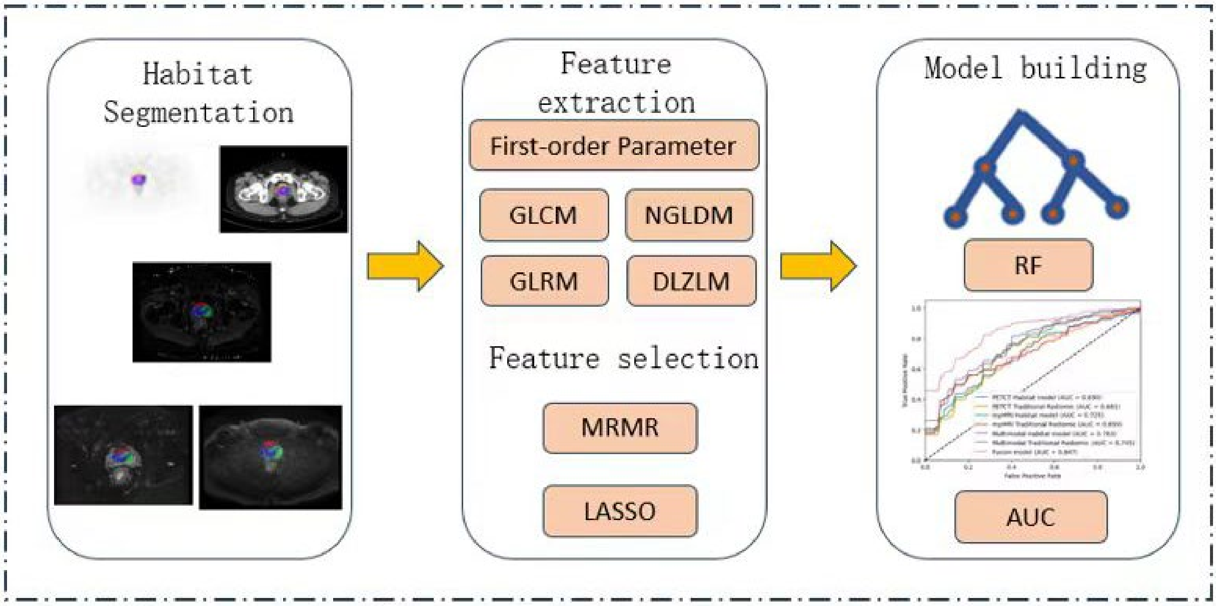

Figure 2. Comparison of receiver operating characteristic curves for various models.

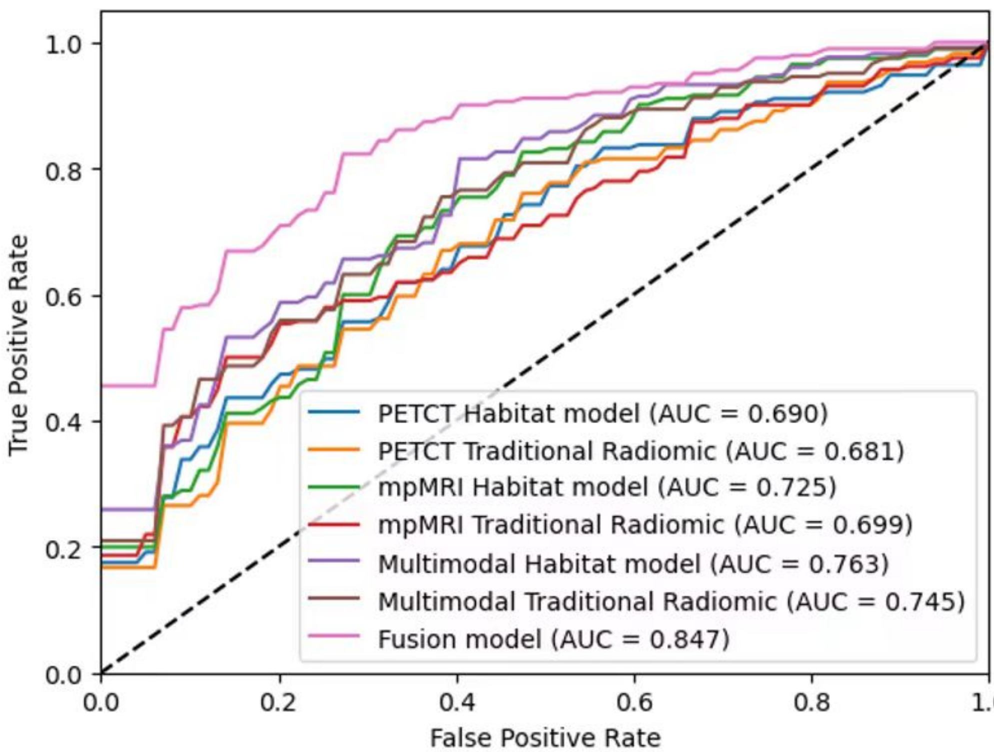

Keywords : Prostate cancer, Multimodal imaging, Adverse pathology

[Poster Presentation 1]

GU-Uro-07

Diagnostic Validity and Inter-reader Reproducibility of the PI-FAB System for Detecting Local Recurrence Following Irreversible Electroporation of Prostate Cancer

Yu Ri Shin[1*], Bohyun Kim[1], Hokun Kim[1], Seo Yeon Youn[1], Sung Eun Rha[1]

[1]Radiology, Seoul St Mary's Hospital, Korea

To evaluate the diagnostic performance and inter-reader reproducibility of the Prostate Imaging after Focal Ablation (PI-FAB) scoring system in detecting biopsy-proven local recurrence after irreversible electroporation (IRE) for localized prostate cancer.

This retrospective single-center study included 152 consecutive patients who underwent IRE for localized prostate cancer between 2019 and 2022 and had subsequent multiparametric MRI (mpMRI) with histopathologic confirmation. Two radiologists, blinded to the clinical outcomes and biopsy results, independently reviewed all post-IRE mpMRI examinations and assigned PI-FAB scores (1–3). The diagnostic performance metrics—sensitivity, specificity, positive predictive value (PPV), and negative predictive value (NPV)—were calculated using histopathology as the reference standard, with two thresholds: PI-FAB ≥2 (suspicious) and PI-FAB =3 (highly suspicious). Inter-reader agreement was assessed using Gwet's Agreement Coefficient (AC1). Clinical and imaging factors associated with inter-reader disagreement were analyzed using Wilcoxon two-sample and chi-square tests.

Biopsy-proven local recurrence was identified in 60 of the 152 patients (39.5%). Inter-reader agreement was substantial when PI-FAB =3 was used as the positive threshold (Gwet's AC1=0.609) compared with fair agreement with PI-FAB ≥2 (AC1=0.385). Using PI-FAB ≥2 as the threshold, the sensitivity was 77% and the NPV was 82%, demonstrating the effectiveness of ruling out recurrence. The stricter PI-FAB =3 threshold yielded a specificity of 84% and PPV of 57%, supporting its utility for confirming recurrence and directing biopsy. Cases with inter-reader discordance were associated with significantly higher initial PSA (p=0.029) and nadir PSA (p=0.0029) levels, and a greater number of positive biopsy cores at diagnosis (p=0.0018), indicating that interpretive uncertainty is concentrated in clinically complex cases.

The PI-FAB scoring system demonstrates acceptable diagnostic validity and inter-reader reproducibility for MRI surveillance after IRE for prostate cancer. A PI-FAB =3 threshold provides superior inter-reader agreement and high specificity for guiding biopsy, whereas a PI-FAB ≥2 threshold offers higher sensitivity for excluding recurrence. These findings support adoption of PI-FAB as a standardized imaging framework for post-IRE surveillance, with threshold selection tailored to clinical objectives.

Keywords : Prostate cancer, IRE, PI-FAB

[Poster Presentation 1]

GU-Uro-08

MRI-Pathology Sizing Discordance in Prostate Cancer: A Lesion-Based Analysis

Honghao Xu[1], Xiaohui Ding[2], Baichuan Liu[1], Xu Bai[1], Jian Zhao[3], Haiyi Wang[1*]

[1]Radiology, First Center of Chinese PLA General Hospital, China
[2]Pathology, First Center of Chinese PLA General Hospital, China
[3]Radiology, Second Center of Chinese PLA General Hospital, China

In focal therapy for prostate cancer, the risk of incomplete ablation arises when pre-procedural MRI underestimates the true tumor size. Identifying which tumors are prone to this underestimation is critical for optimizing patient selection. This research aims to identify pathological factors associated with accurate measurement of the maximum tumor diameter on multiparameter MRI (mpMRI) using histopathology as the reference standard.

This retrospective study enrolled patients who underwent prostate MRI prior to radical prostatectomy. All mpMRIs were acquired on a 3T scanner (Discovery 750; GE Healthcare) following a standard MRI prostate protocol (**Table 1**). The maximum tumor diameter on MRI was compared with histopathological measurements from whole-mount sections. All lesions were initially assigned a PI-RADS v2.1 score by a radiologist blinded to the pathological findings. Lesions with PI-RADS category ≥3 were considered MRI-visible and included for further analysis. The location of each MRI-visible lesion was subsequently matched with the histopathological findings using a standardized 12-segment prostate map, which divides the gland into apex, mid, and base levels, with each level subdivided into 4 sectors (**Fig 1**). This co-localization process was performed by a genitourinary pathologist in conjunction with a senior radiologist. The following pathological parameters were evaluated: Gleason grade (GG), the presence of cribriform architecture, dense growth pattern, tumor volume percentage, and extraprostatic extension. The accuracy of mpMRI, defined as A = (MRI-measured size) / (Pathological size), was assessed using a generalized linear mixed model to identify influencing factors.

The study cohort comprised 63 patients, yielding 82 MRI-visible and 25 MRI-invisible tumor. Among the visible lesions, 56 (68.3%) were classified into the underestimation group (A <1) and 26 (31.7%) into the overestimation group (A ≥ 1) based on MRI-pathology size discrepancy. Analysis of the visible lesions revealed that univariate generalized linear mixed model analysis identified presence of cribriform architecture (β = -0.272, 95% CI: -0.473 to -0.070, P = 0.008), GG (β = -0.130, 95% CI: -0.202 to -0.059, P < 0.001), and dense growth pattern (β = -0.287, 95% CI: -0.488 to -0.086, P = 0.005) as significant factors associated with MRI measurement accuracy. On multivariate analysis, only GG remained an independent predictor of accurate tumor sizing (β = -0.093, P=0.027).

This study demonstrates an inverse relationship between GG and MRI tumor sizing accuracy. These findings support the clinical utility of mp-MRI for precise focal ablation planning in low-grade prostate cancer.

Table 1 MRI sequences and parameter

TR = repetition time; TE = echo time; FOV = field of view; Sag = sagittal; Cor = coronal; Ax = axial; T2WI = T2-weighted Imaging; DWI = diffusion-weighted imaging.

* For the GE 750 scanner, NEX counts of 1, 6, and 12 are used for DWI scans with b values of 0, 1000, and 2000, respectively.

Table 1 MRI sequences and parameter

Center/ MR scanner	Sequence	TR/TE (ms/ms)	FOV（mm²）	Matrix	Slice/Gap (mm)	NEX
Center 1 GE 750	Ax T2WI	6271/124	200×200	288×288	3.0 / 0.3	2
	Ax DWI	2436/77	200×200	130×128	3.0 / 0.3	1,6,12*
	Sag T2WI	10467 / 119	200×200	288×288	3.0 / 0.5	1.5
	Cor T2WI	6283 / 124	180×180	288×288	3.0 / 0.3	2.0
	Ax T2WI-fs	9679 / 80	380×380	320×320	5.0 / 0.5	1.5
	Ax T1WI-fs	4 / 2	380×380	288×192	4.0 / 0.0	1.0

TR = repetition time; TE = echo time; FOV = field of view; Sag = sagittal; Cor = coronal; Ax = axial; T2WI = T2-weighted Imaging; T1WI = T1-weighted Imaging; fs = fat suppression; DWI = diffusion-weighted imaging.

* For the GE 750 scanner, NEX counts of 1, 6, and 12 are used for DWI scans with b values of 0, 1000, and 2000, respectively.

Schematic illustrations of localization of each lesion on MRI and pathological registration. A-D Axial T2-weighted images (Ax T2), Sagittal T2-weighted image (Sag T2), diffusion-weighted images (DWI) at b = 2000 s/mm2, apparent diffusion coefficient (ADC) maps. E. Whole-mount histopathology (hematoxylin-eosin staining) revealed two distinct lesions in the mid-gland (outlined by blue lines). While the lesion in the right upper region was invisible on MRI, the one in the left inferior region was clearly visible (red arrow at A). This MRI-visible lesion was subsequently designated by the pathologist and radiologist as being localized to the mid-gland, left inferior region.

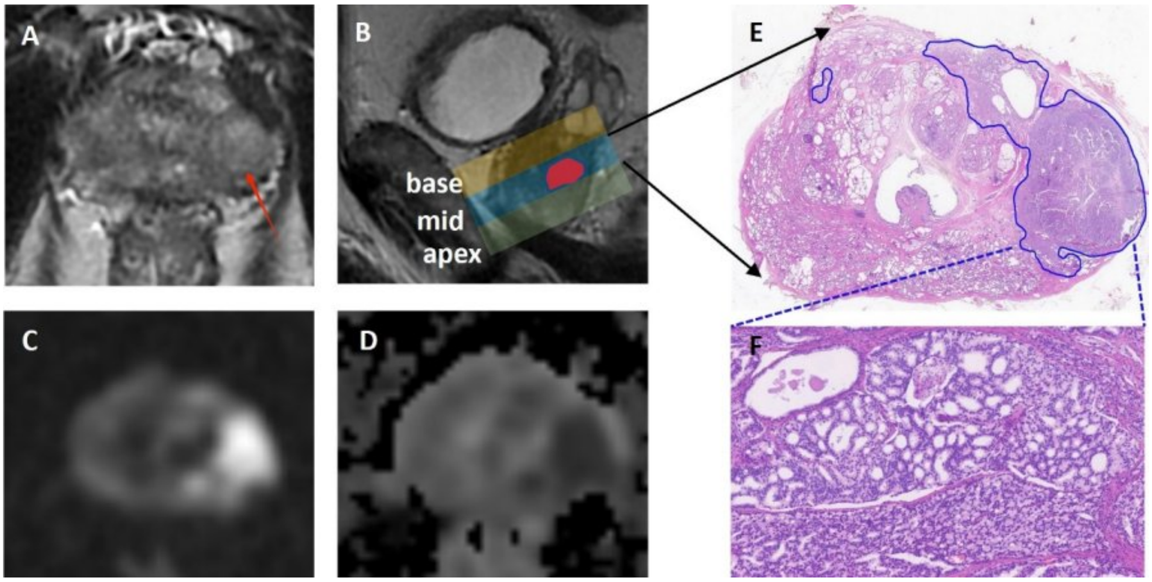

Keywords : Prostate Cancer, Histology, MRI

[Poster Presentation 1]

GU-Uro-10

Rad-VI-RADS: A Fused Radiomics and VI-RADS Model for Improved Detection of Muscle-Invasive Bladder Cancer

Haili Liu[1,2], Yuanhao Ma[1], Huiping Guo[1], Tianran Li[2], Jian Zhao[3], Haiyi Wang[1*]

[1]Radiology, First Medical Center Chinese PLA General Hospital, China
[2]Radiology, Fourth Medical Center Chinese PLA General Hospital, China
[3]Radiology, Second Medical Center Chinese PLA General Hospital, China

To explore the diagnostic efficacy of the fusion model Rad-VI-RADS, which combines the radiomics signature (Radscore) based on multi-parameter MRI radiomics and the VI-RADS, in evaluating muscle invasion of bladder cancer (BCa).

From January 2019 to July 2024, 205 patients with pathologically confirmed BCa who underwent preoperative bladder mpMRI in First Medical Center, PLA General Hospital were included retrospectively. Based on pathological results, the patients were classified into the NMIBC group (n = 139) and the MIBC group (n = 66). Blinded to the clinical and pathological information, two radiologists independently evaluated bladder cancers according to the VI-RADS scoring criteria and reached consensus. Student's *t* test or Mann-Whitney *U* test was used for comparison between the two groups. The weighted Kappa coefficient (κ) was used to assess interobserver agreement. All cases were randomly divided into a training set (n = 143) and a test set (n = 62) at a ratio of 7:3. One radiologist extracted the radiomics features of T2WI, ADC, and DCE sequences and selected the features using the least absolute shrinkage and selection operator (LASSO), maximum relevance and minimum redundancy (mRMR), and ICC (>0.75) methods. Seven machine learning algorithms were used to construct machine learning models. Finally, the machine learning model with higher diagnostic efficacy was selected to construct the radiomics label Radscore. The fusion model of Radscore and VI-RADS (Rad-VI-RADS) was established based on the optimal cutoff value of Radscore determined by the training set. The diagnostic efficacy of VI-RADS, Radscore, and Rad-VI-RADS was evaluated by ROC curves, and the differences in AUC values were compared using the Delong test. The McNemar test was used to compare the sensitivity and specificity.

In the test set, the AUC values of VI-RADS, Radscore, and Rad-VI-RADS for diagnosing MIBC were 0.895 (95% CI 0.790 - 0.958), 0.794 (95% CI 0.672 - 0.886), and 0.947 (95% CI 0.859 - 0.988), respectively. The AUC value of Rad-VI-RADS was significantly higher than that of VI-RADS (P = 0.04) and Radscore (P = 0.02).

The radiomics model based on multi-parametric MRI can effectively evaluate the muscle layer invasion of bladder cancer. Rad-VI-RADS, which is formed by the integration of Radscore and VI-RADS, can significantly improve the diagnostic efficacy of preoperative differentiation of MIBC and show significant clinical additional value.

Keywords : Vesical Imaging-Reporting and Data System (VI-RADS), Muscle-Invasive Bladder Cancer, Radiomics

ACAR 2026

THE 13th ASIAN CONGRESS OF ABDOMINAL RADIOLOGY

Poster Presentation

Mar. 20 (Fri.)

! Abstracts can be found by searching with the Presentation Code !

[Poster Presentation 2 – ISP Format]

ABD-ISP-05

3D Gradient and Spin-Echo MRCP with Deep Learning Reconstruction at 3T: Achieving Non-Inferior Image Quality with Reduced Acquisition Time

Kumi Ozaki[1*], Takafumi Iyoda[1], Satoshi Funayama[1], Yukichi Tanahashi[1], Satoshi Goshima[1]

[1]Radiology, Hamamatsu University School of Medicine, Japan

Magnetic resonance cholangiopancreatography (MRCP) is a noninvasive diagnostic method for imaging biliary and pancreatic ducts. MRCP is routinely performed using respiratory-triggered three-dimensional (3D) acquisitions, yielding thin sections without interslice gaps. However, it usually requires a long acquisition time and depends on the respiratory rhythm, often increasing the risk of motion artifacts. Therefore, we attempted to evaluate whether breath-hold imaging parameters using deep learning reconstruction (DLR) could achieve visually non-inferior image quality within a short acquisition time.

To evaluate the clinical feasibility and image quality of BH 3D-MRCP using a gradient and spin-echo (GRASE) technique with DLR (GRASE-DLR), compared to 3D-GRASE without DLR and 3D-BH-MRCP using a turbo spin-echo sequence with DLR (TSE-DLR) at 3 T.

In total, 65 consecutive patients who underwent MRCP at 3.0 T were prospectively included. Three 3D-BH MRCP protocols were compared: GRASE-DLR, GRASE without DLR, and TSE-DLR. Two radiologists independently analyzed the overall image quality, background suppression, artifacts, and visualization of pancreaticobiliary ducts including the common bile duct (CBD), right and left hepatic ducts (RHD, LHD), second-order intrahepatic ducts, cystic duct, and main pancreatic duct (MPD) using a five-point scale. The signal-to-noise ratio (SNR) of the CBD, contrast-to-noise ratio (CNR) of the CBD and liver, and contrast ratio between the periductal tissue and CBD were measured. The Friedman test was performed to compare the three protocols. A subgroup qualitative analysis was performed in patients with poor breath-holding cooperation (n=8).

GRASE-DLR achieved significantly shorter acquisition time (9.6 seconds) compared with TSE-DLR (16.3 seconds) and GRASE without DLR (17.7 seconds). SNR values were comparable among the three protocols (8.82 ± 3.79 vs. 9.50 ± 3.72 vs. 8.44 ± 3.79, $p = 0.612$). However, TSE-DLR demonstrated significantly higher CNR (25.13 ± 9.28) compared with both GRASE protocols (14.66 ± 4.56 for without DLR and 16.77 ± 6.28 for DLR, $p < 0.001$), with no significant difference between the two GRASE protocols ($p = 0.183$). Similarly, the contrast ratio was significantly higher in TSE-DLR (14.63 ± 5.12) than in both GRASE protocols (5.76 ± 2.18 for without DLR and 6.43 ± 2.88 for DLR, $p < 0.001$), with no significant difference between the two GRASE protocols ($p = 1.000$). Qualitative image analysis showed no significant differences among the three protocols in overall image quality, artifacts, background suppression, or visualization of any pancreaticobiliary ducts. In the poor breath-holding subgroup (n=8), GRASE-DLR demonstrated superior image quality and artifact reduction compared with TSE-DLR and GRASE without DLR, enabling reliable visualization of all pancreaticobiliary structures despite motion degradation.

GRASE-DLR provides comparable image quality to TSE-DLR and GRASE without DLR while significantly reducing scan time. Although quantitative measures such as CNR and contrast ratio were lower in GRASE protocols, qualitative assessment showed no significant differences in the visualization of pancreaticobiliary structures in the overall population. Notably, GRASE-DLR demonstrated particular clinical value in patients with poor breath-holding cooperation. This technique may be clinically useful for improving patient comfort and workflow efficiency in MRCP examinations.

Figure 1.

A 70-year-old woman with pancreatic cystic lesions. Comparison of 3D MRCP images: (a) TSE with DLR, (b) GRASE without DLR, and (c) GRASE with DLR. GRASE sequences (b, c) provide better visualization of the cystic duct (arrows) than TSE. GRASE with DLR (c) demonstrates superior image quality of the pancreatic cystic lesion of the uncs (arrowheads) compared with GRASE without DLR (b).

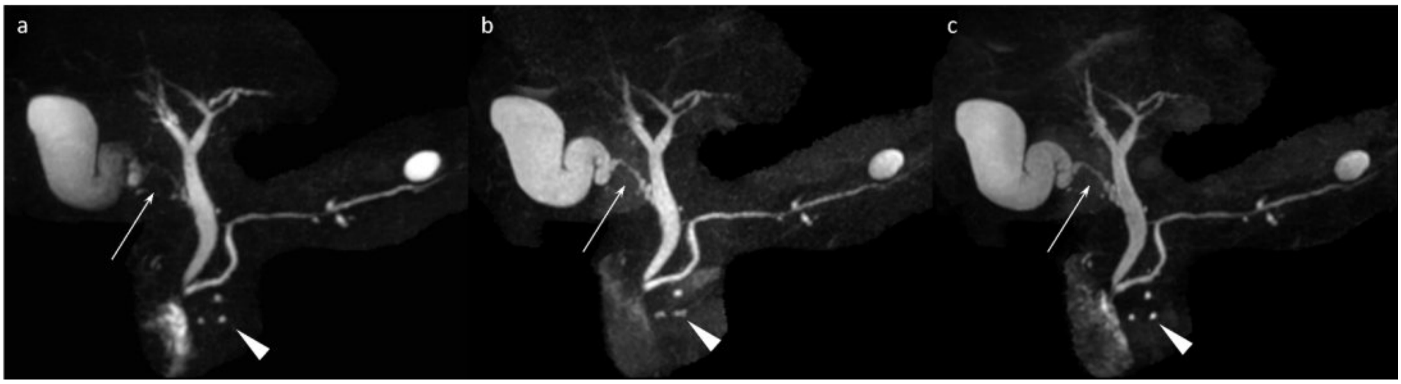

Figure 2.

A 39-year-old man with primary sclerosing cholangitis. Comparison of 3D MRCP images: (a) TSE with DLR, (b) GRASE without DLR, and (c) GRASE with DLR. Due to motion artifacts, image quality with TSE (a) was extremely poor, and multiple stenosis of the biliary duct was not observed (average overall image quality score: 1.0). Although GRASE without DLR (b) demonstrated improved image quality compared with image (a), GRASE with DLR (c) clearly depicts multiple stenosis of the intrahepatic biliary ducts (arrowheads) and common bile duct (arrows).

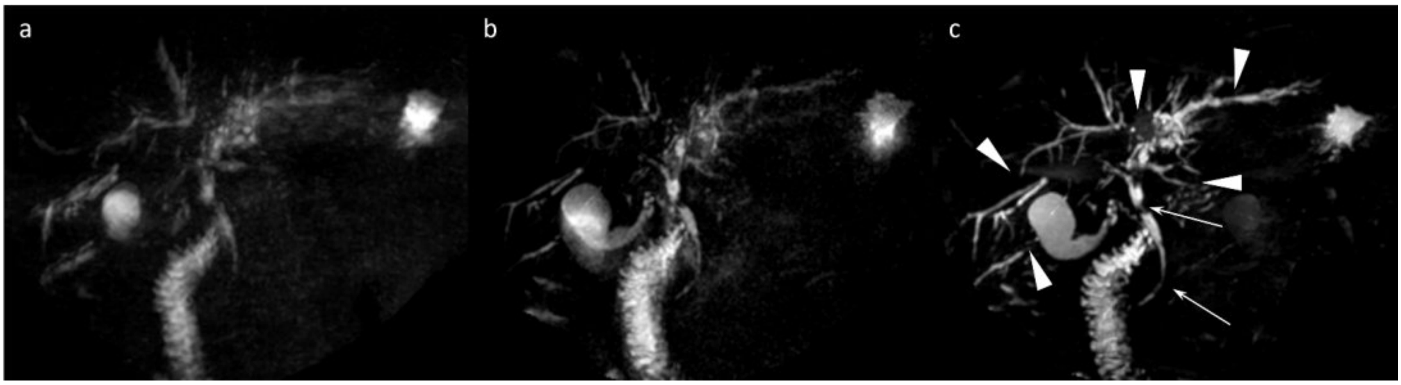

Figure 3.

A 70-year-old woman with pancreatic cystic lesions. Comparison of 3D MRCP images: (a) TSE with DLR, (b) GRASE without DLR, and (c) GRASE with DLR. Inadequate breath-holding during acquisition resulted in significant motion artifacts in both TSE with DLR (a) and GRASE without DLR (b), which precluded assessment of the common bile duct, intrahepatic bile ducts, and main pancreatic duct. Conversely, GRASE with DLR (c), requiring only brief breath-holding (<10 seconds), provides adequate visualization of the overall ductal system including the main pancreatic duct (arrows) despite the same challenging breathing conditions. In GRASE with DLR (c), the cystic duct is clearly visualized (arrowhead). The absence of gallbladder signal reflects gallbladder contraction with concentrated intraluminal bile.

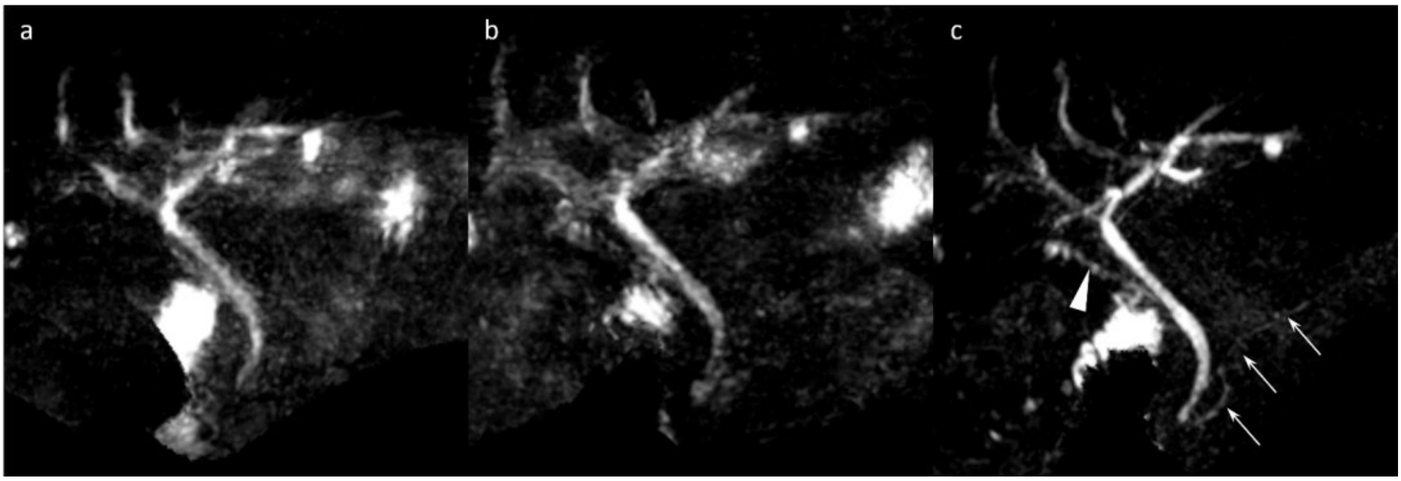

Keywords : MRCP, Grace, Common bile duct

[Poster Presentation 2 – ISP Format]

ABD-ISP-06

Super-Resolution Deep Learning Reconstruction for Three-Dimensional T1-weighted Gradient Echo Imaging in Gadoxetic Acid-Enhanced MRI: Comparison with Conventional and Deep Learning Reconstructions

Kazuma Tsukamoto[1,2], Keitaro Sofue[3*], Yuichiro Somiya[1], Ryuji Shimada[4], Tomohiro Noda[1], Naoki Yoshida[1], Shintaro Horii[1], Akiko Kusaka[1], Takahiro Tsuboyama[3], Yoshiko Ueno[3], Kentaro Nishiuchi[3], Takamichi Murakami[3]

[1]Center for Radiology and Radiation Oncology, Kobe University Hospital, Japan
[2]Graduate school of Medicine Department of Medical Device Engineering, Kobe University, Japan
[3]Radiology, Kobe University Hospital, Japan
[4]Radiological Technology, Faculty of Health Science Kobe Tokiwa, Japan

Gadoxetic acid-enhanced MRI is a key modality for assessing focal liver lesions, offering both dynamic and hepatobiliary phase imaging. However, dynamic imaging demands rapid acquisition within breath-hold limits, forcing trade-offs between spatial resolution, signal-to-noise ratio (SNR), and motion artifact. Deep learning-based reconstruction (DLR) has improved image quality, but its potential to enhance spatial resolution remains limited. Recently, super-resolution DLR (SR-DLR) has emerged, combining deep learning denoising with k-space interpolation. This study aimed to evaluate the image quality of SR-DLR for 3D T1-weighted GRE imaging during gadoxetic acid-enhanced MRI, with particular focus on multiplanar reformatted (MPR) images, compared to conventional and standard DLR.

This retrospective study included 50 consecutive patients (26 men, 24 women; mean age, 71.5 ± 12.8 years) who underwent 3T gadoxetic acid–enhanced MRI. Portal venous phase images were acquired using a 3D fat-suppressed spoiled GRE T1-weighted sequence and reconstructed with Conv., DLR, and SR-DLR algorithms. Quantitative analyses included liver SNR and contrast ratio (CR) between liver and lesions, and edge rise distance (ERD) and edge rise slope (ERS) were calculated for indicators of spatial resolution. Two radiologists independently evaluated image noise, image sharpness, image contrast, motion artifacts, overall image quality, and lesion conspicuity using a 5-point scale. Coronal multiplanar reformatted (MPR) images were also generated and assessed on overall image quality and lesion conspicuity. Statistical comparisons among the three reconstruction methods were performed using the Friedman test with Bonferroni correction.

Liver SNR did not differ significantly between SR-DLR and DLR ($P = 0.186$), but both demonstrated significantly higher SNR than Conv. ($P < 0.001$). SR-DLR achieved significantly sharper edges, with lower ERD (2.63 ± 0.54 mm) and higher ERS (43.4 ± 17.9 mm) compared with Conv. (ERD, 4.43 ± 1.05 mm; ERS, 20.6 ± 7.7 mm) and DLR (ERD, 4.23 ± 0.98 mm; ERS, 20.3 ± 7.7 mm; all $P < 0.001$). The mean CR between liver and lesions was significantly higher for SR-DLR (0.27 ± 0.26) than for Conv. (0.24 ± 0.23) or DLR (0.24 ± 0.23 ($P < 0.001$ for both). Subgroup analyses showed that this improvement in CR was mainly attributed to liver cysts, while malignant lesions demonstrated smaller differences. Qualitatively, SR-DLR achieved the highest ratings for image sharpness, overall image quality, and lesion conspicuity

(P < 0.001). On coronal MPR images, SR-DLR markedly improved overall image quality and lesion conspicuity compared with Conv. and DLR (P < 0.001 for all). SR-DLR exhibited slightly increased image noise and motion artifacts compared with DLR Interobserver agreement for all qualitative parameters ranged from moderate to good (κ = 0.415–0.721).

SR-DLR improved spatial resolution, sharpness, and lesion conspicuity in gadoxetic acid-enhanced MRI compared with conventional reconstruction and DLR. The improvements in image quality, particularly for MPR reconstructions, suggest that SR-DLR has the potential to enhance the clinical utility of dynamic liver MRI. Further optimization of reconstruction algorithms and validation in further studies will be essential to translate these benefits into routine clinical practice for the evaluation of liver disease.

Derivation of the ERD and ERS from portal venous phase liver MRI reconstructed with conventional reconstruction (a), deep learning reconstruction (b), and super-resolution deep learning reconstruction (c). A linear region of interest was positioned across the perpendicular to the second right portal venous branch (red lines).

ERD was defined as the distance between the points corresponding to the maximum and minimum signal intensities measured on the signal intensity profile obtained from a linear region of interest (ROI) placed across the perpendicular to the second right portal venous branch. ERS was calculated as the difference between the maximum and minimum signal intensities divided by ERD . A sharper ERD and a higher ERS indicate a sharper delineation of the images.

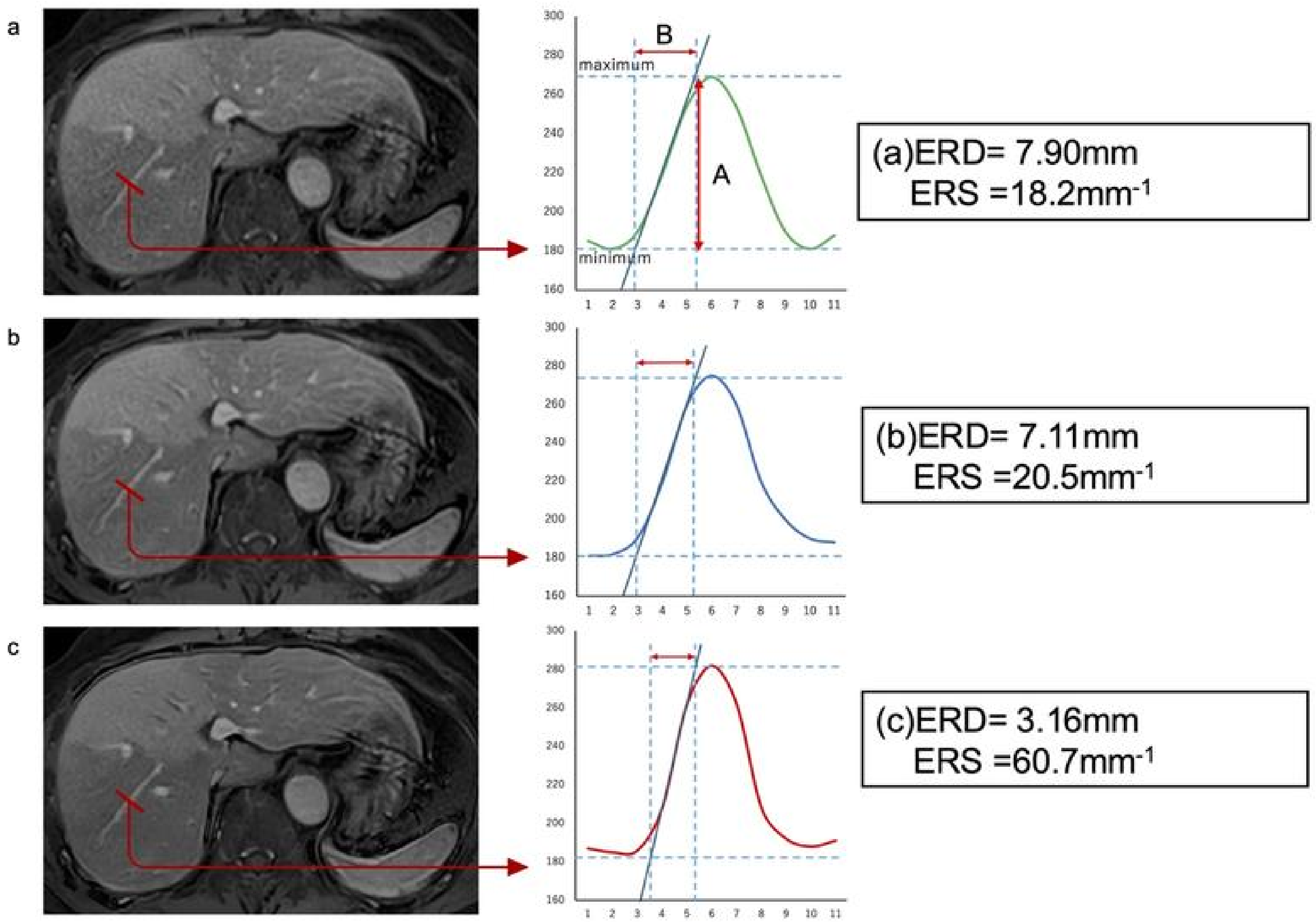

Axial portal venous phase images show hypointense lesion (arrows) in the segment 7 of the liver. Lesion conspicuity is similar between deep learning reconstruction **(b)** and super-resolution deep learning reconstruction **(c)**, while better than conventional reconstruction **(a)**. Coronal reformat image with super-resolution deep learning reconstruction **(f)** demonstrates the highest image quality and lesion conspicuity (arrows) compared with conventional reconstruction **(d)** and deep learning reconstruction **(e)**.

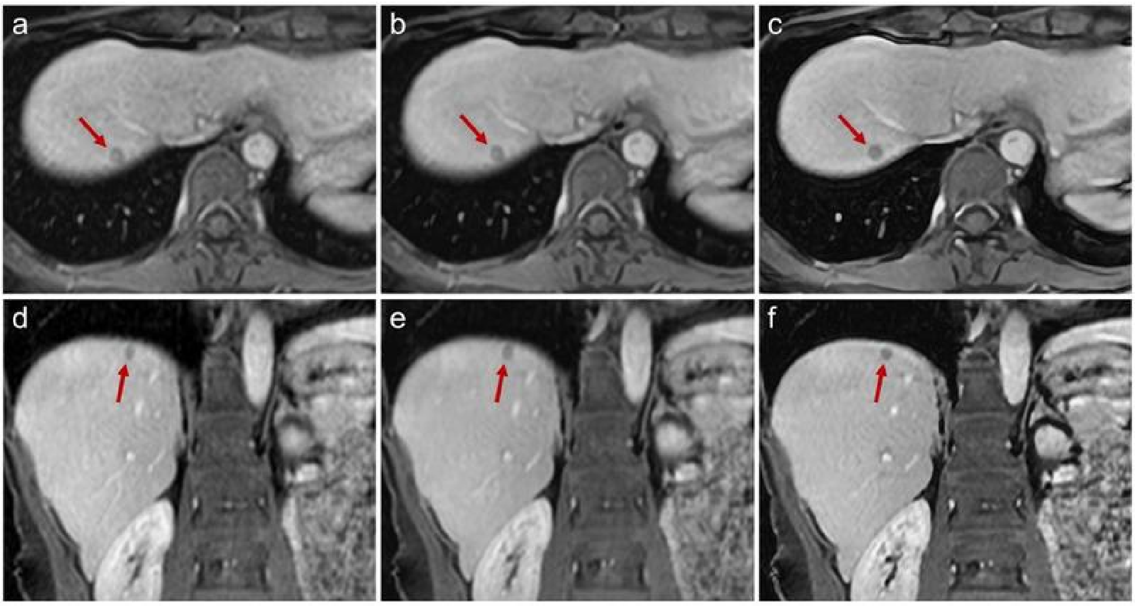

Keywords : Magnetic Resonance Imaging, Super-Resolution Imaging, Gadoxetate Disodium

[Poster Presentation 2 – ISP Format]

ABD-ISP-07

Imaging Findings in Early Pancreatic Adenocarcinoma - When the Duct Speaks First

Xinyi Wong[1], Pearlyn Wong[1*], Hsien Min Low[1]

[1]Diagnostic Radiology, Tan Tock Seng Hospital, Singapore

This poster aims to display a pictorial review of a selection of cases performed at our institution which highlights the subtle imaging findings and clues of the presence of early pancreatic adenocarcinoma (PDAC).

PDAC is frequently detected late because of its nonspecific clinical presentation, lack of specific tumor markers and the limitations in imaging early-stage neoplasms, resulting in a poor prognosis. Imaging plays an important role in the detection of early PDAC, especially in lesions that appear isoattenuating and non-contour deforming.

PDACs usually present as a hypoattenuating infiltrative mass with or without desmoplastic reaction, as well as with presence of a double -duct sign. These are however, often not seen in early PDACs, with secondary signs being the only clues to detection. Secondary imaging signs include abrupt truncation or calibre change of the main pancreatic duct, focal atrophy of the upstream pancreatic parenchyma, faint parenchymal enhancement or restricted diffusion without mass.

This educational poster will highlight these atypical findings through a series of images of patients performed at our institution, all of which did not display the classic imaging findings of a hypoattenuating/hypointense mass.

Radiologists play a paramount role in all stages of patient management in PDAC; from early diagnosis, guiding biopsy as well as in staging and treatment planning (resection, neoadjuvant therapy or palliative care). Due to the varying appearances of PDAC, especially in the early stages, being aware of the secondary imaging signs could aid us in early detection of PDAC.

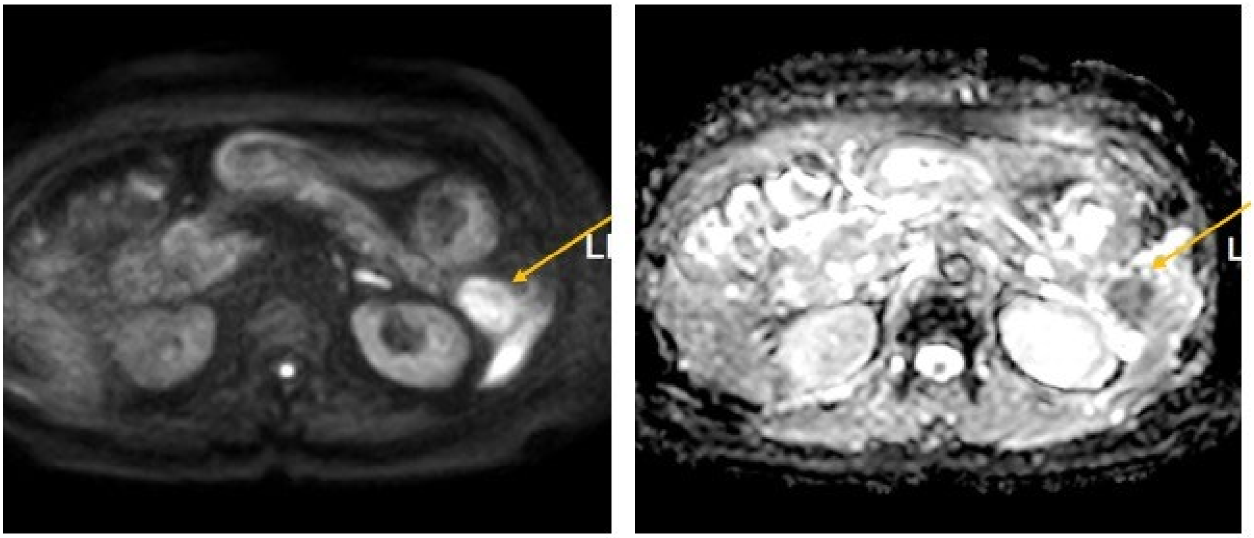

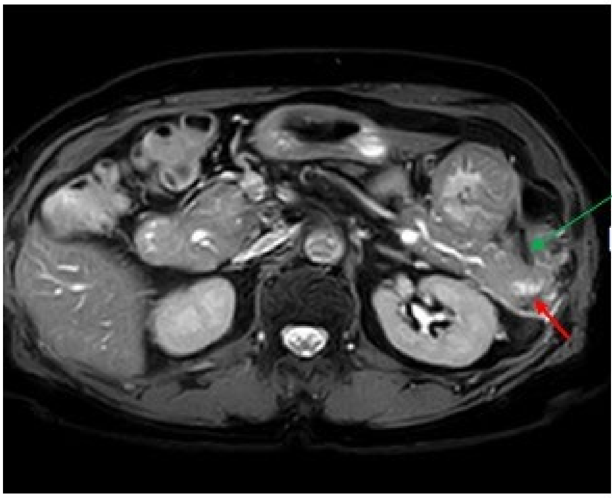

Axial BTFE F/S and DWI/ADC images demonstrate presence of a pancreatic tail isointense mass (green arrow) causing mild upstream dilatation of the pancreatic duct at the tail (red arrow), with associated restricted diffusion (yellow arrows).

Keywords : Pancreatic, Adenocarcinoma, Imaging

[Poster Presentation 2 – ISP Format]

ABD-ISP-08

Gd-EOB-DTPA-Enhanced MRI for Differentiation of Scirrhous Hepatocellular Carcinoma and Intrahepatic Cholangiocarcinoma in an HBV-Infected Cohort：A bi-center study

Haoran He[1], Weiguo Zhang[1*]

[1]Radiology, The Fourth Affiliated Hospital of Soochow University Suzhou, China

This study aimed to investigate the differential imaging features on gadoxetate disodium-enhanced MR imaging for scirrhous hepatocellular carcinoma(S-HCC) and intrahepatic cholangiocarcinoma (ICC) in HBV-infected patients , and to develop a diagnostic model based on these features for preoperative discrimination.

A retrospective analysis was conducted on the clinical and MRI imaging manifestations of 53 patients with pathologically confirmed HBV-positive scirrhous hepatocellular carcinoma and 106 patients with HBV-positive intrahepatic cholangiocarcinoma, who were admitted to two research institutions between January 2015 and January 2025. Univariate and multivariate logistic regression analyses were employed to identify independent diagnostic factors for sclerosing hepatocellular carcinoma and to construct an imaging-based diagnostic model.

Compared to intrahepatic cholangiocarcinoma (ICC), scirrhous hepatocellular carcinoma (SHCC) demonstrates a significantly lower incidence of necrosis (16.3% vs. 35.7%, p=0.031) and a markedly higher frequency of satellite nodules (58.1% vs. 26.8%, p=0.001). On univariate analysis non-thin rim enhancement in arterial phase, enhancing “capsule”, signal loss on opposed-phase T1-weighted imaging, and intratumoral septations (all $p < 0.05$) showed significant differences between ICC and SHCC. A multivariable diagnostic model incorporating non-thin rim enhancement in the arterial phase, enhancing capsule, and signal loss on opposed-phase T1-weighted imaging achieved an area under the curve (AUC) of 0.874, with corresponding sensitivity, specificity, and accuracy of 77.4%, 86.3%, and 83.1%, respectively. Moreover, in patients presenting with the EOB-cloud sign, the EOB-cloud-to-muscle signal intensity ratio emerged as a potentially useful discriminator between the two entities.

Gd-EOB-DTPA-enhanced MRI findings—specifically non-thin rim enhancement in arterial phase, an enhancing “capsule”, and signal loss on opposed-phase imaging—aid in differentiating SHCC from ICC in high-risk, HBV-infected patients.

Liver neoplasms, Scirrhous Hepatocellular Carcinoma, Cholangiocarcinoma

Parameter	AUC(95% CI)	Sensitivity	Specificity	Accuracy	PPV	NPV
Non-thin rim	0.733(0.644-0.823)	60.4	86.3	70.3	56.3	83.1
Opposed-phase loss	0.714(0.627-0.801)	75.5	67.4	77.0	71.1	79.6
Enhancing capsule	0.642(0.547-0.737)	54.7	73.7	66.9	53.7	74.5
Combination	0.874(0.816-0.932)	77.4	86.3	83.1	83.1	87.2

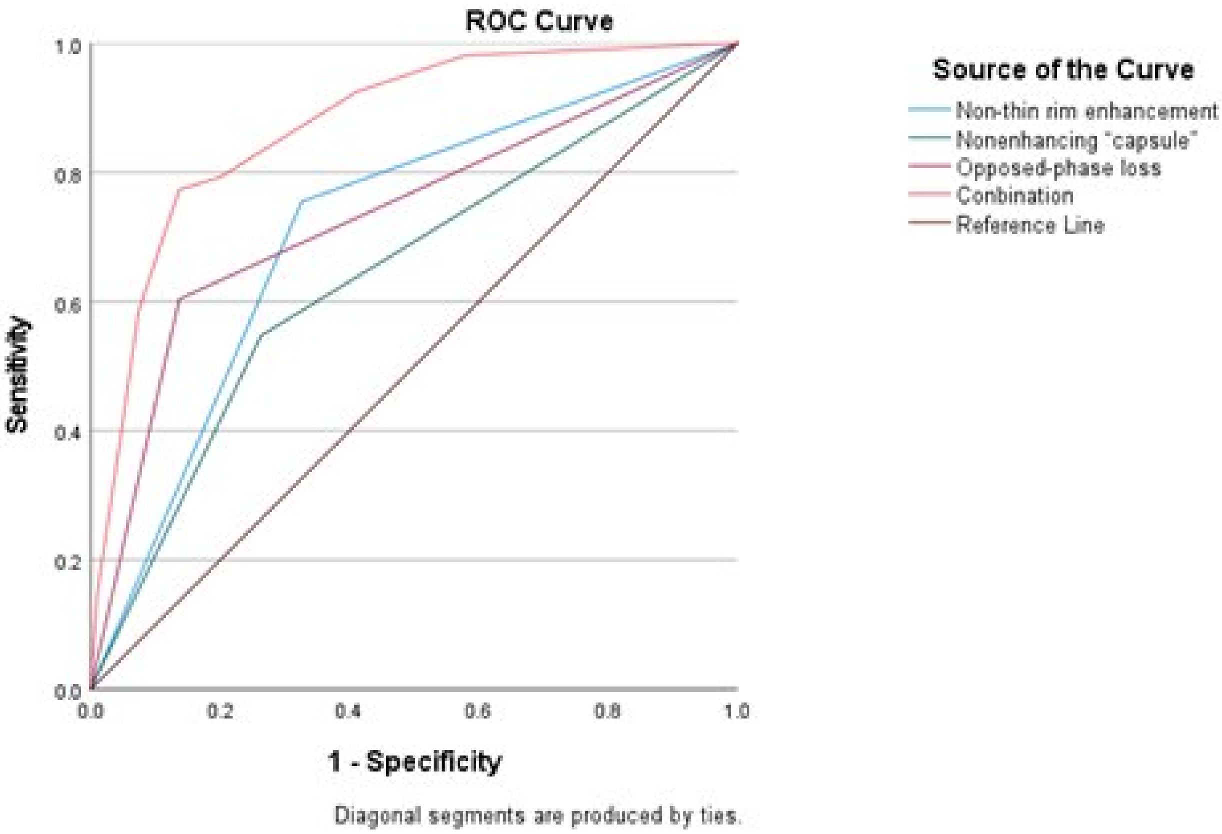

Variables	SHCC(n=53)	ICC(n=95)	χ2/t	Comparison (P value)*
LI-RADS			5.03	0.08
LR-3/4	3(5.7)	3(3.2)		
LR-5	9(17.0)	6(6.3)		
LR-M	41(77.4)	86(90.5)		
Major Imaging Features				
Arterial enhancement			24.9	**<0.001**
Thin rim	13(24.5)	63(66.3)		
Thick rim	17(32.1)	15(15.8)		
Diffuse high	13(24.5)	7(7.4)		
No enhancement	10(18.9)	10(10.5)		
Enhancement pattern			9.65	**0.022**
Wash-in and wash-out	12(22.6)	6(6.3)		
Gradual enhancement	31(58.5)	69(72.6)		
persistent enhancement	6(11.3)	17(17.9)		
Absence	4(7.5)	5(5.3)		
Enhancing capsule	29(54.7)	24(25.6)	23.2	**<0.001**
Ancillary features				
T2WI signal intensity			7.42	**0.024**
hypointense signal	25(47.2)	37(38.9)		
isointense signal	19(35.8)	22(23.2)		
hyperintense signal	9(17.0)	36(37.9)		
Target on DWI	30(56.6)	60(63.2)	0.61	0.43
Target on HBP	13(24.5)	62 (65.3)	22.59	**<0.001**
Target on TP	17(32.1)	48(50.5)	4.70	**0.03**
EOB-Cloud in HBP	34(64.2)	75(78.9)		0.055
EOB-Cloud SI	1.4880(1.3413,1.6966)	1.6519(1.4957,1.8409)		**0.003***
non-EOB-Cloud SI	1.2778(1.0939,1.5128)	1.2510(1.1830,1.3477)		0.736
Opposed-phase loss	32(60.4)	12(12.6)	37.12	**<0.001**
shape			1.69	0.19
Irregular	31(58.8)	45(47.4)		
smooth	22(41.5)	50(52.6)		
Surface retraction	17(32.1)	32(33.7)	0.04	0.842
Septum	31(58.5)			

Keywords : Liver neoplasms, Scirrhous Hepatocellular Carcinoma, Cholangiocarcinoma

[Poster Presentation 2 – ISP Format]

ABD-ISP-09

Diversity of Imaging Features in Intrahepatic Mass-forming Cholangiocarcinoma Across Different Background Liver Conditions

Kazuto Kozaka[1*], Taichi Kitagawa[1], Hirohito Osanai[1], Saya Igarashi[1], Norihide Yoneda[1], Azusa Kitao[2], Kenichi Harada[3], Osamu Matsui[1], Satoshi Kobayashi[1]

[1]Radiology, Kanazawa University Hospital, Japan
[2]Health Sciences Institute of Medical Pharmaceutical and Health Sciences, Kanazawa University, Japan
[3]Human Pathology, Kanazawa University Graduate School of Medicine, Japan

Intrahepatic mass-forming cholangiocarcinoma (IMCC) exhibits marked morphologic and radiological heterogeneity. While prior work has described pathological subtypes and molecular alterations, the relationship between background liver condition—normal liver (NL), chronic hepatitis (CH), or cirrhosis (LC)—and imaging phenotype has not been fully clarified. This study aimed to characterize the variability of imaging features among IMCCs arising in different background liver conditions and to assess whether liver background is a major driver of radiologic appearance.

Thirty-six patients with pathologically proven IMCC were retrospectively analyzed. Background liver condition was categorized as normal liver (NL, n = 12), chronic hepatitis (CH, n = 13), or cirrhosis (LC, n = 11). Imaging variables included CT, MRI, and FDG uptake on PET (SUVmax). Additional imaging-derived parameters included qualitative assessment of vascular and biliary involvement and metabolic activity. Groupwise comparisons across background liver categories were performed using nonparametric tests for continuous variables and χ^2-based analyses for categorical variables.

None of the assessed imaging variables—including arterial-phase enhancement pattern, FDG uptake (SUVmax), delayed contrast enhancement pattern, presence of a capsular restriction, intrahepatic bile duct involvement (IHBD), vascular/biliary interface abnormalities (including vessel involvement/invasion into the tumor and periductal invasion), central hypersignal in the hepatobiliary phase on gadoxetic acid–enhanced MRI (the so-called "EOB cloud sign"), tumor size, or multiplicity—showed a statistically significant difference among NL, CH, and LC. FDG-PET demonstrated numerically higher SUVmax in IMCCs arising in NL compared with CH or LC; however, this difference did not reach statistical significance in this cohort. Similarly, tumor size and other imaging-derived features did not show a consistent or statistically significant monotonic shift across NL, CH, and LC. Aside from patient sex, clinical variables did not show statistically significant differences across background liver conditions.Initial management showed a tendency toward higher rates of surgical resection in patients with chronic hepatitis compared with those with cirrhosis, whereas cirrhotic livers were less frequently resected; this pattern appeared to reflect hepatic functional reserve rather than a distinct imaging phenotype.

IMCC demonstrates substantial imaging heterogeneity that is preserved across normal, chronic hepatitis, and cirrhotic livers. In this cohort, background liver condition did not result in statistically significant differences in imaging features. These findings indicate that the radiologic phenotype of IMCC is driven more by intrinsic tumor biology than by the degree of underlying liver damage. Clinically, IMCC in a cirrhotic liver should not be assumed to follow a stereotypical "cirrhotic pattern". Radiologists should therefore avoid relying on liver background alone when differentiating IMCC from other hepatic malignancies.

Imaging appearance of mass-forming intrahepatic cholangiocarcinoma (IMCC) arising in normal liver.

Four representative cases (78F, 20 mm; 71M, 45 mm; 42M, 94 mm; 66F, 92 mm).

Even in the absence of chronic liver disease, IMCC shows variable arterial phase appearance on gadolinium-enhanced MRI or dynamic CT, including peripheral rim enhancement and heterogeneous internal enhancement. The lesions commonly demonstrate delayed enhancement and imaging features of vessel co-option (VCO) without upstream intrahepatic bile duct dilatation (IHBD). White arrows indicate the tumor.

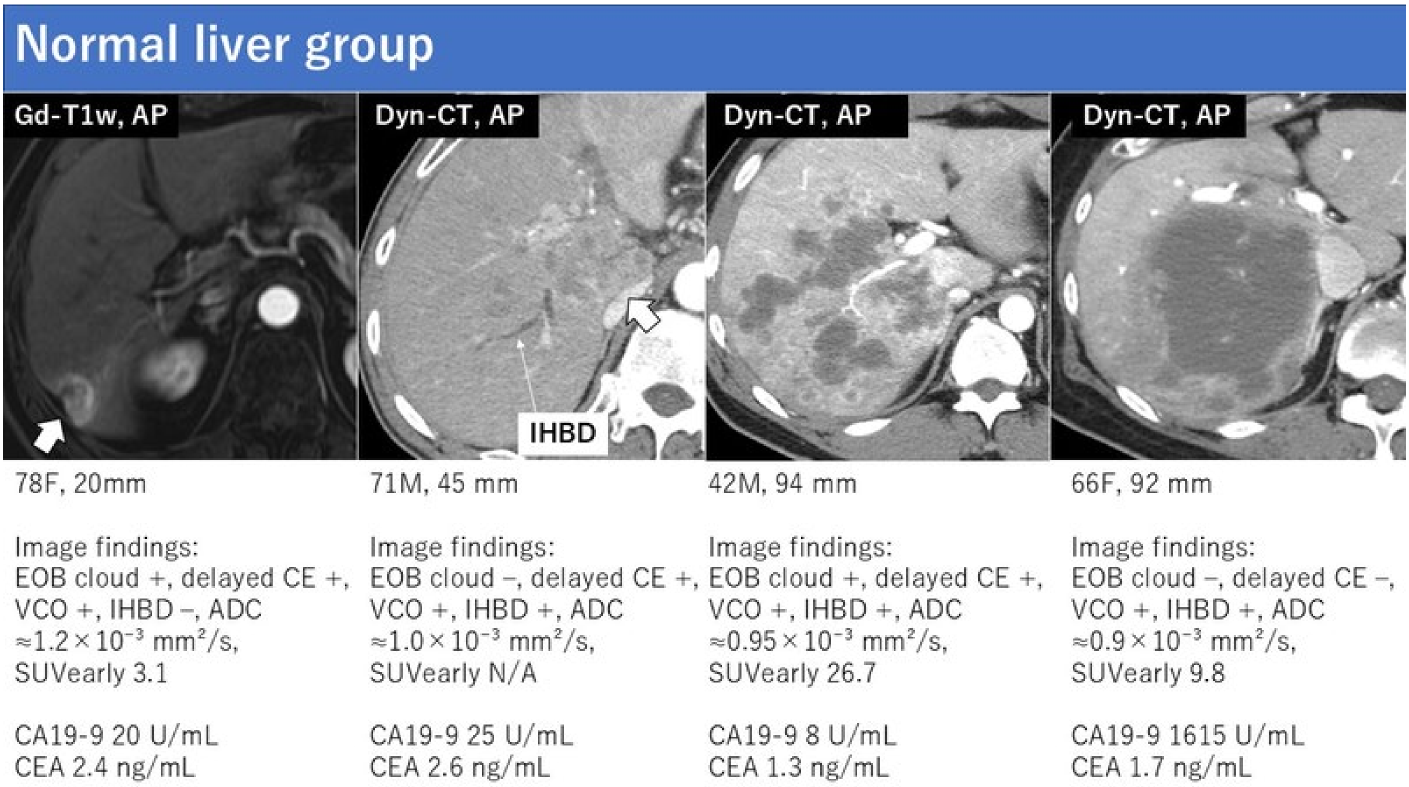

Imaging appearance of mass-forming intrahepatic cholangiocarcinoma (IMCC) arising in cirrhotic liver.

Four representative cases in cirrhotic background liver (79M, HCV, 13 mm; 65M, NASH, 45 mm; 74M, NBNC, 35 mm; 77M, NBNC, 184 mm).

In cirrhosis, IMCC demonstrates arterial phase hyperenhancement or peripheral rim enhancement on dynamic CT, with progressive delayed enhancement and frequent vessel co-option (VCO). Upstream intrahepatic bile duct dilatation (IHBD) can be present, particularly in larger tumors. White arrows indicate the tumor.

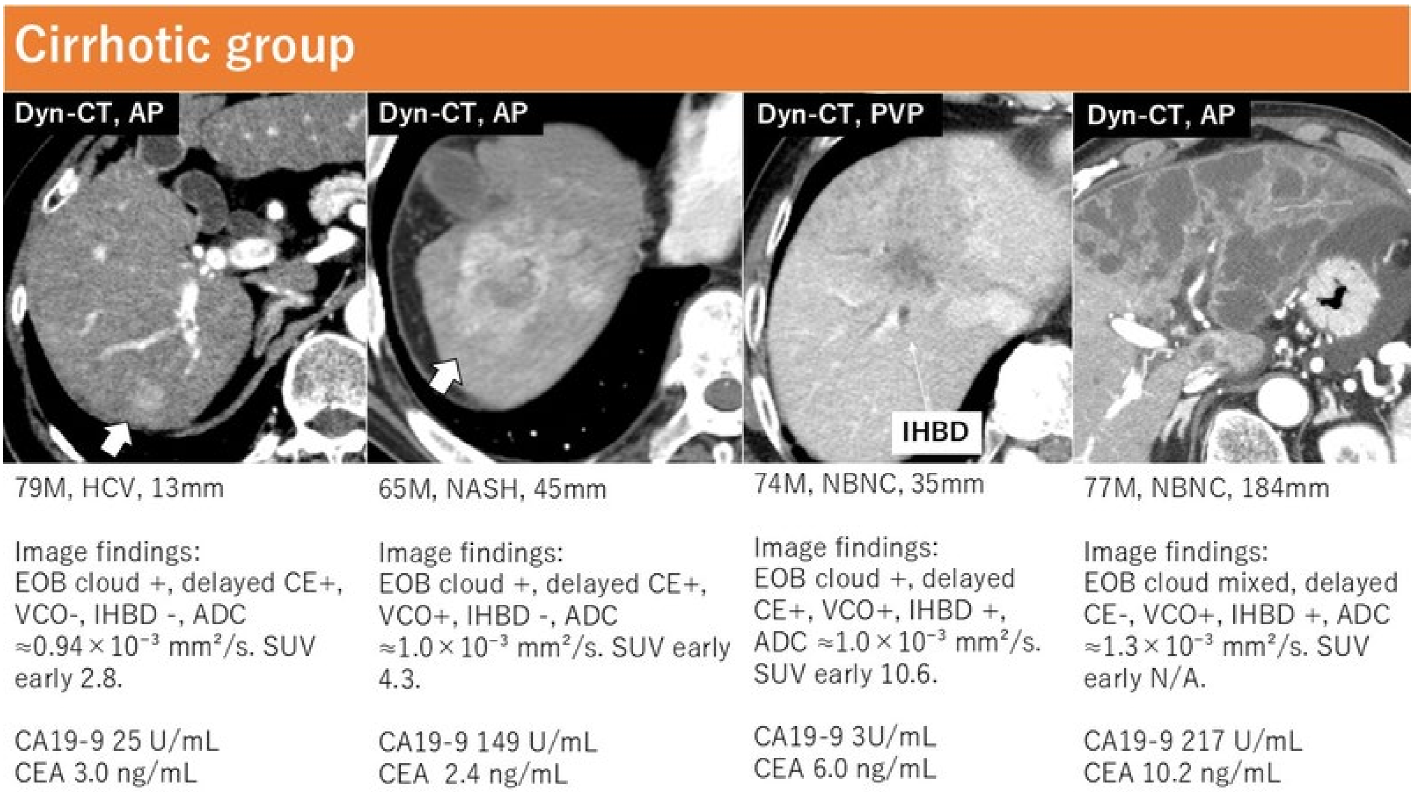

Keywords : Intrahepatic mass-forming cholangiocarcinoma, Background liver condition, Imaging heterogeneity

[Poster Presentation 2]

ABD-Liver-10

Interpreting LI-RADS CEUS Nonradiation TRA v2024: Practical Tips, Pitfalls, and Diagnostic Pearls

Jeremy Jia Qi Soon[1*], Jia Ren Perry Liew[1], Jeremy Jia Hong Lam[1], Wey Chyi Teoh[1]

[1]Radiology, Changi General Hospital, Singapore

Contrast-enhanced ultrasound (CEUS) is increasingly adopted for post-treatment evaluation of hepatocellular carcinoma (HCC), offering real-time assessment of tumor viability without radiation exposure. The 2024 update of the Liver Imaging Reporting and Data System (LI-RADS) CEUS Nonradiation Treatment Response Assessment (TRA) introduced a standardized framework for interpreting enhancement patterns after nonradiation locoregional therapy. However, practical application can be challenging, particularly when differentiating between intralesional and perilesional enhancement or recognizing artifacts that mimic residual disease. This pictorial review illustrates common interpretive pitfalls, shares practical tips for applying LI-RADS CEUS TRA v2024, and highlights strategies to improve diagnostic confidence and interobserver consistency.

A curated selection of illustrative CEUS cases was extracted from a recent institutional audit evaluating the inter-reader reliability and diagnostic performance of LI-RADS CEUS TRA v2024. Cases were chosen to reflect interpretive challenges encountered in everyday clinical practice. Key findings, interpretive dilemmas, and final TRA categorizations are summarized, with emphasis on diagnostic reasoning and error prevention.

Interpretive uncertainty:
When enhancement characteristics are indeterminate, it is recommended to assign the category of lesser certainty (e.g., TR-Equivocal). Areas of hypoenhancement within the ablation zone and perilesional hyperemia frequently contribute to inter-reader variability. These situations underscore the importance of adopting a cautious approach and adhering to the “lesser certainty” principle when perfusion patterns are equivocal.

Differentiating mimics from true enhancement:
Non-linear artifacts and pseudoenhancement artifacts can simulate intralesional viability, highlighting the need to recognize them when they are present. Similarly, enhancing foci straddling the ablation margin may represent adjacent vessels rather than tumor, emphasizing the value of color Doppler interrogation to avoid misclassification.

Boundary ambiguity:
Ambiguity in delineating the ablation margin poses another recurring challenge. Lesions with definite intralesional enhancement may extend across indistinct ablation boundaries, making it difficult to identify if there is any perilesional viability. While this differentiation may be less clinically relevant when intralesional viability is clearly present, recognizing such uncertainty remains important for consistent reporting. Enhancing foci contiguous with the ablation zone may also mimic new separate lesions, and

appreciating their spatial relationship to the treated area supports correct classification as TR-Viable rather than new tumor.

Collectively, these cases illustrate key interpretive principles and reinforce the value of integrating temporal enhancement characteristics with other supporting imaging to enhance diagnostic accuracy and reader consistency.

The LI-RADS CEUS Nonradiation TRA v2024 provides a robust and standardized framework for assessing treatment response in HCC. However, awareness of common pitfalls, including indeterminate enhancement, imaging artifacts, vascular mimics, and boundary ambiguity, is essential for accurate application. Adhering to the “lesser certainty” rule when uncertain and incorporating complementary imaging assessments can improve confidence, reproducibility, and clinical utility in CEUS-based treatment response evaluation.

Enhancing focus straddling the ablation zone and perilesional area after contrast administration (arrow) is shown to be a vessel on doppler (arrow). Pseudoenhancement artifact also noted in the ablation zone (arrowhead).

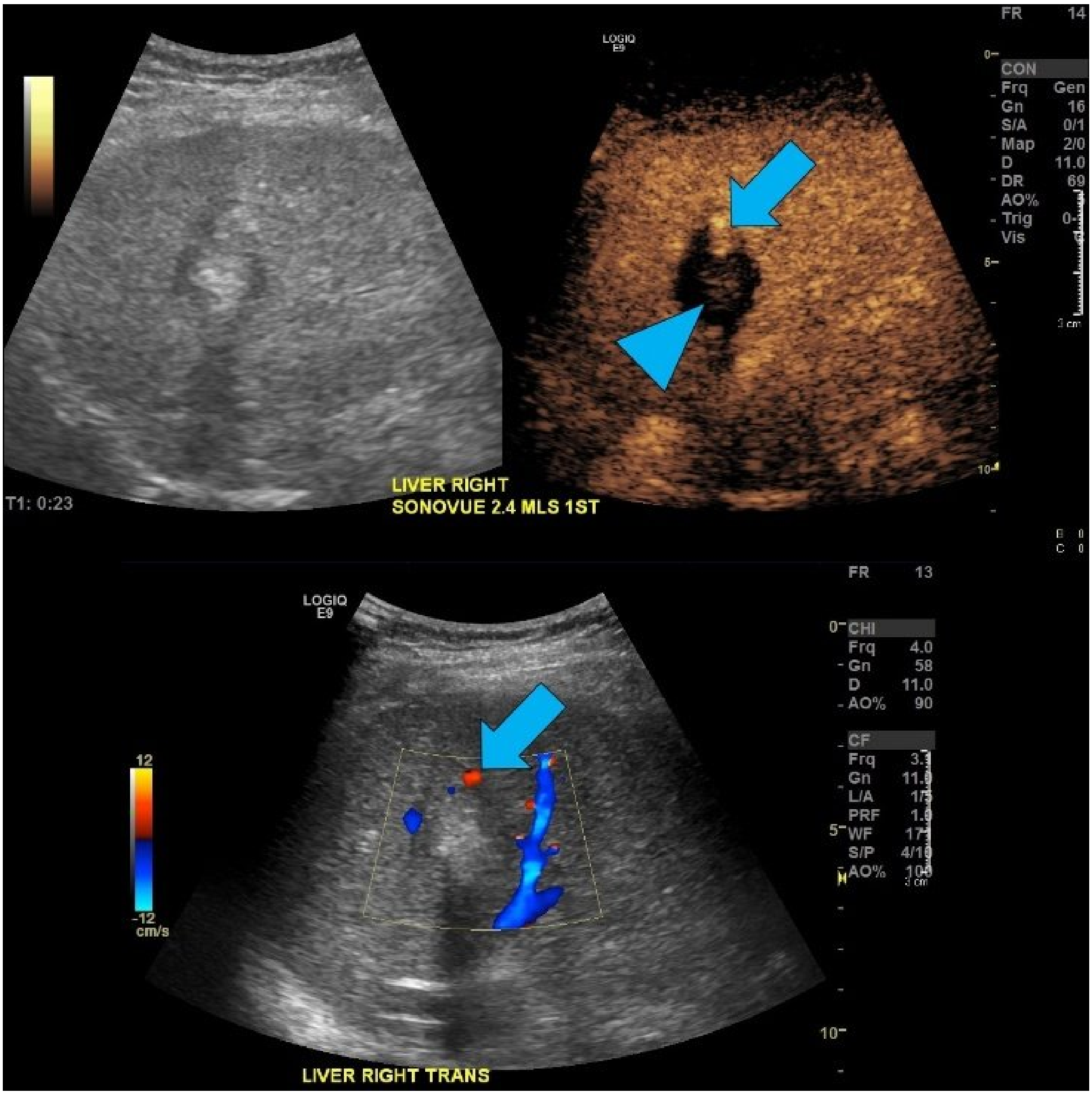

Apparent enhancement in the centre of the ablation zone (arrowhead) that is seen on arterial phase and persists on delayed imaging, corresponds to echogenic component on gray-scale image, compatible with pseudoenhancment artifact.

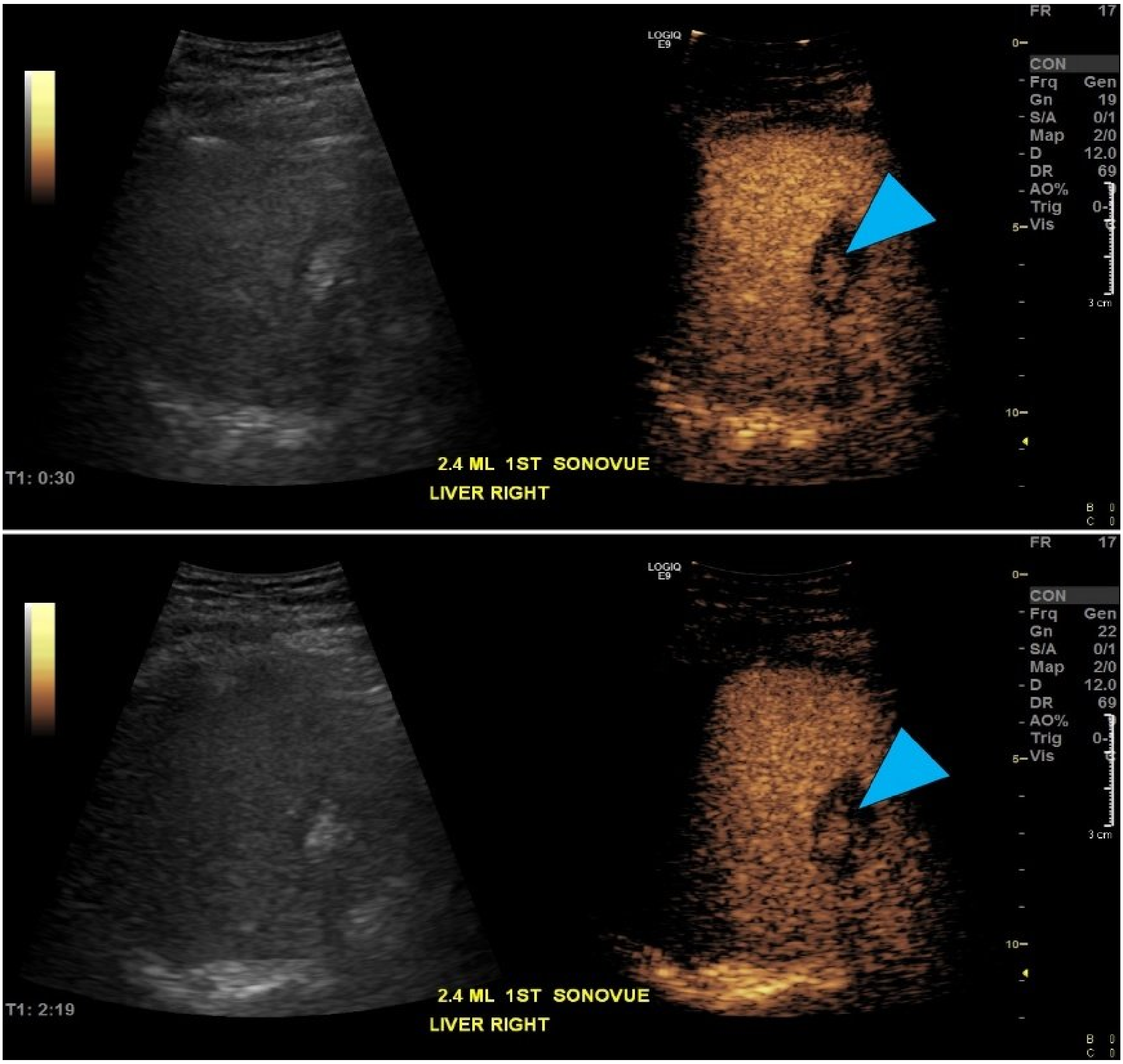

Keywords : CEUS, LI-RADS, HCC

[Poster Presentation 2]

ABD-Liver-11

Prognostic Value of Arterial Enhancement Fraction in Unresectable Hepatocellular Carcinoma Following Conversion Therapy

Xinrui Zhou[1], Bin Song[1*]

[1]Radiology, West China Hospital Sichuan University, China

To evaluate the prognostic value of arterial enhancement fraction (AEF) in predicting recurrence free survival (RFS) in unresectable hepatocellular carcinoma (HCC) patients undergoing combined locoregional-systemic therapy followed by curative-intent liver resection or transplantation.

Between June 2018 and March 2023, consecutive patients with unresectable HCC who underwent combination of locoregional (TACE) and systemic therapy followed by liver curative-intent therapy were retrospectively enrolled. Two radiologists blinded to clinicopathological information independently evaluated 40 CT imaging features. Univariate and multivariable Cox proportional hazards regression analyses were performed to identify significant HCC features associated with RFS, which were subsequently incorporated into a risk score. Risk score performance was assessed using KM curve.

A total of 92 HCC patients with a median age of 54 years (IQR: 46.3 - 63.8) were included. Tumor burden (HR: 1.07, 95% CI: 1.01-1.13, P = 0.027), bilobar involvement (HR: 3.41, 95% CI: 1.69-6.85, P = 0.001), < 50% arterial phase hyperenhancement (APHE) (HR: 1.95, 95% CI: 1.10-3.47, P = 0.023), contiguous multinodular or infiltrative growth subtype(HR: 2.62, 95% CI: 1.41-4.86, P = 0.002) , AFP > 7 (HR: 3.72, 95% CI: 1.34-10.38, P = 0.012), MVI (HR: 2.47, 95% CI: 1.31-4.67, P = 0.005), and AEF change (HR: 0.37, 95% CI: 0.19-0.72, P = 0.004) were independently associated with RFS. The final Cox proportional hazards model incorporating imaging and serum biomarkers [bilobar tumor involvement (HR: 3.52, 95% CI: 1.65-7.49, P = 0.001), < 50% APHE(HR: 2.10, 95% CI: 1.14-3.87, P = 0.017), AFP > 7 (HR: 4.41, 95% CI: 1.53-12.75, P = 0.006) , and AEF change (HR: 0.30, 95% CI: 0.15-0.63, P = 0.001)] achieved c-index of 0.732 (95%CI 0.67-0.80). Incorporating the above 4 variables, a risk score was developed. The optimal cut-off value for the risk score was determined using X-tile software, which identified a threshold of 11.39. Based on this value, patients were stratified into high-risk (≥11.39, n = 63) and low-risk (<11.39, n = 29) groups. Kaplan-Meier analysis revealed markedly reduced RFS in the high-risk cohort compared to the low-risk group (log-rank, P < 0.0001).

AEF change represents an independent prognostic biomarker for RFS in unresectable HCC patients undergoing combined locoregional-systemic therapy.

Keywords : Hepatocellular carcinoma, Arterial enhancement fraction, Combined locoregional-systemic therapy

[Poster Presentation 2]

ABD-Liver-12

Deep Learning for Preoperative Microvascular Invasion Prediction in Hepatocellular Carcinoma: A Systematic Review and Meta-Analysis

Bin Song[1*], **Zhanfei Tian[1]**

[1]Radiology, West China Hospital Sichuan University, China

Hepatocellular carcinoma is one of the most common and lethal malignancies worldwide, and microvascular invasion (MVI) is a critical histopathologic predictor of postoperative recurrence that guides individualized treatment strategies. Although medical imaging–based radiomics and artificial intelligence, particularly deep learning, show promise for noninvasive preoperative MVI prediction, existing studies are highly heterogeneous in populations, imaging protocols, and model designs, and prior meta-analyses have focused largely on radiomics while underrepresenting deep learning. In addition, despite the rapid adoption of large language models (LLMs) in radiology, their potential to enhance the efficiency and accuracy of evidence synthesis in this context remains unclear.

We conducted a PROSPERO-registered (CRD420251174861) systematic review and diagnostic test accuracy meta-analysis of deep learning models for preoperative prediction of microvascular invasion in hepatocellular carcinoma, following PRISMA-DTA and AI-specific reporting and bias-assessment guidelines (TRIPOD-AI, PROBAST-AI). PubMed, Embase, and Web of Science were searched to October 29, 2025, and eligible full-text English studies in humans were screened and extracted independently by two reviewers. A human–AI collaborative workflow additionally compared three large language models with human extractors. Bivariate random-effects models and HSROC curves were used to pool sensitivity and specificity, with meta-regression, sensitivity analyses, and Deeks' tests exploring heterogeneity and publication bias.

Among 51 eligible deep learning studies (all from China; 15 CT, 32 MRI, 4 combined CT/MRI), sample sizes ranged from 97 to 2096 patients and most used retrospectively collected cohorts. Pooled sensitivity and specificity for MVI prediction were 0.85 (95% CI, 0.80–0.88) and 0.83 (95% CI, 0.78–0.87) in internal validation (AUC 0.91), and 0.75 (95% CI, 0.70–0.79) and 0.79 (95% CI, 0.75–0.83) in external validation (AUC 0.84), with substantial between-study heterogeneity but little evidence of publication bias. Over half of studies were rated at high risk of bias or applicability concerns and showed frequent deficiencies in key TRIPOD-AI items, while a human–AI comparison revealed heterogeneous error profiles across three large language models, underscoring the need for human oversight in AI-assisted evidence extraction.

Deep learning analysis of preoperative CT and MRI shows promising potential for noninvasive prediction of microvascular invasion in hepatocellular carcinoma, but current diagnostic accuracy is likely overestimated due to limited external validation, single-country data, and substantial methodological heterogeneity. Our findings also indicate that large language models can substantially accelerate evidence extraction yet remain prone to omissions and hallucinations, supporting their role

as assistants within a multi-LLM, human-supervised workflow rather than replacements for expert reviewers.

Hierarchical summary receiver operating characteristic (HSROC) curves for internal validation. The 95% prediction region is a visual representation of between-study heterogeneity.

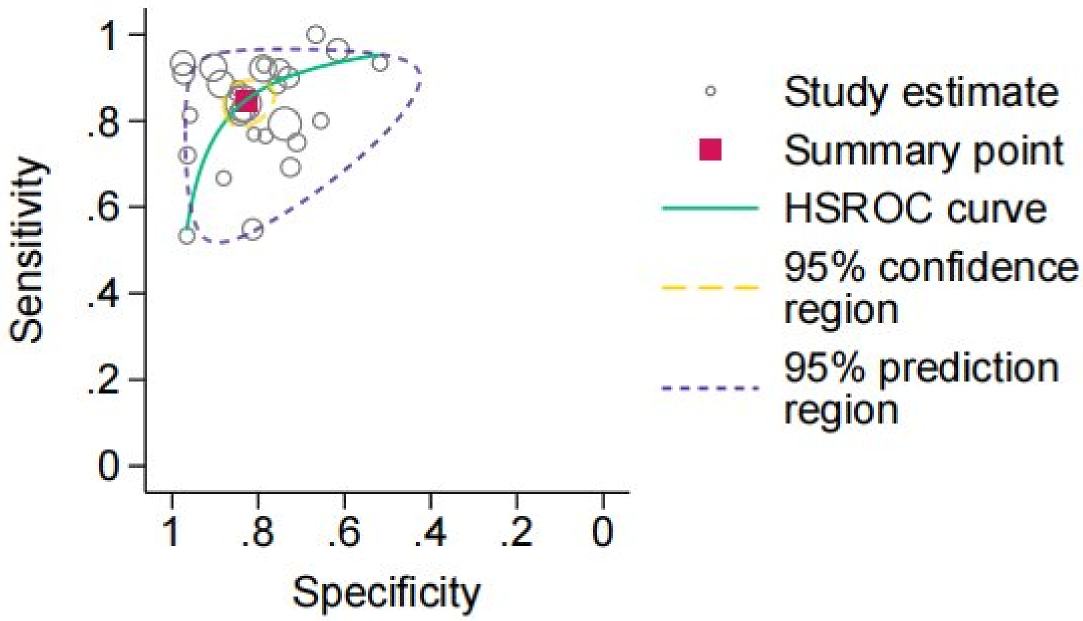

Hierarchical summary receiver operating characteristic (HSROC) curves for external validation. The 95% prediction region is a visual representation of between-study heterogeneity.

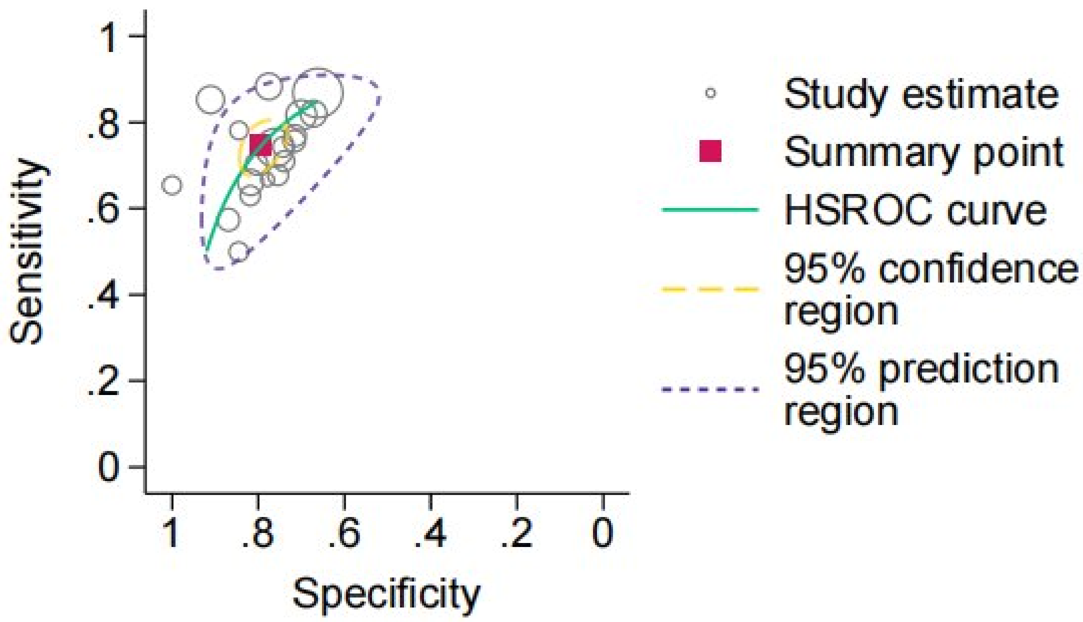

Keywords : Microvascular Invasion, Artificial Intelligence, Meta Analysis

[Poster Presentation 2]

ABD-Liver-13

Imaging Features of Hepatic Epithelioid Hemangioendothelioma: Two Rare Case Reports and Literature Revie

ANH NGUYEN QUYNH[1*]

[1]Radiology, Hanoi Medical University, Vietnam

Hepatic epithelioid hemangioendothelioma (HEHE) is an exceptionally rare malignant vascular tumor of the liver, with an estimated incidence of 1–2 cases per million population, and is characterized by highly variable clinical and imaging manifestations, frequently resulting in diagnostic uncertainty. Because of its rarity and nonspecific presentation, HEHE is often misdiagnosed as other primary or secondary hepatic malignancies. Recognition of characteristic imaging signs is therefore essential to improve diagnostic confidence and optimize patient management.

We report two patients with histopathologically confirmed HEHE diagnosed at Hanoi Medical University Hospital. Both patients underwent abdominal ultrasound and contrast-enhanced magnetic resonance imaging (MRI). Imaging findings were systematically analyzed with particular attention to lesion number, morphology, distribution, signal characteristics, enhancement patterns, and the presence of specific imaging signs, including the “target sign” and “lollipop sign.” Imaging features were correlated with clinical presentation and histopathological and immunohistochemical results. Relevant published literature was also reviewed to contextualize our observations.

The first case involved a 32-year-old woman presenting with persistent dull pain in the right upper quadrant. Ultrasound demonstrated multiple hepatic lesions, and MRI revealed peripheral progressive enhancement, a classic “target sign,” and tapering intralesional vessels extending toward the lesion margin, producing the typical “lollipop sign.” The second case involved a 23-year-old man who presented with systemic symptoms, including significant unintentional weight loss and intermittent epigastric pain for two months. Ultrasound showed multiple heterogeneous hypoechoic nodules. On MRI, only a subset of lesions exhibited the characteristic “target” and “lollipop” signs, while others demonstrated atypical peripheral enhancement patterns. In both cases, ultrasound-guided core needle biopsy confirmed the diagnosis of HEHE by histopathology and immunohistochemistry.

HEHE demonstrates a wide and heterogeneous imaging spectrum, from classic to atypical patterns. Familiarity with key radiologic signs across multimodality imaging enables radiologists to suggest this rare diagnosis with greater confidence, minimize misdiagnosis with other hepatic malignancies, and contribute to more timely and appropriate patient management.

Abdominal ultrasound images
(A): Multiple heterogeneous hypoechoic nodules in the hepatic parenchyma with a surrounding hypoechoic halo (white arrows).
(B): A right hepatic lesion showing a portal venous branch extending from the periphery toward the margin of the lesion (yellow arrow).

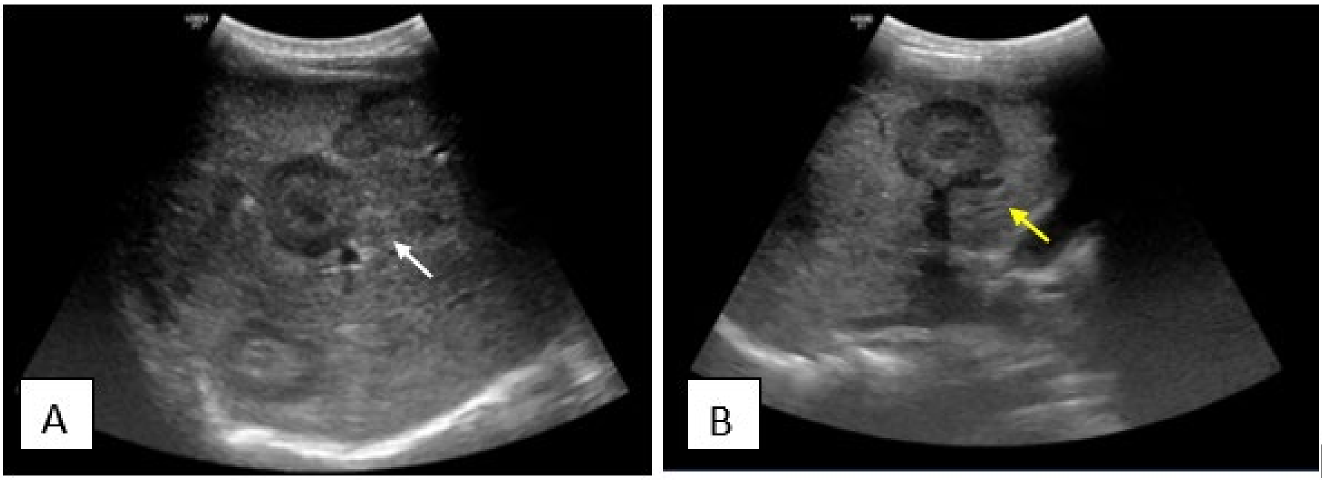

Figure 1. Ultrasound image of the tumor

Contrast-enhanced MRI images
(A): Fat-suppressed T2-weighted images showing multiple peripheral hepatic lesions with concentric hyperintense and hypointense layers, producing a “target sign” (white arrows).
(B): Post-contrast T1-weighted images demonstrating a portal venous branch extending to the margin of the lesion, creating the characteristic “lollipop sign” (yellow arrows).
(C): Illustration of the “lollipop sign”\

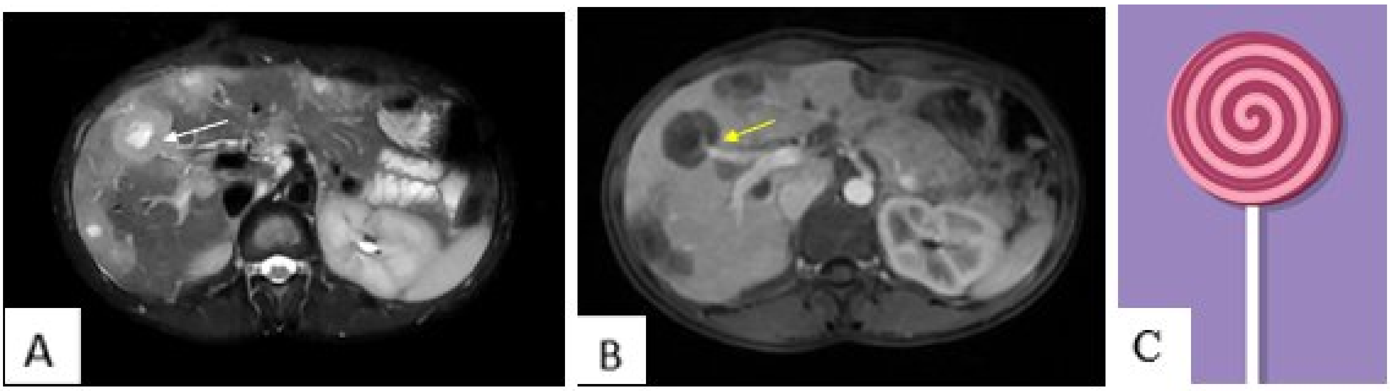

Figure 2. Magnetic resonance imaging (MRI) before and after contrast administration

Keywords : Hepatic epithelioid hemangioendothelioma, Target sign, Lollipop sign

[Poster Presentation 2]

ABD-Pancreas-02

Unmasking the Mimics of Pancreatic Cancer

Ankur Goyal[1*], Raju Sharma[1], Krishna Kumar R G[1], Piyush Agarwal[1]

[1]Radiodiagnosis and Interventional Radiology, All India Institute of Medical Sciences, New Delhi, India

Background: Pancreatic ductal adenocarcinoma (PDAC) is an aggressive malignancy with poor prognosis. The presence of a hypoenhancing pancreatic mass lesion with ductal dilatation is highly suggestive of PDAC. However, there may be situations when a radiologist should consider alternative possibilities. These may include a large lesion in the pancreatic head region or the absence of an abrupt cut-off of the pancreatic duct (PD), or a clinically well-preserved young patient. Thus, it is essential to recognise which other conditions may mimic PDAC on imaging.

Learning objectives: To discuss the imaging differential diagnoses of PDAC and highlight the distinctive features on various imaging modalities.

Based on retrospective review, cases will be showcased where PDAC was considered as a differential diagnosis but the final histology was something else.

The following mimics of PDAC will be discussed along with their differentiating points:

- Mass-forming chronic pancreatitis: Differentiating points include duct cut-off, duct-gland ratio, relative enhancement, vessel irregularity and diffusion restriction
- Autoimmune pancreatitis: absence of PD dilatation, extrapancreatic manifestations
- Paraduodenal pancreatitis: epicentre of the lesion, duodenal wall thickening and displacement of the gastroduodenal artery
- Hypoenhancing neuroendocrine tumors: enhancement ratios, T2 hyperintensity, well-defined smooth round margins
- Cystic neoplasms with pseudosolid appearance like serous cystic neoplasm and solid pseudopapillary tumor
- Metastases: in a known case of extrapancreatic malignancy such as lung or renal carcinoma
- Lymphoma
- Gastric / Duodenal GIST
- Peripancreatic lymphadenopathy
- Granulomatous infections like tuberculosis

Summary: Certain imaging features may suggest alternative diagnoses, like the absence of PD dilatation and presence of duct penetrating sign, T2w hyperintensity, hyperenhancement, hemorrhage, multifocal biliary and pancreatic strictures, duodenal wall thickening, soft tissue in pancreatoduodenal groove and multiple lesions. Such findings may prompt further work-up, including MRI, serum chromogranin, IgG4 levels, DOTANOC-PET CT, endoscopic ultrasound, work-up for inflammatory bowel disease and / or tissue sampling.

Clinical Implications: Knowledge of these mimics and their distinctive features is important to suggest alternative diagnoses and guide further investigations to reach the correct conclusion and avoid mismanagement.

mimics of pancreatic carcinoma

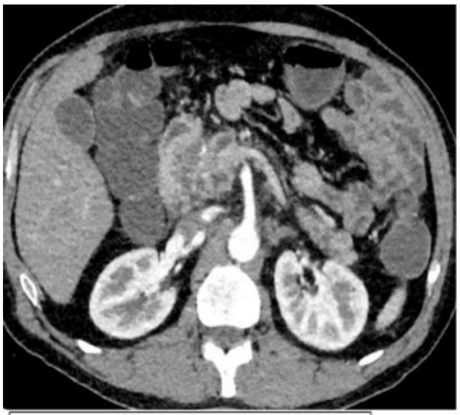

Paraduodenal Pancreatitis
Hypodense soft tissue in pancreaticoduodenal groove

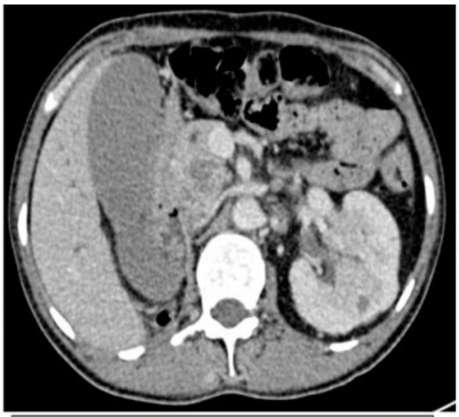

Pancreatic Metastasis, left renal RCC

Pancreatic involvement in Lymphoma with liver lesions

mimics of pancreatic carcinoma

Pancreatic Tuberculosis with necrotic nodes

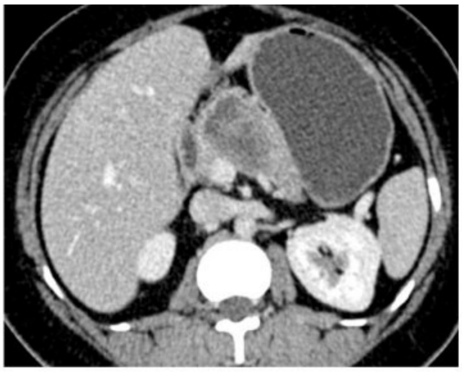

Heterogeneous mass lesion on CECT

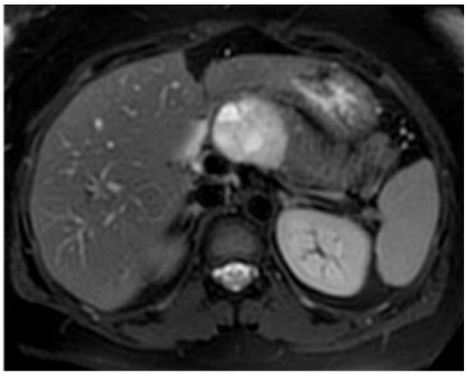

Mixed solid-cystic appearance with fluid levels on T2w MRI

Solid Pseudopapillary tumor

Keywords : Mass-forming chronic pancreatitis, Autoimmune pancreatitis, Neuroendocrine tumor

[Poster Presentation 2]

ABD-Pancreas-03

Integrating Systemic Metabolic Profiles and Dual-Phase CT-Based Habitat Radiomics via Vision Transformer for Predicting the Aggressiveness of Pancreatic Neuroendocrine Neoplasms: A Multicenter Study

Weinuo Qu[1], Chenxi Lyu[1], Zhibo Wang[1], Jiali Li[1], ShaSha Li[3], Feng Li[2], Zhen Li[1*]

[1]Radiology, Tongji Hospital Tongji Medical College Huazhong University of Science and Technology, China
[2]Radiology, Xiangyang Central Hospital, China
[3]Radiology, Shanxi Bethune Hospital, China

Accurate preoperative evaluation of tumor aggressiveness is crucial for optimizing surgical planning and prognosis assessment in pancreatic neuroendocrine neoplasms (PNENs). This study aimed to develop and validate a dual-phase CT-based multimodal framework integrating habitat radiomics, a vision transformer (ViT), and systemic metabolic indicators to noninvasively predict PNEN aggressiveness and explore the systemic-local metabolic interplay.

This retrospective multicenter study included 432 patients confirmed PNENs from three institutions between May 2012 and May 2024. The aggressiveness of PNENs was defined as a composite measure including G3 grading, N+, distant metastases, and/ or disease recurrence after at least 1 year of follow-up. Arterial- and venous-phase tumor regions of interest (ROIs) were first automatically segmented using a pretrained nnUNet-based segmentation model and manually corrected by two radiologists. Based on the corrected masks, a 3-mm peritumoral expansion zone was generated. K-means clustering was applied to both phases to construct habitat subregions. A ViT-based deep learning model was trained using dual-phase CT data.Body composition volume were automatically segmented from CT images using an nnUNetv2-based algorithm. Systemic metabolic indicators, including body composition volumes (visceral, subcutaneous, intermuscular fat, and muscle) and biochemical parameters reflecting glucose-lipid metabolism were used to characterize systemic metabolic status. Features including mean arterial and venous CT attenuation, ΔHU(V-A), the proportion and mean intensity of the highest-enhancement subregion, and radiomics descriptors (first-order, GLCM, GLSZM, and NGTDM) were extracted to represent local metabolic activity. Six models were constructed: (1) habitat model, (2) ViT model, (3) habitat + ViT fusion model, (4) local metabolic model, (5)systemic metabolic model, (6) integrated systemic metabolic+ habitat + ViT fusion model.Model performance was assessed using ROC curves and DeLong tests, with calibration and decision curve analyses for clinical evaluation.To explore the potential relationships between systemic metabolic indicators and tumor-local metabolic features, multiple correlation analyses were conducted, including Spearman's rank correlation, canonical correlation analysis (CCA), partial least squares (PLS), mutual information, distance correlation, and locally weighted regression (LOESS).

The dual-phase Habitat + ViT fusion model achieved superior performance compared with single-

phase and single-modality models,with an AUC of 0.86 in the internal validation cohort and 0.81 in the external test cohort, outperforming both the Habitat model (AUC = 0.83/0.77) and ViT model (AUC = 0.75/0.71). Adding systemic metabolic indicators further improved predictive performance (AUC = 0.89/0.83).Models based solely on local or systemic metabolic features achieved moderate accuracy (AUC = 0.76/0.73 and 0.72/0.74, respectively).

The dual-phase CT-based Habitat+ViT model effectively characterizes intratumoral and peritumoral heterogeneity and provides an accurate, noninvasive approach for predicting PNENs aggressiveness. Integration of systemic and local metabolic information further enhances model performance, offering valuable support for preoperative risk stratification and personalized management.

Keywords : Pancreatic Neuroendocrine Neoplasms, Habitat Radiomics, Vision Transformer

[Poster Presentation 2]

ABD-Pancreas-04

Deep Learning-Accelerated Respiratory-Triggered 3D MR Cholangiopancreatography: Sub-Minute Acquisition with Preserved Image Quality

Naoki Yoshida[1,2], Keitaro Sofue[1*], Kazuma Tsukamoto[2], Tomohiro Noda[2], Tatsuya Nishitani[2], Shintaro Horii[2], Yuichiro Somiya[1,2], Akiko Kusaka[2], Tetsuya Wakayama[3], Xucheng Zhu[4], Ty Cashen[5], Takeru Yamaguchi[1], Yoshiko Ueno[1], Takahiro Tsuboyama[1], Izumi Imaoka[1], Takamichi Murakami[1]

[1]Ragiology, Kobe University Graduate School of Medicine, Japan
[2]Center for Radiology and Radiation Oncology, Kobe University Hospital, Japan
[3]MR Clinical Solutions and Research Collaborations, GE HealthCare, Japan
[4]MR Clinical Solutions and Research Collaborations, GE HealthCare, CA, USA
[5]MR Clinical Solutions and Research Collaborations, GE HealthCare, WI, USA

Magnetic resonance cholangiopancreatography (MRCP) is a noninvasive and reliable technique for evaluating pancreatobiliary diseases. Three-dimensional (3D) MRCP enables multiplanar reconstruction, providing detailed visualization of the biliary and pancreatic ducts and facilitating the detection of small lesions.
Respiratory-triggered 3D-MRCP (RT-3D-MRCP) is widely used for high-quality imaging, but its long acquisition time often leads to image degradation in patients with irregular breathing. To address this limitation, Sonic DL (SDL), a deep learning–based image reconstruction applied to randomly under-sampled data, has been developed to markedly shorten scan time. However, reports on the clinical application of SDL to RT-3D-MRCP remain limited. This study aimed to evaluate and compare image quality of conventional RT-3D-MRCP and SDL-accelerated RT-3D-MRCP protocols in the same patients.

Twenty patients (aged 51–90 years) underwent RT-3D-MRCP using a 3T scanner (Signa Premier, GE Healthcare). RT-3D-MRCP images were acquired with three protocols: a conventional protocol and two SDL-accelerated protocols with 6- and 9-breaths acquisition (SDL-6 and SDL-9). The protocols included: repetition time, 1 × respiratory cycle; echo time, 700, 400, and 400 ms; echo train lengths, 130, 400, 250; voxel size (mm), 0.7×1.0×1.4, 1.0×1.0×1.4, 1.0×1.0×1.4; the number of slices, 160, 100, 100; acceleration factor, 3.75, 10, 10; number of breaths in acquisition, 43, 6, 9, respectively. The estimated scan times were 2 min 49 s (Conventional), 22 s (SDL-6), and 33 s (SDL-9).

Quantitative analysis included signal-to-noise ratio (SNR), contrast ratio (CR), and contrast-to-noise ratio (CNR). Regions of interest were manually placed in the upper, middle, and lower common bile duct (CBD). SNR was calculated as: $SNR = SI_{CBD}/SD_{CBD}$, CR was calculated as $CR = (SI_{CBD}-SI_{BG})/(SI_{CBD} + SI_{BG})$, and CNR was calculated as $CNR = (SI_{CBD}-SI_{BG})/SD_{CBD}$. A board-certified radiologist visually assessed overall image quality, background suppression, image sharpness, artifacts, bile duct visibility, and pancreatic duct visibility on a 5-point scale. Statistical analysis was performed using the Friedman test with Bonferroni correction.

In the quantitative analysis, SDL-9 showed a significantly higher SNR than the conventional protocol (P = 0.034). SDL-6 showed a significantly lower CR than conventional (P = 0.013). CNRs were comparable among the three protocols. In qualitative assessment, overall image quality and sharpness of SDL-9 (3.33 ± 1.03 and 3.27 ± 1.24) were similar to the conventional protocol (3.67 ± 1.02 and 3.53 ± 0.88), whereas SDL-6 (2.80 ± 0.85 and 2.60 ± 0.84) demonstrated significantly lower scores in overall image quality (P < 0.001), background suppression (P < 0.001), image sharpness (P < 0.001), and bile duct visibility (P = 0.002). No significant differences were observed in artifact (P > 0.05) or pancreatic duct visibility scores (P > 0.05). Overall, SDL-9 achieved diagnostically acceptable image quality and contrast comparable to the conventional method, while markedly reducing scan time, whereas SDL-6 showed inferior image quality despite further acceleration.

Accelerated RT-3D-MRCP using Sonic DL achieved diagnostically acceptable image quality and contrast compared with the conventional method, while markedly reducing acquisition time. This approach may help minimize respiratory-oriented image degradation and improve clinical workflow efficiency.

Maximum intensity projection (MIP) images obtained using Conventional (a), Sonic DL-6 (b), and Sonic DL-9 (c) RT-3D-MRCP protocols. Estimated acquisition times were 160s, 22s, and 33s, for conventional, Sonic DL-6, and Sonic DL-9, respectively. Quantitative comparisons of SNR, CR, and CNR are shown in (d), (e), and (f), respectively. Each plot represents data from 20 cases, with horizontal bars indicating mean values.

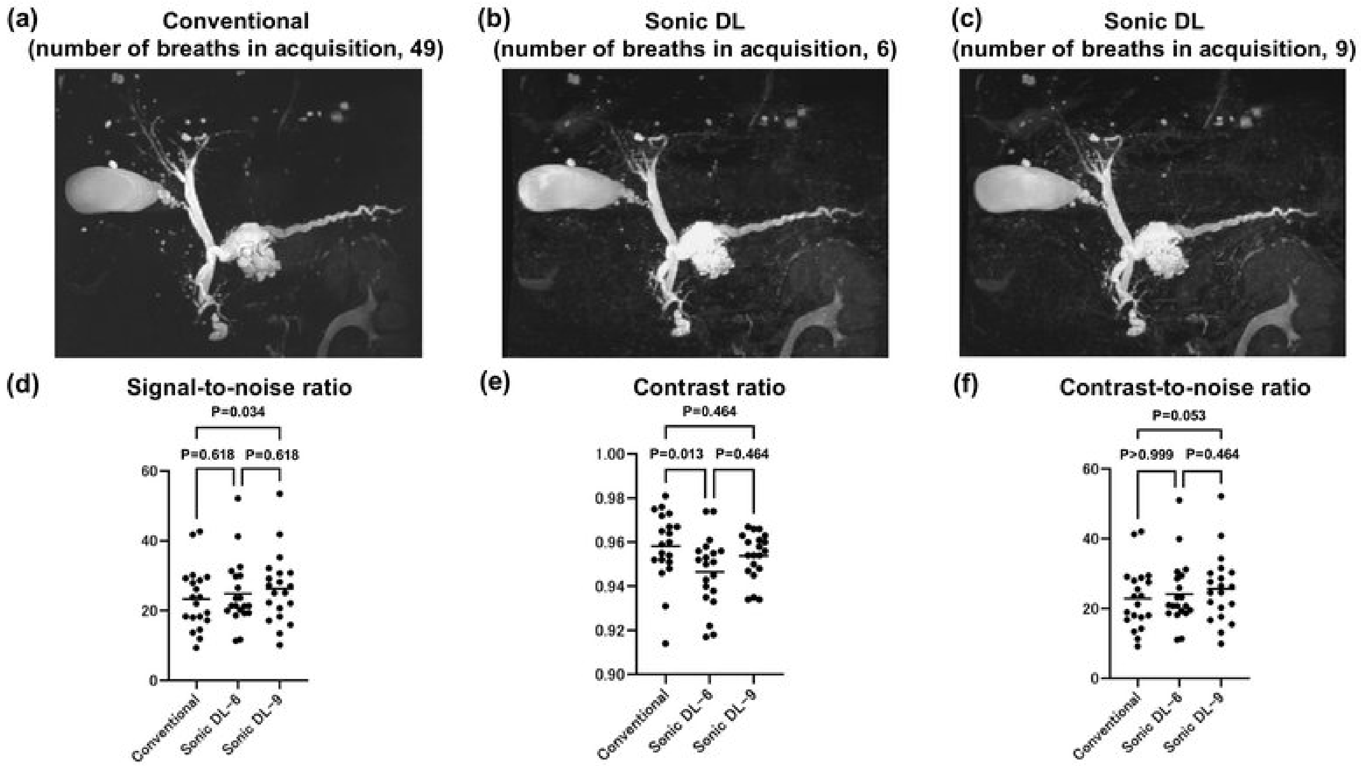

Results of the qualitative (visual) assessment. Graphs (a–f) show scores for overall image quality (a), background suppression (b), image sharpness (c), artifacts (d), bile duct visibility (e), and pancreatic duct visibility (f). Each graph displays the distribution of scores on a five-point scale, with 5 representing the highest and 1 the lowest rating.

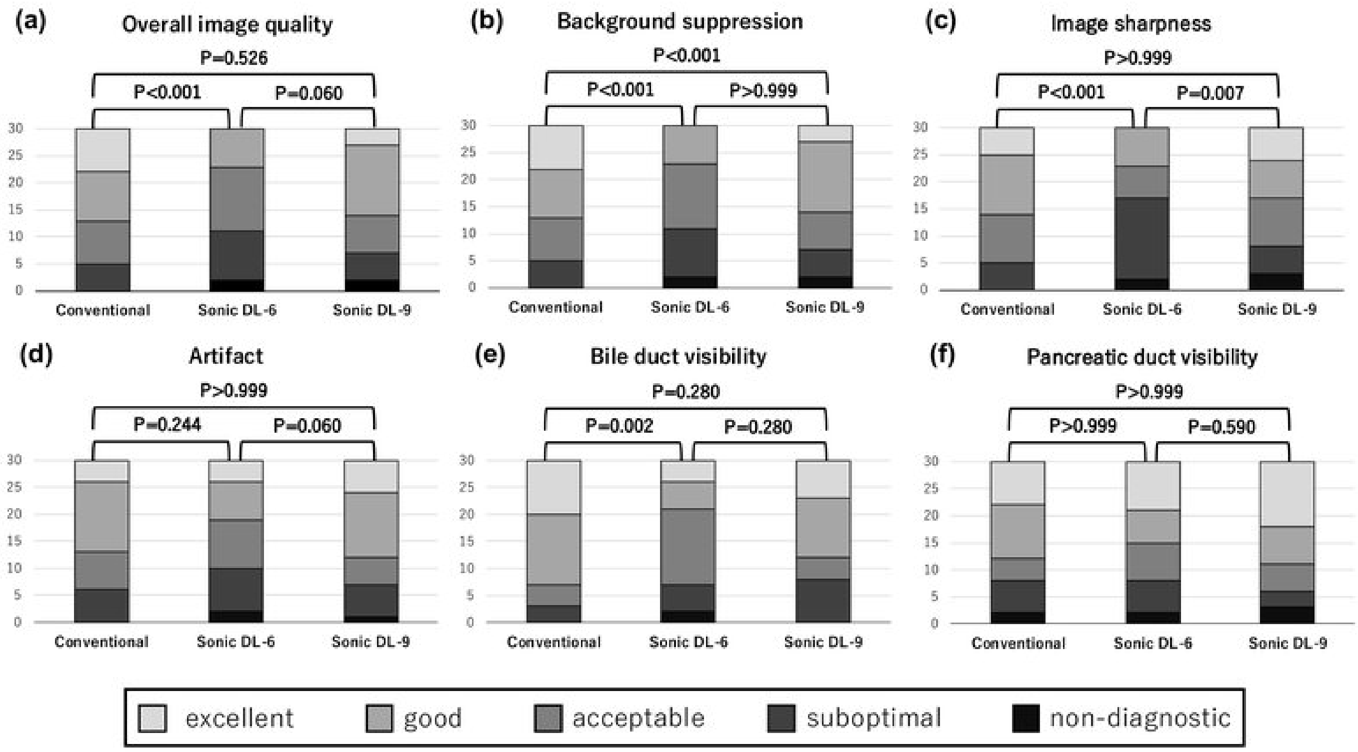

Keywords : MRCP, Deep Learning Reconstruction, MRI

[Poster Presentation 2]

ABD-Biliary-04

Association of Gallbladder Polyps with Intercurrent Degree of Hepatic Steatosis in Patients Who Underwent Abdominal Sonography in a Tertiary Hospital – A Retrospective Study

Charlene Noelle Duante[1], Maynard Redor[1*]

[1]Radiology, FEU-NRMF, Philippines

This study investigated the association between gallbladder polyps (GBP) and hepatic steatosis at a Tertiary Hospital with 500-Bed Capacity. It aimed to describe patient demographics (age and gender), the prevalence and degree of hepatic steatosis, and the presence of GBP among patients with fatty liver disease. Additionally, the study assessed whether there was a relationship between GBP size and the degree of hepatic steatosis.

A total of 562 abdominal ultrasound scans of patients aged 18 years and over, who underwent routine abdominal ultrasound at the Tertiary Hospital from January 2021 to December 2023, were examined for the presence of GBP. The scans were of the whole abdomen or upper abdomen and were performed on patients with symptomatic or asymptomatic abdominal pain. Only the first or initial scans of patients with multiple ultrasound scans were included in the study. The images were obtained from the Picture Archiving and Communication System (PACS) of the said hospital. The scans were performed by the Radiology residents (levels 2-3) and verified by 2-3 Radiology consultants (Consultant A with 10 years experience, Consultant B with 20 years experience and Consultant C with 25 years experience).

The average patient age was 44.6 years, with males having a higher average age (54.8 years) compared to females (45.2 years). Males predominantly fell within the 18 to 29 age group, while females were most commonly in the 30 to 39 age group. Of the 422 GBP cases, 58.1% were male and 41.9% female. The majority of patients with GBP (75.4%) had no hepatic steatosis, and there was no significant difference between sexes regarding hepatic steatosis. Only 2.1% of the polyps were larger than 0.9 cm. Univariate analysis showed that patients aged 40 to 49 years had a higher likelihood of GBP, and males were more prone to GBP compared to females. The degree of hepatic steatosis did not show a significant association with GBP.

This study highlights that age and sex are significant factors in the likelihood of developing GBP, with males and those aged 40 to 49 years being more susceptible. The degree of hepatic steatosis, however, does not appear to significantly impact the occurrence of GBP.

Presence of GBP by sex, age group (n=562)

Table 5. Presence of GBP by sex, age group (n=562)

Variables	n	Without GBP		With GBP		p-value
		n	prop	n	prop	
Sex						
Males	308	63	45.0	245	58.1	
Females	254	77	55.0	177	41.9	0.008
Age group						
18-29	114	24	17.1	90	21.3	
30-39	120	36	25.7	24	19.9	
40-49	109	19	13.6	90	21.3	0.134
50-59	107	29	20.7	78	18.5	
60 and above	112	32	22.9	80	19.0	

Factors associated with Gallbladder polyps using Multiple Logistic Regression

Table 6. Factors associated with Gallbladder polyps using Multiple Logistic Regression

			95 Confidence Interval	
	AOR	p-value	Lower limit	Upper limit
Age group				
18-29	Reference			
30-39	1.5	0.414	0.6	3.6
40-49	3.9	0.003	1.6	9.8
50-59	2.3	0.072	0.9	5.6
60 and above	1.4	0.475	0.6	3.5
Sex				
Male	Reference			
Female	0.6	0.050	0.3	1.0
Hepatic Steatosis				
None	Reference			
Mild	0.004	0.000	0.0	0.0
Moderate to Severe	0.005	0.000	0.0	0.0

Keywords : Gallbladder Polyp, Hepatic Steatosis, Association

[Poster Presentation 2]

ABD-UGI-03

Tumor Subregion-based CT Habitat Radiomics to Improve Prediction of Nodal Disease in Esophageal Squamous Cell Carcinoma

Hao Wen[1], Tian-wu Chen[1*], Xu-rui Liu[1]

[1]Radiology, The Second Affiliated Hospital of Chongqing Medical University, China

To develop and validate a contrast-enhanced CT (CECT) habitat radiomics model focusing on assessing independent predictive contribution of each intratumoral subregion to improve prediction of lymph node metastasis (LNM) in esophageal squamous cell carcinoma (ESCC).

This retrospective study included 246 consecutive patients with confirmed ESCC undergoing preoperative CECT from two centers. Patients from Center 1 (n=194) were randomly divided into training (n=136) and internal-validation (n=58) cohorts, and an external-validation cohort comprised 52 patients from Center 2. Conventional radiomics features were extracted from the whole-tumor. Habitat radiomics features were from three habitat subregions using K-means clustering. The selected core features were used to develop the corresponding support vector machine (SVM) classifiers followed with logistic regression (LR), k-nearest neighbors (KNN), and Light Gradient Boosting Machine (LightGBM) classifiers. Predictive performance of models was evaluated using area under the receiver operating characteristic curve (AUC).

For SVM classifiers, habitat 3 (with high-entropy) based model showed better predictive performance than the conventional whole-tumor model, and habitats 1 and 2 based models (AUC: 0.925 vs. 0.911, 0.865 and 0.882; 0.898 vs. 0.871, 0.741 and 0.781; and 0.844 vs. 0.754, 0.744 and 0.812 in the training, internal-validation and external-validation cohorts, respectively) (all p-values < 0.05). Using the same preprocessing, three types of other classifiers, including LR, KNN and LightGBM, reproduced superiority of habitat 3 with consistent predictive performance, supporting algorithms' robustness.

Habitat with high-entropy based models provided the strongest performance for predicting LNM in ESCC, with SVM performing best and outperforming the whole-tumor models.

Study workflow and radiomics model performance.

ESCC tumors were segmented into three habitat subregions, and features were used to build SVM models.

OC curves show model performance in the training, internal validation, and external validation cohorts.

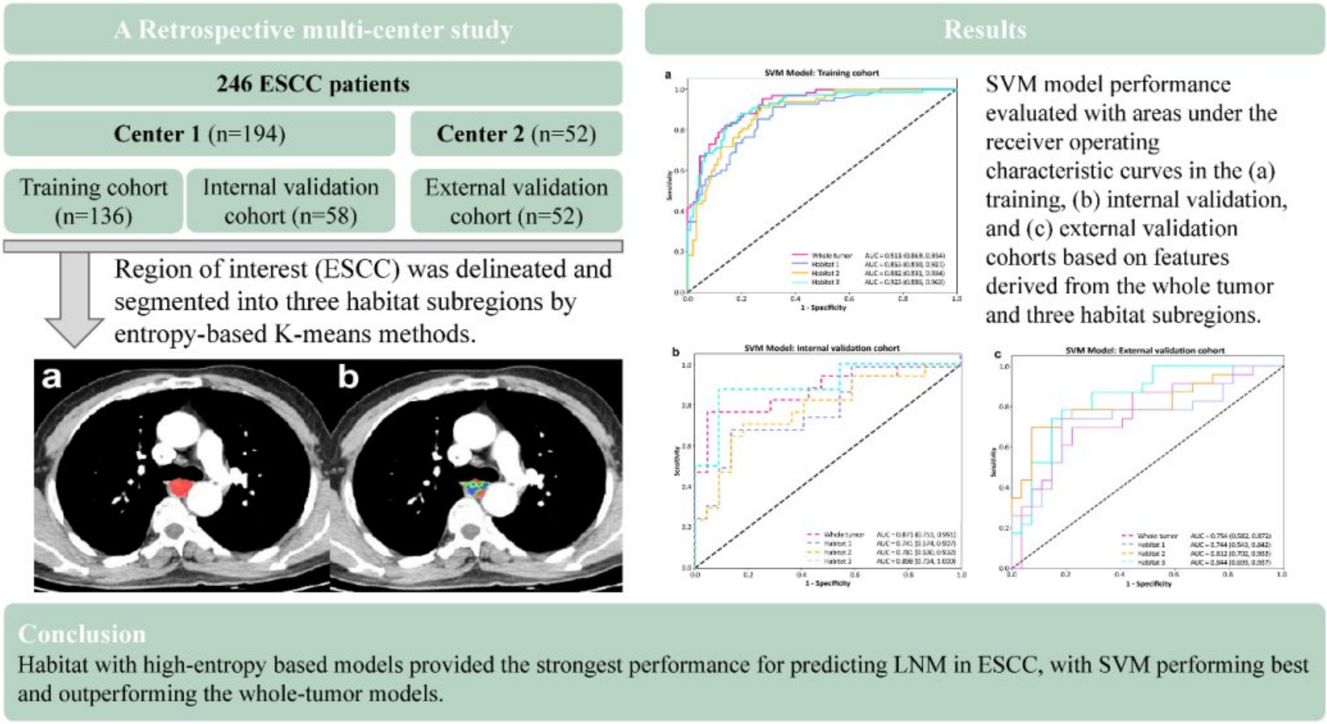

Keywords : Esophageal cancer, Lymph node metastasis, Habitat radiomics

[Poster Presentation 2

ABD-LGI-04

Temporal AI-assisted Compressed Sensing Enables High-resolution, Motion-robust Small-bowel MR Enterography without Antiperistaltic Agents

Ziman Xiong[1*], Xiaopeng Song[2], Wei Mao[2], Zhen Li[1], Yaqi Shen[1]

[1]Radiology, Tongji Hospital of Tongji Medical College of HUST, China
[2]United Imaging Healthcare, China

To evaluate whether temporal AI-assisted compressed sensing (tACS) enables high-resolution, motion-robust magnetic resonance enterography (MRE) without antiperistaltic agents and improves acquisition efficiency and motility visualization.

This prospective single-center study enrolled consecutive patients who underwent both routine and tACS MRE on a 3.0-T scanner between October 2024 and June 2025, without antiperistaltic agents. The tACS protocol acquired axial and coronal T2-weighted images (T2WI); the routine protocol included a coronal Cine sequence. Acquisition time and total temporal frames for non-fat-saturated T2WI (routine and tACS) and Cine were recorded to calculate imaging efficiency (frames/min). Primary outcomes included total temporal frames, scan time, efficiency, subjective image-quality scores, quantitative signal-to-noise ratio (SNR), contrast-to-noise ratio (CNR), maximum local variation (MLV) sharpness, peri-enteric fat-plane clarity, and ileocecal-valve (ICV) motility. Paired statistical tests compared within-subject differences; Kendall's W assessed inter-reader agreement.

Thirty patients completed both protocols. Compared with routine protocol (107 frames in 241 s), tACS acquired 504 frames in 287 s, a 4.7-fold increase in temporal frames for a 46-second time increase. Imaging efficiency improved from 26.6 to 105.4 frames/min (4.0-fold; $p < 0.001$). Subjective image quality favored tACS (median 5.0 vs ≤4.0; $p < 0.01$) with perfect reader agreement ($W = 1.00$). Quantitative SNR and CNR increased 9–10-fold with tACS and MLV sharpness was significantly higher (all $p < 0.001$). Peri-enteric fat-plane clarity reached perfect scores in 93.3% (28/30) with tACS (median 3.0 vs 2.5; $p < 0.001$). ICV motility scoring favored tACS (median 3.0, IQR 2.0–3.0) over Cine (median 2.0, IQR 1.0-2.0); inter-reader agreement remained excellent.

tACS markedly improves temporal resolution and image quality for MRE without antiperistaltic agents, with minimal extra scan time and potential to simplify clinical workflows. This prospective study provides initial clinical validation and includes reproducibility information.

Comparison of acquisition efficiency and image quality: routine T2WI and Cine vs. tACS T2WI.

(A) Total scan time (routine 4:01 [241 s] vs tACS 4:47 [287 s]; paired test, $p < 0.001$).
(B) Subjective image-quality scores (median, IQR; Wilcoxon, $p < 0.001$).
(C) Quantitative SNR and CNR (median, IQR; paired tests; $p < 0.001$).
(D) Image sharpness by MLV (median, IQR; paired tests; $p < 0.001$).

SNR = signal-to-noise ratio; CNR = contrast-to-noise ratio; MLV = maximum local variance; IQR = interquartile range.

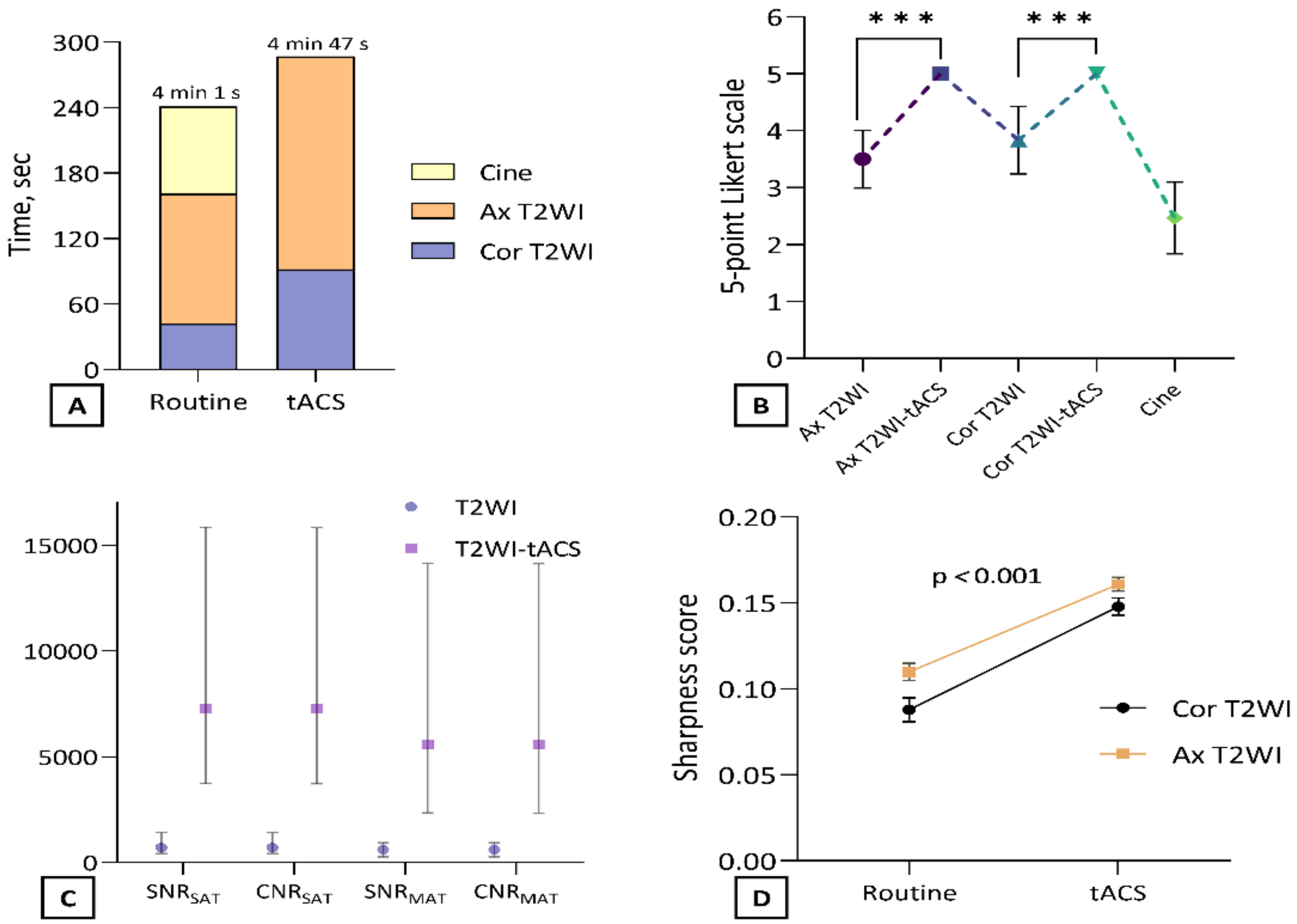

Two representative examples showing visualization of bowel-adjacent organ fat planes on non-fat-saturated T2WI: routine protocol versus tACS.

(A)-(B) Compared with the routine protocol, T2WI-tACS images demonstrate clearer delineation of the fat plane between the bowel and uterus.

(C)-(D) T2WI-tACS images likewise show improved delineation of the fat plane between the bowel and bladder compared with routine acquisitions.

This demonstrating the superior clarity of peri-enteric fat planes with tACS.

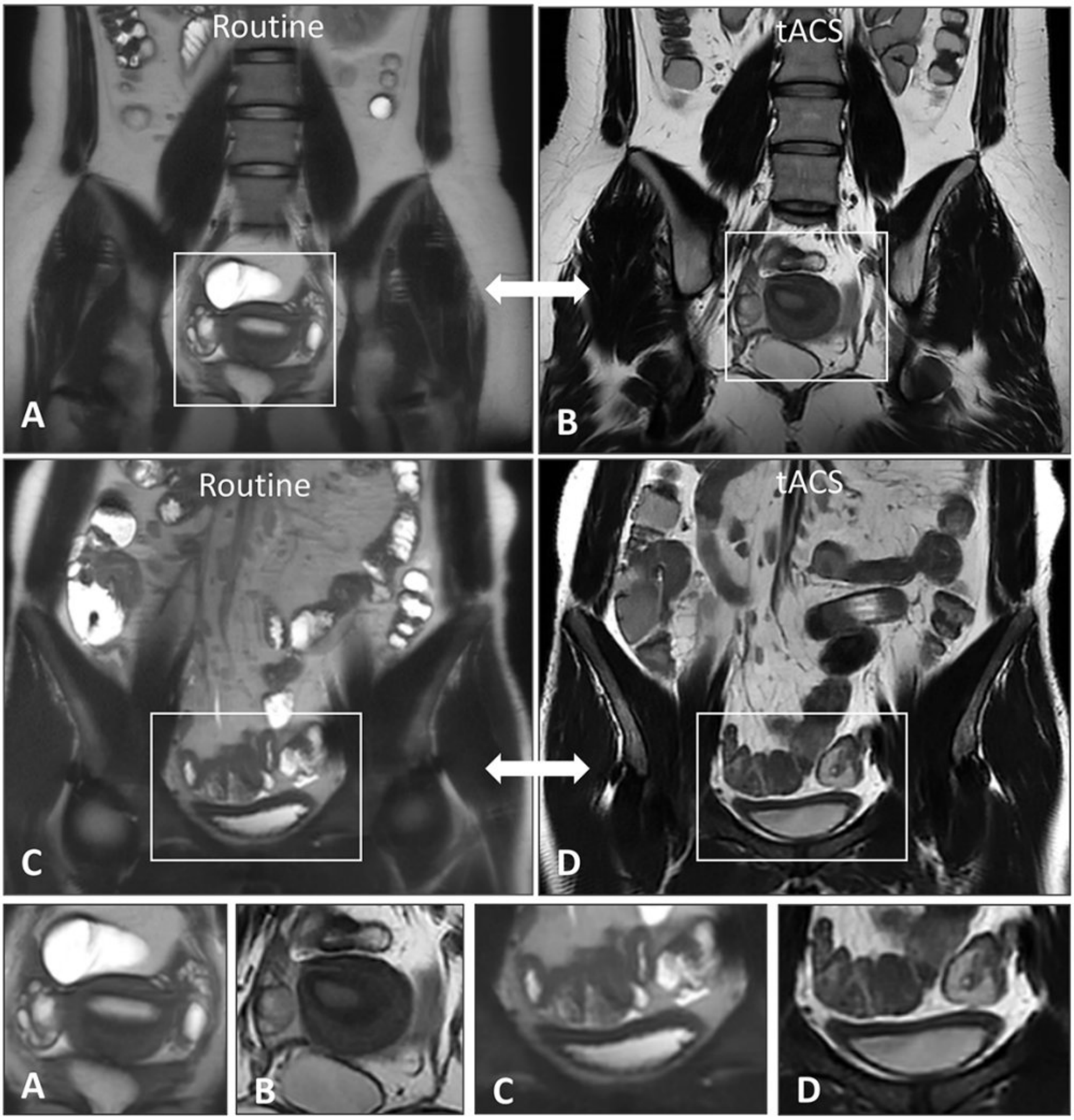

Keywords : Magnetic resonance enterography, AI-assisted image reconstruction, Motion-robust imaging

[Poster Presentation 2]

ABD-LGI-05

Deep Learning–Accelerated Magnetic Resonance Enterography for the Assessment of Crohn's Disease

Sohyun Park[1*]

[1]Radiology, Seoul National University Bundang Hospital, Korea

To compare the image quality (IQ) of deep learning–accelerated magnetic resonance enterography (MRE) with that of conventional MRE in patients with Crohn's disease.

From August 2023 to July 2024, we retrospectively reviewed patients who underwent MRE using either conventional or deep learning (DL)–accelerated sequences. Two radiologists independently evaluated the overall IQ, sharpness, motion artifacts, and artificial appearance for single-shot fast spin echo (SSFSE), diffusion-weighted imaging (DWI), and precontrast and dynamic phases.

A total of 39 patients were included (male, n = 23; median age, 31.0 years; conventional group, n = 15; DL group, n = 24). The mean overall IQ scores for SSFSE, DWI, and the arterial phase were 4.27 ± 0.70 and 4.79 ± 0.41 (P = 0.028), 3.00 ± 0.65 and 3.92 ± 0.65 (P = 0.001), and 3.60 ± 1.06 and 4.33 ± 0.70 (P = 0.044) for the conventional and DL groups, respectively. The DL group demonstrated higher overall IQ than the conventional group across all sequences. No examinations were classified as nondiagnostic (overall IQ < 2) in either group. Across all phases, the DL group exhibited fewer motion artifacts but a more artificial appearance than the conventional group.

DL-MRE achieved adequate IQ in patients with Crohn's disease while reducing scan time.

Keywords : Crohn's disease, Enterography, Deep learning

[Poster Presentation 2]

ABD-LGI-06

CT Utilization in Diagnosing Atypical Causes of Small Bowel Obstruction in the Emergency Room: A Case Series

Jose Ricardo Samson[1], Ma Lourdes Badion[1*]

[1]Radiology, Metropolitan Medical Center, Philippines

Small bowel obstruction (SBO) is one of the most common diagnoses for emergency room consult and subsequent admission, adhesions being the usual cause. However, radiologists should further investigate and entertain other etiologies if no apparent cause for SBO is distinguished. The hallmark finding for cases of SBO is the transition zone which can be further supported by identifying a “small bowel fecalization,” or “small bowel feces sign”. This review aims to highlight uncommon causes of small bowel obstruction.

Selection of uncommon post-pandemic small bowel obstruction cases were retrieved from the picture archiving and communication system (PACS) of Metropolitan Medical Centre Hospital, Manila, Philippines, from January 1, 2022 to September 3, 2025. GE 128 slice multi-detector CT scanner was used for acquisition of whole abdominal images with 16 cm coverage as 256 × 0.625 mm collimations. Multiplanar reconstructions were then reviewed on a 3D imaging workstation. Diagnoses were supported by surgery and histological findings.

A total of 157 cases of SBO were identified. All patients were ages 5 to 94 (86 male and 71 female) complaining of abdominal pain and vomiting were assessed in the emergency room prior to being admitted. Majority of CT findings were due to adhesions (48.0%), followed by malignancy (17.8%), infectious (10.8%), hernias (10.2%), volvulus (3.8%), intussusception (2.5%), fecal stasis or impaction (1.9%), intestinal tuberculosis (1.3%), gallstone ileus (1.2%), necrotizing enterocolitis (0.6%), and congenital bands (0.6%). In the abdominal hernias, the most common were inguinal hernias (43.7%), followed by incisional hernias (26%), umbilical hernias (24%), and spigelian hernias (6.2%).

In the emergency room setting, it is of utmost importance to make accurate diagnoses. Therefore, knowledge and awareness of different pathologies would aid in making more definitive diagnoses. These cases were presented in order to aid and supplement the interpretation and management of patients with rare causes of small bowel obstruction.

Congenital Peritoneal Band in an adult. 54/M presenting with bloatedness and epigastric pain with no prior history for surgery. Saggital reconstruction of the abdomen (A) shows a focal point of narrowing seen at the distal jejunum (arrow head). On coronal view (B) Retrograde dilatation and wall thickening of the proximal jejunal segments (thick arrows). Grossly there were two bands, a small (C) and large (D) band, compressing the mesenteric root causing decreased perfusion in portions of the jejunum and ileum.

Gallstone Ileus cases. 51/F presenting with epigastric pain with associated vomiting in the ER. Plain CT on coronal view (E) shows a radiopaque gallstone (arrow head) seen at the distal ileum measuring 3.7 x 2.5 cm with anterograde collapse of the terminal ileum (thin arrow). The small bowel loops are dilated (thick arrows) with the largest diameter measuring 4.1 cm at the proximal jejunum. Contrast enhanced images shows wall thickening and enhancement (arrows) (F). 76/F complaining of generalized crampy and intermittent abdominal pain with associated vomiting. Contrast enhanced CT axial reconstruction (G) shows a radiopaque lamellated calcific density (arrow head) is seen approximately at the distal jejunum, measuring 2.9 x 2.8 cm. There is retrograde distention of the small bowel loops and mucosal wall thickening of the proximal jejunal segments (thick arrows) (H).

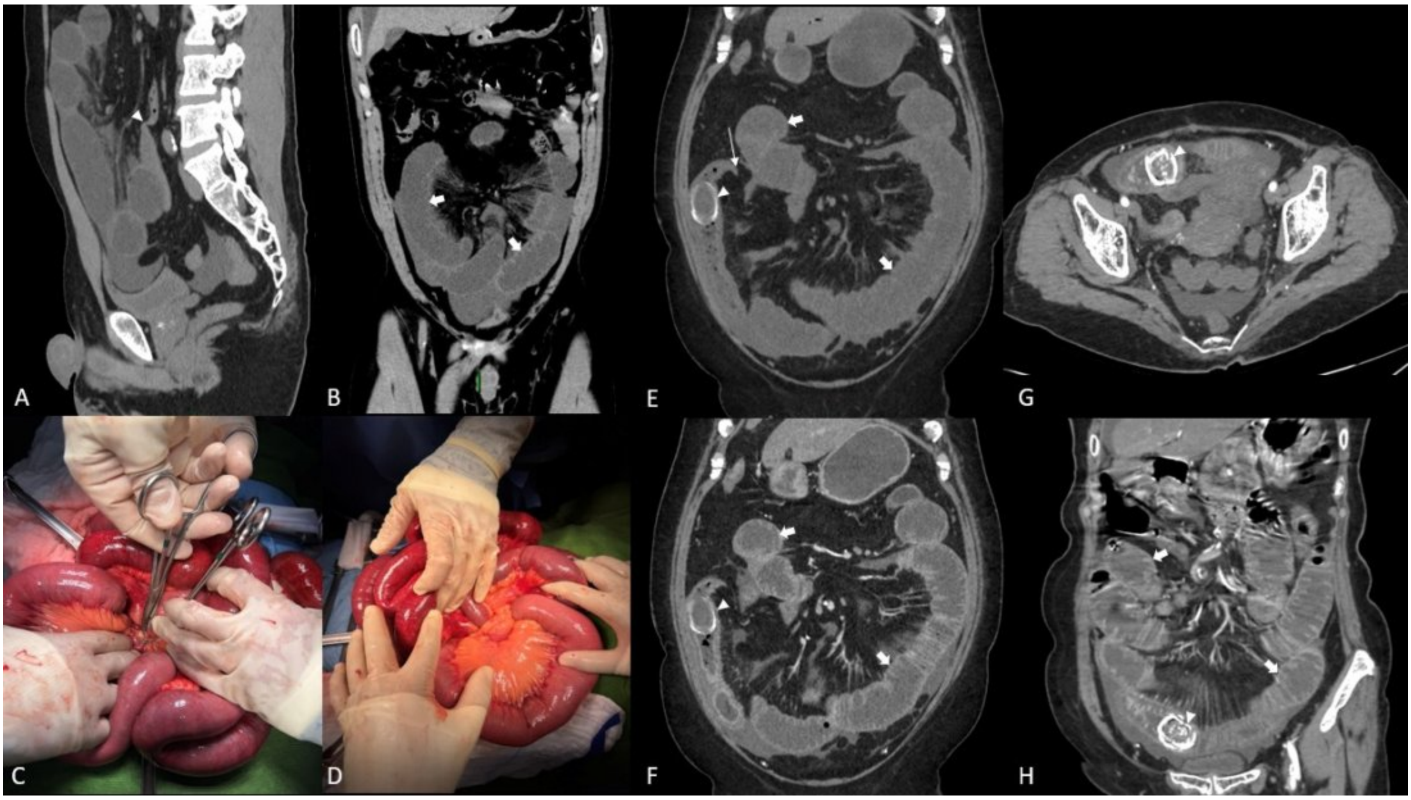

Necrotizing Enterocolitis in an adult. 59/M complaining of bilateral lower quadrant pain and vomiting in the ER. Axial reconstruction (A) demonstrates a transition zone (arrow head) with adjacent pneumatosis intestinalis. On coronal view (B), long segment wall thickening seen in the distal ileum (thick arrows) with surrounding mesenteric stranding and fluid collections extending to the left paracolic region. Grossly necrotic ileal segments were seen on exploratory laparotomy (C, D).

Intestinal Tuberculosis in an adult. 34/M complaining of generalized abdominal pain and vomiting. Saggital view (E) shows ileo-cecal thickening (arrow head) the transition zone (thin arrow) and a normal appendix (thick arrow). On axial reconstruction (F), focal segmental wall thickening and enhancement of the ileo-cecal region with surrounding mesenteric stranding and enlarged lymph nodes.

Pediatric Intestinal Tuberculosis. 12/F complaining of right lower quadrant pain. Coronal view (G) shows thickening of the cecum (arrow head) and dilated small bowel loops (thick arrow). Contrast enhaced images (H) show wall thickening and enhancement with surrounding mesenteric lymphadenopathy.

Spigelian hernia. 43/M complaining of right lower quadrant pain in the ER. Axial reconstruction (I) demonstrates a defect (arrow heads) between the lateral border of the right rectus abdominis muscle and the medial border of the oblique muscle measuring 3.5 cm in diameter. Coronal view (J) shows herniating omental fat as well as small bowel loops demonstrating a transition zone (thin arrow) as it exits through the defect. There is retrograde dilatation of the ileal and jejunal segments with small bowel feces sign (thick arrows).

Keywords : Small Bowel Obstruction, Atypical, Emergency Room

[Poster Presentation 2]

ABD-LGI-07

Review of Gastrointestinal Involvement in Vasculitis: Imaging and Biomarker Perspectives

Yaqi Shen[1], Jiayi Li[1*]

[1]Radiology, Tongji Hospital Affiliated with Tongji Medical College of Huazhong University of Science and Technology, China

Clinical manifestations of gastrointestinal involvement in systemic vasculitis are often insidious and nonspecific, frequently presenting initially with abdominal pain, bleeding, or perforation, leading to frequent misdiagnosis or delayed treatment. Traditional classification frameworks based on vessel size (macrovascular, mesovascular, microvascular) primarily serve rheumatology and immunology clinical diagnosis, offering limited guidance for radiologists in imaging identification and subtype determination. This study systematically reviews gastrointestinal involvement across various vasculitis subtypes, synthesizing insights from imaging, pathology, and biomarkers to propose an incidence-based classification framework. By integrating high-prevalence subtypes in Asian populations and regional variations, it provides radiologists with a systematic reference for early identification, differential diagnosis, and clinical risk stratification, thereby promoting interdisciplinary collaboration and precision medicine.

We systematically searched PubMed, Web of Science, and Embase from January 1990 to June 2025 using keywords including “vasculitis”, “gastrointestinal involvement”, “CT enterography”, “MR enterography”, and specific vasculitis entity names. We included literature focusing on epidemiology of gastrointestinal involvement, imaging findings and biomarkers, with particular emphasis on studies of Asian populations.

Based on the incidence of gastrointestinal involvement, vasculitis was categorized into three groups:

(1) High-incidence group (> 30%): IgA vasculitis (IgAV), polyarteritis nodosa (PAN), and Behçet’s disease (BD). In IgAV the typical CT findings include segmental bowel-wall thickening and mesenteric hyperemia; elevated galactose-deficient IgA1 and D-dimer may indicate active disease. In PAN, CTA/MRA may show microaneurysms and “string-of-beads” changes; in Asian patients PAN is often closely associated with HBV infection. In BD, the ileocecal region is frequently involved; CT enterography/MR enterography may reveal deep large ulcers, and HLA-B51 positivity is an important risk marker.

(2) Moderate-incidence group (5–30%): ANCA-associated vasculitis (AAV), Takayasu arteritis (TA), and lupus vasculitis (LV). AAV commonly presents with multi-segment bowel-wall thickening, and MPO/PR3-ANCA are key diagnostic markers. Takayasu arteritis may lead to mesenteric ischemia; CTA/MRA show concentric arterial-wall thickening and stenosis, and faecal S100A12 is a potential marker of disease activity. In LV, imaging may demonstrate a “target sign”; diagnosis requires correlation with anti-dsDNA positivity and hypocomplementemia.

(3) Low-incidence group (< 5%): Giant cell arteritis (GCA), in which gastrointestinal involvement is rare but associated with high mortality; radiologists should pay attention to differentiation from atherosclerosis and other causes of vascular bowel complications.

In Asian populations, the proportions of gastrointestinal involvement are higher in IgAV, HBV-associated PAN, HLA-B51-associated BD and Takayasu arteritis, and clinical & imaging features show regional differences.

Gastrointestinal involvement in vasculitis is highly heterogeneous. A classification framework based on incidence may highlight high-risk diseases. Integrating imaging features with biomarkers may improve diagnostic accuracy and reduce the risk of serious complications.

Keywords : Gastrointestinal vasculitis, Multimodal Imaging, Biomarkers

[Poster Presentation 2]

ABD-LGI-08

Effectiveness of Deep-Learning-Based Denoising Software on Image Quality and Diagnostic Performance of Low-Dose Abdominal CT for evaluation of Acute Appendicitis

Young Hwan Lee[1*], Cheonghwan Shin[1], Youe Ree Kim[1]

[1]Radiology, Wonkwang University Hospital, Korea

The aim of this study is to evaluate the effectiveness of deep-learning-based denoising on low-dose abdominal CT in terms of image quality and diagnostic performance for evaluating acute appendicitis.

We retrospectively analysed 100 patients who underwent low-dose abdominal CT for suspected acute appendicitis. Images were reconstructed using filtered-back-projection (FBP) and iterative reconstruction (IR), then processed with deep-learning-based denoising software (ClariCT.AI, Claripi), resulting in four image sets per patient. For quantitative analysis, image noise and signal-to-noise ratio were measured. Two radiologists independently scored for qualitative analysis (noise, sharpness, artifacts, overall) on a 4-point Likert scale and assessed the presence of acute appendicitis. Statistical analyses included repeated-measures ANOVA, Friedman test, Wilcoxon signed-rank test, and McNemar's test.

The four image sets demonstrated significant differences in both noise and SNR ($p<0.001$). The noise progressively decreased in the order of FBP(25.62±2.01), IR(11.74±1.36), denoised FBP(11.50±0.86), a nd denoised IR(8.38±0.71). SNR was highest in denoised IR (23.39±2.84), followed by denoised FBP(1 7.11±2.04), IR(11.49±1.38), and FBP(7.73±0.94). Denoised images achived higher score in noise and s harpness in both readers. For artifacts, both readers assigned significantly lower scores to denoised I R than to other series. Overall quality was highest in denoised FBP, followed by denoised IR, IR, and FB P in both readers. There was no significant difference in sensitivity and specificity for acute appendicit is. But numerically, the denoised series showed higher specificities in both readers.

Deep-learning-based denoising achieved significant reductions in quantitative noise, increases in SNR, and consistent improvements in subjective noise, sharpness, and overall image quality. Denoised FBP images showed the highest overall quality. Diagnostic sensitivity and specificity for acute appendicitis did not differ significantly across conditions, even though the denoised images had numerically higher specificity.

Axial abdominopelvic CT images of a 49-year-old man with suspected acute appendicitis. FBP (a) and denoised FBP (b) images show a normal appendix (arrow). Mean image noise decreased from 21.71 to 9.74 on denoised FBP, and subjective image quality scores (noise/sharpness/overall) improved from 2/3/3 to 4/4/4 for both readers

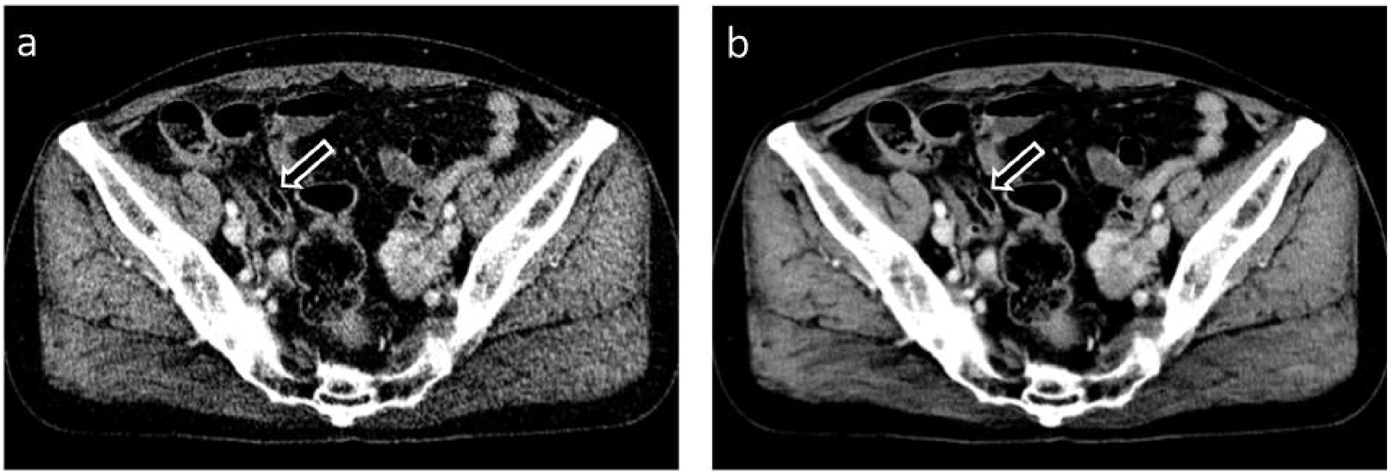

Axial abdominopelvic CT images of a 32-year-old woman with suspected acute appendicitis. IR (a) and denoised IR (b) images. For the artifact score, the denoised IR images was worse because of deformation and a plastic-looking texture, with scores decreasing from 3 to 2 for both readers.

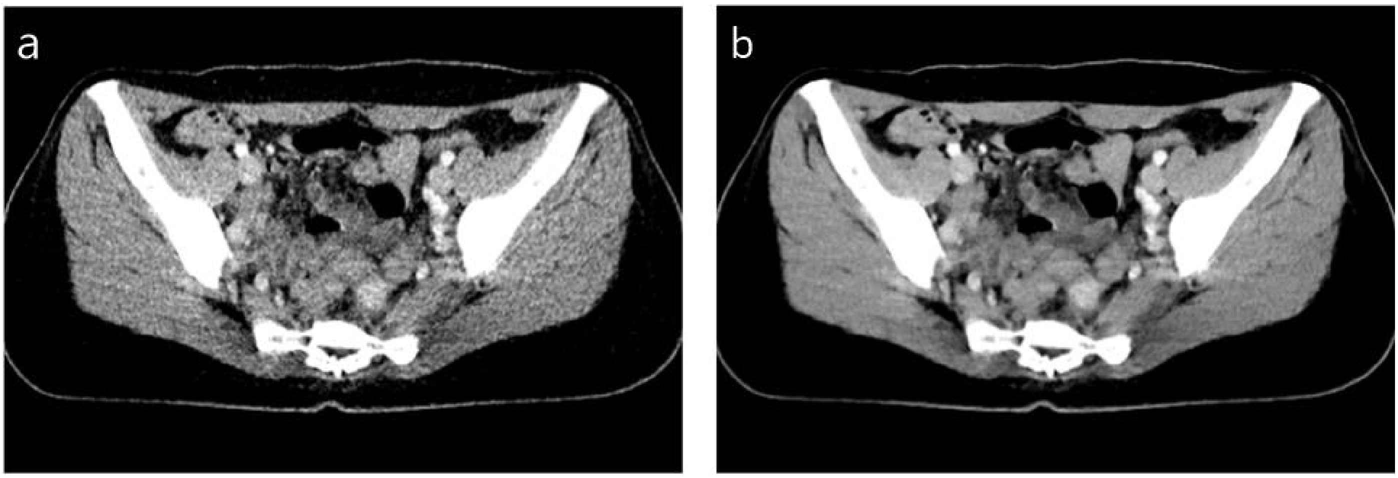

Keywords : Acute appendicitis, CT, Denoising

[Poster Presentation 2]

ABD-CT-02

Manifestations of Tuberculosis in the Abdomen: A Pictorial Review with Corresponding CT Cases

Phoebe Hay Pui Yeung[1*], Christine Tang[1], Chi Man Chau[1], Lik Fai Cheng[1]

[1]Diagnostic and Interventional Radiology, Princess Margaret Hospital, Hong Kong, China

Abdominal and genitourinary tuberculosis (TB) present diagnostic challenges due to their diverse and often nonspecific imaging appearances. With the global resurgence of TB and increasing immunocompromised populations, radiologists must be familiar with its manifestations beyond the lungs. Imaging modalities, particularly computed tomography (CT) and targeted ultrasound (US), are essential for detecting extrapulmonary TB involving the abdomen, pelvis, and scrotum. This pictorial review aims to illustrate key radiologic manifestations of abdominal and scrotal TB, emphasizing characteristic CT and US findings to enhance recognition among radiology trainees. By correlating representative CT and US cases with anatomy-specific features, this poster seeks to enhance trainees' diagnostic confidence and improve early identification of abdominal and genitourinary TB.

This review is based on literature analysis combined with curated institutional imaging cases of microbiologically and/ or histopathologically confirmed abdominal and scrotal TB. CT cases demonstrate involvement of the liver, spleen, bowel, peritoneum, lymph nodes, and kidneys, while additional US cases depict epididymal and testicular involvement. Imaging patterns such as hypodense lesions in solid organs, ileocecal wall thickening, lymph node necrosis, renal calcifications or strictures, and heterogeneous testicular masses were analyzed. Each imaging feature is correlated with clinical context and differential diagnoses. Annotated CT and US images with explanatory notes are provided to aid understanding among junior trainees.

- Solid Organs: CT typically reveals hypodense nodular lesions or diffuse organomegaly in the liver and spleen, occasionally mimicking neoplasms or abscesses. Enhancement patterns vary with disease stage, and calcifications may be observed in chronic cases.

- Bowels and Peritonitis: The hallmark is ileocecal involvement featuring thickened bowel walls, strictures, and adjacent lymphadenopathy. Tuberculous peritonitis shows variable ascites with higher attenuation, smooth peritoneal thickening, and omental thickening, distinguishing it from carcinomatosis. Loculated ascites and mesenteric stranding are also demonstrated.

- Lymph Nodes: Enlarged abdominal lymph nodes exhibit characteristic peripheral rim enhancement with central low attenuation necrosis, aiding differentiation from lymphoma, which typically shows homogeneous enhancement. Calcifications may be present.

- Kidneys: CT typically shows papillary necrosis, caliectasis, and renal scarring with associated dystrophic calcifications. Ureteric strictures and pelvicalyceal abnormalities are common, with perinephric fat stranding in active inflammation.

- Scrotum (Ultrasound): Epididymal TB manifests as heterogeneous, hypoechoic enlargement with increased vascularity, while testicular TB exhibits focal or diffuse hypoechoic lesions and associated hydroceles, sometimes mimicking tumors.

Each category is illustrated with multiple annotated CT and US images highlighting classical and atypical presentations, facilitating pattern recognition.

This pictorial review with corresponding CT and US cases provides a valuable educational tool for junior radiology trainees, fostering a deeper understanding of abdominal and genitourinary tuberculosis imaging features. Familiarity with these radiological patterns can improve diagnostic accuracy, expedite biopsy decisions, and guide appropriate management. This targeted review aids trainees in distinguishing TB from mimics such as malignancy and inflammatory diseases, ultimately contributing to better patient outcomes.

Figure 1a, 1b: Contrast CT abdomen in patient A showing multiple hypoenhancing masses in the liver and spleen. USG-guided biopsy of the liver masses revealed granulomatous inflammation with caseous necrosis.

Figure 1c, 1d: Contrast CT abdomen and pelvis in patient B with background history of Crohn's disease. A segment of mural edema with pericolic stranding is seen at the ascending colon. Subsequent colonoscopy and biopsy revealed acute chronic colitis with ulcer and granulomatous inflammation, which was subsequently positive for Mycobacterium tuberculosis.

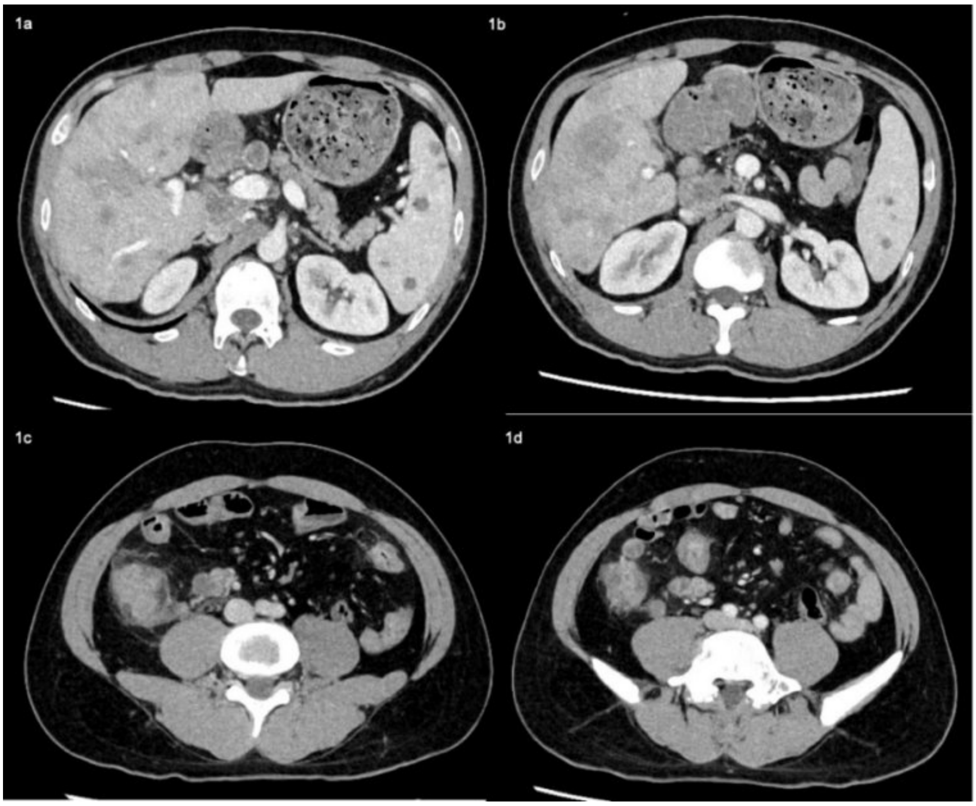

Figure 2a, 2b: Plain CT abdomen and pelvis (axial and coronal MIP) in patient C showing atrophic right kidney with diffuse dystrophic calcifications, in keeping with tuberculosis autonephrectomy.
Figure 2c, 2d: US scrotum in patient D showing swollen bilateral testes and epididymis (only left side shown on this abstract) with numerous hypoechoic lesions and calcifications. Early morning urine subsequently was positive for Mycobacterium Tuberculosis.

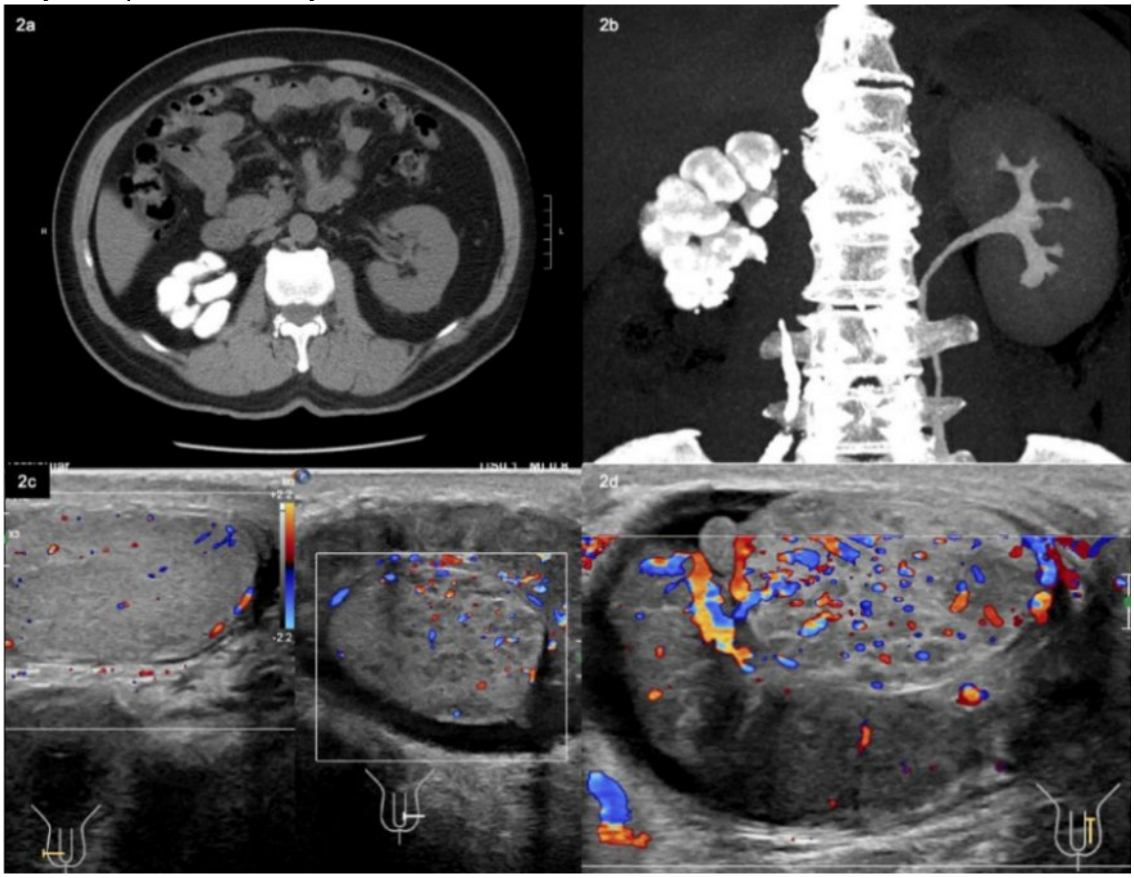

Keywords : Abdominal tuberculosis, Scrotal tuberculosis, Computed tomography

[Poster Presentation 2]

ABD-Others-03

Vascular or Lymphoid? The Role of Temporal Evolution in Differentiating Splenic Mass Lesions – A Local Case Series

Xu Hao Isaac Tan[1*], Shawn Shi Xian Kok[2], Srinivas Anandswaroop Uppaluri[1], Sandeep Venkatesh Halagatti[1], Aftab Syed[1], Srujana Ganti[1], Sze Ying Yee[1], Yogendra Praveen Mogan[1], Freda Jawan[1], Min On Tan[1]

[1]Radiology, Sengkang General Hospital, Singapore
[2]Radiology, Parkway Radiology, Singapore

Splenic masses are usually discovered incidentally during imaging performed for other indications. As such, they often pose a diagnostic challenge due to absence of clinical signs and symptoms to aid in diagnosis. Overlapping features between benign vascular and malignant lymphoid entities may cause further diagnostic dilemmas. While vascular lesions such as sclerosing angiomatoid nodular transformation (SANT) and haemangiomas typically demonstrate characteristic enhancement patterns, early lymphoid malignancies may mimic benign masses. In real-world clinical practice, tissue diagnosis is not always feasible, making temporal stability an important discriminator of benignity.

We explore how imaging features and temporal evolution can aid in differentiating vascular splenic lesions from lymphoid malignancy and demonstrate that benign vascular lesions may occasionally mimic malignant behaviour.

Five splenic lesions diagnosed between 2018 and 2025 were retrospectively reviewed. These included one histologically confirmed marginal zone lymphoma, two lesions radiologically consistent with SANT, one biopsy-proven vascular lesion favouring haemangioma, and one probable haemangioma. Multiphase CT and gadoterate-enhanced MRI were assessed together with serial ultrasound or CT follow-up, when available.

The marginal zone lymphoma showed characteristics of a well-defined, hypoenhancing splenic lesion with peripheral enhancement, mimicking a vascular mass. Over two years, progressive enlargement and the emergence of aggressive features prompted biopsy, confirming marginal zone lymphoma (Figure 1A-B). Two lesions demonstrated the typical "spoke-wheel" progressive enhancement with internal radiating septations, low T2 signal, and long-term stability (> 2 years), consistent with SANT (Figure 1C-D)
A vascular splenic lesion which was absent on serial ultrasound, but newly developed as a 5-6 cm mass on CT and subsequently showing mild growth on MRI with peripheral and septal enhancement, as well as progressive filling in. Although these features were suggestive of a vascular lesion, interval enlargement prompted splenectomy, and histology confirmed a benign vascular lesion favoring haemangioma, highlighting that slow-growing vascular masses may occasionally mimic malignancy (Figure 2A-B). The final splenic lesion showed T2 hyperintense signal with peripheral nodular enhancement with incomplete centripetal fill in. It remains stable over serial imaging for 5 years and was proven to be metabolically inactive on PET/CT, consistent with findings of a haemangioma (Figure 2C-D).

Across cases, lesions that remained stable or decreased in size on follow-up imaging were indicative of a benign vascular origin, while interval growth or splenomegaly suggested malignant transformation.

Characteristic enhancement patterns offer significant diagnostic clues in differentiating vascular from lymphoid splenic lesions. However, imaging appearances can overlap, and early lymphoid malignancies may mimic benign vascular lesions. Temporal stability over serial imaging remains a key indicator of benignity, although occasional slow-growing vascular lesions may mimic malignant behaviour and warrant histological correlation. This case series underscores the complementary role of multimodality imaging and longitudinal follow-up in guiding safe and accurate management of splenic masses.

Figure 1. Malignant progression versus classic benign vascular pattern.

(A–B) Contrast-enhanced CT of marginal zone lymphoma: a well-defined hypoenhancing splenic lesion with peripheral enhancement that enlarges on follow-up, prompting biopsy which confirmed marginal lymphoma.

(C–D) Contrast-enhanced MRI of SANT: central radiating septa with progressive “spoke-wheel” enhancement and long-term stability (>2 years), in keeping with a benign vascular lesion.

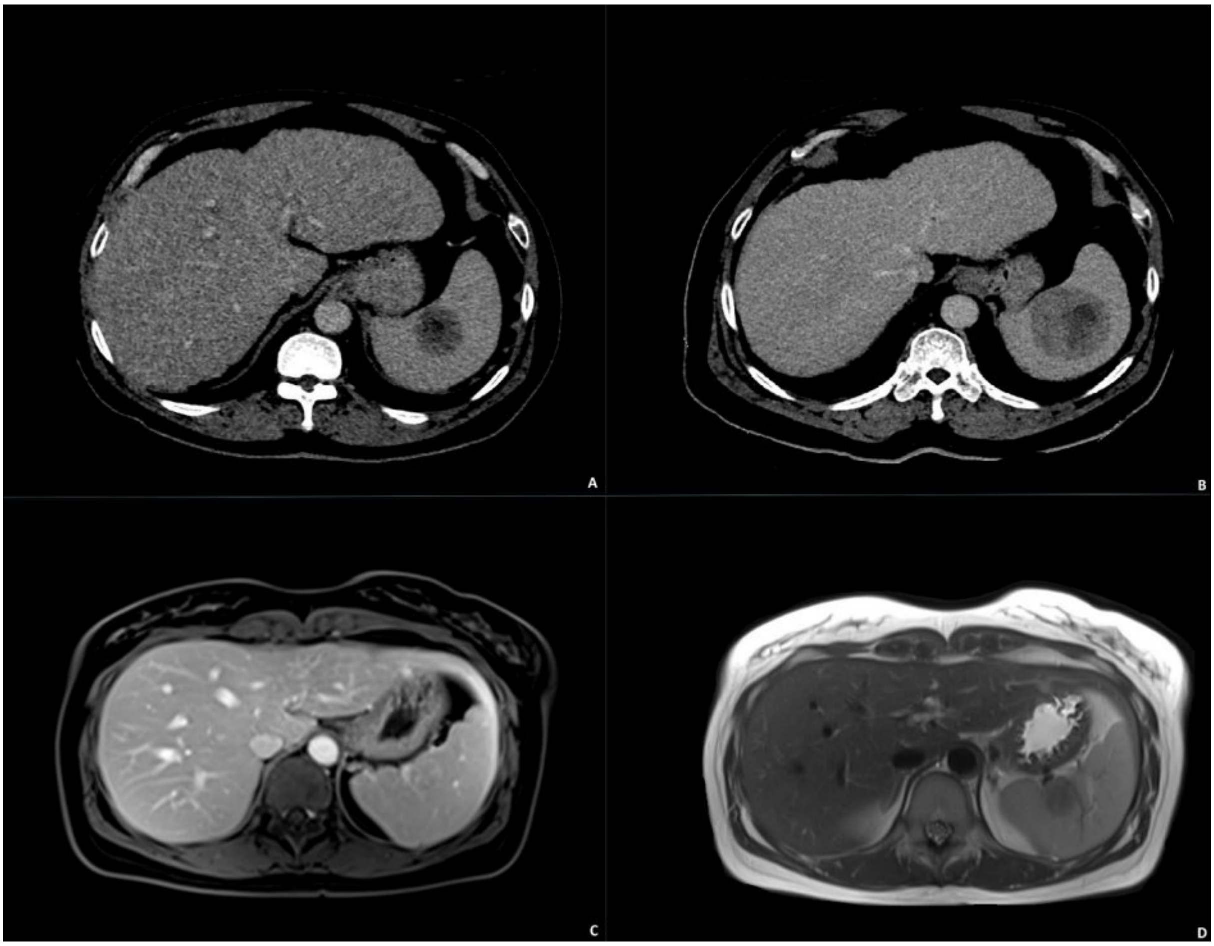

Figure 2. Benign vascular spectrum with differing temporal behaviour.

(A–B) Contrast-enhanced CT of a biopsy-proven vascular lesion favouring haemangioma - Began as de-novo development of a 5–6 cm mass with peripheral and septal enhancement and progressive fill-in; mild growth led to splenectomy, histology confirming a benign vascular lesion favouring haemangioma.

(C–D) Contrast enhanced MRI of a probable haemangioma: T2-hyperintense lesion with peripheral nodular enhancement and incomplete centripetal fill-in, stable over 5 years, consistent with haemangioma.

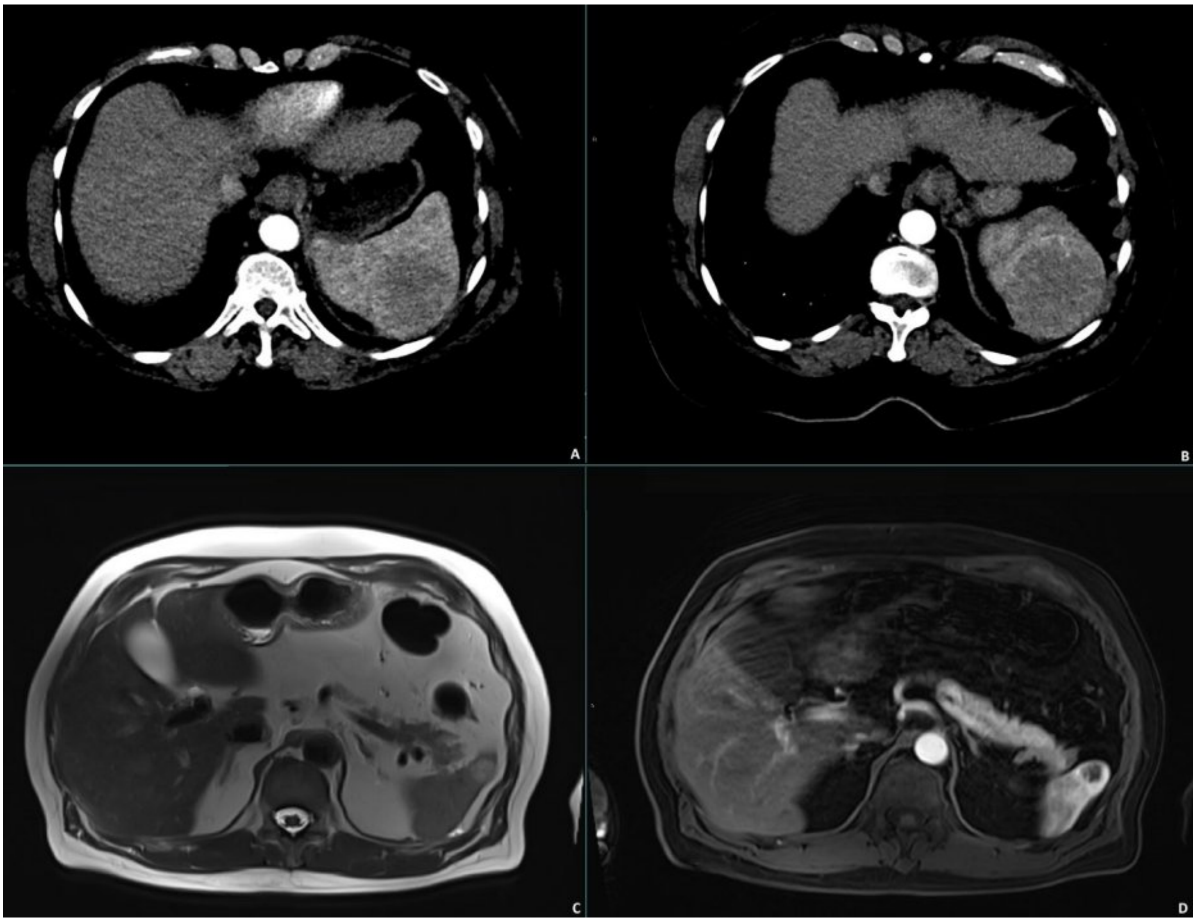

Keywords : Splenic mass

[Poster Presentation 2]

ABD-Others-04

Bladder Wall and Rectus Sheath Hematomas as Rare Hemorrhagic Manifestations of Dengue Fever: Importance of CT for Accurate Diagnosis

Abigail Christie[1], Taufik A Wibowo[1,2*]

[1]Radiology, Cipto Mangunkusumo General Hospital Universitas Indonesia, Indonesia
[2]Abdominal Radiology, Cipto Mangunkusumo General Hospital Universitas Indonesia, Indonesia

The acute abdomen is a common and potentially life-threatening presentation, accounting for 5–12% of emergency department visits. Its causes range from inflammatory, infectious, obstructive, vascular, and neoplastic conditions to traumatic injuries. While inflammatory etiologies such as appendicitis, cholecystitis, and diverticulitis are frequently encountered, spontaneous abdominal bleeding should not be overlooked, particularly in patients with coagulopathy or dengue-related thrombocytopenia. Dengue fever can present with various hemorrhagic manifestations; however, rectus sheath hematoma (RSH) remains an uncommon occurrence occurring in approximately 1.5–2% of hospitalized patients, and concurrent bladder wall hematoma is even rarer. These atypical findings can clinically and radiologically mimic acute surgical conditions, posing significant diagnostic challenges.

Case: A 55- year old female patient, presented with fever and right lower quadrant abdominal pain 4 days before admission. Pain was aggravated by movements of anterior abdominal wall including respiration. Abdominal distension and persistent nausea is present.

Initial suspicion: perforated appendicitis and abdominal mass.

Imaging:

CT revealed a large lobulated hyperdense mass posterior to the right rectus abdominis muscle, protruding into the pelvic cavity and compressing the bladder and uterus. The lesion demonstrated heterogeneous contrast enhancement, surrounding fat stranding, and adjacent fluid collection, initially mimicking a giant perforated appendicitis or soft-tissue tumor.

CECT remains gold standard for characterizing acute abdominal hemorrhage; however, non-contrast CT is often overlooked, despite its critical role in the initial assessment. In this case, the lobulated, well-confined hyperdense mass within the right rectus muscle, lacking rim enhancement or intralesional gas, was characteristic of a rectus sheath hematoma rather than an abscess or soft-tissue tumor. A sentinel clot was also visualized on non-contrast imaging, appearing as a focal area of higher attenuation adjacent to lower-density blood. Recognizing these signs is essential to avoid misinterpretation of enhancement patterns and to guide accurate diagnosis and conservative management.

The concurrent intramural bladder wall hematoma underscores the importance of meticulously reviewing all pelvic structures. Diffuse bladder wall thickening with intramural hyperdensity should raise suspicion for hemorrhage rather than inflammatory or neoplastic disease. Absence of contrast enhancement within the bladder wall further supported the diagnosis of hematoma, differentiating it from active inflammation or tumor infiltration. The similar attenuation of the bladder and rectus sheath lesions supports a shared hemorrhagic etiology.

Key diagnostic signs:

- Hyperdense collections on non-contrast CT.
- Lack of contrast enhancement.
- Sentinel clot sign
- Anatomic confinement consistent with muscle compartments or organ walls.
- Active contrast extravasations suggesting ongoing hemorrhage.
- Secondary signs such as surrounding fat stranding or mild adjacent fluid, which may mimic infection but should be interpreted in the clinical context.

Radiologists should not overlook non-contrast CT and must include spontaneous bleeding in the differential diagnosis of acute abdomen especially in Dengue fever. Prompt recognition of hyperdense collections and sentinel clot signs on non-contrast imaging can steer management toward conservative treatment and prevent inappropriate surgical intervention.

Rectus Sheath Hematoma (A) Non- Contrast axial CT (B) CECT

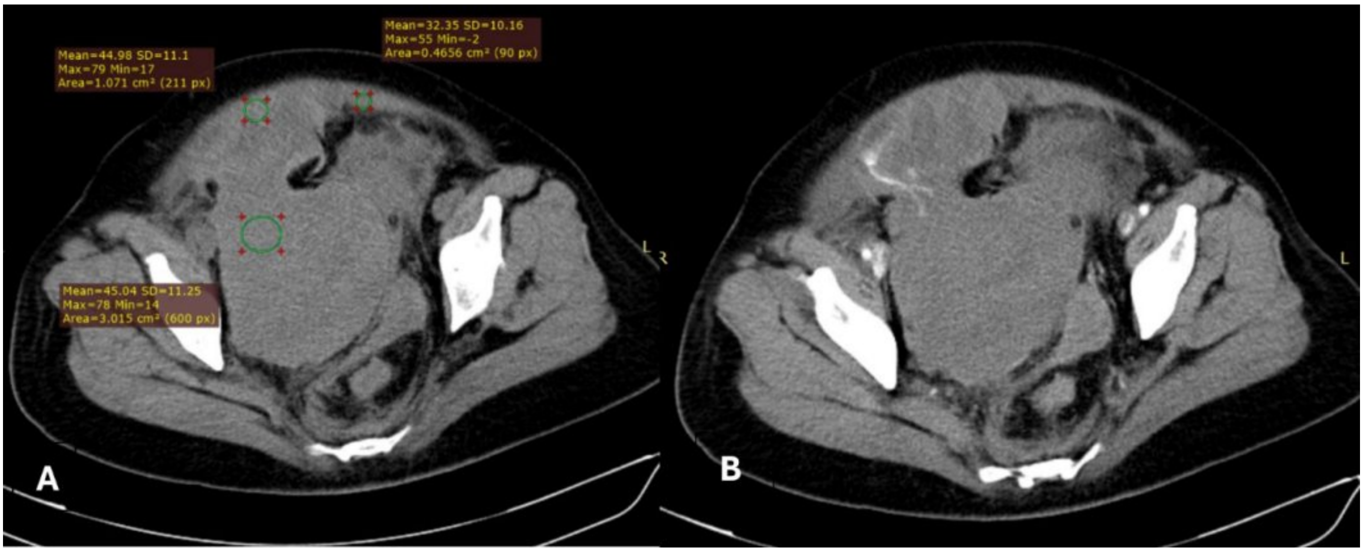

Intramural Bladder Hematoma (A) Non-Contrast axial CT, (B) CECT

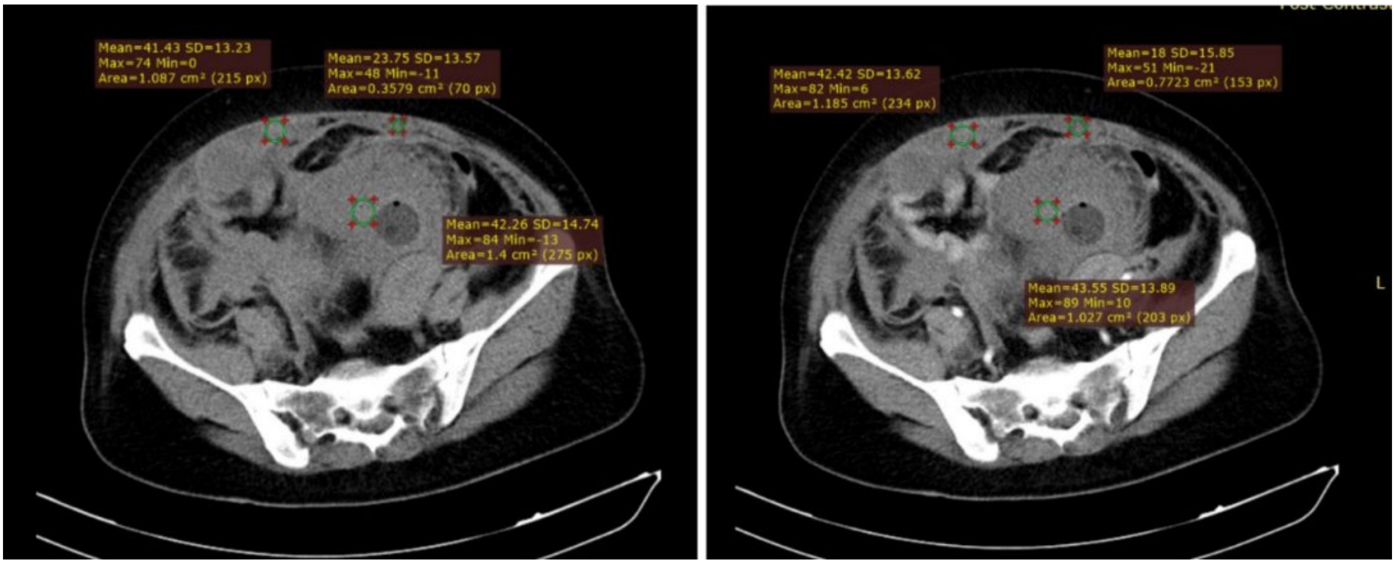

Keywords : Intramural Bladder Hematoma, Rectus Sheath Hematoma, Dengue Manifestations

[Poster Presentation 2]

ABD-Others-05

Wet vs. Dry, Two Faces of Mimicry: Case Series on Tuberculous Peritonitis and Complications

Jose Rafael M. Aldaba[1], Josefina Marie Medina[2*]

[1]Radiology, St. Luke's Medical Center Quezon City, Philippines
[2]Consultant, St. Luke's Medical Center Quezon City, Philippines

Tuberculous peritonitis is an uncommon manifestation of extrapulmonary tuberculosis, representing only 1–3% of pediatric tuberculosis cases, and is classified into wet, fibrotic, and dry types[1]. Its variable presentations and potential complications including abscess formation and the rare occurrence of tuberculous appendicitis often mimic more common abdominal conditions, leading to diagnostic delays. This case series aims to describe two distinct presentations of tuberculous peritonitis with complications, emphasizing the imaging features and diagnostic challenges encountered [2,3].

This case series includes two patients who presented with chronic or subacute abdominal symptoms at our institution. Both underwent comprehensive diagnostic evaluation, including laboratory testing, abdominal and pelvic contrast-enhanced CT imaging, and chest CT or radiography to assess for concurrent pulmonary involvement. Radiologic features were correlated with intraoperative findings following exploratory laparotomy, during which peritoneal, omental, abscess, and appendiceal samples were obtained. All specimens underwent histopathologic evaluation for granulomatous inflammation with or without necrosis. Confirmation of Mycobacterium tuberculosis infection was achieved using MTB-PCR analysis of tissue and fluid samples. Clinical course, operative details, and final diagnoses were documented and compared.

Case 1 involved an 18-year-old female with a three-month history of crampy abdominal pain initially managed as presumed appendicitis. CT imaging demonstrated omental and peritoneal nodularity, mesenteric lymphadenopathy, a dilated fluid-filled appendix, and a localized intra-abdominal abscess (Figure 1). Chest imaging showed reticulonodular densities and tree-in-bud opacities suggestive of pulmonary tuberculosis (Figure 2). Intraoperative findings and histology confirmed dry-type tuberculous peritonitis with chronic tuberculous appendicitis (Figure 3), supported by MTB-PCR positivity in appendiceal tissue and peritoneal samples.

Case 2 involved a 19-year-old male with abdominal distention, vague pain, fever, and weight-related symptoms. Imaging revealed a large, thick-walled abdominopelvic abscess containing feculent material and diffuse peritoneal enhancement consistent with the wet type of tuberculous peritonitis (Figure 4). Laparotomy showed thickened friable peritoneum, adherent omentum, and multiple subcentimeter nodules. Histopathology demonstrated necrotizing granulomatous inflammation, and MTB-PCR of the abscess cavity and peritoneal fluid confirmed infection.

Both cases showcased distinct imaging patterns (dry vs. wet type) and complications, including abscess formation and appendiceal involvement, which initially obscured the underlying diagnosis of tuberculosis.

These cases demonstrate the broad spectrum of tuberculous peritonitis, underscoring how Mycobacterium tuberculosis can produce divergent radiologic patterns and mimic a variety of abdominal pathologies. The presence of abscesses, appendiceal inflammation, or nonspecific peritoneal thickening may lead clinicians toward more common diagnoses, delaying appropriate management. In regions where tuberculosis is endemic or in patients with compatible risk factors, tuberculous peritonitis should be included in the differential diagnosis for persistent abdominal pain, unexplained intra-abdominal collections, or atypical imaging findings. Early recognition and integration of radiologic, surgical, and molecular diagnostic tools remain essential for timely treatment.

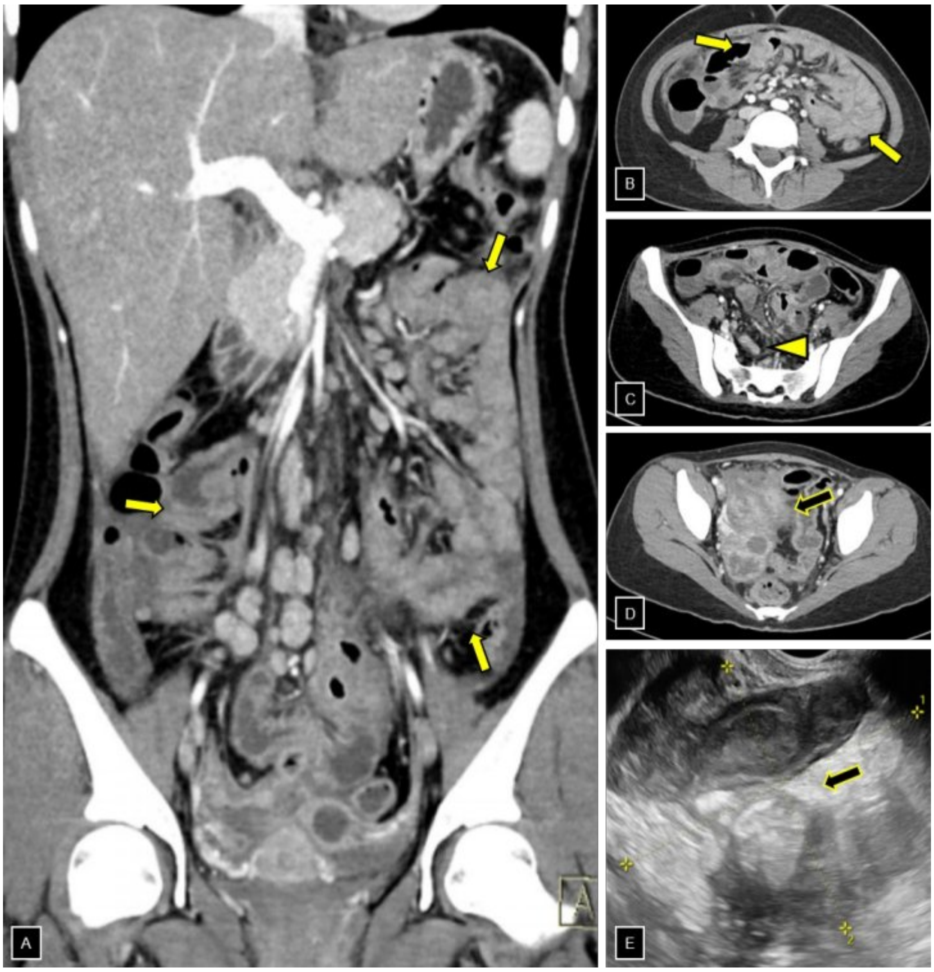

[Case 1] Figure 1. Coronal(A) and axial contrast-enhanced CT study(B) showed omental and peritoneal nodular thickening and disseminated small-sized to enlarged lymph nodes in the abdominal and pelvic regions (yellow arrows). Axial CE CT(C) showed a fluid-filled and dilated appendix (yellow arrowhead) with surrounding minimal fat stranding densities and haziness. Axial CE CT(D) and longitudinal US image(E) showed an irregular fluid collection (black arrow), indicative of abscess.

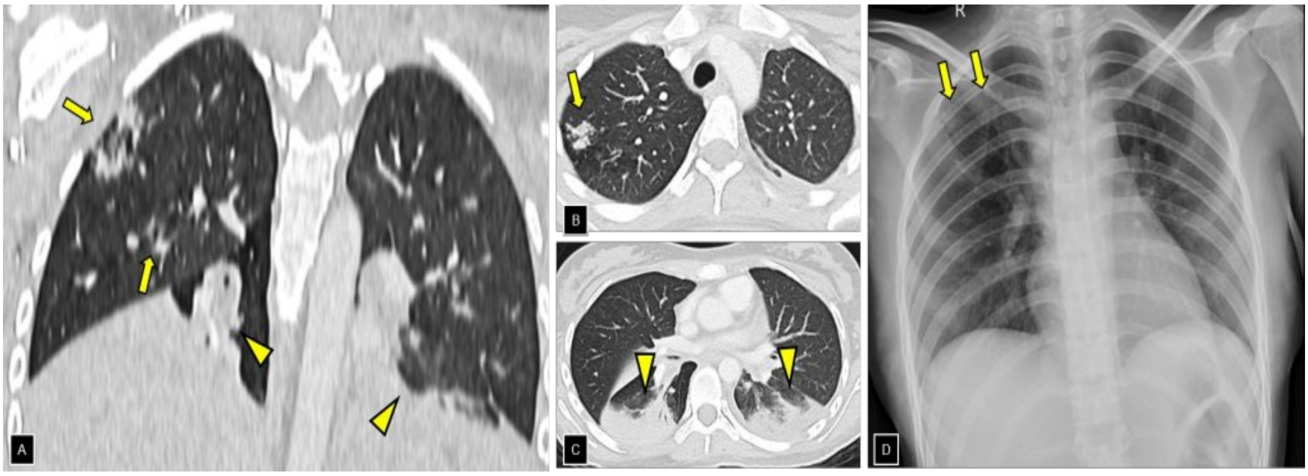

[Case 1] Figure 2. AP view of CXR(D) showed streaky and nodular opacities in the right upper lobe (yellow arrows) and confirmed in the coronal(A) and axial lung window CT(B) which showed reticulonodular densities with bronchiectasis demonstrating "tree-in-bud" configuration (yellow arrows). Consolidation and pleural effusion were also noted both lower lobes (yellow arrowheads).

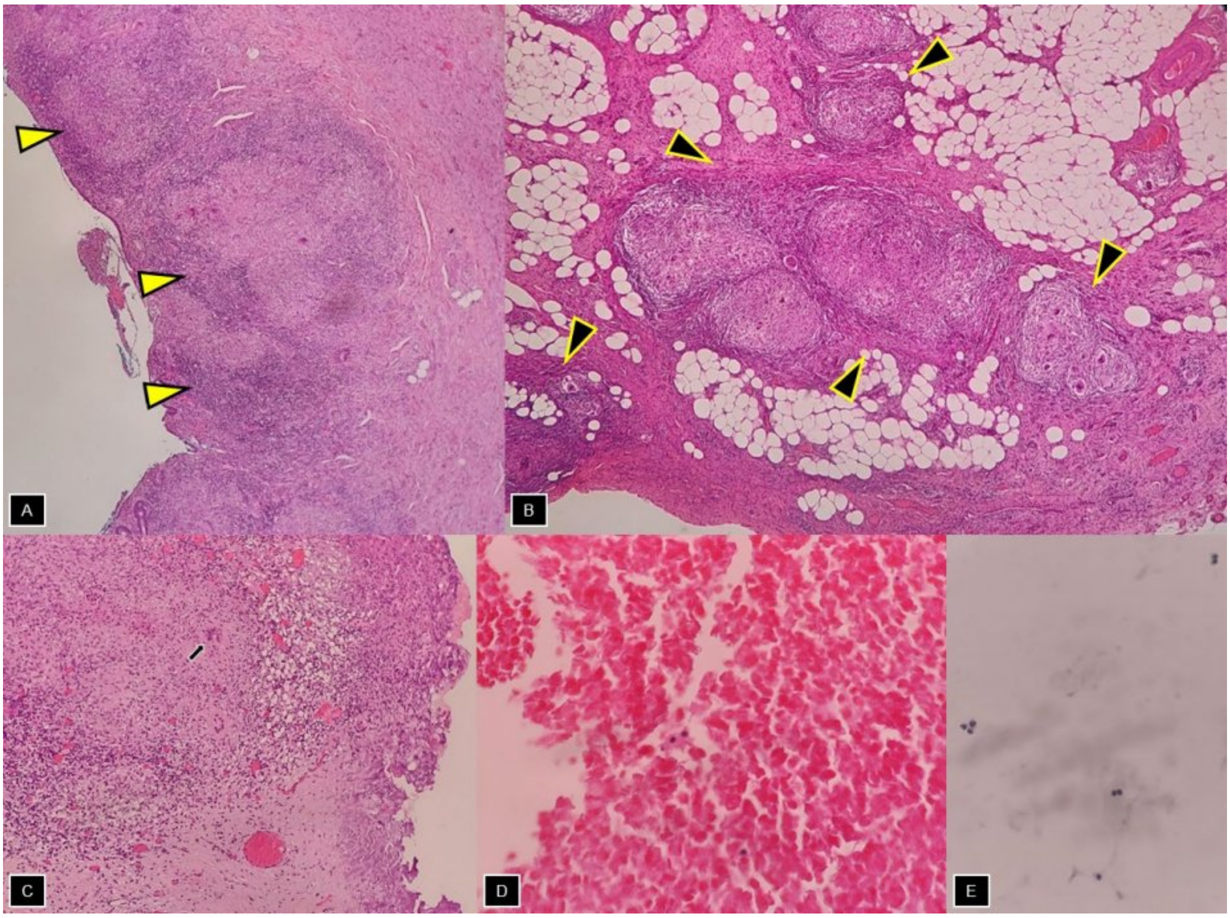

[Case 1] Figure 3. Histopathologic slides(A) revealed appendix with granulomas (yellow arrowheads), (B)fibroadipose tissues with necrotizing granulomatous inflammation (black arrowheads), (C)fibroadipose and fibrocollagenous tissue with granulomatous inflammation (black arrow) and (D, E)inflammatory cells without atypical cells.

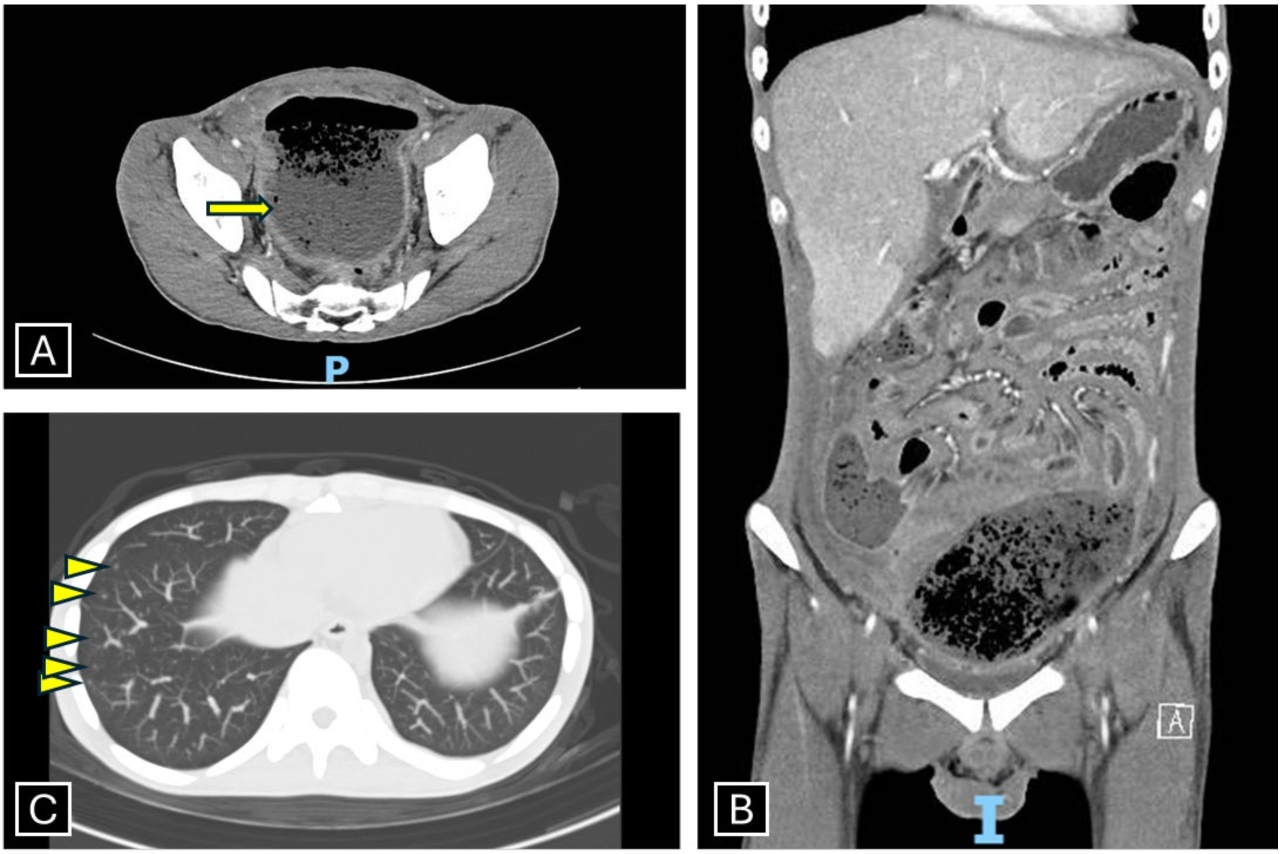

[Case 2] Figure 4.. Axial contrast-enhanced CT (A) shows a large peripherally enhancing thick-walled abdominopelvic fluid collection, containing air-fluid levels, feculent debris and small calcific foci, consistent with abscess formation (yellow arrow). Coronal view notes (B) diffuse thickening and enhancement of the parietal peritoneum. Lung window with maximum intensity projection (C) shows centrilobular nodules in the right lower lobe (yellow arrowheads).

Keywords : Abdomen, Peritoneum, Tuberculosis

[Poster Presentation 2]

ABD-Others-06

When to Suspect Systemic Vasculitis on Abdominal CT?

Raju Sharma[1*], Ankur Goyal[1], Sanchita Gupta[1], Rajendra Behera[1], Shivanand Gamanagatti[1]

[1]Radiology, All India Institute of Medical Sciences, India

To discuss the abdominal imaging features of systemic vasculitis on abdominal CT and stratify these findings to direct further work-up

Background: Systemic vasculitides are difficult to diagnose and may present with abdominal symptoms or apparently incidental findings on an abdominal CT examination. The presence of certain subtle imaging findings may be overlooked if the interpreting radiologist does not have a high index of suspicion. These may include direct vascular findings (vascular irregularity / beading) or end-organ features (splenic / renal infarcts). Thus, it is important to flag these findings and direct further diagnostic work-up.

A retrospective review of the abdominal imaging data of patients with systemic vasculitis was done from our data base.

The findings were summarized and reviewed with the final diagnosis.

The presence of the following imaging features should lead the radiologist to suspect the presence of an underlying vasculitis:

- Circumferential wall thickening +/- stenosis/occlusion of the abdominal aorta/SMA/celiac /renal arteries in large-vessel vasculitis (in young age)
- Contour irregularity/attenuation of hepatic / renal / splenic artery and/or their branches in medium vessel vasculitis
- Aneurysmal changes, transmural calcification
- Development of collaterals
- Visceral (splenic/ renal) infarcts / Bowel ischemia
- Long segment edematous bowel wall thickening

In the presence of suspicious imaging features, further workup for skin / mucosal ulcers, bleeding per rectum, and laboratory tests (ANCA, ANA, urine protein) must be undertaken to investigate for systemic vasculitis

Clinical Implications: Certain imaging features on abdominal CT scans may prompt radiologists to direct further work-up to establish a diagnosis of systemic vasculitis, allowing for appropriate management to be initiated.

CASE: 30-year-old female with recurrent post-prandial abdominal pain and unintentional weight loss

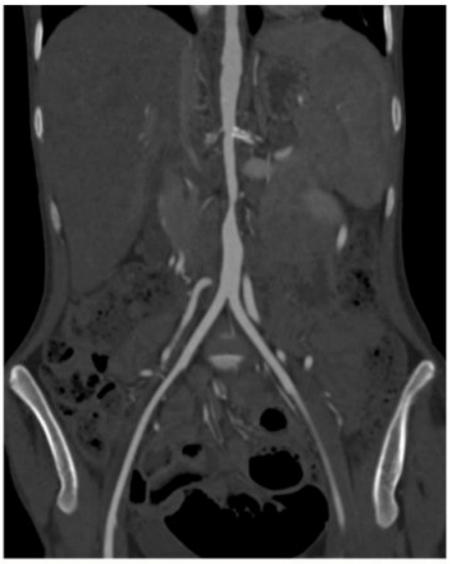

Narrowing of the abdominal aorta (white arrow) and RT renal artery (yellow arrow), with a left renal artery stent (red arrow)

Narrowing of the SMA (arrow)

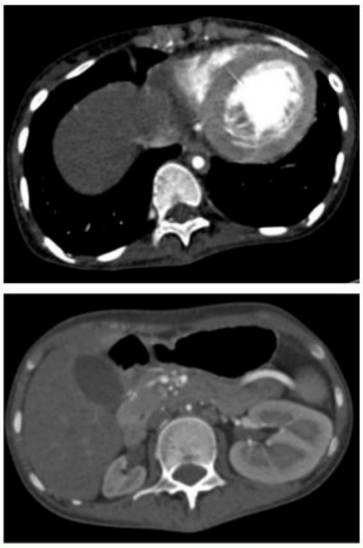

Circumferential hypoenhancing thickening of the abdominal aorta (arrowhead), small right kidney (*)

Takayasu arteritis (TAK)

- 2nd to 3rd decade
- Female
- Asian descent
- Aorta and its thoracic branches
- Mesenteric branches may be involved
- Presents with chronic mesenteric ischemia due to involvement of celiac artery and SMA

Keywords : Vasculitis, Stenosis, Aneurysm

[Poster Presentation 2]

ABD-Others-07

Beyond Active Bleeding: CTA-Guided Culprit Artery Mapping for Targeted Embolization in Acute Gastrointestinal Bleeding.

Viet Tran Doan Khac[1*], Triet Pham Ngoc Minh[1], Viet Dang Quoc[1], Huyen Le Duy Mai[1], Hy Le Nguyen Gia[1], Duc Vo Tan[1], Bac Nguyen Hoang[1]

[1]Radiology, University Medical Center Ho Chi Minh City, Vietnam

In acute gastrointestinal (GI) hemorrhage, catheter angiography with intent to embolize is typically pursued when computed tomography angiography (CTA) demonstrates active contrast extravasation. While CTA is widely used to confirm ongoing bleeding, its procedural value may extend to pre-angiographic vessel mapping. In practice, the direct culprit artery—a clearly traceable arterial branch leading to the bleeding point—is often not identifiable on CTA. We therefore defined an indirect culprit artery as the bowel-supplying arterial branch or closest branch to the suspected bowel wall segment, where the suspected segment was the bowel wall immediately adjacent to the site of intraluminal contrast extravasation on CTA. This study aimed (1) to quantify the frequency of direct culprit-artery visualization on CTA and (2) to evaluate the accuracy of indirect culprit-artery assignment using digital subtraction angiography (DSA) as the reference standard.

From January 2020 to January 2025, 57 consecutive patients with GI bleeding underwent CTA demonstrating active bleeding and were referred for catheter angiography for potential embolization. On CTA, culprit artery designation was categorized as direct and indirect. Bleeding branch on DSA served as the reference for culprit-artery confirmation.

Active bleeding was confirmed on DSA in 44/57 cases (77.2%). Among DSA-positive cases, direct culprit-artery visualization on CTA was observed in 11/44 cases (25.0%). Indirect culprit-artery assignment was applied in the remaining 33/44 cases (75.0%). Concordance between the CTA-designated indirect culprit artery and the culprit vessel on DSA was achieved in 32/33 cases, corresponding to an accuracy of 97.0% for the indirect method.

In angiographically confirmed acute GI hemorrhage, direct culprit-vessel depiction on CTA is achievable in only one-quarter of cases. A pragmatic CTA-based indirect culprit-artery approach demonstrates very high concordance with DSA. This strategy may enhance CTA's procedural utility by improving pre-angiographic targeting and supporting efficient, selective embolization planning in emergent GI bleeding.

Figure 1. Illustration of an acute lower GI bleeding at the splenic flexure, demonstrating concordance of the **indirect culprit arterial branch** between **CTA** and **DSA**.

(A) Sagittal CTA. The crosshairs localize the **indirect culprit artery**—defined as the arterial branch (arising from the **inferior mesenteric artery**) adjacent to the **suspected bowel wall segment**, with the suspected segment being the bowel wall **closest to the focus of intraluminal contrast extravasation**.
(B) Coronal CTA. The crosshairs again indicate the designated **indirect culprit arterial branch**.
(C) Corresponding DSA demonstrating the arterial branch matching the CTA-identified vessel.
(D) Superselective DSA confirming **active contrast extravasation**.

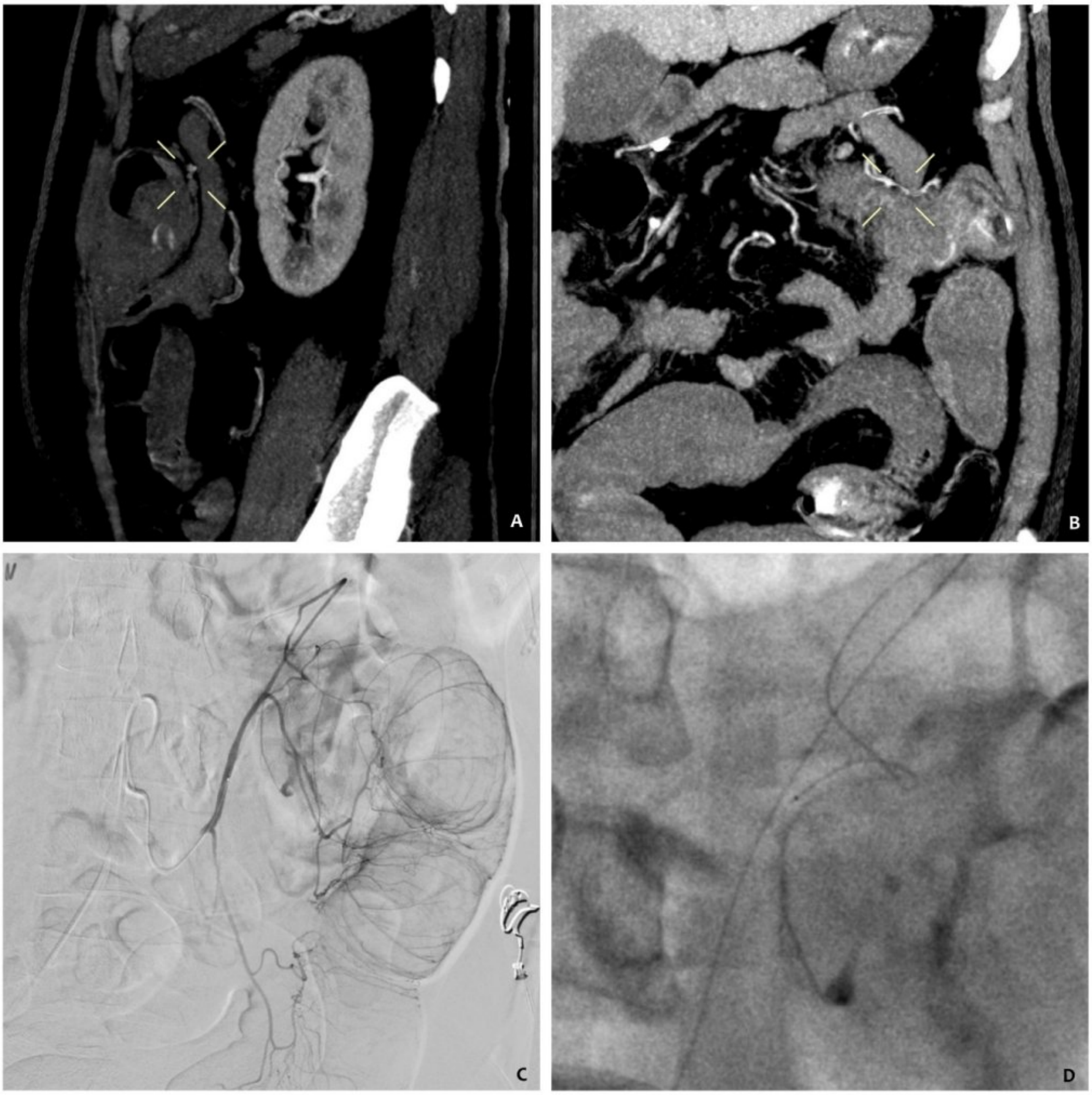

Figure 2. Illustration of an acute upper GI bleeding at the third portion of the duodenum (D3), showing **non-concordance** of the **indirect culprit arterial branch** between **CTA** and **DSA**.

(E) CTA localizes a presumed culprit arterial branch arising from the **superior mesenteric artery (SMA)** (yellow arrow).
(F) DSA of the arterial branch corresponding to the CTA-designated vessel (yellow arrow).
(G)–(H) The actual bleeding focus (orange arrow) originates from the **gastroduodenal anastomotic network** between the **celiac trunk** and the **SMA**.

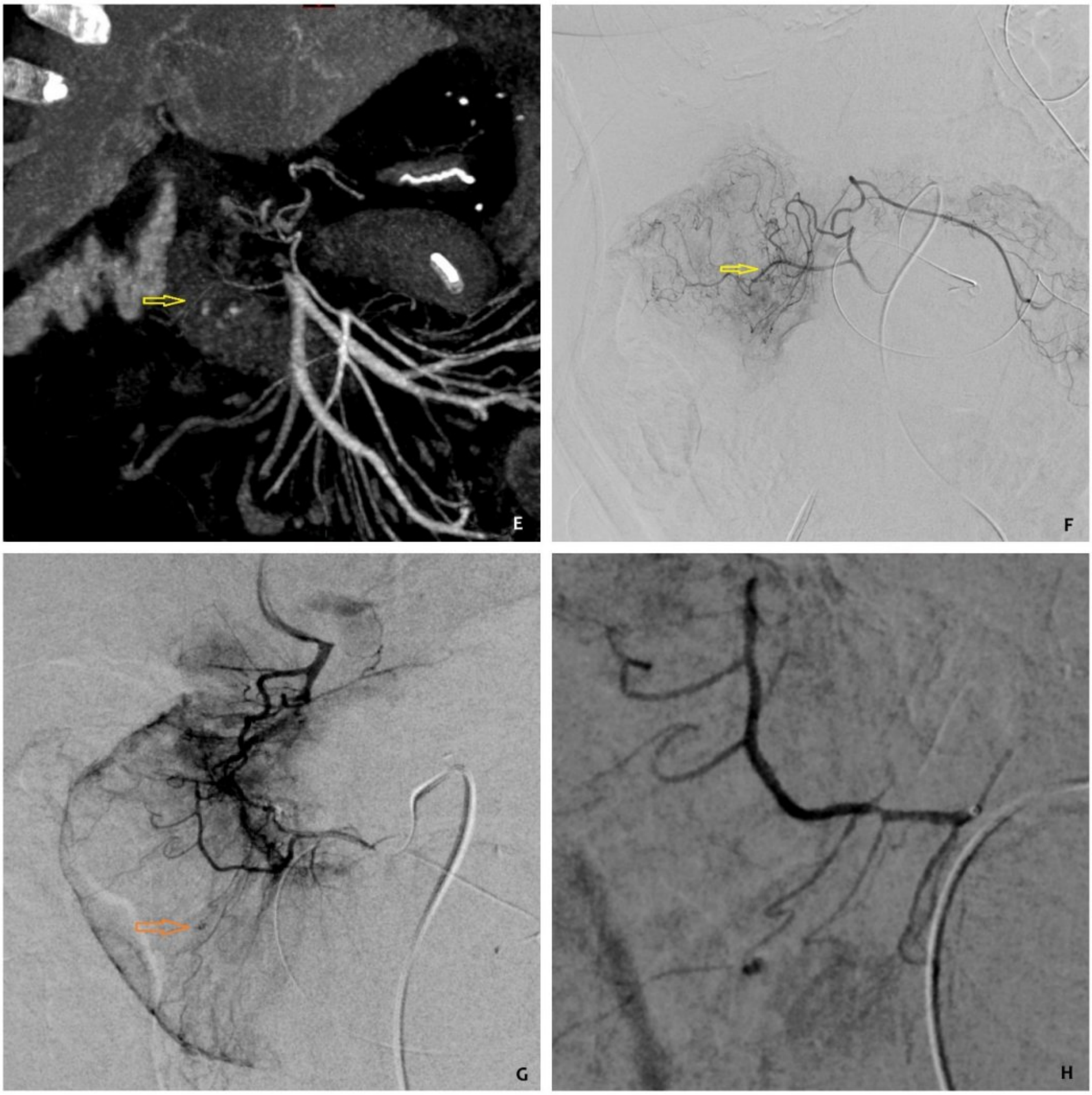

Keywords : Gastrointestinal bleeding, CT Angiography, Catheter Angiography

[Poster Presentation 2]

GU-Uro-11

Fused Pelvic Kidney: A Rare Congenital Fusion Anomaly and Diagnostic Challenge

Mary Grace Yamson[1*]

[1]Medical imaging and therapeutic radiology, National Kidney and Transplant Institute, Philippines

Fused pelvic kidney, also known as a discoid or pancake kidney, is a rare congenital anomaly in which both kidneys are completely fused at the renal pelvis without an intervening septum. It shows a male predilection, with a prevalence ranging from 1 in 65,000 to 1 in 375,000 live births, and is often detected incidentally. To our knowledge, this study represents the first reported case of fused pelvic kidneys with ultrasonographic, voiding cystourethrogram and CT urogram findings in the Philippines.

This study reviews the case of an 11-month-old male with known multiple congenital anomalies who sought consultation due to recurrent urinary tract infections. Initial sonographic findings showed a fusion anomaly resembling a horseshoe kidney. However, further evaluation via computed tomography confirmed a pancake configuration with a single draining ureter and associated vesicoureteral reflux.

Radiologic imaging plays a central role in the diagnosis and management of renal fusion anomalies. Ultrasound is the first line modality for the diagnosis and follow-up of renal anomalies due to its noninvasiveness, lack of radiation and widely available. In this case, initial ultrasound of the patient showed a fusion anomaly resembling a horseshoe kidney, wherein the inferior poles of both kidneys appeared to extend into the midabdominal region., but it was limited in defining the precise anatomy.

VCUG provided valuable information on bladder morphology, vesicoureteral reflux, and residual urine volume, all of which are relevant in recurrent UTI. Radionuclide scintigraphy with DMSA allowed assessment of cortical integrity and differential renal function, though interpretation was complicated by the abnormal renal configuration. The definitive diagnosis was made with CT urogram, which provided detailed anatomic information, including the location, orientation, and fusion of the renal moieties as well as ureteral drainage patterns. CT remains the gold standard in delineating complex fusion anomalies, though radiation exposure and contrast use must be considered. In select cases, magnetic resonance imaging urography may serve as an alternative for detailed anatomical and functional evaluation without ionizing radiation. However, its disadvantages include higher cost, possible claustrophobia, contraindications in the presence of metal implants or foreign bodies, and the need for sedation in pediatric patients.

This case illustrates the difficulty of differentiating pancake kidney from other renal fusion anomalies and stresses the role of advanced imaging in achieving an accurate diagnosis. Early recognition of associated anomalies, careful radiologic evaluation, and coordinated multidisciplinary care are essential to reduce risk infection, preserve renal function, and improve long-term outcomes in affected patients.

Baseline ultrasound of the kidney, ureter and bladder region showed a normal-sized for age right kidney and an enlarged for age left kidney. There is severe left pelvocaliectasia with resultant parenchymal thinning. The inferior poles of both kidneys extend into the midabdominal region, resembling a horseshoe kidney.

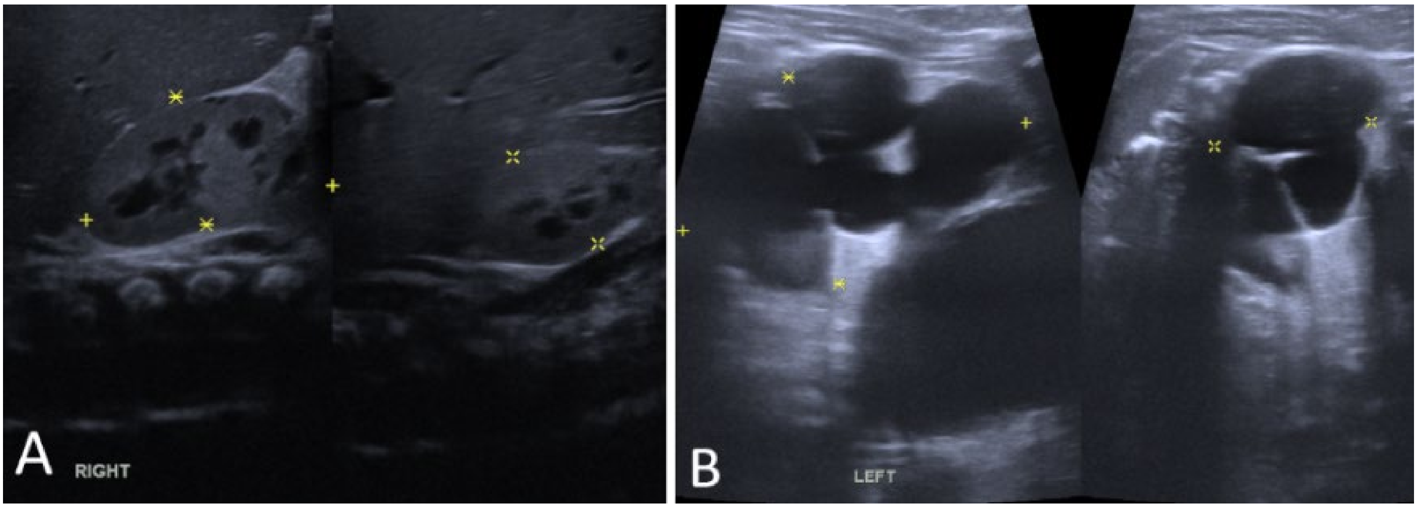

CT urogram was performed and revealed both kidneys located in the right side of the abdomen. The orthotopic right renal moiety was in the right renal fossa, with the renal pelvis directed laterally. The ectopic left renal moiety was situated inferior and medial to the right moiety with renal pelvis directed anteriorly and laterally. The two moieties were extensively fused along the superior to inferior poles, forming a single structure with mild external lobulation.

Keywords : Pancake Kidney, Horseshoe Kidney, Recurrent Urinary Tract Infection

[Poster Presentation 2]

GU-Uro-12

Autosomal Recessive Polycystic Kidney Disease in Fraternal Twins: A Case Report with Radiological Review

Raissa Guldam[1], Riza Marquez-Planta[1*]

[1]Medical Imaging and Therapeutic Radiology, Resident, Philippines

Autosomal recessive polycystic kidney disease (ARPKD) is a rare genetic condition caused by the mutations of the *PKHD1* gene on chromosome 6p12. This mutation leads to clinical manifestations such as enlarged kidneys, progressive renal insufficiency, arterial hypertension, and fibrocystic abnormalities in both kidneys and liver. It has an incidence of approximately 1:20,000 live births. The primary radiologic modality for the evaluation of ARPKD is ultrasonography. In older children, CT and MRI are often used to evaluate liver disease.

This is a case of the two-month-old fraternal male twins who both presented in ultrasound with bilaterally enlarged and globular kidneys, with echogenic parenchyma and loss of corticomedullary differentiation. Upon use of the high-frequency linear probe, multiple tiny cortical cysts were seen in the superior to inferior poles of both kidneys, measuring up to 0.7 cm in twin 1 and up to 0.4 cm in twin 2. These ultrasound findings are suggestive of ARPKD. Bilateral pelvicalyceal fullness was also noted in both kidneys of the twins. An MRI of the upper abdomen with MRCP was also done, in which both twins showed bilaterally enlarged and globular kidneys, indistinct corticomedullary junction, heterogeneous renal parenchyma that was predominantly T2-hyperintense, and multiple small cysts scattered in both kidneys. Also, both babies have normal-sized livers, with homogeneous tissue intensity and unremarkable biliary trees.

No family history of polycystic kidney disease was known on either the maternal or paternal side. Also, no family member was diagnosed with any kidney disease. As per the parents' decision, no genetic testing was done for the twins.

ARPKD can present in perinatal, neonatal, infantile, juvenile, or even adult populations. In patients who present early (perinatal/neonatal), renal disease dominates the clinical picture, whereas in older children (infantile/juvenile), liver disease dominates. Children who survive the first month of life have as much as an 80% chance of living for more than 15 years.

Autosomal recessive polycystic kidney disease (ARPKD) is primarily evaluated using ultrasonography, which typically shows enlarged, echogenic, and heterogeneous kidneys with loss of corticomedullary differentiation and multiple small cysts. Ultrasonography of the liver may also show hepatomegaly, with echogenic and heterogeneous parenchyma, along with hepatic cysts and dilation of the biliary ducts. MRI can also aid in the diagnosis of ARPKD, as it avoids ionizing radiation and shows hepatic lesions well. It can demonstrate enlarged kidneys that are darker than normal on T1-W images and brighter than normal on T2-W images owing to the large amount of water in the dilated ducts within the kidneys. Cysts are best imaged on T2-weighted sequences. Genetic testing is recommended to confirm the diagnosis of ARPKD if the clinical picture and imaging findings are inconclusive.

ARPKD is a rare genetic condition involving the kidneys and liver. In most cases, the diagnosis of ARPKD is made based on a combination of renal ultrasound findings, clinical presentation, and the absence of a family history of kidney disease. CT and MRI scans play complementary roles in the evaluation of ARPKD but are not necessary for its diagnosis.

Ultrasound images (sagittal view) of the kidneys of the twins show bilaterally enlarged kidneys (twin 1, right = 8.6 cm, left = 8.6 cm; twin 2, right = 8.6 cm, left = 8.2 cm) with echogenic parenchyma and loss of corticomedullary junction. Upon use of the high-frequency linear probe, multiple tiny cysts are seen from the superior to inferior poles of both kidneys of the twins. Pelvicalyceal fullness is also noted bilaterally in both twins.

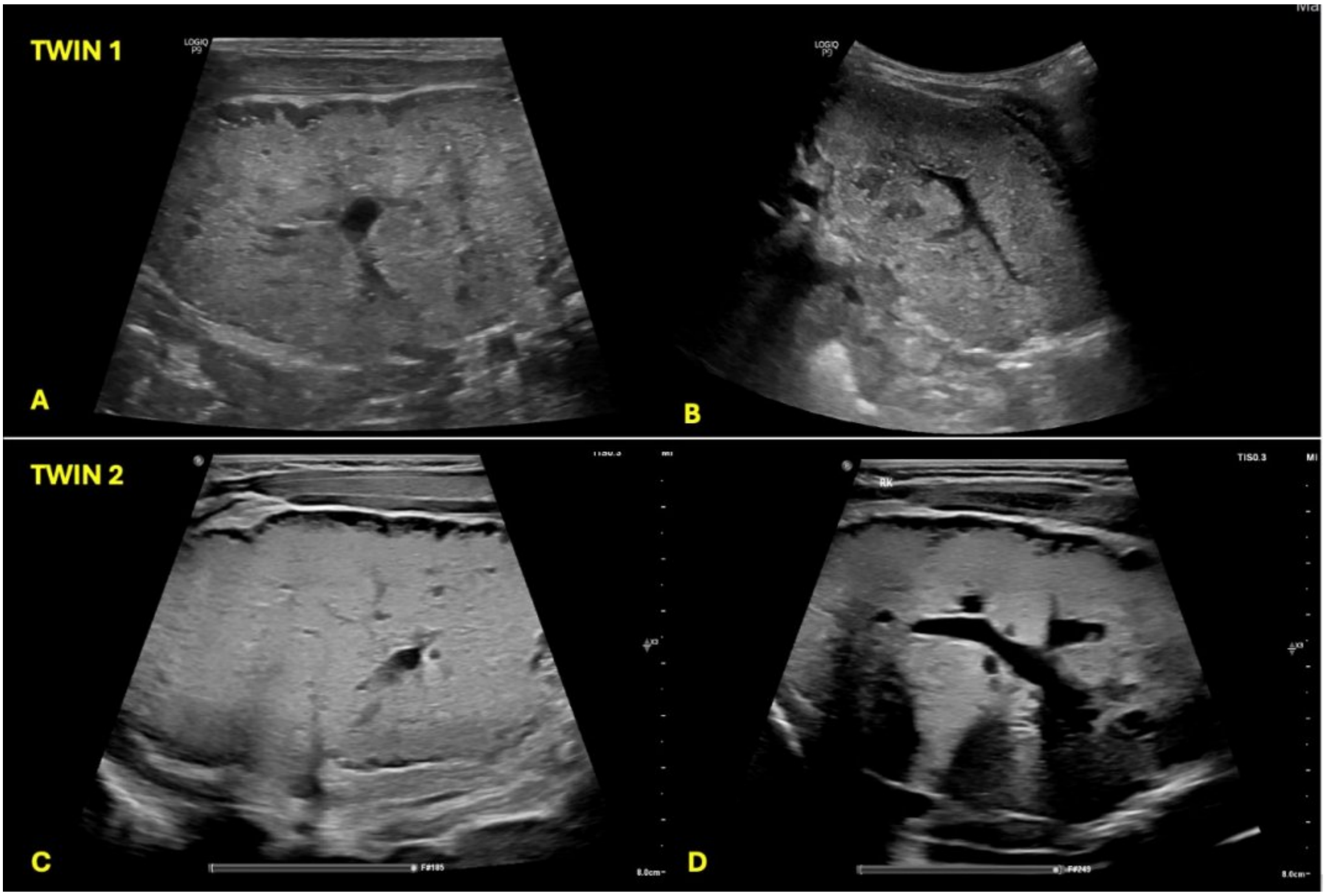

T2 contrast study of the upper abdomen (coronal view) shows the bilaterally enlarged and globular kidneys of both twins, with heterogeneous parenchyma that is predominantly T2-hyperintense, an indistinct corticomedullary junction, and multiple small cysts scattered in the parenchyma.

Keywords : Autosomal recessive polycystic kidney disease, Ultrasonography, Twins

[Poster Presentation 2]

GU-Uro-13

MRI-based Interpretable Habitat Radiomics for Assessing Synchronous Metastatic Risk in Renal Cell Carcinoma: A Multicenter Study

Xu Bai[1], Haiyi Wang[1*]

[1]Radiology, Chinese PLA General Hospital, China

Renal cell carcinoma (RCC) remains a lethal malignancy, with 30% of patients presenting metastases at diagnosis. Current imaging often fails to detect micrometastases, limiting preoperative assessment. While radiomics helps characterize tumor heterogeneity, its performance is hindered by pathological subtype diversity. To overcome this, we propose a habitat-based radiomics approach using MRI. By segmenting tumors into distinct subregions based on the clear cell likelihood score (ccLS)—using corticomedullary-phase (CP) and T2-weighted images (T2WI)—this interpretable model aims to improve non-invasive identification of synchronous metastatic RCC and support personalized treatment planning.

This study retrospectively collected 241 patients with RCC who underwent nephrectomy and lymphadenectomy at four centers between 2010 and 2023. MRI data from the first center were divided into a training set (n = 150) and an internal test set (n=38); data from the other centers (n = 53) were used for external testing. Based on CP and T2WI signal intensity, primary lesions were segmented into 15 habitat subregions. Radiomic features were extracted from the whole-tumor and habitat subregions, respectively. Machine learning algorithms were employed to construct models. Clinical indicators were then integrated to establish a combined model, and performance comparisons and subgroup analyses were conducted based on both the internal and external test sets.

Among the 241 patients (mean age 53 ± 13 years; 169 males), 36.1% exhibited distant or regional lymph node (RLN) metastases. The habitat model achieved a higher area under the curve (AUC) compared with the whole-tumor model in the external test set (0.81 vs. 0.62, P = 0.015). By incorporating RLN size, the combined model outperformed the habitat model in the internal test set (AUC, 0.88 vs. 0.82, P = 0.020) and the clinical model integrating RLN size and hematuria in the external test set (AUC, 0.89 vs. 0.73, P = 0.012). Subgroup analyses indicated that the combined model can independently identify distant and RLN metastases, unaffected by pathological subtypes.

The MRI-based interpretable habitat radiomics model outperformed the whole-tumor radiomics model in identifying metastatic RCC. By combining RLN short diameter, the predictive performance is significantly improved, enabling effective identification of both distant and RLN metastases, unaffected by pathological subtypes.

Habitat radiomics analysis and model construction workflow. The workflow of habitat radiomics can be divided into the following six steps: Step 1, MRI image segmentation following preprocessing; Step 2, registration of T2WI and CP images using EP images; Step 3, generation of habitat subregions based on T2WI and CP images; Step 4, extraction and selection of radiomic features from different habitat subregions; Step 5, model construction using four machine learning algorithms (ET, SVM, RF, GBDT); Step 6, predictive performance evaluation across different datasets and subgroups using ROC curves. CP, corticomedullary phase; EP, excretory phase; ET, extremely randomized trees; SVM, support vector machines; RF, random forests; GBDT, gradient boosting decision trees; ROC, receiver operating characteristic.

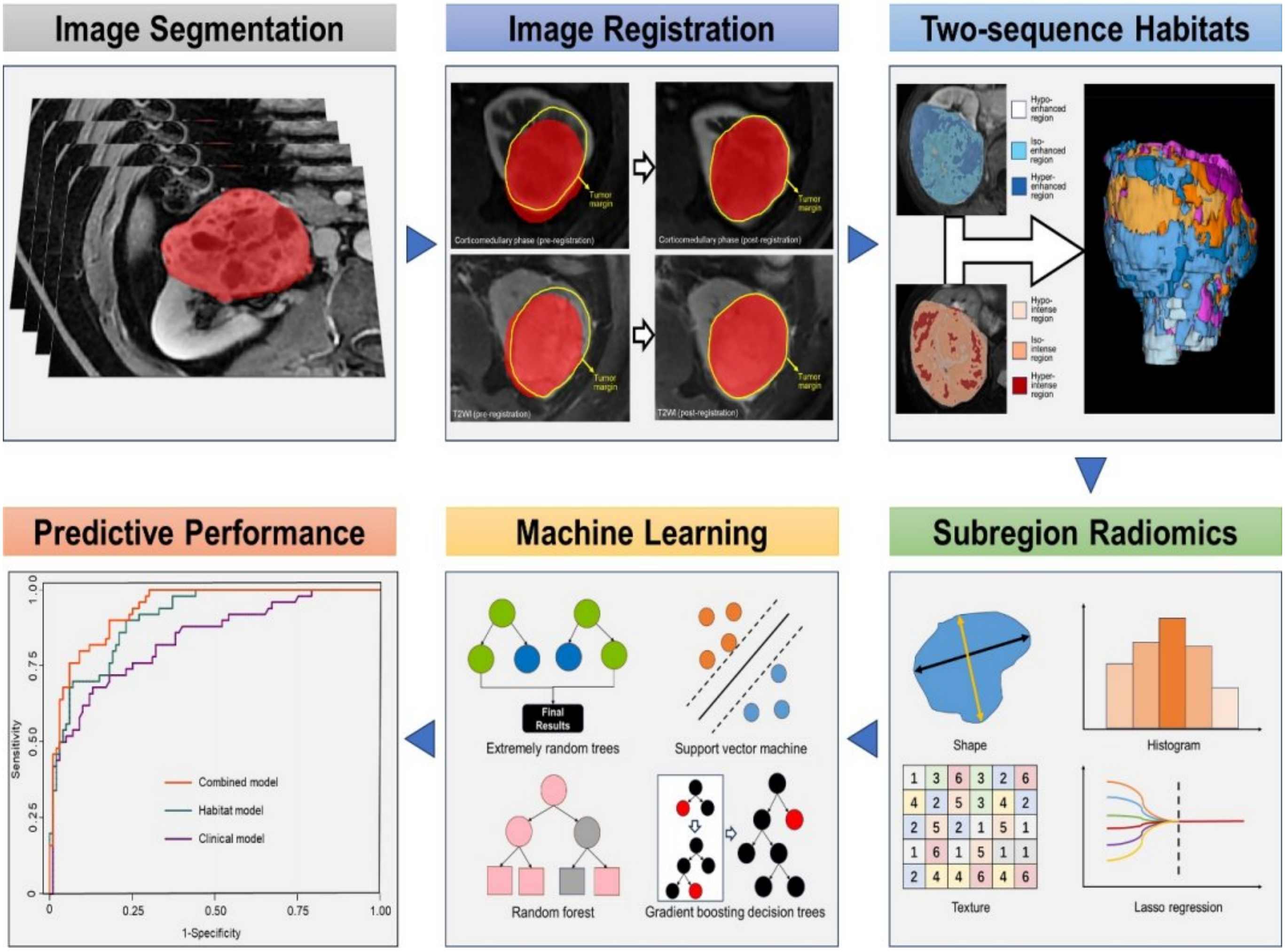

Performance comparison, subgroup analysis, and individual predicted probability distribution. (a-c) AUC comparisons of the habitat combined model, habitat radiomics model, and clinical model across the training set, internal test set, and external test set, respectively. The habitat combined model exhibited higher AUCs than both the clinical model and the habitat radiomics model. **(d)** ROC curves for identifying RLN metastasis and for identifying distant metastasis in patients without RLN metastasis, utilizing the habitat combined model. **(e)** ROC curves for identifying metastatic RCC using the habitat combined model, presented separately for the ccRCC and non-ccRCC groups. **(f)** The individual predicted probability distribution of the habitat combined model in the two test sets, indicating that a cut-off value of 0.240 effectively differentiates between metastatic RCC and non-metastatic RCC. AUC, area under the receiver operating characteristic curve; ROC, receiver operating characteristic; RLN, regional lymph node; ccRCC, clear cell renal cell carcinoma.

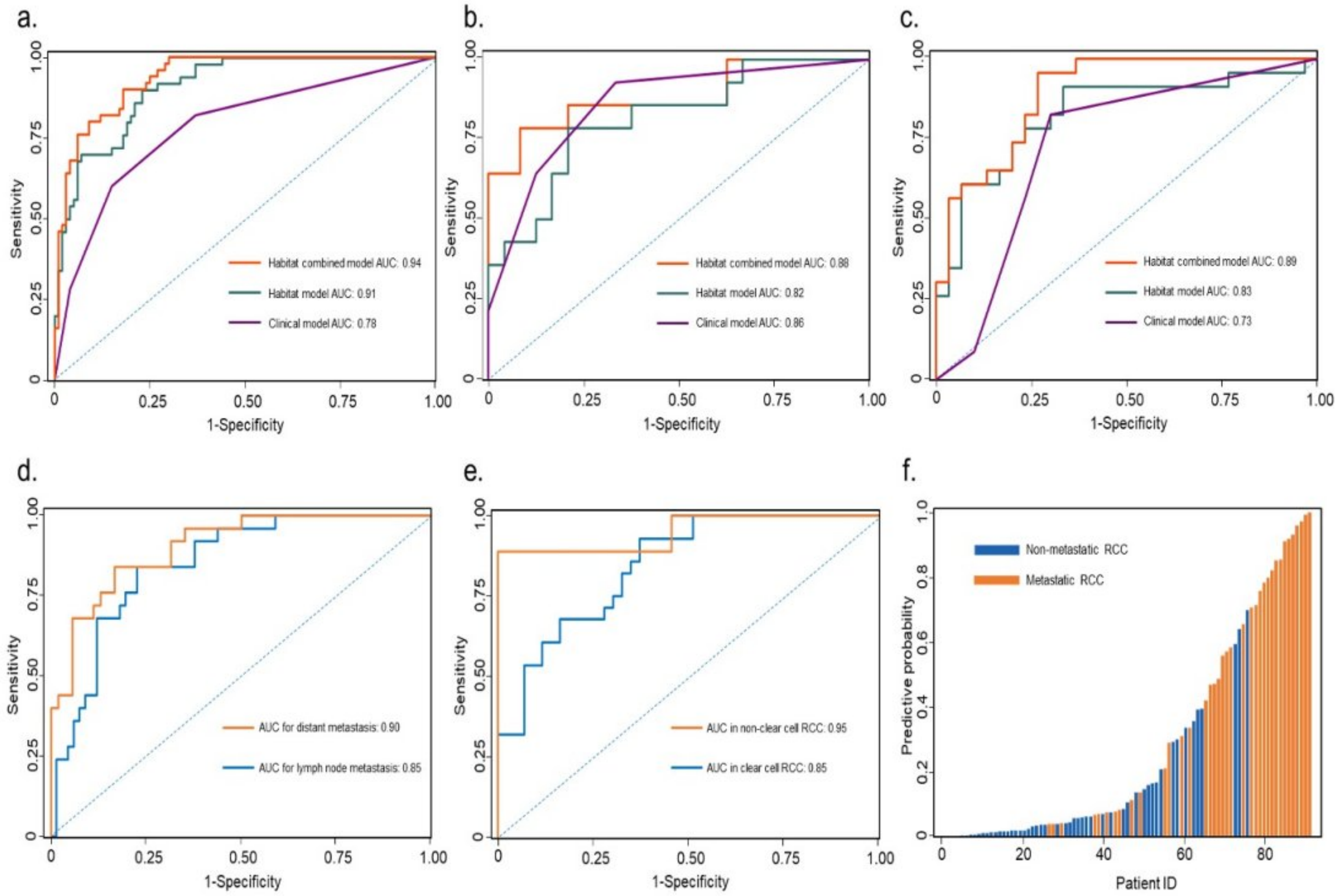

Keywords : Renal cell carcinoma, Magnetic resonance imaging, Habitat

[Poster Presentation 2]

GU-Uro-14

A 11-year Cohort Study Assessing the Management and Outcomes of Renal Injury Focusing on Renal Artery Embolisation at a Level 1 Trauma Centre

Kaiwen Cabbabe[1*], Saman Salaran[1], Samyak Shah[1], Kim Quach[1], Warren Clements[1], Matthew Lukies[1]

[1]Interventional Radiology, Alfred Health, Australia

Renal trauma represents up to 5% of presentations to major trauma centres and encompasses injuries ranging from minor contusions to renovascular disruption. For CTs in which active extravasation or perinephric hematomas are identified, renal artery embolisation has a clinical success rate of up to 93% as reported in the literature. Although management strategies have primarily shifted towards conservative measures, there is a paucity of contemporary data outlining injury patterns, presentations, active management strategies and outcomes. This study provides an 11-year overview of renal injury at our major trauma centre. We aim to provide contemporary data on evidence-based renal trauma management with a specific emphasis on renal artery embolisation.

We performed a retrospective review of all patients with CT-confirmed traumatic renal injury recorded at a level 1 trauma centre between 2013 and 2024. Demographics, mechanism of injury, injury laterality, and American Association for the Surgery of Trauma (AAST) grades were collected. Clinical parameters assessed were hemodynamic status and shock index. Management modalities (conservative, embolisation or nephrectomy), 30-day mortality, and renal function based on eGFR were assessed. Descriptive statistics and comparisons between groups were performed to assess relationships between injury severity, clinical presentation, management and renal outcomes.

A total of 589 renal trauma cases were identified (median age 38 years, 82% male). Most injuries resulted from blunt trauma mechanisms (84%). Overall, 92% were managed conservatively, 5.3% underwent renal artery embolisation, and 2.7% nephrectomy, stenting or laparoscopic repair. Injured renal units were stratified by right (51.3%), left (50.8%) and both (1.8%). AAST injury severity distribution was 40.2% Grade I and II, 31.6% Grade III, and 28% Grade IV and V. High-grade injuries (AAST IV-V) were predominantly managed conservatively (83%). Active contrast extravasation was identified on CT in 77 patients (13.1%). Embolisation was performed in 41 patients (6.7%), of which 31 (5.3%) underwent embolisation as primary management and 10 (1.7%) as secondary management. Secondary embolisation was required for active bleeding that did not cease with conservative management or for the management of ongoing hemodynamic instability. In the embolisation cohort, 30-day mortality was 7.3%, and eGFR remained stable (>90) in 31 patients (75.6%) at follow-up across all injury grades, indicating preserved renal function regardless of injury severity. The shock index was ≥1 within the first 48 hours of presentation in 40 embolised patients (97.5%), and 33 (80.5%) had a high-grade injury (AAST IV-V).

Renal trauma at our centre was predominantly caused by blunt injury with most cases safely managed conservatively. Embolisation was reserved for patients with active bleeding or instability and achieved excellent renal preservation with minimal mortality. A shock index ≥1 at presentation strongly predicted the need for embolisation, identifying a high-risk cohort that benefits from early involvement of interventional radiology. These findings support the safety of contemporary conservative and endovascular strategies to guide renal trauma management.

Keywords : Renal trauma, Renal artery embolization, Management outcomes

[Poster Presentation 2]

GU-Uro-15

Coexistence of Chromophobe Renal Cell Carcinoma and Perirenal Lipomatous Angiomyolipoma: A Case Report

Jin Yunfeng[1*], Cui Mengqiu[2], Ren Shoujun[1], Li Yuan[1], Yu Pingnian[1], Wang Haiyi[2]

[1]CT and MRI, Tonghua Central Hospital, China
[2]Radiology, The Seventh Medical Center of Chinese PLA General Hospital, China

Chromophobe renal cell carcinoma (CRCC) is a rare subtype of renal carcinoma typically characterized by homogeneous imaging features, while renal angiomyolipoma (AML) is a common benign tumor. The coexistence of both tumors in a single patient is itself uncommon. The diagnostic challenge is further compounded when the AML presents atypically—located within the perirenal fat capsule, dominated by smooth muscle components, and lacking characteristic fat signals—and when the CRCC exhibits non-classical imaging findings, such as T2 hyperintensity, hemorrhage, and cystic changes, mimicking clear cell renal carcinoma. This report presents such a unique case to analyze these atypical imaging features and the reasons for misdiagnosis. It aims to emphasize the importance of broadening the differential diagnostic approach when evaluating complex renal masses and to reaffirm the central role of histopathology as the diagnostic gold standard.

The clinical data of a patient with pathologically confirmed dual renal tumors were retrospectively analyzed. The patient was a 50-year-old female who was admitted to the hospital due to an "incidentally discovered right renal mass for 1 month." The patient was asymptomatic. After admission, laboratory tests were completed, and abdominal ultrasonography, contrast-enhanced computed tomography (CT), and contrast-enhanced magnetic resonance imaging (MRI) of the kidneys were performed to evaluate the lesions. Imaging revealed two distinct masses with different characteristics, one within the right kidney and another in the perirenal region. Based on the imaging evaluation, to achieve definitive diagnosis and treatment, the patient underwent retroperitoneal laparoscopic radical nephrectomy under general anesthesia, with simultaneous excision of the mass located within the perirenal fat capsule superior to the right kidney. The resected specimens were sent for routine pathological examination, and the final diagnosis was confirmed through histomorphological observation. This report aims to describe the imaging findings, diagnostic and therapeutic course, and pathological results of this rare case.

Firstly, the imaging features of chromophobe renal cell carcinoma (CRCC) demonstrate heterogeneity. As illustrated in this case, atypical manifestations such as predominantly hyperintense signal on T2-weighted imaging, along with hemorrhage, cystic changes, and moderate heterogeneous enhancement, can easily be mistaken for the more common clear cell renal cell carcinoma (CRCC), leading to preoperative misdiagnosis. Secondly, an angiomyolipoma (AML) occurring within the perirenal fat capsule and composed predominantly of smooth muscle is also an uncommon variant, which further complicates the diagnosis. The coexistence of both tumors in a single patient is extremely rare in clinical practice.

The central message of this case is that when imaging reveals atypical or multifocal renal masses, clinical diagnostic reasoning must maintain openness and vigilance. The possibility of rare tumor types (such as chromophobe renal cell carcinoma) and the coexistence of tumors with different biological behaviors (benign and malignant) should be included in the differential diagnosis.

Figure 1. Imaging findings in a 50-year-old female with pathologically proven chromophobe renal cell carcinoma in the right kidney. A. Axial T2-weighted image shows a heterogeneous, hyperintense mass in the mid portion of the right kidney. B, C. Axial in-phase (B) and opposed-phase (C) images demonstrate intralesional hemorrhage. No definite signal loss is observed on the opposed-phase image. D-G. Axial pre-contrast (D) and contrast-enhanced (E-G) images. The pre-contrast scan reveals a mass with mixed high and low signal intensity. The lesion exhibits moderate heterogeneous enhancement during the corticomedullary phase (E), with persistent enhancement in the nephrographic (F) and delayed (G) phases. A small non-enhancing area is noted within the lesion.

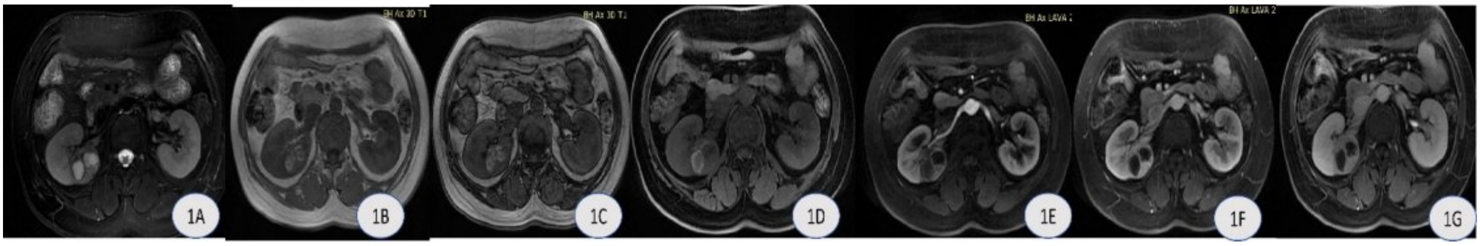

Figure 2. Imaging findings in the same 50-year-old female with a pathologically proven perirenal lipomatous angiomyolipoma on the right side. A. Axial T2-weighted image demonstrates an irregular mass with iso- to hypointense signal within the perirenal fat superior to the right kidney. B, C. Axial in-phase (B) and opposed-phase (C) images. No definite signal loss is observed within the lesion on the opposed-phase image. D-G. Axial pre-contrast (D) and contrast-enhanced (E-G) images. The lesion shows slightly hypointense signal on the pre-contrast scan. It exhibits marked heterogeneous enhancement during the corticomedullary phase (E), persistent enhancement in the nephrographic phase (F), and becomes homogeneously and markedly hyperintense in the delayed phase (G).

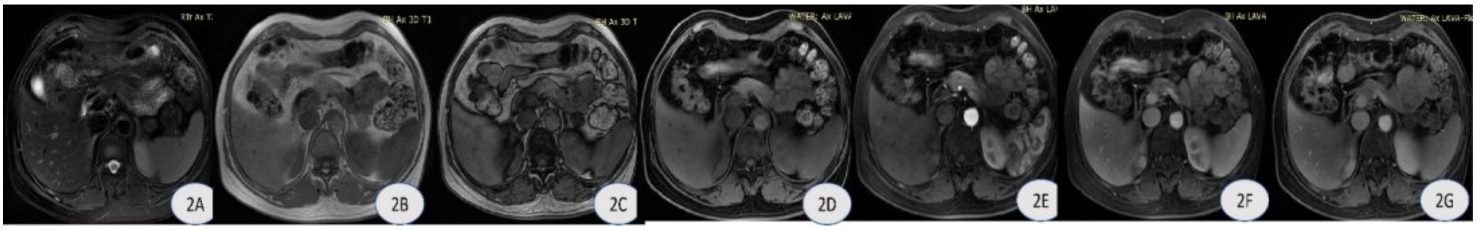

Keywords : Chromophobe, Angiomyolipoma, Magnetic Resonance Imaging

[Poster Presentation 2]

GU-Uro-16

Metanephric Adenoma - A Rare Case Report and Literature Review

Linh Tran Thi[1*]

[1]Radiology, Hanoi Medical University, Vietnam

Metanephric adenoma (MA) is an extremely rare benign epithelial renal tumor, accounting for only 0.2–0.7% of all renal epithelial neoplasms. Because MA lacks specific clinical or radiologic features and may closely mimic malignant renal tumors such as Wilms tumor or papillary renal cell carcinoma, preoperative differentiation remains challenging. Definitive diagnosis relies on histopathology and immunohistochemistry. In this setting, percutaneous renal biopsy plays a crucial role in establishing an accurate diagnosis and ruling out malignancy, thereby enabling kidney-preserving management.

A 46-year-old woman underwent routine health screening, during which an incidental left renal mass was detected. Contrast-enhanced abdominal computed tomography (CT) was performed to characterize the lesion. Ultrasound-guided percutaneous renal biopsy was conducted to obtain diagnostic tissue. Clinical and imaging follow-up was implemented after diagnosis.

Contrast-enhanced CT revealed a well-defined left renal mass demonstrating homogeneous enhancement, progressively increasing from the corticomedullary phase to the nephrogenic phase, though consistently lower than the surrounding renal parenchyma. Percutaneous biopsy under ultrasound guidance was successfully performed with no complications. Histopathological evaluation confirmed metanephric adenoma. Based on the benign diagnosis, the patient underwent conservative management and was placed on periodic surveillance.

This case illustrates the diagnostic difficulty of metanephric adenoma due to its nonspecific imaging appearance and similarity to malignant renal tumors. Ultrasound-guided percutaneous biopsy proved essential in establishing the diagnosis and preventing unnecessary surgical intervention. Early, accurate identification of MA facilitates optimal kidney-preserving management and appropriate follow-up planning.

A: Abdominal ultrasound shows a mixed echogenic cortical nodule in the upper one-third of the left kidney (arrow), with smooth margins, well-defined borders, and no evidence of increased vascularity.

B: Contrast-enhanced abdominal CT: (a) on the unenhanced phase, the lesion is located in the renal cortex and is isoattenuating to the surrounding renal parenchyma; (b, c) after contrast administration, during the corticomedullary and nephrogenic phases, the lesion demonstrates gradual enhancement but remains less enhanced than the normal renal parenchyma.

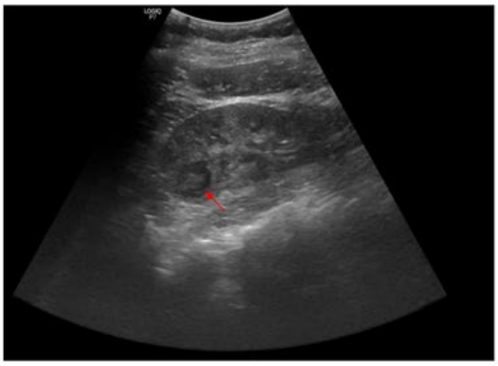

A

B

Histopathological findings: the tumor cells have round, uniformly small nuclei, arranged to form tubular structures with round lumina; some tubules are elongated or show glomeruloid-like structures. Mitotic figures are extremely rare.

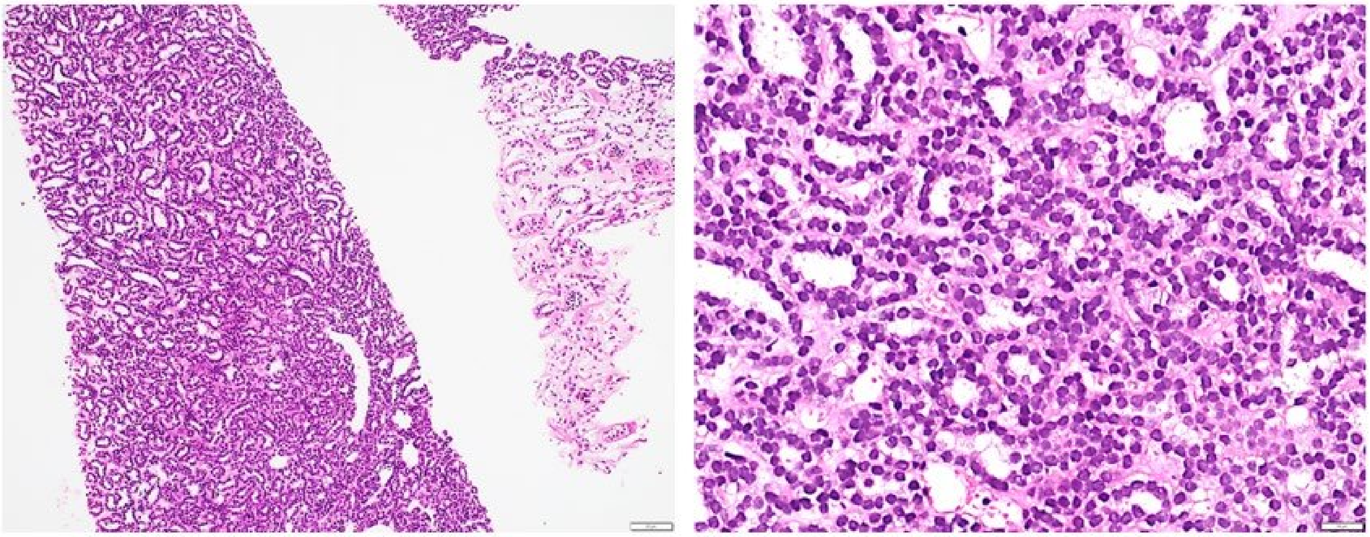

Keywords : Metanephric adenoma, Percutaneous biopsy, Computed tomography

[Poster Presentation 2]

GU-Uro-17

Congenital Megacalycosis with Megaureter: A Rare Masquerader of Obstructive Uropathy

Justin Seah[1*], Shawn Kok[2], Min On Tan[1]

[1]Radiology, Singapore Health Services, Singapore
[2]Radiology, Parkway Radiology, Singapore

Congenital megacalycosis with megaureter is a rare urological abnormality characterised by dilatation of renal calyces and ureter in the absence of true obstruction. This condition is a congenital developmental anomaly of the urinary tract that may remain asymptomatic for years and is often discovered incidentally. While it is a benign condition by itself, it is both a mimicker as well as a potential precursor of obstructive uropathy, making it difficult to diagnose accurately on imaging. We present a series of cases to highlight key imaging findings that aid in accurate diagnosis and appropriate patient management.

There are four cases of megacalycosis and/ or megaureter, all of which detected incidentally during imaging for an unrelated presenting symptom.

Three of the cases are benign findings with no sequelae (at present). In these cases, renal calyceal and/ or ureter dilatation is present without any evidence of mechanical obstruction, luminal narrowing or external compression of the urinary tract. Renal parenchyma is preserved. The fourth case is a patient who subsequently developed obstructive uropathy as a complication of his congenital condition. This was detected during a follow-up surveillance renal function study (mercaptoacetyltriglycine, or MAG3 for short) and required timely intervention to relieve obstruction and preserve renal function.

In conclusion, megacalycosis with megaureter is a rare but important entity that should be considered in cases of renal calyceal and ureteric dilatation without any mechanical obstruction. Recognition of this benign condition can prevent misdiagnoses and unnecessary intervention. It also allows for appropriate surveillance and early detection of secondary complications such as calculi, infection, or progressive ureteric dysmotility.

Keywords : Megacalycosis

[Poster Presentation 2]

GU-Uro-18

A Novel Decision Tree Model Integrating Morphology Variations, ADC ratio and VI-RADS for Detecting Muscle Invasion in Bladder Cancer

Yuanhao Ma[1], Haili Liu[1], Yijian Chen[1], Honghao Xu[1], Xu Bai[1], Jian Zhao[1], Xiaohui Ding[2], Haiyi Wang[1*]

[1]Radiology, First Medical center of Chinese PLA General Hospital, China
[2]Pathology, First Medical center of Chinese PLA General Hospital, China

Background Bladder cancer (BCa) is a common malignant tumor of the genitourinary system in middle-aged and elderly males. The presence or absence of muscle invasion in BCa significantly influences clinical management and patient prognosis.

Purpose To investigate the impact of heterogeneous tumor morphologies in BCa on the VI-RADS-based assessment of muscle invasion using multiparametric MRI (mpMRI) and to propose optimization strategies for enhancing diagnostic performance.

Materials and Methods This retrospective study consecutively enrolled patients with BCa who underwent preoperative bladder mpMRI between January 2019 and June 2024, followed by radical cystectomy, partial cystectomy, or transurethral resection of bladder tumor (TURBT). All lesions were classified into four morphological subtypes based on imaging characteristics: exophytic, endophytic, flat, and mixed types. The diagnostic performance of VI-RADS scores for muscle invasion assessment was evaluated within each morphological subgroup, including interobserver agreement analysis using Gwet's AC test and receiver operating characteristic (ROC) curve comparisons via the DeLong test. Multivariable logistic regression was employed to identify independent predictors of muscle invasion within specific morphological subtypes, guided by VI-RADS performance variations. Subsequently, a decision tree model integrating tumor morphology, quantitative mpMRI parameters, and VI-RADS scores was developed to optimize muscle invasion classification accuracy.

Results Among the 169 BCa patients ultimately enrolled (mean age 64 ± 12 years, 139 males), the muscle invasion rates for exophytic, endophytic, flat, and mixed tumor morphologies were 24.6% (30/122), 95.5% (21/22), 42.9% (9/21), and 50.0% (2/4), respectively. Based on consensus VI-RADS scores from three readers, the AUCs for exophytic and flat tumors were 0.771 and 0.769 (AUC was not calculated for endophytic tumors due to only one non-invasive case and for mixed tumors due to limited cases [n=4]). Interobserver agreement (Gwet's AC) was excellent for endophytic tumors (0.87, 95% CI: 0.76–0.98), good for exophytic tumors (0.70, 95% CI: 0.62–0.78), and moderate for flat tumors (0.42, 95% CI: 0.24–0.60). Given the exceptionally high muscle invasion rate in endophytic tumors and the lower overall AUC for non-endophytic morphologies compared to all subtypes (0.782 vs. 0.833, P<0.001), optimization efforts focused on non-endophytic BCa. Multivariable logistic regression identified ADC ratio (odds ratio [OR] = 0.03, P<0.001) and VI-RADS score (OR = 2.71, P=0.008) as independent predictors of muscle invasion in non-endophytic tumors. A morphology-integrated decision tree (MDT) was developed. This decision tree demonstrated significantly higher AUCs than standalone VI-RADS scores in non-endophytic tumors (0.871 vs. 0.782, P<0.001) and across all morphologies (0.908 vs. 0.833, P<0.001).

Conclusions Endophytic BCa exhibits a high muscularis propria invasion rate, while VI-RADS scoring demonstrates lower diagnostic performance for non-endophytic lesions compared to its performance across all lesion types. The morphology decision tree integrating tumor morphology, ADC ratio, and VI-RADS scoring demonstrates significantly higher diagnostic performance than VI-RADS alone for assessing muscularis propria invasion in BCa.

Figure 1. Morphology-specific decision tree for optimizing VI-RADS scoring based on anatomical regions and ADC ratios**.** The specific rules are as follows: (1) For non-endophytic bladder lesions: i) When VI-RADS score is 1 or 5, the final score remains unchanged; ii) When VI-RADS score is 2–4: a) VI-RADS 2 with ADC ratio >1: maintain score 2; b) VI-RADS 2 with ADC ratio ≤1: upgrade to score 3; c) VI-RADS 3 with ADC ratio >1: downgrade to score 2; d) VI-RADS 3 with ADC ratio ≤1: upgrade to score 4; e) VI-RADS 4 with ADC ratio >1: downgrade to score 3; f) VI-RADS 4 with ADC ratio ≤1: maintain score 4. (2) For endophytic BCa, given its exceptionally high muscularis propria invasion rate, it is directly classified as score 5.

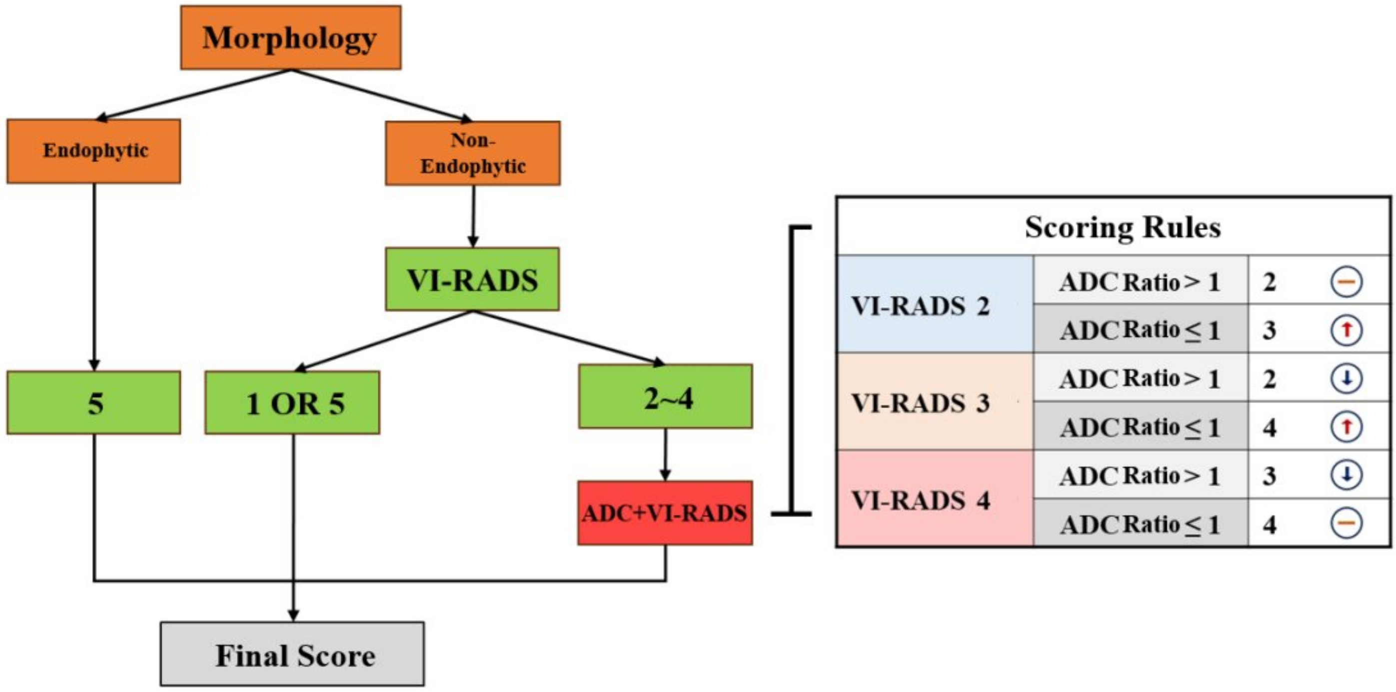

Figure 2. A. Based on the comparison of ROC curves using non-endophytic BCa, the AUC of morphological decision trees is significantly higher than that of VI-RADS; B. Based on the comparison of ROC curves for all lesions, the AUC of the morphological decision tree is significantly higher than that of VI-RADS.

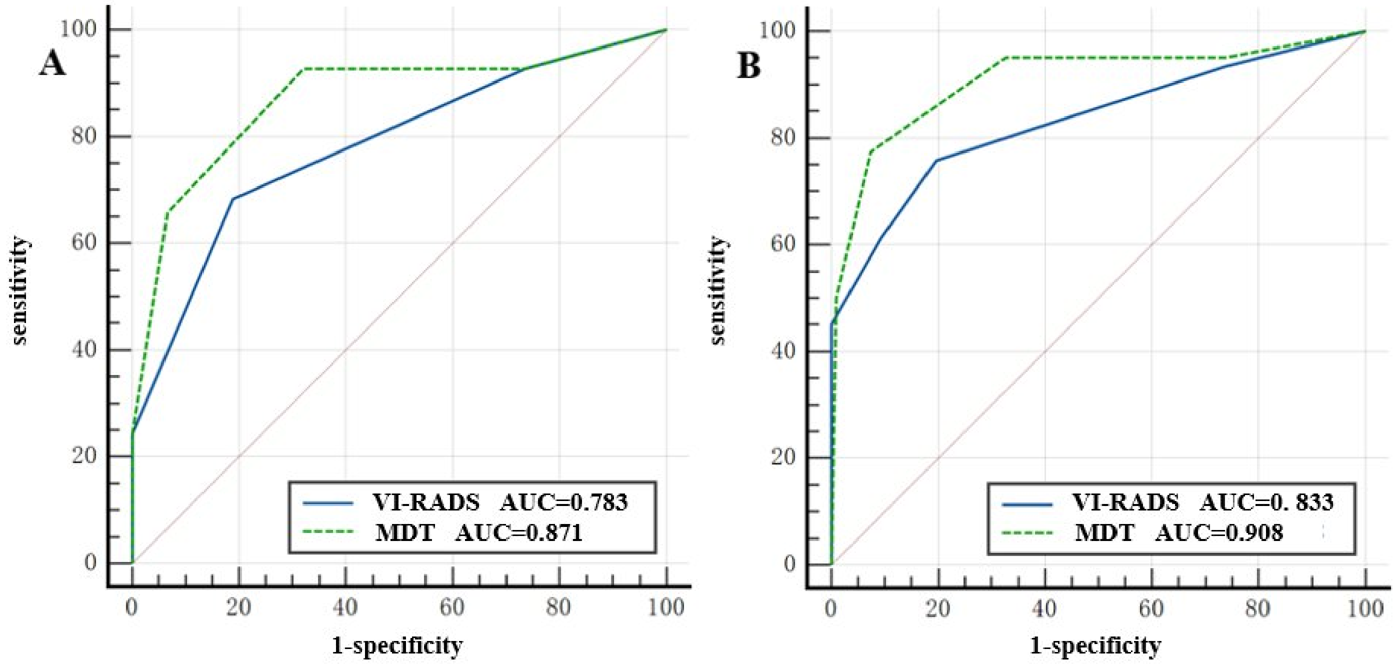

Keywords : Bladder cancer, VI-RADS, ADC

[Poster Presentation 2]

GU-OBGY-01

Rapidly Enlarging Uterine Mass in a Postmenopausal Breast Cancer Survivor : Differentiating Leiomyosarcoma from Degenerated Leiomyoma

Muhammad Arief Saputra[1*], Trifonia Pingkan Siregar[1], Hanna Dwi Wiranti[1], Adinda Amalia[2], Adila Salsabila[1], Rais Izzan Basyari[1]

[1]Radiology, Department of Radiology Faculty of Medicine Universitas Indonesia, Indonesia
[2]Internal Medicine, Department of Internal Medicine Faculty of Medicine Universitas Indonesia, Indonesia

Uterine leiomyosarcoma is a rare but aggressive smooth muscle malignancy that often mimics benign uterine leiomyomas, particularly those undergoing cystic or degenerative changes. Distinguishing these entities preoperatively remains challenging, especially in postmenopausal women where rapid enlargement of a pelvic mass raises significant concern for malignancy. The diagnostic complexity further increases in patients with a history of primary cancer, such as breast carcinoma, in whom pelvic masses must be evaluated for the possibility of metastatic disease or a new primary tumor. This case illustrates the importance of multimodal imaging and clinical correlation in evaluating a rapidly enlarging uterine mass in a breast cancer survivor.

A 58-year-old postmenopausal woman presented with progressive abdominal enlargement over three months without abdominal pain or vaginal bleeding. Her medical history included right breast invasive carcinoma of no special type (NST), grade III with lymphovascular invasion, treated with mastectomy and adjuvant chemotherapy from 2024 to 2025. Physical examination revealed a firm pelvic-abdominal mass extending to one finger below the umbilicus. Laboratory findings showed hemoglobin 10.8 g/dL, leukocytes 5,710/μL, platelets 241,000/μL, HbA1c 7.2%, electrolytes within normal limits, and normal PT/APTT. Chest radiography demonstrated cardiomegaly without pulmonary abnormalities.

Ultrasound showed an 8.8 × 7.3 cm mixed solid–cystic uterine mass. A contrast-enhanced CT scan revealed a heterogeneous 12 × 12 cm pelvic mass. Reassessment of a prior whole-abdomen CT scan demonstrated a lobulated, partially ill-defined, markedly heterogeneous uterine mass with central necrosis measuring 11.4 × 12.7 × 11.4 cm. The lesion displaced the ovaries and urinary bladder without radiologic evidence of invasion. No abdominal–pelvic lymphadenopathy was seen. Multiple hyperdense calculi in the CHD and CBD with associated bilateral intrahepatic biliary dilatation were also noted.

The patient underwent total hysterectomy with bilateral salpingo-oophorectomy. Intraoperative findings revealed a large intramural uterine mass approximately 15 cm in size with smooth external contours. Both ovaries and fallopian tubes appeared normal, and no evidence of peritoneal seeding or extrauterine involvement was observed. Surgical specimens were submitted for histopathological evaluation to differentiate leiomyosarcoma from degenerative leiomyoma.

A rapidly enlarging uterine mass in a postmenopausal woman should raise strong suspicion for uterine leiomyosarcoma, particularly when imaging demonstrates marked heterogeneity and central necrosis. Detailed multimodal imaging and clinical correlation are essential to guide differential diagnosis and surgical planning. Complete surgical excision remains the definitive approach for diagnosis and management, with histopathological examination serving as the gold standard for distinguishing malignant from benign uterine tumors.

Figure 1. Contrast-Enhanced CT Scan of the Pelvis (Sagittal, Coronal, and Axial Views).

Sagittal, coronal, and axial contrast-enhanced CT images demonstrate a large heterogeneous uterine mass (arrows) with central necrosis and lobulated contours, displacing the urinary bladder inferiorly and the ovaries laterally without clear evidence of direct invasion. No pelvic or para-aortic lymphadenopathy is observed.

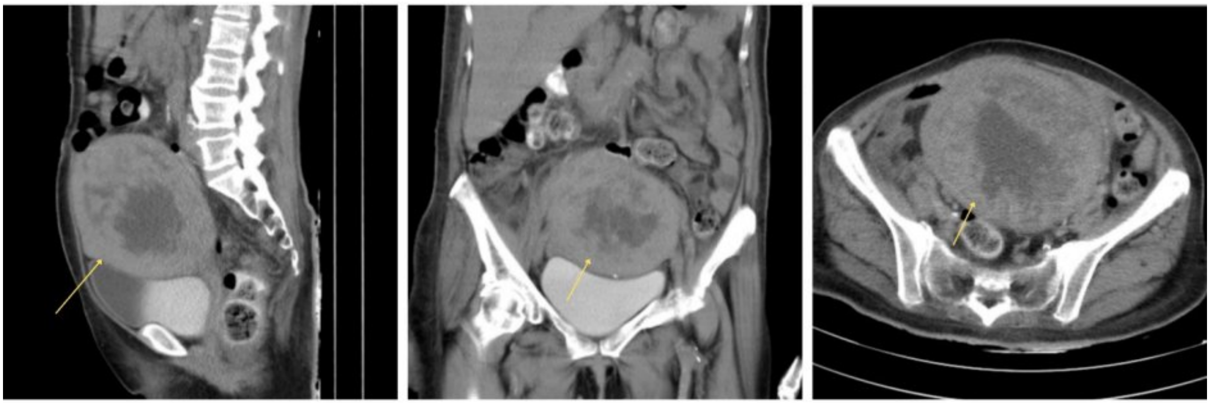

Figure 2. Histopathological appearance of uterine leiomyosarcoma (H&E stain).

High-power view demonstrates densely packed atypical spindle cells arranged in intersecting fascicles, with marked nuclear pleomorphism and hyperchromasia, consistent with leiomyosarcoma.

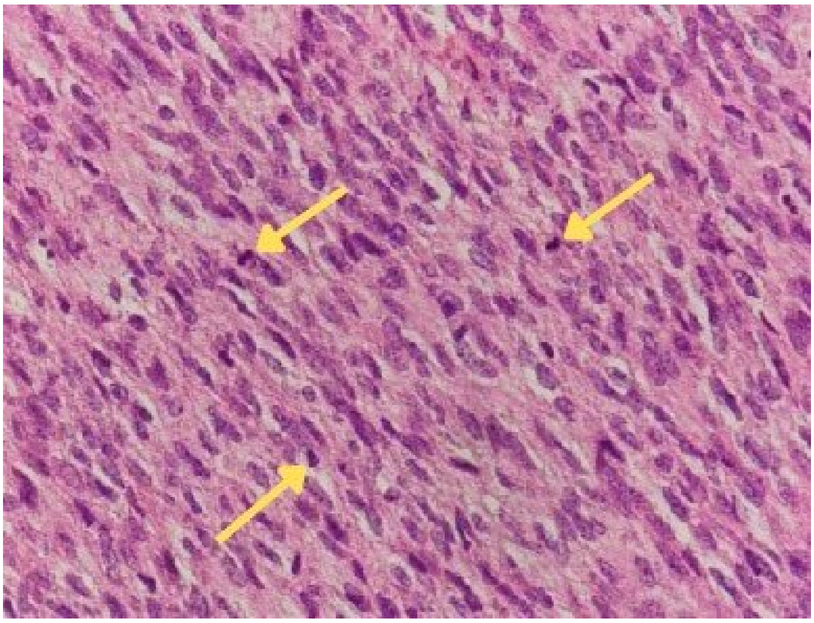

Keywords : Uterine leiomyosarcoma, Pelvic mass, Contrast-enhanced CT

[Poster Presentation 2]

GU-OBGY-02

Massive Ovarian Edema on MRI with Clinicopathologic Correlation

Sung Bin Park[1*], Mi Yeon Park[1], Kye Jin Park[1], Mi-Hyun Kim[1], Jeong Kon Kim[1]

[1]Radiology, Asan Medical Center, Korea

Massive ovarian edema is a rare condition in which the ovary is seen to have a solid tumor due to various causes. Primary cause is torsion of the ovary or twisting of the ovarian pedicle that brings about venous blood supply problem and secondary cause is due to original lesion in the ovary such as neoplasm causes lymphatic insufficiency. Due to its tumorous condition, it is mistaken for neoplasm, causing clinical challenges, and excessive management is often performed. But in fact, massive ovarian edema can be conservatively improved in some cases. Thus, providing appropriate management by predicting these clinical courses through imaging findings can be of great help in preserving the fertility of patients. The purpose of this presentation is to describe the various manifestations of massive ovarian edema on MRI.

In this presentation, we demonstrate seven cases on MRI to massive ovarian edema. 7 patients (mean age ± standard deviation [SD], 31.71 ± 4.38 years, range 26–39 years). Among them, 4 patients were pregnant.

We classify them into three groups according to the management; first, improved conservatively (n=2) and second, improved only by torsion detorsion surgery (n=1), while third, there were cases that were found to be massive edema or hemorrhagic necrosis (n=2) and metastatic adenocarcinoma (n=2) by resection. The overt ‘twisted vascular pedicle’ is key features to determining the treatment methods either conservative or operative.

We correlate imaging features with clinical and pathologic features. Through the clinicopathological correlation of each case, it is considered that the cause of massive ovarian edema could be identified through image findings and appropriate management could be possible.

Familiarity with the clinical setting and imaging appearances of massive ovarian edema can lead to a more accurate diagnosis and treatment.

Keywords : Massive ovarian edema, Ovarian torsion

[Poster Presentation 2]

GU-OBGY-03

Bumps and Bellyaches: Unmasking Non-Obstetric Mimics of Acute Abdominal Pain in Pregnancy

Ying Jie Toh[1*], Wenwen Ni[1], Elizabeth Chen[1], Thida Win[1]

[1]Diagnostic and Interventional Imaging, KK Women's and Children's Hospital, Singapore

Acute abdominal pain in pregnancy poses a diagnostic dilemma due to physiological and anatomical changes that obscure clinical and imaging assessment. While obstetric causes are often considered first, non-obstetric and non-gynaecologic conditions may present similarly and require distinct management.

This pictorial review aims to illustrate the imaging features and diagnostic challenges of non-obstetric causes of acute abdominal pain in pregnant patients and key differentiating findings.

Cases were selected from our institutional radiology database, comprising pregnant patients who presented with acute abdominal or pelvic pain and had confirmed non-obstetric aetiologies.

Imaging modalities included ultrasound (US) as first-line assessment, in keeping with its safety and accessibility during pregnancy, complemented by magnetic resonance imaging (MRI) where clinically indicated. Cases were chosen for their educational diversity, clinical relevance, and diagnostic diversity, representing both common and unusual pathologies encountered in emergency practice.

Non-obstetric causes of acute abdominal pain in pregnancy encompass a broad spectrum of gastrointestinal, genitourinary, and gynaecologic pathologies. Illustrative examples include acute appendicitis and its mimics such as epiploic appendagitis; neoplastic conditions ranging from primary colonic carcinoma to metastatic Krukenberg tumours; genitourinary lesions such as bleeding renal angiomyolipoma; and gynaecologic mimics like ovarian torsion occurring within the gravid pelvis. Each case highlights the importance of recognizing characteristic imaging findings while maintaining a broad differential amidst this challenging patient population.

Non-obstetric causes of abdominal pain in pregnancy can masquerade as obstetric or gynaecologic emergencies. Familiarity with their imaging appearances and pitfalls ensures timely diagnosis and appropriate management while safeguarding maternal and foetal health. This pictorial review reinforces the radiologist’s pivotal role in navigating these diagnostic challenges.

Keywords : Acute Abdominal Pain, Pregnancy, Non-Obstetric